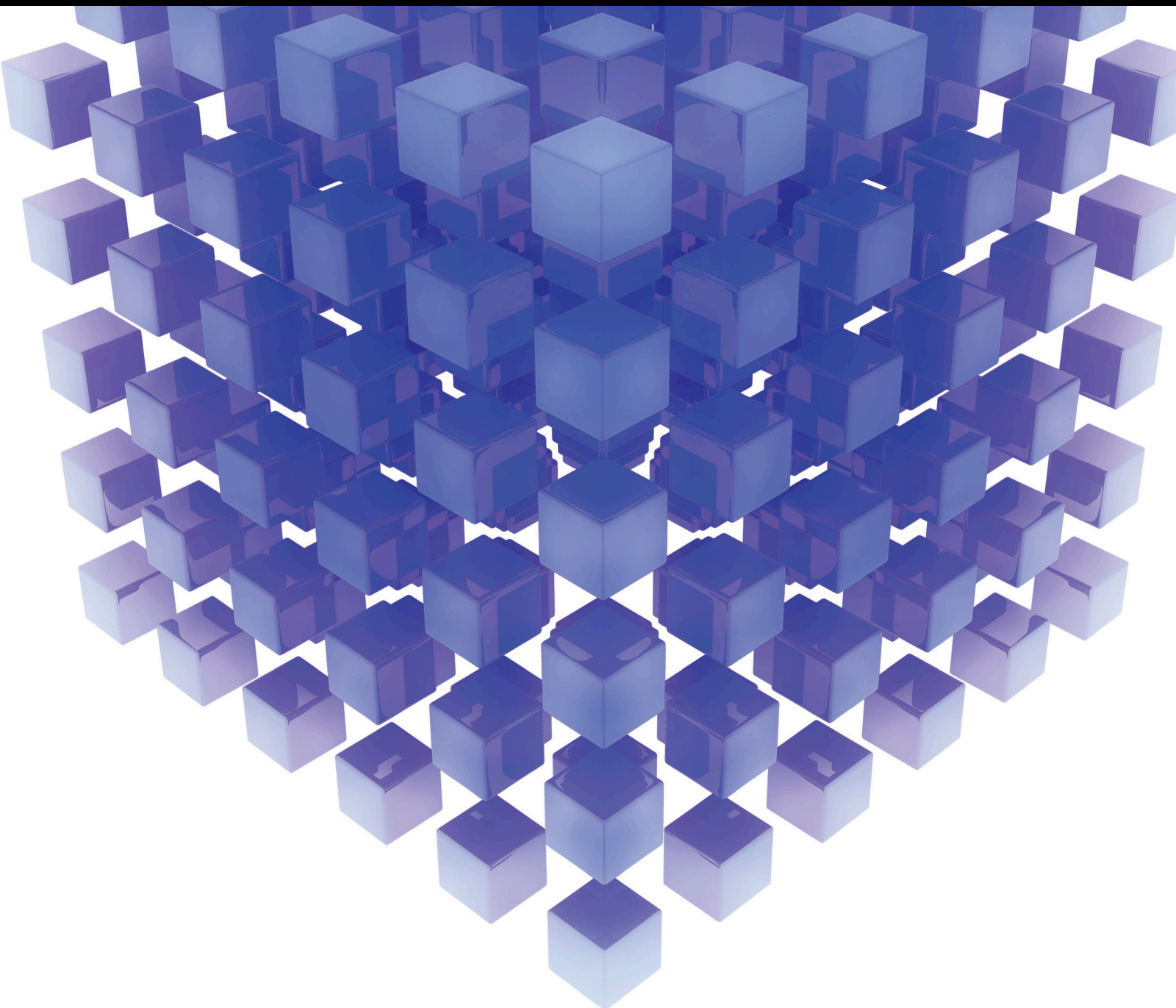# Recent Advances in Multiphase Flows in Engineering

Lead Guest Editor: Muhammad Mubashir Bhatti
Guest Editors: Marin Marin and Ahmad Zeeshan

Recent Advances in Multiphase Flows in Engineering

Recent Advances in Multiphase Flows in Engineering

Lead Guest Editor: Muhammad Mubashir Bhatti
Guest Editors: Marin Marin and Ahmad Zeeshan
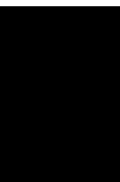
Alberto Borboni, Italy
Marco Bortolini, Italy
Paolo Boscariol, Italy
Daniela Boso, Italy
Guillermo Botella-Juan, Spain
Boulaïd Boulkroune, Belgium
Abdesselem Boulkroune, Algeria
Fabio Bovenga, Italy
Francesco Braghin, Italy
Ricardo Branco, Portugal
Maurizio Brocchini, Italy
Julien Bruchon, France
Matteo Bruggi, Italy
Michele Brun, Italy
Maria Elena Bruni, Italy
Vasilis Burganos, Greece
Maria Angela Butturi, Italy
Raquel Caballero-Águila, Spain
Guillermo Cabrera-Guerrero, Chile
Filippo Cacace, Italy
Pierfrancesco Cacciola, United Kingdom
Salvatore Caddemi, Italy
zuowei cai, China
Roberto Caldelli, Italy
Alberto Campagnolo, Italy
Eric Campos, Mexico
Salvatore Cannella, Italy
Francesco Cannizzaro, Italy
Maosen Cao, China
Javier Cara, Spain
Raffaele Carli, Italy
Ana Carpio, Spain
Rodrigo Carvajal, Chile
Caterina Casavola, Italy
Sara Casciati, Italy
Federica Caselli, Italy
Carmen Castillo, Spain
Inmaculada T. Castro, Spain
Miguel Castro, Portugal
Giuseppe Catalanotti, United Kingdom
Nicola Caterino, Italy
Alberto Cavallo, Italy
Gabriele Cazzulani, Italy
Luis Cea, Spain
Fatih Vehbi Celebi, Turkey
Song Cen, China
Miguel Cerrolaza, Venezuela

M. Chadli, France
Gregory Chagnon, France
Ludovic Chamoin, France
Xiaoheng Chang, China
Kuei-Lun Chang, Taiwan
Ching-Ter Chang, Taiwan
Qing Chang, USA
Kacem Chehdi, France
Peter N. Cheimets, USA
Chih-Chiang Chen, Taiwan
Xiao Chen, China
He Chen, China
Zhiwen Chen, China
Xinkai Chen, Japan
Chien-Ming Chen, China
Shyi-Ming Chen, Taiwan
Kebing Chen, China
Xue-Bo Chen, China
Xizhong Chen, Ireland
Qiang Cheng, USA
Luca Chiapponi, Italy
Ryoichi Chiba, Japan
Francisco Chicano, Spain
Nicholas Chileshe, Australia
Tirivanhu Chinyoka, South Africa
Adrian Chmielewski, Poland
Seongim Choi, USA
Ioannis T. Christou, Greece
Hung-Yuan Chung, Taiwan
Simone Cinquemani, Italy
Roberto G. Citarella, Italy
Joaquim Ciurana, Spain
John D. Clayton, USA
Francesco Clementi, Italy
Piero Colajanni, Italy
Giuseppina Colicchio, Italy
Vassilios Constantoudis, Greece
Francesco Conte, Italy
Enrico Conte, Italy
Alessandro Contento, USA
Mario Cools, Belgium
Gino Cortellessa, Italy
Juan Carlos Cortés, Spain
Carlo Cosentino, Italy
Paolo Crippa, Italy
Erik Cuevas, Mexico
Guozeng Cui, China

Maria C. Cunha, Portugal
Mehmet Cunkas, Turkey
Peter Dabnichki, Australia
Luca D'Acierno, Italy
Zhifeng Dai, China
Weizhong Dai, USA
Purushothaman Damodaran, USA
Bhabani S. Dandapat, India
Giuseppe D'Aniello, Italy
Sergey Dashkovskiy, Germany
Adiel T. de Almeida-Filho, Brazil
Fabio De Angelis, Italy
Samuele De Bartolo, Italy
Abílio De Jesus, Portugal
Pietro De Lellis, Italy
Alessandro De Luca, Italy
Stefano de Miranda, Italy
Filippo de Monte, Italy
José António Fonseca de Oliveira Correia,
Portugal
Jose Renato de Sousa, Brazil
Michael Defoort, France
Alessandro Della Corte, Italy
Laurent Dewasme, Belgium
Sanku Dey, India
Gianpaolo Di Bona, Italy
Angelo Di Egidio, Italy
Roberta Di Pace, Italy
Francesca Di Puccio, Italy
Ramón I. Diego, Spain
Yannis Dimakopoulos, Greece
Rossana Dimitri, Italy
Alexandre B. Dolgui, France
José M. Domínguez, Spain
Georgios Dounias, Greece
Bo Du, China
Z. Du, China
George S. Dulikravich, USA
Emil Dumic, Croatia
Bogdan Dumitrescu, Romania
Saeed Eftekhar Azam, USA
Antonio Elipe, Spain
Anders Eriksson, Sweden
R. Emre Erkmen, Canada
Ricardo Escobar, Mexico
Francisco Periago Esparza, Spain
Gilberto Espinosa-Paredes, Mexico

Leandro F. F. Miguel, Brazil
Andrea L. Facci, Italy
Giovanni Falsone, Italy
Hua Fan, China
Nicholas Fantuzzi, Italy
Muhammad Shahid Farid, Pakistan
Mohammad Fattahi, Iran
Yann Favennec, France
Fiorenzo A. Fazzolari, United Kingdom
Giuseppe Fedele, Italy
Roberto Fedele, Italy
Zhongyang Fei, China
Mohammad Ferdows, Bangladesh
Arturo J. Fernández, Spain
Jesus M. Fernandez Oro, Spain
Massimiliano Ferraioli, Italy
Massimiliano Ferrara, Italy
Francesco Ferrise, Italy
Constantin Fetecau, Romania
Eric Feulvarch, France
Iztok Fister Jr., Slovenia
Thierry Floquet, France
Eric Florentin, France
Gerardo Flores, Mexico
Alessandro Formisano, Italy
FRANCESCO FOTI, Italy
Francesco Franco, Italy
Elisa Francomano, Italy
Juan Frausto-Solis, Mexico
Shujun Fu, China
Juan C. G. Prada, Spain
Matteo Gaeta, Italy
Mauro Gaggero, Italy
Zoran Gajic, USA
Jaime Gallardo-Alvarado, Mexico
Mosè Gallo, Italy
Akemi Gálvez, Spain
Rita Gamberini, Italy
Maria L. Gandarias, Spain
Xingbao Gao, China
Hao Gao, Hong Kong
Shangce Gao, Japan
Zhong-Ke Gao, China
Yan Gao, China
Zhiwei Gao, United Kingdom
Giovanni Garcea, Italy
José García, Chile

Reza Jazar, Australia
Khalide Jbilou, France
Isabel S. Jesus, Portugal
Chao Ji, China
Linni Jian, China
Qing-Chao Jiang, China., China
Bin Jiang, China
Peng-fei Jiao, China
Emilio Jiménez Macías, Spain
Xiaoliang Jin, Canada
Maolin Jin, Republic of Korea
Zhuo Jin, Australia
Dylan F. Jones, United Kingdom
Viacheslav Kalashnikov, Mexico
Mathiyalagan Kalidass, India
Tamas Kalmar-Nagy, Hungary
Zhao Kang, China
Tomasz Kapitaniak, Poland
Julius Kaplunov, United Kingdom
Konstantinos Karamanos, Belgium
Michal Kawulok, Poland
Irfan Kaymaz, Turkey
Vahid Kayvanfar, Iran
Krzysztof Kecik, Poland
Chaudry M. Khalique, South Africa
Mukhtaj khan, Pakistan
Abdul Qadeer Khan, Pakistan
Mostafa M. A. Khater, Egypt
Kwangki Kim, Republic of Korea
Nam-Il Kim, Republic of Korea
Philipp V. Kiryukhantsev-Korneev, Russia
P.V.V Kishore, India
Jan Koci, Czech Republic
Ioannis Kostavelis, Greece
Sotiris B. Kotsiantis, Greece
Frederic Kratz, France
Vamsi Krishna, India
Petr Krysl, USA
Edyta Kucharska, Poland
Krzysztof S. Kulpa, Poland
Kamal Kumar, India
Michal Kunicki, Poland
Cedrick A. K. Kwuimy, USA
Kyandoghere Kyamakya, Austria
Ivan Kyrchei, Ukraine
Davide La Torre, Italy
Márcio J. Lacerda, Brazil

Risto Lahdelma, Finland
Giovanni Lancioni, Italy
Jaroslaw Latalski, Poland
Antonino Laudani, Italy
Hervé Laurent, France
Aimé Lay-Ekuakille, Italy
Nicolas J. Leconte, France
Kun-Chou Lee, Taiwan
Dimitri Lefebvre, France
Eric Lefevre, France
Marek Lefik, Poland
Gang Lei, Saudi Arabia
Yaguo Lei, China
Kauko Leiviskä, Finland
Thibault Lemaire, France
afonso lemonge, Brazil
Ervin Lenzi, Brazil
Roman Lewandowski, Poland
Zhen Li, China
ChenFeng Li, China
Jun Li, China
Yang Li, China
Yueyang Li, China
Jian Li, USA
Jian Lin, China
En-Qiang Lin, USA
Zhiyun Lin, China
Yao-Jin Lin, China
Bo Liu, China
Sixin Liu, China
Wanquan Liu, China
Yu Liu, China
Heng Liu, China
Yuanchang Liu, United Kingdom
Lei Liu, China
Jianxu Liu, Thailand
Bin Liu, China
Bonifacio Llamazares, Spain
Alessandro Lo Schiavo, Italy
Jean Jacques Loiseau, France
Francesco Lolli, Italy
Paolo Lonetti, Italy
Sandro Longo, Italy
António M. Lopes, Portugal
Sebastian López, Spain
Pablo Lopez-Crespo, Spain
Cesar S. Lopez-Monsalvo, Mexico

Higinio Ramos, Spain
Angel Manuel Ramos, Spain
Muhammad Afzal Rana, Pakistan
Amer Rasheed, Pakistan
Muhammad Rashid, Saudi Arabia
Manoj Rastogi, India
Alessandro Rasulo, Italy
S.S. Ravindran, USA
Abdolrahman Razani, Iran
Alessandro Reali, Italy
Jose A. Reinoso, Spain
Oscar Reinoso, Spain
Haijun Ren, China
X. W. Ren, China
Carlo Renno, Italy
Fabrizio Renno, Italy
Shahram Rezapour, Iran
Ricardo Riaza, Spain
Francesco Riganti-Fulginei, Italy
Gerasimos Rigatos, Greece
Francesco Ripamonti, Italy
Marcelo Raúl Risk, Argentina
Jorge Rivera, Mexico
Eugenio Roanes-Lozano, Spain
Bruno G. M. Robert, France
Ana Maria A. C. Rocha, Portugal
Luigi Rodino, Italy
Francisco Rodríguez, Spain
Rosana Rodríguez López, Spain
Alessandra Romolo, Italy
Abdolreza Roshani, Italy
Francisco Rossomando, Argentina
Jose de Jesus Rubio, Mexico
Weiguo Rui, China
Rubén Ruiz, Spain
Ivan D. Rukhlenko, Australia
Chaman Lal Sabharwal, USA
Kishin Sadarangani, Spain
Andrés Sáez, Spain
Bekir Sahin, Turkey
John S. Sakellariou, Greece
Michael Sakellariou, Greece
Salvatore Salamone, USA
Jose Vicente Salcedo, Spain
Alejandro Salcido, Mexico
Alejandro Salcido, Mexico
Salman saleem, Pakistan

Ahmed Salem, Saudi Arabia
Nunzio Salerno, Italy
Rohit Salgotra, India
Miguel A. Salido, Spain
Zabidin Salleh, Malaysia
Roque J. Saltarén, Spain
Alessandro Salvini, Italy
Abdus Samad, India
Nikolaos Samaras, Greece
Sylwester Samborski, Poland
Ramon Sancibrian, Spain
Giuseppe Sanfilippo, Italy
Omar-Jacobo Santos, Mexico
J Santos-Reyes, Mexico
José A. Sanz-Herrera, Spain
Evangelos J. Sapountzakis, Greece
Musavarah Sarwar, Pakistan
Marcelo A. Savi, Brazil
Andrey V. Savkin, Australia
Tadeusz Sawik, Poland
Roberta Sburlati, Italy
Gustavo Scaglia, Argentina
Thomas Schuster, Germany
Oliver Schütze, Mexico
Lotfi Senhadji, France
Junwon Seo, USA
Michele Serpilli, Italy
Joan Serra-Sagrista, Spain
Silvestar Šesnić, Croatia
Erhan Set, Turkey
Gerardo Severino, Italy
Ruben Sevilla, United Kingdom
Stefano Sfarra, Italy
Mohamed Shaat, United Arab Emirates
Mostafa S. Shadloo, France
Kamal Shah, Pakistan
Leonid Shaikhet, Israel
Xingling Shao, China
Hao Shen, China
hang shen, China
Xin Pu Shen, China
Bo Shen, Germany
Dimitri O. Shepelsky, Ukraine
Weichao SHI, United Kingdom
Jian Shi, China
Suzanne M. Shontz, USA
Babak Shotorban, USA

Yong Wang, China
Guoqiang Wang, China
J.G. Wang, China
Zhenbo Wang, USA
Ji Wang, China
Shuo Wang, China
Yung-Chung Wang, Taiwan
Hui Wang, China
Zhibo Wang, China
Yongqi Wang, Germany
Xinyu Wang, China
Fu-Kwun Wang, Taiwan
Weiwei Wang, China
Dagang Wang, China
Bingchang Wang, China
Roman Wan-Wendner, Austria
Fangqing Wen, China
P.H. Wen, United Kingdom
Waldemar T. Wójcik, Poland
Wai Lok Woo, United Kingdom
Zhizheng Wu, China
Zhibin Wu, China
Qiuhong Wu, China
Yuqiang Wu, China
Xianyi Wu, China
Changzhi Wu, China
Michalis Xenos, Greece
hao xiao, China
Xiao Ping Xie, China
Xue-Jun Xie, China
Qingzheng Xu, China
Lingwei Xu, China
Hang Xu, China
Zeshui Xu, China
Lei Xu, China
Qilong Xue, China
Joseph J. Yame, France
Chuanliang Yan, China
Zhiguo Yan, China
Xinggang Yan, United Kingdom
Ray-Yeng Yang, Taiwan
Weilin Yang, China
Jixiang Yang, China
Mijia Yang, USA
Min Ye, China
Jun Ye, China
Luis J. Yebra, Spain

Peng-Yeng Yin, Taiwan
Muhammad Haroon Yousaf, Pakistan
Yuan Yuan, United Kingdom
Qin Yuming, China
Abdullahi Yusuf, Nigeria
Akbar Zada, Pakistan
Elena Zaitseva, Slovakia
Arkadiusz Zak, Poland
Daniel Zaldivar, Mexico
Ernesto Zambrano-Serrano, Mexico
Francesco Zammori, Italy
Vittorio Zampoli, Italy
Rafal Zdunek, Poland
Ahmad Zeeshan, Pakistan
Ibrahim Zeid, USA
Nianyin Zeng, China
Bo Zeng, China
Junyong Zhai, China
Tongqian Zhang, China
Wenyu Zhang, China
Jian Zhang, China
Xuping Zhang, Denmark
Haopeng Zhang, USA
Kai Zhang, China
Xiaofei Zhang, China
Qian Zhang, China
Hao Zhang, China
Xianming Zhang, Australia
Yong Zhang, China
Tianwei Zhang, China
Lingfan Zhang, China
Yifan Zhao, United Kingdom
Yongmin Zhong, Australia
Jian G. Zhou, United Kingdom
Debao Zhou, USA
Zebo Zhou, China
Wu-Le Zhu, China
Quanxin Zhu, China
Gaetano Zizzo, Italy
Zhixiang Zou, China

Contents

Editorial

Recent Advances in Multiphase Flows in Engineering

Muhammad Mubashir Bhatti ⓘ,[1] **Marin Marin** ⓘ,[2] and **Ahmad Zeeshan** ⓘ[3]

[1]*College of Mathematics and Systems Science, Shandong University of Science and Technology, Qingdao 266590,
Shandong, China*
[2]*Department of Mathematics and Computer Science, Transilvania University of Brasov, Brasov 500093, Romania*
[3]*Department of Mathematics and Statistics, FBAS, International Islamic University, Islamabad 44000, Pakistan*

Correspondence should be addressed to Muhammad Mubashir Bhatti; muhammad09@shu.edu.cn

1. Introduction

Multiphase phase flows include the flow of matter in two or
more than two thermodynamic phases and involve solid-gas
flows, bubbly flows, and sprays. They pervaded practically every
feature of human life, and enhanced comprehension of mul-
tiphase flows can play a significant role in ensuring three es-
sential requirements of humans, for instance, sustainable food
production, clean water, and clean air. The understanding of
multiphase flows is beneficial to examine the key mechanisms
of the natural environment and in man-made systems. Mul-
tiphase flows have numerous applications in nanotechnology,
chemical process, energy, environmentally sustainable tech-
nologies, critical infrastructures, and biological and healthcare
applications, i.e., pharmaceuticals, manufacturing processes,
and design materials. Table 1 shows the various classifications
of multiphase flows. The examples given in the table are
intended only to show the reader an overview of the appli-
cations and different types of multiphase flows that appear in
various biological, industrial, and diverse natural systems.

Considering the importance of multiphase flows in
engineering, this Special Issue was introduced. In total, 17
papers were submitted to this Special Issue, and out of them,
12 were selected for publication.

2. Recent Advances in Multiphase
Flows in Engineering

Alqahtani et al. [1] discussed the heat and mass transfer
process through a wedge. The applications of the problems
mainly occur in civil engineering. The effects of magnetic

field and cross-diffusion gradients are also taken into con-
sideration. According to their results, they found that the
Prandtl number diminishes the temperature profile. How-
ever, mass transport increases due to higher values of Soret
number and the converse effects shown for Schmidt number.

Rashid et al. [2] studied gold nanoparticles suspended in
the water-based nanofluid under heat transfer effects. They
contemplated various forms of nanoparticles, including
lamina, hexahedron, column, sphere, and tetrahedron. The
mathematical formulation is performed via similarity
transformations, and the homotopy analysis method was
used to determine the solutions. According to the results, it
is found that heat transfer is maximum for the lamina shape
nanoparticles and the sphere shape nanoparticles show a
considerable behavior in temperature profile as compared to
other types of nanoparticles.

Chu et al. [3] studied the cross-flow in the streamwise
direction towards a moving surface under viscous dissipa-
tion and magnetic effects. They further determined the
stability analysis and presented dual solutions. They found
that the velocities in the direction of streamwise in addition
to cross-flow reduces in the upper branch solution; at the
same time, a converse impact is observed for the lower
branch solution. Furthermore, the impact of suction on the
velocities uplifts the solutions in the upper branch and
diminishes the solutions in the lower branch.

Han et al. [4] used the CFD-DEM coupling technique to
set up the simulation model of two-phase flow through a
drill pipe. They determined the impact of cutting removal on
air velocity, the mass flow rate of cutting on the flow
properties, the cutting removal impact, and the pressure

TABLE 1: Classification of multiphase flows.

	Gas-solid flows	Liquid-solid flows	Gas-liquid flows	Liquid-liquid flows	Gas-solid flows
Natural	Sand storms, volcanoes, and avalanches	Sediment transport of sand in rivers and sea, soil erosion, mud slides, debris flows, and iceberg formation	Rain droplets, ocean waves, and mist formation	—	—
Biological	Aerosols (dust particles) and smoke (fine soot particles)	Blood flow	Aerosols (liquid droplets)	—	—
Industrial	Pneumatic conveyers, dust collectors, fluidized beds, and solid propellant Rockets, pulverized solid particles, spray drying, and spray casting	Slurry transportation, flotation, fluidized beds, water jet cutting, and sewage treatment plants	Boiling water and pressurized water nuclear reactors, chemical reactor desalination systems, boilers, heat exchangers, internal combustion engines, liquid propellant rockets, and fire sprinkler suppression systems	Emulsifiers, fuel-cell systems, microchannel applications, and extraction systems	Air lift pumps and fluidized beds

drop of cutting-gas-two-phase flow. According to their analysis, they found that the drag force of drilling cuttings becomes higher with an increment in air velocity. When the mass flow rate of cutting is constant, it enhances the air velocity for cutting removal and tends to enhance the pressure drop in the inner hole of the drill pipe. On the contrary, when the air velocity of cutting removal is constant, then the mass flow rate of cutting and the pressure drop in the inner hole of the drill pipe rises.

Gonzalez-Trejo et al. [5] studied fluid dynamics within a pair of submerged entry nozzle models with a square cross-section bore. They contemplated water as a working fluid with the Froude similarity criterion. The proposed model comprises a square-shaped tube having one inlet and two lateral squared exits at the bottom; however, the model does not have exit ports. The proposed turbulence model is presented as a large eddy simulation having dynamics k-equation filtering. According to the results, it is found that with one large vortex, the flow pattern within the pool nozzle can be defined, whereas, in the nozzle without the pool, the flow pattern depicts a complex mechanism distinguished by two small vortexes.

Yousaf et al. [6] presented a novel method known as the cubic trigonometric B-spline technique based on the Hermite formula. They used this method to solve the convection-diffusion equation. They found that the main benefit of this scheme is that the approximate solution is obtained as a smooth piecewise continuous function, which enables us to determine the approximate solution at any point in the location with higher accuracy.

Basit et al. [7] examined heat transfer with forced convection from arrays of prolate particles is formulated by employing the second-order immersed boundary Lattice Boltzmann technique. They found that Reynolds number and solid volume fraction significantly enhanced the Nusselt number and Hermans orientation factor. Furthermore, they noticed that the impact of orientation on Nusselt number is remarkable.

Irfan et al. [8] examined the theoretical impact of magnetized stagnation point flow on heat and mass transfer towards a shrinking and stretching porous surface. Furthermore, they elaborated the behavior of chemical reaction, thermal radiation, swimming of gyrotactic microorganisms, and heat source/sink. MATLAB software has been used to examine the solutions using the bvp4c command. They concluded that the skin friction coefficient increases due to an increment in porosity and magnetic parameters. Moreover, they discussed that the Peclet number and Lewis number enhanced the motile microorganism profile.

Arain et al. [9] studied bioconvection flow with nanoparticles under the presence of an induced magnetic field. They have contemplated Carreau fluid which is moving between a pair of rotating circular plates. Furthermore, they used the DTM-Pade approximation to determine the numerical solutions. They also discussed the effects of shear-thinning, shear-thickening, and Newtonian fluid models as a special case of the proposed study.

Song et al. [10] presented a design and implementation of the array logging tool for horizontal production logging. The proposed project has designed a staggered probe array flow meter well logging apparatus based on the characteristic of electromagnetic wave specific retention meter that can fully cover the wellbore fluid and improve the flow measurement accuracy. According to the application in horizontal wells, the accuracy of this measuring instrument has been proved to be more than 90%. It can meet the requirements of production logging interpretation in horizontal wells.

Farooq et al. [11] employed a simplified finite difference technique to examine the nanofluid mechanism through an exponentially stretching surface under the effects of thermal radiation. They discussed the efficiency of the proposed scheme by comparing the results with other similar methods. Their outcomes found that the Eckert number enhanced the velocity profile; however, the thermal Grashof number opposes the temperature profile.

Riaz et al. [12] discussed the entropy mechanism of a three-dimensional wavy flow using Eyring–Powell nanofluid. Mathematical and physical modeling is performed based on the lubrication approach. Furthermore, they used the homotopy perturbation approach to solve the coupled nonlinear differential equations. They showed that entropy generation reduces due to concentration parameters but upsurges due to viscous dissipation. Moreover, it is presented that Eyring–Powell depicts the difference in behavior in the entropy generation and the presence of nanoparticles due to the significant dissipation effects. In addition, it travels faster than the viscous fluid. This study may be helpful for cancer therapy in biomedicine by nanofluid properties in multiple drugs contemplated as a non-Newtonian fluid.

Conflicts of Interest

The editors declare that there are no conflicts of interest.

Muhammad Mubashir Bhatti
Marin Marin
Ahmad Zeeshan

References

[1] A. M. Alqahtani, U. Khan, N. Ahmed, S. T. Mohyud-Din, and I. Khan, "Numerical investigation of heat and mass transport in the flow over a magnetized wedge by incorporating the effects of cross-diffusion gradients: applications in multiple engineering systems," *Mathematical Problems in Engineering*, vol. 2020, Article ID 2475831, 10 pages, 2020.

[2] U. Rashid, T. Abdeljawad, H. Liang, A. Iqbal, M. Abbas, and M. Siddiqui, "The shape effect of gold nanoparticles on squeezing nanofluid flow and heat transfer between parallel plates," *Mathematical Problems in Engineering*, vol. 2020, Article ID 9584854, 12 pages, 2020.

[3] Y. M. Chu, U. Khan, A. Zaib, and S. H. Shah, "Numerical and computer simulations of cross-flow in the streamwise direction through a moving surface comprising the significant impacts of viscous dissipation and magnetic fields: stability analysis and dual solutions," *Mathematical Problems in Engineering*, vol. 2020, Article ID 8542396, 2020.

[4] X. Han, P. Li, and J. Li, "CFD-DEM simulation of reverse circulation pneumatic cuttings removal during coal seam drilling," *Mathematical Problems in Engineering*, vol. 2020, Article ID 3707864, 2020.

[5] J. Gonzalez-Trejo, C. A. Real-Ramirez, I. Carvajal-Mariscal et al., "Hydrodynamic analysis of the flow inside the submerged entry nozzle," *Mathematical Problems in Engineering*, vol. 2020, Article ID 6267472, 14 pages, 2020.

[6] A. Yousaf, T. Abdeljawad, M. Yaseen, and M. Abbas, "Novel cubic trigonometric B-spline approach based on the Hermite formula for solving the convection-diffusion equation," *Mathematical Problems in Engineering*, vol. 2020, Article ID 8908964, 17 pages, 2020.

[7] R. Basit, X. Li, Z. Huang, and Q. Zhou, "Heat transfer studies of arrays of prolate particles in gas-solid flows," *Mathematical Problems in Engineering*, vol. 2020, Article ID 6639172, 12 pages, 2020.

[8] M. Irfan, M. A. Farooq, A. Mushtaq, and Z. H. Shamsi, "Unsteady MHD bionanofluid flow in a porous medium with thermal radiation near a stretching/shrinking sheet," *Mathematical Problems in Engineering*, vol. 2020, Article ID 8822999, 14 pages, 2020.

[9] M. B. Arain, M. M. Bhatti, A. Zeeshan, T. Saeed, and A. Hobiny, "Analysis of Arrhenius kinetics on multiphase flow between a pair of rotating circular plates," *Mathematical Problems in Engineering*, vol. 2020, Article ID 2749105, 17 pages, 2020.

[10] W. Song, H. Chen, Q. Zhang, and J. Zhang, "Design and implementation of the array logging tool on horizontal production logging," *Mathematical Problems in Engineering*, Article ID 6903970, 7 pages, 2020.

[11] M. A. Farooq, A. Salahuddin, A. Mushtaq, and M. Razzaq, "A simplified finite difference method (SFDM) solution via tridiagonal matrix algorithm for MHD radiating nanofluid flow over a slippery sheet submerged in a permeable medium," *Mathematical Problems in Engineering*, vol. 2021, Article ID 6628009, 17 pages, 2021.

[12] A. Riaz, A. Zeeshan, and M. M. Bhatti, "Entropy analysis on a three-dimensional wavy flow of eyring–powell nanofluid: a comparative study," *Mathematical Problems in Engineering*, vol. 2021, Article ID 6672158, 14 pages, 2021.

Research Article

Entropy Analysis on a Three-Dimensional Wavy Flow of Eyring–Powell Nanofluid: A Comparative Study

Arshad Riaz,[1] Ahmed Zeeshan,[2] and M. M. Bhatti [3]

[1]*Department of Mathematics, Division of Science and Technology, University of Education, Lahore 54770, Pakistan*
[2]*Department of Mathematics and Statistics, Faculty of Basic and Applied Sciences, International Islamic University, Islamabad 44000, Pakistan*
[3]*College of Mathematics and Systems Science, Shandong University of Science and Technology, Qingdao, Shandong 266590, China*

Correspondence should be addressed to M. M. Bhatti; muhammad09@shu.edu.cn

The thermal management of a system needs an accurate and efficient measurement of exergy. For optimal performance, entropy should be minimized. This study explores the enhancement of the thermal exchange and entropy in the stream of Eyring–Powell fluid comprising nanoparticles saturating the vertical oriented dual cylindrical domain with uniform thermal conductivity and viscous dissipation effects. A symmetrical sine wave over the walls is used to induce the flow. The mathematical treatment for the conservation laws are described by a set of PDEs, which are, later on, converted to ordinary differential equations by homotopy deformations and then evaluated on the Mathematica software tool. The expression of the pressure rise term has been handled numerically by using numerical integration by Mathematica through the algorithm of the Newton–Cotes formula. The impact of the various factors on velocity, heat, entropy profile, and the Bejan number are elaborated pictorially and tabularly. The entropy generation is enhanced with the variation of viscous dissipation but reduced in the case of the concentration parameter, but viscous dissipation reveals opposite findings for the Newtonian fluid. From the abovementioned detailed discussion, it can be concluded that Eyring–Powell shows the difference in behavior in the entropy generation and in the presence of nanoparticles due to the significant dissipation effects, and also, it travels faster than the viscous fluid. A comparison between the Eyring-Powell and Newtonian fluid are also made for each pertinent parameter through special cases. This study may be applicable for cancer therapy in biomedicine by nanofluid characteristics in various drugs considered as a non-Newtonian fluid.

1. Introduction

Nonlinear fluid models are the center of consideration of several theoretical and experimental evaluations due to their massive applicability in the engineering sciences, biomechanics, and mechanical manufacturing such as the petroleum industry, flow of blood in the body, and transport of sewage. Working in the domain of nonlinear fluid flows creates challenges to the mathematician and simulation engineers with its diversity and complexity. As the complexity of such fluids offers no unique constitutive equation which encounters all the properties, for such fluids, several non-Newtonian models are presented in

[1–4]. The polymeric liquids reveal diverse rheological attributes apparent in the flow, such as polymer accumulation, mechanical mortification, and solvent composition. [5]. Kwack [6] explained that all these polymer properties influence the elasticity of the fluids. Mathematical models such as the Carreau fluid model [7], Ellis fluid model [8], and Powell–Eyring fluid model [9] effectively discuss elastic properties of the fluid. Out of these models, the Powell-Eyring model stands out because of its fluid elasticity property and ease for its applicability to both experimental and theoretical studies. These advantages lead many scientists to unveil these hidden properties of such fluids in different flow situations. Patel and

Timol [10] found a numerical solution to debate on the characteristics of the Powell-Eyring type model. They used the so-called MSABC scheme to find an asymptotically convergent solution. Hayat et al. [11] found a series solution using the so-called HAM to define the momentum and heat transfer about the stagnation point for the Powell-Eyring fluid. They also analyzed melting heat transfer effects. Jalil et al. [12] discovered self-similar solutions of parallel free stream flow of this fluid. The flow is considered on a moving plate. Islam et al. [13] considered the flow of the Powell-Eyring fluid in slider bearings. They employed HPM to develop the analytic series solution of the current flow. Hina et al. [14] elaborated the study of Powell-Eyring fluids between curved compliant walls of the channel. The effects on temperature variations are also discussed. Hayat et al. [15] evaluated MHD Powell-Eyring liquid flow on a radially stretching cylinder. They exclusively focused on the effects of Newtonian heating.

In recent times, the study of flows driven by peristaltic waves has become more and more popular in physiology and biomedical industry. The idea of peristalsis was driven from the food transport duct in the human body. Other than food transport from the mouth to stomach, this phenomenon can be seen in the spermatozoa movement in the male genital region and ovum in the females and also in urine travelling and chyme movement through the gastrointestinal tract, etc. In industry, machine-like rollers and finger pumps and blood filtration devices in dialysis employ the mechanism of peristalsis. Shapiro [16] and Latham [17] presented the idea of peristalsis theoretically and verified experimentally. Ever since, numerous studies, both theoretically and experimentally, have been published in the domain of nonlinear fluids [18–20]. The peristaltic mechanism of certain elastic fluids is a matter of great interest. Recent studies are indicative of the importance of these in industrial applications. Ellahi et al. [21] used 3D analysis of a peristaltic stream of Carreau fluid in the magnetic environment. Hayat et al. [22] worked with the Carreau-Yasuda fluid with nanosized particle theoretically. They considered that flow is driven due to the sinusoidal motion of the wall. Also, they examined both convective and no-mass flux on the wall. Prakash and Tripathi [23] examined the effects of the electric double layer on Williamson ionic liquid with homogeneously distributed particles of nanosize. They considered a tapered channel with peristaltic waves on the wall. Effects of thermal radiation are also discovered. Zeeshan et al. [24] focused on the flow of the bio-Jeffrey fluid and the sustainability character in the human body. Tanveer et al. [25] checked the flow through a curved channel. They revealed mixed convection impacts and elastic properties of the walls on pumping transport of Eyring-Powell liquid with nanomaterial. Bhatti et al. [26] presented the effects of the Darcy porous medium of a two-phase nanofluid in a channel.

The applications such as paper drying, thermal coating, hot rolling, and glass fiber stretching divert one's focus towards the heat transfer of non-Newtonian fluids. Motivated by this, it stimulates an extensive literature in this field [27–30] which includes analysis in flexible channels. Presence of nanoparticles shows a positive trend in enhancing the heat transfer of fluid. The theme of nanofluids is the concept of Choi [31]. The concept was to add nanosized particles in a fluid which has low thermal conductivity. Hence, fluid behavior and metallic conductivity both combine to obtain an enhanced heat conductor which can be transported like a fluid. It was one of the promising aspects of such fluids. Many mathematical models using continuum formulation [32] or two-phase suspension models [33] are developed over the years now. One such model due to Buongiorno [34] was developed in many ways. Some researchers [35–39] revealed the basics of nanofluids' contribution in different geometries with the peristaltic wave.

It is essential to generate the systems or the machines which perform and help in efficient energy transport. Such a machine is broadly utilized in power plants, manufacturing plants, and transportation. The warm productivity of the framework relies upon the material used for thermal vitality. It is fundamental to understand the factor which diminishes warm proficiency. As indicated by the laws of thermodynamics, vitality of the framework stays to save, yet can be changed over into different structures for the utility. All the more regularly, we state all the energies of the framework are spent in accomplishing work or to expand the temperature of the body. Numerous frictional powers emerging from the attractive field, permeable spaces, and so on are explained in the improvement of the temperature of the framework. The warm messiness in the framework is consistently on the ascent. Realizing the elements engaged with entropy rise is consistently imperative to get ideal warm effectiveness of the framework. Ascend being used of nanofluids is one approach to decrease the loss of vitality. Entropy generation and exergy are one of the most dynamic examination fields in thermodynamics. Most recently, Naz et al. [40] optimized entropy generated in the flow of pseudoplastic fluid. The fluid also comprises of microorganisms. Abbas et al. [41] analyzed the entropy generated theoretically in the stream of magnetized nanofluid. They use statistical techniques to get results. Abbas et al. [42] also analyzed entropy for peristaltic flow of nanofluids. Ellahi et al. [43] extended the work with a porous medium. Hayat et al. [44] use modified Darcy's porous medium and the effects of the endoscope.

The limited literature on entropy generation of nanoelastic fluid, useful characteristics of the Eyring-Powell model, and the applicability in the industrial usage of such flows is the main motivation for the current analysis. With the cited literature in mind, the existing study designed to investigate the distribution of nanoparticles in a Powell-Eyring viscoelastic fluid having enhanced elastic properties and viscous dissipation effects through a cylindrical structure with the peristaltic wave is focused. Energy loss in the transport is also an area of interest. The observations for the Newtonian fluid are also taken into consideration as a limiting case of the readings. The obtained PDEs are simplified with the help of laminar

movement of the liquid and small wave amplitude approximations and then solved analytically. The results are elaborated comprehensively and displayed in the graphical way. Conclusions which highlight the key findings are placed in the end.

2. Mathematical Treatment

We take the peristaltic flow of an Eyring-Powell liquid situated in an annular part of two eccentric cylinders by introducing nanoparticles. We also consider the term of viscous dissipation and entropy generation occurring during the process due to the irreversibilities of viscous factors, thermal analysis, and mass exchanging phenomenon of nanoparticles. The geometry is assumed to be having flexible outer surfaces. The flow is taken inside the annular region of two eccentric annuli with eccentricity ϵ. Moreover, the inner cylinder is considered as rigid with radius δ, and the outer cylinder with radius a is producing a sinusoidal wave propagating along the axial root. The walls of the inner and outer annuli have been described in [30]. The conservation laws for an incompressible and unsteady flow of non-Newtonian nanofluid are described in [30, 35]. The temperatures and nanoparticle concentrations at the inner cylinder are fixed at the amount of T_o and C_o, while those of the outer cylinder are maintained at T_1 and $C_1 \simeq$ accordingly. The mathematical model of the stress matrix representing the Eyring-Powell fluid is described as follows [15]:

$$S_{\mathrm{LM}} = \mu \frac{\partial V_p}{\partial x^i} + \frac{1}{\beta} \operatorname{Arc\,sinh}\left(c^{-1}\frac{\partial V_p}{\partial x^i}\right), \quad (1)$$

$$\operatorname{Arc\,sinh}\left(c^{-1}\frac{\partial V_p}{\partial x^i}\right) \approx c^{-1}\frac{\partial V_p}{\partial x^i} - \frac{1}{6}\left(c^{-1}\frac{\partial V_p}{\partial x^i}\right)^3 + O\left| c^{-1}\frac{\partial V_p}{\partial x^i}\right|^5, \quad (2)$$

where μ represents the shear viscosity coefficient and β and c are the material constants. Now, we introduce local wave frame coordinates (r, θ, z) running with the same wave velocity relative to the fixed frame (x^1, x^2, x^3) through the following transformations:

$$\begin{aligned}
z &= x^3 - c_1 t, \\
r &= x^1, \\
\theta &= x^2, \\
w &= \underline{W} - c_1, \\
p &= P, \\
u &= \underline{U}, \\
S_{\mathrm{LM}} &= s_{\mathrm{lm}}.
\end{aligned} \quad (3)$$

We use the following dimensionless parameters in the problem:

$$p' = \frac{a^2}{\mu c_1 \lambda} p,$$

$$w' = \frac{w}{c_1},$$

$$u' = \frac{\lambda}{a c_1} u,$$

$$V' = \frac{V}{c_1},$$

$$z' = \frac{z}{\lambda},$$

$$r' = \frac{r}{a},$$

$$\theta' = \theta,$$

$$t' = \frac{c}{\lambda} t,$$

$$\phi = \frac{b}{a},$$

$$\epsilon' = \frac{\epsilon}{a},$$

$$R_e = \frac{\rho c_1 a}{\mu},$$

$$\delta' = \frac{\delta}{a},$$

$$\overline{\theta} = \frac{T - T_o}{T_1 - T_o},$$

$$\delta_o = \frac{a}{\lambda},$$

$$r'_1 = r_1,$$

$$r'_2 = \frac{r_2}{a},$$

$$\sigma = \frac{C - C_o}{C_1 - C_o},$$

$$P_r = \frac{\mu}{\rho \alpha},$$

$$S_c = \frac{\mu}{\rho D_B},$$

$$\alpha_f = \frac{k}{(\rho c)_f},$$

$$\tau = \frac{(\rho c)_p}{(\rho c)_f},$$

$$B_r = \frac{\rho_f g \alpha a^2}{\mu c}(T_1 - T_o),$$

$$G_r = \frac{\rho_f g \alpha a^2}{\mu c}(C_1 - C_o),$$

$$N_b = \frac{\tau D_B}{\alpha_f}(C_1 - C_o),$$

$$N_t = \frac{\tau D_T}{T_o \alpha_f}(T_1 - T_o),$$

$$\dot{S} = \frac{a}{\mu c_1} S,$$

$$G_c = \frac{\mu c^2}{k(T_1 - T_o)},$$

$$M = \frac{1}{\beta \mu c},$$

$$K = \frac{Mc_1^2}{6c^2 a^2},$$

(4)

where $V, \phi, R_e, \delta_o, P_r, N_b, N_t, G_c, G_r$, and B_r evaluate the velocity of the inner rod, amplitude fraction, Reynolds number factor, nondimensional wave number, the Prandtl number, the Brownian motion parameter, the thermophoresis constant parameter, Brinkman number, localized temperature Grashof number, and localized nanoparticles Grashof number, separately. After employing the above-mentioned nondimensional parameters and wave frame, we approach to the following dimensionless form of the equations of motion defined in [30] under the physiological limitations of long wavelength ($\lambda \longrightarrow \infty$) and low Reynolds number ($R_e \longrightarrow 0$):

$$\frac{\partial u'}{\partial r'} + \frac{\partial w'}{\partial z'} + \frac{u'}{r'} = 0,$$

(5)

$$0 = -\frac{\partial p'}{\partial z'} + \frac{1}{r'}\frac{\partial(r'S'_{rz})}{\partial r'} + \frac{1}{r'}\frac{\partial S'_{\theta z}}{\partial \theta'} + Gr\overline{\theta} + Br\sigma,$$

(6)

$$0 = \left(\frac{\partial^2 \overline{\theta'}}{\partial r'^2} + \frac{1}{r'^2}\frac{\partial^2 \overline{\theta'}}{\partial \theta'^2} + \frac{1}{r'}\frac{\partial \overline{\theta'}}{\partial r'}\right) + N_b\left(\frac{\partial \sigma}{\partial r'}\frac{\partial \overline{\theta'}}{\partial r'} + \frac{1}{r'^2}\frac{\partial \sigma}{\partial \theta'}\frac{\partial \overline{\theta'}}{\partial \theta'}\right) + N_t\left(\left(\frac{\partial \overline{\theta'}}{\partial r'}\right)^2 + \frac{1}{r'^2}\left(\frac{\partial \overline{\theta'}}{\partial \theta'}\right)^2\right)$$
$$+ G_c\left(S'_{rz}\frac{\partial w'}{\partial r'} + \frac{1}{r'}S'_{z\theta}\frac{\partial w'}{\partial \theta'}\right),$$

(7)

$$0 = \left(\frac{\partial^2 \sigma}{\partial r'^2} + \frac{1}{r'^2}\frac{\partial^2 \sigma}{\partial \theta^2} + \frac{1}{r'}\frac{\partial \sigma}{\partial r'}\right) + \frac{N_t}{N_b}\left(\frac{\partial^2 \overline{\theta'}}{\partial r'^2} + \frac{1}{r'^2}\frac{\partial^2 \overline{\theta'}}{\partial \theta'^2} + \frac{1}{r'}\frac{\partial \overline{\theta'}}{\partial r'}\right).$$

(8)

The needed nondimensional components of stress tensor S_{LM} calculated from relation (1) can be collected as follows:

$$S'_{rz} = \frac{\partial w'}{\partial r'} + M\frac{\partial w'}{\partial r'} - K\left(\frac{\partial w'}{\partial r'}\right)^3,$$

$$S'_{z\theta} = \frac{1}{r'}\frac{\partial w'}{\partial \theta'} + \frac{M}{r'}\frac{\partial w'}{\partial \theta'} - K\left(\frac{1}{r'}\frac{\partial w'}{\partial \theta'}\right)^3,$$

$$S'_{z\theta} = 0.$$

(9)

Now, we use $S'_{rz}, S'_{\theta z}$, and $S'_{z\theta}$ in (6) and (7) and also omit the prime symbols to have the resulting structure as follows:

$$\frac{1}{(1+M)}p'(z) = \frac{\partial^2 w}{\partial r^2} + \frac{1}{r}\frac{\partial w}{\partial r} + \frac{1}{r^2}\frac{\partial^2 w}{\partial \theta^2} - \frac{3K}{(1+M)}\left(\frac{\partial w}{\partial r}\right)^2\frac{\partial^2 w}{\partial r^2} - \frac{K}{r(1+M)}\left(\frac{\partial w}{\partial r}\right)^3$$

$$- \frac{3K}{r^4(1+M)}\left(\frac{\partial w}{\partial \theta}\right)^2\frac{\partial^2 w}{\partial \theta^2} + \frac{1}{(1+M)}(Gr\overline{\theta} + Br\sigma),$$

(10)

$$0 = \left(\frac{\partial^2 \overline{\theta}}{\partial r^2} + \frac{1}{r}\frac{\partial \overline{\theta}}{\partial r} + \frac{1}{r^2}\frac{\partial^2 \overline{\theta}}{\partial \theta^2}\right) + N_b\left(\frac{\partial \sigma}{\partial r}\frac{\partial \overline{\theta}}{\partial r} + \frac{1}{r^2}\frac{\partial \sigma}{\partial \theta}\frac{\partial \overline{\theta}}{\partial \theta}\right) + N_t\left(\left(\frac{\partial \overline{\theta}}{\partial r}\right)^2 + \frac{1}{r^2}\left(\frac{\partial \overline{\theta}}{\partial \theta}\right)^2\right)$$

$$+ G_c\left(\left(\frac{\partial w}{\partial r}\right)^2 + M\left(\frac{\partial w}{\partial r}\right)^2 - K\left(\frac{\partial w}{\partial r}\right)^4\right),$$

(11)

$$0 = \left(\frac{\partial^2 \sigma}{\partial r^2} + \frac{1}{r}\frac{\partial \sigma}{\partial r} + \frac{1}{r^2}\frac{\partial^2 \sigma}{\partial \theta^2}\right) + \frac{N_t}{N_b}\left(\frac{\partial^2 \overline{\theta}}{\partial r^2} + \frac{1}{r}\frac{\partial \overline{\theta}}{\partial r} + \frac{1}{r^2}\frac{\partial^2 \overline{\theta}}{\partial \theta^2}\right). \tag{12}$$

The relevant no-slip walls' conditions in a nondimensional format are described as follows [30]:

$$w = \{V \text{ when } r = r_1 = \delta + \varepsilon \cos\theta, 0 \text{ when } r = r_2 = 1 + \phi \cos 2\pi z\},$$
$$(\overline{\theta}, \sigma) = \{0 \text{ when } r = r_1 = \delta + \varepsilon \cos\theta, 1 \text{ when } r = r_2 = 1 + \phi \cos 2\pi z\}. \tag{13}$$

3. Solution Procedure

The solutions of the overhead nonlinear partial equations, (10), (11), and (12), are achieved analytically. The deformation expressions for the considering problems are evaluated as follows [30, 37]:

$$(1 - q'')\left(\mathcal{L}[\widetilde{w}] - \mathcal{L}[\widetilde{w}_o]\right) + q''\left[\begin{array}{c}\mathcal{L}[\widetilde{w}] + \frac{1}{r^2}\frac{\partial^2 \widetilde{w}}{\partial \theta^2} - \frac{3K}{(1+M)}\left(\frac{\partial \widetilde{w}}{\partial r}\right)^2\frac{\partial^2 \widetilde{w}}{\partial r^2} - \frac{K}{r(1+M)}\left(\frac{\partial \widetilde{w}}{\partial r}\right)^3 - \frac{3K}{r^4(1+M)}\left(\frac{\partial \widetilde{w}}{\partial \theta}\right)^2\frac{\partial^2 \widetilde{w}}{\partial \theta^2} \\ + \frac{1}{(1+M)}\left(G_r\Theta + Br\Omega - p'(z)\right)\end{array}\right] = 0, \tag{14}$$

$$(1 - q)\left(\mathcal{L}[\Theta] - \mathcal{L}[\widetilde{\theta}_o]\right) + q''\left[\begin{array}{c}\mathcal{L}[\Theta] + \frac{1}{r^2}\frac{\partial^2 \Theta}{\partial \theta^2} + Nb\left(\frac{\partial \Theta}{\partial r}\frac{\partial \Omega}{\partial r} + \frac{1}{r^2}\frac{\partial \Theta}{\partial \theta}\frac{\partial \Omega}{\partial \theta}\right) \\ + N_t\left(\left(\frac{\partial \Theta}{\partial r}\right)^2 + \frac{1}{r^2}\left(\frac{\partial \Theta}{\partial \theta}\right)^2\right) + G_c\left(\left(\frac{\partial \widetilde{w}}{\partial r}\right)^2 + M\left(\frac{\partial \widetilde{w}}{\partial r}\right)^2 - K\left(\frac{\partial \widetilde{w}}{\partial r}\right)^4\right)\end{array}\right] = 0, \tag{15}$$

$$(1 - q)\mathcal{L}[\Omega - \widetilde{\sigma}_o] + q''\left[\mathcal{L}[\Omega] + \frac{1}{r^2}\frac{\partial^2 \Omega}{\partial \theta^2} + \frac{N_t}{N_b}\left(\frac{\partial^2 \Theta}{\partial r^2} + \frac{1}{r^2}\frac{\partial^2 \Theta}{\partial \theta^2} + \frac{1}{r}\frac{\partial \Theta}{\partial r}\right)\right] = 0. \tag{16}$$

Let us choose the linear operator as $\mathcal{L} = (\partial/\partial r^2) + (1/r)(\partial/\partial r)$. We observe the following initial choices for $w, \overline{\theta}$, and σ:

$$\widetilde{w}_o = V(\log r - \log r_2)(\log r_1 - \log r_2)^{-1},$$
$$\overline{\theta}_o = \overline{\sigma}_o = (\log r_1 - \log r)(\log r_1 - \log r_2)^{-1}. \tag{17}$$

Now, using the perturbation technique on the parameter q'', we have

$$\widetilde{w}(r, \theta, z, q'') = w_o + q''w_1 + \ldots, \tag{18}$$

$$\widetilde{\Theta}(r, \theta, z, q'') = \overline{\theta}_o + q''\overline{\theta}_1 + \ldots, \tag{19}$$

$$\widetilde{\Omega}(r, \theta, z, q'') = \sigma_o + q''\sigma_1 + \ldots. \tag{20}$$

After substituting the abovementioned equations into equations (14)–(16), the solution of velocity w_1 contains a very large output, so it is not displayed here, and the solutions of $\overline{\theta}_1$ and σ_1 are given in Appendix. Now, for $(q'' \longrightarrow 1)$, we approach the final solutions. So, from equations (18)–(20), we get

$$w(r, \theta, z) = w_o + w_1,$$
$$\overline{\theta}_o(r, \theta, z) = \theta_o + \theta_1, \tag{21}$$
$$\sigma(r, \theta, z) = \sigma_o + \sigma_1.$$

The instant value of volume rate of flow $\overline{Q''}$ is taken by

$$\overline{Q''} = 2\pi \int_{r_1}^{r_2} rw dr. \tag{22}$$

The periodic mean volumetric rate of stream Q is found mathematically as follows [30]:

$$\overline{Q''}(z, t) = \frac{Q}{\pi} - \frac{\phi^2}{2} + 2\phi \cos[2\pi(z - t)] + \phi^2\cos^2[2\pi z]. \tag{23}$$

One can get the measure of pressure rate $p'(z)$ by decoding (22) and (23). The dimensionless pressure rise _$\Delta p$is defined as follows [30]:

$$\Delta p = \int_0^1 p'(z)dz. \tag{24}$$

The integration is performed numerically by using Newton–Cotes formulas through the NIntegrate tool on Mathematica 7.

4. Entropy Measures

The expression of entropy generation under the irreversibility of heat exchange, nanoparticles, and viscous effects of the nanofluid is defined as follows [30]:

$$
S'_{\text{gen}} = \frac{K}{T_o^2}\left(\left(\frac{\partial T}{\partial r}\right)^2 + \frac{1}{r^2}\left(\frac{\partial T}{\partial \theta}\right)^2 + \left(\frac{\partial T}{\partial z}\right)^2\right) + \frac{D_B}{C_o}\left(\left(\frac{\partial C}{\partial r}\right)^2 + \frac{1}{r^2}\left(\frac{\partial C}{\partial \theta}\right)^2 + \left(\frac{\partial C}{\partial z}\right)^2\right)
$$
$$
+ \frac{D_B}{T_o}\left(\frac{\partial C}{\partial r}\frac{\partial T}{\partial r} + \frac{1}{r^2}\frac{\partial C}{\partial \theta}\frac{\partial T}{\partial \theta} + \frac{\partial C}{\partial z}\frac{\partial T}{\partial z}\right) + \frac{1}{T_o}\left(S_{rr}\frac{\partial u}{\partial r} + \frac{1}{r}S_{r\theta}\frac{\partial u}{\partial \theta} + S_{rz}\left(\frac{\partial u}{\partial z} + \frac{\partial w}{\partial r}\right) + \frac{1}{r}S_{z\theta}\frac{\partial w}{\partial \theta} + S_{zz}\frac{\partial w}{\partial z} + \frac{u}{r}S_{\theta\theta}\right).
$$

$$(25)$$

The dimensionless factors used in these equations are considered as follows:

$$
N_s = \frac{S'_{\text{gen}}}{S_G},
$$
$$
S_G = \frac{K(T_1 - T_o)^2}{a^2 T_o^2},
$$
$$
\Gamma = \frac{D_B T_o (C_1 - C_o)}{K(T_1 - T_o)}, \tag{26}
$$
$$
\Lambda = \frac{T_1 - T_o}{T_o},
$$
$$
\Omega = \frac{(C_1 - C_o)}{C_o}.
$$

Now, we substitute the abovementioned manipulated factors in equation (25); we have

$$
N_s = \left(\left(\frac{\partial \overline{\theta}}{\partial r'}\right)^2 + \frac{1}{r'^2}\left(\frac{\partial \overline{\theta}}{\partial \theta'}\right)^2 + \delta_O^2\left(\frac{\partial \overline{\theta}}{\partial z'}\right)^2\right) + \frac{\Gamma\Lambda}{\Omega}\left(\left(\frac{\partial \sigma}{\partial r'}\right)^2 + \frac{1}{r'^2}\left(\frac{\partial \sigma}{\partial \theta'}\right)^2 + \delta_O^2\left(\frac{\partial \sigma}{\partial z'}\right)^2\right)
$$
$$
+ \Gamma\left(\frac{\partial \sigma}{\partial r'}\frac{\partial \overline{\theta}}{\partial r'} + \frac{1}{r'^2}\frac{\partial \sigma}{\partial \theta'}\frac{\partial \overline{\theta}}{\partial \theta'} + \delta_O^2\frac{\partial \sigma}{\partial z'}\frac{\partial \overline{\theta}}{\partial z'}\right) \tag{27}
$$
$$
+ \frac{G_c}{\Omega}\left(\delta_o S'_{rr}\frac{\partial u'}{\partial r'} + \delta_o\frac{1}{r'}S'_{r\theta}\frac{\partial u'}{\partial \theta'} + S'_{rz}\left(\delta_O^2\frac{\partial u'}{\partial z'} + \frac{\partial w'}{\partial r'}\right) + \frac{1}{r'}S'_{z\theta}\frac{\partial w'}{\partial \theta'} + \delta_o S'_{zz}\frac{\partial w'}{\partial z'} + \delta_o\frac{u'}{r'}S'_{\theta\theta}\right).
$$

Incorporating the lubrication strategy in the abovementioned equation, it will take the form

$$
N_s = \left(\left(\frac{\partial \overline{\theta}}{\partial r'}\right)^2 + \frac{1}{r'^2}\left(\frac{\partial \overline{\theta}}{\partial \theta'}\right)^2\right) + \frac{\Gamma\Lambda}{\Omega}\left(\left(\frac{\partial \sigma}{\partial r'}\right)^2 + \frac{1}{r'^2}\left(\frac{\partial \sigma}{\partial \theta'}\right)^2\right)
$$
$$
+ \Gamma\left(\frac{\partial \sigma}{\partial r'}\frac{\partial \overline{\theta}}{\partial r'} + \frac{1}{r'^2}\frac{\partial \sigma}{\partial \theta'}\frac{\partial \overline{\theta}}{\partial \theta'}\right) + \frac{G_c}{\Omega}\left(S'_{rz}\frac{\partial w'}{\partial r'} + \frac{1}{r'}S'_{z\theta}\frac{\partial w'}{\partial \theta'}\right).
$$

$$(28)$$

Now, using the values of S'_{rz} and $S'_{z\theta}$ in the abovementioned equation,

$$N_s = \left(\left(\frac{\partial \bar{\theta}}{\partial r'} \right)^2 + \frac{1}{r'^2} \left(\frac{\partial \bar{\theta}}{\partial \theta'} \right)^2 \right) + \frac{\Gamma \Lambda}{\Omega} \left(\left(\frac{\partial \sigma}{\partial r'} \right)^2 + \frac{1}{r'^2} \left(\frac{\partial \sigma}{\partial \theta'} \right)^2 \right) + \Gamma \left(\frac{\partial \sigma}{\partial r'} \frac{\partial \bar{\theta}}{\partial r'} + \frac{1}{r'^2} \frac{\partial \sigma}{\partial \theta'} \frac{\partial \bar{\theta}}{\partial \theta'} \right)$$
$$+ \frac{G_c}{\Omega} \left(\frac{\partial w'}{\partial r'} \frac{\partial w'}{\partial z'} + M \frac{\partial w'}{\partial r'} \frac{\partial w'}{\partial z'} - K \left(\frac{\partial w'}{\partial r'} \right)^3 \frac{\partial w'}{\partial z'} \right). \tag{29}$$

By ignoring the prime symbols of the abovementioned equation, we obtain

$$N_s = \left(\left(\frac{\partial \bar{\theta}}{\partial r} \right)^2 + \frac{1}{r^2} \left(\frac{\partial \bar{\theta}}{\partial \theta} \right)^2 \right) + \frac{\Gamma \Lambda}{\Omega} \left(\left(\frac{\partial \sigma}{\partial r} \right)^2 + \frac{1}{r^2} \left(\frac{\partial \sigma}{\partial \theta} \right)^2 \right) + \Gamma \left(\frac{\partial \sigma}{\partial r} \frac{\partial \bar{\theta}}{\partial r} + \frac{1}{r^2} \frac{\partial \sigma}{\partial \theta} \frac{\partial \bar{\theta}}{\partial \theta} \right)$$
$$+ \frac{G_c}{\Omega} \left(\frac{\partial w}{\partial r} \frac{\partial w}{\partial z} + M \frac{\partial w}{\partial r} \frac{\partial w}{\partial z} - K \left(\frac{\partial w}{\partial r} \right)^3 \frac{\partial w}{\partial z} \right). \tag{30}$$

Moreover, the Bejan number (B_e) is defined as [30]

$$B_e = \left(\left(\frac{\partial \bar{\theta}}{\partial r} \right)^2 + \frac{1}{r^2} \left(\frac{\partial \bar{\theta}}{\partial \theta} \right)^2 \right) \left(\left(\left(\frac{\partial \bar{\theta}}{\partial r} \right)^2 + \frac{1}{r^2} \left(\frac{\partial \bar{\theta}}{\partial \theta} \right)^2 \right) + \frac{\Gamma \Lambda}{\Omega} \left(\left(\frac{\partial \sigma}{\partial r} \right)^2 + \frac{1}{r^2} \left(\frac{\partial \sigma}{\partial \theta} \right)^2 \right) \right.$$
$$+ \Gamma \left(\frac{\partial \sigma}{\partial r} \frac{\partial \bar{\theta}}{\partial r} + \frac{1}{r^2} \frac{\partial \sigma}{\partial \theta} \frac{\partial \bar{\theta}}{\partial \theta} \right) + \frac{G_c}{\Omega} \left(\frac{\partial w}{\partial r} \frac{\partial w}{\partial z} + M \frac{\partial w}{\partial r} \frac{\partial w}{\partial z} - K \left(\frac{\partial w}{\partial r} \right)^3 \frac{\partial w}{\partial z} \right) \right)^{-1}. \tag{31}$$

5. Discussion on Results

This segment is assigned to giving the graphical appearance dedicating the key features of the study by drawing figures against the most pertinent parameters by taking the solution series up to the first two orders of the summation. These results also reflect the physical logic through a mathematical model of the real phenomenon. It also helps the engineers and scientist to work on such problems experimentally. The numerical data of velocity, temperature, entropy, and Bejan number profiles have been presented in Tables 1–4, respectively. From Tables 1 and 2, one can clarify that this study reproduces the results of Nadeem et al. [45] which notify the validity of the current analysis. These tables have been prepared also to estimate the variations of physical properties and imagine a difference of the behavior of Newtonian and non-Newtonian fluids under similar circumstances.

From here, we can clearly find out the viscous effects on the different viscosity model which are also manipulated latterly through graphics. The graphs for velocity of the nanofluid, temperature profile, entropy generation, and Bejan number have also been invoked in this study. The data for obtained quantities have been collected from the achieved analytical solutions. The main focus is kept on analyzing the difference of behavior shown by Newtonian $M = K = 0$ and the Eyring-Powell fluid model $M = K = 0.2$ under the variation of different flow factors. The velocity radial component w can be understood diagrammatically from Figures 1–3. Figures 4–6 exhibit the deportment of temperature distribution θ. The entropy generation analysis can be perceived from graphs of N_S which are placed in Figures 7–10, and the Bejan number variation has been offered through Figures 11–14.

5.1. Velocity Profile. It is observed from Figure 1 that the Eyring-Powell fluid travels faster as compared to the Newtonian fluid under the variation of the Grashof number G_r. It is deeply observed that the rise in values of Grashof number G_r shows that the peak value tends to shift toward the upper cylinder. It is for the verity that uplift in the

TABLE 1: Comparative data of velocity w.

r	Nadeem et al. [45]	Current study when $K = M = 0$	Eyring-Powell fluid when $K = M = 0.2$
0.1	0.93621	0.93621	1.07305
0.2	1.20280	1.20280	1.06557
0.3	1.33809	1.33809	1.23787
0.4	1.36955	1.36955	1.32323
0.5	1.31354	1.31354	1.30876
0.6	1.17896	1.17896	1.20033
0.7	0.97092	0.97092	1.00403
0.8	0.69251	0.69251	0.72443
0.9	0.34569	0.34569	0.36479
1.0	−0.06832	−0.06832	−0.07258
1.1	−0.54873	−0.54873	−0.58602

TABLE 2: Comparative data of temperature profile θ.

r	Nadeem et al. [45]	Current study when $K = M = 0$	Eyring-Powell fluid when $K = M = 0.2$
0.1	−2.65812	−2.65812	0.29081
0.2	0.00717	0.00717	0.00323
0.3	0.94041	0.94041	0.59033
0.4	1.33187	1.33187	0.95761
0.5	1.48432	1.48432	1.15508
0.6	1.51257	1.51257	1.24405
0.7	1.46984	1.46984	1.26306
0.8	1.38411	1.38411	1.23571
0.9	1.27134	1.27134	1.17683
1.0	1.14125	1.14125	1.09610
1.1	1.00000	1.00000	1.00000

TABLE 3: Comparative data of entropy generation profile N_s.

r	Newtonian fluid when $K = M = 0$	Eyring-Powell fluid when $K = M = 0.2$
0.1	50.1938	62.9615
0.2	10.5518	12.1126
0.3	4.34614	4.79125
0.4	2.33529	2.51282
0.5	1.44690	1.53105
0.6	0.97960	1.02353
0.7	0.70457	0.72868
0.8	0.52948	0.54288
0.9	0.41134	0.41857
1.0	0.32800	0.33149
1.1	0.26708	0.26822

TABLE 4: Comparative data of the Bejan number profile B_e.

r	Newtonian fluid when $K = M = 0$	Eyring-Powell fluid when $K = M = 0.2$
0.1	0.18389	0.15935
0.2	0.33130	0.29225
0.3	0.46349	0.41517
0.4	0.58363	0.53109
0.5	0.69574	0.64370
0.6	0.80377	0.75691
0.7	0.91142	0.87478
0.8	1.02216	1.00175
0.9	1.13951	1.14304
1.0	1.26728	1.30530
1.1	1.40994	1.49768
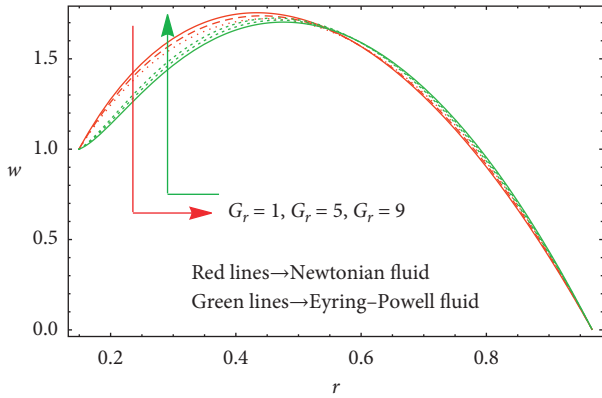
FIGURE 1: Structure of velocity factor w with G_r for fixed $\theta = 0.8$, $\phi = 0.1$, $B_r = 1$, $\delta = 0.1$, $Q = 0.1$, $K = 2$, $M = 5$.

FIGURE 2: Structure of velocity factor w with B_r for fixed $\theta = 0.8$, $\phi = 0.1$, $\delta = 0.1$, $G_r = 1$, $Q = 0.1$, $K = 2$, $M = 5$.

FIGURE 3: Structure of velocity factor w with ϵ for fixed $\theta = 1$, $\phi = 0.1$, $\delta = 0.1$, $G_r = 1$, $B_r = 1$, $Q = 0.25$, $K = 0.1$, $M = 0.1$.

FIGURE 4: Alteration of heat factor $\overline{\theta}$ for N_b when $\theta = 0.1 B_r = 0.5$, $\delta = 0.1$, $\phi = 0.5$, $V = 0.3$, $K = 1$, $M = 1$, $G_c = 1$, $N_t = 0.2$, $\varepsilon = 0.1$.

FIGURE 5: Alteration of heat factor $\overline{\theta}$ for N_t when $\theta = 0.1$, $\phi = 0.5$, $N_b = 0.2$, $\delta = 0.1$, $B_r = 0.5$, $V = 0.3$, $K = 1$, $M = 1$, $G_c = 1$, $\varepsilon = 0.1$.
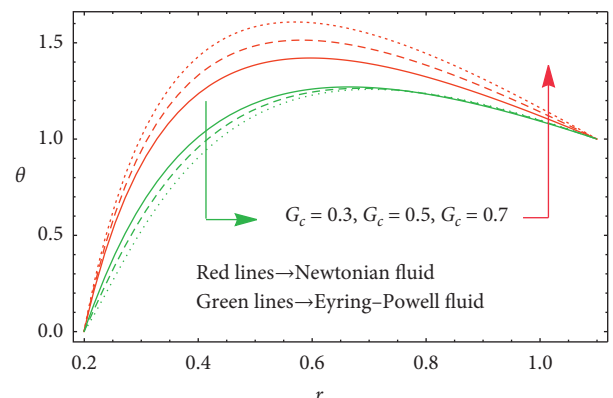
FIGURE 6: Alteration of heat factor $\overline{\theta}$ for G_c when $\theta = 0.1$, $\phi = 0.5$, $N_t = 0.2$, $\delta = 0.1$, $B_r = 0.5$, $V = 0.3$, $K = 1$, $M = 1$, $N_b = 1$, $\varepsilon = 0.1$.

values of G_r buoyancy impacts raising the fluid, which happens to generate free convection. Normally, the density tends to rise with the reduction in temperature, but in case of the Newtonian fluid, the uniform viscosity measures the inverse behavior against the same factor. With the large

value of B_r, the energy dissipates due to thermal enhancement and, hence, rises the flow near the outer cylinder which are observed in Figure 2, and the same observation is reported for viscous and nonlinear fluids. In Figure 3, variation
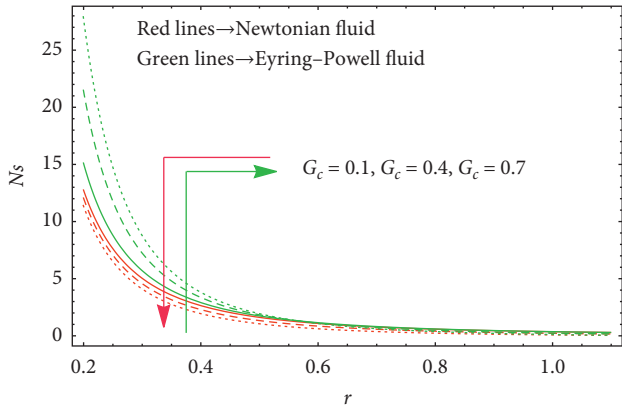
FIGURE 7: For N_s with fixed G_c where $\delta = 0.01, \theta = 0.1, \phi = 0.8, \varepsilon = 0.01, \Gamma = 0.4, N_b = 0.9, N_t = 0.5, B_r = 1, G_r = 1, V = 0.3, K = 2, M = 1, Q = 1, \Lambda = 0.1, \Omega = 0.3.$
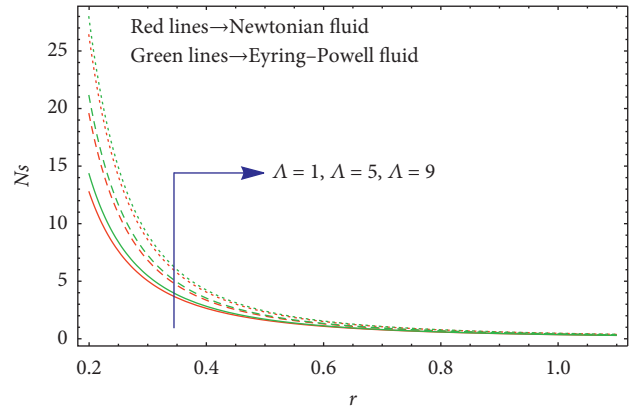
FIGURE 10: For N_s with fixed Λ where $\delta = 0.01, \theta = 0.1, \phi = 0.8, \epsilon = 0.1, \quad G_c = 0.01, N_b = 0.9, N_t = 0.5, B_r = 1, G_r = 3, V = 0.1, K = 1, M = 1, Q = 1, \Gamma = 0.4, \Omega = 0.3.$
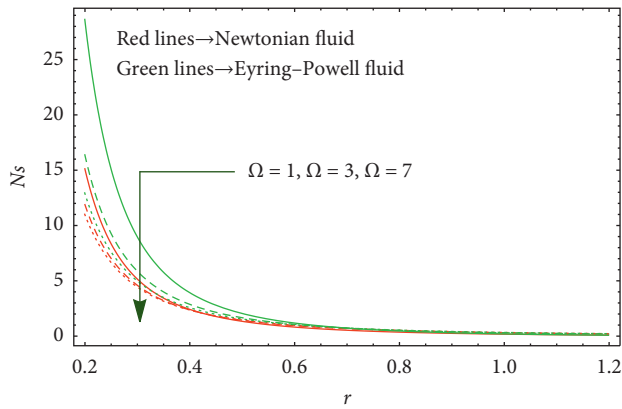
FIGURE 8: For N_s with fixed Ω where $\delta = 1.5, \theta = 0.1, \phi = 2, \varepsilon = 0.01, \Gamma = 0.4, N_b = 0.9, N_t = 0.5, \quad B_r = 1, G_r = 5, V = 0.3, K = 1, M = 1, Q = 1, \Lambda = 1, G_c = 0.01.$
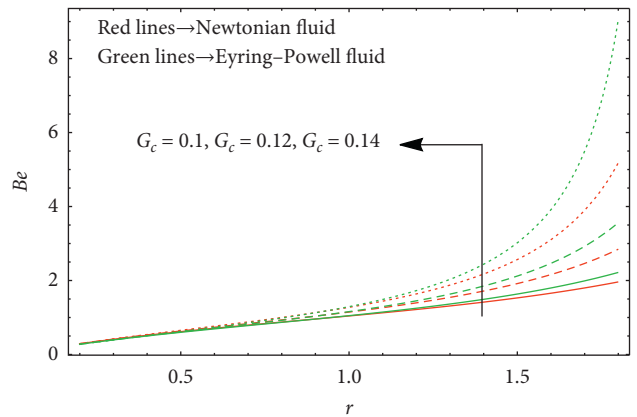
FIGURE 11: For B_e, Be with fixed G_c where $\delta = 0.1, \theta = 0.1, \phi = 0.5, \epsilon = 0.01, \Lambda = 1, N_b = 0.9, N_t = 0.5, B_r = 1, G_r = 5, V = 0.3, K = 1, M = 3, Q = 1, \Gamma = 0.4, \Omega = 0.3.$
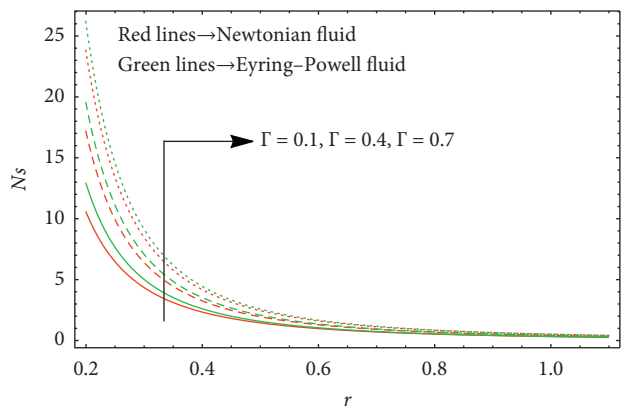
FIGURE 9: For N_s with fixed Γ where $\delta = 0.01, \theta = 0.3, \phi = 0.8, \epsilon = 0.01, G_c = 0.01, N_b = 0.9, N_t = 0.5, \quad B_r = 1, G_r = 3, V = 0.3, K = 1, M = 1, Q = 1, \Lambda = 0.4, \Omega = 0.3.$
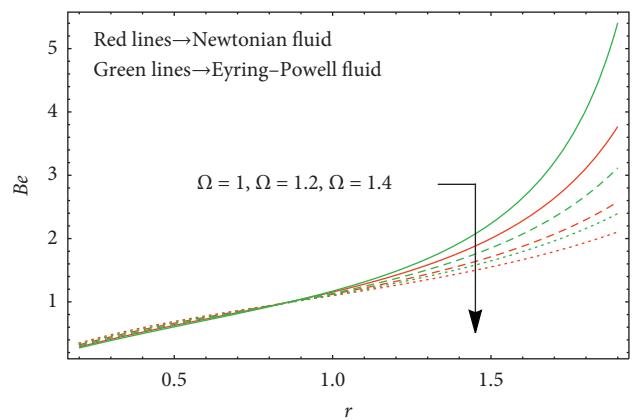
FIGURE 12: For B_e, Be with fixed Ω where $\delta = 0.1, \theta = 0.1, \phi = 0.5, \varepsilon = 0.2, \Lambda = 1, N_b = 0.9, N_t = 0.5, B_r = 1, G_r = 5, V = 0.3, K = 1, M = 3, Q = 1, \Gamma = 0.4, G_c = 0.01.$
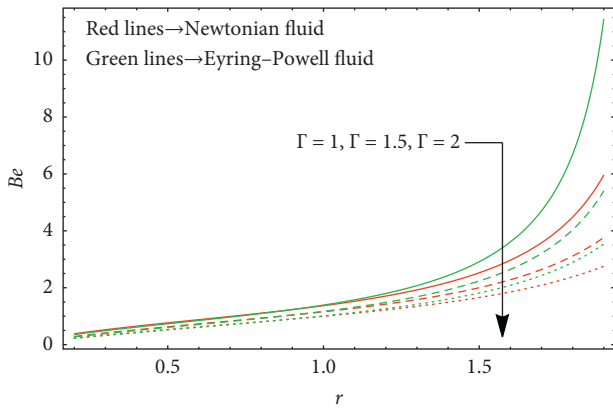
FIGURE 13: For B_e with fixed Γ where $\delta = 0.1, \theta = 0.1, \phi = 0.5, \varepsilon = 0.2, \Lambda = 0.1, N_b = 0.9, N_t = 0.5, B_r = 5, G_r = 1, V = 0.2, K = 1, M = 1, Q = 1, \Omega = 0.3, G_c = 0.01$.
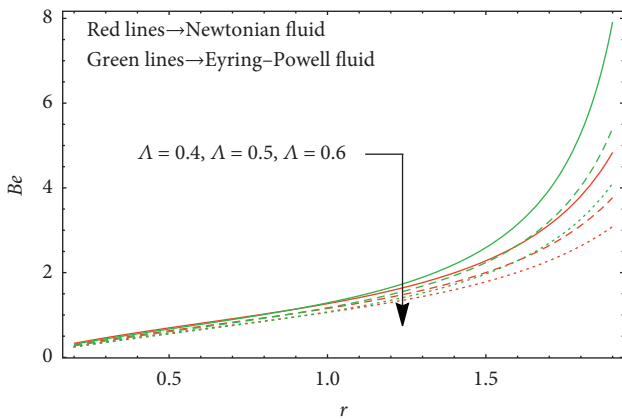
FIGURE 14: For B_e with fixed Λ where $\delta = 0.1, \theta = 0.1, \phi = 0.5, \varepsilon = 0.2, \Gamma = 0.4, N_b = 0.9, N_t = 0.5, B_r = 1, G_r = 5, V = 0.3, K = 1, M = 1, Q = 1, \Omega = 0.3, G_c = 0.01$.

of velocity is observed for the change in eccentricity of the cylinders. It is observed that velocity declines when the eccentricity enhanced, whereas it shows the opposite behavior for the Newtonian fluid case. It is found due to the fact that Eyring-Powell fluid is higher in its viscosity with the detraction of the inner cylinder from the central axis which was not in the case of a linear model.

5.2. Temperature Dispersion Profile.

The variation in temperature distribution is observed from Figures 4–6. The parameters of interest are the Brownian motion factor N_b, thermophoresis coefficient N_t, and nanoparticles Grashof factor G_c. Examining the results, we observe that a more parabolic nature is exhibited in case of temperature profile than velocity curves. With the rise in the value of the Brownian motion parameter N_b, Brownian motion increases that leads to a rise in temperature of the fluid; it is validated from Figure 4. In Figure 5, the variation of the thermophoresis parameter N_t is observed. It is clear from here that temperature increases in the flow domain since the rise in thermal diffusion. The Brinkman number G_c shows a

reduction in temperature in the flow domain due to the rise in energy dissipation due to viscosity diffusion which is contradictory to the Newtonian fluid case where an opposite behavior is provoked (see Figure 6). In the abovementioned three discussed results, it is very obvious that temperature variation for the viscous and nonlinear model of fluid shows a similar situation against N_b and N_t, but there are inverse calculations for the two different phases of fluid just because of the viscosity alteration aspect.

5.3. Entropy Measurements.

The factor which is the most important one for thermal analysis of liquid flow is the dissipation analysis of energy which is defined by the entropy generation parameter (N_s). The variation in entropy generation is graphically displayed for various values $G_C, \Omega, \Gamma,$ and Λ in Figures 7–10, respectively. Entropy generation decreases for larger values of the Brinkman number G_C since temperature profile shows a rise for G_c (Figure 7). From Figure 8, the findings made are described as with the rise in the concentration parameter, entropy decreases. An opposite behavior of the temperature parameter Γ is observed from Figure 9. From Figure 10, it is reflected that the ratio of the concentration parameter Λ is responsible for higher entropy generation. From Figures 7–10, the interesting aspect which is pointed out is that only G_c puts opposite impacts on viscous fluid but other parameters make no prominent change for the Newtonian fluid, and an important notable thing is that entropy peaks are measured in the neighborhood of the inner cylinder which becomes flat at the surface of the outer one.

5.4. Bejan Number Curves.

A graphical representation of B_e is displayed in Figures 11–14. It is defined as the entropy generation due to heat loss divided by total entropy. It is observed from Figure 11 that, with a rise in the Brinkman number G_c, the Bejan Number B_e increases due to the increase in thermal entropy for the rise in temperature which comes from high values of the Brinkman number. It indicates that the contribution of G_c in entropy increases with r for higher values of G_c. Figure 12 shows a decrease in the entropy ratio for large values of Ω, which means that an increase in the concentration parameter produces less entropy due to thermal transfer and more entropy due to collective aspects generating entropy, whereas the temperature parameter Γ and temperature to concentration parameter Λ show an opposite behavior than the Brinkman number as seen from Figures 13 and 14, respectively. On the parallel side, these plots also investigate that the Bejan number curves are reflecting similar results for both the viscous and nonlinear fluids. The only thing that is prominent from these graphs is that the thermal entropy is maximum near the outer cylinder.

6. Concluding Remarks

In the current paper, we have elaborated entropy measures occurring during the biological movement of a viscoelastic-type fluid in between an annular region of two cylinders

having distinct centers. The nanoparticles phenomenon is also taken into consideration. The equations have been assembled in the light of the lubrication strategy and steady format by transformation used in a newly arranged wave frame of reference. In terms of solution, expressions have been analytically gathered with the help of HPM and numerical integration is operated to the expression of pressure rise on mathematical computing the Mathematica tool. The expressions of the entropy generation factor and Bejan number are incorporated by obtained data of viscous dissipation, heat, and energy terms. Comparison of two different models of the fluid is kept under key observation in all figures. The final headings extracted from the whole analysis are reflected in the following:

(i) It is found that the velocity of the substance is getting lower by increasing eccentricity measures of the cylinders and the local temperature Grashof number but higher in front of the local nanoparticles Grashof number. It is also seen that the Newtonian fluid shows opposite readings against the eccentricity and local nanoparticles Grashof number but the same for the temperature Grashof number

(ii) Temperature of the fluid is enhanced for both of the factors, the Brownian motion parameter and thermophoresis parameter, but suppressed against the Brinkman number which is a contradictory result in the Newtonian fluid

(iii) It is noted that entropy generation gets lowered with the increase in the concentration parameter, but it is enhanced under the variation of the Brinkman number, temperature variance representative, and the factor showing the ratio of the thermal factor and concentration factors, but the difference of variation for the viscous fluid is only reported in the case of the Brinkman number

(iv) Bejan number curves are showing totally inverse characteristics than the entropy generation curves

(v) It can be resulted from abovementioned detailed discussion that the Eyring-Powell fluid shows the difference of behavior mostly for viscous dissipation effects in entropy generation and in the presence of nanoparticles, and it travels faster than the viscous fluid

(vi) This study is validated by the result of Nadeem et al. [45] and also compares the characteristics of both the viscous and Eyring-Powell fluid model through special cases $K = M = 0$

Abbreviations

S_{LM}:   Stress tensor of the Eyring-Powell fluid
μ: Viscosity of the fluid
V_p: Velocity field
x^i: Coordinates in fixed frame
β, c: Material constants for the fluid
p: Pressure term

a: Radius of the outer tube
c_1:   Wave speed
λ: Wavelength
δ: Radius of the inner tube
t: Time factor
u, v, w: Dimensionless velocity components
r, θ, z: Dimensionless cylindrical coordinates
b: Wave amplitude
ϵ: Dimensionless eccentricity factor
R_e: Reynolds number
T, T_0, T_1:   Temperature factors
C, C_0, C_1:   Nanoparticles concentration
$(\rho c)_f$:   Fluid heat capacity
$(\rho c)_p$:   Nanoparticles heat capacity
P_r: Prandtl number
S_c: Schmidt number
k: Thermal conductivity of the fluid
B_r: Local temperature Grashof number
G_r: Local nanoparticle Grashof number
N_b: Brownian motion parameter
N_t: Thermophoresis parameter
G_c: Brinkman number
M, K: Eyring-Powell dimensionless factors
V: Velocity of the inner tube
r_1, r_2:   Inner and outer boundary functions
q'':   Homotopy parameter
$\mathscr{L}$:   Linear operator
$\overline{\theta}$:   Dimensionless temperature
σ: Dimensionless volume fraction.

Data Availability

No data were used to support this study.

Conflicts of Interest

The authors declare no conflicts of interest.

Authors' Contributions

All the authors contributed equally.

Acknowledgments

References

[1] M. B. Arain, M. M. Bhatti, A. Zeeshan, T. Saeed, and A. Hobiny, "Analysis of arrhenius kinetics on multiphase flow between a pair of rotating circular plates," *Mathematical Problems in Engineering*, vol. 2020, Article ID 2749105, 17 pages, 2020.

[2] M. Irfan, M. A. Farooq, A. Mushtaq, and Z. H. Shamsi, "Unsteady MHD bionanofluid flow in a porous medium with thermal radiation near a stretching/shrinking sheet," *Mathematical Problems in Engineering*, vol. 2020, Article ID 8822999, 14 pages, 2020.

[3] H. Maleki, M. R. Safaei, A. A. A. A. Alrashed, and A. Kasaeian, "Flow and heat transfer in non-Newtonian nanofluids over porous surfaces," *Journal of Thermal Analysis and Calorimetry*, vol. 135, no. 3, pp. 1655–1666, 2019.

[4] H. Maleki, M. R. Safaei, H. Togun, and M. Dahari, "Heat transfer and fluid flow of pseudo-plastic nanofluid over a moving permeable plate with viscous dissipation and heat absorption/generation," *Journal of Thermal Analysis and Calorimetry*, vol. 135, no. 3, pp. 1643–1654, 2019.

[5] H. K. Yoon, *An experimental and analytical study of heat transfer to polymer solutions in turbulent pipe flows under constant wall heat flux*, Ph.D. thesis, Oklahoma State University, Stillwater, OK, USA, 1986.

[6] E. Y. Kwack, *Effect of Weissenberg number on turbulent heat transfer and friction factor of viscoelastic fluids*, Ph.D. thesis, University of Illinois at Chicago, Chicago, IL, USA, 1983.

[7] M. Khan, M. Irfan, W. A. Khan, and A. S. Alshomrani, "A new modeling for 3D Carreau fluid flow considering nonlinear thermal radiation," *Results in Physics*, vol. 7, pp. 2692–2704, 2017.

[8] S. Matsuhisa and R. B. Bird, "Analytical and numerical solutions for laminar flow of the non-Newtonian ellis fluid," *AIChE Journal*, vol. 11, no. 4, pp. 588–595, 1965.

[9] H. K. Yoon and A. J. Ghajar, "A note on the Powell-Eyring fluid model," *International Communications in Heat and Mass Transfer*, vol. 14, no. 4, pp. 381–390, 1987.

[10] M. Patel and M. G. Timol, "Numerical treatment of Powell–Eyring fluid flow using method of satisfaction of asymptotic boundary conditions (MSABC)," *Applied Numerical Mathematics*, vol. 59, no. 10, p. 2592, 2009.

[11] T. Hayat, M. Farooq, A. Alsaedi, and Z. Iqbal, "Melting heat transfer in the stagnation point flow of powell-Eyring fluid," *Journal of Thermophysics and Heat Transfer*, vol. 27, no. 4, pp. 761–766, 2013.

[12] M. Jalil, S. Asghar, and S. M. Imran, "Self similar solutions for the flow and heat transfer of Powell-Eyring fluid over a moving surface in a parallel free stream," *International Journal of Heat and Mass Transfer*, vol. 65, pp. 73–79, 2013.

[13] S. Islam, A. Shah, C. Y. Zhou, and I. Ali, "Homotopy perturbation analysis of slider bearing with Powell-Eyring fluid," *Zeitschrift für Angewandte Mathematik und Physik*, vol. 60, no. 6, p. 1178, 2009.

[14] S. Hina, M. Mustafa, T. Hayat, and A. Alsaedi, "Peristaltic transport of Powell-Eyring fluid in a curved channel with heat/mass transfer and wall properties," *International Journal of Heat and Mass Transfer*, vol. 101, pp. 156–165, 2016.

[15] T. Hayat, Z. Hussain, M. Farooq, and A. Alsaedi, "Magnetohydrodynamic flow of Powell-Eyring fluid by a stretching cylinder with Newtonian heating," *Thermal Science*, vol. 22, no. 1, pp. 371–382, 2018.

[16] A. H. Shapiro, "Pumping and retrograde diffusion in peristaltic waves," in *Proceedings of the Workshop in Ureteral Reflux in Children*, pp. 109–126, Washington, DC, USA, 1967.

[17] T. W. Latham, "Fluid motions in a peristaltic pump," Doctoral dissertation, Massa-Chusetts Institute of Technology, Cambridge, MA, USA, 1966.

[18] M. Y. Jaffrin and A. H. Shapiro, "Peristaltic pumping," *Annual Review of Fluid Mechanics*, vol. 3, no. 1, pp. 13–37, 1961.

[19] L. Zhang, M. M. Bhatti, M. Marin, and K. S. Mekheimer, "Entropy analysis on the blood flow through anisotropically tapered arteries filled with magnetic zinc-oxide (ZnO) nanoparticles," *Entropy*, vol. 22, no. 10, p. 1070, 2020.

[20] K. Javid, M. Hassan, M. Imran Asjad et al., "Rheological effects of biomimetic propulsion on fluid flow: an application of bio-

[21] R. Ellahi, M. M. Bhatti, and C. M. Khalique, "Three-dimensional flow analysis of Carreau fluid model induced by peristaltic wave in the presence of magnetic field," *Journal of Molecular Liquids*, vol. 241, pp. 1059–1068, 2017.

[22] T. Hayat, B. Ahmed, A. Alsaedi, and F. M. Abbasi, "Numerical study for peristalsis of Carreau-Yasuda nanomaterial with convective and zero mass flux condition," *Results in Physics*, vol. 8, pp. 1168–1177, 2018.

[23] J. Prakash and D. Tripathi, "Electroosmotic flow of Williamson ionic nanoliquids in a tapered microfluidic channel in presence of thermal radiation and peristalsis," *Journal of Molecular Liquids*, vol. 256, pp. 352–371, 2018.

[24] A. Zeeshan, N. Ijaz, T. Abbas, and R. Ellahi, "The sustainable characteristic of bio-bi-phase flow of peristaltic transport of MHD Jeffrey fluid in the human body," *Sustainability*, vol. 10, no. 8, p. 2671, 2018.

[25] A. Tanveer, T. Hayat, F. Alsaadi, and A. Alsaedi, "Mixed convection peristaltic flow of Eyring-Powell nanofluid in a curved channel with compliant walls," *Computers in Biology and Medicine*, vol. 82, pp. 71–79, 2017.

[26] M. M. Bhatti, A. Zeeshan, R. Ellahi, and G. C. Shit, "Mathematical modeling of heat and mass transfer effects on MHD peristaltic propulsion of two-phase flow through a Darcy-Brinkman-Forchheimer porous medium," *Advanced Powder Technology*, vol. 29, no. 5, pp. 1189–1197, 2018.

[27] M. Afridi, M. Qasim, A. Wakif, and A. Hussanan, "Second law analysis of dissipative nanofluid flow over a curved surface in the presence of Lorentz force: utilization of the Chebyshev-Gauss-Lobatto spectral method," *Nanomaterials*, vol. 9, no. 2, p. 195, 2019.

[28] S. Nazari, R. Ellahi, M. M. Sarafraz, M. R. Safaei, A. Asgari, and O. A. Akbari, "Numerical study on mixed convection of a non-Newtonian nanofluid with porous media in a two liddriven square cavity," *Journal of Thermal Analysis and Calorimetry*, vol. 140, pp. 1121–1141, 2019.

[29] S. R. R. Reddy, P. B. A. Reddy, and A. M. Rashad, "Activation energy impact on chemically reacting Eyring–Powell nanofluid flow over a stretching cylinder," *Arabian Journal for Science and Engineering*, vol. 45, pp. 5227–5242, 2020.

[30] A. Riaz, A. Gul, I. Khan et al., "Mathematical analysis of entropy generation in the flow of viscoelastic nanofluid through an annular region of two asymmetric annuli having flexible surfaces," *Coatings*, vol. 10, no. 3, p. 213, 2020.

[31] M. Sheikholeslami, M. Jafaryar, S. Saleem, Z. Li, A. Shafee, and Y. Jiang, "Nanofluid heat transfer augmentation and exergy loss inside a pipe equipped with innovative turbulators," *International Journal of Heat and Mass Transfer*, vol. 126, pp. 156–163, 2018.

[32] S. U. Choi, "Nanofluids: from vision to reality through research," *Journal of Heat Transfer*, vol. 131, no. 3, 2009.

[33] R. K. Shukla and V. K. Dhir, "Numerical study of the effective thermal conductivity of nanofluids," in *Proceedings of the ASME 2005 Summer Heat Transfer Conference Collocated with the ASME 2005 Pacific Rim Technical Conference and Exhibition on Integration and Packaging of MEMS, NEMS, and Electronic Systems*, pp. 449–457, American Society of Mechanical Engineers Digital Collection, San Francisco, CA, USA, July 2005.

[34] A. Behzadmehr, M. Saffar-Avval, and N. Galanis, "Prediction of turbulent forced convection of a nanofluid in a tube with uniform heat flux using a two phase approach," *International*

Journal of Heat and Fluid Flow, vol. 28, no. 2, pp. 211–219, 2007.

[35] J. Buongiorno, "Convective transport in nanofluids," *Journal of Heat Transfer*, vol. 128, no. 3, pp. 240–250, 2006.

[36] Y. M. Chu, U. Khan, A. Zaib, and S. H. Shah, "Numerical and computer simulations of cross-flow in the streamwise direction through a moving surface comprising the significant impacts of viscous dissipation and magnetic fields: stability analysis and dual solutions," *Mathematical Problems in Engineering*, vol. 2020, Article ID 8542396, 11 pages, 2020.

[37] A. Riaz, H. Alolaiyan, and A. Razaq, "Convective heat transfer and magnetohydro-dynamics across a peristaltic channel coated with nonlinear nanofluid," *Coatings*, vol. 9, no. 2, p. 816, 2019.

[38] U. Rashid, T. Abdeljawad, H. Liang, A. Iqbal, M. Abbas, and M. Siddiqui, "The shape effect of gold nanoparticles on squeezing nanofluid flow and heat transfer between parallel plates," *Mathematical Problems in Engineering*, vol. 2020, Article ID 9584854, 12 pages, 2020.

[39] S. U. Khan, K. Al-Khaled, and M. M. Bhatti, "Bioconvection analysis for flow of Oldroyd-B nanofluid configured by a convectively heated surface with partial slip effects," *Surfaces and Interfaces*, vol. 23, Article ID 100982, 2021.

[40] R. Naz, M. Noor, Z. Shah, M. Sohail, P. Kumam, and P. Thounthong, "Entropy generation optimization in MHD pseudoplastic fluid comprising motile microorganisms with stratification effect," *Alexandria Engineering Journal*, vol. 59, no. 1, pp. 485–496, 2020.

[41] M. A. Abbas and I. Hussain, "Statistical analysis of the mathematical model of entropy generation of magnetized nanofluid," *Inventions*, vol. 4, no. 2, p. 32, 2019.

[42] M. Abbas, Y. Bai, M. Rashidi, and M. Bhatti, "Analysis of entropy generation in the flow of peristaltic nanofluids in channels with compliant walls," *Entropy*, vol. 18, no. 3, p. 90, 2016.

[43] R. Ellahi, M. Raza, and N. S. Akbar, "Study of peristaltic flow of nanofluid with entropy generation in a porous medium," *Journal of Porous Media*, vol. 20, no. 5, 2017.

[44] T. Hayat, S. Nawaz, and A. Alsaedi, "Entropy generation and endoscopic effects on peristalsis with modified Darcy's law," *Physica A: Statistical Mechanics and Its Applications*, vol. 536, p. 120846, 2019.

[45] S. Nadeem, A. Riaz, R. Ellahi, and N. S. Akbar, "Effects of heat and mass transfer on peristaltic flow of a nanofluid between eccentric cylinders," *Applied Nanoscience*, vol. 4, no. 4, pp. 393–404, 2014.

Research Article

A Simplified Finite Difference Method (SFDM) Solution via Tridiagonal Matrix Algorithm for MHD Radiating Nanofluid Flow over a Slippery Sheet Submerged in a Permeable Medium

M. Asif Farooq [ORCID],[1] A. Salahuddin,[1] Asif Mushtaq [ORCID],[2] and M. Razzaq[3]

[1]*Department of Mathematics, School of Natural Sciences (SNS), National University of Sciences and Technology (NUST), Sector H-12, Islamabad 44000, Pakistan*
[2]*Seksjon for Matematikk, Nord Universitet, Bodø 8026, Norway*
[3]*Department of Mathematics, Lahore University of Management Sciences (LUMS), Lahore 54792, Pakistan*

Correspondence should be addressed to Asif Mushtaq; asif.mushtaq@nord.no

In this paper, we turn our attention to the mathematical model to simulate steady, hydromagnetic, and radiating nanofluid flow past an exponentially stretching sheet. A numerical modeling technique, simplified finite difference method (SFDM), has been applied to the flow model that is based on partial differential equations (PDEs) which is converted to nonlinear ordinary differential equations (ODEs) by using similarity variables. For the resultant algebraic system, the SFDM uses the tridiagonal matrix algorithm (TDMA) in computing the solution. The effectiveness of numerical scheme is verified by comparing it with solution from the literature. However, where reference solution is not available, one can compare its numerical results with the results of MATLAB built-in package *bvp4c*. The velocity, temperature, and concentration profiles are graphed for a variety of parameters, i.e., Prandtl number, Grashof number, thermal radiation parameter, Darcy number, Eckert number, Lewis number, and Brownian and thermophoresis parameters. The significant effects of the associated emerging thermophysical parameters, i.e., skin friction coefficient, local Nusselt number, and local Sherwood numbers are analyzed and discussed in detail. Numerical results are compared from the available literature and found a close agreement with each other. It is found that the Eckert number upsurges the velocity curve. However, the dimensionless temperature declines with the Grashof number. It is also shown that the SFDM gives good results when compared with the results obtained from *bvp4c* and results from the literature.

1. Introduction

The stretching sheet flow has several interesting engineering applications such as in a chemical engineering plant's polymer handling unit and in metallurgy for the metal working system. Crane [1] researched the continuous two-dimensional boundary layer flow induced by stretching the sheet moving in its own plane at a velocity linearly varying from a fixed point on the sheet. Immediately after Crane [1], abundant work in this direction is reported and discussed.

Makinde and Aziz [2] explored the effect of boundary layer flow over linearly stretching nanofluid while Mustafa et al. [3] concentrated on boundary layer flow for an exponentially stretching sheet and solved the issue using the technique of the homotopy analysis method to calculate analytical solutions. Realistically, as discussed by Gupta and Gupta [4], stretching a plastic sheet may not necessarily be linear.

Since Choi and Eastman's pioneering research [5], surveys associated to nanofluid dynamics have risen significantly in contemporary times due to the low thermal conductivity of prevalent heat transfer liquids, which causes the device to function inefficiently and consume additional energy. A new method has been introduced to optimize machine operation by dispersing solid particles with a base fluid. Nanofluid defines the suspension in standard base liquids such as water, ethylene glycol, and motor oil of strong particles of a nanometer size. References from [2, 3, 5] give a

thorough overview of the nanofluid literature. Innovative fluid types are needed in these days to achieve more effective output. Sheikholeslami and Bhatti [6] studied forced convection of nanofluid considering nanoparticles' shape impacts. The Brownian motion impact on nanofluid flow within a porous cavity was recently regarded by Sheikholeslami [7]. He found that convective flow enhances with increase in Darcy number.

The research of electrically conductive fluid flow has many applications in engineering issues such as MHD generators, plasma research, nuclear reactors, geothermal energy extraction, and aerodynamic boundary layer control [8]. Reddy et al. [9] studied the effects of frictional and irregular temperature on non-Newtonian MHD fluid flows owing to stretched surface.

Mishra and Singh [10] addressed dual solutions of mixed convection flow with momentum and heat slip over a permeable shrinking cylinder. When studying the flow models in nanoscales or microscales, the interaction of the fluid surface is mostly controlled by models of slip flow. These models were checked from asymptotic solution using the Boltzmann technique where the internal kinetic solution matches the outer (i.e., bulk) Navier–Stokes solution, and matching is only achieved when the slip/jump coefficient is regarded at the border or surface (Hadjiconstantinou [11, 12]). Therefore, the slip coefficients are the result of these assessments. Due to its simplicity, the slip flow phenomenon is always preferred to no-slip situations. The Navier–Stokes equations are still valid here, and only the boundary conditions change in compliance with the slip flow model. With the newly suggested second-order slip flow model, Fang et al. [13] evaluated the slip flow over a permeable shrinking surface. Ullah et al. [14] examined the two-dimensional flow of Reiner–Philippoff fluid thin films over an unstable stretching sheet in the variable heat distribution and radiation.

Khan et al. [15] provided thermal radiation and viscous dissipation impacts on the unstable nanofluid boundary layer flow over a stretching sheet. In this research, they accounted for the viscous dissipation impact and discovered that the heat boundary layer thickness is increased by increasing the values of Eckert number. Ibrahim and Shankar [16] evaluated the impact of thermophoresis on Brownian fluid movement owing to stretching sheet.

Several technological systems depend on the impact of buoyancy. Makinde et al. [17] examined combined impacts of buoyancy force, convective warming, Brownian movement, thermophoresis, and magnetic field on stagnation point stream and heat exchange due to nanofluid stream towards an extending sheet. Ali and Yousef [18] analyzed laminar mixed convection heat transfer from continuously stretching vertical surface with energy functional form for wall temperature by considering the impact of buoyancy. Mixed convection heat transfer from an exponentially stretching sheet was explored by Partha et al. [19]. They also analyzed influence of buoyancy along with viscous dissipation, and the flow is governed by the mixed convection parameter (Gr/Re^2). The effect of viscous dissipation in natural convection process has been investigated by Gebhart

[20] and Gebhart and Mollendorf [21]. Magyari and Keller [22] analytically as well as numerically evaluated the continuous free fluid flow and thermal transfer from an exponentially stretching vertical surface with an exponential temperature distribution. Unsteady flow of thermally radiating nanofluid over nonlinearly stretching sheet was discussed by Seth et al. [23]. They noted that the nanofluid's velocity curve depends on the unsteadiness, velocity slip, and stretching velocity nonlinearity. Makinde et al. [24] reported the two-dimensional unsteady MHD radiating electrically conducting fluid past a slippery stretching sheet embedded in a porous medium. Using the explicit finite difference scheme, they solved the system of higher-order nonlinear PDEs. Hamid and Khan [25] have discussed the thermophysical properties of the flow of Williamson nanofluid and solved their problem numerically. They concluded that the stronger the magnetic field resulted in decreasing of boundary layer thickness. Some other references in this direction can be consulted in [26–28].

Qing et al. [29] researched the entropy generation of nanofluid owing to a magnetic field over a stretching surface. Hosseini et al. [30] discussed heat transfer of nanofluid flow in microchannel heat sink (MCHS) in the presence of a magnetic field. The influence of chemical reaction and heat generation/ absorption on mixed convective flow of nanofluid past an exponentially stretched surface has been examined by Eid [31], and numerical solutions have been obtained by utilizing the shooting technique along with the Runge–Kutta–Fehlberg method. Afify and Elgazery [32] investigated numerically the boundary layer flow of Maxwell nanofluid with convective boundary condition and heat absorption. The result showed that nanoparticle concentration reduces with higher chemical reaction parameter whereas a reverse pattern is noted for temperature. Reviews of viscous fluid flow problems for nonlinear stretching sheet have been presented by Prasad et al. [33], Afzal [34], and Nandeppanavar et al. [35]. Nadeem and Lee [36] studied analytically the problem of steady boundary layer flow of nanofluid over an exponentially stretching surface including the effects of Brownian motion and thermophoresis parameters. The influence of solar energy radiations in the time-dependent Hiemenz flow of nanofluid over a wedge was discussed by Mohamad et al. [37]. In [38], Sheikholeslami et al. discussed natural convection inside a sinusoidal annulus. Tripathi et al. [39] reported shape effects of nanoparticle on blood flow in a microvascular flow. Bhatti et al. [40] have discussed the movement of gyrotactic microorganism in a magnetized nanofluid over a plate. Ibrahim and Anbessa [41] discussed Casson nanofluid with Hall and Ion slip effects. Ibrahim and Negera [42] investigated Williamson nanofluid over a stretching cylinder with activation energy. For similar work in this direction, the reader referred to [43].

In all previous studies, a usual course is followed in one way or the other and discussion is intended towards linearly or nonlinearly stretching sheets in the absence of some important emerging parameters. The aim of this work is to add numerical methodology, SFDM, in the literature so that it can be applicable to many problems containing coupled ODEs. To the best of our knowledge, the current mathematical model along with numerical consideration has not been discussed before.

The paper is planned in the following order. Section 2 commences by laying out the mathematical model of the physical problem. Numerical procedure is opted and discussed in Section 3. In the same section, the detailed description of the SFDM is given. As a consequence of numerical calculations, results and discussion are followed in Section 4. At the end of the paper, the conclusions are presented in Section 5.

2. Mathematical Formulation

We deliberate a two dimensional, steady, incompressible, laminar, and MHD flow of an electrically conducting nanofluid occupied over a slippery stretching sheet submerged in a porous medium. The geometrical description of fluid flow over a sheet is shown in Figure 1. In the figure, x-axis has been chosen along the sheet and y-axis normal to it.

After making use of these assumptions, the set of continuity, momentum, energy, and concentration equations incorporating the Buongiorno model is written as follows [44]:

$$\partial_x(u) + \partial_y(v) = 0, \tag{1}$$

$$uu_x + vu_y = vu_{yy} - \frac{\sigma B_o^2 u}{\rho} - \frac{vu}{K} + g\beta(T - T_\infty), \tag{2}$$

$$uT_x + vT_y = \frac{k}{\rho C_p}(T_{yy}) + \frac{v}{C_p}(u_y)^2 + \frac{\sigma B_o^2 u^2}{\rho C_p} + \frac{vu^2}{C_p K} - \frac{1}{\rho C_p}q_{r,y} + \frac{Q(T - T_\infty)}{\rho C_p} + \tau\left[D_B(C_y T_y) + \frac{D_T}{T_\infty}(T_y)^2\right], \tag{3}$$

$$uC_x + vC_y = D_B(C_{yy}) + \frac{D_T}{T_\infty}(T_{yy}), \tag{4}$$

here the velocity components (u, v) are considered along and normal of the sheet. μ is the coefficient of viscosity, ρ is the density of the fluid, σ is the electrical conductivity of the fluid, T is fluid's temperature, K is the permeability, β is the thermal expansion coefficient, k is the thermal conductivity, C_p is the specific heat capacity at constant pressure, q_r is the radioactive heat flux, Q is the heat source coefficient, C is the concentration, and $\tau = (\rho C)_p/(\rho C)_f$, where $(\rho C)_p$ and $(\rho C)_f$ are heat capacities of the nanofluid and base fluid, respectively. Also, D_B and D_T are Brownian and thermophoretic diffusion coefficients, respectively. T_∞ is the ambient fluid temperature, and C_∞ is the ambient fluid concentration.

2.1. Boundary Conditions. The preceding mathematical model allows the following boundary condition:

$$u(x, 0) = U_w + \frac{\mu}{L_1}u_y,$$

$$v(x, 0) = 0,$$

$$T(x, 0) = T_w,$$

$$C(x, 0) = C_w, \tag{5}$$

$$u \longrightarrow 0,$$

$$T \longrightarrow T_\infty,$$

$$C \longrightarrow C_\infty, \quad \text{as } y \longrightarrow \infty,$$

where L_1 is the slip length. Here, $U_w = U_0 e^{x/L}$ is the stretching velocity, where U_0 is the reference velocity. And, $T_w = T_\infty + T_0 e^{x/(2L)}$ is the variable temperature at the sheet with T_0 being a reference temperature. Also, $C_w = C_\infty + C_0 e^{x/(2L)}$ is the variable concentration at the sheet with C_0 being a constant.

2.2. Method of Solution. By introducing similarity variables η, $\psi(\eta)$, $\theta(\eta)$, and $\phi(\eta)$ as dimensionless independent variable, stream function, temperature and concentration for the momentum, energy and concentration equations (1)–(4), and in the boundary conditions (5),

$$\eta = \sqrt{\frac{U_0}{2vL}}e^{x/(2L)}y,$$

$$\psi(\eta) = \sqrt{2U_0 vL}e^{x/(2L)}f(\eta),$$

$$u = U_0 f' e^{x/L},$$

$$v = -\sqrt{\frac{U_0 v}{2L}}e^{x/(2L)}(f'\eta + f), \tag{6}$$

$$\theta(\eta) = \frac{T - T_\infty}{T_0}e^{-x/(2L)},$$

$$\phi(\eta) = \frac{C - C_\infty}{C_0}e^{-x/(2L)},$$

gives the following nonlinear ordinary differential equations:

$$f''' + ff'' - 2(f')^2 - \left(M + \frac{1}{Da}\right)f' + 2Gr\theta = 0, \quad (7)$$

$$\Pr(\theta f' - f\theta') - (1 + Nr)\theta'' - \Pr Ec(f'')^2$$
$$- \Pr Ec\left(M + \frac{1}{Da}\right)(f')^2 \quad (8)$$
$$- 2\Pr S\theta - \Pr Nb\phi'\theta' - \Pr Nt\theta'^2 = 0,$$

$$\phi'' + \frac{Nt}{Nb}\theta'' + Le(f\phi' - f'\phi) = 0, \quad (9)$$

$$\begin{aligned}
f(\eta) &= 0, \\
f'(\eta) &= 1 + \lambda f''(\eta), \\
\theta(\eta) &= 1, \\
\phi(\eta) &= 1, \quad \text{as } \eta \longrightarrow 0,
\end{aligned} \quad (10)$$

$$\begin{aligned}
f'(\eta) &\longrightarrow 0, \\
\theta(\eta) &\longrightarrow 0, \\
\phi(\eta) &\longrightarrow 0, \quad \text{as } \eta \longrightarrow \infty.
\end{aligned} \quad (11)$$

In the above equations, various parameters appear which are M, Pr, Nt, Nb, Gr, Da, Nr, Ec, S, Le, and λ. In order, these are the magnetic parameter, Prandtl number, thermophoresis parameter, Brownian parameter, Grashof number, Darcy's number, thermal radiation effect, heat source or sink, Lewis number, and the slip parameter. Their expressions are grouped as follows:

$$\begin{aligned}
\Pr &= \frac{\mu C_p}{k}, \\[6pt]
M &= \frac{2L\sigma B_0^2}{U_w \rho}, \\[6pt]
Nt &= \frac{\tau D_T (T_w - T_\infty)}{T_\infty \nu}, \\[6pt]
Nb &= \frac{\tau D_B (C_w - C_\infty)}{\nu}, \\[6pt]
Le &= \frac{\nu}{D_B}, \\[6pt]
Gr &= \frac{\beta g L (T_w - T_\infty)}{U_w^2}, \\[6pt]
Da &= \frac{K U_w}{2\nu L}, \\[6pt]
Ec &= \frac{U_w^2}{T_w C_p}, \\[6pt]
S &= \frac{QL}{U_w \rho C_p}.
\end{aligned} \quad (12)$$
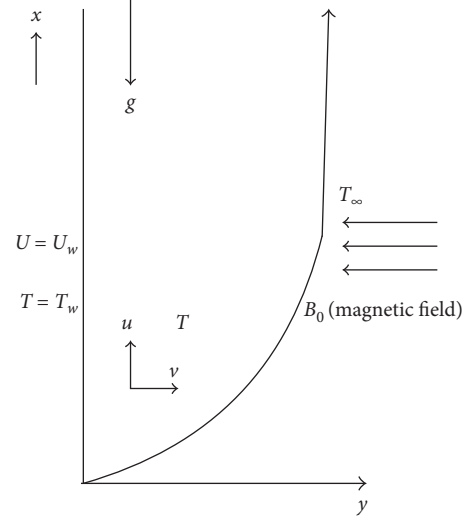
FIGURE 1: Schematic diagram of the problem.

2.3. Physical Quantities.

Now that the flow equations are known, the physical quantities that measures roughness, heat transfer rate, and concentration rate at the sheet can be obtained. First, the skin friction coefficient C_f is given by

$$C_f = \frac{\nu}{U_w^2}\left(\frac{\partial u}{\partial y}\right)_{y=0}. \quad (13)$$

Second, the local Nusselt number Nu_x is written as

$$Nu_x = -(1 + Nr)\frac{x}{(T_w - T_\infty)}\left(\frac{\partial T}{\partial y}\right)_{y=0}. \quad (14)$$

Third, the local Sherwood number Sh_x is defined as

$$Sh_x = -\frac{x}{(C_w - C_\infty)}\left(\frac{\partial C}{\partial y}\right)_{y=0}. \quad (15)$$

After substituting similarity variables in (13)–(15), this yields the expressions as follows:

$$\begin{aligned}
C_f &= \frac{1}{\sqrt{2\mathrm{Re}_x}}f''(0), \\[6pt]
Nu_x &= -(1 + Nr)\sqrt{\frac{x\mathrm{Re}_x}{2L}}\theta'(0), \\[6pt]
Sh_x &= -\sqrt{\frac{x\mathrm{Re}_x}{2L}}\phi'(0).
\end{aligned} \quad (16)$$

Here, $\mathrm{Re}_x = Ux/\nu$ is a local Reynolds number.

3. Numerical Procedures

In search of solution for the above problem given in equations (7)–(9), the only plausible way to compute solution is numerically. We find numerical solutions by using

two numerical techniques. The first numerical method we use is the SFDM, and the second one is the famous algorithm written in MATLAB and commonly known as *bvp4c*. Thus, due details on the SFDM will be presented first followed by brief description on *bvp4c*.

3.1. SFDM. This work is influenced by Na [45] in which some numerical results are displayed for linear ODEs. For coupled nonlinear ODEs, we expand these ideas theoretically and execute them in MATLAB. The algorithm with necessary details for the SFDM is as follows:

(1) Reduce third-order ODEs to a pair of ODEs of the first and second order

(2) Use Taylor series to linearize the system of nonlinear ODEs

(3) Substitute finite difference formulas in the derivatives

(4) Finally, solve the algebraic system by TDMA

The results are shown for $N = 1000$ grid points. Generally, the domain length varies with different parameters. However, the domain value $\eta = 7$ seems enough to show steady state results. To initiate the SFDM procedure, we assume $f' = \overline{F}$ in equation (7) and we get

$$\frac{d^2\overline{F}}{d\eta^2} = -f\frac{d\overline{F}}{d\eta} + 2\overline{F}^2 + \left(M + \frac{1}{Da}\right)\overline{F} - 2Gr\theta, \tag{17}$$

Define a new variable as

$$\xi_1\left(\eta, \overline{F}, \overline{F}'\right) = -f\frac{d\overline{F}}{d\eta} + 2\overline{F}^2 + \left(M + \frac{1}{Da}\right)\overline{F} - 2Gr\theta \tag{18}$$

and approximate $(d\overline{F}/d\eta)$ by forward difference approximation with constant width h

$$\xi_1\left(\eta, \overline{F}, \overline{F}'\right) = -f_i\left(\frac{\overline{F}_{i+1} - \overline{F}_i}{h}\right) + 2\overline{F}_i^2 + \left(M + \frac{1}{Da}\right)\overline{F}_i - 2Gr\theta_i. \tag{19}$$

The coefficients are written as

$$\overline{A}_n = -\frac{\partial f}{\partial \overline{F}'} = -(-f) = f = f_i,$$

$$\overline{B}_n = -\frac{\partial f}{\partial \overline{F}} = -4\overline{F} - \left(M + \frac{1}{Da}\right),$$

$$\overline{B}_n = -4\overline{F}_i - \left(M + \frac{1}{Da}\right), \tag{20}$$

$$\overline{D}_n = \xi_1\left(\eta, \overline{F}, \overline{F}'\right) + \overline{B}_n\overline{F}_i + \overline{A}_n\frac{\overline{F}_{i+1} - \overline{F}_i}{h}.$$

Simplifying the above, we reach at

$$\overline{a}_i\overline{F}_{i-1} + \overline{b}_i\overline{F}_i + \overline{c}_i\overline{F}_{i+1} = \overline{r}_i, \quad i = 1, 2, 3, \ldots, N, \tag{21}$$

where

$$\begin{aligned}
\overline{a}_i &= 2 - h\overline{A}_n, \\
\overline{b}_i &= 2h^2\overline{B}_n - 4, \\
\overline{c}_i &= 2 + h\overline{A}_n, \\
\overline{r}_i &= 2h^2\overline{D}_n.
\end{aligned} \tag{22}$$

In the matrix-vector form, it is written in compact as

$$\overline{A}\,\overline{F} = \overline{s}, \tag{23}$$

where

$$\overline{A} = \begin{bmatrix} \overline{b}_1 & \overline{c}_1 & & & \\ \overline{a}_2 & \overline{b}_2 & \overline{c}_2 & & \\ & & \cdots & & \\ & & & \overline{a}_{N-2} & \overline{b}_{N-2} & \overline{c}_{N-2} \\ & & & & \overline{a}_{N-1} & \overline{b}_{N-1} \end{bmatrix},$$

$$\overline{F} = \begin{bmatrix} \overline{F}_1 \\ \overline{F}_2 \\ \cdot \\ \cdot \\ \overline{F}_{N-1} \end{bmatrix}, \tag{24}$$

$$\overline{s} = \begin{bmatrix} \overline{s}_1 \\ \overline{s}_2 \\ \cdot \\ \cdot \\ \overline{s}_{N-1} \end{bmatrix}.$$

The matrix $\overline{A}$ is a tridiagonal matrix and is written in LU factorization as

$$\overline{A} = \overline{LU}, \tag{25}$$

where

$$\overline{L} = \begin{bmatrix} \overline{\beta}_1 & & & \\ \overline{a}_2 & \overline{\beta}_2 & & \\ & \cdots & & \\ & & \overline{a}_{N-2} & \overline{\beta}_{N-2} \\ & & & \overline{a}_{N-1} & \overline{\beta}_{N-1} \end{bmatrix},$$

$$\overline{U} = \begin{bmatrix} 1 & \overline{\gamma}_1 & & & \\ & 1 & \overline{\gamma}_2 & & \\ & & \cdots & & \\ & & & 1 & \overline{\gamma}_{N-2} \\ & & & & 1 \end{bmatrix}, \tag{26}$$

where $\overline{L}$ and $\overline{U}$ are the lower and upper triangular matrices, respectively. Here, the unknowns $(\overline{\beta}_i, \overline{\gamma}_i)$, $i = 1, 2, \ldots, N - 1$ are to be related as

$$\overline{\beta}_1 = -1 - \frac{\overline{\lambda}}{h},$$

$$\overline{\gamma}_1 = \frac{\overline{\lambda}}{\overline{\beta}_1 h}, \qquad (27)$$

$$\overline{\beta}_i = \overline{b}_i - \overline{a}_i \overline{\gamma}_{i-1}, \quad i = 2, 3, \ldots, N - 1,$$

$$\overline{\beta}_i \overline{\gamma}_i = \overline{c}_i, \quad i = 2, 3, \ldots, N - 2.$$

After defining these relations, (23) becomes

$$\overline{LUF} = \overline{s},$$
$$\overline{UF} = \overline{z}, \qquad (28)$$
$$\overline{Lz} = \overline{s},$$

and we have

$$\begin{bmatrix} \overline{\beta}_1 & & & & \\ \overline{a}_2 & \overline{\beta}_2 & & & \\ & & \cdots & & \\ & & & \overline{a}_{N-2} & \overline{\beta}_{N-2} \\ & & & & \overline{a}_{N-1} \end{bmatrix} \begin{bmatrix} \overline{z}_1 \\ \overline{z}_2 \\ \overline{z}_3 \\ \cdot \\ \cdot \\ \cdot \\ \overline{z}_{N-2} \\ \overline{z}_{N-1} \end{bmatrix} = \begin{bmatrix} \overline{s}_1 \\ \overline{s}_2 \\ \overline{s}_3 \\ \cdot \\ \cdot \\ \cdot \\ \overline{s}_{N-2} \\ \overline{s}_{N-1} \end{bmatrix}. \qquad (29)$$

The unknown elements of $\overline{s}$ are written as

$$\overline{z}_1 = \frac{\overline{s}_1}{\overline{\beta}_1, \overline{s}_i} = \frac{\overline{s}_i - \overline{a}_i \overline{z}_{i-1}}{\overline{\beta}_i}, \quad i = 2, 3, \ldots, N - 1,$$

$$\begin{bmatrix} 1 & \overline{\gamma}_1 & & & \\ & 1 & \overline{\gamma}_2 & & \\ & & \cdots & & \\ & & & 1 & \overline{\gamma}_{N-2} \\ & & & & 1 \end{bmatrix} \begin{bmatrix} \overline{F}_1 \\ \overline{F}_2 \\ \cdot \\ \cdot \\ \cdot \\ \overline{F}_{N-2} \\ \overline{F}_{N-1} \end{bmatrix} = \begin{bmatrix} \overline{z}_1 \\ \overline{z}_2 \\ \cdot \\ \cdot \\ \cdot \\ \overline{z}_{N-2} \\ \overline{z}_{N-1} \end{bmatrix}. \qquad (30)$$

We get

$$\overline{F}_{i-1} = \overline{z}_{i-1},$$
$$\overline{F}_i = \overline{z}_i - \overline{\gamma}_i \overline{F}_{i+1}, \quad i = N - 2, N - 3, \ldots, 3, 2, 1, \qquad (31)$$

which is a solution of (17). We can easily find f from $f' = \overline{F}$ which is in the discretization form written as follows:

$$\frac{f_{i+1} - f_i}{h} = \overline{F}_i, \qquad (32)$$

which gives a required solution of (7). A similar procedure can also be opted for solutions θ and ϕ. For the sake of brevity, we only present coefficients for these ODEs and leave the details which follows on the same line as presented above. For example, we have the energy and concentration equation as follows:

$$\frac{d^2\theta}{d\eta^2} =$$

$$\frac{1}{1+N_r}\left\{\Pr\left(\theta\overline{F}-f\frac{d\theta}{d\eta}\right)-\Pr Ec\left(\frac{d\overline{F}}{d\eta}\right)^2-\Pr Ec\left(M+\frac{1}{Da}\right)\overline{F}^2-2\Pr S\theta-\Pr Nb\frac{d\phi}{d\eta}\frac{d\theta}{d\eta}-\Pr Nt\left(\frac{d\theta}{d\eta}\right)^2\right\},$$

$$\xi_2(\eta,\theta,\theta')=\frac{1}{1+N_r}\left\{\Pr\left(\theta_i\overline{F}_i-f_i\frac{\theta_i-\theta_{i-1}}{h}\right)-\Pr Ec\left(\frac{\overline{F}_i-\overline{F}_{i-1}}{d\eta}\right)^2-\Pr Ec\left(M+\frac{1}{Da}\right)\overline{F}_i^2-2\Pr S\theta_i\right\}$$

$$-\frac{1}{1+N_r}\left\{\Pr Nb\frac{\phi_i-\phi_{i-1}}{h}\frac{\theta_i-\theta_{i-1}}{h}-\Pr Nt\left(\frac{\theta_i-\theta_{i-1}}{d\eta}\right)^2\right\},$$

$$A_{nn}=-\frac{\partial f}{\partial\theta'}=-\frac{1}{1+N_r}\left\{-\Pr f-\Pr Nb\frac{d\phi}{d\eta}-2\Pr Nt\frac{d\theta}{d\eta}\right\},$$

$$A_{nn}=-\frac{\partial f}{\partial\theta'}=\frac{1}{1+N_r}\left\{\Pr f_i+\Pr Nb\frac{d\phi_i-\phi_{i-1}}{h}+2\Pr Nt\frac{d\theta_i-\theta_{i-1}}{h}\right\},$$ (33)

$$B_{nn}=-\frac{\partial f}{\partial\theta}=\frac{-1}{1+N_r}\{\Pr\overline{F}-2\Pr S\},$$

$$B_{nn}=-\frac{\partial f}{\partial\theta}=\frac{-1}{1+N_r}\{\Pr\overline{F}_i-2\Pr S\},$$

$$\frac{d^2\phi}{d\eta^2}=\frac{-Nt}{Nb}\frac{d^2\theta}{d\eta^2}-Le\left(f\frac{d\phi}{d\eta}-\overline{F}\phi\right),$$

$$\xi_3(\eta,\phi,\phi')=\frac{-Nt}{Nb}\frac{\theta_{i-1}-2\theta_i+\theta_{i+1}}{d\eta^2}-Le\left(f_i\frac{\phi_i-\phi_{i-1}}{h}-\overline{F}_i\phi_i\right).$$

Similarly, the coefficients for (9) are written as

$$A_{nnn}=Lef_i,$$
$$B_{nnn}=-Le\overline{F}_i.$$ (34)

Boundary conditions are discretized as

$$\overline{F}_1=1+\lambda\left(\frac{\overline{F}_2-\overline{F}_1}{h}\right).$$ (35)

3.2. bvp4c. This section presents the second numerical method of the studied problem given in (7)–(9) which subject to the boundary conditions (10) and (11). We use MATLAB built-in function *bvp4c* for this purpose. For description and details of this method, one can refer to [46]. Let us define the variables as

$$y_1=f,$$
$$y_2=f',$$
$$y_3=f'',$$
$$y_4=\theta,$$ (36)
$$y_5=\theta',$$
$$y_6=\phi,$$
$$y_7=\phi'.$$

The system of first-order equations is given as follows:

$$
\begin{aligned}
y_1' &= f' = y_2, \\
y_2' &= f'' = y_3, \\
y_3' &= f''' = -y_1 y_3 + 2(y_2)^2 + \left(M + \frac{1}{Da}\right) y_2 - 2Gr y_4, \\
y_4' &= \theta' = y_5, \\
y_5' &= \theta'' = \frac{1}{1 + Nr}\left(\Pr y_4 y_2 - \Pr y_1 y_5 - \Pr Ec y_3^2 - \left(M + \frac{1}{Da}\right) Ec \Pr y_2^2 - 2\Pr S y_4 - \Pr Nb y_7 y_5 - Nt \Pr y_5^2\right), \\
y_6' &= \phi' = y_7, \\
y_7' &= \phi'' = Le y_6 y_2 - Le y_1 y_7 - \frac{Nt}{Nb} y_5',
\end{aligned}
\tag{37}
$$

and boundary conditions are given as follows:

$$
\begin{aligned}
y_0(1) &= 0, \\
y_0(2) - 1 - \lambda y_0(3) &= 0, \\
y_0(4) - 1 &= 0, \\
y_0(6) - 1 &= 0, \\
y_{\inf}(2) &= 0, \\
y_{\inf}(4) &= 0, \\
y_{\inf}(6) &= 0.
\end{aligned}
\tag{38}
$$

4. Results and Discussion

In this section, the focus is to analyze the role of embedded parameters on the velocity, temperature, and concentration. Results of the current study are displayed in the tabular as well as graphical form.

For $-f''(0)$, the results are compared with the solutions published in the literature, and this comparison is listed in Table 1. The results demonstrate that the numerical values of SFDM are accurate and closely agreed with one another.

In Table 2, when the admissible values of the magnetic parameter increase resultantly, the skin friction coefficient also increases. However, reduction in both temperature and concentration gradients is observed. One can also observe that the magnitude of the local Nusselt and the local Sherwood numbers increases and the skin friction coefficient decreases with the rise of values of Darcy's number. Grashof number enhances local Nusselt number and local Sherwood number whereas this reduces the skin friction coefficient. However, Lewis number Le causes slight change in skin friction coefficient while concentration gradient and wall temperature gradient reduce.

It is also evident from Table 2 that local Sherwood number increases by increasing Nt, but the effect is seen to be reverse on skin friction coefficient while local Nusselt number remains constant. The skin friction coefficient, local Nusselt number, and local Sherwood number decrease with respect to thermophoretic parameter Nb (see Table 3). From Table 3, one can observe an increase in local Sherwood number along the range of Ec. This also causes a surge in local Sherwood number whereas its effect on the skin friction coefficient and local Nusselt number is opposite.

4.1. Effect of Magnetic Parameter M. Figure 2 shows a decreasing trend in velocity profiles against M $(2 \le M \le 8)$ to the point where $\eta \approx 2.50$. After this point, the boundary layer thickness demonstrates the opposite behaviour. Figure 3 illustrates an increase in thermal boundary layer thickness due to an increase in a magnetic parameter. However, minor increase in concentration profile is presented in Figure 4. The reduction of the momentum boundary layer is strongly influenced by the magnetic parameter strength which produces Lorentz force and that offer resistance to the flow.

4.2. Effects of Darcy Number Da. Darcy number Da characterizes the strength of permeability of the porous medium. Figures 5 and 6 depict increasing values of Darcy number $(0.5 \le Da \le 15.5)$ that increase the velocity profile while concentration profile decreases. However, the temperature decreases in the boundary layer region. Thus, the thickness of the thermal boundary layer decreases as shown in Figure 7.

4.3. Effects of Lewis Number Le. Figure 8 displays the variations of velocity profiles due to the variations in the values of Lewis number $(0.5 \le Le \le 2)$. It is observed that the velocity profile decreases with an increase in Le. For $Le \ge 1$, the mass transport is dominant that resists the flow. One can also observe that in Figure 9, the temperature profile as well

TABLE 1: The comparison of skin friction coefficient to previous data for $\lambda = S = Ec = Nr = Gr = 0$ and $Da = \infty$ and for various values Pr, M, Nb, Nt, and Le.

						Present result	
Pr	M	Nb	Nt	Le	Sharif et al. [47]	bvp4c	SFDM
0.7	0	0.5	0.5	1	1.28183	1.2818089	1.2646694
—	0.1	—	—	—	1.32104	1.3210148	1.3030810
—	0.2	—	—	—	1.35895	1.3589575	1.3402296
—	0.3	—	—	—	1.39581	1.3957745	1.3762525

TABLE 2: Results for $-f''(0)$, $-\theta'(0)$, and $-\phi'(0)$ obtained by fixing values of parameters $Pr = 6.2$, $Nt = 2$, $Ec = 0.2$, $Nb = 8$, $S = 0.1$, $Nr = 5$, and $\lambda = 3$.

				bvp4c			SFDM		
M	Da	Gr	Le	$-f''(0)$	$-\theta'(0)$	$-\phi'(0)$	$-f''(0)$	$-\theta'(0)$	$-\phi'(0)$
1	4	0.3	8	0.1945	0.0100	2.2070	0.1945175	0.0099219	2.196740
1.1	—	—	—	0.1977	0.0094	2.1769	0.1977045	0.0093481	2.1669909
1.2	—	—	—	0.2008	0.0088	2.1477	0.2007573	0.0087879	2.1380916
1.3	—	—	—	0.2037	0.0083	2.1193	0.2036818	0.0082440	2.1100172
1	5	0.3	8	0.1929	0.0103	2.2223	0.1928713	0.0102230	2.2119414
—	6	—	—	0.1918	0.0105	2.2327	0.1917538	0.010423	2.2221985
—	7	—	—	0.1910	0.0106	2.2401	0.1909458	0.0105674	2.2295847
—	8	—	—	0.1903	0.0107	2.2458	0.1903340	0.0106763	2.2351598
1	5	0.4	8	0.1754	0.0121	2.3805	0.1753267	0.0121091	2.3689312
−2	—	0.5	—	0.1592	0.0136	2.5161	0.1591568	0.0136077	2.5033457
—	—	0.6	—	0.1441	0.0149	2.6354	0.1440571	0.0148417	2.6216478
—	—	0.7	—	0.1299	0.0159	2.7426	0.1298239	0.0158828	2.7277798
1	5	0.7	9	0.1302	0.0159	2.9079	0.1301768	0.0149605	2.8912397
—	—	—	13	0.1313	0.0124	3.4900	0.1312932	0.0124113	3.4660959
—	—	—	17	0.1321	0.0108	3.9863	0.1321069	0.0108305	3.9552333
—	—	—	21	0.1328	0.0097	4.4263	0.1327388	0.0097292	4.3880280

TABLE 3: Results for $-f''(0)$, $-\theta'(0)$, and $-\phi'(0)$ obtained by various values of parameters $Pr = 6.2$, $M = 2$, $Da = 5$, $Gr = 0.7$, $Nr = 5$, $Le = 8$, and $\lambda = 3$.

			bvp4c			Simplified FDM		
Nb	Nt	Ec	$-f''(0)$	$-\theta'(0)$	$-\phi'(0)$	$-f''(0)$	$-\theta'(0)$	$-\phi'(0)$
2	2	0.2	0.1660	0.0270	2.4876	0.1682158	0.0746442	2.4973830
6	—	—	0.1648	0.0148	2.4800	0.1647564	0.0148202	2.4679691
8	—	—	0.1641	0.0104	2.4777	0.1640238	0.0104038	2.4656461
10	—	—	0.1636	0.0081	2.4774	0.1635227	0.0081378	2.4652570
10	0.5	0.1	0.1656	0.0106	2.4477	0.1655962	0.0105904	2.4350691
—	1	—	0.1650	0.0106	2.4580	0.1649419	0.0106063	2.4455417
—	1.5	—	0.1644	0.0106	2.4668	0.1643695	0.0106205	2.4546071
—	2	—	0.1639	0.0106	2.4745	0.163872	0.0106326	2.4624605
15	2	0	0.1634	0.0086	2.4739	0.1632997	0.0086251	2.4618319
—	—	0.1	0.1631	0.0070	2.4763	0.1630272	0.0069807	2.4641318
—	—	0.2	0.1628	0.0053	2.4787	0.1627443	0.0053296	2.4665070
—	—	0.3	0.1625	0.0037	2.4812	0.1624500	0.0036714	2.4689664

as the thickness of the boundary layer initially increases and then decreases with an increase due to Lewis number. This implies that the momentum boundary layer thickness decreases when a ratio of thermal diffusivity to a mass diffusivity increases. Figure 10 demonstrates the nanoparticle volume fraction for several values of Lewis number Le accompanying reduction in concentration boundary layer thickness.

4.4. Effects of Grashof Number Gr. The Gr approximates the ratio of buoyancy to viscous forces and represents how dominant is buoyancy force which is responsible for the conviction comparing to viscous forces. Either convection or viscous forces are dominant, and the results are displayed in Figures 11–13. It can be observed that temperature and concentration decrease with the Grashof number $Gr (3 \leq Gr \leq 6.5)$, but there is an abrupt change in a velocity profile.

$Pr = 6.2, Da = 5, Gr = 2, Nr = 5, Nb = 2, Nt = 0.5,$
$Ec = 0.1, Le = 5, \lambda = 0.5, S = 0.1$

FIGURE 2: Velocity profiles for different M.

$Pr = 6.2, Da = 5, Gr = 2, Nr = 5, Nb = 2, Nt = 0.5,$
$Ec = 0.1, Le = 5, \lambda = 3, S = 0.1$
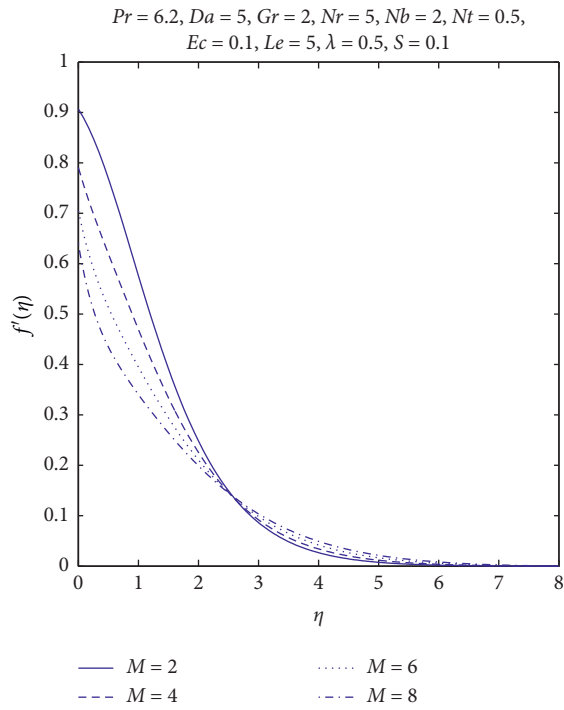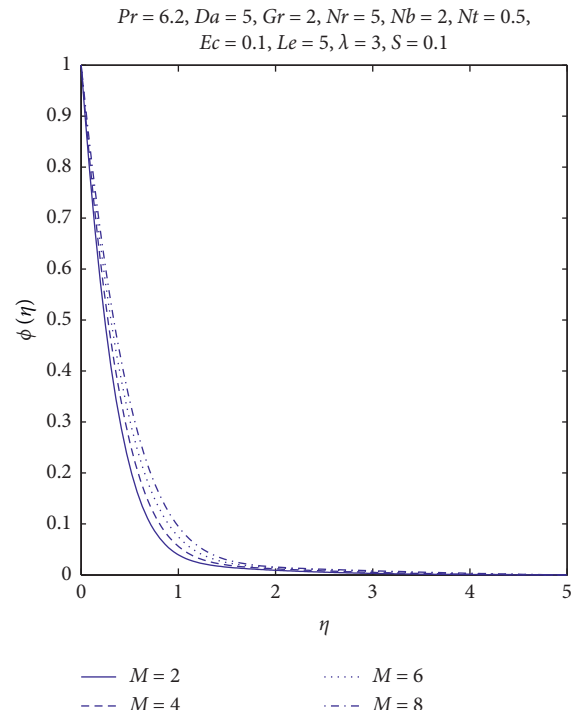
FIGURE 4: Concentration profiles for different M.

$Pr = 6.2, Da = 5, Gr = 2, Nr = 5, Nb = 2, Nt = 0.5,$
$Ec = 0.1, Le = 5, \lambda = 3, S = 0.1$
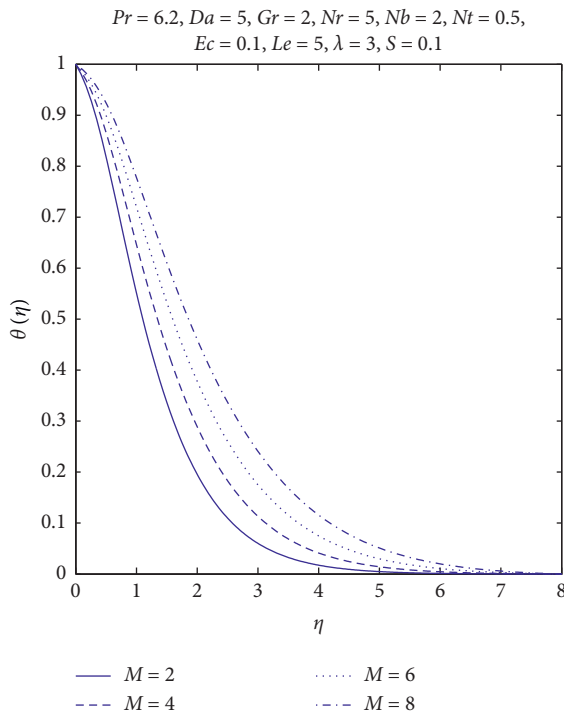
FIGURE 3: Temperature profiles for different M.

$Pr = 6.2, M = 2, Gr = 2, Nr = 5, Nb = 2, Nt = 0.5,$
$Ec = 0.1, Le = 5, \lambda = 3, S = 0.1$
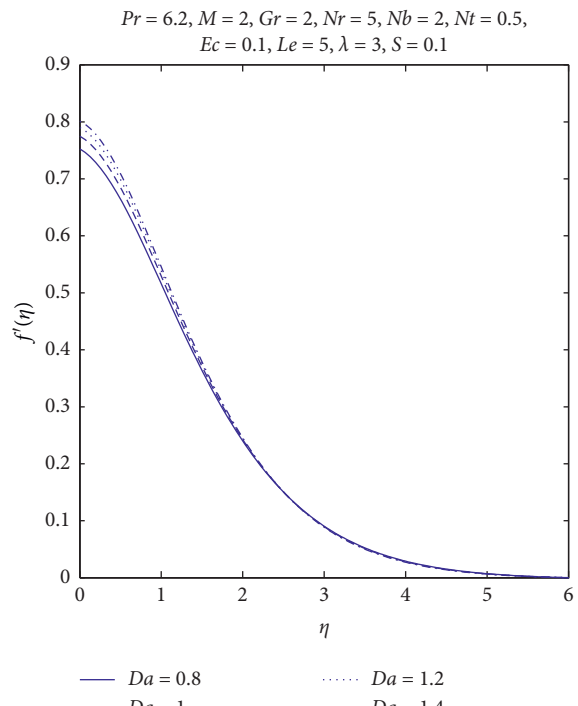
FIGURE 5: Velocity profiles for different Da.

4.5. Effects of Nt. Figure 14 shows that the velocity profile increases with Nt in the range $(0.5 \leq Nt \leq 2)$. Figure 15 illustrates the variations of thermophoretic parameter on temperature profile. It validated the fact that thermophoretic parameter enhances the temperature profile. Since the thermophoretic phenomenon transferred nanoparticles from hot surface to the cold region, it resulted in increasing the temperature of the fluid. Figure 16 suggests that a stronger thermophoretic parameter produces minor change in nanoparticle volume fraction.

$Pr = 6.2, M = 2, Gr = 2, Nr = 5, Nb = 2, Nt = 0.5,$
$Ec = 0.1, Le = 5, \lambda = 3, S = 0.1$
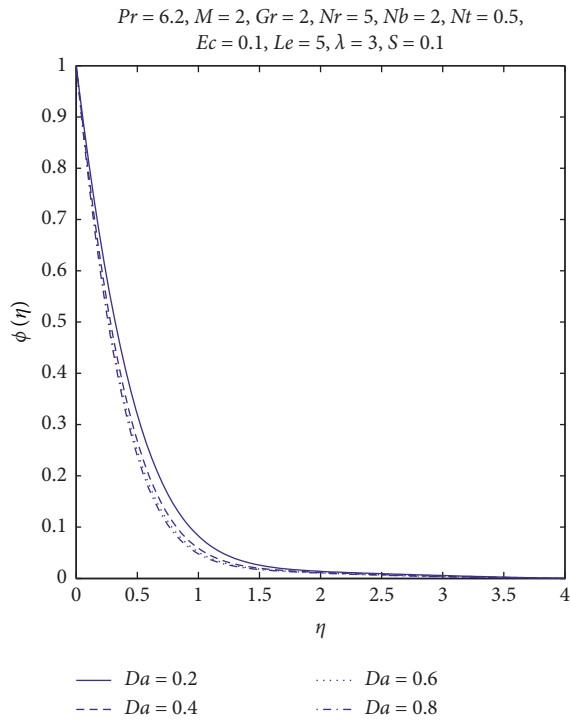
Figure 6: Concentration profiles for different Da.

$Pr = 6.2, M = 2, Gr = 2, Nr = 5, Nb = 10, Nt = 2,$
$Ec = 0.1, Da = 5, \lambda = 3, S = 0.1$
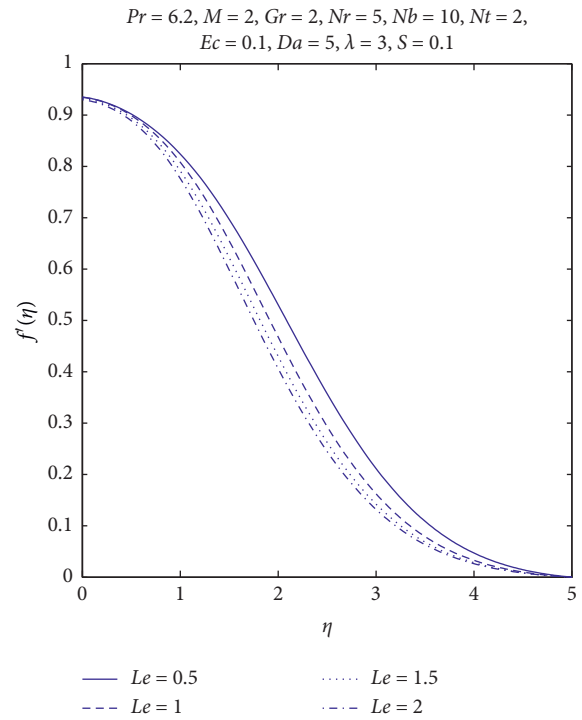
Figure 8: Velocity profiles for different Le.

$Pr = 6.2, M = 2, Gr = 2, Nr = 5, Nb = 2, Nt = 0.5,$
$Ec = 0.1, Le = 5, \lambda = 3, S = 0.1$

Figure 7: Temperature profiles for different Da.

$Pr = 6.2, M = 2, Gr = 2, Nr = 5, Nb = 10, Nt = 2,$
$Ec = 0.1, Da = 5, \lambda = 3, S = 0.1$
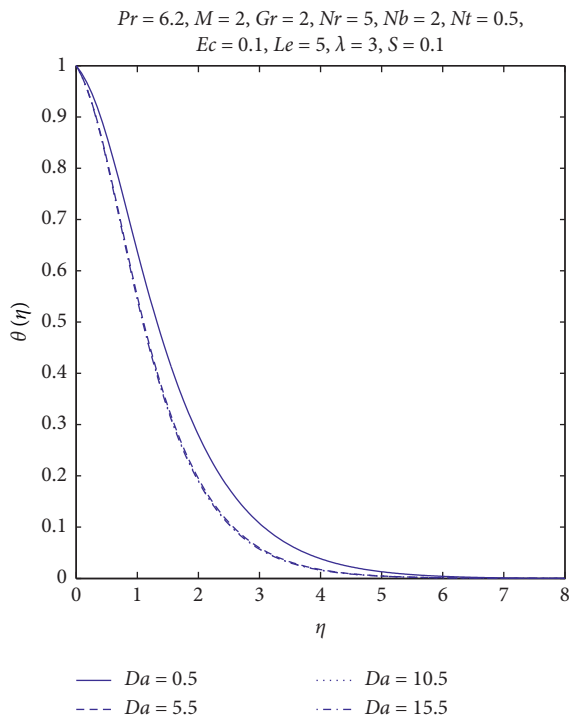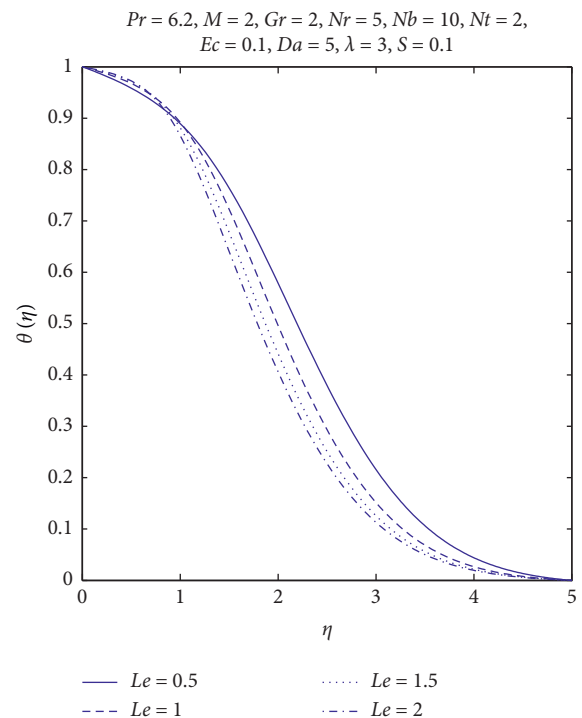
Figure 9: Temperature profiles for different Le.

4.6. Effects of Nb. Incremental Brownian parameter $Nb\,(5 \leq Nb \leq 20)$ causes slight change in nanoparticles volume fraction which increases the velocity profile as presented in Figures 17 and 18. Figure 19 suggests that a stronger Brownian motion is responsible for an increase in thermal boundary layer thickness.

4.7. Effects of Eckert Number Ec. Eckert number plays an important role in high speed flows for which viscous dissipation is significant. It gives relative importance of the kinetic energy in heat transfer flows. For $Ec \ll 1$, the energy equation gives the balance between conduction and convection. From Figures 20–22, the effects of this dissipation on velocity,

$Pr = 6.2, M = 2, Gr = 2, Nr = 5, Nb = 10, Nt = 2,$
$Ec = 0.1, Da = 5, \lambda = 3, S = 0.1$

— $Le = 0.5$ ⋯⋯ $Le = 1.5$
- - - $Le = 1$ -·- $Le = 2$
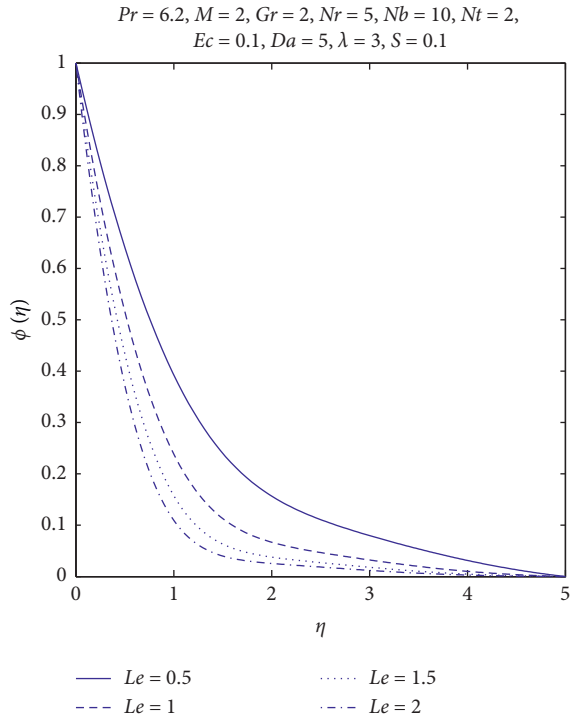
FIGURE 10: Concentration profiles for different Le.

$Pr = 6.2, M = 2, Da = 5, Nr = 5, Nb = 10, Nt = 0.5,$
$Ec = 0.1, Le = 5, \lambda = 3, S = 0.1$

— $Gr = 3$ ⋯⋯ $Gr = 5$
- - - $Gr = 4$ -·- $Gr = 6$
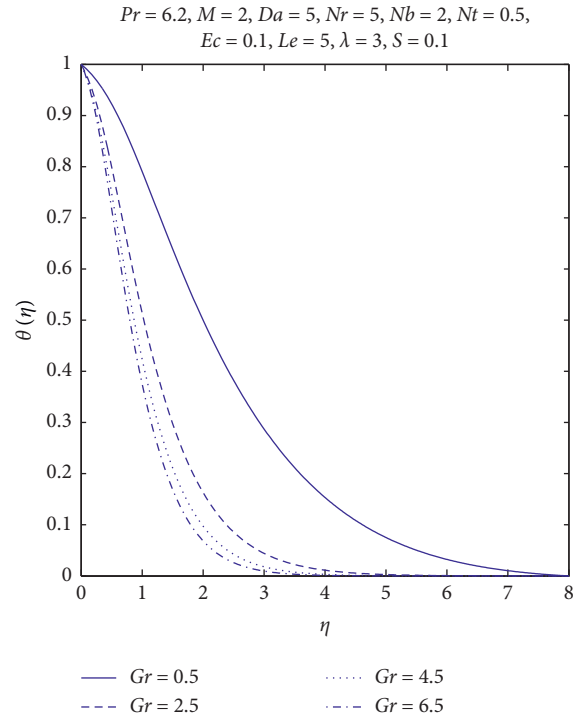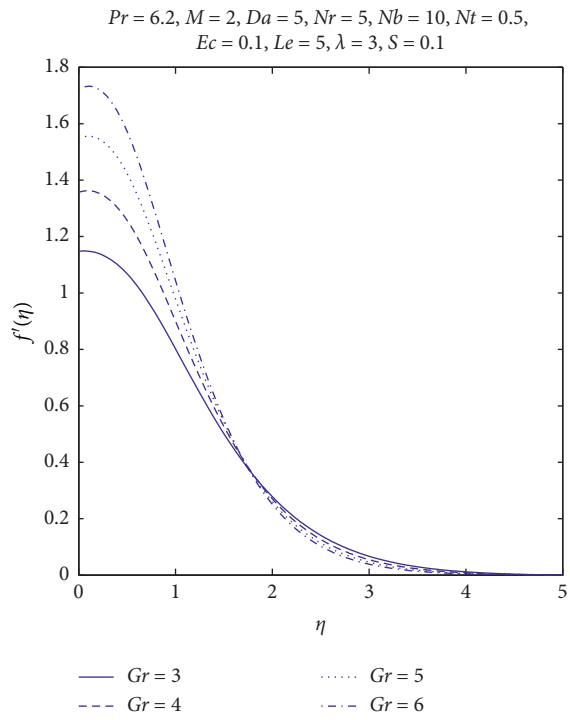
FIGURE 11: Velocity profiles for different Gr.

$Pr = 6.2, M = 2, Da = 5, Nr = 5, Nb = 2, Nt = 0.5,$
$Ec = 0.1, Le = 5, \lambda = 3, S = 0.1$

— $Gr = 0.5$ ⋯⋯ $Gr = 4.5$
- - - $Gr = 2.5$ -·- $Gr = 6.5$

FIGURE 12: Temperature profiles for different Gr.

$Pr = 6.2, M = 2, Da = 5, Nr = 5, Nb = 2, Nt = 0.5,$
$Ec = 0.1, Le = 5, \lambda = 3, S = 0.1$

— $Gr = 0.5$ ⋯⋯ $Gr = 4.5$
- - - $Gr = 2.5$ -·- $Gr = 6.5$
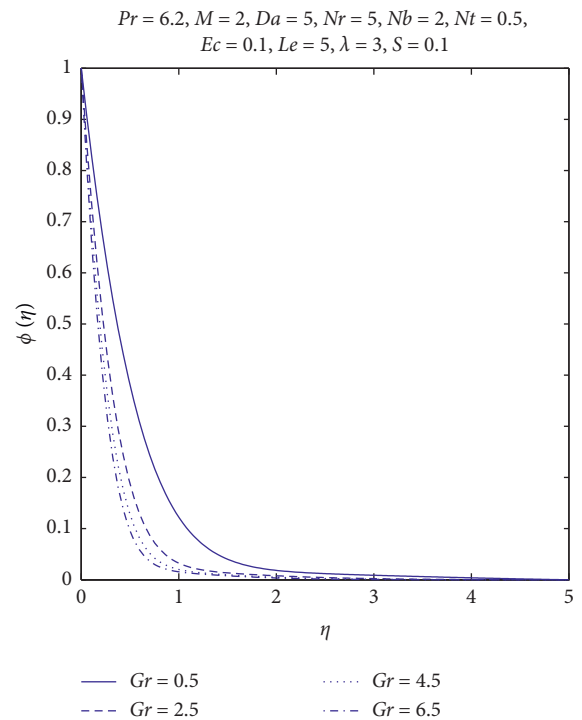
FIGURE 13: Concentration profiles for different Gr.

temperature, and concentration profile have been shown. It depicts that, in the absence of Ec, the dimensionless velocity is lowest at the surface and then increases with increasing Ec. The

dimensionless temperature is lowest inside the thermal boundary layer and increases with Ec while the effect of a viscous dissipation is insignificant on concentration profile.
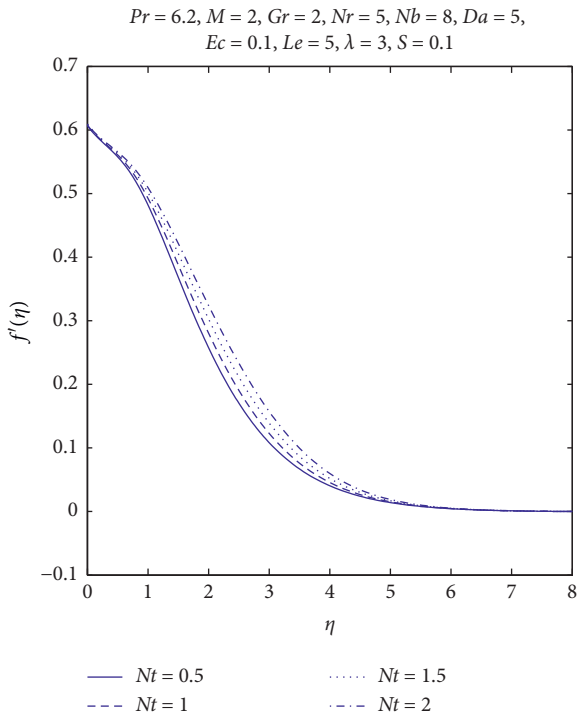
Figure 14: Velocity profiles for different Nt.
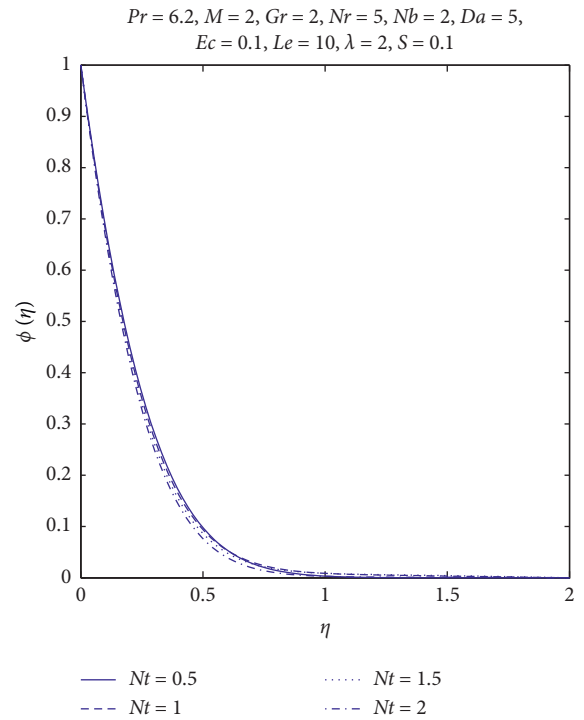
Figure 16: Concentration profiles for different Nt.
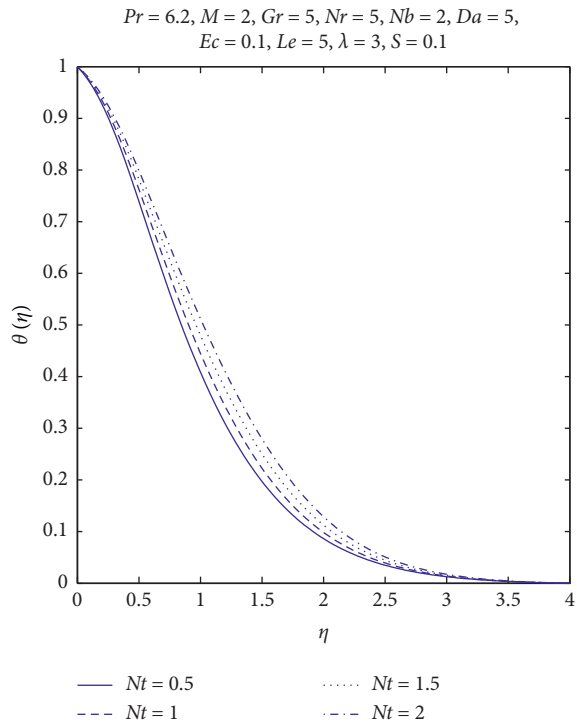
Figure 15: Temperature profiles for different Nt.
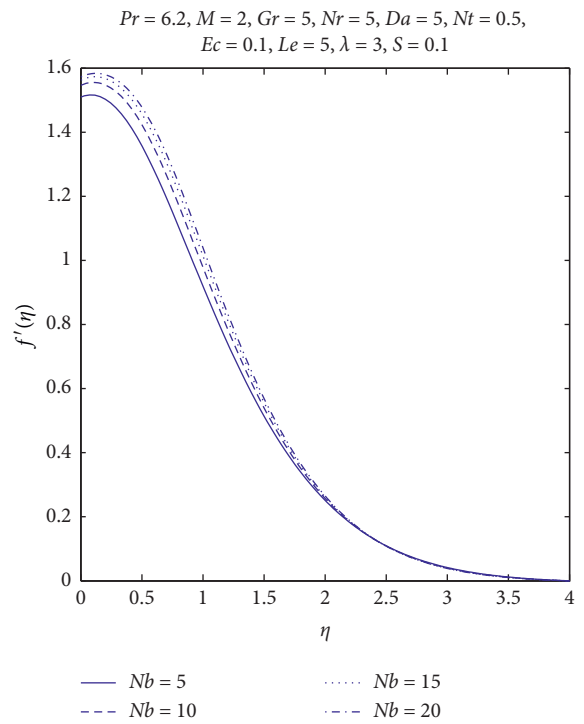
Figure 17: Velocity profiles for different Nb.

$Pr = 6.2, M = 2, Gr = 5, Nr = 5, Da = 5, Nt = 2,$
$Ec = 0.1, Le = 2, \lambda = 3, S = 0.1$
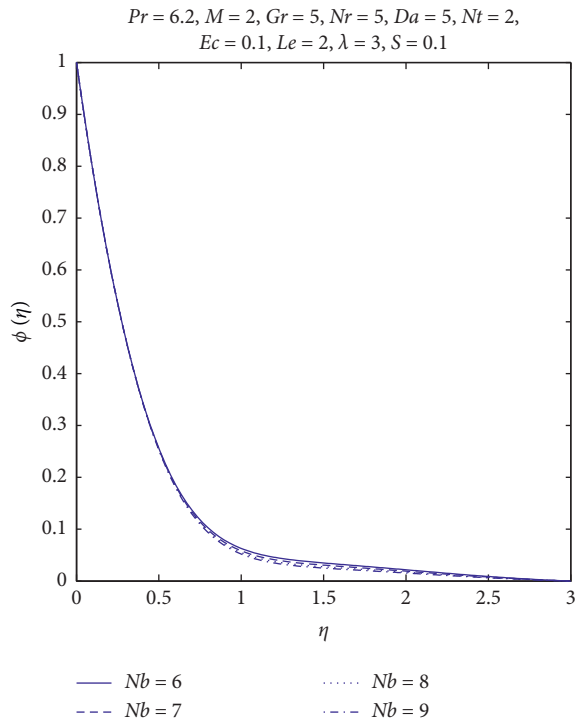
FIGURE 18: Concentration profiles for different Nb.

$Pr = 6.2, M = 2, Gr = 9, Nr = 5, Nb = 2,$
$Nt = 0.5, Da = 5, Le = 5, \lambda = 3, S = 0.1$
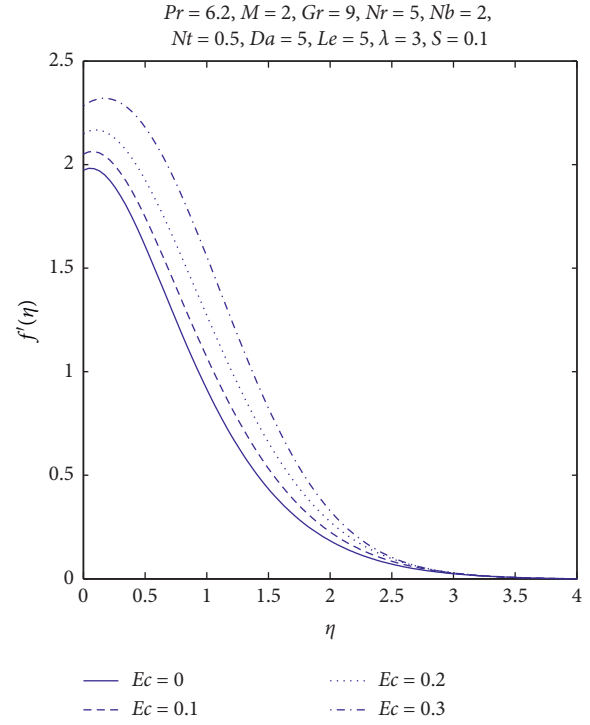
FIGURE 20: Velocity profiles for different Ec.

$Pr = 6.2, M = 2, Gr = 5, Nr = 5, Da = 5, Nt = 0.5,$
$Ec = 0.1, Le = 5, \lambda = 3, S = 0.1$
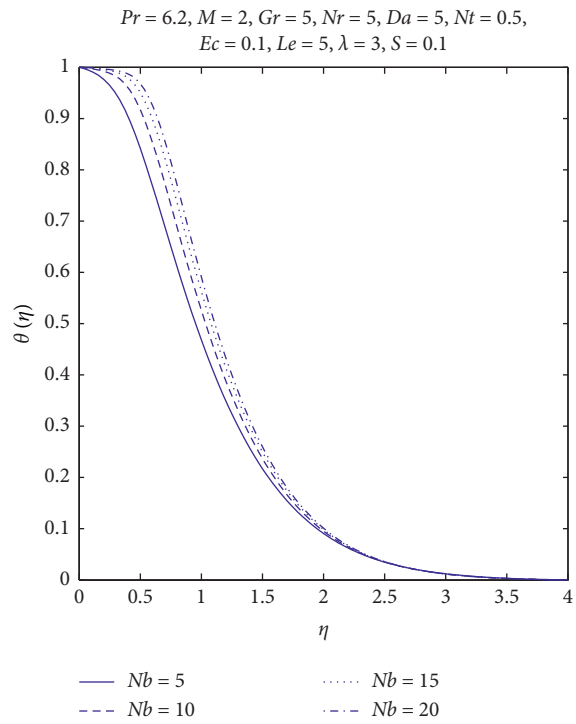
FIGURE 19: Temperature profiles for different Nb.

$Pr = 6.2, M = 2, Gr = 2, Nr = 5, Nb = 2, Nt = 0.5,$
$Da = 5, Le = 5, \lambda = 3, S = 0.1$
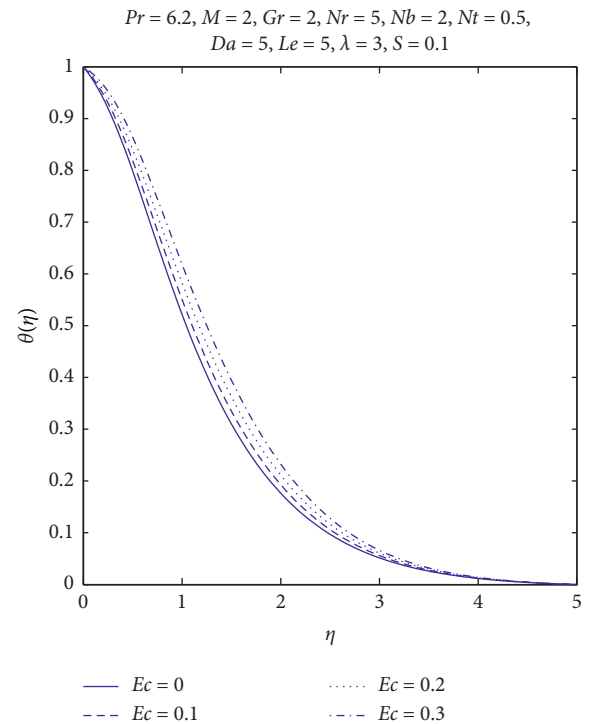
FIGURE 21: Temperature profiles for different Ec.

$Pr = 6.2, M = 2, Gr = 5, Nr = 5, Nb = 2,$
$Nt = 0.5, Da = 3, Le = 2, \lambda = 3, S = 0.1$
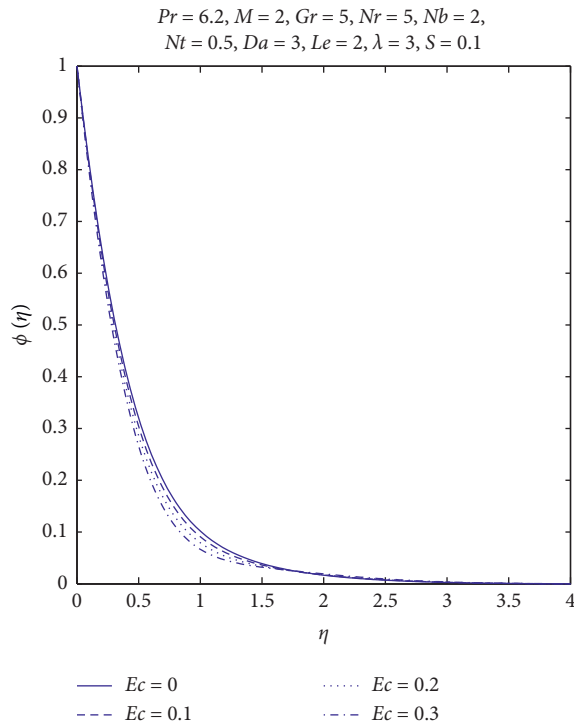
Figure 22: Concentration profiles for different Ec.

5. Conclusions

This study focuses on two objectives as follows: (1) to produce a mathematical model for nanofluid flow considering MHD, radiation, porosity, and slippery exponentially stretching sheet which is immersed in a porous medium and (2) to develop a new numerical scheme for the solution of a general nonlinear ODEs which is applicable not only for the current problem but many others. The key observations of present work are as follows:

(i) The skin friction coefficient grows with a rise of the values of magnetic parameter but local Nusselt and Sherwood numbers reduces The rise of magnetic parameter causes decrease in velocity initially after that the reverse effects can be seen. It enhances temperature and nanoparticle concentration of the boundary layer regime.

(ii) The Darcy number causes the thermal boundary layer and solute concentration to reduce whereas it enhances the momentum boundary layer. The skin friction coefficient decreases yet the wall temperature gradient and nanoparticle concentration increase with an increase in Darcy number.

(iii) The Grashof number enhances local Nusselt number and local Sherwood number whereas this reduces the skin friction coefficient.

(iv) The Lewis number increases momentum and concentration boundary layers. Although it causes a slight change in the skin friction coefficient, wall temperature gradient and boosts nanoparticle concentration are reduced.

(v) The thermophoresis parameter causes both the thermal and momentum boundary layer to increase while its effect on nanoparticle volume fraction is insignificant. The skin friction coefficient and local Sherwood number increase while local Nusselt number remains unaltered.

(vi) The Brownian parameter increases thickness of the thermal boundary layer and momentum boundary layer while there is a slight change in the concentration boundary layer. It causes a reduction in wall temperature gradient, the skin friction coefficient, the local Nusselt number, and the local Sherwood number.

(vii) The Eckert number Ec reduces the skin friction coefficient, local Nusselt number, and concentration boundary layer while momentum boundary layer, thermal boundary layer, and local Sherwood number increase.

(viii) The SFDM has been successfully developed and applied in the current problem. One can show that the SFDM is easy to implement and converges quickly.

(ix) To validate, one compares the SFDM results with $bvp4c$ and those with the literature which gives a good account of agreement with each other.

Data Availability

There are no experiment data involved in this study.

Conflicts of Interest

The authors declare that they have no conflicts of interest.

Acknowledgments

References

[1] L. J. Crane, "Flow past a stretching plate," *Zeitschrift für angewandte Mathematik und Physik ZAMP*, vol. 21, no. 4, pp. 645–647, 1970.

[2] O. D. Makinde and A. Aziz, "Boundary layer flow of a nanofluid past a stretching sheet with a convective boundary condition," *International Journal of Thermal Sciences*, vol. 50, no. 7, pp. 1326–1332, 2011.

[3] M. Mustafa, T. Hayat, and S. Obaidat, "Boundary layer flow of a nanofluid over an exponentially stretching sheet with convective boundary conditions," *International Journal of Numerical Methods for Heat and Fluid Flow*, vol. 23, no. 6, pp. 945–959, 2013.

[4] P. S. Gupta and A. S. Gupta, "Heat and mass transfer on a stretching sheet with suction or blowing," *The Canadian Journal of Chemical Engineering*, vol. 55, no. 6, pp. 744–746, 1977.

[5] S. U. Choi and J. Eastman, *Enhancing thermal conductivity of fluids with nanoparticles, ASME International Mechanical Engineering Congress and Exhibition*, American Society of Mechanical Engineers (ASME), San Francisco, CL, USA, 1995.

[6] M. Sheikholeslami and M. M. Bhatti, "Forced convection of nanofluid in presence of constant magnetic field considering shape effects of nanoparticles," *International Journal of Heat and Mass Transfer*, vol. 111, pp. 1039–1049, 2017.

[7] M. Sheikholeslami, "CuO-water nanofluid flow due to magnetic field inside a porous media considering Brownian motion," *Journal of Molecular Liquids*, vol. 249, pp. 921–929, 2018.

[8] M. Xenos, N. Kafoussias, and G. Karahalios, "Magnetohydrodynamic compressible laminar boundary-layer adiabatic flow with adverse pressure gradient and continuous or localized mass transfer," *Canadian Journal of Physics*, vol. 79, no. 10, pp. 1247–1263, 2001.

[9] J. R. Reddy, K. A. Kumar, V. Sugunamma, and N. Sandeep, "Effect of cross diffusion on MHD non-Newtonian fluids flow past a stretching sheet with non-uniform heat source/sink: a comparative study," *Alexandria Engineering Journal*, vol. 57, no. 3, pp. 1829–1838, 2018.

[10] U. Mishra and G. Singh, "Dual solutions of mixed convection flow with momentum and thermal slip flow over a permeable shrinking cylinder," *Computers & Fluids*, vol. 93, pp. 107–115, 2014.

[11] N. G. Hadjiconstantinou, "Comment on Cercignani's second-order slip coefficient," *Physics of Fluids*, vol. 15, no. 8, pp. 2352–2354, 2003.

[12] N. G. Hadjiconstantinou, "The limits of Navier-Stokes theory and kinetic extensions for describing small-scale gaseous hydrodynamics," *Physics of Fluids*, vol. 18, no. 11, Article ID 111301, 2006.

[13] T. Fang, S. Yao, J. Zhang, and A. Aziz, "Viscous flow over a shrinking sheet with a second order slip flow model," *Communications in Nonlinear Science and Numerical Simulation*, vol. 15, no. 7, pp. 1831–1842, 2010.

[14] A. Ullah, E. Alzahrani, Z. Shah, M. Ayaz, and S. Islam, "Nanofluids thin film flow of reiner-philippoff fluid over an unstable stretching surface with brownian motion and thermophoresis effects," *Coatings*, vol. 9, no. 1, p. 21, 2019.

[15] M. S. Khan, I. Karim, L. E. Ali, and A. Islam, "Unsteady MHD free convection boundary-layer flow of a nanofluid along a stretching sheet with thermal radiation and viscous dissipation effects," *International Nano Letters*, vol. 2, no. 1, p. 24, 2012.

[16] W. Ibrahim and B. Shankar, "MHD boundary layer flow and heat transfer of a nanofluid past a permeable stretching sheet with velocity, thermal and solutal slip boundary conditions," *Computers & Fluids*, vol. 75, pp. 1–10, 2013.

[17] O. D. Makinde, W. A. Khan, and Z. H. Khan, "Buoyancy effects on MHD stagnation point flow and heat transfer of a nanofluid past a convectively heated stretching/shrinking sheet," *International Journal of Heat and Mass Transfer*, vol. 62, pp. 526–533, 2013.

[18] M. Ali and F. Al-Yousef, "Laminar mixed convection from a continuously moving vertical surface with suction or injection," *Heat and Mass Transfer*, vol. 33, no. 4, pp. 301–306, 1998.

[19] M. Partha, P. Murthy, and G. Rajasekhar, "Effect of viscous dissipation on the mixed convection heat transfer from an exponentially stretching surface," *Heat and Mass Transfer*, vol. 41, no. 4, pp. 360–366, 2005.

[20] B. Gebhart, "Effects of viscous dissipation in natural convection," *Journal of Fluid Mechanics*, vol. 14, no. 2, pp. 225–232, 1962.

[21] B. Gebhart and J. Mollendorf, "Viscous dissipation in external natural convection flows," *Journal of Fluid Mechanics*, vol. 38, no. 1, pp. 97–107, 1969.

[22] E. Magyari and B. Keller, "Heat and mass transfer in the boundary layers on an exponentially stretching continuous surface," *Journal of Physics D: Applied Physics*, vol. 32, no. 5, p. 577, 1999.

[23] G. S. Seth, A. Bhattacharyya, R. Kumar, and A. J. Chamkha, "Entropy generation in hydromagnetic nanofluid flow over a non-linear stretching sheet with Navier's velocity slip and convective heat transfer," *Physics of Fluids*, vol. 30, no. 12, Article ID 122003, 2018.

[24] O. D. Makinde, Z. H. Khan, R. Ahmad, and W. A. Khan, "Numerical study of unsteady hydromagnetic radiating fluid flow past a slippery stretching sheet embedded in a porous medium," *Physics of Fluids*, vol. 30, no. 8, Article ID 083601, 2018.

[25] A. Hamid and M. Khan, "Unsteady mixed convective flow of Williamson nanofluid with heat transfer in the presence of variable thermal conductivity and magnetic field," *Journal of Molecular Liquids*, vol. 260, pp. 436–446, 2018.

[26] M. Jafaryar, M. Sheikholeslami, and Z. Li, "CuO-water nanofluid flow and heat transfer in a heat exchanger tube with twisted tape turbulator," *Powder Technology*, vol. 336, pp. 131–143, 2018.

[27] A. Hamid, M. Hashim, and M. Khan, "Impacts of binary chemical reaction with activation energy on unsteady flow of magneto-Williamson nanofluid," *Journal of Molecular Liquids*, vol. 262, pp. 435–442, 2018.

[28] M. Khan, A. Hashim, and A. Hafeez, "A review on slip-flow and heat transfer performance of nanofluids from a permeable shrinking surface with thermal radiation: dual solutions," *Chemical Engineering Science*, vol. 173, pp. 1–11, 2017.

[29] J. Qing, M. Bhatti, M. Abbas, M. Rashidi, and M. Ali, "Entropy generation on MHD Casson nanofluid flow over a porous stretching/shrinking surface," *Entropy*, vol. 18, no. 4, p. 123, 2016.

[30] S. R. Hosseini, M. Sheikholeslami, M. Ghasemian, and D. D. Ganji, "Nanofluid heat transfer analysis in a microchannel heat sink (MCHS) under the effect of magnetic field by means of KKL model," *Powder Technology*, vol. 324, pp. 36–47, 2018.

[31] M. R. Eid, "Chemical reaction effect on MHD boundary-layer flow of two-phase nanofluid model over an exponentially stretching sheet with a heat generation," *Journal of Molecular Liquids*, vol. 220, pp. 718–725, 2016.

[32] A. A. Afify and N. S. Elgazery, "Effect of a chemical reaction on magnetohydrodynamic boundary layer flow of a Maxwell fluid over a stretching sheet with nanoparticles," *Particuology*, vol. 29, pp. 154–161, 2016.

[33] K. V. Prasad, K. Vajravelu, and P. S. Datti, "Mixed convection heat transfer over a non-linear stretching surface with variable fluid properties," *International Journal of Non-linear Mechanics*, vol. 45, no. 3, pp. 320–330, 2010.

[34] N. Afzal, "Momentum and thermal boundary layers over a two-dimensional or axisymmetric non-linear stretching surface in a stationary fluid," *International Journal of Heat and Mass Transfer*, vol. 53, no. 1–3, pp. 540–547, 2010.

[35] M. M. Nandeppanavar, K. Vajravelu, M. S. Abel, and C. O. Ng, "Heat transfer over a nonlinearly stretching sheet with non-uniform heat source and variable wall temperature,"

International Journal of Heat and Mass Transfer, vol. 54, no. 23-24, pp. 4960–4965, 2011.

[36] S. Nadeem and C. Lee, "Boundary layer flow of nanofluid over an exponentially stretching surface," *Nanoscale Research Letters*, vol. 7, no. 1, p. 94, 2012.

[37] R. B. Mohamad, R. Kandasamy, and I. Muhaimin, "Enhance of heat transfer on unsteady Hiemenz flow of nanofluid over a porous wedge with heat source/sink due to solar energy radiation with variable stream condition," *Heat and Mass Transfer*, vol. 49, no. 9, pp. 1261–1269, 2013.

[38] M. Sheikholeslami, R. Ellahi, and C. Fetecau, "CuO–Water nanofluid magnetohydrodynamic natural convection inside a sinusoidal annulus in presence of melting heat transfer," *Mathematical Problems in Engineering*, vol. 2017, 19 pages, Article ID 5830279, 2017.

[39] D. Tripathi, J. Prakash, A. K. Tiwari, and R. Ellahi, "Thermal, microrotation, electromagnetic field and nanoparticle shape effects on Cu-CuO/blood flow in microvascular vessels," *Microvascular Research*, vol. 132, Article ID 104065, 2020.

[40] M. M. Bhatti, A. Shahid, T. Abbas, S. Z. Alamri, and R. Ellahi, "Study of activation energy on the movement of gyrotactic microorganism in a magnetized nanofluids past a porous plate," *Processes*, vol. 8, no. 3, p. 328, 2020.

[41] W. Ibrahim and T. Anbessa, "Three-dimensional MHD mixed convection flow of Casson nanofluid with Hall and Ion slip effects," *Mathematical Problems in Engineering*, vol. 2020, Article ID 8656147, 16 pages, 2020.

[42] W. Ibrahim and M. Negera, "The investigation of MHD Williamson nanofluid over stretching cylinder with the effect of activation energy," *Advances in Mathematical Physics*, vol. 2020, Article ID 9523630, 18 pages, 2020.

[43] A. F. Elelamy, N. S. Elgazery, and R. Ellahi, "Blood flow of MHD non-Newtonian nanofluid with heat transfer and slip effects," *International Journal of Numerical Methods for Heat & Fluid Flow*, vol. 62, no. 3, 2020.

[44] J. Buongiorno, "Convective transport in nanofluids," *Journal of Heat Transfer*, vol. 128, no. 3, pp. 240–250, 2006.

[45] T. Y. Na, *Computational methods in engineering boundary value problems*, Academic Press, Cambridge, MA, USA, 1980.

[46] L. F. Shampine, J. Kierzenka, and M. W. Reichelt, "Solving boundary value problems for ordinary differential equations in MATLAB with *bvp4c*," *Tutorial notes*, vol. 16, pp. 1–27, 2000.

[47] R. Sharif, M. A. Farooq, and A. Mushtaq, "Magnetohydrodynamic study of variable fluid properties and their impact on nanofluid over an exponentially stretching sheet," *Journal of Nanofluids*, vol. 8, no. 6, pp. 1249–1259, 2019.

Research Article

Hydromagnetic Flow of Prandtl Nanofluid Past Cylindrical Surface with Chemical Reaction and Convective Heat Transfer Aspects

Kottakkaran Sooppy Nisar,[1] S. Bilal [ORCID],[2] Imtiaz Ali Shah,[2] M. Awais,[3] Khalil-Ur-Rehman,[2] Ilyas Khan,[4] and Phatiphat Thonthong[5]

[1]*Department of Mathematics, College of Arts and Sciences, Prince Sattam bin Abdulaziz University, Wadi Aldawaser 11991, Saudi Arabia*
[2]*Department of Mathematics, Air University, PAF Complex E-9, Islamabad 44000, Pakistan*
[3]*Department of Mathematics, Quaid-i-Azam University, Islamabad 44000, Pakistan*
[4]*Department of Mathematics, College of Science Al-Zulfi, Majmaah University, Al-Majmaah 11952, Saudi Arabia*
[5]*King Mongkut's University of Technology North Bangkok Renewable Energy Research Centre (RERC) Wongsawang, Bangsue, Bangkok 10800, Thailand*

Correspondence should be addressed to S. Bilal; smbilal@math.qau.edu.pk

Thermodynamical attributes of non-Newtonian fluids over stretched surfaces have gained pervasive essence due to extensive utilization in extruding plastic sheet procedures, liquid film condensation, glass blowing, paper production, biopolymer cylinder coatings, and so forth. So, currently communication is aimed to candidly explicate flow characteristic of Prandtl fluid generated by axial stretching of cylindrical surface. Mathematical modelling by using conservation laws of momentum, energy and concentration fields containing the aspects of magnetic field, convective heating, and chemical reaction are presented initially in the form of partial differential expressions. Later on, these attained PDEs are transmuted into nonlinear ordinary differential equations with implementation of similarity variables. Numerical approach renowned as shooting technique with improved coefficient of the Runge–Kutta (R–K) method by Cash and Karp is used to access accurate solution. Linear curved fitting analysis is also performed to analyze results. Influence of flow-controlling parameters on associated profiles is revealed through graphical visualization. Stream line plots representing flow behavior of Prandtl fluid versus different magnitudes of the curvature parameter are adorned. Variation in friction drag force at wall, heat flux, and concentration gradient are evaluated through numerical data and with interpolation of linear curved fittings. It is deduced from results that increasing curvature parameter momentum and temperature distributions enriches whereas skin-friction coefficient depicts reverse pattern. It is also inferred that temperature shows incrementing deviation in the absence of chemical reaction whereas concentration profiles exhibit reduction with consideration of influence of chemical reaction parameter. Magnetic field tends to reduce the velocity and create thinness of boundary layer thickness.

1. Introduction

Analysis of non-Newtonian fluids has attained superb attention of researchers due to numerous scientific implementations in multiple fields such as food mixing, multigrade oils, composition of materials, wire drawing, hot rolling, petroleum productions, metallurgical procedures, manufacturing of materials, preventive coating, lubricating products, polymerization processes, ink-jet printers, geophysical flows, liquid crystallizations, and several others. Taking into consideration the aforementioned extensive applicability in different technological and industrial

frameworks, a lot of analysis has been conducted in this direction in recent years. However,, the complexity about the non-Newtonian model is its mathematical modelling on behalf of different rheological features. Hence, there is no single constitutive mathematical model which is present, which expresses the fluid characteristics of all non-Newtonian fluids single handedly. Consequently, non-Newtonian fluid models are categorized into time-dependent, time-independent, viscoelastic, and viscoinelastic fluids. Among these subclasses, the most practicing fluids are viscoinelastic fluids. Dunn [1] presented pioneering investigation on the properties of viscoinelastic fluids and depicted behavior of strain of such fluids against application of stress. In the literature, a lot of fluid models are presented to elaborate characteristics of viscoinelastic fluids, but it is found that Prandtl fluid is the most fittest to explicate features of viscoinelastic fluids. Peristaltic movement of Prandtl fluid in endoscope was investigated by Nadeem et al. [2] by calculating perturbation solution of modelled problem with implementation of analytical approach. Akbar [3] considered blood as viscoinelastic fluid and delineated flow features in stenosed tapered arteries by computing perturbation solution. Jothi et al. [4] discussed the physical aspects of magnetically effected Prandtl fluid flow in a symmetric channel. Nazari et al. [5] analyzed convective heat transfer of Prandtl nanofluid flow saturated in lid-driven enclosure. Hossainy et al. [6] discussed the influence of yielding stress on magneto hydrodynamic boundary layer fluid flow of 3D Casson nanofluid over stretched surface entrenched in a porous medium. Bilal et al. [7] adumbrated flow features of the Prandtl fluid model over stretching sheet along with effectiveness of double-diffusive heating.

The mass transport phenomenon in many scientific disciplines involves molecular and convective transport of atoms and molecules. The driving force for producing such type of molecular diffusion is the concentration differences which can generate to application of chemical reaction within flow domain. The process of chemical reaction arises with addition of multiple dissimilar natured particles, and an outcome interaction of particles is produced. Mass transport procedures with effectiveness of chemical reactions have many practical applications, e.g., combustion system, metallurgy, distribution of fertilizers in agriculture field, nuclear reactor safety, and many more. In view of such extensive applications several interesting studies are conducted. For the sake of brevity, some of them are mentioned. Effect of chemical reactions on viscous fluid flow over horizontal plate was discussed by Anjalidevi and Kandasamy [8]. Zhang and Zheng [9] reported influence of chemical reactive species in thermosolutal Marangoni flow of electrified viscous fluid and predicted reduction in nanoparticle concentration with respect to uplift in chemical reaction magnitude. Chaudhary and Merkin [10] investigated thermophysical attributes of viscous fluid influenced by chemical reaction effects. Nandkeolyar et al. [11] described stagnant dissipative nanofluid in the attendance of chemically reaction and magnetic field. Hossainy and Eid [12] analyzed hydrothermal efficiency of non-Newtonian hybrid nanofluid in a heat-exchange channel by generation of chemical

reactions in domain. Eid and Makinde [13] studied collaborative aspects of radiative heat energy and chemical reaction on electrically conducting nanofluid flow over a stretching sheet immersed in a permeable medium. The effects of slip velocity and chemical reaction generated in stagnant flow of nanofluid over a stretching sheet embedded in a porous medium were studied by Eid [14]. In precise, investigators are still working to explore hidden features of chemical reaction on Newtonian and non-Newtonian flows [7, 15, 16].

In the today technological world, nanotechnology is considered one of momentous inventions which have brought advancement in industrial rebellion. Nanotechnology based on nanofluids is engineered colloidal suspension of nanometer-sized particles in host fluids. Before the discovery of nanoparticles, liquids with low thermophysical characteristics are capitalized in multiple procedures which produce deficiencies in output. So, Choi [17] proposed the idea of nanofluids by experimentally measuring their intrinsic features possessed by nanoparticles. Buongiorno [18] evaluated enhancement in thermal conductance of ordinary fluids with the induction of nanoparticles. Flow analysis of viscous fluid generated by an exponential stretching of surface by adding nanoparticles was probed by Nadeem et al. [19]. Reza et al. [20] interrogated influence of carbon nanotubes in peristaltic movement of water in a permeable channel under the impact of magnetic field. Peyghambarzadeh et al. [21] disclosed application of nanofluids in increasing automotive cooling. In recent years, extensive work on nanofluid flow analysis in numerical computational domains along with applications was manifest. So, for interest of readers and getting their motivation in this work few references are mentioned. Alaidrous and Eid [22] adumbrated nanofluid flow of non-Newtonian liquid under impedance of electromagnetic radiations and highly rated reactions. Eid and Mabood [23] irreversibility entropy generated aspects of carbon nanotube (CNT) placement in micropolar dusty fluid mixed with kerosene oil. The uplift in thermal characteristics of blood flow with induction of gold plated hybridized nanoparticles past a stretching sheet was analyzed by Eid [24]. Also, [25–30] presented the literature discusses by various researchers on nanoliquids.

Analysis of fluid flows under impression of magnetic field has been demanding research area among researchers due to overwhelming implications in industry, engineering, medical technology, and so many. In recent years, magneto hydrodynamics of electrically conducting flows has been investigated extensively in multiple physical configurations. Likewise, Lahmar et al. [31] examined transportation of an unsteady ferro magnetic nanofluid between two parallel plates by considering thermal heat conduction as a function of temperature in the presence of magnetic source. Some recent investigations in this direction are enclosed in [32, 33].

The abovementioned literature survey reflects prominence about thermophysical features of non-Newtonian fluid flow. However, it is seen that analysis of the Prandtl fluid model in the presence of chemical reaction and

magnetic field over melted heating cylinder has not been scrutinized yet. So, current effort is made to fill this gap. In this regards, mathematical modelling of the non-Newtonian fluid rheological model with heat transfer aspects is attained in the form of partial differential equations by applying boundary layer approach. Afterwards, suitable scaling transformations are used for conversion into ordinary differential expressions. Improved numerical simulations by means of the Runge–Kutta method with improved coefficients presented by Cash and Karp are used. Computed results are presented through graphical and tabular manners.

2. Mathematical Formulation

Assume 2-D, in-compressed, time-independent, and electrified Prandtl nanoliquid persuaded by an axially stretchable cylinder. Let v and u be the velocity constituents along r and x directions, respectively, as shown in Figure 1. The cylinder is stretched axially with linear velocity. The magnetic field of strength $B°$ is applied perpendicular to cylinder axis. Furthermore, the generated magnetic field is very small in comparison with applied one due to low magnetic Reynolds number assumption.

Prandtl proposed the following rheological model [16]:

$$S = \left(\frac{A}{\dot{\gamma}} \sin^{-1}\left(\frac{1}{c}\dot{\gamma} \right) \right) A_1, \tag{1}$$

where fluid parameters are denoted with A and c, A_1 is first Rivlin–Ericksen tensor, and $\dot{\gamma}$ is defined as

$$\dot{\gamma} = \sqrt{\frac{1}{2} tr A_1^2}. \tag{2}$$

By expanding $\sin^{-1}(\cdot)$ function up to second-order approximation using Taylor's series,

$$\sin^{-1}\left(\frac{\dot{\gamma}}{c} \right) = \frac{\dot{\gamma}}{c} + \frac{\dot{\gamma}^3}{6c^3}, \quad \text{where } \left| \frac{1}{c}\dot{\gamma} \right| < 1. \tag{3}$$

By means of usual boundary layered approximations, the constitutive expressions become

$$\frac{\partial(ru)}{\partial x} + \frac{\partial(rv)}{\partial r} = 0, \tag{4}$$

$$u\frac{\partial u}{\partial x} + v\frac{\partial u}{\partial r} = \frac{A}{\rho c}\frac{\partial^2 u}{\partial r^2} + \frac{A}{2\rho c^3}\left(\frac{\partial u}{\partial r} \right)^2 \frac{\partial^2 u}{\partial r^2} + \frac{A}{r\rho c}\frac{\partial u}{\partial r}$$
$$+ \frac{A}{6r\rho c^3}\left(\frac{\partial u}{\partial r} \right)^3 - \sigma\frac{B_0^2}{\rho}u, \tag{5}$$

$$u\frac{\partial T}{\partial x} + v\frac{\partial T}{\partial r} = \frac{\dot{\alpha}}{r}\frac{\partial}{\partial r}\left(r\frac{\partial T}{\partial r} \right) + \tau D_B\left(\frac{\partial C}{\partial r}\frac{\partial T}{\partial r} \right)$$
$$+ \frac{\tau D_T}{T_\infty}\left(\frac{\partial T}{\partial r} \right)^2 + \frac{A}{c\rho c_p}\left(\frac{\partial u}{\partial r} \right)^2 + \frac{A}{6c^3\rho c_p}\left(\frac{\partial u}{\partial r} \right)^3, \tag{6}$$
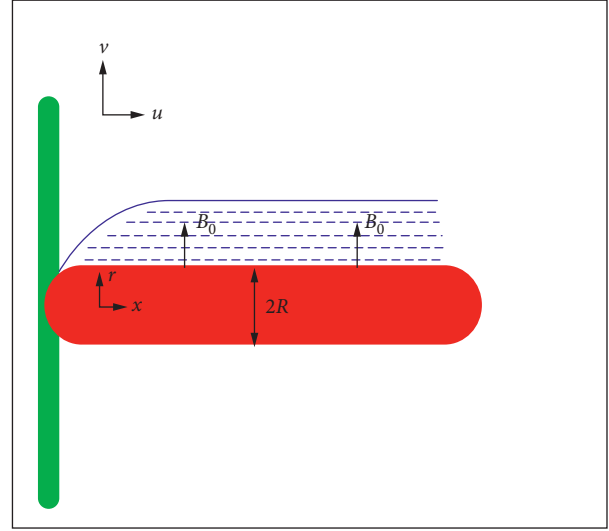
FIGURE 1: Diagram of physical configuration of problem.

$$u\frac{\partial C}{\partial x} + v\frac{\partial C}{\partial r} = \frac{D_B}{r}\frac{\partial}{\partial r}\left(r\frac{\partial C}{\partial r} \right) + \frac{D_T}{rT_\infty}\frac{\partial}{\partial r}\left(r\frac{\partial T}{\partial r} \right)$$
$$- K(C - C_\infty). \tag{7}$$

Accompanied to boundary conditions,

$$u = U_w(x) + L\frac{\partial u}{\partial r},$$

$$v = 0,$$

$$k(T)\frac{\partial T}{\partial r} = -h_w[T_w - T],$$

$$C = C_m(x), \quad \text{at } r = R, \tag{8}$$

$$u \longrightarrow 0,$$

$$T \longrightarrow T_\infty(x),$$

$$C \longrightarrow C_\infty, \quad \text{as } r \longrightarrow \infty.$$

In the above equations σ is the electrical conductance, κ is the thermal conductivity, R is the radius of the cylinder, $\dot{\alpha} = (v/\rho c_p)$ denotes the thermal diffusivity, c_p is the specific heat at constant pressure, D_B is Brownian motion diffusion coefficient, D_T is the thermophoresis diffusion coefficient, K is chemical reaction rate constant, $U_w(x) = ax$ is linear stretching velocity, and wall heat flux coefficient is denoted with h_w.

The stream function which satisfied the continuity equation is mentioned as follows:

$$u = \frac{1}{r}\frac{\partial \psi}{\partial r},$$

$$v = \frac{-1}{r}\frac{\partial \psi}{\partial x}. \tag{9}$$

Equations (4)–(7) can be transformed into nonlinearized ordinary differential equation by employing the following transmutations:

$$\left.\begin{array}{l} \eta = \dfrac{r^2 - R^2}{2R}\left(\dfrac{U_w}{\nu}\right)^{(1/2)} \\[2mm] \psi = (U_w \nu x)^{(1/2)} R f(\eta) \\[2mm] \theta(\eta) = \dfrac{T - T_\infty}{T_w - T_\infty} \\[2mm] \varphi(\eta) = \dfrac{C - C_\infty}{C_w - C_\infty} \end{array}\right\}. \tag{10}$$

After applying the abovementioned transformations, the governing equations, i.e., equations (4)–(7), are transformed into following form:

$$\alpha(1 + 2\gamma\eta)f''' + \alpha\beta(1 + 2\gamma\eta)^2 f''^2 f''' + \frac{4}{3}\gamma\alpha\beta(1 + 2\gamma\eta)(f'')^3$$

$$+ 2\gamma\alpha f'' - (f')^2 + ff'' - M_f^2 f' = 0,$$

$$(1 + 2\gamma\eta)\theta'' + 2\gamma\theta' + \Pr f\theta' + \Pr(1 + 2\gamma\eta)$$

$$\cdot\left(\mathrm{Nb}\theta'\phi' + \mathrm{Nt}\theta'^2\right) = 0,$$

$$(1 + 2\gamma\eta)\phi'' + 2\gamma\phi' + \mathrm{LePr}\left(f\phi' - \delta_c\phi\right)$$

$$+ \frac{\mathrm{Nt}}{\mathrm{Nb}}\left(2r\theta' + (1 + 2\gamma\eta)\theta''\right) = 0. \tag{11}$$

The associated boundary conditions take the following form:

$$\begin{aligned} f(\eta) &= 0, \\ f'(\eta) &= 1 + \lambda f''(0), \quad \text{at } \eta = 0, \\ f'(\eta) &\longrightarrow 0, \quad \text{at } \eta \longrightarrow \infty, \\ \theta'(\eta) &= -k(1 - \theta(\eta)), \quad \text{at } \eta = 0, \\ \theta(\eta) &\longrightarrow 0, \quad \text{as } \eta \longrightarrow \infty, \\ \phi(\eta) &= 1, \quad \text{at } \eta = 0, \\ \phi(\eta) &= 0, \quad \text{at } \eta \longrightarrow \infty, \end{aligned} \tag{12}$$

where α is the fluid parameter, β is the elastic parameter, γ is the curvature parameter, Nb is the Brownian motion parameter, M_f is the magnetic strength parameter, Pr is the Prandtl number, Re is the Reynolds number, Le is the Lewis number, Nt is the thermophoresis parameter, and δ_c is the chemical reactive parameter defined as follows:

$$\left.\begin{array}{l} \alpha = \dfrac{A}{\mu c} \\[2mm] \beta = \dfrac{a^3 x^2}{2c^2 v} \\[2mm] \gamma = \dfrac{1}{R}\sqrt{\dfrac{\nu}{a}} \\[2mm] \mathrm{Nb} = \dfrac{\tau D_B(C_w - C_\infty)}{\rho c_p v} \\[2mm] \delta_c = \dfrac{KL}{a} \\[2mm] M_f = \sqrt{\dfrac{\sigma x B_0^2}{\rho U_w}} \\[2mm] \Pr = \dfrac{\nu}{\dot{\alpha}} \\[2mm] \mathrm{Re} = \dfrac{U_w x}{v} \\[2mm] \mathrm{Le} = \dfrac{\dot{\alpha}}{D_B} \\[2mm] \mathrm{Nt} = \dfrac{\tau D_T(T_w - T_\infty)}{T_\infty \rho c_p v} \end{array}\right\}. \tag{13}$$

The physical parameters of interest, i.e., coefficients of wall drag, wall heat flux, and wall mass flux, are defined as

$$\begin{aligned} C_f &= \frac{\tau_w}{(1/2)\rho U_w^2}, \\ Nu_w &= \frac{x q_w}{k(T_\infty - T_m)}, \\ Sh &= \frac{x j_w}{(C_\infty - C_m)}, \end{aligned} \tag{14}$$

where τ_w is the surface drag force, q_w is the surface heat flux, and j_w is the surface mass flux given as follows:

$$\begin{aligned} \tau_w &= \left[\frac{A}{C}\left(\frac{\partial u}{\partial r}\right) + \frac{A}{6C^3}\left(-\frac{\partial u}{\partial r}\right)^3\right]_{r=R}, \\ q_w &= -k\left(\frac{\partial T}{\partial r}\right)_{r=R}, \\ J_w &= -D\left(\frac{\partial C}{\partial r}\right). \end{aligned} \tag{15}$$

Coefficients of wall drag, thermal flux, and mass flux are defined as

$$\left.\begin{array}{l} \dfrac{1}{2}C_f\mathrm{Re}^{(-1/2)} = \alpha f''(\eta) + \dfrac{\alpha\beta}{3}\left(f''(\eta)\right)^3, \quad \text{at } \eta \longrightarrow 0 \\[4mm] Nu_w\mathrm{Re}^{(-1/2)} = -\theta'(\eta), \quad \text{at } \eta \longrightarrow 0 \\[4mm] Sh\mathrm{Re}^{(-1/2)} = -\phi'(\eta), \quad \text{at } \eta \longrightarrow 0 \end{array}\right\}. \tag{16}$$

3. Computational Algorithm

Shooting technique along with the Runge–Kutta–Fehlberg method (by using Cash and Carp coefficients) is adopted to solve flow-govern problem (Table 1). For this process, flow-govern equations are transformed into

$$f'' = \frac{f'^2 - ff'' - 2\gamma\alpha f'' + M_f^2 f - (4/3)\gamma\alpha\beta(1+2\gamma\eta)f''^3}{\left(\alpha(1+2\gamma\eta) + \alpha\beta(1+2\gamma\eta)^2 f''^2\right)},$$

$$\theta'' = \frac{-\left(\mathrm{Pr} f\theta' + \mathrm{Pr}(1+2\gamma\eta)\left(\mathrm{Nb}\theta'\phi' + \mathrm{Nt}\theta'^2\right) + 2\gamma\theta'\right)}{(1+2\gamma\eta)},$$

$$\phi'' = \frac{-(2\gamma\phi' + \mathrm{LePr}\left(f\phi' - \delta_c\phi\right) + (\mathrm{Nt}/\mathrm{Nb})\left(2r\theta' + (1+2\gamma\eta)\theta''\right))}{(1+2\gamma\eta)}. \tag{17}$$

By letting a new set of variables,

$$\begin{aligned} e_1 &= f, \\ e_2 &= f', \\ e_3 &= f'', \\ e_4 &= \theta, \\ e_5 &= \theta', \\ e_6 &= \phi, \\ e_7 &= \phi'. \end{aligned} \tag{18}$$

After using new variables, the governing equations take the following form:

$$e_1' = e_2, \tag{19}$$

$$e_2' = e_3, \tag{20}$$

$$e_3' = \frac{(e_2)^2 - e_1 e_3 - 2\gamma\alpha e_3 + \left(M_f\right)^2 e_1 - (4/3)\gamma\alpha\beta(1+2\gamma\eta)\left(e_3\right)^3}{\left(\alpha(1+2\gamma\eta) + \alpha\beta(1+2\gamma\eta)^2 \left(e_3\right)^2\right)}, \tag{21}$$

$$e_4' = e_5, \tag{22}$$

$$e_5' = \frac{-\left(\mathrm{Pr}e_1 e_5 + \mathrm{Pr}(1+2\gamma\eta)\left(\mathrm{Nb}e_5 e_7 + \mathrm{Nt}e_5^2\right) + 2\gamma e_3\right)}{(1+2\gamma\eta)}, \tag{23}$$

$$e_6' = e_7, \tag{24}$$

$$e_7' = \frac{-(2\gamma e_7 + \mathrm{LePr}\left(e_1 e_7 - \delta_c e_6\right) + (\mathrm{Nt}/\mathrm{Nb})\left(2\gamma e_5 + (1+2\gamma\eta)e_5'\right))}{(1+2\gamma\eta)}. \tag{25}$$

along boundary conditions

$$\begin{aligned} e_1(\eta) &= 0, \\ e_2(\eta) &= 1 + \lambda e_3(\eta), \\ e_4(\eta) &= -(1/k), \\ e_5(\eta) &- 1, \\ e_6(\eta) &= 1, \quad \text{at } \eta \longrightarrow 0, \\ e_2(\eta) &\longrightarrow 0, \\ e_4(\eta) &\longrightarrow 0, \\ e_6(\eta) &\longrightarrow 0, \quad \text{as } \eta \longrightarrow \infty. \end{aligned} \tag{26}$$

The Runge–Kutta–Fehlberg method is applicable on initial value problem, and in addition, Cash and Karp coefficients are used to raise the accuracy of solution. So, the given boundary conditions are transformed into initial conditions:

$$e_1(0) = 0,$$

$$e_2(0) = 1 + \lambda e_3(0),$$

$$e_3(0) = \omega_1, \quad \text{(unknown initial condition)},$$

$$e_4(0) = -\left(\frac{1}{k}\right)e_5(0) - 1, \tag{27}$$

$$e_5(0) = \omega_2, \quad \text{(unknown initial condition)},$$

$$e_6(0) = 1,$$

$$e_7(0) = \omega_3, \quad \text{(unknown initial condition)}.$$

Then, initial value problem is solved and error is computed by comparing given and calculated boundary values. If error is larger than tolerance, i.e., 10^{-6}, then initial values are modified with Newton's method and process is repeated unless differences are less than 10^{-6}.

4. Graphs and Tables

Impacts and influences of different variables in absence of δ_c are shown in Figures 2–14.

TABLE 1: Numerical values of the coefficient given by Cash and Karp.

I	A_i	B_{ij}					C_i	D_i
1	–	–	–	–	–	–	(37/378)	(2825/27648)
2	(1/5)	(1/5)	–	–	–	–	0	0
3	(3/10)	(3/40)	(9/40)	–	–	–	(250/621)	(18575/48384)
4	(3/5)	(3/10)	(−9/40)	(6/5)	–	–	(125/594)	(13525/55296)
5	1	(−11/54)	(5/2)	(−70/27)	(35/27)	–	0	(277/14336)
6	(7/8)	(1631/55296)	(175/512)	(575/13824)	(44275/110592)	(253/4096)	(512/1771)	(1/4)
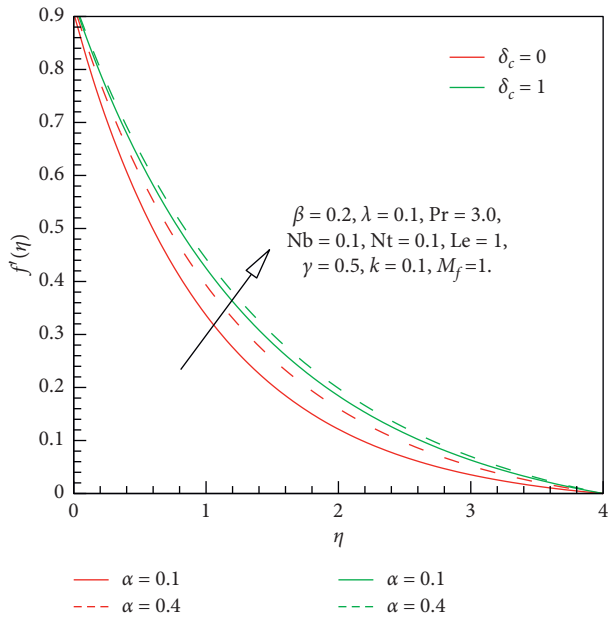
FIGURE 2: Impacts of α on $f'(\eta)$ in absence/presence of δ_c.
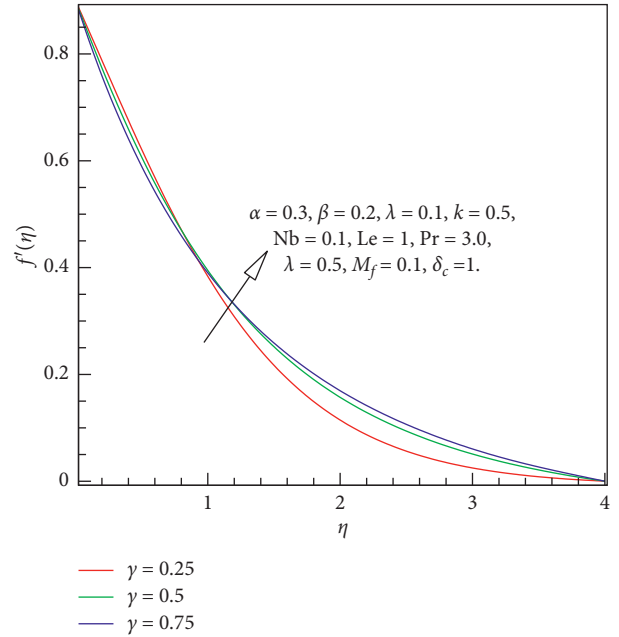
FIGURE 4: γ influences on $f'(\eta)$ in absence/presence of δ_c.
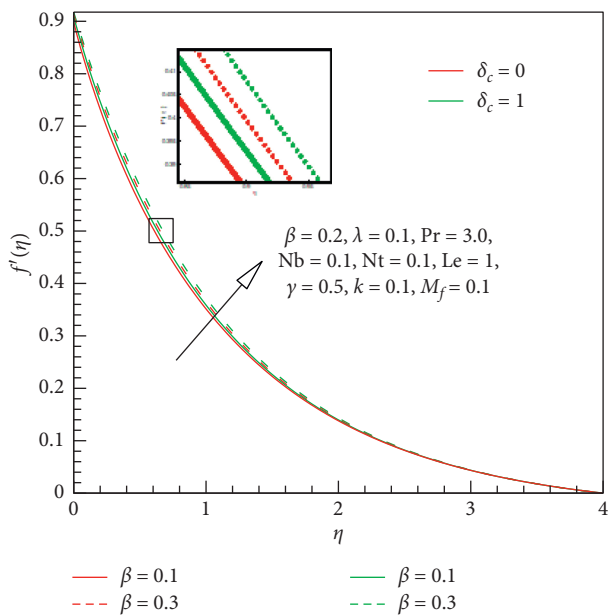
FIGURE 3: Influence of β on $f'(\eta)$ in absence/presence of δ_c.
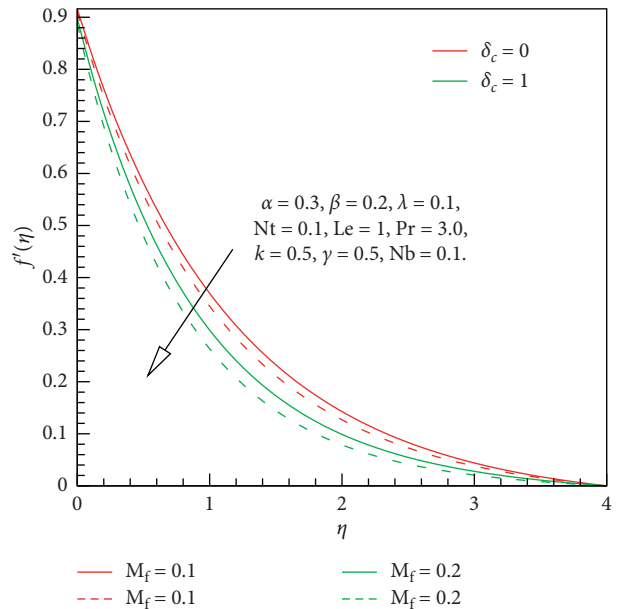
FIGURE 5: M_f impacts on $f'(\eta)$ in absence/presence of δ_c.
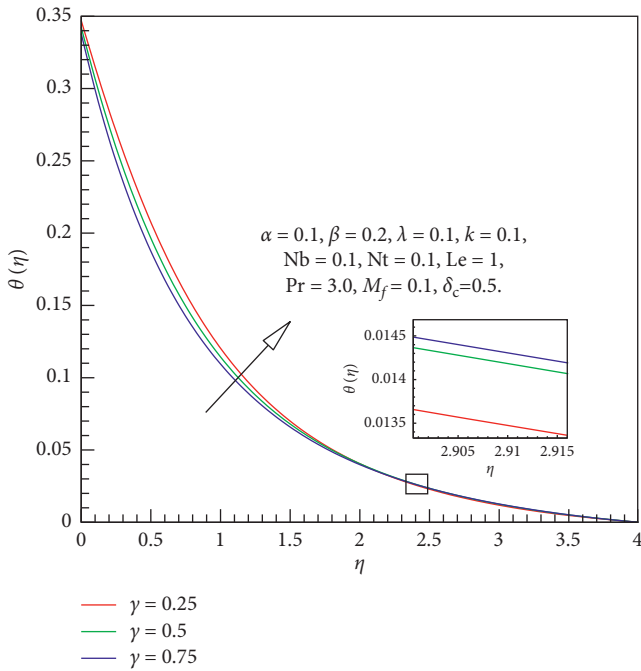
FIGURE 6: γ impacts on $\theta(\eta)$ in the absence/presence of δ_c.
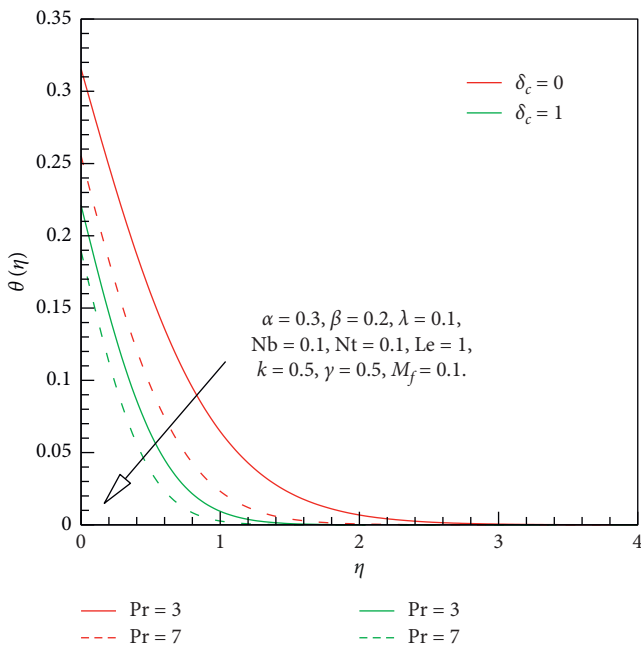
FIGURE 7: **Pr** impacts on $\theta(\eta)$ in the absence/presence of δ_c.

FIGURE 8: **Nb** influences on $\theta(\eta)$ in the absence/presence of δ_c.
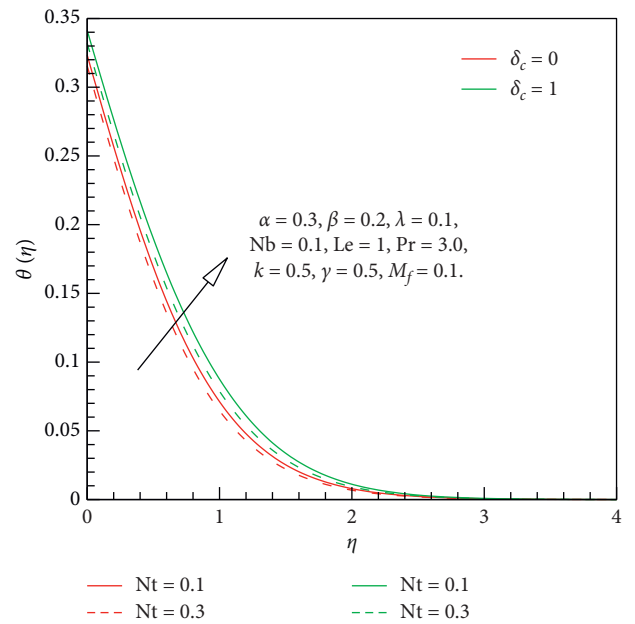
FIGURE 9: Nt influences on $\theta(\eta)$ in the absence/presence of δ_c.

5. Straight Line Curve-Fitting Analysis

The behavior of wall drag, wall heat flux, and wall mass flux is analyzed via straight linearized curved fitting for Prandtl fluid parameter, elastic parameter, curvature parameter, velocity slip, magnetic field, Prandtl number, thermophoretic, Brownian motion, Biot number, Lewis number, and chemical reactive parameters. The Guass and Legendre method was adopted. The expressions for linear approximations are defined such as

$$na_0 + a_1 \sum \chi_i = \sum \xi_i,$$
$$a_0 \sum \chi_{ii} + a_1 \sum \chi_i^2 = \sum \chi_i \xi_i. \tag{28}$$

We trace out linearized fitting for wall drag coefficient towards Prandtl fluid, elastic, curvature, velocity slip, and magnetic parameters, i.e., α, β, γ, λ, and M_f. Let $\chi_i = (\alpha)_i$ and $\xi_i = (\alpha f''(0) + (\alpha\beta/3)(f''(0))^3)_i$, then we get
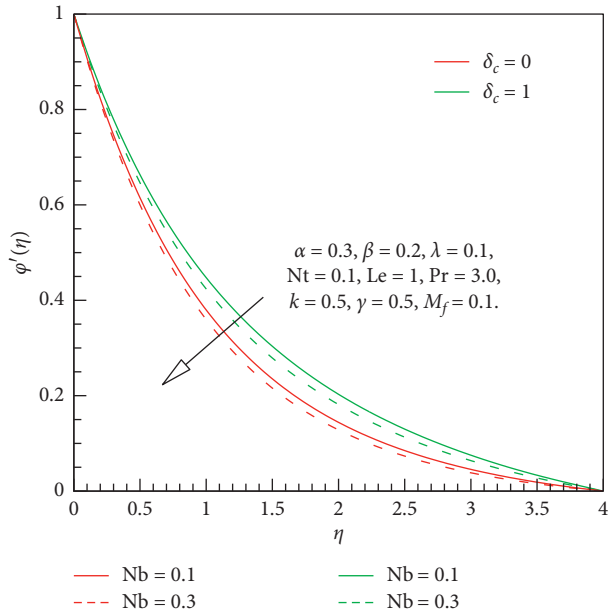
FIGURE 10: **Nb** impacts on $\phi(\eta)$ in the absence/presence of δ_c.
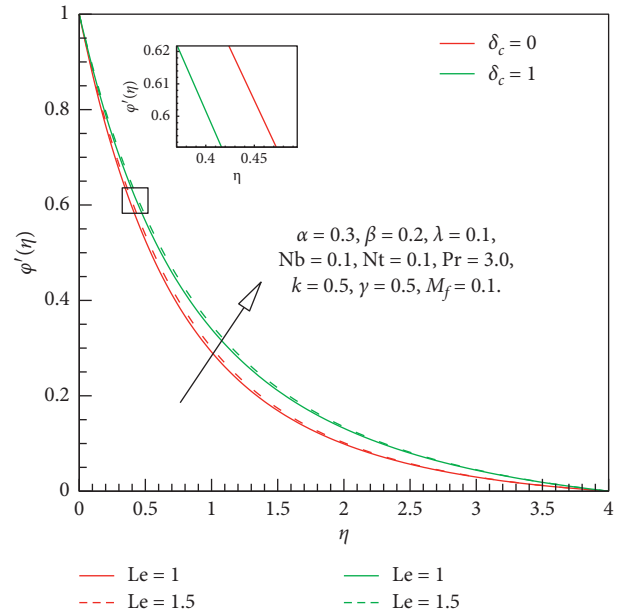
FIGURE 12: Le influences on $\phi(\eta)$ in the absence/presence of δ_c.
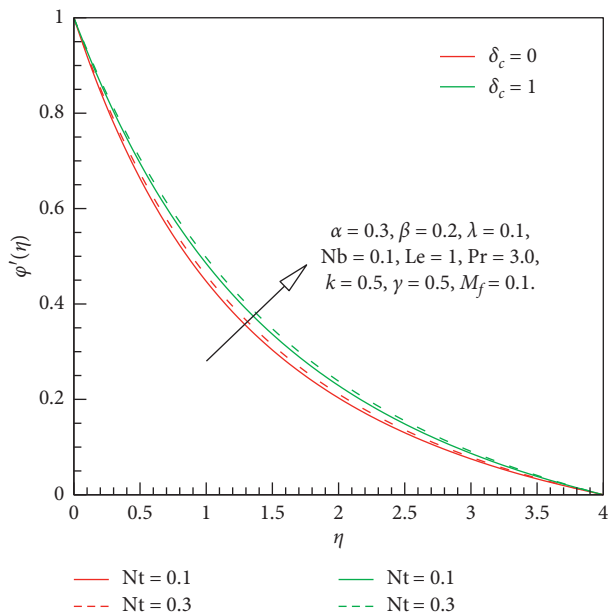
FIGURE 11: Nt influences on $\phi(\eta)$ in the absence/presence of δ_c.
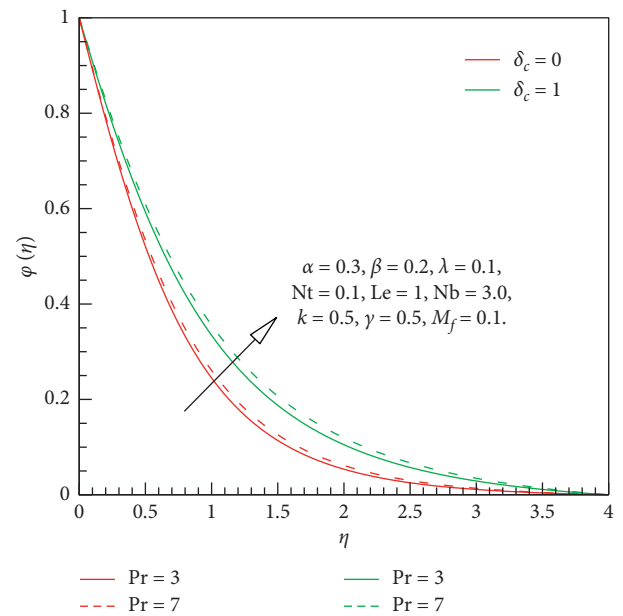
FIGURE 13: **Pr** impacts on $\theta(\eta)$ in the absence/presence of δ_c.

$$\sum (\alpha)_i = 0.7,$$

$$\sum (\alpha)_i^2 = 0.25,$$

$$\sum \left(\alpha f''(0) + \frac{\alpha \beta}{3} (f''(0))^3 \right)_i = -1.3085, \tag{29}$$

$$\sum (\alpha)_i \left(\alpha f''(0) + \frac{\alpha \beta}{3} (f''(0))^3 \right)_i = -0.4826.$$

For straight line approximation, we inserted above expressions in equation (23) and got

$$2a_0 + 0.7a_1 = -1.3085, \tag{30}$$
$$0.7a_0 + 0.25a_1 = -0.4826.$$

By evaluating systemized expression given by (24), we get

$$\alpha f''(0) + \frac{\alpha \beta}{3} (f''(0))^3 = a_0 + a_1 \alpha, \tag{31}$$

where $a_0 = 1.0694$ and $a_1 = -4.9249$.

Linearized curve fitting for wall shear stress versus elastic parameter β is found such as
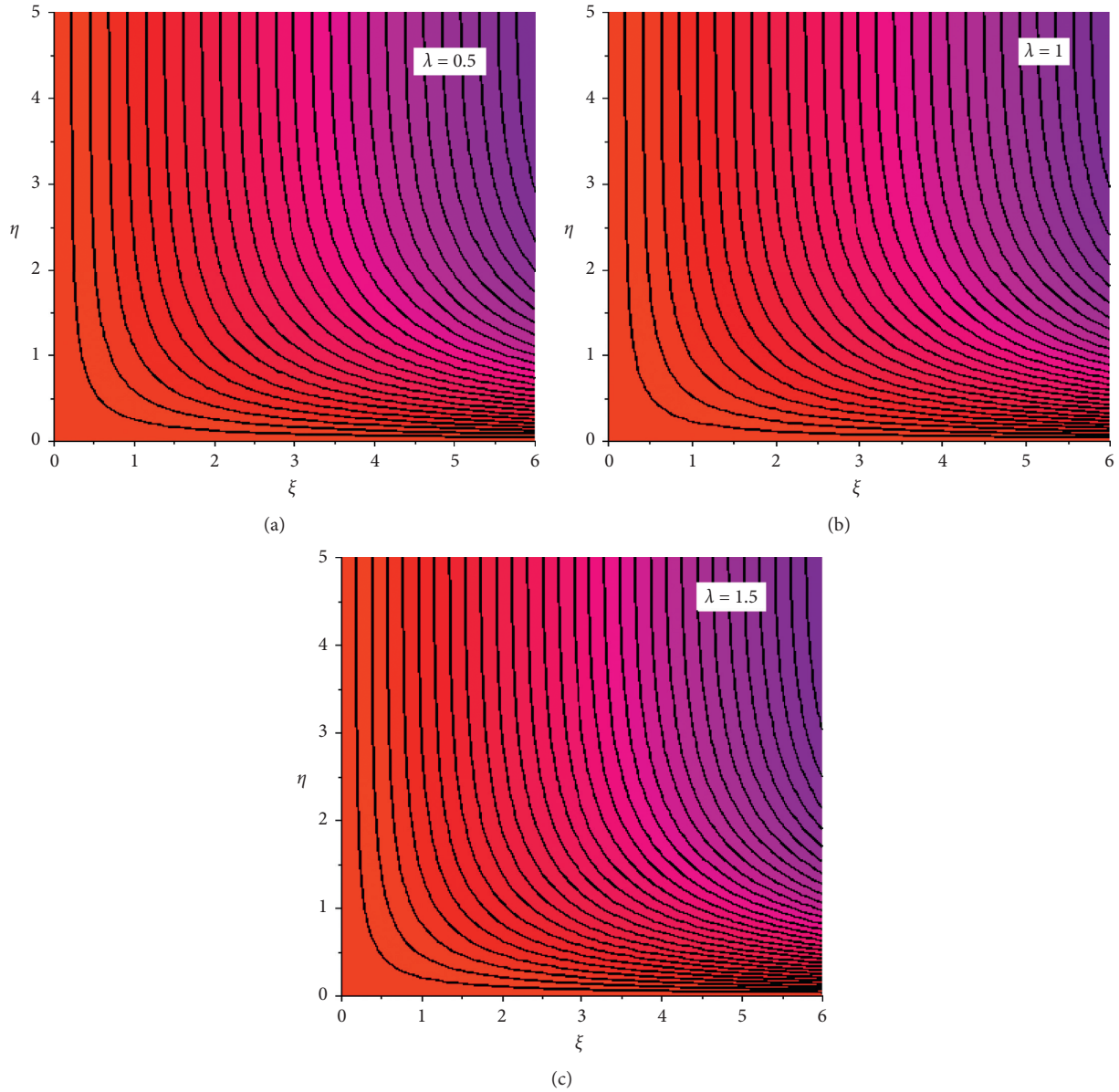
Figure 14: (a) Stream lines against curvature parameter. (b) Stream lines against curvature parameter. (c) Stream lines against curvature parameter.

$$\sum (\beta)_i = 0.7,$$

$$\sum (\beta)_i^2 = 0.29,$$

$$\sum \left(\alpha f''(0) + \frac{\alpha \beta}{3} (f''(0))^3 \right)_i = -1.1708,$$

$$\sum (\beta)_i \left(\alpha f''(0) + \frac{\alpha \beta}{3} (f''(0))^3 \right)_i = -0.4632,$$

$$2b_0 + 0.7b_1 = -1.1708,$$

$$0.7b_0 + 0.29b_1 = -0.4632.$$

(32)

The linearized approximation for fluid elastic variable is specified by

$$\alpha f''(0) + \frac{\alpha \beta}{3} (f''(0))^3 = P(\beta) = b_0 + b_1 \beta, \qquad (33)$$

where $b_0 = -0.1699$ and $b_1 = -1.1871$.

The straight line-curved fitted model for the dragged wall number for curvature parameter γ is disclosed as follows:

$$\sum (\gamma)_i = 1.5,$$

$$\sum (\gamma)_i^2 = 1.25,$$

$$\sum \left(\alpha f''(0) + \frac{\alpha \beta}{3} (f''(0))^3 \right)_i = -1.5347,$$

$$\sum (\beta)_i \left(\alpha f''(0) + \frac{\alpha \beta}{3} (f''(0))^3 \right)_i = -1.3299,$$

$$2c_0 + 1.5c_1 = -1.5347,$$

$$1.5c_0 + 1.25c_1 = -1.3299.$$

(34)

Then, the linear approximations for the curvature parameter are given by

$$\alpha f''(0) + \frac{\alpha\beta}{3}(f''(0))^3 = P(\gamma) = c_0 + c_1\gamma, \qquad (35)$$

where $c_0 = -0.3059$ and $c_1 = -1.4310$.

Straight line curve fitting for wall drag coefficient against velocity slip parameter λ is defined as

$$\sum(\lambda)_i = 0.4,$$

$$\sum(\lambda)_i^2 = 0.1,$$

$$\sum\left(\alpha f''(0) + \frac{\alpha\beta}{3}(f''(0))^3\right)_i = -0.6685,$$

$$\sum(\lambda)_i\left(\alpha f''(0) + \frac{\alpha\beta}{3}(f''(0))^3\right)_i = -0.1191, \qquad (36)$$

$$2d_0 + 0.4d_1 = -0.6685,$$

$$0.4d_0 + 0.1d_1 = -0.1191.$$

Then, the straight line curves versus the curvature parameter are defined as follows:

$$\alpha f''(0) + \frac{\alpha\beta}{3}(f''(0))^3 = P(\lambda) = d_0 + d_1\lambda, \qquad (37)$$

where $d_0 = -0.4802$ and $d_1 = 0.7300$.

Straight line curve fitting for skin-friction coefficient towards velocity slip parameter λ is computed as

$$\sum(M_f)_i = 0.4,$$

$$\sum(M_f)_i^2 = 0.1,$$

$$\sum\left(\alpha f''(0) + \frac{\alpha\beta}{3}(f''(0))^3\right)_i = -0.9699,$$

$$\sum(M_f)_i\left(\alpha f''(0) + \frac{\alpha\beta}{3}(f''(0))^3\right)_i = -0.2095, \qquad (38)$$

$$2e_0 + 0.4e_1 = -0.9699,$$

$$0.4e_0 + 0.1e_1 = -0.2095.$$

Then, the straight line approximations towards the curvature parameter are given by

$$\alpha f''(0) + \frac{\alpha\beta}{3}(f''(0))^3 = P(M_f) = e_0 + e_1 M_f, \qquad (39)$$

where $e_0 = -0.3297$ and $e_1 = -0.7759$.

Now, to trace curve-fitted approximation for convectional wall transfer against the curvature parameter, Prandtl number, thermophoresis parameter, Brownian movement parameter, and Biot number are calculated as follows:

$$\sum(\gamma)_i = 1.5,$$

$$\sum(\gamma)_i^2 = 1.25,$$

$$\sum(-\theta'(0))_i = 0.5973,$$

$$\sum(\gamma)_i(-\theta'(0))_i = 0.4764, \qquad (40)$$

$$2f_0 + 1.5f_1 = 0.5973,$$

$$1.5f_0 + 1.25f_1 = 0.4764.$$

After simplifying, we get

$$-\theta'(0) = P(\gamma) = f_0 + f_1\gamma, \qquad (41)$$

where $f_0 = 0.1281$ and $f_1 = 0.2274$.

Wall heat flux straight line approximation towards the Prandtl number is assessed as

$$\sum(\mathrm{Pr})_i = 3,$$

$$\sum(\mathrm{Pr})_i^2 = 5,$$

$$\sum(-\theta'(0))_i = 0.6737,$$

$$\sum(\mathrm{Pr})_i(-\theta'(0))_i = 2.8851, \qquad (42)$$

$$2g_0 + 8g_1 = 0.6737,$$

$$8g_0 + 34g_1 = 0.4320.$$

After computing by usual algebraic practice, we attain

$$-\theta'(0) = P(\mathrm{Pr}) = g_0 + g_1\mathrm{Pr}, \qquad (43)$$

where $g_0 = 4.8624$ and $g_1 = 1.1314$.

Linear approximation for heat transferal rate towards the thermophoresis parameter is calculated by

$$\sum(\mathrm{Nt})_i = 0.1,$$

$$\sum(\mathrm{Nt})_i^2 = 0.2,$$

$$\sum(-\theta'(0))_i = 0.4558,$$

$$\sum(\mathrm{Nt})_i(-\theta'(0))_i = 0.0669, \qquad (44)$$

$$2h_0 + 0.3h_1 = 0.4558,$$

$$0.3h_0 + 0.05h_1 = 0.0669.$$

After solving by common algebraic practice, we get

$$-\theta'(0) = P(\mathrm{Nt}) = h_0 + h_1\mathrm{Nt}, \qquad (45)$$

where $h_0 = 4.8624$ and $h_1 = 1.1314$.

Straight line approximation by varying thermophoresis parameter for wall heat flux is found as

$$\sum (\text{Nb})_i = 0.1,$$
$$\sum (\text{Nb})_i^2 = 0.2,$$
$$\sum (-\theta'(0))_i = 0.2417,$$
$$\sum (\text{Nb})_i (-\theta'(0))_i = 0.2212,$$
$$2j_0 + 0.3j_1 = 0.4829,$$
$$0.3j_0 + 0.05j_1 = 0.0644. \tag{46}$$

After simplifying, we get

$$-\theta'(0) = P(\text{Nb}) = j_0 + j_1 \text{Nb}. \tag{47}$$

where $j_0 = 0.4825$ and $j_1 = -1.6070$.

Straight line approximations of wall heat flux against the Biot number are found as

$$\sum (k)_i = 0.4,$$
$$\sum (k)_i^2 = 0.1,$$
$$\sum (-\theta'(0))_i = 0.2417,$$
$$\sum (\text{Nb})_i (-\theta'(0))_i = 0.2212,$$
$$2l_0 + 0.4l_1 = 1.2262,$$
$$0.4l_0 + 0.1l_1 = 0.2257. \tag{48}$$

After computing by usual algebraic practice, we attain

$$-\theta'(0) = P(k) = l_0 + l_1 k. \tag{49}$$

where $l_0 = 1.0694$ and $l_1 = -4.9242$.

Wall mass flux straight line approximations versus Lewis number, Prandtl number, thermophoresis parameter, Brownian motion parameter, and chemical reaction parameter are examined as follows:

$$\sum (\text{Le})_i = 1.5,$$
$$\sum (\text{Le})_i^2 = 1.25,$$
$$2m_0 + 1.5m_1 = 1.3397,$$
$$1.5m_0 + 1.25m_1 = 1.0665. \tag{50}$$

After simplifying, we get

$$-\phi'(0) = P(\text{Le}) = m_0 + m_1 k. \tag{51}$$

where $m_0 = 0.2995$ and $m_1 = 0.4938$.

Straight line approximation for surface mass flux for the Prandtl number is calculated as

$$\sum (\text{Pr})_i = 1.5,$$
$$\sum (\text{Pr})_i^2 = 1.25,$$
$$\sum (-\phi'(0))_i = 1.1471,$$
$$\sum (\text{Pr})_i (-\phi'(0))_i = 0.8739,$$
$$2n_0 + 1.5n_1 = 1.2262,$$
$$1.5n_0 + 0.1n_1 = 0.8739. \tag{52}$$

After computing by usual algebraic way, we attain

$$-\phi'(0) = P(\text{Pr}) = n_0 + n_1 \text{Pr}, \tag{53}$$

where $n_0 = 0.4921$ and $n_1 = 1.0847$.

Linear approximation for mass flux towards thermophoresis variable is scrutinized as follows:

$$\sum (\text{Nt})_i = 0.3,$$
$$\sum (\text{Nt})_i^2 = 0.05,$$
$$\sum (-\phi'(0))_i = 1.1587,$$
$$\sum (\text{Nt})_i (-\phi'(0))_i = 0.1771,$$
$$2q_0 + 0.3q_1 = 1.1587,$$
$$0.3q_0 + 0.05q_1 = 0.1771. \tag{54}$$

After computing by usual algebraic way, we attain

$$-\phi'(0) = P(\text{Nt}) = q_0 + q_1 \text{Nt}, \tag{55}$$

where $q_0 = 0.4825$ and $q_1 = 0.6589$.

Surface mass flux straight line approximation for chemical reaction parameter is computed as

$$\sum (\delta_c)_i = 0.3,$$
$$\sum (\delta_c)_i^2 = 0.05,$$
$$\sum (-\phi'(0))_i = 1.1505,$$
$$\sum (\delta_c)_i (-\phi'(0))_i = 0.1754,$$
$$2s_0 + 0.3s_1 = 1.1505,$$
$$0.3s_0 + 0.05s_1 = 0.1754. \tag{56}$$

After simplifying, we get

$$-\phi'(0) = P(\delta_c) = s_0 + s_1 \delta_c, \tag{57}$$

where $s_0 = 0.4905$ and $s_1 = 0.5649$.

6. Physical Outcomes

This section is fascinated to examine impact of embedded parameters on fluid concerning profiles. Moreover, physical quantities of interest, i.e., coefficients of wall friction, wall heat flux, and wall mass flux, are reported by means of both straight line curve fitting and tabular structure. In detail, impacts of α and β on fluid velocity in the absence/presence of δ_c are presented in Figures 1–3, respectively. From graphical trends, it is seen that both α and β cause declination in momentum of fluid flow and associated boundary layer thickness. The reason behind this variation is that with increase in α and β, viscosity of fluid increases, and hence, movement of fluid decays. It is also divulged that flow regime depicts higher magnitude in the absence of chemical reaction as compared to the presence of chemical reaction. These trends in similar were reported by Eid et al. [14] and Nadeem and Lee [19]. Figure 4 reveals the variation of fluid velocity towards γ. The fluid velocity accelerated by increasing γ (see Figure 4) because larger values of γ correspond to reduce

cylindrical radius which in turn reduces surface area; hence, fluid particles experienced less resistance due to which motion is accelerated. Figure 5 elucidates the impact of M_f on velocity. It is clear from these curves that the fluid velocity shows decline trend because an increase in $\mathbf{M_f}$ leads to an increase in Lorentz force and it has tendency to resist the movement of fluid particles, so that velocity decreases. Figure 6 interprets the variations in temperature profile by varying γ. This figure predicts that the fluid temperature increases by enlarging the curvature parameter. This is due to the fact that when γ enlarges, the surface heat flux increases due to which temperature drops adjacent to the cylindrical surface but temperature away from the cylindrical surface enhances. Figure 7 shows impact of $\mathbf{Pr}$ on fluid temperature. The graphical plotting depicts decrement in temperature distribution against $\mathbf{Pr}$. It is also noticed that $\delta_c = 0$ (in absence of chemical reactions), and fluid temperature declines by enlarging the values of $\mathbf{Pr}$, but for $\delta_c > 0$, the decline in fluid temperature is more rapid by enlarging the values of $\mathbf{Pr}$. Figure 8 deliberates the fluctuations in fluid temperature by varying Nb in the absence/presence of the chemical reaction phenomenon. Since Brownian motion accelerates the particle movement, thus collision process is expedited and hence produces more thermal energy (which can be observed from the graph that fluid temperature rises for larger values of Nb in both cases). On the other hand, presence of chemical reactive species drops the fluid temperature. Figure 9 shows the temperature profile variations versus Nt in the absence/presence of chemical reaction. Temperature profile shows increase versus Nt both zero and nonzero δ_c. Figure 10 displays the variations in concentration profile versus combined effect of Nb and δ_c. This graph reveals that the larger values of Nb lessen the nanoparticle concentration because enhancement in Nb corresponds to accelerate random motion of nanoparticles. However, in presence of destructive chemical reaction case, the concentration profile increases. Figure 11 reveals the effect of Nt in absence and presence of the chemical reaction parameter. It is clear from these curves that both parameters have the same impact on nanoparticle concentration. Figure 12 divulges the influence of Le on nanoparticle volume fraction in absence/presence of chemical reaction. This figure predicts that the concentration profile enlarges versus Le irrespective of absence/presence of chemical reaction. Figure 13 examines the physical significance of Pr on concentration profile in absence/presence of chemical reaction. It is evident that by increasing Pr and δ_c, nanoparticle volume fraction increases significantly. Figures 14(a)–14(c) are provided to inspect the flow pattern of Prandtl fluid over the stretching cylinder by sketching stream lines against curvature parameter γ. From stream line plots, it is seen that intensification in magnitude of lines is found with increase in γ because as curvature parameter γ increases, contact of fluid particles reduces, and as an outcome, less resistance is provided. So, rapid movement in fluid is observed versus γ. Furthermore, these curves show that γ enhances the fluid momentum versus positive alteration in velocity. Figure 15 deliberates variation in skin-friction coefficient against $\alpha, \beta, \gamma, \lambda$, and $\mathbf{M}_f$. It is observed that with increase in

α, β, and $\mathbf{M}_f$, wall shear stress increases because all of these mentioned parameters uplift the viscosity forces for reduction in velocity whereas reverse pattern is depicted in case of λ and γ. The reason behind increase in skin friction is the uplift of viscosity force in flow domain against these mentioned parameters. Figure 16 displays fluctuations in wall heat flux by varying $\gamma, \mathbf{Pr}$ while $\mathbf{Nt}, \mathbf{Nb}$, and $\mathbf{k}$. It is found that wall heat flux coefficient increases by enhancing $\gamma, \mathbf{Pr}$ while $\mathbf{for\ Nt, Nb}$ and $\mathbf{k}$ reduce. The reason behind enhancement in temperature gradient at wall against γ and $\mathbf{Pr}$ is due to the fact that by increasing these parameters, resistance is provided by surface to molecules decrease, and hence, average kinetic energy of molecules increases which raise thermal flux. Figure 17 explicates variation in mass flux against $\mathbf{Le}, \mathbf{Pr}, \mathbf{Nt}, \mathbf{Nb}$, and δ_c. It is seen that all mentioned parameters diminish concentration distribution and create motion in fluid molecules, which raises the mass flux with in flow domain. Table 2 delineates the variations in wall friction coefficient versus $\alpha, \beta, \gamma, \lambda$, and, $\mathbf{M}_f$ and increasing pattern of wall friction coefficient against α, β, γ while both λ and $\mathbf{M}_f$ decrease it. Table 3 is designed to explain the fluctuations in wall heat flux by varying governing parameters. Wall heat flux coefficient increases by enhancing $\gamma, \mathbf{Pr}$ while $\mathbf{Nt}, \mathbf{Nb}$, and $\mathbf{k}$ reduce it. Table 4 depicts the variations in the local Sherwood number via $\mathbf{Le}, \mathbf{Pr}, \mathbf{Nt}, \mathbf{Nb}$, and δ_c, and we observed that with respect to defined parameters, enhancement in the local Sherwood number is manipulated. Tables 5 and 6 provide comparison with the previously published literature and given assurance about collected values in this work.

7. Key Results

The current study investigates the magnetic field influences on partial slip flow of Prandtl nanofluid over the stretching cylinder. The fluid flow regime is manifested with the chemical reaction phenomenon. The modelled mathematical equations are reduced in terms of the system of ODEs, and then, the numerical method shooting is implemented to interpret physical aspects of involved parameters. In the presence or absence of the chemical reaction phenomenon, the main findings of present analysis are itemized as follows:

(1) Prandtl fluid velocity reflects an inciting trend towards both Prandtl fluid and elastic parameters

(2) Both fluid velocity and temperature are increasing function of curvature parameter

(3) Magnetic field parameter declines both fluid velocity and temperature

(4) Fluid temperature is increasing function of both Brownian motion and thermophoresis parameters

(5) Nanoparticle concentration shows diminishing variations towards Brownian motion parameter while the opposite trend is noticed versus thermophoresis parameter

(6) Nanoparticle concentration remarks inciting values towards Lewis and Prandtl numbers
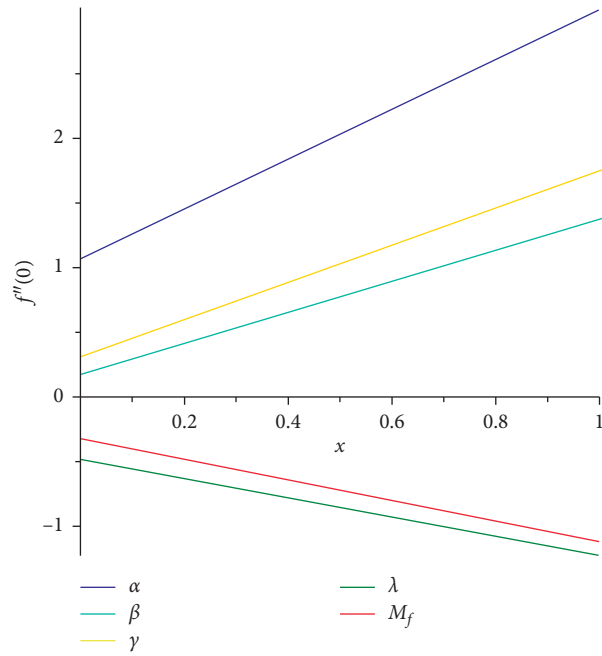
FIGURE 15: Straight line curve fitting for wall shear stress.
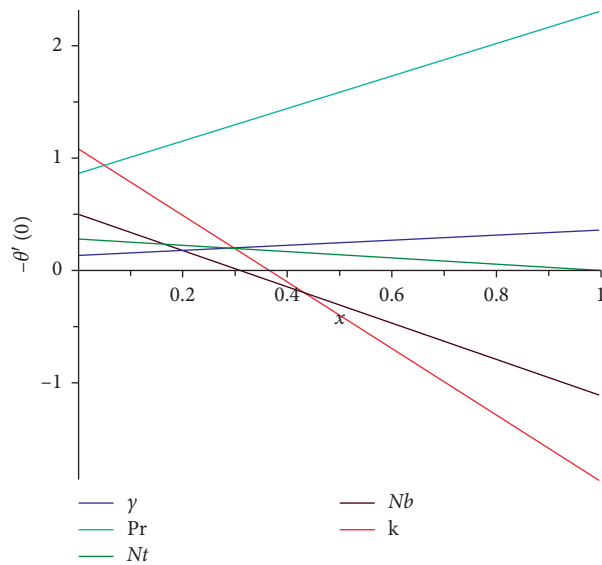
FIGURE 16: Straight line curve fitting for heat transfer rate.

(7) The skin-friction coefficient shows increasing nature for α, β, γ, but opposite behavior is observed for λ and M_f

(8) Wall heat flux coefficient increases against γ, Pr while it decreases for Nt, Nb, and k

(9) The local Sherwood number shows an inciting value via Le, Pr, Nt, Nb, and δ_c

Nomenclature

B_o: Uniform magnetic field
$f'(\eta)$:   Dimensionless radial velocity profile
C_f: Skin-friction coefficient
$\theta(\eta)$:   Dimensionless temperature profile
A and c: Dimensional fluid parameters
$\phi(\eta)$:   Dimensionless concentration profile
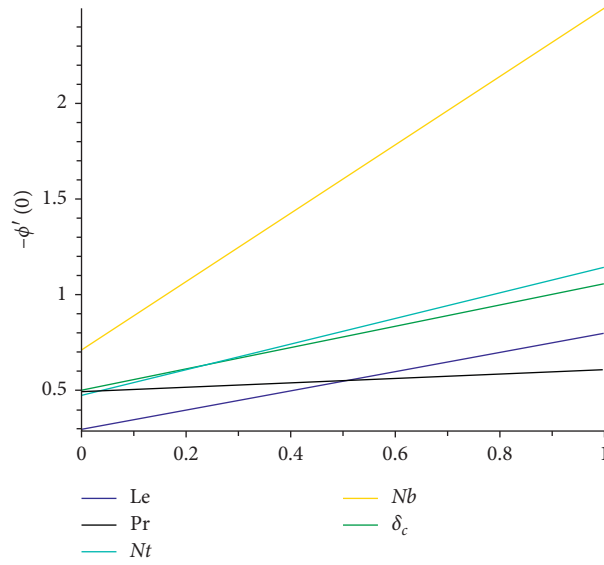
FIGURE 17: Straight line curve fitting for wall mass flux.

TABLE 2: Numerical variation of wall friction coefficient for different parameters.

α	β	γ	λ	$\mathbf{M_f}$	$\alpha f''(0) + (\alpha\beta/3)[f''(0)]^3$
0.3	0.2	0.5	0.1	0.1	−0.4073
0.4	–	–	–	–	−0.9012
0.5	–	–	–	–	−1.4121
0.3	0.2	–	–	–	−0.4073
–	0.4	–	–	–	−0.6481
–	0.5	–	–	–	−0.7635
–	0.2	0.5	–	–	−0.4096
–	–	1	–	–	−1.1251
–	–	1.5	–	–	−1.7481
–	–	0.5	0.1	–	−0.4073
–	–	–	0.3	–	−0.2612
–	–	–	0.5	–	−0.1815
–	–	–	0.1	0.1	−0.4073
–	–	–	–	0.3	−0.5626
–	–	–	–	0.7	−0.2253

TABLE 3: Numerical variation of HTR for different parameters.

γ	$\mathbf{Pr}$	$\mathbf{Nt}$	$\mathbf{Nb}$	k	$-\theta'(0)$
0.5	3	0.1	0.1	0.5	0.2417
1	–	–	–	–	0.3556
1.5	–	–	–	–	0.4517
0.5	3	–	–	–	0.2417
–	5	–	–	–	0.4320
–	7	–	–	–	0.7121
–	3	0.1	–	–	0.2417
–	–	0.2	–	–	0.2141
–	–	0.3	–	–	0.1782
–	–	0.1	0.1	–	0.2417
–	–	–	0.2	–	0.2212
–	–	–	0.3	–	0.2031
–	–	–	0.1	0.1	0.7104
–	–	–	–	0.3	0.5158
–	–	–	–	0.7	0.1715

TABLE 4: Numerical variation of MTR for different parameters.

Le	Pr	Nt	Nb	δ_c	$-\phi'(0)$
0.5	0.5	0.1	0.1	0.1	0.5463
1	–	–	–	–	0.7934
1.5	–	–	–	–	0.9946
0.5	0.5	–	–	–	0.5463
–	1	–	–	–	0.6008
–	1.5	–	–	–	0.6458
–	0.5	0.1	–	–	0.5463
–	–	0.2	–	–	0.6124
–	–	0.3	–	–	0.7314
–	–	0.1	0.1	–	0.5463
–	–	–	0.2	–	0.8201
–	–	–	0.3	–	1.1241
–	–	–	–	0.1	0.5463
–	–	–	–	0.2	0.6042
–	–	–	–	0.3	0.6513

TABLE 5: Comparison of wall shear stress by varying magnetic field parameter M_f while considering other parameters to zero.

M_f	Akbar at el. [32]	Malik at el. [33]	Present
0.0	−1	−1	−1
0.5	−1.11803	−1.11803	−1.1180
1.0	−1.41421	−1.41419	−1.4137
5.0	−2.44949	−2.44945	−2.4495
10	−3.31663	−3.31657	−3.3166
100	−10.04988	−10.04981	−10.0500
500	−22.38303	−22.38294	−22.3835
1000	−31.63859	−31.63851	−31.6391

TABLE 6: Comparison of results for the reduced Nusselt number $-\theta'(0)$ against Pr and considering all other parameters zero.

Pr	Present results	Wang [30]	Gorla and Sidawi [31]
0.07	0.0663	0.0656	0.0656
0.20	0.1619	0.1619	0.1619
0.70	0.4539	0.4539	0.4539
2.00	0.9113	0.9114	0.9114
7.00	1.8954	1.8954	1.9805
20.00	3.3539	3.3539	3.3539
70.00	6.4621	6.4622	6.4622

A_1: First Rivlin–Ericksen tensor
v: Kinematic viscosity
M: Magnetic parameter
μ: Dynamic viscosity
Pr: Prandtl number
ρ: Density
r, x: Cylindrical coordinate system
ρC_P: Volumetric heat capacity
K: Dimensionless chemical reaction parameter
γ: Curvature parameter
α: Fluid parameter
β: Elastic parameter
Nu: Nusselt number
Nb: Brownian motion parameter
Nt: Thermophoresis parameter
δ_c: Dimensionless chemical reaction parameter

Greek symbols

$\dot{\alpha}$: Thermal diffusivity [m^2/s]
η: Independent similarity variable.

Data Availability

The data used to support the findings of this study are available from the corresponding author after acceptance of publication.

Conflicts of Interest

The authors declare that they have no conflicts of interest.

Acknowledgments

References

[1] M. W. Dunn, "Non-newtonian fluid flow through fabrics: national textile center," *Annual Report*, vol. M98–P02, p. 1, 1999.

[2] S. Nadeem, H. Sadaf, and N. S. Akbar, "Analysis of peristaltic flow of prandtl fluid model in an endoscope," *Journal of Power Technology*, vol. 94, pp. 1–11, 2014.

[3] N. S. Akbar, "Blood flow analysis of prandtl fluid model in tapered stenosed arteries," *Ain Shams Engineering Journal*, vol. 5, no. 4, pp. 1267–1275, 2014.

[4] S. Jothi, A. R. Parasad, and M. V. S. Reddy, "Perestaltic flow of prandtl fluid in a symmetric channel under the effect of magnetic field," *Advances in Applied Science Research*, vol. 3, pp. 2108–2119, 2012.

[5] S. Nazari, R. Ellahi, M. M. Sarafraz, M. R. Safaei, A. Asgari, and O. A. Akbari, "Numerical study on mixed convection of a non-newtonian nanofluid with porous media in a two lid-driven square cavity," *Journal of Thermal Analysis and Calorimetry*, vol. 140, no. 3, pp. 1121–1145, 2020.

[6] A. F. A. Hossainy, M. R. Eid, and M. S. Zoromba, "SQLM for external yield stress effect on 3D MHD nanofluid flow in a porous medium," *Physica Scripta*, vol. 94, p. 10, 2019.

[7] S. Bilal, K. U. Rehman, M. Y. Malik, A. Hussain, and M. Awais, "Effect logs of double diffusion on MHD prandtl nano fluid adjacent to stretching surface by way of numerical approach," *Results in Physics*, vol. 7, pp. 470–479, 2017.

[8] S. P. Anjalidevi and R. Kandasamy, "Effects of chemical reaction, heat and mass transfer on laminar flow along a semi infinite horizontal plate," *Heat and Mass Transfer*, vol. 35, no. 6, pp. 465–467, 1999.

[9] Y. Zhang and L. Zheng, "Analysis of MHD thermosolutal marangoni convection with the heat generation and a first-order chemical reaction," *Chemical Engineering Science*, vol. 69, no. 1, pp. 449–455, 2012.

[10] M. A. Chaudhary and J. H. Merkin, "A simple isothermal model for homogeneous-heterogeneous reactions in boundary-layer flow. I equal diffusivities," *Fluid Dynamics Research*, vol. 16, no. 6, pp. 311–333, 1995.

[11] R. Nandkeolyar, S. S. Motsa, and P. Sibanda, "Viscous and joule heating in the stagnation point nanofluid flow through a stretching sheet with homogenous-heterogeneous reactions and nonlinear convection," *Journal of Nanotechnology in Engineering and Medicine*, vol. 4, no. 4, 2013.

[12] A. F. A. Hossainy and M. R. Eid, "Structure, DFT calculations and heat transfer enhancement in [ZnO/PG + H2O]C hybrid nanofluid flow as a potential solar cell coolant application in a double-tube," *Journal of Materials Science: Materials in Electronics*, vol. 31, pp. 15243–15257, 2020.

[13] M. R. Eid and O. D. Makinde, "Solar radiation effect on a magneto nanofluid flow in a porous medium with chemically reactive species," *International Journal of Chemical Reactor Engineering*, vol. 16, pp. 2017–0212, 2018.

[14] M. R. Eid, K. L. Mahny, A. Dar, and T. Muhammad, "Numerical study for carreau nanofluid flow over a convectively heated nonlinear stretching surface with chemically reactive species," *Physica A: Statistical Mechanics and Its Applications*, vol. 540, p. 123063, 2020.

[15] L. Zhang, M. M. Bhatti, and E. E. Michaelides, "Entropy generation in magnetized blood flow through a finite wavy channel under slip conditions," *Journal of Non-equilibrium Thermodynamics*, vol. 45, no. 4, p. 419, 2020.

[16] M. M. Bhatti, A. Riaz, L. Zhang, S. M. Sait, and R. Ellahi, "Biologically inspired thermal transport on the rheology of williamson hydromagnetic nanofluid flow with convection: an entropy analysis," *Journal of Thermal Analysis and Calorimetry*, 2020.

[17] C. SU, "Enhancing thermal conductivity of fluids with nanoparticles," *ASME-Publications*, vol. 231, pp. 99–106, 1995.

[18] J. Buongiorno, "Convective transport in nanofluids," *Journal of Heat Transfer*, vol. 128, no. 3, pp. 240–250, 2006.

[19] S. Nadeem and C. Lee, "Boundary layer flow of nanofluid over an exponentially stretching surface," *Nanoscale Research Letters*, vol. 7, no. 1, p. 7, 2012.

[20] M. Raza, R. Ellahi, S. M. Sait, M. M. Sarafraz, M. S. Shadloo, and I. Waheed, "Enhancement of heat transfer in peristaltic flow in a permeable channel under induced magnetic field using different CNTs," *Journal of Thermal Analysis and Calorimetry*, vol. 140, no. 3, pp. 1277–1291, 2020.

[21] S. M. Peyghambarzadeh, S. H. Hashemabadi, M. S. Jamnani, and S. M. Hoseini, "Improving the cooling performance of automobile radiator with Al_2O_3/water nanofluid," *Applied Thermal Engineering*, vol. 31, no. 10, pp. 1833–1838, 2011.

[22] A. A. Alaidrous and M. R. Eid, "3D electromagnetic radiative non-newtonian nanofluid flow with Joule heating and higher-order reactions in porous materials," *Scientific Reports*, vol. 10, no. 4, pp. 41598–42020, 2020.

[23] M. R. Eid and F. Mabood, "Entropy analysis of a hydromagnetic micropolar dusty carbon NTs-kerosene nanofluid with heat generation: darcy-forchheimer scheme," *Journal of Thermal Analysis and Calorimetry*, 2020.

[24] M. R. Eid, "Effects of NP shapes on non-newtonian bio-nanofluid flow in suction/blowing process with convective condition: sisko model," *Journal of Non-equilibrium Thermodynamics*, vol. 45, 2020.

[25] W. A. Khan and I. Pop, "Boundary-layer flow of a nanofluid past a stretching sheet," *International Journal of Heat and Mass Transfer*, vol. 53, no. 11-12, pp. 2477–2483, 2010.

[26] L. A. Khan, M. Raza, N. A. Mir, and R. Ellahi, "Effects of different shapes of nanoparticles on peristaltic flow of MHD nanofluids filled in an asymmetric channel," *Journal of Thermal Analysis and Calorimetry*, vol. 140, no. 3, pp. 879–890, 2020.

[27] A. Ahmed, "Flow of ReinerPhilippoff based nano-fluid past a stretching sheet," *Journal of Molecular Liquids*, vol. 219, pp. 643–646, 2016.

[28] C. Y. Wang, "Free convection on a vertical stretching surface," *ZAMM - Journal of Applied Mathematics and Mechanics/ Zeitschrift für Angewandte Mathematik und Mechanik*, vol. 69, no. 11, pp. 418–420, 1989.

[29] R. S. R. Gorla and I. Sidawi, "Free convection on a vertical stretching surface with suction and blowing," *Applied Science Research*, vol. 52, pp. 247–257, 1994.

[30] M. R. Eid, A. F. A. Hossainy, and M. S. Zoromba, "FEM for blood-based SWCNTs flow through a circular cylinder in a porous medium with electromagnetic radiation," *Communications in Theoretical Physics*, vol. 71, p. 12, 2019.

[31] Lahmar, "Examined the fluid flow and thermal transportation of an unsteady nanofluid (fe3o4–water) between two plates parallel to each other, observing the case where the thermal heat conduction is a function of temperature in the presence of magnetic field," 2020.

[32] N. S. Akbar, A. Ebai, and Z. H. Khan, "Numerical analysis of magnetic field effects on eyring-powell fluid flow towards a stretching sheet," *Journal of Magnetism and Magnetic Materials*, vol. 382, pp. 355–358, 2015.

[33] M. Y. Malik, T. Salahuddin, A. Hussain, and S. Bilal, "MHD flow of tangent hyperbolic fluid over a stretching cylinder: using keller box method," *Journal of Magnetism and Magnetic Materials*, vol. 395, pp. 271–276, 2015.

Research Article

Design and Implementation of the Array Logging Tool on Horizontal Production Logging

Wenguang Song [ID],[1] **Haiyu Chen** [ID],[2] **Qiujuan Zhang**,[1] and **Jiahao Zhang**[1]

[1]*School of Computer Science, Yangtze University, Jingzhou 434023, Hubei, China*
[2]*Department of Computer, Zhaoqing Medical College, Zhaoqing 526020, Guangdong, China*

Correspondence should be addressed to Haiyu Chen; jsj-3782036@126.com

The measuring instruments have some errors in the measurement of high water cut production wells, and many domestic oil fields are also in high water cut state. The measured data from the conventional production logging instrument are all almost inaccurate. This project has designed a staggered probe array flow meter well logging apparatus based on the characteristic of electromagnetic wave specific retention meter that can fully cover the wellbore fluid and improve flow measurement accuracy. According to the application in horizontal wells, the accuracy of this measuring instrument now has been proved to be more than 90% and can meet the requirements of production logging interpretation in horizontal wells.

1. Introduction

Directional well drilling technology is becoming more and more perfect. Related completion technology is also constantly improved [1]. The number of horizontal wells is also increasing. Horizontal wells have gradually become one of the key technologies for high and stable production of various oil and gas fields. A large number of oil and gas fields have developed a certain scale of high angle wells and horizontal wells [2]. But, in production, many horizontal wells have low production and high water cut. The aquifer is located by production logging technology. This is very necessary. Several new horizontal well logging technologies have been developed by engineering and technical personnel through technical innovation [3]. For example, positioning and wet cable head pipe conveyed logging technology. Because the fluid in horizontal well is affected by gravity, the upper part is light phase and the lower part is heavy phase [4]. In the lower half, there is sediment and other phenomena, especially in the horizontal shaft of the horizontal well. This sediment can cause the measuring instrument not to operate normally [5].

Therefore, the array measurement instrument is used to reduce the interference of sediment on measurement data. This is a better method of measurement. According to this measurement method, the corresponding interpretation method and interpretation model are studied. This can improve the measurement accuracy of horizontal wells, and can lay the foundation for accurately finding aquifers [6].

Many oil fields at home and abroad are mining a large number of highly deviated wells and horizontal wells to improve the single well production capacity and improve the recovery of oil and gas [7]. But, in production logging, conventional measuring instruments cannot carry out the measurement work for high water cut and low yield horizontal wells. Foreign RAT [8], CAT [9], and other instruments are only suitable for high output of oil wells [10]. As for the low yield of oil well, the measurement accuracy needs to be further improved [11]. This project has found that using the 12 packer water holdup meter-combined electromagnetic wave measuring instruments can improve the measurement accuracy of a horizontal well through several experimental studies [12].

2. The Designing of the Double Array Logging Tool

Through the preliminary study, the temperature of fluid in the horizontal well is not more than 155 degrees Celsius, and the formation pressure is generally not more than 32 MPa [13]. If the domestic production wells are in high water cut, the instrument can measure the water holding rate range between 0~100%, and the precision should be above 98%. Moreover, there may be a problem that is not easy to operate if the 12 holding water rate measuring instrument is in the same cross section of the array type measuring instrument [14] because of the limited working space in the production well [15]. So, here, the structure is designed as shown in Figures 1 and 2.

As shown in Figure 1, measuring probes are installed on the two cross section of the measuring instrument [16]. As shown in Figure 2, 6 water holding capacity measuring apparatus are distributed on each probe equally [17]. At the same time, the two cross sections of the probe are required to be uniformly distributed within the wellbore [18]. As shown in Figure 3, the effect of the distribution of 12 probes will be found in the longitudinal direction of the cross section [19].

As shown in Figure 3, probe 1, 3, 5, 7, 9, and 11 are 6 water holding capacity measuring apparatus at the same cross section, and probe 2, 4, 6, 8, 10, and 12 are another 6 water holding capacity measuring apparatus at another same cross section [20]. As all these 12 probes are designed like this, the diameter of the instrument after contraction is reduced and contributes to the instrument carrying out survey work in wellbore [21].

Because the measuring instrument is limited by the diameter of the measuring shaft [22], the length of the probe is 120 mm, the outer radius for the inner conductor is 2 mm, the inner radius of the outer conductor is 7 mm, and the outer radius of the outer conductor is 9 mm [23].

According to the transmission theory of electromagnetic field [24], the highest cutoff frequency or the minimum cutoff wavelength calculation formula of the transmission of the TEM wave (Transverse electric and magnetic field) inside a detector is

$$f_T \text{EM} \max = \frac{300}{\pi (a + b)\varepsilon_m},$$

$$\lambda_T \text{EM} \min = \pi \sqrt{(a + b)\varepsilon_m}.$$

(1)

The $f_T\text{EM}\max$ in (1) is the highest cutoff frequency of the TEM mode with the same axis [25], and the $\lambda_T\text{EM}$ mim is the minimum cutoff wavelength of the TEM mode with the same axis [26]. a is the outer radius for the inner conductor of the coaxial line [27]. b is the inner radius of the outer conductor of the coaxial line. ε_m is the dielectric constant of the medium in the same axis [28]. In the whole water, $a = 2$ mm, $b = 7$ mm, $\varepsilon_m = 80$ in (1 in = 2.54 cm), the highest cutoff frequency is 132.7 MHz, and the minimum cutoff wavelength calculation formula is 253 mm, as mentioned above [29]. Therefore, the circuit structure of the probe of the 12 holding water rate measuring instruments [30] is as shown in Figure 4.
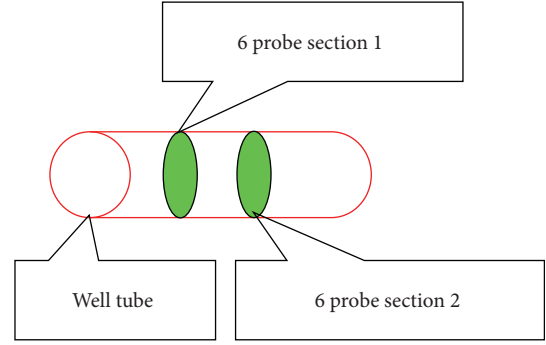
Figure 1: The instrument is measured in two cross sections in the wellbore.
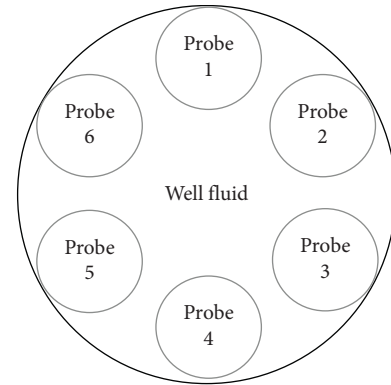
Figure 2: Six probes of the probe section distribution diagram.
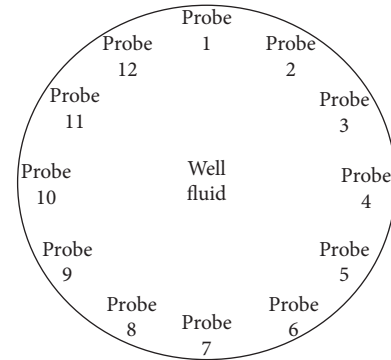
Figure 3: Twelve array probes are evenly distributed within the instrument.

3. The Realization of the Measuring Instrument

According to the previously described content, 12 probe array flow meter logging apparatus is designed as in Figure 5.

As shown in Figure 5, there two groups of the electromagnetic wave water holding rate meter measuring instrument; each group had 6 measuring probes, and 12 probes are covering the whole wellbore section equally. It is called the array logging tool.

There are 12 probes of the array logging tool in radial distribution of borehole to measure the accurate local stalemate rate. These cylindrical probes are 0.157 inches in
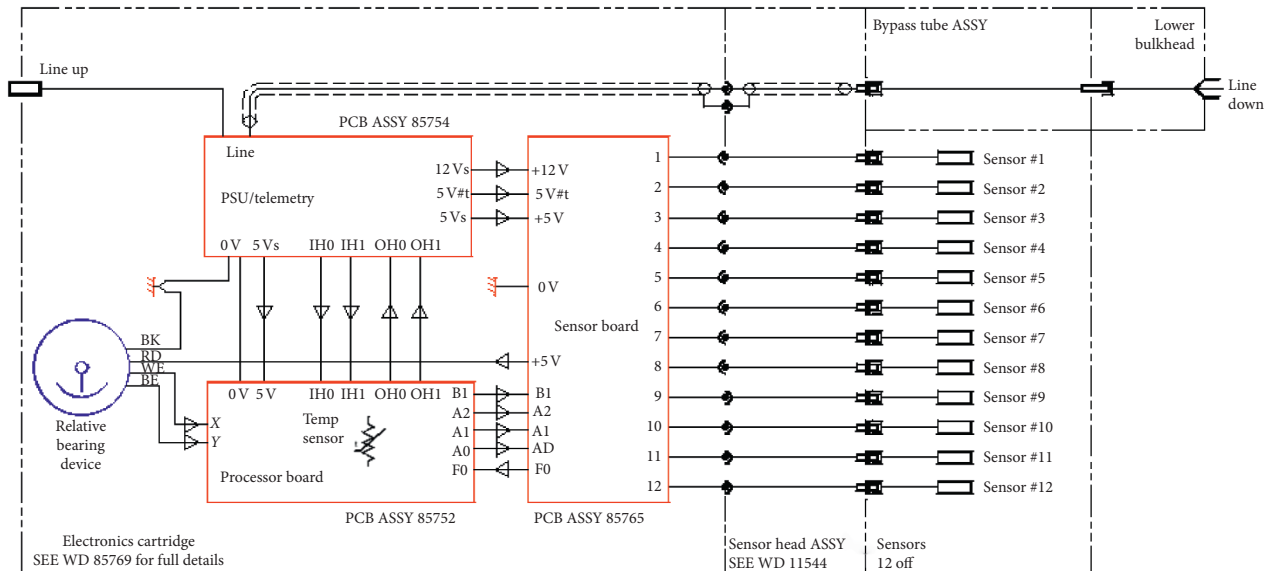
FIGURE 4: Twelve probes circuit logic structure.
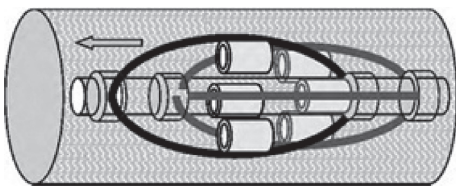
FIGURE 5: Twelve probes electromagnetic wave water holding rate meter measuring instrument.

diameter and 0.055 inches in length. It is set 0.35 inches away from the end of the movable support arm. Each probe resonates at different frequencies in oil [31], gas, and water. The tool judges the distribution of oil, gas, and water in the given area of the well by the difference of frequency resonance in the oil, gas, and water [32].

Corresponding to the capacitance value of the probe phase, the oscillation circuit produces a lower frequency in the water, a higher frequency in the oil, and the highest in the gas [33]. Probe frequency is typically sampled 72 times per minute. It can be repeated on the ground surface, which can process data and display the results [34]. The probe radius of each probe is about 0.01 inches. The probe can only reflect the capacitance value of the local environment around it. The calibration of the probe response can accurately measure the holdup of any two-phase mixture [35].

There are 6 probes are on the same cross section of the double array logging tool. The array logging tool is suitable for measuring the cross section holdup near the top and bottom of the wellbore perpendicular to the shaft [36]. The array of probe provides full coverage of the borehole. It can accurately determine the fluid in horizontal wells and highly deviated wells [37].

The probe calibration works are as follows. First, the borehole fluid is captured, and then, the probe is measured in the fluid, and the measured value is marked. For example, probe measures its value in the produced water and marks its measured value. The probe measures its value in the produced oil and marks its measured value. Probe calibration can take into account each probe specific fluid endpoint value and probe measurements in pure water or pure oil. For oil and water, these responses do not change much from the ground to the bottom. The next, the air point of each probe is recorded as the calibration value of the gas. Unlike the fluid, the air point varies with temperature and pressure. So, if possible, the gas needs to be calibrated on the spot.

Each probe has its own calibration value relative to oil, gas, and water [38]. Therefore, the probe can accurately measure the values of oil, gas, and water in wellbore [39]. For all probes, normalization is made so that each probe has the same measurement value for the same phase. Normalization allows minimal probe differences to be minimized, allowing 12 probe to achieve consistent response. All probes are normalized so that each phase has its own response value. Each probe also has a specific response value to the two-phase mixture. The standardization process is controlled by borehole fluid and special logging tools used. Calibration must be performed before logging. This requires the use of collected borehole fluids. If there is no borehole fluid, it needs to be processed later to correct the logging data [40].

Once the double array logging tool is calibrated and the data are normalized, an image can be formed by processing the curves recorded by 12 probe. The oil, gas, and water have the corresponding color coding in the image. The single-phase water is blue. Single-phase oil is green. The single-phase gas is red. Bracket arm 1 can be positioned relative to the upper part of the borehole. So, when drawing a graph, we can use arm 1 to correct the position.

The double array logging tool can distinguish oil, gas, and water three phase. Therefore, according to the data measured by the array logging tool, the holdup of oil, gas, and water phases can be calculated.

This measuring apparatus has obtained good results in the process of horizontal well measurement construction
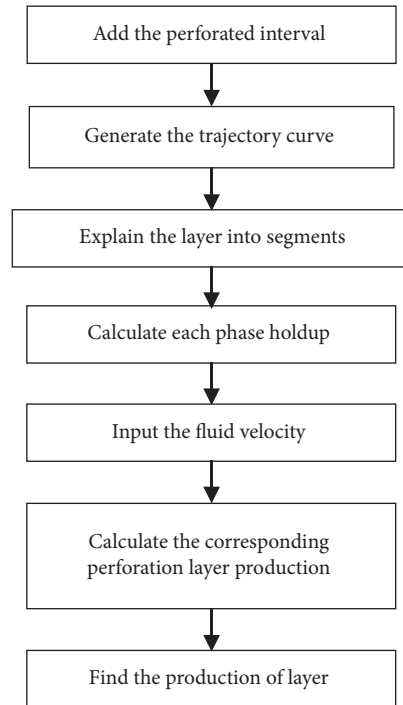
FIGURE 6: The chart of software design.
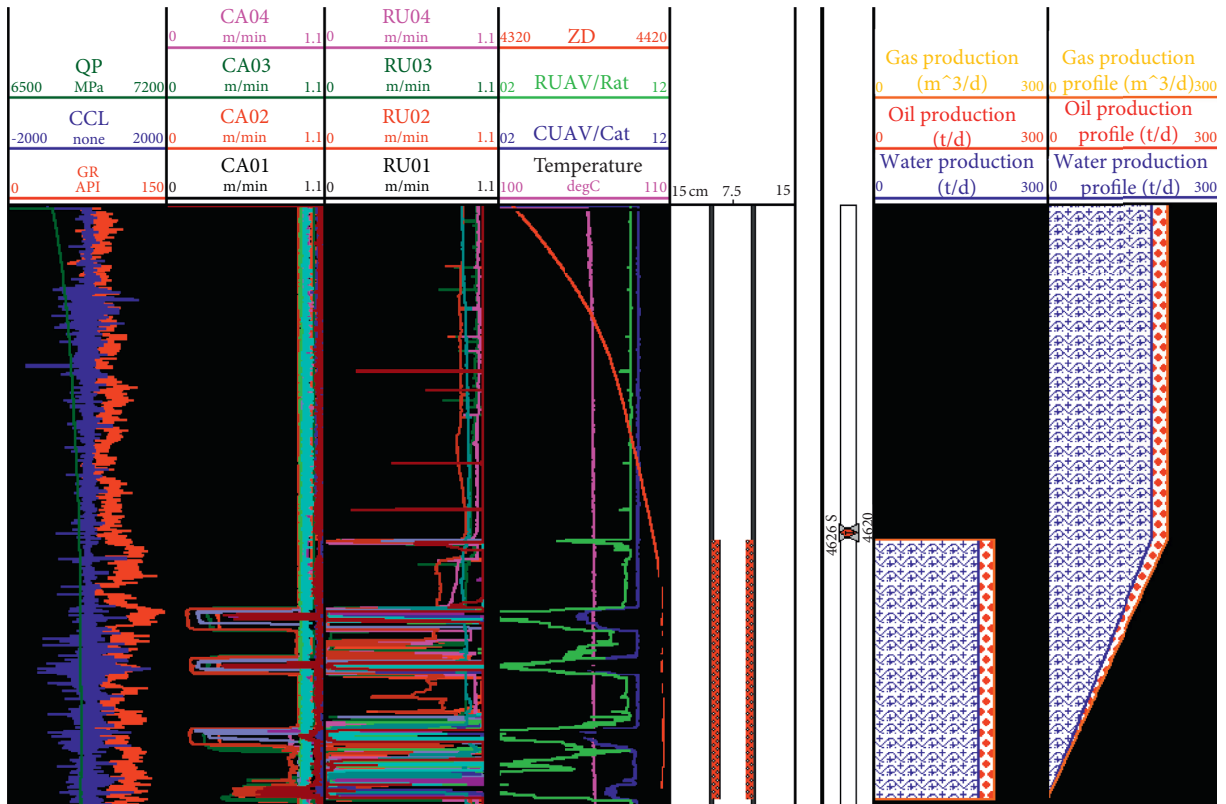
FIGURE 7: Simulation results calculated by the software.

conducted by a well area of Northwest China which is served by Shengli Oilfield Logging Company. We got the corresponding measurement data from using the flow meter well logging apparatus of the staggered probe array to carry out

the production logging task and combined well logging interpretation software for production logging interpretation. Also, a set of horizontal well production interpretation software is developed. It is realized by using VC++ 6.0 as the

TABLE 1: The deviation of calculation and realistic of water holdup Y_w.

Well serial number	Measured value (%)	Actual value (%)	Relative error (%)
1	40.2	44	9.37
2	31.7	34.5	9.01
3	90.2	90.2	0.04
4	60.7	64.6	6.49
5	39.2	40.1	2.19
6	62.8	66.1	5.26
7	32.3	30.2	6.54

TABLE 2: The deviation of calculation and realistic results.

	Calculation results (square per day)	Realistic results (square per day)	Variation (square per day)	Deviation (%)
Oil production	27.031	25.5	1.531	6
Liquid yield	208.463	201.3	7.163	3.56

development on the basis of FORWARD2.71. This software is designed as in Figure 6.

The emphasis is the calculation water holdup. That is described in the paper titled The Calculation Method of Production Log Holdup.

We developed a set of horizontal well production interpretation software. It is realized by using VC++ 6.0 as the development on the basis of FORWARD2.7. The emphasis is the calculation water holdup. That is described in detail in the paper titled The Calculation Method of Production Log Holdup about CAT Instrument.

We can use the computer language to achieve the production log well software and use in the low production horizontal wells. We input the measured value of CAT, RAT, GR, CCL, QP, and ZD. The software can calculate the liquid-producing profile map. That is shown in Figure 7.

4. The Application in Two-Phase Production Logging of Horizontal Wells

We can use the computer language to achieve the production log well software and use in the low-production horizontal wells. We input the measured value of GR, CCL, QP, ZD, and 12 measurement of the electromagnetic wave holding capacity. The software can calculate the liquid-producing profile map. We use the double array logging tool to measure 7 horizontal wells and calculate the water holdup Y_w.

The data of 7 wells are shown in Table 1. Measured value is the value obtained from the double array logging tool measurements. Actual value is the actual water cut value of a well. Relative error is the error between measured value and actual value. Through data analysis, the maximum error is found to be 9.37%. The minimum error is 0.04%. The precision of the double array logging tool is more than 90%. This kind of measuring instrument can meet the production requirement of horizontal well holdup measurement.

It can explain the wellhead metering data and interpretation of results data compared to the results, as shown in Table 2.

The production log interpretation is in accordance with the realistic results. It can measure the moisture content of the production log well. So, this method can accuracy

calculate the results more than 90%, and it can satisfy the requirements of production. The conclusion shows that this method has a certain practical value.

5. Conclusions

Because of the gravity factors, the differentiation of fluid in the horizontal wellbore occurs that the light phase is in the upper part and the lower part is in the lower part. The traditional production logging instrument cannot truly reflect the fluid shape in horizontal wells. So, it must analyze the flow pattern of multiphase flow in horizontal wells. It researches the importance of the multiphase flow mechanism in horizontal wells to interpretation of production profile data.

The double array logging tool can be designed according to the flow pattern of multiphase flow in horizontal wells. It can well measure the fluid holdup values in the horizontal wellbore. The paper developed the horizontal section interpretation module for single-phase and two-phase flow (oil-water two-phase; gas water two-phase) horizontal well production, according to the research model, in the Visual C++ compiling environment. Also, this paper applied the double array logging tool in one Western China horizontal well. We use the module to interpretation of actual logging data. The interpretation results are basically consistent with the actual production situation of the wellhead. It is proved that the developed double array logging tool and the interpretation model of the interpretation method are feasible. It can solve the problem of quantitative interpretation of production profile logging data in horizontal wells.

The paper developed the interpretation module of the array capacitance instrument and array resistance instrument in horizontal well. It can further improve the accuracy of qualitative interpretation by the double array logging tool, which accumulated experience for further quantitative interpretation of array data. There are two novelty points in this study.

First, the design of simulation experiment on the large diameter used in the actual production logging instrument is continuous and packer. This paper analyzed numerical

simulation, the flow, fluid flow characteristics, and the response of the holdup measurement instrument.

Second, it designed the double array logging tool. Also, this paper compiled the interpretation module of the horizontal well production section. This module is used to interpret the actual logging data of horizontal wells, and the interpretation results are basically consistent with the actual production situation at the wellhead, which indicates that that the proposed interpretation model is feasible.

The system has problems and suggestions. First, it will improve the production logging technique in the horizontal well and make full use of the existing domestic conventional production profile measuring instrument. Second, it can measure multiprobe, multi-instrument integral, and local combination on the same target parameters and verify the accuracy of the instrument response. Third, we can also absorb the advanced technology of foreign countries, use the physical theory of electricity (such as a microrotor flow meter) and optics (such as GHOST), and constantly develop new or improved measurement sensor for two-phase flow of a horizontal well.

6. The Future Work

The array logging tools will be introduced furthermore, and the response rules will be clarified. Then, the cooperative interpretation of various logging information will be carried out. Further research on multiphase flow simulation will put forward the appropriate instrument combination and interpretation model.

Data Availability

The data used to support the findings of this study can be obtained from the corresponding author upon request.

Conflicts of Interest

The authors declare that they have no conflicts of interest.

Acknowledgments

References

[1] G. Frisch, T. Perkins, and Q. John, "Integra-ting wellbore flow images with a conventional production log interpretation method," in *Proceedings of the SPE Annual Technical Conference and Exhibition*, San Antonio, TX, USA, September 2002.

[2] W. Song, H. Guo, and X. Shi, "Levenberg-marquardt algorithm used in reservoir damage production of logging prediction," in *Proceedings of the 2011 2nd International Conference on Information Technology and Scientific Management*, pp. 62–65, Nanjing, China, September 2011.

[3] W. Song, H. Guo, and J. Wang, "The BP algorithm used in reservoir damage predictionof speed-sensitive by improved," in *Proceedings of the 2011 2nd International Conference on Information Technology and Scientific Management*, pp. 58–61, Nanjing, China, September 2011.

[4] X.-D. Wang, G.-D. Yu, and Z.-P. Li, "Productivity of horizontal wells with complex branches," *Petroleum Exploration and Development*, vol. 6, pp. 729–733, 2006.

[5] J. Wang and R. Jiang, "Physical modeling of a sidetrack horizontal well production to improve oil recovery," *Science in China (Series E: Technological Sciences)*, vol. 44, no. 4, pp. 353–364, 2002.

[6] H. Zhao and X. Lu, "China's crude oil production from 2005 to 2010 (10,000 tons)," *China Oil & Gas*, vol. 25, no. 2, pp. 22–25, 2011.

[7] Q. Zhao and T. Wenguang, "Achievements of China's coal-bed methane exploration and development," *China Oil & Gas*, vol. 2, pp. 27–31, 2008.

[8] L. Liming, Q. Jishun, S. Yang et al., "Analysis and evaluation on horizontal well seepage models and their developing trends," *Oil & Gas Geology*, vol. 34, no. 6, pp. 821–827, 2013.

[9] B. Ji, "Progress and prospects of enhanced oil recovery technologies at home and abroad," *Oil & Gas Geology*, vol. 33, no. 1, pp. 111–117, 2012.

[10] Y. Han, "Application of horizontal well technology to liaohe oilfield," *China Oil & Gas*, vol. 1, pp. 35–37, 2008.

[11] J. Xu, N. Dong, C. Zhu et al., "Application of seismic data to the design of horizontal well trajectory in tight sandstone reservoirs," *Oil & Gas Geology*, vol. 33, no. 6, pp. 909–913, 2012.

[12] L.-S. Zhai, N. D. Jin, X. K. Zheng et al., "The analysis and modeling of measuring data acquired by using combination production logging tool in horizontal simulation well," *Chinese Journal of Geophysics*, vol. 55, no. 4, pp. 1411–1421, 2012.

[13] Q. Tang, "Application of gesturing technology in the development of Sulige gas field—case studies of the Su10 and Su53 blocks," *Oil & Gas Geology*, vol. 34, no. 3, pp. 388–393, 2013.

[14] Y. Zong, *Measurement of the Properties of Oil-Water Two-Phase Flow in Inclined and Horizontal Pipes*, Tianjin University, Tianjin, China, 2009.

[15] D. Piron, B. Hubert, D. Heddadj, G. Pérès, H. Vincent, and D. Cluzeau, "Indicators of earth wormbioturbation to improve visual assessment of soil structure," *Soil&Tillage Research*, vol. 173, pp. 53–63, 2017.

[16] H. Xu, W. Huang, Q. Hou et al., "The effects of probiotics administration on the milk production, milk components and fecal bacteria microbiota of dairy cows," *Science Bulletin*, vol. 62, no. 11, pp. 767–774, 2017.

[17] Y. Sun, M. Liang, X. Jin, P. Ji, and J. Shan, "Experimental and modeling study of the regular polygon angle-spiral liner in ball mills," *Chinese Journal of Mechanical Engineering*, vol. 30, no. 2, pp. 363–372, 2017.

[18] Y. Li, B. Li, C. Tian, Y. Zhu, B. Song, and Q. Qian, "A method of production profile quick prediction based on typical curves: a case study of the upper shale large multi-layered sandstone

reservoir, Rumaila Oilfield, Iraq," *Petroleum Exploration and Development Online*, vol. 43, no. 6, pp. 189–201, 2016.

[19] A. Patel, N. Arora, J. Mehtani, V. Pruthi, and A. P. Pruthi, "Assessment of fuel properties on the basis of fatty acid profiles of oleaginous yeast for potential biodiesel production," *Renewable and Sustainable Energy Reviews*, vol. 77, pp. 604–616, 2017.

[20] M. O. Igono, G. Bjotvedt, and H. T. Sanford-Crane, "Environmental profile and critical temperature effects on milk production of Holstein cows in desert climate," *International Journal of Biometeorology*, vol. 36, no. 2, pp. 38–45, 1992.

[21] R. Mikuła, W. Nowak, J. Jaśkowski, P. Maćkowiak, and E. Oszmałek, "Effects of different starch sources on metabolic profile, production and fertility parameters in dairy cows," *Polish Journal of Veterinary Sciences*, vol. 14, no. 1, pp. 79–86, 2011.

[22] V. T. Dosseva-Panova, C. L. Popova, and V. E. Panov, "Subgingival microbial profile and production of proinflammatory cytokines in chronic periodontitis," *Folia Medica*, vol. 56, no. 3, pp. 152–160, 2014.

[23] C. Barton and M. Cai, "Equatorial wave expansion of instantaneous flows for diagnosis of equatorial waves from data: formulation and illustration," *Advances in Atmospheric Sciences*, vol. 34, no. 10, pp. 1219–1234, 2017.

[24] C. Liu, X. L. Wang, D. Deng et al., "Optimal spacing of sequential and simultaneous fracturing in horizontal well," *Journal of Natural Gas Science and Engineering*, vol. 29, pp. 85–96, 2016.

[25] M. Wei, Y. Duan, M. Dong, and Q. Fang, "Blasingame decline type curves with material balance pseudo-time modified of a multi-fractured horizontal well in a shale gas reservoir," *Journal of Natural Gas Science and Engineering*, vol. 31, pp. 340–350, 2016.

[26] B. Li, Y.-P. Liang, X.-S. Li, and L. Zhou, "A pilot-scale study of gas production from hydrate deposits with two-spot horizontal well system," *Applied Energy*, vol. 176, pp. 48–57, 2016.

[27] L. Cao, X. Li, C. Luo, L. Yuan, J. Zhang, and X. Tan, "Horizontal well transient rate decline analysis in low permeability gas reservoirs employing an orthogonal transformation method," *Journal of Natural Gas Science and Engineering*, vol. 33, pp. 59–67, 2016.

[28] J. Hou, B. Wei, Q. Du, J. Wang, Q. Wang, and G. Zhang, "Production prediction of cyclic multi-thermal fluid stimulation in a horizontal well," *Journal of Petroleum Science and Engineering*, vol. 146, pp. 949–958, 2016.

[29] Z. Wang, D. Gao, and J. Liu, "Multi-objective sidetracking horizontal well trajectory optimization in cluster wells based on DS algorithm," *Journal of Petroleum Science and Engineering*, vol. 147, pp. 771–778, 2016.

[30] Y. S. Wei, A. L. Jia, D. B. He, and J. L. Wang, "A new method in predicting productivity of multi-stage fractured horizontal well in tight gas reservoirs," *Journal of Natural Gas Geoscience*, vol. 1, pp. 397–406, 2016.

[31] W. Cheng, H. Gao, Y. Jin, M. Chen, and G. Jiang, "A study to assess the stress interaction of propped hydraulic fracture on the geometry of sequential fractures in a horizontal well," *Journal of Natural Gas Science and Engineering*, vol. 37, pp. 69–84, 2016.

[32] G. Cui, S. Ren, L. Zhang et al., "Geothermal exploitation from hot dry rocks via recycling heat transmission fluid in a horizontal well," *Energy*, vol. 128, pp. 156–162, 2017.

[33] X.-P. Li, L.-N. Cao, C. Luo, B. Zhang, J.-Q. Zhang, and X.-H. Tan, "Characteristics of transient production rate performance of horizontal well in fractured tight gas reservoirs with stress-sensitivity effect," *Journal of Petroleum Science and Engineering*, vol. 158, pp. 92–106, 2017.

[34] L. Xu, W. Xu, C. Zhang, X. Liu, and J. Hu, "Multiple parameters' estimation in horizontal well logging using a conductance-probe array," *Flow Measurement and Instrumentation*, vol. 40, pp. 152–160, 2014.

[35] L. Wan, X. Kong, and F. Xia, "Joint range-Doppler-angle estimation for intelligent tracking of moving aerial targets," *IEEE Internet of Things Journal*, vol. 5, no. 3, pp. 1625–1636, 2018.

[36] L. Wan, L. Sun, X. Kong, Y. Yuan, K. Sun, and F. Xia, "Task-driven resource assignment in mobile edge computing exploiting evolutionary computation," *IEEE Wireless Communications*, vol. 26, no. 6, pp. 94–101, 2019.

[37] F. Wen, Z. Zhang, K. Wang, G. Sheng, and G. Zhang, "Angle estimation and mutual coupling self-calibration for ULA-based bistatic MIMO radar," *Signal Processing*, vol. 144, pp. 61–67, 2018.

[38] F. Wen and J. Shi, "Fast direction finding for bistatic EMVS-MIMO radar without pairing," *Signal Process*, vol. 173, Article ID 107532, 2020.

[39] D. Meng, X. Wang, M. Huang, L. Wan, and B. Zhang, "Robust weighted subspace fitting for DOA estimation via block sparse recovery," *IEEE Communications Letters*, vol. 24, no. 3, pp. 563–567, 2020.

[40] X. Wang, L. Wang, X. Li, and G. Bi, "Nuclear norm minimization framework for DOA estimation in MIMO radar," *Signal Processing*, vol. 135, pp. 147–152, 2017.

Research Article

Analysis of Arrhenius Kinetics on Multiphase Flow between a Pair of Rotating Circular Plates

M. B. Arain,[1] M. M. Bhatti [ID],[2] A. Zeeshan,[1] Tareq Saeed,[3] and Aatef Hobiny[3]

[1]*Department of Mathematics and Statistics, International Islamic University, Islamabad 44000, Pakistan*
[2]*College of Mathematics and Systems Science, Shandong University of Science and Technology, Qingdao, Shandong 266590, China*
[3]*Nonlinear Analysis and Applied Mathematics (NAAM)-Research Group, Department of Mathematics, Faculty of Science, King Abdulaziz University, P.O. Box 80203, Jeddah 21589, Saudi Arabia*

Correspondence should be addressed to M. M. Bhatti; mmbhatti@sdust.edu.cn

In this study, we aim to deal with the flow behavior betwixt a pair of rotating circular plates filled with Carreau fluid under the suspension of nanoparticles and motile gyrotactic microorganisms in the presence of generalized magnetic Reynolds number. The activation energy is also contemplated with the nanoparticle concentration equation. The appropriate similarity transformations are used to formulate the proposed mathematical modeling in the three dimensions. The outcomes of the torque on both plates, i.e., the fix and the moving plate, are also contemplated. A well-known differential transform method (DTM) with a combination of Padé approximation will be implemented to get solutions to the coupled nonlinear ordinary differential equations (ODEs). The impact of different nondimensional physical aspects on velocity profile, temperature, concentration, and motile gyrotactic microorganism functions is discussed. The shear-thinning fluid viscosity decreases with shear strain due to its high velocity compared to the Newtonian and shear-thickening case. The impact of Carreau fluid velocity for shear-thinning $(n < 1)$, Newtonian case $(n = 0)$, and shear-thickening $(n > 1)$ cases on axial velocity distribution $f'(\lambda)$ has been discussed in tabular form and graphical figures. For the validation of the current methodology, a comparison is made between DTM-Padé and the numerical shooting scheme.

1. Introduction

A nanofluid is a substance that contains nanosized particles suspended in the base fluid. These nanoparticles are usually made of oxides, metals, carbon nanotubes, or carbides, while base fluids are often taken as water, oil, and ethylene glycol. The potential use of nanofluids can be found in many applications in industry, i.e., heat transfer, especially in pharmaceutical processes, microelectronics, engine cooling (vehicle heat management), hybrid-power engines, chiller, fuel cells, heat exchanger, grinding, and boiler flue gas temperature reduction. The non-Newtonian fluids have significant applications in science and engineering, such as coating of wire and blade, textile dying, papers, manufacturing of plastics, the flow of biological liquids, and food processing. In industrial applications, the flow of non-

Newtonian viscoelastic Carreau nanofluids is essential to increase energy performance. For example, it is used to release polymer sheets from the die or in plastic film drawing. Non-Newtonian fluids have drawn considerable interest among researchers and scientists due to their broad applications. Examples include apple sauce, chyme, photographic emulsion, dirt, soaps, blood, and shampoos at low shear stress that may be noted as non-Newtonian fluids. In the chemical engineering industry, the viscosity of fluid plays a significant role. Viscosity is dependent on the shear rate in the case of generalized Newtonian fluids. The idea of the generalized non-Newtonian fluid was introduced by Bird et al. [1]. Fluid flow past a rigid surface has also been investigated, and literature suggests that the microlevel surface forces are essential and that fluid layering increases viscosity. They help to increase the viscosity of fluid due to fluid

coating. In the power-law model, the limitation is that when the shear rate is extremely low or high, the viscosity is not adequately addressed. To tackle this problem, the model of the Carreau fluid model is presented [2]. The Carreau fluid model gains the attention of many researchers for several years because of their essential characteristics. The flow on the magnetized permeable shrinking sheet and radiation due to heat was discussed by Yahya et al. [3]. Eid et al. [4] analyzed flow over a nonlinear permeable stretching sheet due to Carreau fluid under the influence of chemical reaction. Santoshi et al. [5] numerically studied the Carreau nanofluids in three dimensions on a stretching sheet in addition to considering mass slip and nonlinear thermal radiation. The effects of the internal energy in the porous von Karman model in steady electrical Carreau fluid under ohmic heating and transverse magnetohydrodynamics were studied by Khan et al. [6]. They considered a cylindrical coordinate system, and similarity transformations are applied to obtain the ordinary differential equation for the proposed problem and implement a well-known shooting scheme to achieve the results. Bilal et al. [7] investigated flow features of Carreau fluid by conferring the stimulating traits of thermal stratification. Appropriate use of MHD and infinite shear rate viscosity flow equation are modeled. They concluded that the thermal stratification characterizes fluid flow's thermal distribution, and Carreau fluid acts in a reverse direction for shear-thickening and shear-thinning liquids. Khan et al. [8] examined the mass and heat transfer for convection in non-Newtonian Carreau nanofluid on a cylinder in the presence of temperature-dependent thermal conductivity. They considered a well-known model, i.e., Buongiorno's model, which contains the Brownian and thermophoresis parameters. The key finding of this study was that the temperature profile and concentration of nanoparticle were increasing functions for the thermophoresis parameter in shear-thickening and shear-thinning fluids. Some recent critical studies related to the current topic are given in [9–13].

In previous decades, the study of magnet fields in fluid flow grabbed substantial attention because magnetohydrodynamics (MHD) is frequently used in many areas such as crystal growth process, pumping, agriculture, and polymer industry. MHD was recently identified as very useful in biotechnology as it is used in multiple testing processes for diseases. Recently, Lu et al. [14] studied mathematical models for the axisymmetric steady magnetohydrodynamic flow of Carreau nanofluids across radially stretched surfaces under nonlinear radiation of heat and chemical reaction. The additional feature of the problem, which makes it unique, is the generation/absorption of heat connected with new applied zero mass flux conditions. The flow due to boundary conditions due to convection with Carreau nanofluid with a magnetic field is studied by Wakif et al. [15] in addition to jump and slip conditions on a stretching cylinder. Khan et al. [16, 17] examined the flow induced by non-Newtonian Carreau fluid on a stretching cylinder with a magnetic field.

Further, the flow on a stretching cylinder affected by homogenous and heterogeneous conditions was examined by them and applied to convective boundary conditions

numerically. This study mainly aims at the direct influence of homogenous and different reactions of Carreau fluid on a stretching cylinder with a magnetic field. A practical method for two-dimensional Carreau nanofluid for a nonsimilar solution with a magnetic field (applied) and mixed convection was analyzed by Sardar et al. [18]. They showed that increasing the buoyancy parameter boosts both skin friction and Nusselt number. In the presence of infinite shear rate viscosity, the stagnation point and the MHD flow of a Carreau fluid are also detected. Salahuddin et al. [19] examined the generalized slip effects of the magnetic field on Carreau nanofluid for a linear stretching cylinder with reactive species. Bhatti et al. [20] investigated the peristaltic motion of small particles suspended in a Carreau nanofluid with constant density. Laminar flow in two-dimensional past a stretching cylinder covered with the porous surface was studied with the effects of the magnetic field by Bovand et al. [21]. This article presented the findings of a numerical study of the circulatory cylindrical fluid flow under the influence of magnetohydrodynamics. Another numerical analysis is made by Amanulla et al. [15]. They studied the two-dimensional steady convective boundary layer flow over the surface of an isothermal sphere with the radial magnetic field and slip conditions. They perceived that growth in momentum slip parameters allows the skin friction coefficient to be reduced. In contrast, the local Nusselt number declined as the Carreau fluid parameter increases. Rudraswamy et al. [22] examined the Carreau fluid flow in a two-dimensional stretchable surface with the magnetic field. They concluded with a statement that when Brownian motion parameter and thermophoretic parameters are enhanced, the temperature of the fluid increases. Kumar et al. [23] investigated the Cattaneo–Christov heat flux model with Carreau fluid under the magnetic field on a varying thickness of the melting surface. Akbar et al. [24] investigated the flow of stagnation point for Carreau fluid on a wrinkled sheet in two dimensions. They presented a dual solution for the problem under consideration, and the graphs for various parameters in the equations are drawn. Shit et al. [25] investigated the nanofluid flow with MHD and thermal radiation. They studied the system of energy efficiency through the Bejan number.

Due to the complicated nature of the chemical reactions system, restricting to binary type alone becomes more comfortable and straightforward. A chemical reaction requires a quantity of activation energy to start. In the Arrhenius equation, a reaction's activation energy is obtained by describing constant rate changes with the temperature. A chemical reaction is a chemical change in which reactants with varying properties may yield one or more products. Several industries need chemical reactions as an essential phase in the manufacturing process. Traditionally these types of responses occur in chemical reactors and are generally constrained to mass transfer. The response is sufficient when reagent volume and energy inputs enhance, and waste is reduced; then the optimum product can be obtained. Bestman [26] applied the model of binary reaction in the Arrhenius equation to produce a chemical reaction. The effects of energy of activation and binary chemical

change on a two-dimensional radiative magnetohydrodynamics boundary layer flow for nanofluid on a vertical plate were discussed by Anuradha and Yegammai [27]. They scrutinized that the temperature distribution was accelerated, and the nanoparticle concentration profile decelerates under the effects of the heat generation, viscous dissipation, and MHD. Irfan et al. [28] discussed the Carreau nanofluid time-dependent flow for Arrhenius activation energy by using properties of binary chemical reaction with mixed convection. Khan et al. [29] explored the incompressible flow past a stretchable sheet of the Carreau–Yasuda model. Kumar et al. [30] analyzed the effects of nonlinear radiation with heat transfer attributes and activation energy. Khan et al. [29] reported a new nanofluid relation which examines the characteristics of the energy of activation with mixed convection Carreau nanofluid. They studied radiation and magnetic field parameters on both the entropy generation and the Bejan number.

Bioconvection flow is the flow of macroscopic convection of the fluid due to the density gradient generated by the collective swimming of motile microorganisms. Due to the swimming of these motile microorganisms in a particular direction, the density of the fluid increases, which results in the phenomenon of bioconvection. Slip effects and the movement of motile gyrotactic microorganisms on an exponentially stretching sheet were examined by Nayak at el. [31]. They discussed the temperature profile, velocity profile, nanoparticle concentration profile, and gyrotactic microorganism profile associated with different physical parameters. The thermal radiation effects with activation energy over a stretching cylinder with Oldroyd-B fluid due to the flow of microorganisms under the impact of the magnetic field were examined by Tlili et al. [32]. The thermal developmental nanofluid flow propagating on an extended surface was analyzed by Abdelmalek et al. [33] with additional activation energy characteristics, second-order, and viscous dissipation slip. Atif et al. [34] inspected the flow of the stratified micropolar MHD fluid with nanoparticles that contains gyrotactic microorganisms. The process of ohmic heating and radiated heat has also been taken into consideration. Khan et al. [35] determined the suspension of nanoparticles in Sisko nanofluid, utilizing the idea of microorganisms with activation energy and chemical reaction. Bhatti et al. [36] demonstrated the movement of motile gyrotactic microorganisms past a stretched surface filled with nanofluid. They applied the Successive Local Linearization Method (SLLM) for solving the modeled formulation and showed that the current method is stable and gives excellent results compared with similar methods. Nagendramma et al. [37] developed a mathematical model for Casson fluid through a slandering sheet in the existence of microorganisms for Cattaneo–Christov thermal flux and nonuniform heat source/sink. References [38–42] depict the flow in different geometries with different fluid models.

After investigating the above literature, it is found that no efforts are devoted to determining the analysis of activation energy for the Carreau non-Newtonian nanofluid with gyrotactic microorganism through a pair of rotating circular disks with generalized magnetic Reynolds number.

In the present formulation, we considered the induced magnetic field in the axial and tangential direction. The Carreau nanofluid with gyrotactic microorganisms is suspended betwixt the set of rotating circular disks. The effects of activation energy are also contemplated with nanoparticle concentration. A well-known differential transform method (DTM) with Padé approximant is employed to obtain the solutions of the given coupled highly nonlinear ordinary differential equations. The effects of all the parameters associated with velocity profile, temperature profile, induced magnetic field, nanoparticle concentration, and motile microorganism functions are discussed in detail via graphs and tables.

2. Mathematical and Physical Modeling

Let us contemplate the flow in three-dimensional axisymmetry in a squeezed lubricant film of a Carreau nanofluid betwixt a set of two circular rotating parallel plates with finite length. The coordinate system is chosen as cylindrical polar axis (r, θ, z) with the associated velocity field $V = [v_r, v_\theta, v_z]$. The heights of two parallel rotating circular plates are considered and taken as $\widehat{\Gamma}(t) [= (-\alpha t + 1)^{1/2} D]$ at time t. The lower disk is stationary and upper disk is moving towards fix disk. The velocity of upper disk is denoted by $\widehat{\Gamma}'(t)$. The z−axis indicates the symmetry axis in which the plates are rotating. The external magnetic field on the moving plate is applied with axial and azimuthal components, i.e.,

$$
\begin{cases}
\widehat{H}_\theta = \dfrac{rN_0}{\mu_2} \sqrt{\dfrac{D}{\widehat{\Gamma}(t)}}, \\[4mm]
\widehat{H}_z = -\dfrac{\alpha M_0 D}{\mu_1 \widehat{\Gamma}(t)},
\end{cases}
\tag{1}
$$

in which M_0, N_0 are the dimensionless quantities which make $\widehat{H}_\theta, \widehat{H}_z$ dimensionless and μ_1, μ_2 are the magnetic permeability's of the squeeze film and the medium external to the disks, respectively. For the liquid metals, $\mu_2 = \mu_\ell$ where μ_ℓ denotes the permeability of free space. H_θ, H_z on the lower plate is assumed to be zero here. In present investigation, induced magnetic field $\widehat{B}(r, \theta, z)$ having the component $\widehat{B}_r, \widehat{B}_\theta, \widehat{B}_z$ is generated by the magnetic field (applied) in a squeezed film between the plates. Figure 1 shows the geometrical coordinates. The upper and lower plate are held at fixed temperature (T_0, T_1) and concentration (C_0, C_1). The fluid is electrically conducting under the suspension of nanoparticles and gyrotactic microorganisms.

2.1. Rheological Model for Carreau Fluid. The Carreau fluid model is defined as [43]

$$
\widetilde{\tau}_{ij} = \left[\mu_\infty + (\mu_0 - \mu_\infty)\left(1 + (\Gamma \dot{\gamma})^2\right)^{(n-1/2)} \right] \widehat{A}_1,
\tag{2}
$$

in which $\widetilde{\tau}_{ij}$ represents the stress tensor, μ_0 represents the zero shear rate viscosity, μ_∞ represents the limiting constant viscosity at infinite shear rate viscosity, Γ represents the
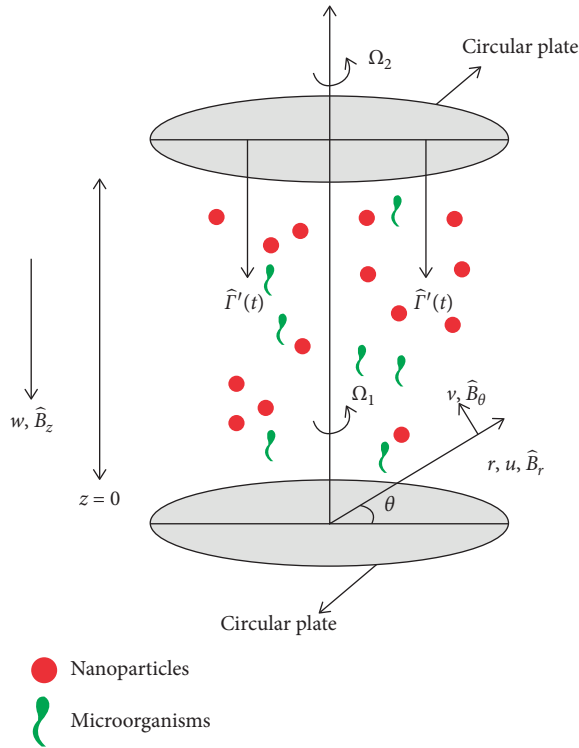
FIGURE 1: The schematic diagram of nanoparticles between parallel finite plates in the presence of microorganisms.

constant of time, n represents the power law index, $\widehat{A}_1$ represents the first Rivlin–Ericksen tensor, and $\dot{\gamma}$ represents the second invariant rate of strain tensor which is defined as

$$\dot{\gamma} = \sqrt{\frac{1}{2} tr\left(\widehat{A}_1\right)},$$

$$\widehat{A}_1 = \left(L + L^T\right) = \left[\left(\nabla V + \nabla V^T\right)\right]. \tag{3}$$

Assume that μ_∞ is zero, and by using binomial series approximation of first order of (2), we have

$$\widetilde{\tau}_{ij} = \left[\mu_0\left(1 + \frac{n-1}{2}(\Gamma\dot{\gamma})^2\right)\right]\widehat{A}_1. \tag{4}$$

The Carreau fluid model in component form is given in Appendix.

2.2. Problem Formulation. The governing flow equations by taking the above assumptions, the MHD squeezed film regime for Carreau fluid model, the equation of continuity, and momentum in r, θ, z direction can be read as

$$\frac{1}{r}\frac{\partial}{\partial r}\left(rv_r\right) + \frac{1}{r}\frac{\partial}{\partial \theta}\left(v_\theta\right) + \frac{\partial}{\partial z}\left(v_z\right) = 0, \tag{5}$$

$$\rho\left(\frac{\partial v_r}{\partial t} + v_r\frac{\partial v_r}{\partial r} + \frac{v_\theta}{r}\frac{\partial v_r}{\partial \theta} + v_z\frac{\partial v_r}{\partial z} - \frac{v_\theta}{r}\right) = -\frac{\partial p}{\partial r}$$
$$+ \frac{1}{r}\frac{\partial}{\partial r}\left(r\widetilde{\tau}_{rr}\right) + \frac{1}{r}\frac{\partial \widetilde{\tau}_{r\theta}}{\partial \theta} - \frac{\widetilde{\tau}_{\theta\theta}}{r} + \frac{\partial \widetilde{\tau}_{rz}}{\partial z} - \frac{\partial B_r}{\partial z}B_z - \frac{\partial B_\theta}{\partial z}B_\theta, \tag{6}$$

$$\rho\left(\frac{\partial v_\theta}{\partial t} + v_r\frac{\partial v_\theta}{\partial r} + \frac{v_\theta}{r}\frac{\partial v_\theta}{\partial \theta} + v_z\frac{\partial v_\theta}{\partial z} - \frac{v_r v_\theta}{r}\right) = -\frac{1}{r}\frac{\partial p}{\partial \theta}$$
$$+ \frac{1}{r}\frac{\partial \widetilde{\tau}_{\theta\theta}}{\partial \theta} + \frac{1}{r^2}\frac{\partial\left(r^2\widetilde{\tau}_{r\theta}\right)}{\partial r} + \frac{\partial \widetilde{\tau}_{\theta z}}{\partial z} - \frac{\partial B_\theta}{\partial z}B_z - \frac{\partial B_\theta}{\partial r}B_r, \tag{7}$$

$$\rho\left(\frac{\partial v_z}{\partial t} + v_r\frac{\partial v_z}{\partial r} + \frac{v_\theta}{r}\frac{\partial v_z}{\partial \theta} + v_z\frac{\partial v_z}{\partial z}\right) = -\frac{\partial p}{\partial z}$$
$$+ \frac{1}{r}\frac{\partial}{\partial r}\left(r\widetilde{\tau}_{rz}\right) + \frac{1}{r}\frac{\partial \widetilde{\tau}_{\theta z}}{\partial \theta} + \frac{\partial \widetilde{\tau}_{zz}}{\partial z} - \frac{\partial B_\theta}{\partial z}B_\theta + \frac{\partial B_r}{\partial z}B_r, \tag{8}$$

where $\rho, \mu, \widetilde{\tau}, p$ are denoted by fluid density, viscosity, stress tensor, and pressure, respectively. The equation of magnetic field can be read as

$$\frac{1}{r}\frac{\partial}{\partial r}\left(rB_r\right) + \frac{1}{r}\frac{\partial B_\theta}{\partial \theta} + \frac{\partial B_z}{\partial z} = 0, \tag{9}$$

$$\frac{\partial B_r}{\partial t} + u\frac{\partial B_r}{\partial r} + v\frac{\partial B_r}{\partial \theta} + w\frac{\partial B_r}{\partial z} = -\frac{\partial}{\partial z}\left(v_r B_z - v_z B_r\right) + \frac{1}{\delta\mu_2}\left(\frac{\partial^2 B_r}{\partial z^2}\right), \tag{10}$$

$$\frac{\partial B_\theta}{\partial t} + u\frac{\partial B_\theta}{\partial r} + v\frac{\partial B_\theta}{\partial \theta} + w\frac{\partial B_\theta}{\partial z} = \frac{\partial}{\partial r}\left(v_r B_\theta - v_\theta B_r\right) - \frac{\partial}{\partial z}\left(v_\theta B_z - B_\theta v_z\right) + \frac{1}{\delta\mu_2}\left(\frac{\partial^2 B_\theta}{\partial z^2}\right), \tag{11}$$

$$\frac{\partial B_z}{\partial t} + u\frac{\partial B_z}{\partial r} + v\frac{\partial B_z}{\partial \theta} + w\frac{\partial B_z}{\partial z} = \frac{\partial}{\partial r}\left(v_r B_z - v_z B_r\right) + \frac{1}{\delta\mu_2}\left(\frac{\partial^2 B_z}{\partial z^2}\right), \tag{12}$$

where δ represents the electrical conductivity.

The energy equation for the proposed problem is read as

$$\frac{\partial \breve{T}}{\partial t} + v_r \frac{\partial \breve{T}}{\partial r} + v_z \frac{\partial \breve{T}}{\partial z} = \breve{\alpha} \frac{\partial^2 \breve{T}}{\partial z^2} + \tau \left[D_B \left(\frac{\partial \breve{T}}{\partial r} \frac{\partial \breve{C}}{\partial r} + \frac{\partial \breve{T}}{\partial z} \frac{\partial \breve{C}}{\partial z} \right) + \frac{D_T}{T_\infty} \left[\left(\frac{\partial \breve{T}}{\partial r} \right)^2 + \left(\frac{\partial \breve{T}}{\partial z} \right)^2 \right] \right], \tag{13}$$

where $\breve{T}, \breve{C}, \breve{T}_m, D_B, \tau = (\rho c)_f / (\rho c)_p$, $\breve{\alpha} = k/(\rho c)_p\, D_T$ are the temperature, concentration, mean fluid temperature, Brownian diffusivity, the proportion of the effected heat capacitance of the nanoparticle to the base fluid, and thermophoretic diffusion coefficient, respectively, where k is the thermal conductivity and $(\rho c)_p$ is the heat capacity of the nanofluid.

The concentration of nanoparticle equation with activation energy reads

$$\frac{\partial \breve{C}}{\partial t} + v_r \frac{\partial \breve{C}}{\partial r} + v_z \frac{\partial \breve{C}}{\partial z} = D_B \frac{\partial^2 \breve{C}}{\partial z^2} + \frac{D_T}{\breve{T}} \frac{\partial^2 \breve{T}}{\partial z^2} - k_r^2 (C - C_\infty) \left(\frac{\breve{T}}{\breve{T}_\infty} \right)^{\bar{n}}$$

$$\cdot \exp \left(-\frac{E_a}{1 + \kappa \breve{T}} \right), \tag{14}$$

where κ, k_r^2, $\bar{n}$, and E_a represent the Boltzmann constant, reaction rate, rate constant, and activation energy, respectively.

The conservation of microorganism reads

$$\frac{\partial n}{\partial t} + v_r \frac{\partial n}{\partial r} + v_\theta \frac{\partial n}{\partial \theta} + v_z \frac{\partial n}{\partial z} + \frac{\bar{b} W_{mo}}{C_\infty} \left[\frac{\partial}{\partial z} \left(n \frac{\partial \breve{C}}{\partial z} \right) \right]$$

$$= D_{mo} \left(\frac{\partial^2 n}{\partial z^2} \right), \tag{15}$$

where chemotaxis constant is combined with maximal speed of cell swimming and is denoted by $\bar{b} W_{mo}$ ($\bar{b} W_{mo}$ is considered as a constant) and diffusivity of microorganisms is denoted by D_{mo}.

The initial and boundary conditions for (5)–(15) with our assumptions are the same as considered in [44]

$$u = 0, \; v = \Omega_1 r \frac{D^2}{\widehat{\Gamma}^2 (t)}, \; w = 0, \; B_z = B_\theta = 0, \; C = \breve{C}_l, \; T = \breve{T}_l, \; n = n_l \quad at \; z = 0, \tag{16}$$

$$\begin{cases} u = 0, \; v = \Omega_2 r \dfrac{D^2}{\widehat{\Gamma}^2 (t)}, \; B_\theta = N_0 r \dfrac{D^2}{\widehat{\Gamma}^2 (t)}, \; B_z = -\dfrac{\beta D M_0}{\widehat{\Gamma} (t)}, \; w = -\dfrac{\beta D^2}{2 \widehat{\Gamma} (t)}, & \\[2mm] T = \breve{T}_u, \; C = \breve{C}_u, \; n = n_u, & \end{cases} \quad at \; z = \widehat{\Gamma} (t), \tag{17}$$

2.3. Similarity Transformations.
The set of similarity transformations are introduced as

$$\begin{cases} v_r = r \dfrac{\partial F}{\partial z} = \dfrac{\alpha r}{2} \dfrac{D^2}{\widehat{\Gamma}^2 (t)} f' (\lambda), \; v_\theta = r G (z, t) = r \Omega_1 \dfrac{D^2}{\widehat{\Gamma}^2 (t)} g (\lambda), \\[3mm] B_r = r \dfrac{\partial M}{\partial z} = \dfrac{\alpha r\, D M_0}{2 \widehat{\Gamma}^2 (t)} m' (\lambda), \; B_\theta = r N (z, t) = r N_0 \dfrac{D^2}{\widehat{\Gamma}^2 (t)} n (\lambda), \\[3mm] B_z = -2 M (z, t) = -\dfrac{\alpha\, D M_0 m (\lambda)}{\widehat{\Gamma} (t)}, \; v_z = -2 F (z, t) = -\dfrac{\alpha D^2 f (\lambda)}{\widehat{\Gamma} (t)}, \\[3mm] \phi (\lambda) = \dfrac{\breve{C} - \breve{C}_u}{\breve{C}_l - \breve{C}_u}, \; \chi (\lambda) = \dfrac{n - n_u}{n_l - n_u}, \; \breve{\theta} = \dfrac{\breve{T} - \breve{T}_u}{\breve{T}_l - \breve{T}_u}, \; \lambda = \dfrac{z}{\widehat{\Gamma} (t)}. \end{cases} \tag{18}$$

Now substituting the abovementioned similarity transformation in (5)–(15), the following highly coupled nonlinear ordinary differential equations (ODEs) with unit-spaced variable λ are obtained as

$$f^{(iv)} = 8S_Q\left[3f'' - 2\left(\frac{R_\Omega}{S_Q}\right)^2 gg' + 2F_T^2\left(mm''' + m'm''\right) - (2f - \lambda)f''' + 2F_A^2\left(\frac{R_\Omega}{S_Q}\right)^2 nn'\right]$$

$$-4(n-1)We\left[\begin{array}{l}\dfrac{1}{S_Q}\left(2f'g'g'' + f''g'^2\right) + \dfrac{S_Q}{R_\Omega^2}\left[7f'f''f''' + 3f''^3 + \dfrac{1}{2}f'^2f^{iv} - \dfrac{3Re}{4R_\Omega}\left(2f''f'''^2 + f''^2 f^{iv}\right)\right] \\[2mm] -\dfrac{Re}{2R_\Omega S_Q}\left[\left(g'f''g''' + g'f'''g'' + f''g''^2\right) - \dfrac{1}{4}\left(g'^2 f^{iv} + 2g'g''f'''\right)\right]\end{array}\right], \tag{19}$$

$$g''(\eta) = 2S_Q^2\left[2g + \lambda g' + 2gf' - fg' + 2F_A F_T\left(mn' + nm'\right)\right]$$

$$-(n-1)WeS_Q\left[\frac{2S_Q}{R_\Omega^2}\left(f'^2 g'' + 2f'f''g'\right) - \frac{3Re}{2S_Q R_\Omega}g'^2 g'' - \frac{ReS_Q}{R_Q^3}\left(\frac{3f''^2 g''}{4} + g'f''f'''\right)\right], \tag{20}$$

$$m'' = Re_M\left[m + \lambda m' + 2mf' - 2fm'\right], \tag{21}$$

$$n'' = Re_M\left[2n - fn' + \lambda n' + 2\left(\frac{F_A}{F_T}\right)mg'\right], \tag{22}$$

$$\breve{\theta}'' + S_Q P_t f\overline{\theta'} + T_t\theta''^2 + T_{b\breve{}}\,\theta'\phi' = 0, \tag{23}$$

$$\phi'' + \frac{T_t}{T_b}\,\breve{\theta}'' + S_Q S_M f\phi' - S_M\sigma(1 + \widetilde{\delta}\breve{\theta})^{\overline{n}}\exp\left(-\frac{E}{1 + \widetilde{\delta}\breve{\theta}}\right)\phi = 0, \tag{24}$$

$$\chi'' - S_Q B_s\left(\frac{\lambda}{2}\right)\chi' + B_s S_Q f\chi' - P_l\left[\chi'\phi' + (\chi + \Phi)\phi''\right] = 0, \tag{25}$$

where squeezed Reynolds number is represented by S_Q, rotational Reynolds number is denoted by R_Ω, magnetic field strength in axial and azimuthal direction is represented by F_A, F_T, respectively, magnetic Reynolds number is represented by Re_M, Weissenberg number is represented by We, Brownian motion parameter is represented by T_b, thermophoresis parameter is represented by T_t, Prandtl number is represented by P_t, Schmidt number is represented by S_M, chemical reaction parameter is represented by σ, temperature difference is represented by $\widetilde{\delta}$, bioconvection Schmidt number is represented by B_s, Peclet number is represented by P_l, and Φ represents constant number. They are defined as

$$\begin{cases} S_Q = \dfrac{\alpha D^2}{2v}, \ R_\Omega = \dfrac{\Omega_1 D^2}{v}, \ F_T = \dfrac{M_0}{D\sqrt{\mu_2\rho}}, \ F_A = \dfrac{N_0}{\Omega_1\sqrt{\mu_2\rho}}, \ We = \Omega_1^2\Gamma^2, \\[4mm] T_b = \dfrac{\tau D_B\left(\breve{C}_l - \breve{C}_u\right)}{\breve{\alpha}}, \ T_t = \dfrac{\tau D_T\left(\breve{T}_l - \breve{T}_u\right)}{\breve{\alpha}}, \ P_t = \dfrac{v}{\breve{\alpha}}, S_M = \dfrac{v}{D_B}, \\[4mm] B_s = \dfrac{v}{D_n}, \ P_l = \dfrac{\overline{b}W_{mo}}{D_{mo}}, \ \Phi = \dfrac{n_\infty}{n_w - n_\infty}, \ Bt = \delta\mu_2 v, \ Re_M = R_Q Bt, \end{cases} \tag{26}$$

where Bt is the Batchelor number.

The corresponding boundary mentioned in (16) and (17) is reduced as

$$\begin{cases} f(0) = 0 = f'(0), \, g(0) = 1, \, m(0) = 0, \, n(0) = 1, \, \breve{\theta}(0) = 1, \, \chi(0) = 1, \phi(0) = 1, \\[2mm] f(1) = \dfrac{1}{2}, \, g(1) = \dot{\xi}, \, m(1) = 1, \, n(1) = 1, \, \breve{\theta}(1) = 0, \, \phi(1) = 0, \, \chi(1) = 0, \end{cases} \tag{27}$$

where f represents the axial and g represents the tangential velocity, m represents the axial and n represents the tangential induced magnetic field components, θ represents the temperature profile, ϕ represents nanoparticles concentration, χ represents the motile density microorganism profile, and $\xi(= \Omega_2/\Omega_1)$ denotes the angular velocity and the range of the velocity betwixt the rotating plates is $-1 \leq \xi \leq 1$, which is useful to analyze various flows characteristics of rotating plates which revolve in the same or opposite directions.

The dimensionless torque can be measured on the moving disk by

$$\dot{T}_{up} = 2\pi\rho \int_0^b \left(\frac{\partial v}{\partial z}\right)_{z=\widehat{\Gamma}(t)} dr. \tag{28}$$

The radius of the disk is denoted by b.

Using (18) in (28), it becomes

$$\dot{T}_{up} = \frac{dg(1)}{d\lambda}, \tag{29}$$

where the nondimensional torque on moving disk by fluid is denoted by $\dot{T}_{up}$, and gradient of the tangential velocity on the moving disk is $dg(1)/d\lambda$.

Similarly, the torque in dimensionless form on the lower (fixed) plate is obtained by the same calculation at $\lambda = 0$; it becomes

$$\dot{T}_{lp} = \frac{dg(0)}{d\lambda}. \tag{30}$$

3. Solution of the Problem: Differential Transform Method (DTM)

The nonlinear dimensionless ordinary differential equations (19)–(25) with boundary conditions (28) are elucidated with DTM. The DTM produces an analytical result based on Taylor series expansion in polynomial form. The differential transform method can easily be applied to linear or nonlinear problems and reduces the size of computational work. With this method, exact solutions may be obtained without cumbersome work, and it is a useful tool for analytical and numerical solutions. In the past decades, DTM has been successfully applied in many models of fluid dynamics, nanofluid dynamics in biotechnology, heat transfer, burgers equations, applications to nonlinear oscillators, plane Couette fluid flow problem, free vibration analysis, micropolar fluid flow, and non-Newtonian nanofluids flow analysis [45–48]. The proposed Padé approximation helps to enhance the convergence rate of the solutions of the truncated series. The DTM solutions can not satisfy the given boundary conditions at infinity without the use of Padé approximations. It is, therefore, essential to use DTM-Padé to afford an effective way to deal with infinite boundary value problems. Mathematica (12v) software has been used to obtain approximations. The complete procedure of this method is described by Zhang et al. [49]. Taking differential transform of each term of (19)–(25), the following transformations are obtained:

$$\left.\begin{aligned} f'' &\longrightarrow (k+1)(2+k)f(2+k), \\ f''^3 &\longrightarrow \left[\sum_{m=0}^k \left(\begin{aligned}\sum_{r=0}^m (r+1)(r+2)(-r+m+1)(-m+k+1)(-m+k+2) \\ f(-m+k+2)f(2+r)f(-r+2+k)\end{aligned}\right)\right], \\ f'f''f''' &\longrightarrow \left[\sum_{r=0}^k \left(\begin{aligned}\sum_{m=0}^{k-r} (r+1)(1+m)(2+m)(-r+k-m+1)(-r+2+k-m) \\ (-m+k-r+3)f(1+r)f(2+m)f(-r+k-m+3)\end{aligned}\right)\right], \\ f''f'''^2 &\longrightarrow \left[\sum_{r=0}^k \left(\begin{aligned}\sum_{m=0}^{k-r} (1+r)(r+2)(3+r)(m+1)(2+m)(-m+k+1-r) \\ (-m+k+2-r)(-m+k-r+3)f(3+r)f(2+m)f(-m+k-r+3)\end{aligned}\right)\right], \end{aligned}\right\} \tag{31}$$

$$\left.\begin{aligned} g &\longrightarrow g(k), \\ \lambda g' &\longrightarrow \sum_{r=0}^k ((-r+1+k)\varepsilon(r)g(-r+1+k)), \end{aligned}\right\} \tag{32}$$

$$gf' \longrightarrow \sum_{r=0}^{k}(-r+1+k)g(r)f(-r+1+k),$$

$$fg' \longrightarrow \sum_{r=0}^{k}(-r=1+k)f(r)g(-r+1+k),$$

$$f'g'g'' \longrightarrow \sum_{r=0}^{k}(r+1)(-r+1+k)(-r+2+k)f(1+r)g(1+r)g(-r+2+k),$$

$$g'g''f''' \longrightarrow \sum_{r=0}^{k}(1+r)(r+2)(-r+1+k)(-r+2+k)(-r+k+3)g(1+r)g(2+r)$$
$$g(-r+k+3),$$

$$f'g'f'' \longrightarrow \sum_{r=0}^{k}(1+r)(-r+k+1)(-r+2+k)f(1+r)g(1+r)f(-r+2+k),$$

$$g'f''f''' \longrightarrow \sum_{r=0}^{k}(1+r)(2+r)(-r+1+k)(-r+2+k)(-r+k+3)g(r+1)f(2+r)$$
$$f(-r+3+k),$$

$$f''g'^{2} \longrightarrow \sum_{m=0}^{k}\left(\begin{array}{l}\sum_{r=0}^{m}(1+r)(2+r)(1-r+m)(-m+1+k)g(-m+1+k)f(2+r) \\ g(-r+1+k)\end{array}\right),$$

$$f''g''^{2} \longrightarrow \sum_{r=0}^{k}\left(\begin{array}{l}\sum_{m=0}^{k-r}(r+1)(2+r)(m+1)(m+2)(-m+1-r+k)(-r+2+k-m) \\ g(2+r)f(m+2)g(-r+2+k-m)\end{array}\right),$$

$$f'^{2}g'' \longrightarrow \sum_{m=0}^{k}\left(\begin{array}{l}\sum_{r=0}^{m}(1+r)(2+r)(-r+1+m)(-m+1+k)f(-m+1+k)g(2+r) \\ f(-r+k+1)\end{array}\right),$$

$$(33)$$

$$m'm'' \longrightarrow \sum_{r=0}^{k}(r+1)(2+r)(-r+1+k)(-r+2+k)m(r+1)m(-r+2+k),$$

$$\lambda m' \longrightarrow \sum_{r=0}^{k}((-r+1+k)\varepsilon(r)m(-r+k+1)),$$

$$mf' \longrightarrow \sum_{r=0}^{k}((-r+1+k)m(r)f(-r+1+k)),$$

$$fm' \longrightarrow \sum_{r=0}^{k}((-r+1+k)f(r)m(-r+1+k)),$$

$$mg' \longrightarrow \sum_{r=0}^{k}((-r+1+k)m(r)g(-r+1+k)),$$

$$(34)$$

$$nn' \longrightarrow \sum_{r=0}^{k}((-r+1+k)n(r)n(-r+1+k)),$$

$$fn' \longrightarrow \sum_{r=0}^{k}((-r+1+k)f(r)n(-r+1+k)),$$

$$\lambda n' \longrightarrow \sum_{r=0}^{k}((-r+1+k)\varepsilon(r)n(-r+1+k)),$$

$$(35)$$

$$f \smile \theta' \longrightarrow \sum_{r=0}^{k} \left((-r + 1 + k) f(r) \breve{\theta}(-r + 1 + k) \right),$$

$$\breve{\theta}'^{2} \longrightarrow \sum_{r=0}^{k} \left((1 + r)(-r + 1 + k) \breve{\theta}(1 + r) \breve{\theta}(1 - r + k) \right), \tag{36}$$

$$\smile \theta' \phi' \longrightarrow \sum_{r=0}^{k} \left((1 + r)(-r + 1 + k) \breve{\theta}(1 + r) \phi(-r + 1 + k) \right),$$

$$f \phi' \longrightarrow \sum_{r=0}^{k} \left((-r + 1 + k) f(r) \phi(-r + 1 + k) \right), \tag{37}$$

$$\lambda \chi' \longrightarrow \sum_{r=0}^{k} \left((-r + 1 + k) \varepsilon(r) \chi(-r + 1 + k) \right),$$

$$f \chi' \longrightarrow \sum_{r=0}^{k} \left((-r + 1 + k) f(r) \chi(-r + 1 + k) \right),$$

$$\chi' \phi' \longrightarrow \sum_{r=0}^{k} \left((1 + r)(-r + 1 + k) \chi(r + 1) \phi(-r + 1 + k) \right),$$

$$\chi \phi'' \longrightarrow \sum_{r=0}^{k} \left((-r + 1 + k)(-r + 2 + k) \chi(r) \phi(-r + 2 + k) \right), \tag{38}$$

where the transformed functions of $f(\lambda), g(\lambda), m(\lambda), n(\lambda), \theta(\lambda), \phi(\lambda)$ and $\chi(\lambda)$ are $f(k), g(k), m(k), n(k), \theta(k), \phi(k)$ and $\chi(k)$, respectively, and are expressed as

$$f(\lambda) = \sum_{k=0}^{\infty} f(k) \lambda^{k},$$

$$g(\lambda) = \sum_{k=0}^{\infty} g(k) \lambda^{k},$$

$$m(\lambda) = \sum_{k=0}^{\infty} m(k) \lambda^{k},$$

$$n(\lambda) = \sum_{k=0}^{\infty} n(k) \lambda^{k}, \tag{39}$$

$$\breve{\theta}(\lambda) = \sum_{k=0}^{\infty} \breve{\theta}(k) \lambda^{k},$$

$$\phi(\lambda) = \sum_{k=0}^{\infty} \phi(k) \lambda^{k},$$

$$\chi(\lambda) = \sum_{k=0}^{\infty} \chi(k) \lambda^{k}.$$

The boundary conditions are

$$f(0) = 0, \ f(1) = \frac{1}{2}, \ g(0) = 1, \ m(0) = 0, \ n(0) = 0,$$

$$\breve{\theta}(0) = 1, \ \phi(0) = 0, \ \chi(0) = 0, \ f(2) = \Pi_1, \ f(3) = \Pi_2,$$

$$g(1) = \Pi_3, \ m(1) = \Pi_4, \ n(1) = \Pi_5, \ \breve{\theta}(1) = \Pi_6, \ \phi(1) = \Pi_6,$$

$$\chi(1) = \Pi_8. \tag{40}$$

Substituting transformations given in (31)–(38) into (19)–(25) and solving with the help of boundary conditions given in (40), the series solutions are

$$f(\lambda) = \overline{f}_1 \lambda^2 + \overline{f}_2 \lambda^3 + \overline{f}_3 \lambda^4 + \overline{f}_4 \lambda^5 + \dots, \tag{41}$$

$$g(\lambda) = 1 - \overline{g}_1 \lambda + \overline{g}_2 \lambda^2 + \overline{g}_3 \lambda^3 + \overline{g}_4 \lambda^4 + \dots, \tag{42}$$

$$m(\lambda) = \overline{m}_1 \lambda + \overline{m}_2 \lambda^3 + \overline{m}_3 \lambda^4 + \overline{m}_4 \lambda^5 + \dots, \tag{43}$$

$$n(\lambda) = \overline{n}_1 \lambda + \overline{n}_2 \lambda^3 + \overline{n}_3 \lambda^4 + \overline{n}_4 \lambda^5 + \dots, \tag{44}$$

$$\breve{\theta}(\lambda) = 1 + \overline{\theta}_1 \lambda + \overline{\theta}_2 \lambda^2 + \overline{\theta}_3 \lambda^3 + \overline{\theta}_4 \lambda^4 + \dots, \tag{45}$$

$$\phi(\lambda) = 1 + \overline{\phi}_1 \lambda + \overline{\phi}_2 \lambda^2 + \overline{\phi}_3 \lambda^3 + \overline{\phi}_4 \lambda^4 + \dots, \tag{46}$$

$$\chi(\lambda) = 1 + \overline{\chi}_1 \lambda + \overline{\chi}_2 \lambda^2 + \overline{\chi}_3 \lambda^3 + \overline{\chi}_4 \lambda^4 + \dots, \tag{47}$$

where $\overline{f}_i, \overline{g}_i, \overline{m}_i, \overline{n}_i, \overline{\theta}_i, \overline{\phi}_i \overline{\chi}_i;$ $(i = 1, 2, 3, \dots)$ are constants but difficult to represent here. With the aid of Mathematica (12v) software, the above equations are solved with 30 iterations. However, the rate of convergence is not obtained. Some schemes are available to increase the rate of convergence. One of the easiest ways to enhance the rate of convergence of the truncated series is Padé approximation, which is utilized into the form of rational fraction (ratio of two polynomials). Without the use of Padé approximation, the results attained by DTM do not satisfy the boundary condition at infinity because of the nonlinearity in the governing equations. So it is compulsory to combine the analytic solution obtained by DTM with the Padé approximation which gives good convergence rate at infinity. As a result of numerical values to a desired exactness, the number of terms required is determined by the higher approximation

of the order. The Padé approximation of order $[5 \times 5]$ is applied to (41)–(47); the Padé approximants are as follows:

$$f(\lambda) = \frac{1.90345\lambda^2 - 1.46791\lambda^3 + 0.305748\lambda^4 - 0.096132\lambda^5 + \ldots}{1 + 0.254218\lambda + 0.054450\lambda^2 - 0.00576\lambda^3 - 0.0106312\lambda^4 - 0.00369678\lambda^5 + \ldots},$$

$$g(\lambda) = \frac{1 - 2.5321\lambda + 0.1463087\lambda^2 + 0.8214957\lambda^3 + 0.4412932\lambda^4 + 0.130549\lambda^5}{1 - 1.53185\lambda - 1.38353\lambda^2 - 0.56653\lambda^3 - 0.1264778\lambda^4 - 0.0004279\lambda^5},$$

$$m(\lambda) = \frac{0.70958\lambda + 0.088916\lambda^2 - 0.013768\lambda^3 + 0.301618\lambda^4 - 0.3283745\lambda^5}{1 + 0.12530\lambda - 0.352736\lambda^2 + 0.066053\lambda^3 - 0.0612512\lambda^4 - 0.019786\lambda^5},$$

$$n(\lambda) = \frac{0.93923\lambda + 1.48352\lambda^2 + 0.904482\lambda^3 + 0.462497\lambda^4 + 0.191811\lambda^5}{1 + 1.579508x + 0.7148985x^2 + 0.418387\lambda^3 + 0.296779x^4 - 0.022257\lambda^5}, \qquad (48)$$

$$\breve{\theta}(\lambda) = \frac{1 - 0.80937\lambda - 0.215262\lambda^2 + 0.013511\lambda^3 + 0.004125\lambda^4 + 0.00701\lambda^5}{1 + 0.12854\lambda - 0.0271242\lambda^2 - 0.003919\lambda^3 - 0.010742\lambda^4 + 0.0005623\lambda^5},$$

$$\phi(\lambda) = \frac{1 - 0.121238\lambda - 0.3440942\lambda^2 - 0.48574198\lambda^3 - 0.000109\lambda^4 - 0.04746\lambda^5}{1 + 1.059822\lambda + 0.6555562\lambda^2 + 0.09425\lambda^3 + 0.022888\lambda^4 + 0.001157\lambda^5},$$

$$\chi(\lambda) = \frac{1 - 0.1473267\lambda - 0.6259649\lambda^2 - 0.1604094\lambda^3 - 0.0551968\lambda^4 - 0.011072\lambda^5}{1 + 0.9192844\lambda + 0.266335\lambda^2 + 0.072151\lambda^3 + 0.015844\lambda^4 + 0.00046357\lambda^5}.$$

4. Discussion of Numerical and Graphical Results

The numerical results of DTM-Padé, which is employed to solve nonlinear coupled ordinary differential equations for the governing flow, are discussed in this section. Computational software Mathematica (12v) is used to obtain the solutions of the system of equations. We compare our results with the shooting method [50] to verify the accuracy of the present method. Our primary purpose is to analyze the physical significance of various parameters involved in the energy equation, induced MHD equation, nanoparticle concentration equation, momentum equation, and motile microorganism function. Multiple parameters are discussed, i.e., squeezing Reynolds number S_Q, rotational Reynolds number R_Ω, Weissenberg number We, Reynolds number Re, magnetic Reynolds number Re_M on velocity profiles $\{f'(\lambda), g'(\lambda)\}$, and induced magnetic field $\{m(\lambda), n(\lambda)\}$. Furthermore, the influence of squeezing Reynolds number S_Q, Prandtl number P_t, thermophoresis parameter T_t, Brownian motion T_b, activation energy E, activation rate σ, Schmidt number S_M, bioconvection number B_s, and Peclet number is also discussed. The numerical results for local Nusselt number, local Sherwood number, and motile density number are presented in Tables 1–3. From these tables, it is observed that our outcomes are in good agreement with the numerical shooting method. Equations (28)–(29) are used to calculate the effects of torque on the fixed and moving plate, which is displayed in Table 4. For the graphical outcomes, we have selected the following parametric values against each parameter: $S_M = 0.2$, $Pe = 0.5$, $B_s = 5$, $S_Q = 0.02$, $R_\Omega = 0.2$,

$We = 0.01$, $\text{Re} = 0.001$, $\text{Re}_M = 0.5$, $T_t = 0.03$, $T_b = 0.1$, $P_t = 6.8$, $E = 2$, $\sigma = 2$.

Figure 2 shows the impact on the velocity field in the axial direction $f'(\lambda)$ due to squeezed Reynolds number S_Q and rotational Reynolds number R_Ω. It is observed when the values of squeezed Reynolds number S_Q enhance, the axial velocity distribution decreases. However, when increasing the values of R_Ω, the axial velocity $f'(\lambda)$ increases. This is because the rotation of the plates accelerates the velocity of the fluid. Furthermore, in Figure 3, it is seen that when increasing value of Re, the velocity of the fluid declines and the Weissenberg number We increases the axial velocity profile. Physically, when the values of the Weissenberg number We are increased, the relaxation time increases for the particles of Carreau fluid, so these particles and velocity decrease the resistance. This is because the Weissenberg number We is the ratio of relaxation time of the fluid and particular process time. In Figure 4, the impact of Weissenberg number on Carreau fluid velocity for shear-thinning $(n < 1)$, Newtonian case $(n = 0)$, and thickening $(n > 1)$ cases can be seen on axial velocity distribution $f'(\lambda)$. This is because, in the shear-thinning case, the fluid viscosity is lower with shear strain, and the velocity is high compared to the Newtonian and shear-thickening case. Figures 5 and 6 represent the influence of squeezed Reynolds number and rotational Reynolds number on tangential velocity distribution $g'(\lambda)$. It is observed that, by enhancing the value of squeezed Reynolds number and rotational Reynolds number, the tangential velocity distribution decreases, but the effects are negligible. From Figure 7, it is noticed that the axial and tangential induced magnetic field distributions

TABLE 1: Comparison of Nusselt number $-\theta'(0)$ for various values T_t, T_b, P_t, S_Q by shooting method and DTM-Padé $[5 \times 5]$.

T_t	T_b	P_t	S_Q	$n = -3, We = 0.01$		$n = 1, We = 0$		$n = 3, We = 0.01$	
				Shooting method	DTM-Padé	Shooting method	DTM-Padé	Shooting method	DTM-Padé
0.03	0.01	6.8	0.05	0.89308203	0.89308203	0.89309699	0.89309699	0.89310474	0.89310474
0.06				0.80302479	0.80302479	0.80303833	0.80303833	0.80304535	0.80304535
0.09				0.71985201	0.71985201	0.71986417	0.71986417	0.71987048	0.71987048
0.05	0.1			0.58574689	0.58574689	0.58575671	0.58575671	0.5857618	0.5857618
	0.3			0.24295587	0.25072139	0.24295986	0.24295986	0.24296193	0.24296193
	0.5			0.08998096	0.08998096	0.08998239	0.08998239	0.08998315	0.08998315
	0.01	4		0.89845222	0.89845222	0.89846105	0.89846105	0.89846562	0.89846562
		7		0.82769241	0.82769241	0.82770676	0.82770676	0.82771419	0.82771419
		10		0.76139836	0.76139836	0.76141735	0.76141735	0.76142719	0.76142719
		6.8	−0.05	0.78688575	0.78688575	0.78688221	0.78688221	0.78688033	0.78688033
			0.02	0.81862905	0.81862905	0.81863007	0.81863007	0.81863059	0.81863059
			0.12	0.97452857	0.97452857	0.86421817	0.86421817	0.85056260	0.85056260

TABLE 2: Comparison of $\chi'(0)$ for various values of $S_Q, B_s, _P$ by shooting method and DTM-Padé $[5 \times 5]$.

T_t	T_b	S_Q	S_M	E	σ	$n = -3, We = 0.01$		$n = 1, We = 0$		$n = 3, We = 0.01$	
						Shooting method	DTM-Padé	Shooting method	DTM-Padé	Shooting method	DTM-Padé
0.03	0.01	0.05	5	3	2	−1.48750051	−1.48750051	−1.48747228	−1.48747228	−1.48745764	−1.48745764
0.06						−2.31230089	−2.31230089	−2.31224459	−2.31224459	−2.31221539	−2.31221539
0.09						−3.59230155	−3.59230155	−3.59222994	−3.59222994	−3.59219276	−3.59219276
0.05	0.1					−1.37683310	−1.37683310	−1.37684321	−1.37684321	−1.60791008	−1.60791008
	0.3					−1.29862771	−1.29862771	−1.29864147	−1.29864147	−1.40562686	−1.40562686
	0.5					−1.26476393	−1.26476393	−1.26477795	−1.26477795	−1.33606822	−1.33606822
	0.01	−0.05				−2.16407621	−2.16407621	−2.16408297	−2.16408297	−3.91679239	−3.91679239
		0.02				−2.03817454	−2.03817454	−2.03817048	−2.03817048	−3.69044429	−3.69044429
		0.12				−1.96569720	−1.96569720	−1.85623506	−1.85623506	−3.49325834	−3.49325834
		0.01	5			−2.05625050	−2.05625050	−2.05624885	−2.05624885	−3.72303640	−3.72303640
			10			−2.17949478	−2.17949478	−2.17949321	−2.17949321	−3.77225894	−3.77225894
			15			−2.29665895	−2.29665895	−2.29665738	−2.29665738	−3.82221775	−3.82221775
			5	2		−1.99640130	−1.99640130	−2.81393318	−2.81393318	−3.69971651	−3.69971651
				3		−1.95271335	−1.95271335	−2.29665738	−2.29665738	−3.68433831	−3.68433831
				4		−1.93641884	−1.93641884	−2.07634697	−2.07634697	−3.67871779	−3.67871779
				2	2	−1.99640130	−1.99640130	−2.81393318	−2.81393318	−3.69971651	−3.69971651
					4	−2.06392299	−2.06392299	−3.48018830	−3.48018830	−3.72438933	−3.72438933
					6	−2.12957297	−2.12957297	−4.03630116	−4.03630116	−3.74942313	−3.74942313

TABLE 3: Comparison of $\phi'(0)$ for various values T_t, T_b, S_Q, E, σ by shooting method and DTM-Padé $[5 \times 5]$.

S_Q	B_s	P_l	$n = -3, We = 0.01$		$n = 1, We = 0$		$n = 3, We = 0.01$	
			Shooting method	DTM-Padé	Shooting method	DTM-Padé	Shooting method	DTM-Padé
-0.05	5	0.5	−3.68071264	−3.68071264	−3.68070328	−3.68070328	−3.68069877	−3.68069877
0.02			−3.40398671	−3.40398671	−3.40397880	−3.40397880	−3.40397480	−3.40397480
0.12			−3.24595020	−3.24595020	−3.20633134	−3.20633134	−3.20623463	−3.20623463
0.01	5		−3.44353509	−3.44353509	−3.44353113	−3.44353113	−3.44352914	−3.44352914
	10		−3.44262691	−3.44262691	−3.44262260	−3.44262260	−3.44262046	−3.44262046
	15		−3.44171898	−3.44171898	−3.44171434	−3.44171434	−3.44171203	−3.44171203
	1	0.5	−3.23321118	−3.23321118	−3.23320693	−3.23320693	−3.23320481	−3.23320481
		1.0	−5.75926435	−5.75926435	−5.75925402	−5.75925402	−5.75924883	−5.75924883
		1.5	−8.53042052	−8.53042052	−8.53040286	−8.53040286	−8.53039401	−8.53039401

decline with increases in the value of magnetic Reynolds number Re_M.

Figure 8 shows the influence of the thermophoresis parameter T_t and the Brownian motion parameter T_b on the temperature profile $\breve{\theta}(\lambda)$ by keeping the rest of the parameters unaltered. The effect indicates that increasing the values of both parameters raises the temperature profile. The impact of S_Q and Prandtl number P_t is portrayed in Figure 9. It is seen that, by upgrading the Prandtl number P_t, the temperature profile $\breve{\theta}(\lambda)$ declines. The reason behind this is

Table 4: Values of torque at the lower (fix) and upper (moving) plates.

S_Q	R_Ω	We	Re	$dg(0)/d\lambda$		$dg(1)/d\lambda$	
				DTM-Padé	Shooting method	DTM-Padé	Shooting method
0.01	0.1	0.01	0.01	−1.05591667	−1.05591667	−1.00586254	−0.99994831
0.03				−1.00101432	−1.00101432	−1.00688815	−0.99954622
0.05				−1.03595883	−1.03595883	−1.01803750	−0.99874826
0.01	0.1			−1.00101432	−1.00101432	−1.00586254	−0.99994831
	0.2			−1.00087495	−1.00087495	−1.00030989	−0.99989969
	0.3			−1.00091052	−1.00091052	−1.00062003	−0.99988534
	0.1	0.01		−1.00101432	−1.00101432	−1.00586254	−0.99994831
		0.04		−1.00174207	−1.00174207	−1.02341830	−1.00012927
		0.07		−1.00247679	−1.00247679	−1.04340432	−1.00031195
		0.01	0.0013	−1.00101290	−1.00101290	−1.00054533	−0.99994839
			0.0016	−1.00101295	−1.00101295	−1.00053459	−0.99994839
			0.0019	−1.00101299	−1.00101299	1.00051846	−0.99994839
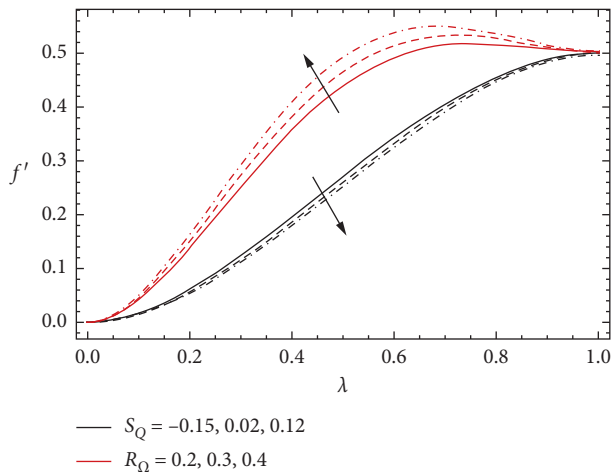
Figure 2: Effect of various values of squeeze Reynolds number S_Q and rotational Reynolds number R_Ω on axial velocity distribution $f'(\lambda)$.
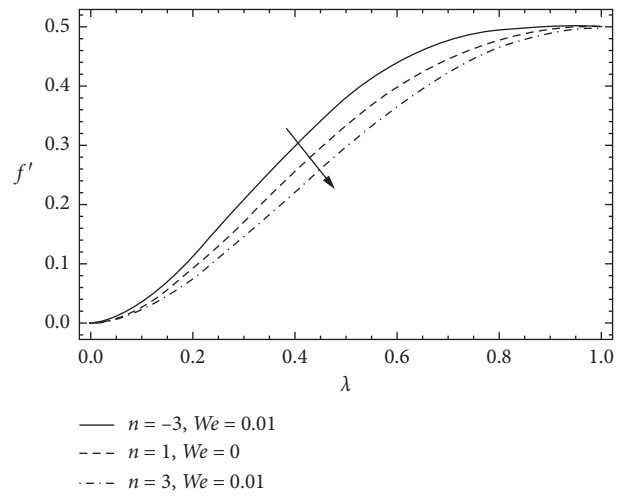
Figure 4: Effect of different values of power law index n and Weissenberg number We on axial velocity distribution $f'(\lambda)$.
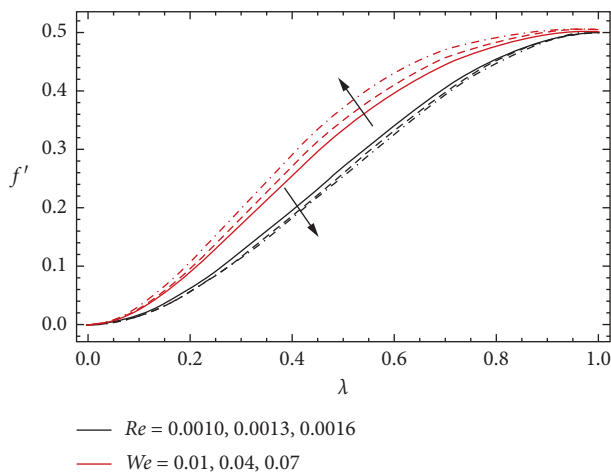
Figure 3: Effect of various values of Reynolds number Re and Weissenberg number We on axial velocity distribution $f'(\lambda)$.
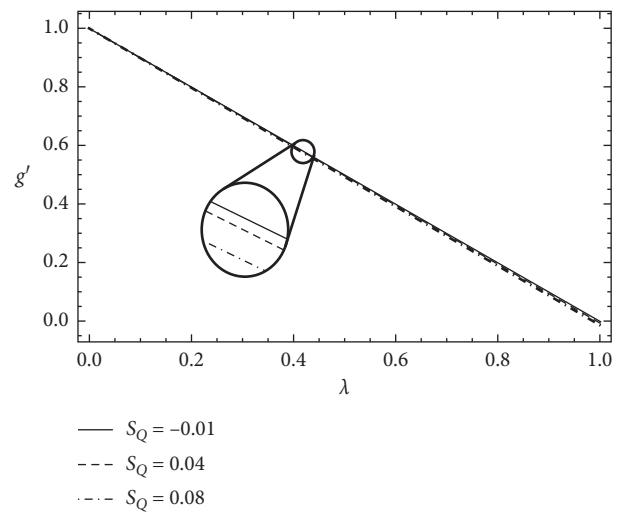
Figure 5: Effect of various values of squeeze Reynolds number S_Q on the tangential velocity distribution $g'(\lambda)$.
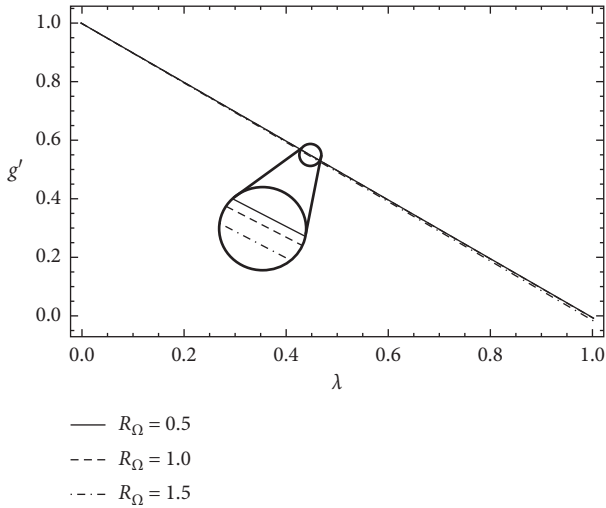
FIGURE 6: Effect of various values of rotational Reynolds number R_Ω on the tangential velocity distribution $g'(\lambda)$.
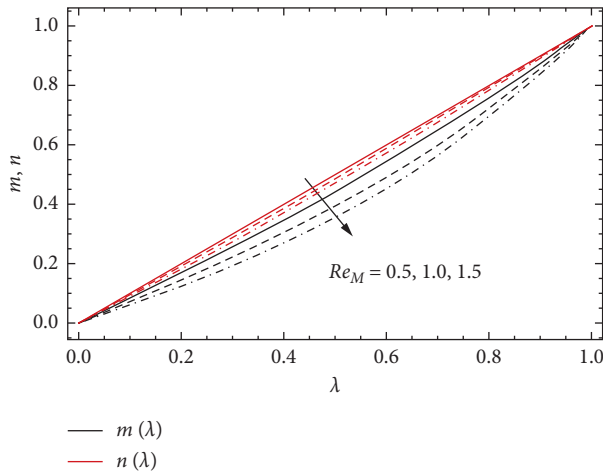
FIGURE 7: Effect of different values of magnetic Reynolds number Re_M on the axial and tangential induced magnetic field distributions $m(\lambda)$, $n(\lambda)$.
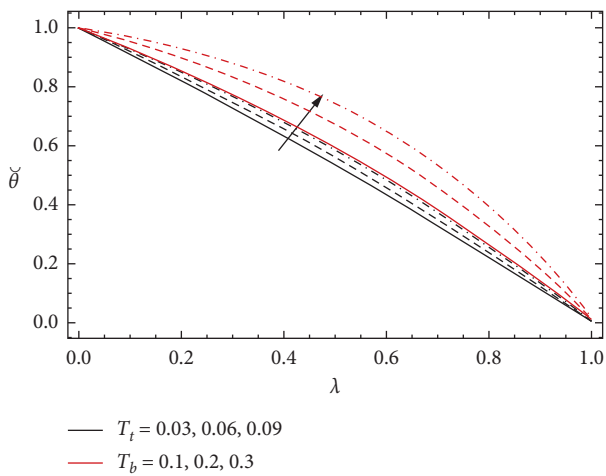
FIGURE 8: Effect of different values of thermophoresis parameter T_t and Brownian motion parameter T_b on the temperature distribution $\breve{\theta}(\lambda)$.
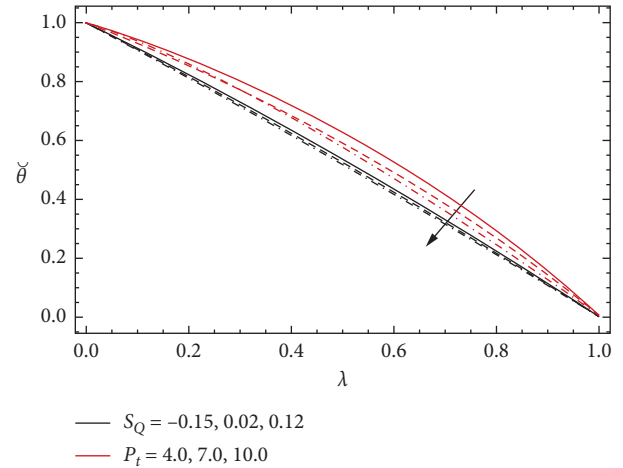
FIGURE 9: Effect of various values of squeeze Reynolds number S_Q and Prandtl number P_t on the temperature distribution $\breve{\theta}(\lambda)$.
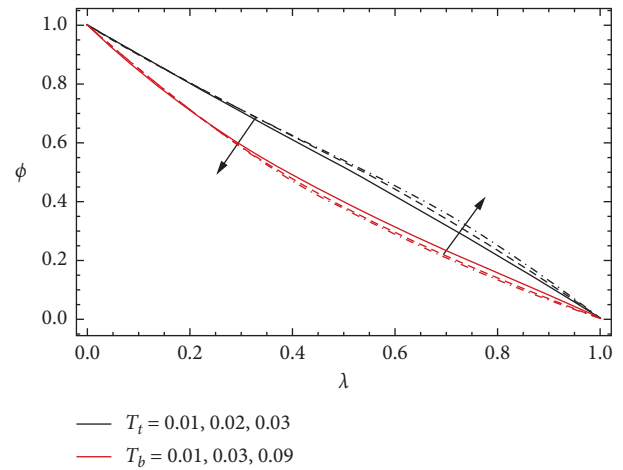
FIGURE 10: Effect of different values of thermophoresis parameter T_t and Brownian motion parameter T_b on the nanoparticle volume fraction $\phi(\lambda)$.
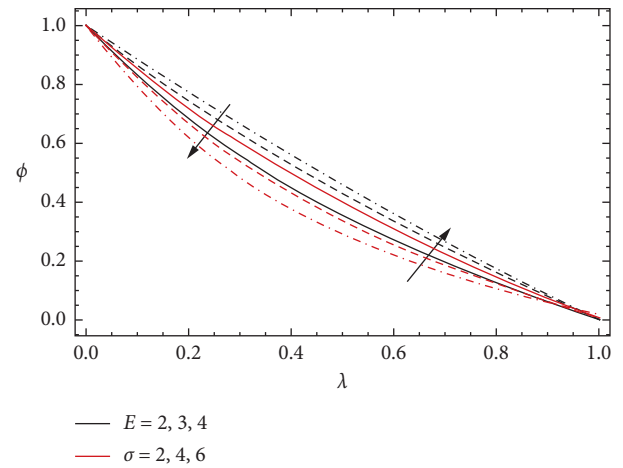
FIGURE 11: Effect of different values of activation energy E and reaction rate σ on the nanoparticle volume fraction $\phi(\lambda)$.
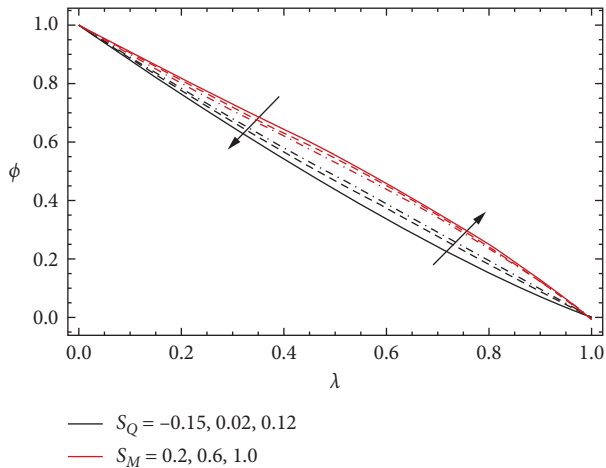
FIGURE 12: Effect of various values of squeeze Reynolds number S_Q and Schmidt number S_M on the nanoparticle volume fraction $\phi(\lambda)$.

FIGURE 13: Effect of various values of squeeze Reynolds number S_Q and Peclet number Pe on the motile microorganism density function $\chi(\lambda)$.

that when increasing the value of the Prandtl number P_t, the thermal conductivity reduces, and due to this reason, the temperature profile declines. It is also seen that temperature profile decreases with an increase in the values of squeezed Reynolds number S_Q.

The impact of the thermophoresis parameter T_t and the Brownian motion T_b on the nanoparticle concentration $\phi(\lambda)$ is displayed in Figure 10. It is noticed that the concentration of nanoparticle declines by enhancing the Brownian motion parameter T_b and concentration of nanoparticle enhances when values of the thermophoresis parameter T_t increase. Figure 11 depicts the influence of activation energy E and reaction rate σ on the nanoparticle concentration $\phi(\lambda)$. It can be seen that, by enhancing the dimensionless activation energy E, the concentration of nanoparticle increases. That is because low temperatures and high energy activation contribute to a constant reaction rate, and thus, the chemical reaction slows down. As a result, the concentration of solute increases. Besides, with higher values of reaction rate σ, the nanoparticle concentration declines. Figure 12 shows the effect of squeezed Reynolds number S_Q and Schmidt number S_M. By enhancing the values of squeezed Reynolds number S_Q, the nanoparticle concentration $\phi(\lambda)$ increases while the opposite behavior is observed when increasing the value of the Schmidt number S_M.

Figure 13 depicts the influence of squeezed Reynolds number S_Q and Peclet number P_l on microorganism density function $\chi(\lambda)$. It is perceived that, with the increase in the value of squeezed Reynolds number S_Q, the microorganism density function increases and it increases in the value of Peclet number P_l; the behavior of the microorganism density function shows the opposite phenomenon. The reason behind this is that the speed of microorganisms is decreased when there is a rise in the value of Peclet number, and therefore diffusivity of the microorganism decreases. Figure 14 demonstrates the physical behavior of the Schmidt number S_M. It is seen that the density of motile microorganism function increases by enhancing the value of the
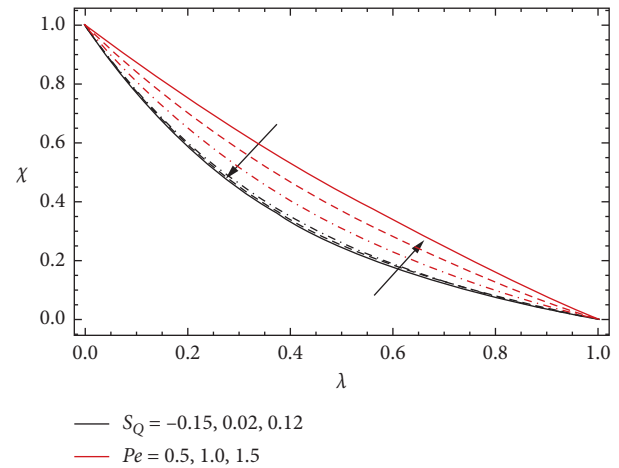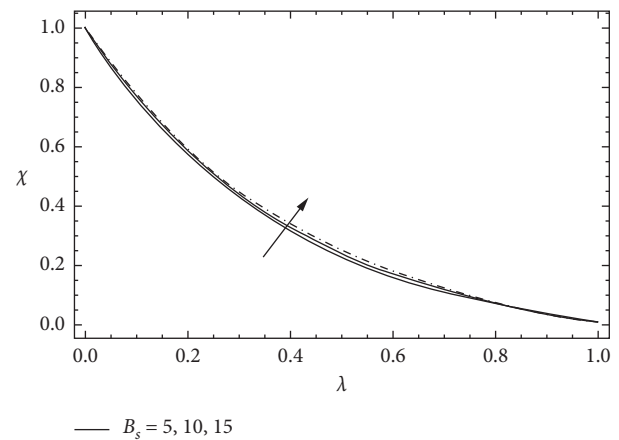
FIGURE 14: Effect of various values of bioconvection number B_s on motile microorganism density function $\chi(\lambda)$.

bioconvection Schmidt number B_s, but the influence is nominal.

5. Conclusion

In this study, the flow behavior betwixt circular rotating plates filled with Carreau fluid under the suspension of nanoparticles and gyrotactic microorganisms in the presence of an induced magnetic field has been investigated. DTM-Padé is used to solve the resulting differential equations. Padé approximant is helpful to provide the swift convergence rate and provide stable results. It is observed that, after merging the differential transform method (DTM) with the Padé approximant, the results are far better, which is confirmed with the numerical shooting method. Tables are drawn for various values of flow parameters, and comparison is obtained with the shooting method, which shows that DTM-Padé is accurate and stable. The main findings are briefed as follows:

(i) Rotational Reynolds number gives opposite behavior for the axial and tangential velocity distribution

(ii) The shear-thinning fluid viscosity decreases with shear strain due to its high velocity compared to Newtonian and shear-thickening fluids

(iii) In axial and tangential velocity distribution, velocity is decreasing by increasing the value of squeezed Reynolds number

(iv) The induced magnetic field in axial and tangential direction tends to reduce by enhancing the values of the magnetic Reynolds number

(v) In the temperature profile, by raising the Brownian motion and thermophoresis parameter, the temperature profile increases, but for nanoparticle concentration opposite effect has been observed

(vi) Squeezed Reynolds number suppresses the temperature profile, but opposite behavior is seen for concentration and microorganism profile

(vii) Activation energy enhances while the reaction rate suppresses the nanoparticle concentration

(viii) Peclet number reduces the microorganism profile, whereas squeezed Reynolds number and bioconvection number intend to enhance the microorganism profile

Appendix

The components form of Carreau fluid model are

$$\tau_{rr} = \mu_0 \left[1 + \frac{(n-1)}{2} \Gamma^2 \left(2\left(\frac{\partial v_r}{\partial r}\right)^2 + \left(\frac{\partial v_r}{\partial z}\right)^2 + \left(\frac{\partial v_\theta}{\partial z}\right)^2 + \left(\frac{\partial v_\theta}{\partial r} - \frac{v_\theta}{r}\right)^2 + 2\left(\frac{v_r}{r}\right)^2 \right) \right] 2\frac{\partial v_r}{\partial r}, \tag{A.1}$$

$$\tau_{r\theta} = \mu_0 \left[1 + \frac{(n-1)}{2} \Gamma^2 \left(2\left(\frac{\partial v_r}{\partial r}\right)^2 + \left(\frac{\partial v_r}{\partial z}\right)^2 + \left(\frac{\partial v_\theta}{\partial z}\right)^2 + \left(\frac{\partial v_\theta}{\partial r} - \frac{v_\theta}{r}\right)^2 + 2\left(\frac{v_r}{r}\right)^2 \right) \right] \left(\frac{\partial v_\theta}{\partial r} - \frac{v_\theta}{r}\right), \tag{A.2}$$

$$\tau_{rz} = \mu_0 \left[1 + \frac{(n-1)}{2} \Gamma^2 \left(2\left(\frac{\partial v_r}{\partial r}\right)^2 + \left(\frac{\partial v_r}{\partial z}\right)^2 + \left(\frac{\partial v_\theta}{\partial z}\right)^2 + \left(\frac{\partial v_\theta}{\partial r} - \frac{v_\theta}{r}\right)^2 + 2\left(\frac{v_r}{r}\right)^2 \right) \right] \frac{\partial v_r}{\partial z}, \tag{A.3}$$

$$\tau_{\theta r} = \mu_0 \left[1 + \frac{(n-1)}{2} \Gamma^2 \left(2\left(\frac{\partial v_r}{\partial r}\right)^2 + \left(\frac{\partial v_r}{\partial z}\right)^2 + \left(\frac{\partial v_\theta}{\partial z}\right)^2 + \left(\frac{\partial v_\theta}{\partial r} - \frac{v_\theta}{r}\right)^2 + 2\left(\frac{v_r}{r}\right)^2 \right) \right] \left(\frac{\partial v_\theta}{\partial r} - \frac{v_\theta}{r}\right), \tag{A.4}$$

$$\tau_{\theta\theta} = \mu_0 \left[1 + \frac{(n-1)}{2} \Gamma^2 \left(2\left(\frac{\partial v_r}{\partial r}\right)^2 + \left(\frac{\partial v_r}{\partial z}\right)^2 + \left(\frac{\partial v_\theta}{\partial z}\right)^2 + \left(\frac{\partial v_\theta}{\partial r} - \frac{v_\theta}{r}\right)^2 + 2\left(\frac{v_r}{r}\right)^2 \right) \right] 2\left(\frac{v_r}{r}\right), \tag{A.5}$$

$$\tau_{\theta z} = \mu_0 \left[1 + \frac{(n-1)}{2} \Gamma^2 \left(2\left(\frac{\partial v_r}{\partial r}\right)^2 + \left(\frac{\partial v_r}{\partial z}\right)^2 + \left(\frac{\partial v_\theta}{\partial z}\right)^2 + \left(\frac{\partial v_\theta}{\partial r} - \frac{v_\theta}{r}\right)^2 + 2\left(\frac{v_r}{r}\right)^2 \right) \right] \frac{\partial v_\theta}{\partial z}, \tag{A.6}$$

$$\tau_{zr} = \mu_0 \left[1 + \frac{(n-1)}{2} \Gamma^2 \left(2\left(\frac{\partial v_r}{\partial r}\right)^2 + \left(\frac{\partial v_r}{\partial z}\right)^2 + \left(\frac{\partial v_\theta}{\partial z}\right)^2 + \left(\frac{\partial v_\theta}{\partial r} - \frac{v_\theta}{r}\right)^2 + 2\left(\frac{v_r}{r}\right)^2 \right) \right] \frac{\partial v_r}{\partial z}, \tag{A.7}$$

$$\tau_{z\theta} = \mu_0 \left[1 + \frac{(n-1)}{2} \Gamma^2 \left(2\left(\frac{\partial v_r}{\partial r}\right)^2 + \left(\frac{\partial v_r}{\partial z}\right)^2 + \left(\frac{\partial v_\theta}{\partial z}\right)^2 + \left(\frac{\partial v_\theta}{\partial r} - \frac{v_\theta}{r}\right)^2 + 2\left(\frac{v_r}{r}\right)^2 \right) \right] \frac{\partial v_\theta}{\partial z}, \tag{A.8}$$

$$\tau_{zz} = 0. \tag{A.9}$$

Data Availability

No data were used to support this study.

Conflicts of Interest

The authors declare that they have no conflicts of interest.

Acknowledgments

References

[1] R. Bird, R. Byron, R. C. Armstrong, and O. Hassager, *Dynamics of Polymeric Liquids. Vol. 1: Fluid Mechanics*, Wiley, London, UK, 1987.

[2] P. J. Carreau, "Rheological equations from molecular network theories," *Transactions of the Society of Rheology*, vol. 16, no. 1, pp. 99–127, 1972.

[3] R. I. Yahaya, N. Md Arifin, and S. S. P. Mohamed Isa, "Stability analysis of MHD Carreau fluid flow over a permeable shrinking sheet with thermal radiation," *Sains Malaysiana*, vol. 48, no. 10, pp. 2285–2295, 2019.

[4] M. R. Eid, K. L. Mahny, A. Dar, and T. Muhammad, "Numerical study for carreau nanofluid flow over a convectively heated nonlinear stretching surface with chemically reactive species," *Physica A: Statistical Mechanics and Its Applications*, vol. 540, Article ID 123063, 2020.

[5] P. N. Santoshi, G. V. R. Reddy, and P. Padma, "Numerical study of Carreau nanofluid flow under slips," *International Journal of Applied and Computational Mathematics*, vol. 5, no. 5, p. 122, 2019.

[6] M. Khan, T. Salahuddin, M. Y. Malik, and F. Khan, "Change in internal energy of Carreau fluid flow along with Ohmic heating: a Von Karman application," *Physica A: Statistical Mechanics and Its Applications*, vol. 547, Article ID 123440, 2020.

[7] S. Bilal, A. S. Shafqatullah, A. S. Alshomrani et al., "Analysis of Carreau fluid in the presence of thermal stratification and magnetic field effect," *Results in Physics*, vol. 10, pp. 118–125, 2018.

[8] M. Khan, M. Azam, and A. S. Alshomrani, "On unsteady heat and mass transfer in Carreau nanofluid flow over expanding or contracting cylinder with convective surface conditions," *Journal of Molecular Liquids*, vol. 231, pp. 474–484, 2017.

[9] N. S. Khan, S. Islam, T. Gul, I. Khan, W. Khan, and L. Ali, "Thin film flow of a second grade fluid in a porous medium past a stretching sheet with heat transfer," *Alexandria Engineering Journal*, vol. 57, no. 2, pp. 1019–1031, 2018.

[10] A. Shafiq, T. N. Sindhu, and C. M. Khalique, "Numerical investigation and sensitivity analysis on bioconvective tangent hyperbolic nanofluid flow towards stretching surface by response surface methodology," *Alexandria Engineering Journal*, 2020.

[11] A. Shafiq, Z. Hammouch, T. Naz Sindhu, and D. Baleanu, "Statistical approach of mixed convective flow of third-grade fluid towards an exponentially stretching surface with convective boundary condition," *Special Functions and Analysis of Differential Equations*, p. 307, 2020.

[12] N. Acharya, K. Das, and P. K. Kundu, "The squeezing flow of Cu-water and Cu-kerosene nanofluids between two parallel plates," *Alexandria Engineering Journal*, vol. 55, no. 2, pp. 1177–1186, 2016.

[13] N. S. Khan, T. Gul, M. A. Khan, E. Bonyah, and S. Islam, "Mixed convection in gravity-driven thin film non-Newtonian nanofluids flow with gyrotactic microorganisms," *Results in Physics*, vol. 7, pp. 4033–4049, 2017.

[14] D. Lu, M. Ramzan, N. ul Huda, J. D. Chung, and U. Farooq, "Nonlinear radiation effect on MHD Carreau nanofluid flow over a radially stretching surface with zero mass flux at the surface," *Scientific Reports*, vol. 8, no. 1, pp. 1–17, 2018.

[15] C. H. Amanulla, A. Wakif, Z. Boulahia, M. S. Reddy, and N. Nagendra, "Numerical investigations on magnetic field modeling for Carreau non-Newtonian fluid flow past an isothermal sphere," *Journal of the Brazilian Society of Mechanical Sciences and Engineering*, vol. 40, no. 9, p. 462, 2018.

[16] I. Khan, M. Shafquatullah, M. Y. Malik, A. Hussain, and M. Khan, "Magnetohydrodynamics Carreau nanofluid flow over an inclined convective heated stretching cylinder with Joule heating," *Results in Physics*, vol. 7, pp. 4001–4012, 2017.

[17] I. Khan, S. Ullah, M. Y. Malik, and A. Hussain, "Numerical analysis of MHD Carreau fluid flow over a stretching cylinder with homogenous-heterogeneous reactions," *Results in Physics*, vol. 9, pp. 1141–1147, 2018.

[18] H. Sardar, M. Khan, and L. Ahmad, "Local non-similar solutions of convective flow of Carreau fluid in the presence of MHD and radiative heat transfer," *Journal of the Brazilian Society of Mechanical Sciences and Engineering*, vol. 41, no. 2, p. 69, 2019.

[19] T. Salahuddin, A. Hussain, M. Y. Malik, M. Awais, and M. Khan, "Carreau nanofluid impinging over a stretching cylinder with generalized slip effects: using finite difference scheme," *Results in Physics*, vol. 7, pp. 3090–3099, 2017.

[20] M. M. Bhatti, R. Ellahi, A. Zeeshan, M. Marin, and N. Ijaz, "Numerical study of heat transfer and Hall current impact on peristaltic propulsion of particle-fluid suspension with compliant wall properties," *Modern Physics Letters B*, vol. 33, no. 35, Article ID 1950439, 2019.

[21] M. Bovand, S. Rashidi, J. A. Esfahani, S. C. Saha, Y. T. Gu, and M. Dehesht, "Control of flow around a circular cylinder wrapped with a porous layer by magnetohydrodynamic," *Journal of Magnetism and Magnetic Materials*, vol. 401, pp. 1078–1087, 2016.

[22] N. G. Rudraswamy, S. A. Shehzad, K. Ganesh Kumar, and B. J. Gireesha, "Numerical analysis of MHD three-dimensional Carreau nanoliquid flow over bidirectionally moving surface," *Journal of the Brazilian Society of Mechanical Sciences and Engineering*, vol. 39, no. 12, pp. 5037–5047, 2017.

[23] K. A. Kumar, J. V. R. Reddy, V. Sugunamma, and N. Sandeep, "MHD Carreau fluid flow past a melting surface with cattaneo-christov heat flux," in *Proceedings of the Applied Mathematics and Scientific Computing*, pp. 325–336, Vellore, India, December 2019.

[24] N. S. Akbar, S. Nadeem, R. U. Haq, and S. Ye, "MHD stagnation point flow of Carreau fluid toward a permeable shrinking sheet: dual solutions," *Ain Shams Engineering Journal*, vol. 5, no. 4, pp. 1233–1239, 2014.

[25] G. C. Shit and S. Mukherjee, "MHD graphene-polydimethylsiloxane Maxwell nanofluid flow in a squeezing channel with thermal radiation effects," *Applied Mathematics and Mechanics*, vol. 40, no. 9, pp. 1269–1284, 2019.

[26] A. R. Bestman, "Radiative heat transfer to flow of a combustible mixture in a vertical pipe," *International Journal of Energy Research*, vol. 15, no. 3, pp. 179–184, 1991.

[27] S. Anuradha and M. Yegammai, "MHD radiative boundary layer flow of nanofluid past a vertical plate with effects of binary chemical reaction and activation energy," *The Global Journal of Pure and Applied Mathematics*, vol. 13, pp. 6377–6392, 2017.

[28] M. Irfan, W. A. Khan, M. Khan, and M. M. Gulzar, "Influence of Arrhenius activation energy in chemically reactive radiative flow of 3D Carreau nanofluid with nonlinear mixed convection," *Journal of Physics and Chemistry of Solids*, vol. 125, pp. 141–152, 2019.

[29] M. I. Khan, M. Irfan, W. A. Khan, M. Waqas, and S. Rashi, "Activation energy analysis in entropy optimized reactive flow," *Applied Nanoscience*, vol. 10, pp. 2673–2683, 2020.

[30] K. G. Kumar, A. Baslem, B. C. Prasannakumara, J. Majdoubi, M. Rahimi-Gorji, and S. Nadeem, "Significance of Arrhenius activation energy in flow and heat transfer of tangent hyperbolic fluid with zero mass flux condition," *Microsystem Technologies*, vol. 26, pp. 2517–2526, 2020.

[31] M. K. Nayak, J. Prakash, D. Tripathi, V. S. Pandey, S. Shaw, and O. D. Makinde, "3D Bioconvective multiple slip flow of chemically reactive Casson nanofluid with gyrotactic microorganisms," *Heat Transfer-Asian Research*, vol. 49, no. 1, pp. 135–153, 2020.

[32] I. Tlili, H. Waqas, A. Almaneea, S. U. Khan, and M. Imran, "Activation energy and second order slip in bioconvection of Oldroyd-B nanofluid over a stretching cylinder: a proposed mathematical model," *Processes*, vol. 7, no. 12, p. 914, 2019.

[33] Z. Abdelmalek, S. Ullah Khan, H. Waqas, H. A. Nabwey, and I. Tlili, "Utilization of second order slip, activation energy and viscous dissipation consequences in thermally developed flow of third grade nanofluid with gyrotactic microorganisms," *Symmetry*, vol. 12, no. 2, p. 309, 2020.

[34] S. M. Atif, S. Hussain, and M. Sagheer, "Magnetohydrodynamic stratified bioconvective flow of micropolar nanofluid due to gyrotactic microorganisms," *AIP Advances*, vol. 9, no. 2, Article ID 25208, 2019.

[35] M. I. Khan, F. Haq, T. Hayat, A. Alsaedi, and M. U. Rahman, "Natural bio-convective flow of Sisko nanofluid subject to gyrotactic microorganisms and activation energy," *Physica Scripta*, vol. 94, no. 12, Article ID 125203, 2019.

[36] M. M. Bhatti, A. Shahid, T. Abbas, S. Z. Alamri, and R. Ellahi, "Study of activation energy on the movement of gyrotactic microorganism in a magnetized nanofluids past a porous plate," *Processes*, vol. 8, no. 3, p. 328, 2020.

[37] V. Nagendramma, C. S. K. Raju, B. Mallikarjuna, S. A. Shehzad, and A. Leelarathnam, "3D Casson nanofluid flow over slendering surface in a suspension of gyrotactic microorganisms with Cattaneo-Christov heat flux," *Applied Mathematics and Mechanics*, vol. 39, no. 5, pp. 623–638, 2018.

[38] M. I. Khan, F. Alzahrani, A. Hobiny, and Z. Ali, "Estimation of entropy optimization in Darcy-Forchheimer flow of Carreau-Yasuda fluid (non-Newtonian) with first order velocity slip," *Alexandria Engineering Journal*, vol. 59, no. 5, pp. 3953–3962, 2020.

[39] R. Muhammad, M. I. Khan, M. Jameel, and N. B. Khan, "Fully developed Darcy-Forchheimer mixed convective flow over a curved surface with activation energy and entropy generation," *Computer Methods and Programs in Biomedicine*, vol. 188, Article ID 105298, 2020.

[40] M. I. Khan and F. Alzahrani, "Binary chemical reaction with activation energy in dissipative flow of non-Newtonian nanomaterial," *Journal of Theoretical and Computational Chemistry*, vol. 19, Article ID 2040006, 2020.

[41] Z. Shah, E. Alzahrani, M. Jawad, and U. Khan, "Microstructure and inertial characteristics of MHD suspended SWCNTs and MWCNTs based maxwell nanofluid flow with bio-convection and entropy generation past A permeable vertical cone," *Coatings*, vol. 10, no. 10, p. 998, 2020.

[42] A. Khan, Z. Shah, E. Alzahrani, and S. Islam, "Entropy generation and thermal analysis for rotary motion of hydromagnetic Casson nanofluid past a rotating cylinder with Joule heating effect," *International Communications in Heat and Mass Transfer*, vol. 119, Article ID 104979, 2020.

[43] P. T. Griffiths, "Flow of a generalised Newtonian fluid due to a rotating disk," *Journal of Non-newtonian Fluid Mechanics*, vol. 221, pp. 9–17, 2015.

[44] M. M. Rashidi, N. Freidoonimehr, E. Momoniat, and B. Rostami, "Study of nonlinear MHD tribological squeeze film at generalized magnetic Reynolds numbers using DTM," *PloS One*, vol. 10, no. 8, Article ID e0135004, 2015.

[45] S. S. Elshekh, M. K. Abd Elhady, and F. N. Ibrahim, "Fluid film squeezed between two rotating disks in the presence of a magnetic field," *International Journal of Engineering Science*, vol. 34, no. 10, pp. 1183–1195, 1996.

[46] R. Abazari and A. Borhanifar, "Numerical study of the solution of the Burgers and coupled Burgers equations by a differential transformation method," *Computers & Mathematics with Applications*, vol. 59, no. 8, pp. 2711–2722, 2010.

[47] M. M. Rashidi, O. A. Beg, M. Asadi, and M. T. Rastegari, "DTM-Padé modeling of natural convective boundary layer flow of a nanofluid past a vertical surface," *International Journal of Thermal & Environmental Engineering*, vol. 4, no. 1, pp. 13–24, 2012.

[48] M. M. Bhatti, S. Ullah Khan, O. Anwar Bég, and A. Kadir, "Differential transform solution for Hall and ion-slip effects on radiative-convective Casson flow from a stretching sheet with convective heating," *Heat Transfer*, vol. 49, no. 2, pp. 872–888, 2020 Mar.

[49] L. Zhang, M. B. Arain, M. M. Bhatti, A. Zeeshan, and H. Hal-Sulami, "Effects of magnetic Reynolds number on swimming of gyrotactic microorganisms between rotating circular plates filled with nanofluids," *Applied Mathematics and Mechanics*, vol. 41, no. 4, pp. 637–654, 2020.

[50] T. Y. Na, *Computational Methods in Engineering Boundary Value Problems*, Vol. 145, Academic Press, Cambridge, MA, USA, 1980.

Research Article

Unsteady MHD Bionanofluid Flow in a Porous Medium with Thermal Radiation near a Stretching/Shrinking Sheet

M. Irfan,[1] M. Asif Farooq (iD),[1] A. Mushtaq (iD),[2] and Z. H. Shamsi (iD)[3]

[1]*Department of Mathematics, School of Natural Sciences (SNS), National University of Sciences and Technology (NUST), Sector H-12, Islamabad 44000, Pakistan*
[2]*Seksjon for Matematikk, Nord Universitet, Bodø 8026, Norway*
[3]*Department of Mathematics, University of the Punjab, Lahore 54590, Pakistan*

Correspondence should be addressed to A. Mushtaq; asif.mushtaq@nord.no

This research aims at providing the theoretical effects of the unsteady MHD stagnation point flow of heat and mass transfer across a stretching and shrinking surface in a porous medium including internal heat generation/absorption, thermal radiation, and chemical reaction. The fundamental principles of the similarity transformations are applied to the governing partial differential equations (PDEs) that lead to ordinary differential equations (ODEs). The transformed ODEs are numerically solved by the shooting algorithm implemented in MATLAB, and verification is done from MATLAB built-in solver *bvp4c*. The numerical data produced for the skin friction coefficient, the local Nusselt number, and the local Sherwood number are compared with the available result and found to be in a close agreement. The impact of involved physical parameters on velocity, temperature, concentration, and density of motile microorganisms profiles is scrutinized through graphs. It is analyzed that the skin friction coefficient enhances with increasing values of an unsteady parameter A, magnetic parameter M, and porosity parameter Kp. In addition, we observe that the density of a motile microorganisms profile enhances larger values of the bioconvection Lewis number Lb and Peclet number Pe and decreases with the increasing values of an unsteady parameter A.

1. Introduction

Nanofluids have been in demand because of its use in energy efficient devices due to its high performance contribution in thermal conductivity compared to a traditional fluid [1–3]. Nanofluids have recently been used in detergent, vehicle coolant, sensing in microelectromechanical systems (MEMS), and thermal energy storage [4]. Thus, it can be used in heating and electronic devices to make it more cost effective by minimization of energy lost in heat transfer process. There are a number of applications where nanofluids have been used such as in biomedical engineering, fluid power, mechanical and manufacturing industry, hydraulics, etc. The nanofluids are a composite solution containing nanoparticles and the base fluid [5].

The scope of nanofluid has been further enlarged by coalescing nanoparticles with blood to cultivate comprehension of biological sciences as well. Such a fluid is ordinarily known as bionanofluid. Recent applications of bionanofluid in medical sciences, such as medicine, cancer therapy, etc., have generated interest in investigating the bionanofluid flow. Moreover, the bionanofluid has instigated research in nanotechnology, biomedical engineering (applying biological in medical innovation), bioengineering (applying engineering principle to biology), and medical devices, etc.

Bioconvection is a process in which microorganisms convection occur in the fluid [6]. Khan and Makinde [7] investigated nanofluids in motile gyrotactic microorganisms. In [8], analytical solution of bioconvection of oxytactic bacteria was found. Mutuku and Makinde [9] discussed hydromagnetic bioconvection due to microorganisms and solution is obtained numerically. Recently, Naganthran et al. [10] applied extrapolation technique in time dependent

bionanofluid. Zaimi et al. [11] discussed stagnation point flow not only containing nanoparticles but also gyrotactic microorganisms. Ali and Zaib [12] discussed unsteady flow of an Eyring-Powell nanofluid near a stagnation point. Zeng and Pedley [13] discussed gyrotactic microorganisms in complex three-dimensional flow. Shah et al. [14] have developed a fractional model in discussing a natural convection of bionanofluids between two vertical plates. Amirsom et al. [15] have discussed melting bioconvection nanofluid with second-order slip and thermal physical properties. Khader et al. [16] performed experimental study to determine the thermal and electrical conductivity to develop a new correlation in bionanofluid. For other details in this direction, see [17–22].

The thermal radiation plays an important role in industrial and engineering processes. Thermal radiation is a phenomenon in which energy is transported through indirect contact. Izadi et al. [23] discussed thermal radiation in a micropolar nanoliquid in a porous chamber. They applied the Galerkin finite element method to compute the numerical solution. Daniel et al. [24] presented a theory on entropy analysis for EMHD nanofluids considering thermal radiation and viscous dissipation. Muhammad et al. [25] obtained numerical solutions via the shooting method and bvp4c for the significant role nonlinear thermal radiation played in 3D Eyring-Powell nanofluid. Sohail et al. [26] described entropy analysis of Maxwell nanofluid in gyrotactic microorganisms with thermal radiation. Gireesha et al. [27] provide hybrid nanofluid flow across a permeable longitudinal moving fin with thermal radiation.

Eid [28] presents two-phase chemical reactions over a stretching sheet. Tripathy et al. [29] research chemical reactive flow over a moving vertical plate. In Pal and Talukdar [30], chemical reaction effects in a mixed convection flow have been covered. Katerina and Patel [31] reported results on radiation and chemical reaction in Casson fluid over an oscillating vertical plate. The works of Shah et al. [32], Rasool et al. [33], Khan et al. [34], and Khan et al. [35] contain chemical reactions as well as entropy generation over a nonlinear sheet. Khan et al. [36] present results on axisymmetric Carreau nanofluid along with chemical reaction. Gharami et al. [37] provide an unsteady flow of tangent nanofluid with a chemical reaction. Hamid et al. [38] simultaneously presented work on chemical reaction and activation energy in the unsteady flow of Williamson nanofluid. Reddy et al. [39] report results on nanofluid over a rotating disk with a chemical reaction. For other references on this topic, the reader is referred to [40–50].

In aforementioned literature studies, the chief emphasis has been made on various physical situations to find an indepth understanding of physics but the route of bionanofluid along with other situations of unsteady effect in a free stream flow is mostly absent from the literature.

The paper is written in the following order. Introduction of the paper is given in Section 1. Problem formulation is presented in Section 2. Numerical method is presented in Section 3. The results and discussion of the work are discussed Section 4. Conclusion is drawn at the end in Section 5.

2. Problem Formulation

Assuming an unsteady two-dimensional MHD stagnation point flow of bionanofluid in the presence of thermal radiation, chemical reaction, and internal heat generation/absorption adjacent to a stretching sheet with thermal radiation, a water-based nanofluid containing nanoparticles and gyrotactic microorganisms is considered. It is assumed that the presence of nanoparticles has no effect on the swimming direction of microorganisms and on their swimming velocity. This assumption holds only for less than 1% concentration of nanoparticles. The magnetic Reynolds number of the flow is taken to be very small, so that the induced magnetic field is presumed to be negligible. The applied magnetic field β_o^2 is taken along the normal to the sheet. It is also assumed that the sheet is stretching/shrinking with a velocity $u_e = \epsilon a x (1 - A_1 t)^{-1}$, $\epsilon > 0$ indicates the stretching sheet whereas $\epsilon < 0$ describes the shrinking sheet while $\epsilon = 0$ represents a stationary sheet. The configuration of the flow is given in Figure 1.

Under the above assumptions, the governing model of flow reads as follows [10, 51]:

$$\frac{\partial u}{\partial x} + \frac{\partial v}{\partial y} = 0, \tag{1}$$

$$\frac{\partial u}{\partial t} + u \frac{\partial u}{\partial x} + v \frac{\partial u}{\partial y} = u_e \frac{\partial u_e}{\partial x} + \frac{\partial u_e}{\partial t} + v \frac{\partial^2 u}{\partial y^2} - \frac{v}{k^*} (u - u_e)$$
$$- \frac{\sigma \beta_o^2}{\rho} (u - u_e), \tag{2}$$

$$\frac{\partial T}{\partial t} + u \frac{\partial T}{\partial x} + v \frac{\partial T}{\partial y} = \alpha \frac{\partial^2 T}{\partial y^2} + \tau_1 \left(D_B \frac{\partial T}{\partial y} \frac{\partial C}{\partial y} + \frac{D_T}{T_\infty} \left(\frac{\partial T}{\partial y} \right)^2 \right)$$
$$- \frac{1}{\rho c_p} \frac{\partial q_r}{\partial y} + \frac{\mu}{\rho c_p} \left(\frac{\partial u}{\partial y} \right)^2 + \frac{(T - T_\infty) Q}{\rho c_p}, \tag{3}$$

$$\frac{\partial C}{\partial t} + u \frac{\partial C}{\partial x} + v \frac{\partial C}{\partial y} = D_B \frac{\partial^2 C}{\partial y^2} + \frac{D_T}{T_\infty} \frac{\partial^2 T}{\partial y^2} - (C - C_\infty) K_c, \tag{4}$$

$$\frac{\partial N}{\partial t} + u \frac{\partial N}{\partial x} + v \frac{\partial N}{\partial y} + \frac{b w_c}{C_w - C_\infty} \left(\frac{\partial}{\partial y} \left(N \frac{\partial C}{\partial y} \right) \right) = D_n \frac{\partial^2 N}{\partial y^2}. \tag{5}$$

However, the boundary conditions corresponding to the considered model is taken as follows:

$$u \to u_e, T \to T_\infty, C \to C_\infty, N \to N_\infty, y \to \infty$$

Microorganism density boundary layer

Concentration boundary layer

Momentum boundary layer

Thermal boundary layer

y axis

x axis

Magnetic field

Stretching sheet

$$u = \epsilon u_w \qquad N = N_w \qquad T = T_w, \qquad C = Cw \qquad y = 0$$
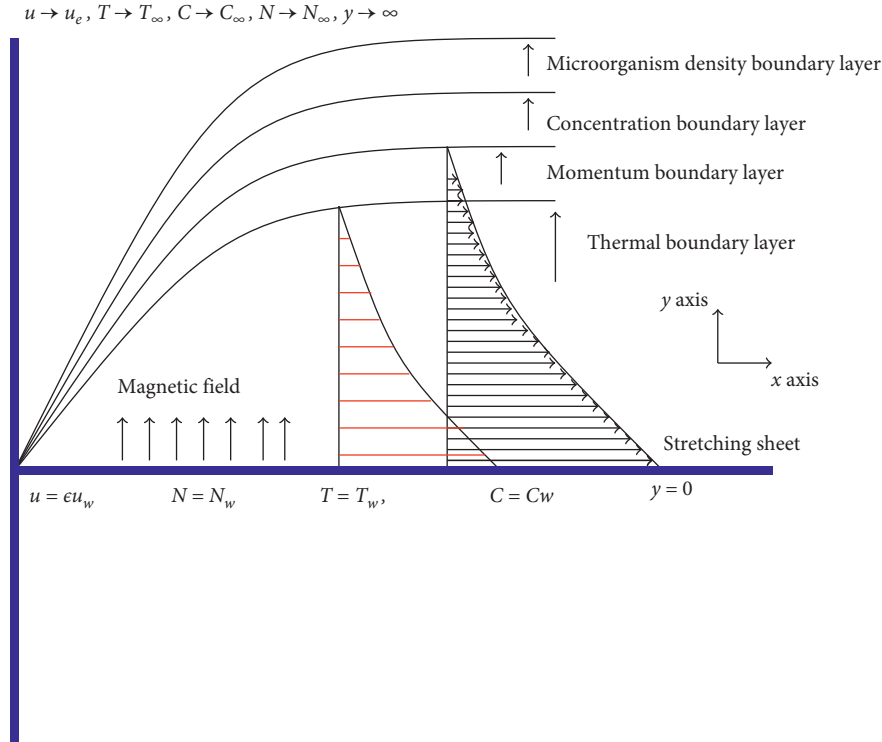
FIGURE 1: Structural diagram of the flow problem.

$$t \leq 0: v = 0, u = 0, T = T_\infty, C = C_\infty, N = N_\infty,$$

$$t > 0: u = \epsilon u_w(x, t) = \epsilon \, ax(1 - A_1 t)^{-1}, \quad \text{with } A_1 t \neq 1, \ v = 0, \ T = T_w,$$

$$C = C_w, N = N_w \text{ at } y = 0, \tag{6}$$

$$u = u_e(x, t) = ax(1 - A_1 t)^{-1}, \quad \text{with } A_1 t \neq 1, \ v = 0, \ T = T_\infty,$$

$$C = C_\infty, N = N_\infty \text{ as } y \longrightarrow \infty,$$

where t is time, u, v are the velocity components in the $x-$ and $y-$ axes, respectively. Furthermore, T is a temperature of the fluid, C is the concentration, N is the density of the motile microorganisms, k^* is the porosity of a porous medium, μ is the dynamic velocity of the fluid, σ is the electrical conductivity of the fluid, ρ is the density of the fluid, α is the thermal diffusivity, c_p is the specific heat capacity at constant temperature, τ_1 is the ratio of the effective heat capacity of the nanoparticle and the base fluid, D_B is the Brownian diffusion coefficient, D_T is thermophoretic diffusion coefficient, D_m is the diffusivity of the microorganisms, q_r is the radiative heat flux, Q is the volumetric heat source, K_c is called a rate of chemical reaction between the base fluid and nanoparticles, W_c is the maximum cell swimming speed, and b is the chemotaxis constant. Moreover, T_w, C_w, and N_w are the temperature, nanoparticle concentration, and the density of the motile microorganisms at the wall and T_∞, C_∞, and N_∞ are the temperature, nanoparticle concentration, and motile microorganisms far away from the sheet, respectively.

Introducing the similarity solutions as follows:

$$\eta = \sqrt{\frac{a}{\nu(1 - A_1 t)}} y,$$

$$\psi = \sqrt{\frac{a\nu}{1 - A_1 t}} \, xf(\eta),$$

$$\theta(\eta) = \frac{T - T_\infty}{T_w - T_\infty}, \tag{7}$$

$$\phi(\eta) = \frac{C - C_\infty}{C_w - C_\infty},$$

$$\chi(\eta) = \frac{N - N_\infty}{N_w - N_\infty}.$$

By inserting equation (7) into equations (1)–(5), we obtain the following transformed nonlinear ordinary differential equations:

$$f''' + ff'' - f'^2 + 1 + A - A\left(f' + \frac{\eta}{2}f''\right) - (M + \text{Kp})(f' - 1) = 0,$$

$$\left(1 + \frac{4}{3}\text{Rd}\right)\theta'' + \text{Pr}\,f\theta' + \text{Nb}\,\theta'\phi' + \text{Nt}\,\theta'^2 + \text{Pr}\left(\text{Ec}\,f''^2 + s\theta - \frac{\eta}{2}\theta' A\right) = 0,$$

$$\phi'' + \frac{\text{Nt}}{\text{Nb}}\theta'' + \text{Le}\,\text{Pr}\,f\phi' - \frac{\eta}{2}\text{Le}\,\text{Pr}\,A\phi' - \text{Le}\,\text{Pr}\,\text{Kr}\,\phi = 0,$$

$$\chi'' + \text{Lb}\,\text{Pr}\,f\chi' - \text{Pe}\left(\phi'\chi' + (\chi + \sigma_1)\phi''\right) - \frac{\eta}{2}\text{Lb}\,\text{Pr}\,A\chi' = 0. \tag{8}$$

Similarly, equations (7) reduces boundary condition (6) into

$$f(0) = 0, f'(0) = \epsilon, \theta(0) = 1, \phi(0) = 1, \chi(0) = 1,$$
$$f'(\infty) = 1, \theta(\infty) = 0, \phi(\infty) = 0, \chi(\infty) = 0, \tag{9}$$

where A is an unsteadiness parameter, porous parameter Kp, magnetic parameter M, Prandtl number Pr, thermal radiation parameter Rd, Brownian motion parameter Nb, thermophoretic parameter Nt, Eckert number Ec, heat source parameter s, Lewis number Le, chemical reaction parameter Kr, bioconvection Lewis number Lb, Peclet number Pe , and bioconvection parameter σ_1 are defined as follows:

$$A = \frac{A_1}{a},$$

$$\text{Kp} = \frac{\nu(1 - A_1 t)}{\text{ak}^*},$$

$$M = \frac{\sigma B_o^2 (1 - A_1 t)}{\rho a},$$

$$\text{Pr} = \frac{\nu}{\alpha},$$

$$\text{Rd} = \frac{4\sigma T_\infty^3}{k_1 k},$$

$$\text{Nb} = \frac{\tau_1 D_B (C_w - C_\infty)}{\alpha},$$

$$\text{Nt} = \frac{\tau_1 D_T (T_w - T_\infty)}{T_\infty \alpha},$$

$$\text{Ec} = \frac{u_e^2}{c_p (T_w - T_\infty)},$$

$$s = \frac{Q(1 - A_1 t)}{a\rho c_p},$$

$$\text{Le} = \frac{\alpha}{D_B},$$

$$K_r = \frac{K_c (1 - A_1 t)}{a},$$

$$\text{Lb} = \frac{\alpha}{D_n},$$

$$\text{Pe} = \frac{bw_c}{D_n},$$

$$\sigma_1 = \frac{N_\infty}{N_w - N_\infty}. \tag{10}$$

The physical quantities of interest in this study are the local skin friction coefficient C_{fx}, the local Nusselt number Nu_x, the local Sherwood number Sh_x , and the local density number of motile microorganisms Nn_x are defined as follows:

$$C_{fx} = \frac{\mu(\partial u/\partial y)_{y=0}}{\rho u_e^2},$$

$$\text{Nu}_x = \frac{-kx(\partial T/\partial y)_{y=0}}{k(T_w - T_\infty)},$$

$$\text{Sh}_x = \frac{-D_B x(\partial C/\partial y)_{y=0}}{D_B (C_w - C_\infty)},$$

$$\text{Nn}_x = \frac{-D_n x(\partial N/\partial y)_{y=0}}{D_n (N_w - N_\infty)}. \tag{11}$$

Inserting equation (7) into equation (11) yields the following expressions:

$$\text{Re}_x^{(1/2)} C_{fx} = f''(0),$$

$$\text{Re}_x^{-(1/2)} \text{Nu}_x = -\left(1 + \frac{4}{3}\text{Rd}\right)\theta'(0),$$

$$\text{Re}_x^{-(1/2)} \text{Sh}_x = -\phi'(0),$$

$$\text{Re}_x^{-(1/2)} \text{Nn}_x = -\chi'(0), \tag{12}$$

where the local Reynolds number is defined as $\text{Re}_x = (u_e x/\nu)$.

3. Numerical Procedure

3.1. Shooting Method. The physical model of ODEs alongside boundary conditions quantitatively evaluated by the shooting method implemented in MATLAB. The shooting approach involves two stages: Converting the boundary value problem (BVP) into an initial value problem (IVP) and the higher-order ODEs into a system of first-order ODEs. We employed the Newton–Raphson approach in locating roots. The Runge–Kutta method of order five is implemented in determining the solution of the IVP. The system of first-order ODEs reads as follows:

$$f = y_1, f' = y_2, f'' = y_3, f''' = y_3' = -y_1 y_3 + y_2^2 - 1 - A + A\left(y_2 + \frac{\eta}{2} y_3\right) + (M + \text{Kp})(y_2 - 1),$$

$$y_4 = \theta, y_5 = \theta', \theta'' = y_5' = \frac{-1}{(1 + (4/3)\text{Rd})}\left(\text{Pr } y_1 y_5 + \text{Nb } y_5 y_7 + \text{Nt } y_5^2 + \text{Pr}\left(\text{Ec } y_3^2 + s y_4 - \frac{\eta}{2} A y_5\right)\right),$$

$$y_6 = \phi, y_7 = \phi', \phi'' = y_7' = -\frac{N_t}{N_b} y_5' - \text{Le Pr } y_1 y_7 + \frac{\text{Le Pr } \eta A}{2} y_7 + \text{Le Pr Kr } y_6,$$

$$y_8 = \chi, y_9 = \chi', \chi'' = y_9' = -\text{Lb Pr } y_1 y_9 + \text{Pe}\left(y_7 y_9 + (y_8 + \sigma_1) y_7'\right) + \frac{\eta}{2} \text{Lb Pr } A y_9.$$

$$(13)$$

The converted form of boundary conditions into an initial condition for the shooting method is rewritten as follows:

$$
\begin{aligned}
y_1(0) &= 0, \\
y_2(0) &= \epsilon, \\
y_4(0) &= 1, \\
y_6(0) &= 1, \\
y_8(0) &= 1, \\
y_3(0) &= \tilde{\lambda}_1, \\
y_5(0) &= \tilde{\lambda}_2, \\
y_7(0) &= \tilde{\lambda}_3, \\
y_9(0) &= \tilde{\lambda}_4.
\end{aligned}
\tag{14}
$$

3.2. bvp4c. Having found numerical results from the shooting method, we verify these results using MATLAB built-in solver bvp4c [52, 53]. The bvp4c is a collocation solver which uses Gauss–Lobatto points to compute accurate results. In bvp4c, the first-order system of ODEs remains the same as discussed in Section 3.1. However, the boundary conditions implemented in MATLAB are as follows:

$$
\begin{aligned}
y_1(0) &= 0, \\
y_2(0) &= \epsilon, \\
y_4(0) &= 1, \\
y_6(0) &= 1, \\
y_8(0) &= 1, \\
y_2(\infty) &= 1, \\
y_4(\infty) &= 0, \\
y_6(\infty) &= 0, \\
y_8(\infty) &= 0.
\end{aligned}
\tag{15}
$$

4. Results and Discussion

A summary of the current and the reported findings is seen with a minimal disparity in Table 1.

The data in Tables 2 and 3 show computational results for the skin friction coefficient, the local Nusselt number, the local Sherwood number, and the local density number of motile microorganisms obtained with the shooting method and the bvp4c. In Table 2, it is revealed that the skin friction coefficient Cf_x increases with increasing values of unsteady parameter A, magnetic parameter M, and porosity parameter Kp. However, decreasing trend is seen in the local Nusselt number Nu_x against an unsteady parameter A, radiation parameter Rd, Brownian motion parameter Nb, thermophoretic parameter Nt, Eckert number Ec, and heat source parameter s. The local Nusselt number enhances the increasing values of Prandtl number Pr. The local Sherwood number Sh_x increases for higher values of Prandtl number Pr, radiation parameter Rd, Brownian motion parameter Nb, Eckert number Ec, heat source parameter s, Lewis number Le, and chemical reaction parameter Kr. The local Sherwood number decreases for higher values of thermophoretic parameter Nt. For the local density number of motile microorganisms, Nn_x shows decreasing trend for higher values of unsteady parameter A and thermophoretic parameter Nt is observed while it increases by enhancing the Prandtl number Pr, radiation parameter Rd, Brownian motion parameter Nb, Eckert number Ec, heat source parameter s, Lewis number Le , and chemical reaction parameter Kr. The local Sherwood number decreases for higher values of the thermophoretic parameter Nt. For the local density number of motile microorganisms, Nn_x shows decreasing trend for higher values of unsteady parameter A and thermophoretic parameter Nt is observed while it increases by enhancing the Prandtl number Pr, radiation parameter Rd, and Brownian motion parameter Nb,Eckert number Ec, heat source parameter s, Lewis number Le, chemical reaction parameter Kr, the bioconvection Lewis number Lb, and Peclet number Pe.

In Figures 2 and 3, we present velocity profile results against parameters M and Kp with $\epsilon = -0.5, 0.5$ corresponding to shrinking and stretching sheets. In both cases, the boundary layer thickness decreases.

Figures 4–6 illustrate the impact of the Brownian motion parameter Nb on the temperature, concentration, and the density of motile microorganisms profiles for the case of stretching sheet ($\epsilon = -0.5$) and shrinking sheet ($\epsilon = -0.5$), respectively. Figure 4 gives an incremental thermal boundary layer thickness results as Nb increases. The thermal boundary layer thickness for the Brownian motion parameter with the stretching sheet is lower than the shrinking sheet. From Figure 5, it is observed that by increasing the Brownian motion parameter Nb, the

TABLE 1: Comparison of the values of $f''(0)$, $-\theta'(0)$ and $-\phi'(0)$ when $\epsilon = 1$, Le $= 2$, $M = $ Kp $= A = $ Rd $= $ Ec $= s = $ Kr $= $ Lb $= $ Pe $= 0$, Nt $= $ Nb $= 0.5$, and Pr $= 1$.

	Ibrahim et al. [51]	Zaimi et al. [11]	Naganthran et al. [10]	Present result (SM)
$f''(0)$	0	0	0	0
$-\theta'(0)$	0.4767	0.476737	0.476737	0.4767
$-\phi'(0)$	1.0452	1.045154	1.045154	1.0452

TABLE 2: Numerical values of $f''(0)$, $-\theta'(0)$, $-\phi'(0)$, and $-\chi'(0)$ for several values of the involved parameter A, M, Kp, Pr, Rd, Nb, Nt, Ec, s, Le, Kr, Lb, Pe with $\epsilon = 0.5$ and $\sigma_1 = 0.1$ (shooting method (SM)).

													SM	SM	SM	SM
A	M	Kp	Pr	Rd	Nb	Nt	Ec	s	Le	Kr	Lb	Pe	$f''(0)$	$-(1+(4/3)Rd)\theta'(0)$	$-\phi'(0)$	$-\chi'(0)$
0.1	0.5	0.2	0.72	0.2	0.1	0.2	0.2	0.1	1	0.1	0.5	0.5	0.8364	0.5104	0.4108	0.5893
0.3													0.8576	0.4687	0.4109	0.5658
0.5													0.8784	0.4238	0.4121	0.5414
0.1	0.1	1	0.72	0.2	0.1	0.2	0.2	0.1	1	0.1	0.5	0.5	0.7749	0.5091	0.4082	0.5859
	0.3												0.8062	0.5098	0.4095	0.5876
	0.5												0.8364	0.5104	0.4108	0.5893
0.1	0.5	0	0.72	0.2	0.1	0.2	0.2	0.1	1	0.1	0.5	0.5	0.8062	0.5098	0.4095	0.5876
		0.3											0.8512	0.5107	0.4115	0.5900
		0.5											0.8799	0.5111	0.4127	0.5915
0.1	0.5	0.2	1	0.2	0.1	0.2	0.2	0.1	1	0.1	0.5	0.5	0.8364	0.5861	0.4919	0.6925
			5										0.8364	1.1092	1.1971	1.5280
			10										0.8364	1.4271	1.7646	2.1553
0.1	0.5	0.2	0.72	0	0.1	0.2	0.2	0.1	1	0.1	0.5	0.5	0.8364	0.4343	0.3812	0.5781
				0.3									0.8364	0.5456	0.4232	0.5940
				0.7									0.8364	0.6722	0.4611	0.6087
0.1	0.5	0.2	0.72	0.2	0.2	0.2	0.2	0.1	1	0.1	0.5	0.5	0.8364	0.4848	0.5386	0.6405
					0.5								0.8364	0.4132	0.6138	0.6709
					0.7								0.8364	0.3697	0.6272	0.6762
0.1	0.5	0.2	0.72	0.2	0.1	0.1	0.2	0.1	1	0.1	0.5	0.5	0.8364	0.5282	0.5116	0.6269
						0.2							0.8364	0.5104	0.4108	0.5893
						0.4							0.8364	0.4765	0.2685	0.5453
0.1	0.5	0.2	0.72	0.2	0.1	0.2	0.2	0.1	1	0.1	0.5	0.5	0.8364	0.5104	0.4108	0.5893
							0.4						0.8364	0.4822	0.4518	0.6109
							0.7						0.8364	0.4398	0.5132	0.6434
0.1	0.5	0.2	0.72	0.2	0.1	0.2	0.2	0	1	0.1	0.5	0.5	0.8364	0.5701	0.3345	0.5508
								0.1					0.8364	0.5104	0.4108	0.5893
								0.2					0.8364	0.4468	0.4916	0.6299
0.1	0.5	0.2	0.72	0.2		0.2	0.2	0.1	0.7	0.1	0.5	0.5	0.8364	0.5150	0.2662	0.5278
									1				0.8364	0.5104	0.4108	0.5893
									1.3				0.8364	0.5073	0.5261	0.6402
0.1	0.5	0.2	0.72	0.2	0.1	0.2	0.2	0.1	1	0.1	0.5	0.5	0.8364	0.5104	0.4108	0.5893
										0.4			0.8364	0.5075	0.6112	0.6861
										0.8			0.8364	0.5047	0.8266	0.7918
0.1	0.5	0.2	0.72	0.2	0.1	0.2		0.1	1	0.1	0.5	0.5	0.8364	0.5104	0.4108	0.5893
											1		0.8364	0.5104	0.4108	0.7446
											2		0.8364	0.5104	0.4108	0.9578
										0.1	0.5	0.5	0.8364	0.5104	0.4108	0.5893
												1	0.8364	0.5104	0.4108	0.7629
												3	0.8364	0.5104	0.4108	1.5188

Table 3: Numerical values of $f''(0)$, $-\theta'(0)$, $-\phi'(0)$, and $-\chi'(0)$ for several values of involved parameter A, M, Kp, Pr, Rd, Nb, Nt, Ec, s, Le, Kr, Lb, Pe with $\epsilon = 0.5$ and $\sigma_1 = 0.1$ (bvp4c).

													bvp4c	bvp4c	bvp4c	bvp4c
A	M	Kp	Pr	Rd	Nb	Nt	Ec	s	Le	Kr	Lb	Pe	$f''(0)$	$-(1+(4/3)Rd)\theta'(0)$	$-\phi'(0)$	$-\chi'(0)$
0.1	0.5	0.2	0.72	0.2	0.1	0.2	0.2	0.1	1	0.1	0.5	0.5	0.8364	0.5104	0.4108	0.5893
0.3													0.8576	0.4687	0.4108	0.5658
0.5													0.8784	0.4238	0.4121	0.5414
0.1	0.1	1	0.72	0.2	0.1	0.2	0.2	0.1	1	0.1	0.5	0.5	0.7749	0.5091	0.4082	0.5859
	0.3												0.8062	0.5098	0.4095	0.5876
	0.5												0.8364	0.5104	0.4108	0.5893
0.1	0.5	0	0.72	0.2	0.1	0.2	0.2	0.1	1	0.1	0.5	0.5	0.8062	0.5098	0.4095	0.5876
		0.3											0.8512	0.5107	0.4115	0.5900
		0.5											0.8798	0.5111	0.4127	0.5915
0.1	0.5	0.2	1	0.2	0.1	0.2	0.2	0.1	1	0.1	0.5	0.5	0.8364	0.5861	0.4919	0.6925
			5										0.8364	1.1092	1.1971	1.5280
			10										0.8364	1.4271	1.7646	2.1553
0.1	0.5	0.2	0.72	0	0.1	0.2	0.2	0.1	1	0.1	0.5	0.5	0.8364	0.4343	0.3812	0.5781
				0.3									0.8364	0.5456	0.4232	0.5940
				0.7									0.8364	0.6722	0.4611	0.6087
0.1	0.5	0.2	0.72	0.2	0.2	0.2	0.2	0.1	1	0.1	0.5	0.5	0.8364	0.4848	0.5387	0.6405
					0.5								0.8364	0.4132	0.6138	0.6709
					0.7								0.8364	0.3697	0.6272	0.6762
0.1	0.5	0.2	0.72	0.2	0.1	0.1	0.2	0.1	1	0.1	0.5	0.5	0.8364	0.5282	0.5116	0.6269
						0.2							0.8364	0.5104	0.4108	0.5893
						0.4							0.8364	0.4764	0.2685	0.5453
0.1	0.5	0.2	0.72	0.2	0.1	0.2	0.2	0.1	1	0.1	0.5	0.5	0.8364	0.5104	0.4108	0.5893
							0.4						0.8364	0.4822	0.4518	0.6109
							0.7						0.8364	0.4398	0.5132	0.6434
0.1	0.5	0.2	0.72	0.2	0.1	0.2	0.2	0	1	0.1	0.5	0.5	0.8364	0.5701	0.3345	0.5508
								0.1					0.8364	0.5104	0.4108	0.5893
								0.2					0.8364	0.4467	0.4916	0.6299
0.1	0.5	0.2	0.72	0.2		0.2	0.2	0.1	0.7	0.1	0.5	0.5	0.8364	0.5150	0.2662	0.5278
									1				0.8364	0.5104	0.4108	0.5893
									1.3				0.8364	0.5073	0.5261	0.6402
0.1	0.5	0.2	0.72	0.2	0.1	0.2	0.2	0.1	1	0.1	0.5	0.5	0.8364	0.5104	0.4108	0.5893
										0.4			0.8364	0.5075	0.6112	0.6861
										0.8			0.8364	0.5047	0.8266	0.7918
0.1	0.5	0.2	0.72	0.2	0.1	0.2		0.1	1	0.1	0.5	0.5	0.8364	0.5104	0.4108	0.5893
											1		0.8364	0.5104	0.4108	0.7446
											2		0.8364	0.5104	0.4108	0.9578
										0.1	0.5	0.5	0.8364	0.5104	0.4108	0.5893
												1	0.8364	0.5104	0.4108	0.7629
												3	0.8364	0.5104	0.4108	1.5189

concentration boundary layer thickness reduces in both stretching and shrinking sheet cases. Figure 6 exhibits that for higher values of the Brownian motion parameter Nb, the density of motile microorganisms decreases. This decrease in the density of motile microorganisms is higher in the shrinking sheet case as compared to the stretching sheet case.

The impact of the thermophoresis parameter Nt on temperature, concentration, and density of motile microorganisms can be seen in Figures 7–9. Figure 7 reveals that the thermal boundary layer thickness increases for larger values of the thermophoresis parameter Nt. Figures 8 and 9 indicate that the concentration and density of motile microorganisms increases by increasing thermophoresis parameter Nt, respectively.

Figure 10 depicts the behavior of a radiation parameter Rd on the temperature profile. We observe that by increasing radiation parameter, thermal boundary layer thickness increases in both stretching and shrinking sheet cases.

Figure 11 characterizes the influence of Eckert number Ec on temperature distribution. We conclude that increment in Eckert number Ec enhances the temperature profile.

Figure 12 scrutinizes the impact of the heat source parameter s on the temperature profile. It is seen that for higher values of the heat source parameter s, the temperature profile increases.

Figure 13 examines the effect of the Prandtl number Pr on the temperature profile. We analyzed that enhancement in Prandtl number Pr causes a reduction in thermal boundary layer thickness.
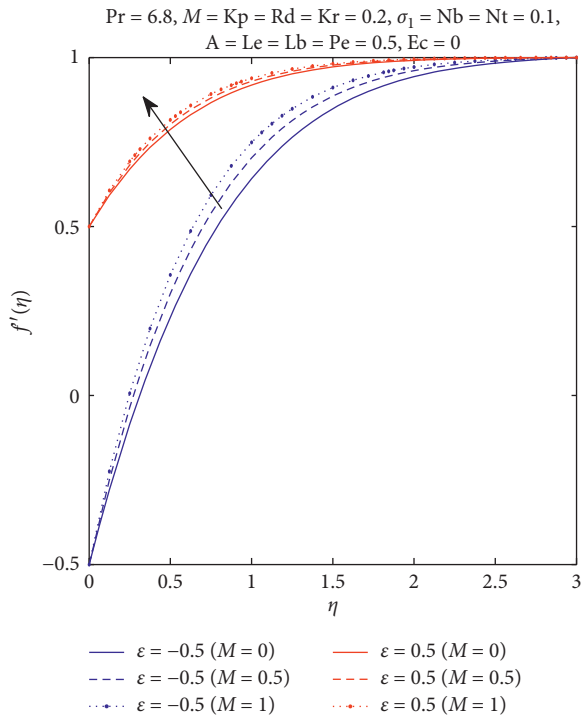
FIGURE 2: Velocity profile $f'(\eta)$ for different M.

FIGURE 3: Velocity profile $f'(\eta)$ for different Kp.
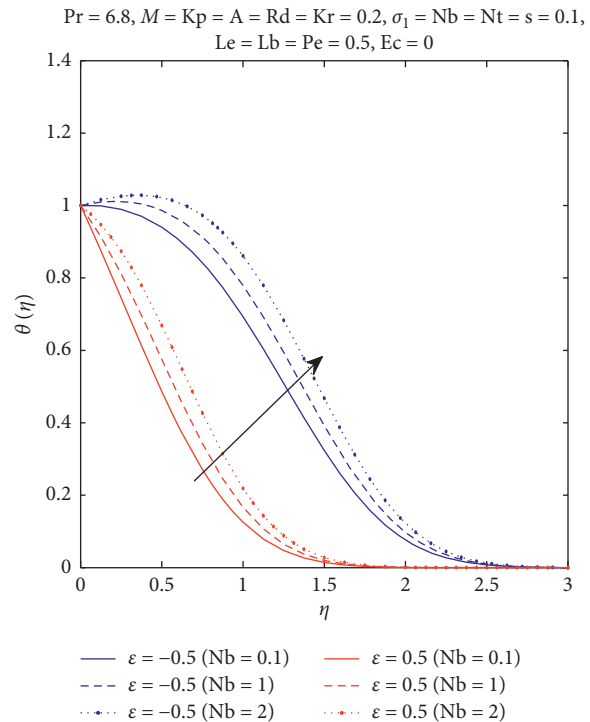
FIGURE 4: Temperature profile $\theta(\eta)$ for different Nb.
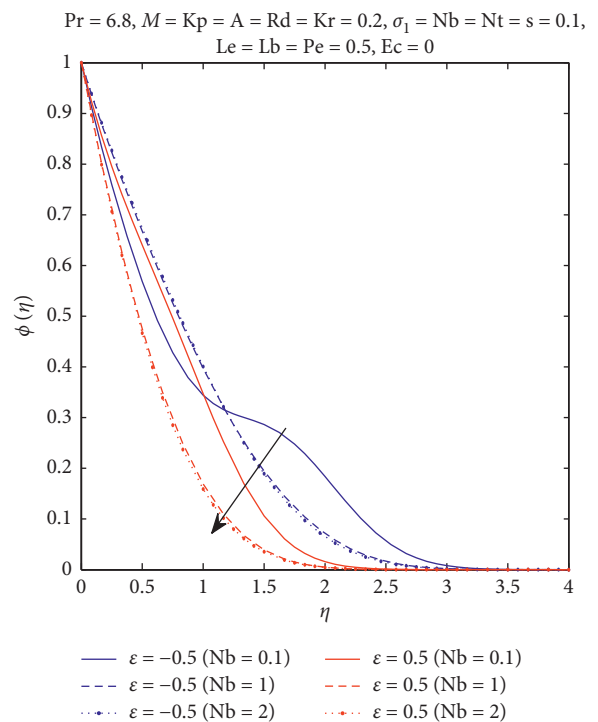
FIGURE 5: Concentration profile $\phi(\eta)$ for different Nb.

Pr = 6.8, M = Kp = A = Rd = Kr = 0.2, σ_1 = Nb = Nt = s = 0.1, Le = Lb = Pe = 0.5, Ec = 0
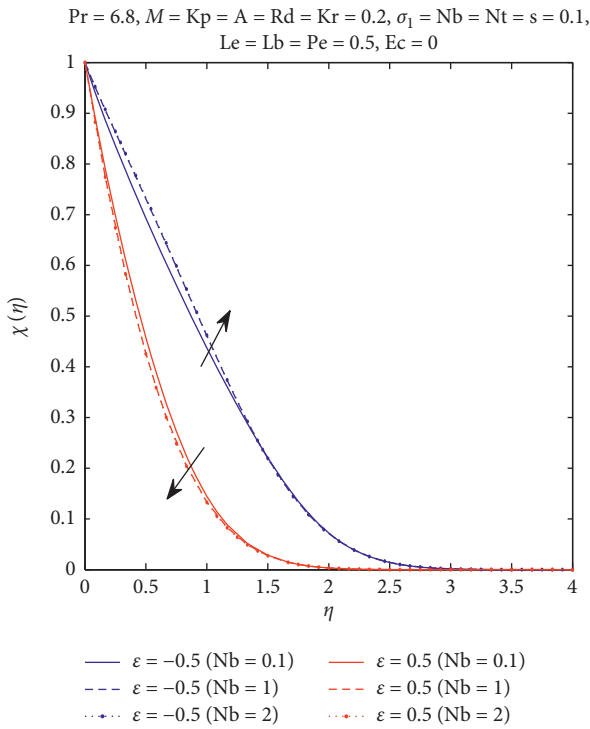
FIGURE 6: Microorganisms profile $\chi(\eta)$ for different Nb.

Pr = 6.8, M = Kp = A = Rd = Kr = 0.2, σ_1 = Nb = Nt = s = 0.1, Le = Lb = Pe = 0.5, Ec = 0
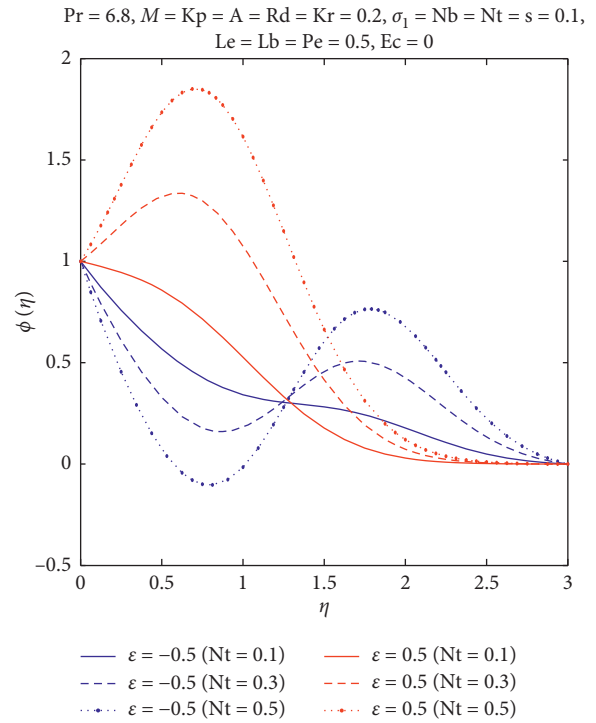
FIGURE 8: Concentration profile $\phi(\eta)$ for different Nt.

Pr = 6.8, M = Kp = A = Rd = Kr = 0.2, σ_1 = Nb = Nt = s = 0.1, Le = Lb = Pe = 0.5, Ec = 0

FIGURE 7: Temperature profile $\theta(\eta)$ for different Nt.

Pr = 6.8, M = Kp = A = Rd = Kr = 0.2, σ_1 = Nb = Nt = s = 0.1, Le = Lb = Pe = 0.5, Ec = 0
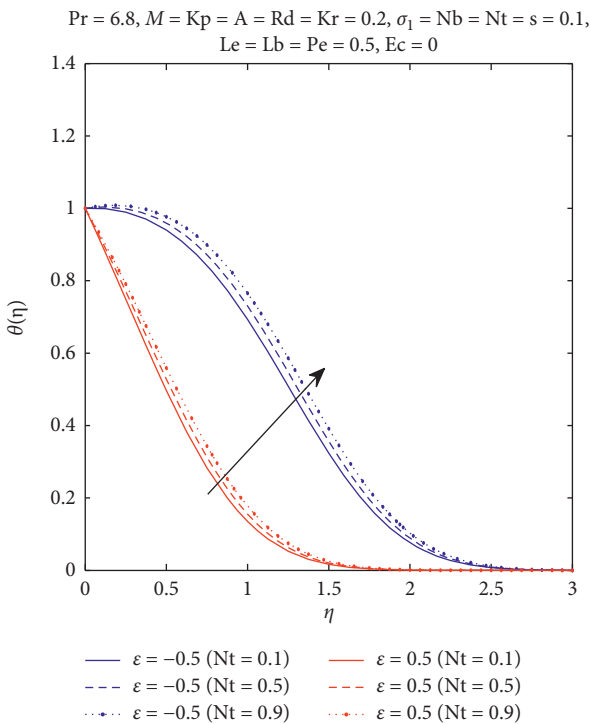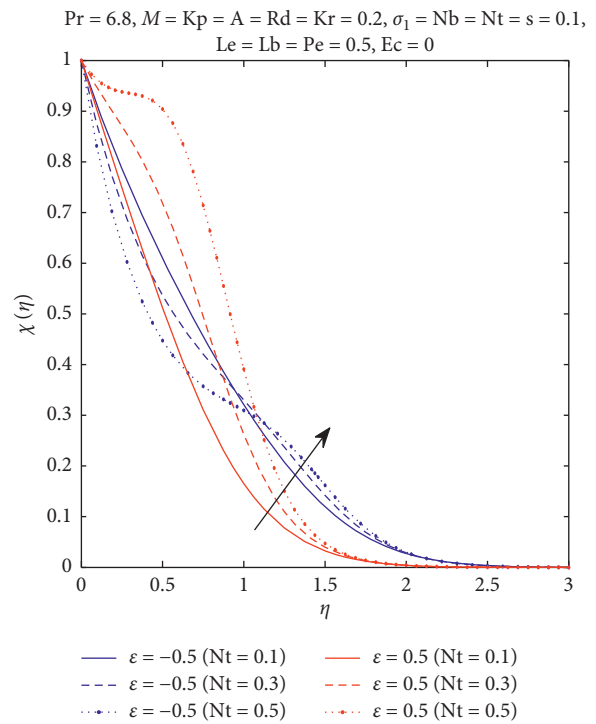
FIGURE 9: Microorganisms profile $\chi(\eta)$ for different Nt.

$Pr = 6.8, M = Kp = Rd = Kr = 0.2, \sigma_1 = Nb = Nt = s = 0.1,$
$A = Le = Lb = Pe = 0.5, Ec = 0$
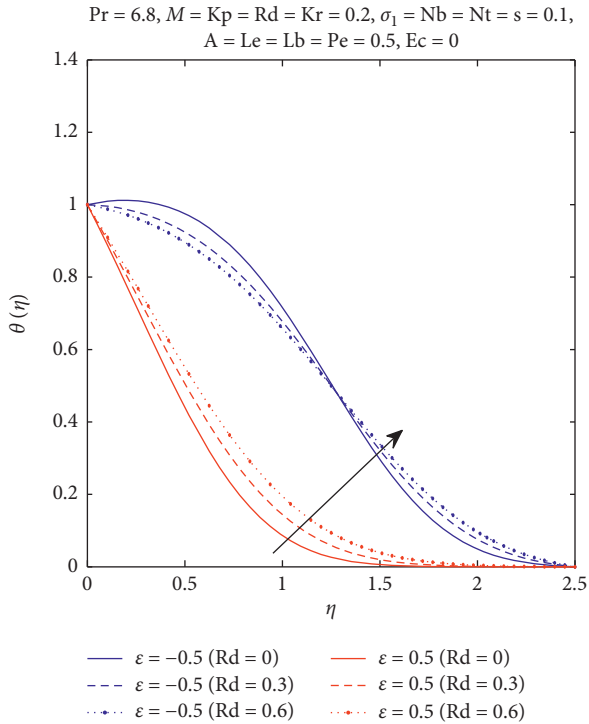
FIGURE 10: Temperature profile $\theta(\eta)$ for different Rd.

Legend:
— $\varepsilon = -0.5$ (Rd = 0)   — $\varepsilon = 0.5$ (Rd = 0)
- - - $\varepsilon = -0.5$ (Rd = 0.3)   - - - $\varepsilon = 0.5$ (Rd = 0.3)
· · · $\varepsilon = -0.5$ (Rd = 0.6)   · · · $\varepsilon = 0.5$ (Rd = 0.6)

$Pr = 6.8, M = Kp = Rd = Kr = 0.2, \sigma_1 = Nb = Nt = s = 0.1,$
$A = Le = Lb = Pe = 0.5, Ec = 0$

FIGURE 12: Temperature profile $\theta(\eta)$ for different s.

Legend:
— $\varepsilon = -0.5$ (s = 0)   — $\varepsilon = 0.5$ (s = 0)
- - - $\varepsilon = -0.5$ (s = 0.1)   - - - $\varepsilon = 0.5$ (s = 0.1)
· · · $\varepsilon = -0.5$ (s = 0.2)   · · · $\varepsilon = 0.5$ (s = 0.2)

$Pr = 6.8, M = Kp = Rd = Kr = 0.2, \sigma_1 = Nb = Nt = s = 0.1,$
$Le = Lb = Pe = 0.5$
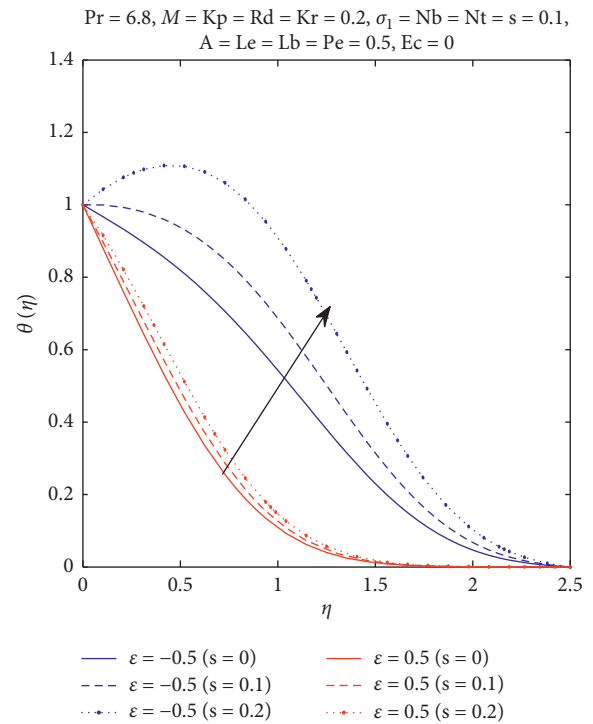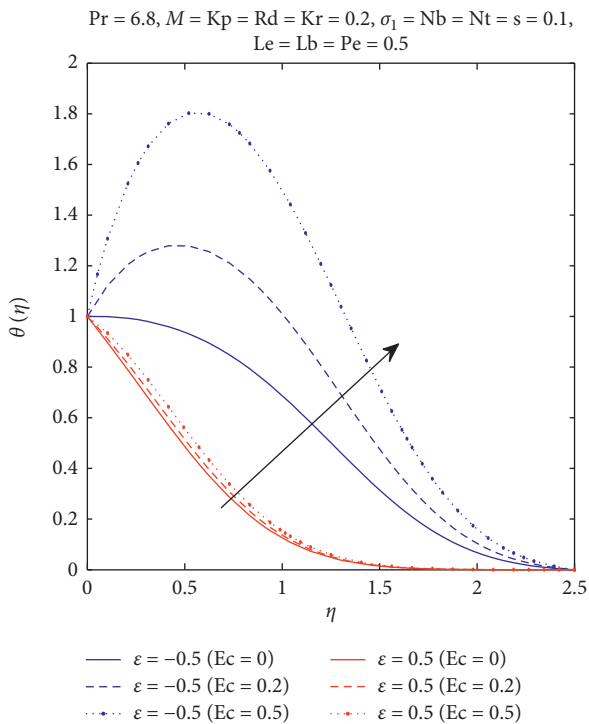
FIGURE 11: Temperature profile $\theta(\eta)$ for different Ec.

Legend:
— $\varepsilon = -0.5$ (Ec = 0)   — $\varepsilon = 0.5$ (Ec = 0)
- - - $\varepsilon = -0.5$ (Ec = 0.2)   - - - $\varepsilon = 0.5$ (Ec = 0.2)
· · · $\varepsilon = -0.5$ (Ec = 0.5)   · · · $\varepsilon = 0.5$ (Ec = 0.5)

$Pr = 1\ M = Kp = Rd = Kr = 0.2, \sigma_1 = Nb = Nt = 0.1,$
$A = Le = Lb = Pe = 0.5, Ec = 0$
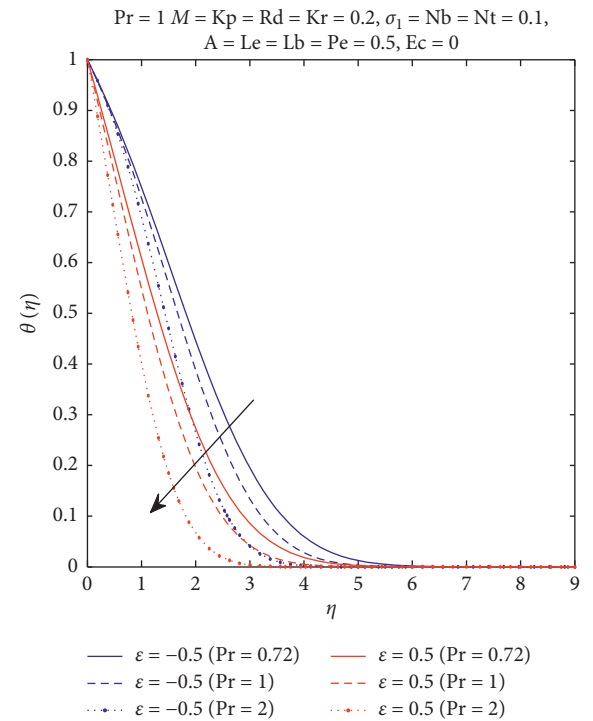
FIGURE 13: Temperature profile $\theta(\eta)$ for different Pr.

Legend:
— $\varepsilon = -0.5$ (Pr = 0.72)   — $\varepsilon = 0.5$ (Pr = 0.72)
- - - $\varepsilon = -0.5$ (Pr = 1)   - - - $\varepsilon = 0.5$ (Pr = 1)
· · · $\varepsilon = -0.5$ (Pr = 2)   · · · $\varepsilon = 0.5$ (Pr = 2)

Figure 14 is drawn to perceive the impact of bio-convection Lewis number Lb on the density of motile microorganisms profile. It is observed that higher values of bioconvection Lewis number Lb lower the boundary layer thickness of motile microorganisms profile.

Figure 15 represents the influence of the Peclet number Pe on the density of motile microorganisms profile. It is validated the fact that increment in Peclet number Pe causes
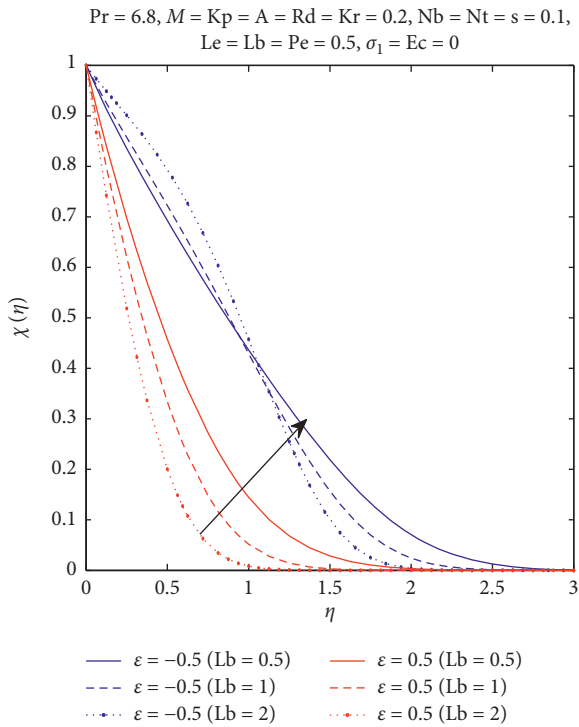
FIGURE 14: Microorganisms profile $\chi(\eta)$ for different Lb.
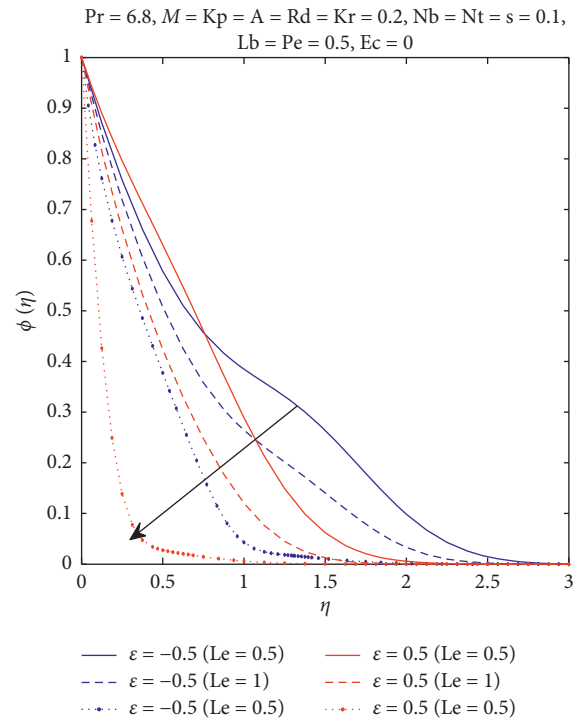
FIGURE 16: Concentration profile $\phi(\eta)$ for different Le.
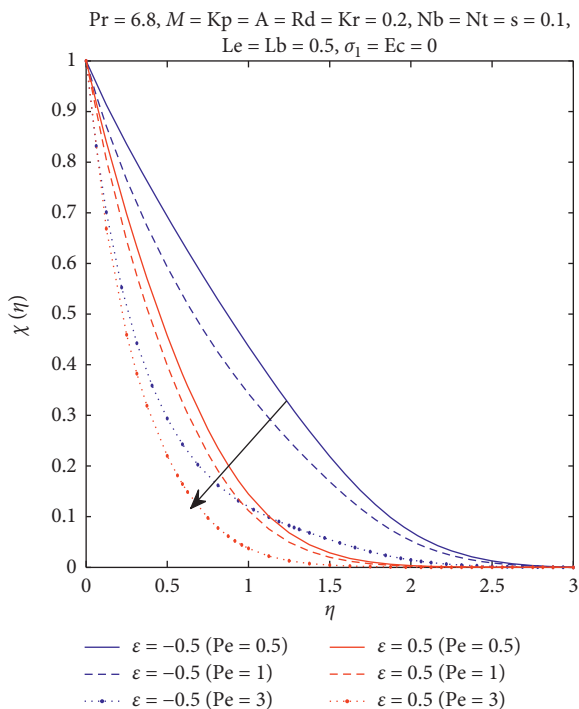
FIGURE 15: Microorganisms profile $\chi(\eta)$ for different Pe.
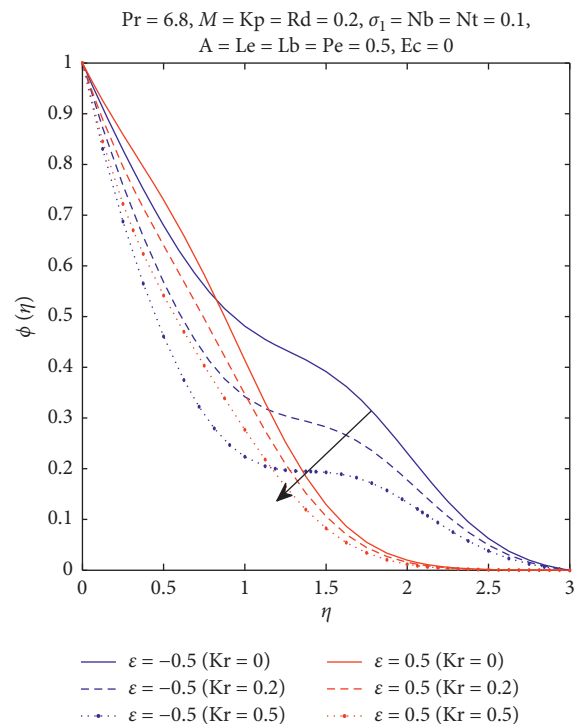
FIGURE 17: Concentration profile $\phi(\eta)$ for different Kr.

a reduction in motile microorganisms boundary layer thickness.

Figures 16 and 17 portray the impact of the Lewis number Le and the chemical reaction Kr on the concentration profile. It is analyzed that by increasing both the parameter Lewis number Le and chemical reaction Kr, the concentration boundary layer thins.

Figure 18 depicts the skin friction coefficient against the porosity parameter K_p with variations A and M. The skin
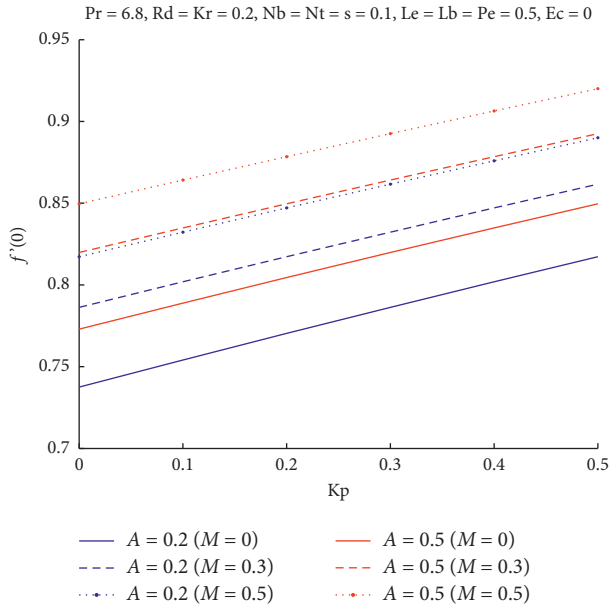
FIGURE 18: The skin friction coefficient with variations of A and M.

friction seems to increase with the porosity parameter and with the increasing values of A and M.

5. Conclusions

The current analysis focuses on the unsteady MHD stagnation point flow of bionanofluid with internal heat generation/absorption in a permeable medium with thermal radiation and chemical reaction into account over a stretching and shrinking sheet. The significant findings of the problem are summarized as follows:

(1) The skin friction coefficient enhances for higher values of the unsteady parameter A, magnetic parameter M, and porosity parameter Kp.

(2) The increment in the Brownian motion parameter Nb, thermophoresis parameter Nt, thermal radiation parameter Rd, Eckert number Ec, heat source parameter s causes enhancement in thermal boundary layer thickness while an increase in Prandtl number Pr causes a reduction in thermal boundary layer thickness.

(3) The concentration boundary layer thickness increases for the thermophoresis parameter Nt , whereas it decreases for higher values of the Brownian motion parameter Nb, Lewis number Le , and chemical reaction parameter Kr.

(4) The increment of the Brownian motion parameter Nb, bioconvection parameter Lb , and Peclet number Pe reduces the density of motile microorganisms while it increases for larger values of the thermophoresis parameter Nt.

(5) Different trends have been seen for boundary layer thickness through graphs. Graphs describe that boundary layer thickness is different in the stretching sheet case when compared to the shrinking sheet case.

(6) The skin friction coefficient increases with the increase in porosity parameter K_P as it can be seen through tables and graphical representation.

Nomenclature

a: Positive constant (s^{-1})
(u, v):   The velocity components (ms^{-1})
(x, y):   Cartesian coordinates (m)
A: Unsteadiness parameter
A_1:   Dimensionless parameter
β_o: Applied magnetic field ($Nm^{-1}A^{-1}$)
μ: The coefficient of viscosity (Pas)
ρ: The density of fluid (kgm^{-3})
σ: The electrical conductivity of the fluid ($S\,m^{-1}$) (S is siemens)
M: Magnetic parameter
Kp: Porosity parameter
ϵ: Stretching/Shrinking parameter
T: Fluid temperature (K)
T_w: Constant temperature at wall (K)
T_∞:   The ambient fluid temperature (K)
k: The thermal conductivity ($Wm^{-1}K^{-1}$)
α: The thermal diffusivity (m^2s^{-1})
k_1:   Mean absorption coefficient (m^{-1})
σ^*:   Stefan–Boltzman constant ($Wm^{-2}K^{-4}$)
C_p: The specific heat capacity ($Jkg^{-1}K^{-1}$)
q_r: The radiative heat flux (Wm^{-2})
Q: Rate of heat generation/absorption
C_f: Skin friction coefficient
Nu_x: Local Nusselt parameter
s: Local heat source/sink parameter
Rd: Thermal radiation parameter
Pr: Ambient Prandtl number
D_B: Brownian diffusion coefficient (m^2s^{-1})
D_T: Thermophoretic diffusion coefficient (m^2s^{-1})
D_m: Diffusivity of microorganisms (m^2s^{-1})
D_n: Diffusivity coefficient (m^2s^{-1})
τ_1:   Ratio of effective heat capacitance of the nanoparticle to the base fluid
$(\rho c)_p$: Nanoparticle heat capacity ($JK^{-1}m^3$)
N_b: Brownian motion parameter
N_t: Thermophoresis parameter
C: The concentration
C_w: The concentration at the wall
C_∞:   The ambient fluid concentration
N: The concentration of microorganisms
N_w: Microorganisms at the wall
N_∞:   Microorganisms far from the wall
Le: Lewis number
Lb: Bioconvection Lewis number
b: Chemotaxis constant (m)
w_c: Maximum cell swimming speed ms^{-1}
Pe: Peclet number
Sh_x: Local Sherwood parameter
Nn_x: Local density parameter of the motile microorganisms.

Data Availability

No experimental data were used to support this study.

Conflicts of Interest

The authors declare that they have no conflicts of interest.

Acknowledgments

References

[1] Q. Z. Xue, "Model for effective thermal conductivity of nanofluids," *Physics Letters A*, vol. 307, no. 5-6, pp. 313–317, 2003.

[2] W. Yu and S. U. S. Choi, "The role of interfacial layers in the enhanced thermal conductivity of nanofluids: a renovated Maxwell model," *Journal of Nanoparticle Research*, vol. 5, no. 1-2, pp. 167–171, 2003.

[3] W. Yu and S. U. S. Choi, "The role of interfacial layers in the enhanced thermal conductivity of nanofluids: a renovated Hamilton?Crosser model," *Journal of Nanoparticle Research*, vol. 6, no. 4, pp. 355–361, 2004.

[4] https://tfaws.nasa.gov/TFAWS10/Proceedings/Interdisciplinary/Debjyoti%20Banerjee.pdf.

[5] X.-Q. Wang and A. S. Mujumdar, "Heat transfer characteristics of nanofluids: a review," *International Journal of Thermal Sciences*, vol. 46, no. 1, pp. 1–19, 2007.

[6] T. J. Pedley, N. A. Hill, and J. O. Kessler, "The growth of bioconvection patterns in a uniform suspension of gyrotactic micro-organisms," *Journal of Fluid Mechanics*, vol. 195, no. 1, pp. 223–237, 1988.

[7] W. A. Khan and O. D. Makinde, "MHD nanofluid bioconvection due to gyrotactic microorganisms over a convectively heat stretching sheet," *International Journal of Thermal Sciences*, vol. 81, pp. 118–124, 2014.

[8] A. V. Kuznetsov, A. A. Avramenko, and P. Geng, "Analytical investigation of a falling plume caused by bioconvection of oxytactic bacteria in a fluid saturated porous medium," *International Journal of Engineering Science*, vol. 42, no. 5-6, pp. 557–569, 2004.

[9] W. N. Mutuku and O. D. Makinde, "Hydromagnetic bioconvection of nanofluid over a permeable vertical plate due to gyrotactic microorganisms," *Computers & Fluids*, vol. 95, pp. 88–97, 2014.

[10] K. Naganthran, M. F. M. Basir, S. O. Alharbi, R. Nazar, A. M. Alwatban, and I. Tlili, "Stagnation point flow with time-dependent bionanofluid past a sheet: richardson extrapolation technique," *Processes*, vol. 7, no. 10, p. 722, 2019.

[11] K. Zaimi, A. Ishak, and I. Pop, "Stagnation-point flow toward a stretching/shrinking sheet in a nanofluid containing both nanoparticles and gyrotactic microorganisms," *Journal of Heat Transfer*, vol. 136, no. 4, 2014.

[12] F. Ali and A. Zaib, "Unsteady flow of an eyring-powell nanofluid near stagnation point past a convectively heated stretching sheet," *Arab Journal of Basic and Applied Sciences*, vol. 26, no. 1, pp. 215–224, 2019.

[13] L. Zeng and T. J. Pedley, "Distribution of gyrotactic microorganisms in complex three-dimensional flows. Part 1. Horizontal shear flow past a vertical circular cylinder," *Journal of Fluid Mechanics*, vol. 852, pp. 358–397, 2018.

[14] N. A. Shah, A. H. Seikh, I. Tlili et al., "Natural convection of bio-nanofluid between two vertical parallel plates with damped shear and thermal flux," *Journal of Molecular Liquids*, vol. 296, p. 111575, 2019.

[15] N. A. Amirsom, M. J. Uddin, M. F. Md Basir, A. Kadir, O. A. Bég, and A. I. Md. Ismail, "Computation of melting dissipative magnetohydrodynamic nanofluid bioconvection with second-order slip and variable thermophysical properties," *Applied Sciences*, vol. 9, no. 12, p. 2493, 2019.

[16] A. M. Khdher, N. A. C. Sidik, W. A. W. Hamzah, and R. Mamat, "An experimental determination of thermal conductivity and electrical conductivity of bio glycol based Al 2 O 3 nanofluids and development of new correlation," *International Communications in Heat and Mass Transfer*, vol. 73, pp. 75–83, 2016.

[17] M. M. Bhatti and E. E. Michaelides, "Study of Arrhenius activation energy on the thermo-bioconvection nanofluid flow over a Riga plate," *Journal of Thermal Analysis and Calorimetry*, pp. 1–10, 2020.

[18] S. M. Atif, S. Hussain, and M. Sagheer, "Magnetohydrodynamic stratified bioconvective flow of micropolar nanofluid due to gyrotactic microorganisms," *AIP Advances*, vol. 9, no. 2, Article ID 025208, 2019.

[19] T. Zhang, S. U. Khan, M. Imran, I. Tlili, H. Waqas, and N. Ali, "Activation energy and thermal radiation aspects in bioconvection flow of rate-type nanoparticles configured by a stretching/shrinking disk," *Journal of Energy Resources Technology*, vol. 142, no. 11, 2020.

[20] Y. Li, H. Waqas, M. Imran, U. Farooq, F. Mallawi, and I. Tlili, "A numerical exploration of modified second-grade nanofluid with motile microorganisms, thermal radiation, and Wu's slip," *Symmetry*, vol. 12, no. 3, p. 393, 2020.

[21] A. M. Alwatban, S. U. Khan, H. Waqas, and I. Tlili, "Interaction of Wu's slip features in bioconvection of eyring powell nanoparticles with activation energy," *Processes*, vol. 7, no. 11, p. 859, 2019.

[22] Y. Wang, H. Waqas, M. Tahir, M. Imran, and C. Y. Jung, "Effective Prandtl aspects on bio-convective thermally developed magnetized tangent hyperbolic nanoliquid with gyrotactic microorganisms and second order velocity slip," *IEEE Access*, vol. 7, pp. 130008–130023, 2019.

[23] M. Izadi, M. A. Sheremet, S. A. M. Mehryan, I. Pop, H. F. Öztop, and N. Abu-Hamdeh, "MHD thermogravitational convection and thermal radiation of a micropolar nanoliquid in a porous chamber," *International Communications in Heat and Mass Transfer*, vol. 110, p. 104409, 2020.

[24] Y. S. Daniel, Z. A. Aziz, Z. Ismail, and F. Salah, "Entropy analysis in electrical magnetohydrodynamic (MHD) flow of nanofluid with effects of thermal radiation, viscous dissipation, and chemical reaction," *Theoretical and Applied Mechanics Letters*, vol. 7, no. 4, pp. 235–242, 2017.

[25] T. Muhammad, H. Waqas, S. A. Khan, R. Ellahi, and S. M. Sait, "Significance of nonlinear thermal radiation in 3D Eyring-Powell nanofluid flow with Arrhenius activation energy," *Journal of Thermal Analysis and Calorimetry*, pp. 1–16, 2020.

[26] M. Sohail, R. Naz, and S. I. Abdelsalam, "On the onset of entropy generation for a nanofluid with thermal radiation and gyrotactic microorganisms through 3D flows," *Physica Scripta*, vol. 95, no. 4, Article ID 045206, 2020.

[27] B. J. Gireesha, G. Sowmya, M. I. Khan, and H. F. Öztop, "Flow of hybrid nanofluid across a permeable longitudinal moving fin along with thermal radiation and natural convection," *Computer Methods and Programs in Biomedicine*, vol. 185, p. 105166, 2020.

[28] M. R. Eid, "Chemical reaction effect on MHD boundary-layer flow of two-phase nanofluid model over an exponentially stretching sheet with a heat generation," *Journal of Molecular Liquids*, vol. 220, pp. 718–725, 2016.

[29] R. S. Tripathy, G. C. Dash, S. R. Mishra, and S. Baag, "Chemical reaction effect on MHD free convective surface over a moving vertical plate through porous medium," *Alexandria Engineering Journal*, vol. 54, no. 3, pp. 673–679, 2015.

[30] D. Pal and B. Talukdar, "Buoyancy and chemical reaction effects on MHD mixed convection heat and mass transfer in a porous medium with thermal radiation and Ohmic heating," *Communications in Nonlinear Science and Numerical Simulation*, vol. 15, no. 10, pp. 2878–2893, 2010.

[31] H. R. Kataria and H. R. Patel, "Radiation and chemical reaction effects on MHD Casson fluid flow past an oscillating vertical plate embedded in porous medium," *Alexandria Engineering Journal*, vol. 55, no. 1, pp. 583–595, 2016.

[32] Z. Shah, P. Kumam, and W. Deebani, "Radiative MHD Casson Nanofluid Flow with Activation energy and chemical reaction over past nonlinearly stretching surface through entropy generation," *Scientific Reports*, vol. 10, no. 1, pp. 1–14, 2020.

[33] G. Rasool, T. Zhang, A. J. Chamkha, A. Shafiq, I. Tlili, and G. Shahzadi, "Entropy generation and consequences of binary chemical reaction on MHD Darcy–forchheimer Williamson nanofluid flow over non-linearly stretching surface," *Entropy*, vol. 22, no. 1, p. 18, 2020.

[34] U. Khan, A. Zaib, I. Khan, and K. S. Nisar, "Activation energy on MHD flow of titanium alloy (Ti6Al4V) nanoparticle along with a cross flow and streamwise direction with binary chemical reaction and non-linear radiation: dual Solutions," *Journal of Materials Research and Technology*, vol. 9, no. 1, pp. 188–199, 2020.

[35] M. I. Khan, S. A. Khan, T. Hayat, S. Qayyum, and A. Alsaedi, "Entropy generation analysis in MHD flow of viscous fluid by a curved stretching surface with cubic autocatalysis chemical reaction," *The European Physical Journal Plus*, vol. 135, no. 2, pp. 1–17, 2020.

[36] M. Khan, T. Salahuddin, M. Y. Malik, A. Tanveer, A. Hussain, and A. S. Alqahtani, "3-D axisymmetric Carreau nanofluid flow near the Homann stagnation region along with chemical reaction: application Fourier's and Fick's laws," *Mathematics and Computers in Simulation*, vol. 170, pp. 221–235, 2020.

[37] P. P. Gharami, S. Reza-E-Rabbi, S. M. Arifuzzaman, M. S. Khan, T. Sarkar, and S. F. Ahmmed, "MHD effect on unsteady flow of tangent hyperbolic nano-fluid past a moving cylinder with chemical reaction," *SN Applied Sciences*, vol. 2, no. 7, pp. 1–16, 2020.

[38] A. Hamid, M. Hashim, and M. Khan, "Impacts of binary chemical reaction with activation energy on unsteady flow of magneto-Williamson nanofluid," *Journal of Molecular Liquids*, vol. 262, pp. 435–442, 2018.

[39] P. S. Reddy, P. Sreedevi, and A. J. Chamkha, "MHD boundary layer flow, heat and mass transfer analysis over a rotating disk through porous medium saturated by Cu-water and Ag-water nanofluid with chemical reaction," *Powder Technology*, vol. 307, pp. 46–55, 2017.

[40] B. Ali, Y. Nie, S. A. Khan, M. T. Sadiq, and M. Tariq, "Finite element simulation of multiple slip effects on MHD unsteady maxwell nanofluid flow over a permeable stretching sheet with radiation and thermo-diffusion in the presence of chemical reaction," *Processes*, vol. 7, no. 9, p. 628, 2019.

[41] M. R. Krishnamurthy, B. C. Prasannakumara, B. J. Gireesha, and R. S. R. Gorla, "Effect of chemical reaction on MHD boundary layer flow and melting heat transfer of Williamson nanofluid in porous medium," *Engineering Science and Technology, an International Journal*, vol. 19, no. 1, pp. 53–61, 2016.

[42] M. Mustafa, J. A. Khan, T. Hayat, and A. Alsaedi, "Buoyancy effects on the MHD nanofluid flow past a vertical surface with chemical reaction and activation energy," *International Journal of Heat and Mass Transfer*, vol. 108, pp. 1340–1346, 2017.

[43] P. B. A. Reddy, "Magnetohydrodynamic flow of a Casson fluid over an exponentially inclined permeable stretching surface with thermal radiation and chemical reaction," *Ain Shams Engineering Journal*, vol. 7, no. 2, pp. 593–602, 2016.

[44] I. Ullah, K. Bhattacharyya, S. Shafie, and I. Khan, "Unsteady MHD mixed convection slip flow of Casson fluid over nonlinearly stretching sheet embedded in a porous medium with chemical reaction, thermal radiation, heat generation/absorption and convective boundary conditions," *PloS One*, vol. 11, no. 10, Article ID e0165348, 2016.

[45] G. T. Thammanna, K. Ganesh Kumar, B. J. Gireesha, G. K. Ramesh, and B. C. Prasannakumara, "Three dimensional MHD flow of couple stress Casson fluid past an unsteady stretching surface with chemical reaction," *Results in Physics*, vol. 7, pp. 4104–4110, 2017.

[46] M. M. Bhatti, S. R. Mishra, T. Abbas, and M. M. Rashidi, "A mathematical model of MHD nanofluid flow having gyrotactic microorganisms with thermal radiation and chemical reaction effects," *Neural Computing and Applications*, vol. 30, no. 4, pp. 1237–1249, 2018.

[47] M. A. Imran, F. Miraj, I. Khan, and I. Tlili, "MHD fractional Jeffrey's fluid flow in the presence of thermo diffusion, thermal radiation effects with first order chemical reaction and uniform heat flux," *Results in Physics*, vol. 10, pp. 10–17, 2018.

[48] S. A. Khan, Y. Nie, and B. Ali, "Multiple slip effects on magnetohydrodynamic axisymmetric buoyant nanofluid flow above a stretching sheet with radiation and chemical reaction," *Symmetry*, vol. 11, no. 9, p. 1171, 2019.

[49] N. V. Ganesh, Q. M. Al-Mdallal, S. Al Fahel, and S. Dadoa, "Riga-Plate flow of γ Al2O3-water/ethylene glycol with effective Prandtl number impacts," *Heliyon*, vol. 5, no. 5, Article ID e01651, 2019.

[50] N. V. Ganesh, Q. M. Al-Mdallal, K. Reena, and S. Aman, "Blasius and Sakiadis slip flow of H2O-C2H6O2 (50:50) based nanoliquid with different geometry of boehmite alumina nanoparticles," *Case Studies in Thermal Engineering*, vol. 16, p. 100546, 2019.

[51] W. Ibrahim, B. Shankar, and M. M. Nandeppanavar, "MHD stagnation point flow and heat transfer due to nanofluid towards a stretching sheet," *International Journal of Heat and Mass Transfer*, vol. 56, no. 1-2, pp. 1–9, 2013.

[52] J. Kierzenka and L. F. Shampine, "A BVP solver based on residual control and the Maltab PSE," *ACM Transactions on Mathematical Software*, vol. 27, no. 3, pp. 299–316, 2001.

[53] J. Kierzenka and L. F. Shampine, "A BVP solver that controls residual and error," *Journal of the Society for Industrial and Applied Mathematics*, vol. 3, no. 1-2, pp. 27–41, 2008.

Research Article

Heat Transfer Studies of Arrays of Prolate Particles in Gas-Solid Flows

Romana Basit [ID],[1] Xinyang Li [ID],[1] Zheqing Huang [ID],[1] and Qiang Zhou [ID][1,2]

[1]School of Chemical Engineering and Technology, Xi'an Jiaotong University, Xi'an 710049, China
[2]State Key Laboratory of Multiphase Flow in Power Engineering, Xi'an Jiaotong University, Xi'an 710049, China

Correspondence should be addressed to Qiang Zhou; zhou.590@mail.xjtu.edu.cn

Numerical study of forced convection heat transfer from arrays of prolate particles is performed using the second-order Immersed Boundary-Lattice Boltzmann Method (IB-LBM). Prolate particle is studied with aspect ratio of 2.5 with solid volume fraction variation from 0.1 to 0.3. For each solid volume fraction, arrays of prolate particles are generated and simulations have been performed to calculate Nusselt number for four different Hermans orientation factors and various Reynolds numbers. From the simulation results, it has been observed that, for any specific value of Hermans orientation factor, Nusselt number increases with the increase of the Reynolds number and solid volume fraction. More importantly, it is found that the effect of orientations on Nusselt number is significant. Nusselt number correlation is developed for ellipsoidal particles as function of Reynolds number, Prandtl number, solid volume fraction, and orientation factors. This correlation is valid for $0.1 \le c \le 0.3$ and $0 < \text{Re} \le 100$.

1. Introduction

Fluid flow and its interaction with solid particles is an essential phenomenon, which has immense applications in the domain of various industries, for example, in pneumatic conveying system, drying of food items, combustion of coal, fluidized bed, waste recycling, and pharmaceutical product formation. Heat transfer of these gas-solid flows is a significant phenomenon that needs to be investigated. A comprehensive understanding of this process is essential for the better operations of equipment in which gas-solid flows take place.

Many studies on the heat transfer of multiparticle systems have been carried out; however, most of the research is done on spherical particles only. In practical engineering applications, most of the particles are nonspherical in shape and form diverse orientations in space. Ellipsoidal particles have many applications in industry, for example, in bio gas, in manufacturing industry, and in char conversion industry for energy conversion process [1]. These industries deal with particles having increasingly stretched shapes more like the prolate. Fuel used in the biomass procedure takes the shape

of prolate particles [2]. Also, particles present in biomass process acquire different orientations. However, detailed analysis of many particle systems of prolate particles with different orientations has not been performed yet. In the present work, these orientations are quantified by using the Hermans orientation factors (S) in the range of −0.5 to 1. In the literature, dependence of Nusselt number (Nu) is only presented in the form of solid volume fraction and Reynolds number. But, in the present research, a new parameter of S is found, which has strong effects on the Nu. The present research aims to study such systems of particles; therefore, it will be an important contribution in the field of gas-solid flows.

Normally people use Gunn's [3] and Wakao et al.'s [4] correlations for predicting the heat transfer and drag in fluid particle systems which fit well only for spherical particle. Many researchers have investigated the heat transfer properties in the arrays of spherical particles [5–8]. Some investigators have performed numerical simulations to study the heat transfer from single nonspheroidal particles. Finite difference numerical procedure was used by Juncu for unsteady heat transfer studies of a prolate and an oblate

particle [9]. The particle temperature was considered only to be a function of time, whereas it was considered uniform in space. In the simulations, Reynolds number range was taken from 10 to 200 and Prandtl number was chosen to be 1 and 10 with axis ratio from 0.1 to 0.9. Richter and Nikrityuk performed numerical simulations in three dimensions for calculating heat transfer and drag force coefficients [10]. They used different shapes including ellipsoidal, spherical, and cuboidal particles in the flow, with Reynolds number in the range from 10 to 250. In the study, they explored that the drag coefficient of a specific particle depended on its normalized longitudinal length, whereas Nusselt number was mostly affected by the crosswise sphericity and sphericity itself. Zhang et al. performed direct numerical simulation (DNS) studies of forced convection from rotating single ellipsoidal particles for five different aspect ratios [11]. They investigated the effect of particle rotations on drag, lift, and moment coefficients. Average value of Nusselt number was also analyzed. They concluded that particle rotations played a substantial role in momentum and heat transfer from ellipsoidal particles.

Yang et al. studied the forced convection heat transfer in packed bed reactors using CFX10 [12]. They employed the SC, BCC, and FCC structured packing of solids for heat transfer studies. They concluded that selection of structured packing affected the pressure drop in the packed bed reactors. They also studied the effect of the shape of particles on heat transfer and flow process. Their work was mainly for higher Reynolds number flows for which RNG $k - \varepsilon$ turbulence model was used. Tavassoli et al. used the DNS for heat transfer studies of nonspherical particles with fixed random arrays [13]. The main objective of the study was to modify the existing correlations of spherical particles to be used for nonspherical objects. Spherocylindrical particles with random distribution were used and the simulations were performed using the immersed boundary method (IBM). Simulation results showed that, by making proper selection of effective diameter, the correlations of spherical particles could be employed for spherocylindrical shape without introducing any significant errors. He and Tafti investigated the heat transfer from ellipsoidal particles for low-to-moderate Reynolds numbers in the range of 10 to 200 [14]. They used a particle aspect ratio of 2.5 with solid volume fraction in the range of 0.1 to 0.35. Random assemblies of particles were generated by using SDK-PhysX. They reported a Nusselt number correlation based on the simulation data. Li et al. studied the effects of spheroid orientations on drag force of prolate particles by using IBM [15]. In particular, they adopted Hermans orientation factor (denoted by S) to quantify the mean orientation of the prolate. By definition, S ranges from −0.5 to 1 and can be used to represent the mean orientation of all possible arrangements of ellipsoids. Different values of S represent arrays of particles with different mean orientations (see Figure 1). Results obtained by Li et al. showed that drag force decreased with the rise of S when flow followed the reference direction. A new drag correlation based on particle orientation, aspect ratio, and solid volume fraction was proposed for ellipsoidal particles.

In the literature, the available investigations of heat transfer phenomenon between prolate particles and the fluid are mostly focusing on an isolated particle or arrays of particles with random orientations. However, practical applications usually involve millions to billions of prolate particles. Therefore, arrays of particles need to be considered in revealing the effect of particle orientations. Li et al. [15] found that S could be used to quantify these orientations. Through systematic DNSs, they have revealed that S has a significant impact on the drag force experienced by arrays of prolate particles. However, the impact of the mean orientation on the heat transfer properties of prolate particles has not been discovered. Therefore, this work aims to quantify this impact and develop new correlation for heat transfer of prolate particles.

In the present work, DNSs of flows past arrays of prolate particles with different S have been performed. The temperature of fluid at the inlet is set different from that of particles to enforce the heat transfer between the two phases. A wide range of solid volume fractions and Reynolds numbers are considered. It has been found that S results in a significant variation in forced convection heat transfer at any specific value of solid volume fraction and Reynolds number. Furthermore, a Nusselt number correlation is proposed in terms of Reynolds number, solid volume fraction, and Hermans orientation factor. It should be mentioned that, as a first step towards exploring the orientation effect on heat transfer from prolate particles, this work focuses on prolate particles with aspect ratio of 2.5 and the proposed correlation is only valid for this specific aspect ratio. The choice of aspect ratio of 2.5 is due to the fact that the only available work in the literature on heat transfer of arrays of prolate particles is performed at this aspect ratio by He and Tafti only at $S = 0$ [14]. Results of the present study have been validated and found to be in good agreement with the results of He and Tafti.

2. Numerical Method

2.1. Governing Equations.
LBM has been used to simulate various flow phenomena in both two and three dimensions. Generally, the model in LBM is described by $D_p Q_q$, where index p denotes the number of dimensions in which specific problem is defined and q depicts the number of lattice velocity vectors. In the present work, $D_3 Q_{19}$ model is used. Mathematical representation of LBM can be expressed in the following form [16]:

$$f_i\left(\mathbf{x} + \mathbf{e_i}\Delta t, t + \Delta t\right) - f_i(\mathbf{x}, t) = -\frac{1}{\tau_f}\left(f_i(\mathbf{x}, t) - f_i^{\text{eq}}(\mathbf{x}, t)\right)$$

$$+ \Delta t F_{A_{\text{F},i}}(\mathbf{F}).$$

$$(1)$$

In the above equation, f_i is the distribution function that shows the histogram representation of frequency of occurrence. These frequencies are the direction-specific fluid densities. e_i are the lattice velocities, having the magnitude of 1 or $\sqrt{2}\,lu/ts$ depending on the values of i; f_i^{eq} is the
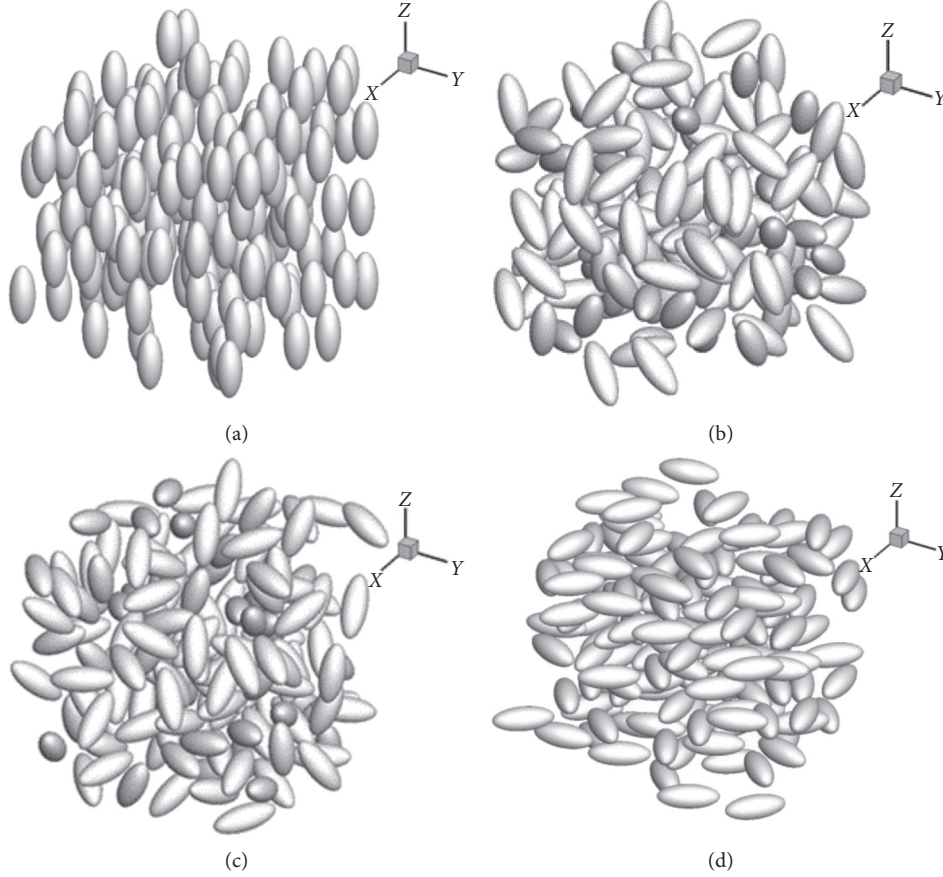
FIGURE 1: Arrays of prolate particles with aspect ratio of 2.5, solid volume fraction of 0.2, and reference direction along z direction: (a) $S = 1$, (b) $S = 0.2$, (c) $S = 0$, and (d) $S = -0.5$.

equilibrium distribution function; τ_f is the relaxation factor. The last term on the right-hand side depicts the effect of force from solid phase to the gas phase. Temperature field in LBM can be obtained by another equation having similar form to that of equation (1) [17]:

$$g_i\left(\mathbf{x} + \mathbf{e_i}\Delta t, t + \Delta t\right) - g_i\left(\mathbf{x}, t\right) = -\frac{1}{\tau_g}\left(g_i\left(\mathbf{x}, t\right) - g_i^{\mathrm{eq}}\left(\mathbf{x}, t\right)\right) + \Delta t Q_{A_{Q,i}}(Q),$$

(2)

where τ_g is the relaxation time and the last term on the right-hand side is the heat source term. For details of the numerical methods, reader can refer to [17], since the same computer code is used except that the simulated particles in this work are prolate ellipsoids. The difference between the sphere and prolate model lies in the distribution of Lagrangian markers on the particle surface. In the case of spherical particles, markers are distributed uniformly on the surface of sphere but in the case of prolate particles more markers are present in region with larger surface curvature of the ellipsoids. Different assumptions are made during the simulations and they are given as follows:

(i) Laminar flow

(ii) Heat capacity and density of the fluid remain constant throughout the simulations

(iii) Effect of temperature alteration on the velocity and density is not considered

(iv) Effects of radiation and viscous dissipation are not considered

2.2. Nusselt Number Calculations.

Nusselt number is defined as the ratio of strength of convection to conductive heat transfer. Its generalized form is [18]

$$\mathrm{Nu} = \frac{hD}{k},$$

(3)

where h is the convective heat transfer coefficient, D is the particle equivalent diameter, and k is the fluid thermal conductivity. For Reynolds number calculations, equivalent diameter and superficial gas velocities (U) have been used; that is, $\mathrm{Re} = \rho U D / \mu$. In IB-LBM, Nusselt number is calculated in computational domain by making slices of unit thickness in the flow direction. Average temperature of the slice is calculated by [17]

$$\langle T_f \rangle = \frac{\int_A \alpha u_z(x, y, z) T(x, y, z) \mathrm{d}x \mathrm{d}y}{\int_A \alpha u_z(x, y, z) \mathrm{d}x \mathrm{d}y}; \quad \alpha \in [0, 1],$$

(4)

where A is the area of slice. Integration is executed over the surface, which is perpendicular to the direction of flow. More details of the heat transfer calculations by this method can be found in the literature [17]. Nusselt number calculations of these slices adopt the following conventions [17]:

$$h_{f,\text{slice}} = \frac{Q_{\text{slice}}}{a_p V_{\text{slice}}\left(T_s - \langle T_f \rangle\right)},$$

$$\text{Nu}_{f,\text{slice}} = \frac{h_{f,\text{slice}} D}{k},$$

$$\text{Nu}_{\text{overall}} = \frac{\sum \text{Nu}_{f,\text{slice}}}{N_{\text{slice}}},$$

where V_{slice}, N_{slice}, a_p, and Q_{slice} denote volume of slice, number of slices, specific surface area, and heat flux from particles to the fluid phase, respectively.

2.3. Creation of Random Arrays.

Random arrays of prolate particles with different Hermans orientation factors are generated by means of the in-house application of Monte Carlo method [19]. The functional form of orientations factors (S) is [15]

$$S = \frac{3 < \cos^2\varnothing > - 1}{2}, \quad \varnothing \in \left[0, \frac{\pi}{2}\right],$$

where $\varnothing$ is angle among reference direction and semimajor axis of the prolate particle. Reference direction is defined as the average direction of all particles' semimajor axes in the domain. S takes the values from -0.5 to 1, $S = 0$ shows random orientations of particles, $S = 1$ corresponds to the perfect alignment of prolate particles with respect to reference direction, and $S = -0.5$ represents perfect normal alignment as shown in Figure 1. Through the random generation process of assemblies, particles overlap is prohibited and if such situation occurs, then that location of particle is rejected and a new location is assigned. Solid particle locations are random in nature, so the present method depicts the true picture of natural process in gas-solid flows. For different values of Hermans orientation factors, heat transfer studies of prolate particles with aspect ratio ar = 2.5 under moderate Reynolds number have not thus far been performed in the literature. Aspect ratio and solid volume fractions are defined by [15]

$$\text{aspect ratio (ar)} = \frac{a}{b}, \begin{cases} a & \text{prolate semi major axis} \\ b & \text{prolate semi minor axis} \end{cases},$$

$$c = \frac{4\pi nab^2}{3L^3}, \begin{cases} n \text{ number of solid particles} \\ L \text{ length of packed cubic section} \end{cases}$$

Prolate particles have three different solid volume fractions, that is, $c = 0.1, 0.2, 0.3$, and for each solid volume fraction four spheroid orientations, that is, $S = \{-0.5, 0, 0.2, 1\}$, are studied.

3. Geometry Description and Code Validation

3.1. Geometry and Boundary Conditions.

Prolate particles with aspect ratio ar = 2.5 at three solid volume fractions {0.1, 0.2, 0.3} are studied. For each solid volume fraction, arrays with four Hermans orientation factors, that is, $S = \{-0.5, 0, 0.2, 1\}$, are simulated. For each solid volume fraction, Reynolds number and Hermans orientation factor results are averaged based on three different configurations. Each configuration represents a realization at the prescribed specific parameters. The simulated Reynolds numbers are confined in the range from 0 to 100. Choice of this aspect ratio is due to the fact that only existing data in literature are for $S = 0$ with ar = 2.5. In industry applications, for example, in drying process, particles are of smaller size. Depending on particle characteristic length, Reynolds number remains smaller. Therefore, in the present research, range of the Reynolds number has been taken up to 100. Range of c is selected according to many practical fluidization reactors. The maximum c of 0.3 is chosen because systems with larger c are difficult to generate with a wide range of S. Lattice unit system is used in all the simulations. The boundary conditions are the same as those used in [17]. Temperature of the solid particles is specified to be 1 and fluid bulk temperature is fixed at 0 at the inlet. Prandtl number is set equal to unity. It means that hydrodynamic and thermal boundary layers are of the same size. A constant pressure gradient is employed across the domain to drive the flow. At the outlet, temperature gradient was set to zero. Gas flows parallel to increasing z direction. Domain size of 1.4 L is used, where L is the side length of packed cubic section. Schematic representation of the complete description of domain is mentioned in Figure 2. Three sizes of grids $d/\Delta x = 8, 12, 16$, are used, where d is the length of the minor axis of the particles. Final results are obtained by Richardson Extrapolation method using three-grid data as shown in Figure 3. This is because many studies, such as [19, 21], reported that the use of Richardson Extrapolation method was necessary for the particle-resolved simulations to obtain the grid-independent results. Particle numbers used for different solid volume fractions are in the range of 120 to 189. More than 500 numerical simulations were performed during this study.

3.2. Code Validation.

Huang et al. have already validated the present code of IB-LBM for spherical single as well as arrays of spherical particles for variety of solid volume fractions [17]. Before doing the heat transfer calculations for arrays of ellipsoidal particles, code validation of single ellipsoidal particle is performed. Richter and Nikrityuk performed the heat transfer calculations of cubes and ellipsoids in flows using ANSYS FLUENT software package. They simulated two cases for ellipsoids: one is parallel to the flow direction; that is, major axis of the ellipsoids was set parallel to the flow (ellipsoid 1) or perpendicular to the flow (ellipsoid 2). Therefore, to check the validity of present code, single-prolate particle is simulated for two orientations: one is parallel and other is perpendicular to the flow direction.
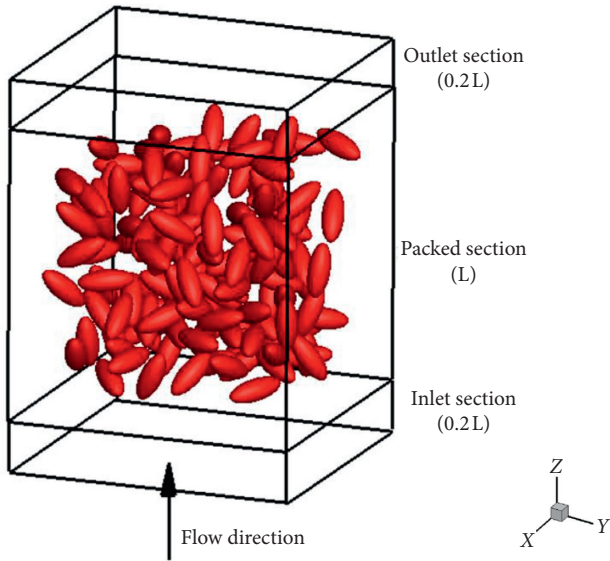
FIGURE 2: Schematic representation of computational domain (ar = 2.5, $S = 0$, and $c = 0.2$).

FIGURE 4: Single ellipsoidal particle. Ellipsoid 1 parallel to flow direction and ellipsoid 2 perpendicular to flow direction.

FIGURE 3: Three symbols are the three grids' values and the intersection between the dashed line and the vertical axis is the Richardson Extrapolation result depending on the three known grid values. The shown results are from a configuration of prolate particles at Re = 24, $c = 0.1$, and $S = 0.2$.
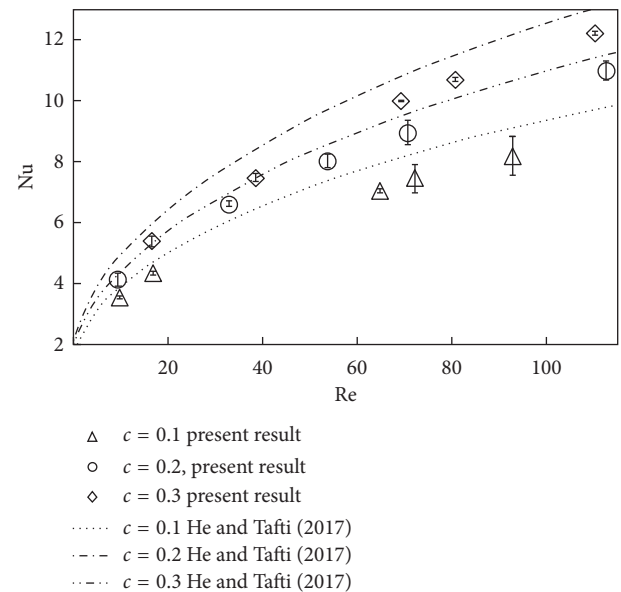
FIGURE 5: Nusselt number variation with respect to Reynolds number for various solid volume fractions at ar = 2.5 and $S = 0$. Error bars represent standard deviation in Nusselt number obtained from three different samples of random configurations.

Here, IB-LBM results are compared with the reported data of Richter and Nikrityuk. Nusselt number of single ellipsoidal particle is obtained by extrapolation at three small solid volume fractions of 0.01, 0.02, and 0.03. Simulation results are presented in Figure 4 with the results of Richter and Nikrityuk [10]. The results are found to be in good agreement with maximum deviation of less than 3% from the literature results. The comparison depicts that IB-LBM can produce the results in good accuracy when compared with commercial computational fluid dynamic software package.

For further validation, arrays of prolate particles at ar = 2.5 and $S = 0$ are considered. Figure 5 shows variation of Nusselt number versus Reynolds number for different solid volume fractions. Results show that Nusselt number increases with the increase of Reynolds number. The results of

the present study are compared with those of He and Tafti [14] who also simulated the prolate particles for solid volume fractions of 0.1 to 0.35. In general, the results are in good agreement with the literature both qualitatively and quantitatively. Minor differences are due to the use of different type of immersed boundary method in the present study. Also, He and Tafti have used constant heat flux boundary condition, whereas constant temperature boundary condition has been employed in the present research work. It is a known fact that the Nusselt number is lower for constant

temperature boundary case as compared to constant heat flux boundary conditions due to lower effective temperature gradient at the wall [18].

4. Results and Discussion

Average Nusselt number at the start of simulations has higher value but after some time steps it achieves its steady state as shown in Figure 6. During the process of forced convection heat transfer from hot particles, the temperature of gas increases as the gas approaches the outlet section as shown in Figure 7. The temperature attained near the outlet of the domains depends upon the Re, solid volume fraction, and S. As the temperature of fluid rises along the fluid direction, the potential for heat transfer decreases as temperature gradient at the particle surfaces is decreased.

Reynolds number plays a significant role in heat transfer phenomenon because it is the driving force behind the forced convection. As flow velocity (or Re) is increased, the fluid temperature in the cross section decreases, as shown in Figure 8, due to enhanced heat transfer.

As the ellipsoidal objects are 3D in nature, the orientations of these particles may modify the flow field around the assembly of particles. Therefore, orientations of these particles in the assembly can significantly influence the heat transfer. To investigate these effects, numerical simulations are performed for various Hermans orientation factors. For parallel arrays with $S = 1$, all particles are positioned such that they are parallel to the flow direction. Figure 9 ellipsoidal particles wh depicts that Nusselt number increases with the increase of Reynolds number due to enhanced convective heat transfer at higher Re. At a fixed Re, Nusselt number increases with solid volume fraction because the small interstitial spaces among the particles cause flow velocity to increase, which enhances the forced convection heat transfer as mentioned by [22].

The results for $S = 0.2$ are shown in Figure 10. Variations of Nu in the cases of $S = 0.2$ and $S = 1$ are not the same because of the different local recirculation zones due to particles orientations. Figure 11 shows the Nusselt number variation versus Reynolds number for $S = -0.5$. For this orientation factor, flow direction and major axes of ellipsoids are normal to each other. Here, difference between Nusselt numbers of two consecutive solid volume fractions is smaller because there is a negligible variation in flow velocity as the solid volume fraction is altered. However, at any fixed Reynolds number, solid volume fractions cause Nu number to increase.

4.1. Influence of Hermans Orientation Factor on Nusselt Number.
Nusselt number is the dimensionless temperature gradient at the surface of particle. Usually heat transfer correlations of Nusselt number are developed using experimental results. However, for arrays of particles, it is difficult and economically expensive to calculate the heat transfer coefficient experimentally. In functional form, it has dependency on the Reynolds number and Prandtl number for single-particle case. But, for multiparticle system, effect of solid volume fraction and its orientation cannot be
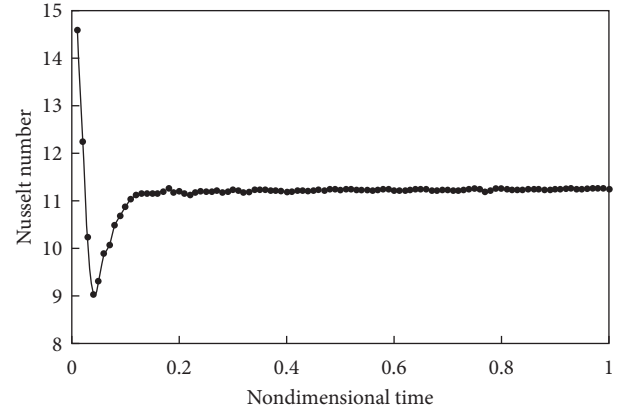
FIGURE 6: Average Nusselt number with Hermans orientation factor of 0.2, with $c = 0.3$ and Re $= 82$.
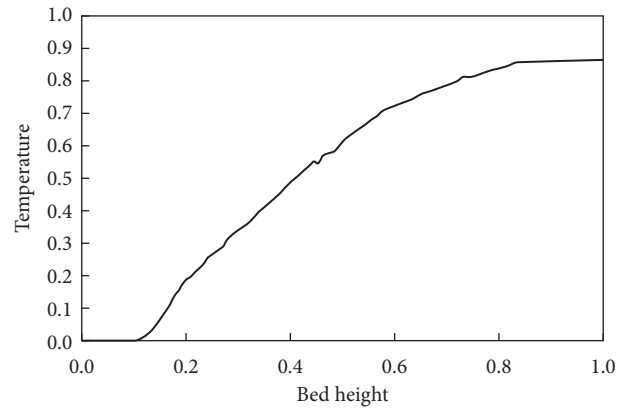
FIGURE 7: Gas temperature rise with bed height. $S = -0.5$, $c = 0.1$, and Re $= 12.72$.

neglected. Therefore, Nu $= f$ (Re, Pr, c, S). By using the simulation data, a correlation has been developed for assembly of ellipsoidal particles with aspect ratio of 2.5 and it reads

$$
\begin{aligned}
\text{Nu} = {}& \left(1.5 - 0.885\,(1 - c) + 0.078\,(1 - c)^2\right) \\
& \cdot \left[2.458 - 0.042\text{Re}^{1.07}\text{Pr}^{1/3}\right] \\
& + \left(1.115 - 0.62\,(1 - c) - 0.08\,(1 - c)^2\right)\text{Re}^{0.68}\text{Pr}^{1/3} \\
& + (-S + 0.08).
\end{aligned}
\tag{8}
$$

Equation (8) is valid for $0 < \text{Re} \leq 100$, $0.1 \leq c \leq 0.3$, and $S = \{-0.5, 0, 0.2, 1\}$ for solid particles with aspect ratio of 2.5. The coefficients of equation (8) are determined by minimizing the difference between the simulated data and predicted correlation. Predicted values of Nusselt number using equation (8) are plotted with simulation results in Figure 12. It can be seen that the proposed correlation gives satisfactory performance and the maximum deviation from the simulated results is less than 10%.

(a)

(b)
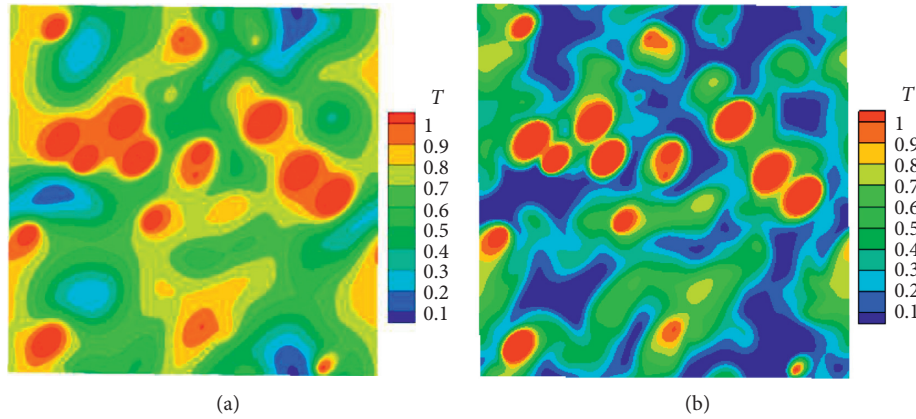
FIGURE 8: Temperature contours in xy plane (middle of packed section), $S = 0$ at 0.1 solid volume fractions. (a) Re = 16.5 and (b) Re = 90.

◇ $c = 0.1$
△ $c = 0.2$
○ $c = 0.3$
—— $c = 0.1$ correlation
⋯⋯ $c = 0.2$ correlation
--- $c = 0.3$ correlation
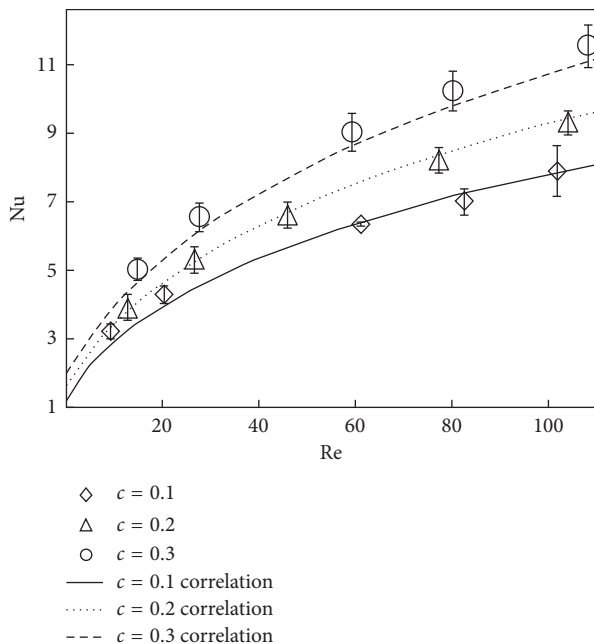
FIGURE 9: Nusselt number variation with Reynolds numbers for ar = 2.5 and $S = 1$ at $c = 0.1$, 0.2, and 0.3. Symbols represent simulation results and lines obtained from correlation in equation (8).

△ $c = 0.1$
◇ $c = 0.2$
× $c = 0.3$
—— $c = 0.1$ correlation
⋯⋯ $c = 0.2$ correlation
--- $c = 0.3$ correlation

FIGURE 10: Nusselt number versus Reynolds number for ar = 2.5 and $S = 0.2$ at $c = 0.1$, 0.2, and 0.3. Symbols represent simulation results and lines obtained from correlation in equation (8).

Impact of Hermans orientation factor on Nusselt number can be probed by using equation (8).

Effects of orientations cannot be neglected in forced convection heat transfer because this phenomenon strongly depends on the flow field variations. For different values of S, Nusselt number varying with the Reynolds number is plotted in Figure 13. Only the results at $c = 0.2$ are shown as illustrative examples. It can be seen that the Nusselt number generally decreases with the increase of S. The proposed correlation agrees favorably well with the DNS results. Also the variation of Nusselt number with Hermans orientation factors is presented in Figures 14(a) to 14(d) at various Reynolds numbers. Figure 14(a) is the plot at Reynolds number of 20, which shows that Nu decreases with the increase of S linearly at various solid volume fractions. This

trend is also observed at other Reynolds numbers, since the proposed equation (8) is indeed a linear function of S when other parameters in the correlation are fixed.

Nusselt numbers at $S = 1$ have minimum values as compared to the other three orientations at the same solid volume fractions. This is due to the less recirculation of flow as particles are aligned along the flow direction.

Figure 14 shows that the effect of S on average Nusselt number is very significant and this behavior remains obvious even with the increase of Reynolds number. It can be realized from Figure 14(a) that, at the Reynolds number of 20, the value of Nusselt number at $c = 0.1$ and $S = -0.5$ is almost 9% more than the respective value at $S = 0$. This may be due to the fact that, for lower solid volume fraction ($c = 0.1$), $S = -0.5$ gives rise to higher value of the effective heat transfer surface area as compared to $S = 0$. Moreover, when compared to $S = 0.2$, Nusselt number for $S = -0.5$ has 13% higher
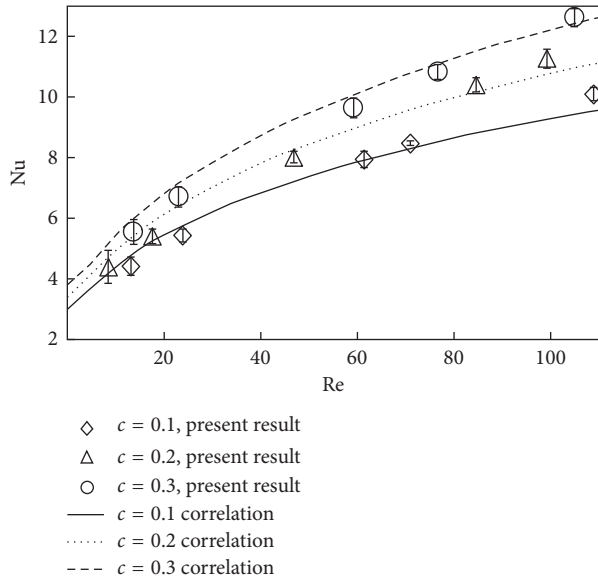
FIGURE 11: Nusselt number versus Reynolds number for $ar = 2.5$ and $S = -0.5$ at $c = 0.1, 0.2,$ and 0.3. Symbols represent simulation results and lines obtained from correlation in equation (8).
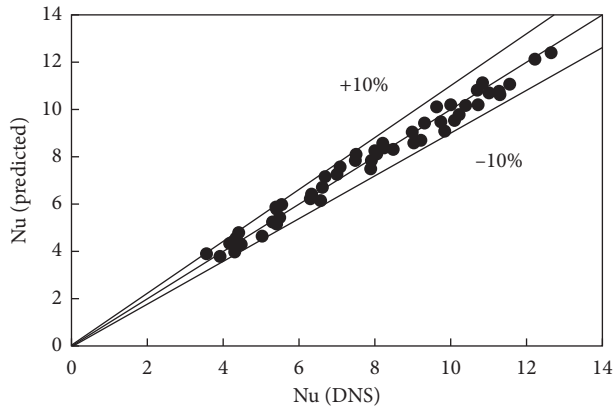
FIGURE 12: Comparison of average Nusselt number from DNS with correlation predicted values.

value. Similarly, the forced convection strength of $S = -0.5$ is 27% higher when compared with $S = 1$ at $c = 0.1$. Highest value of Nusselt number 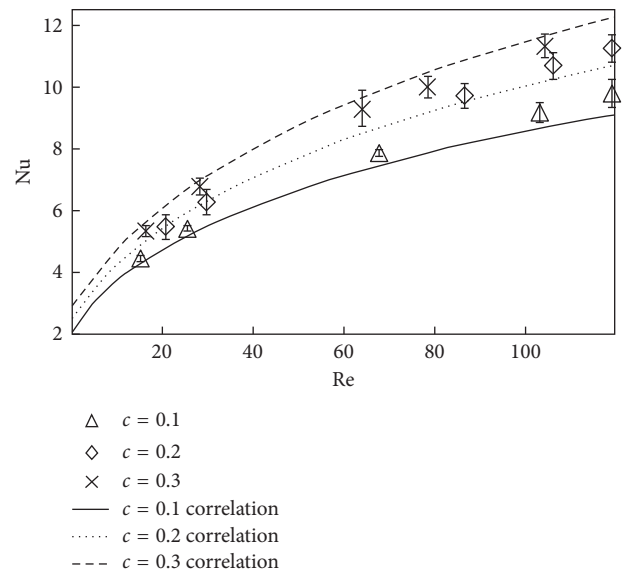occurs for $c = 0.1$ and $S = -0.5$ is due to the impact of jet and enhanced recirculation. Also, the ellipsoidal particles whose major axis is placed parallel to the flow direction have smaller Nu as mentioned in [23].

For $c = 0.2$ and $Re = 50$ in Figure 14(b), it can be observed that prolate particle assembly with $S = -0.5$ again has the highest heat transfer properties as compared to the other orientations. This increase is 6%, 8%, and 17% as compared to $S = 0$, $S = 0.2$, and $S = 1$, respectively. It is observed that, with increase of c, maxima was again achieved at $S = -0.5$. The amount of heat transfer from each assembly depends on many factors including heat transfer surface area, local flow velocity, temperature gradient, and vortices formed near the solid particle [24].
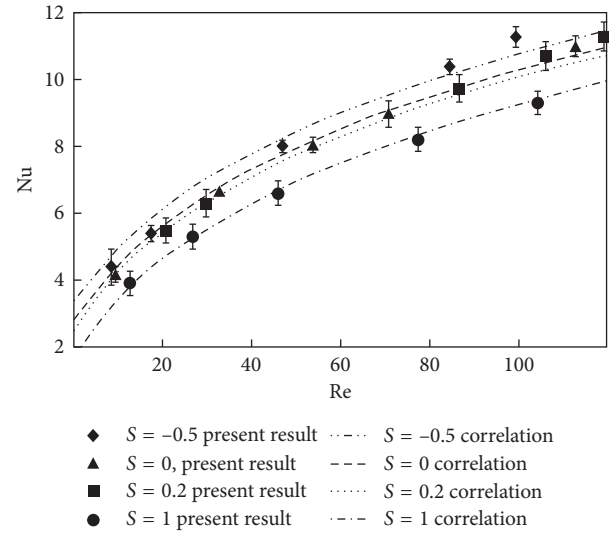
FIGURE 13: Nusselt number variation for different Hermans orientation factor $c = 0.2$.

Figures 14(c) and 14(d) show effect of S on Nusselt number at Reynolds numbers of 90 and 100, respectively. For $c = 0.3$ and $S = -0.5$, average Nusselt number is 4% more than the random orientation ($S = 0$) case. Therefore, it can be concluded that arrays of particles whose major axes are perpendicular to the flow direction have high value of Nusselt number ($Nu_{S=-0.5}$) as compared to the other orientations. Parallel arrays have minimum values of Nusselt number ($Nu_{S=1}$). Overall percent increase in Nusselt number caused by S can be calculated by using equation (9) and is plotted in Figure 15 for different values of solid volume fractions and Reynolds number.

$$\% \text{ increase} = \frac{Nu_{S=-0.5} - Nu_{S=1}}{Nu_{S=-0.5}} \times 100. \tag{9}$$

Figure 16 represents the contours at 0.2 solid volume fractions for three different values of S. All the three cases have distinct local structure that results in unique convective heat transfer behavior. For $S = 1$, the temperature of the gas around the particles is still lower due to less heat transfer as compared to the other two cases.

4.2. Stanton Number.
Stanton number, St, also known as Margoulis number (M), is another dimensionless number that is used in forced convection heat transfer process. It measures the ratio of heat transported into a fluid to the thermal capacity of the fluid. Mathematical expression for this number is [18]

$$St = \frac{Nu}{Re\,Pr}. \tag{10}$$

In the present study, Prandtl number is 1 and Stanton number can also be calculated from the simulation data. Dimensionless numbers have great significance in fluid mechanics. They help in easy parametric investigation of diverse engineering problems. Figure 17 shows the trend of

(a)

(b)

(c)

(d)
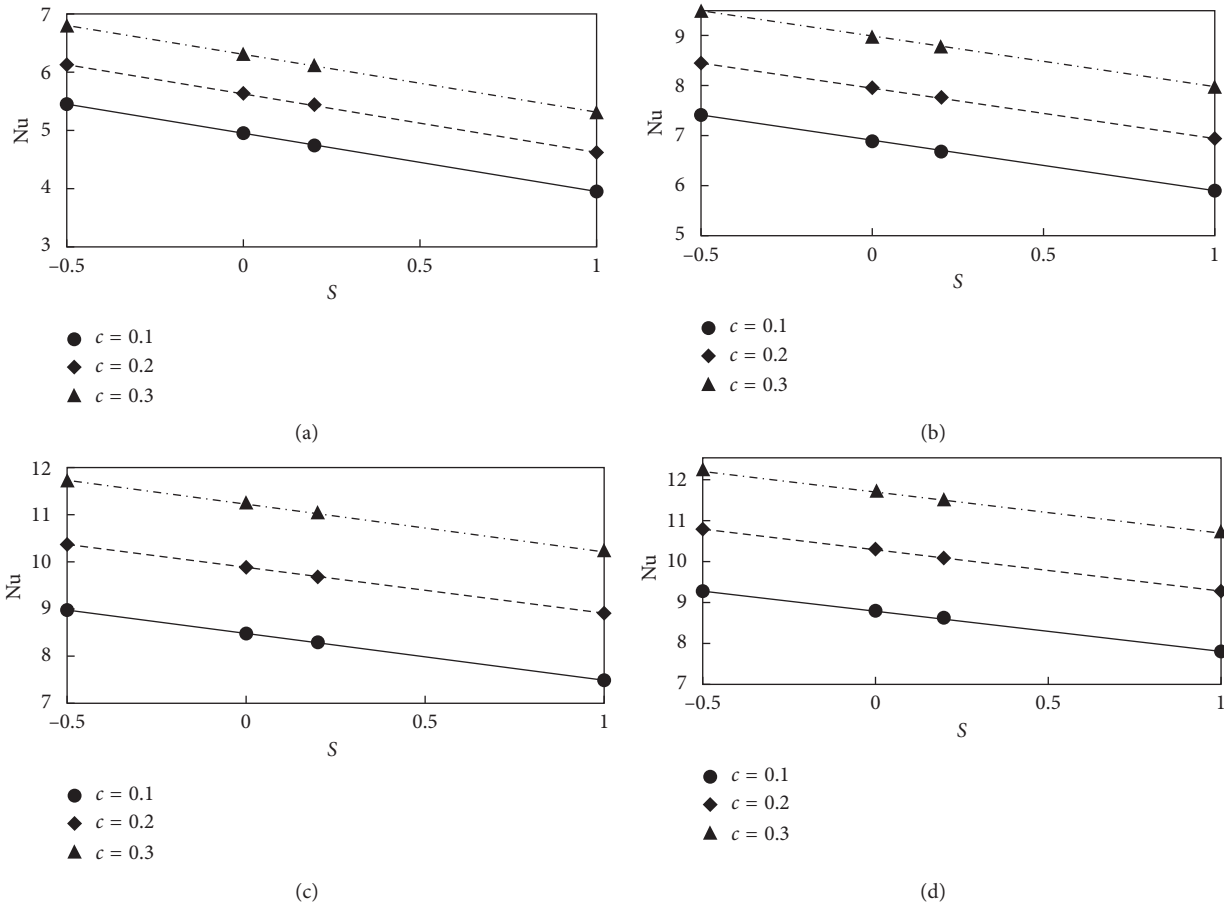
FIGURE 14: Nusselt number variation with Hermans orientation factor. (a) Re = 20, (b) Re = 50, (c) Re = 90, and (d) Re = 100.
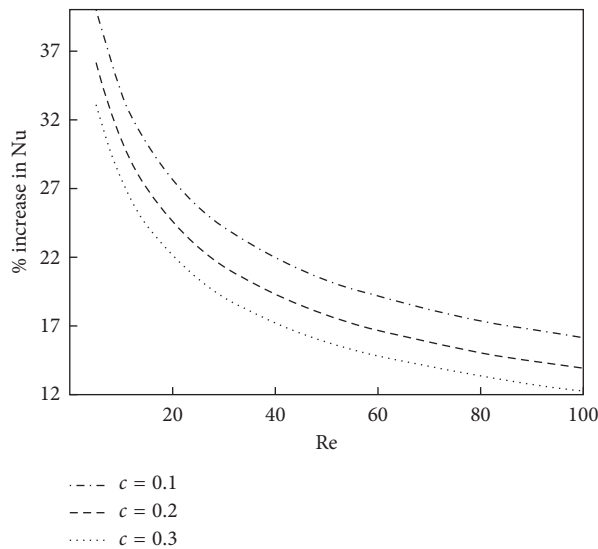
FIGURE 15: Percent increase in Nusselt number caused by S for various solid volume fractions.

Stanton number with Reynolds number. Also Figure 18 shows the effects of Hermans orientation factors on Stanton number at $c = 0.2$. Clearly, Stanton number decreases with the increase of S at fixed value of $c = 0.2$. Close observation shows that the impact of S on Stanton number decreases with the increase of Reynolds number. The trend observed at other solid volume fractions is similar to that reported at $c = 0.2$ and hence is omitted.
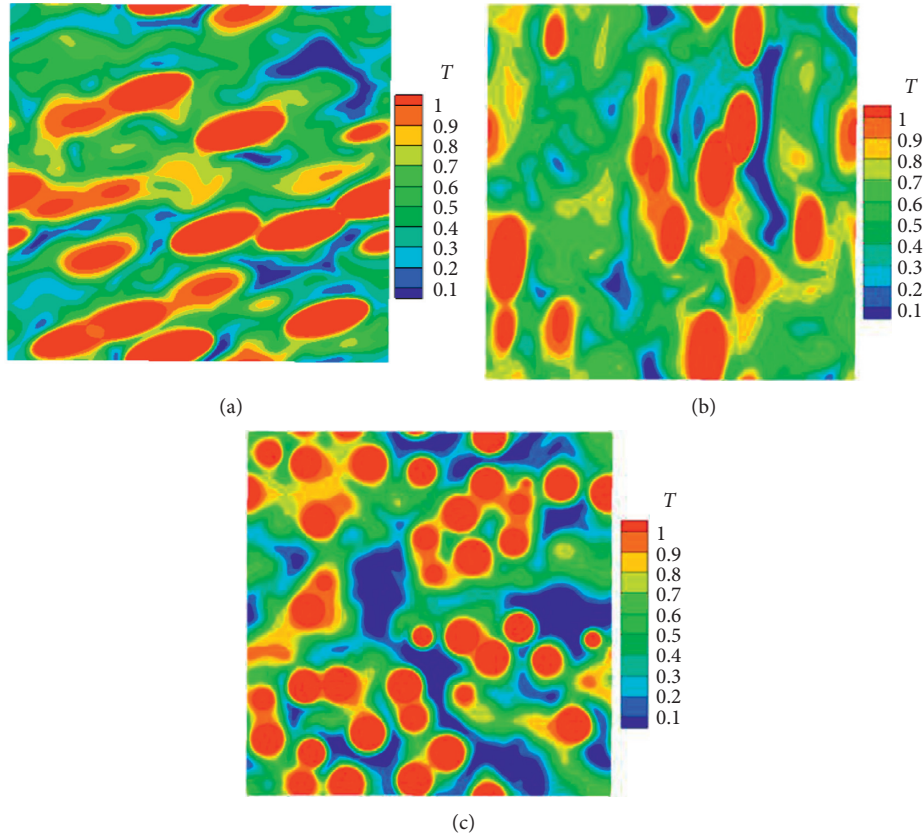
FIGURE 16: Temperature contours in xy plane (middle of packed section), $c = 0.2$. (a) Re = 98.9 and $S = -0.5$. (b) Re = 90.5 and $S = 0$. (c) Re = 100 and $S = 1$.
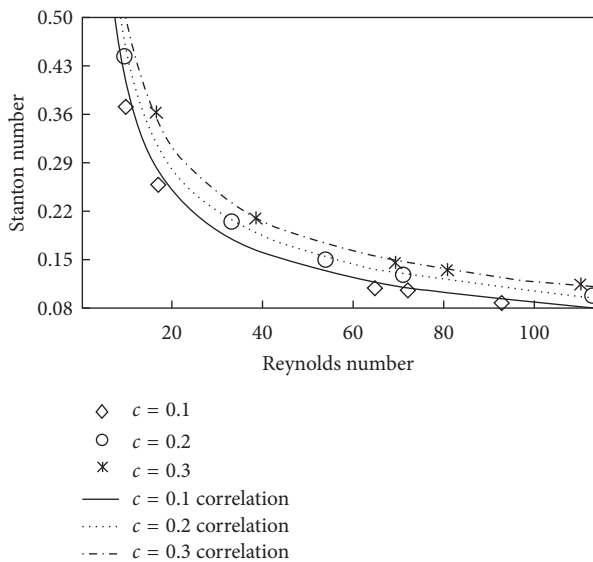
FIGURE 17: Variation of Stanton number with Reynolds number at $S = 0$.

FIGURE 18: Variation of Stanton number for different S at $c = 0.2$.

Stanton number is also widely used in Reynolds analogy concept of boundary layer theory. From the information of Stanton number, the friction coefficient can be calculated because St = $C_f/2$ [18]. This analogy is applicable only if Prandtl number is one and pressure gradient is zero in limiting condition. However, this analogy can be applied with its limitations just to have the first approximation of the magnitudes of flow variables, that is, friction or mass flow rate coefficients. So, heat transfer data can be utilized to have

a good insight into the underlying physical problems. Although this analogy will not give the accurate results, it can provide a firsthand engineering analysis [25].

5. Summary and Conclusions

Heat transfer study of prolate particle arrays is performed using second-order accurate Immersed Boundary-Lattice Boltzmann Method (IB-LBM) [16]. Particles with aspect ratio of 2.5 are studied. Arrays are generated for solid volume fraction from 0.1 to 0.3 by using Monte Carlo method [15]. Moreover, four different values of Hermans orientation factor in the range of –0.5 to 1 are considered. Results are presented by doing averaging on three different random arrays of prolate particles. It is concluded that Nusselt number considerably increases with the increase of Reynolds number and solid volume fractions. Also, Nusselt number significantly decreases with the increase of Hermans orientation factor. For example, at $c = 0.1$ and Re = 20, Nusselt number of arrays with $S = -0.5$ is approximately 27% higher than that in arrays with $S = 1$. The difference between Nusselt number obtained in arrays of $S = -0.5$ and that obtained in arrays of $S = 1$ decreases as the solid volume fraction and Reynolds number increase. This difference is still remarkable at $c = 0.3$ and Re = 100, which is around 12%.

Based on the present simulations, a correlation is presented for heat transfer of prolate particles. The maximum deviation of the proposed correlation from the simulation results is less than 10 percent. It is noted that Nusselt number is a linear function of S when other parameters such as Re, Pr, and c in the correlation are fixed. The proposed correlation would prove beneficial for future studies in practical processes. Stanton number calculations are also performed based on the proposed correlation for Nusselt number. It is found that the impact of S on Stanton number is nonnegligible. Stanton number decreases with the increase of S. The impact of S on Stanton number decreases with the increase of Reynolds number. Overall, the present study shows that the effect of mean particle orientation on Nu for arrays of prolate particles is significant. This indicates that, in practical systems with nonspherical particles, the consideration of the effect of orientation is necessary for accurate prediction of the heat transfer property of the flow. Forthcoming studies will comprise the heat transfer of prolate arrays for several aspect ratios. Consideration of a variety of aspect ratios will be fruitful in biomass applications because in such process enormous particles' aspect ratios exist. In practical applications, particles form different orientations; therefore, the impact of orientations on forced convection for a range of aspect ratio will contribute a lot on the road to the engineering community. In the future, a unified Nusselt number correlation will be presented in the form of aspect ratios, Hermans orientation factor, Reynolds number, and solid volume fraction. The impacts of the orientation on gas-solid heat transfer at even higher Reynolds number and various aspect ratios are recommended for future studies.

Nomenclature

c: Solid volume fraction
D: Particle equivalent diameter
U: Superficial gas velocities
Re: Reynolds number
ρ: Density of gas
μ: Viscosity of gas
S: Hermans orientation factors
f_i, g_i: Distribution functions
f_i^{eq}, g_i^{eq}:   Equilibrium distribution functions
e_i: Lattice velocity
x: Position vector
τ_f, τ_g: Relaxation factors
$F_{A_{F,i}} (F)$:   Source term in momentum equation
$Q_{A_{Q,i}} (Q)$:   Source term in heat equation
k: Fluid thermal conductivity
h: Convective heat transfer coefficient
Pr: Prandtl number
Nu: Nusselt number
$Nu_{f,slice}$:   Nusselt number of slice
T_s: Ellipsoid temperature
$\langle T_f \rangle$:   Average temperature of slice
V_{slice}:   Volume of slice
N_{slice}:   Number of slices
a_p: Specific surface area
Q_{slice}:   Heat flux from particles to the fluid phase
$h_{f,slice}$:   Slice heat transfer coefficient
A: Area of slice
α: Signed level set function
u_z: Gas velocity in flow direction
$\varnothing$:   Angle
a, b: Particle semimajor and minor axis
ar: Aspect ratio
n: Number of solid particles
L: Length of cubic computational domain
St: Stanton number
C_f: Skin friction.

Data Availability

The data used to support the findings of this study are available from the corresponding author upon request.

Conflicts of Interest

The authors declare that they have no known conflicts of interest or personal relationships that could have appeared to influence the work reported in this paper.

Acknowledgments

References

[1] J. Brix, P. A. Jensen, and A. D. Jensen, "Modeling char conversion under suspension fired conditions in O_2/N_2 and O_2/CO_2 atmospheres," *Fuel*, vol. 90, no. 6, pp. 2224–2239, 2011.

[2] A. Panahi, Y. A. Levendis, N. Vorobiev, and M. Schiemann, "Direct observations on the combustion characteristics of Miscanthus and Beechwood biomass including fusion and spherodization," *Fuel Processing Technology*, vol. 166, pp. 41–49, 2017.

[3] D. J. Gunn, "Transfer of heat or mass to particles in fixed and fluidised beds," *International Journal of Heat and Mass Transfer*, vol. 21, no. 4, pp. 467–476, 1978.

[4] N. Wakao, S. Kaguei, and T. Funazkri, "Effect of fluid dispersion coefficients on particle-to-fluid heat transfer coefficients in packed beds," *Chemical Engineering Science*, vol. 34, no. 3, pp. 325–336, 1979.

[5] N. G. Deen, S. H. L. Kriebitzsch, M. A. van der Hoef, and J. A. M. Kuipers, "Direct numerical simulation of flow and heat transfer in dense fluid-particle systems," *Chemical Engineering Science*, vol. 81, pp. 329–344, 2012.

[6] H. Tavassoli, E. A. J. F. Peters, and J. A. M. Kuipers, "Direct numerical simulation of non-isothermal flow through dense bidisperse random arrays of spheres," *Powder Technology*, vol. 314, pp. 291–298, 2017.

[7] S. Das, N. G. Deen, and J. A. M. Kuipers, "A DNS study of flow and heat transfer through slender fixed-bed reactors randomly packed with spherical particles," *Chemical Engineering Science*, vol. 160, pp. 1–19, 2017.

[8] K. Suzuki, T. Kawasaki, N. Furumachi, Y. Tai, and M. Yoshino, "A thermal immersed boundary-lattice Boltzmann method for moving-boundary flows with Dirichlet and Neumann conditions," *International Journal of Heat and Mass Transfer*, vol. 121, pp. 1099–1117, 2018.

[9] G. Juncu, "Unsteady heat transfer from an oblate/prolate spheroid," *International Journal of Heat and Mass Transfer*, vol. 53, no. 17-18, pp. 3483–3494, 2010.

[10] A. Richter and P. A. Nikrityuk, "Drag forces and heat transfer coefficients for spherical, cuboidal and ellipsoidal particles in cross flow at sub-critical Reynolds numbers," *International Journal of Heat and Mass Transfer*, vol. 55, no. 4, pp. 1343–1354, 2012.

[11] H. Zhang, L. Zhang, X. An, and A. Yu, "PR-DNS on the momentum and heat transfer of a rotating ellipsoidal particle in a fluid," *Powder Technology*, vol. 373, pp. 152–163, 2020.

[12] J. Yang, Q. Wang, M. Zeng, and A. Nakayama, "Computational study of forced convective heat transfer in structured packed beds with spherical or ellipsoidal particles," *Chemical Engineering Science*, vol. 65, no. 2, pp. 726–738, 2010.

[13] H. Tavassoli, E. A. J. F. Peters, and J. A. M. Kuipers, "Direct numerical simulation of fluid-particle heat transfer in fixed random arrays of non-spherical particles," *Chemical Engineering Science*, vol. 129, pp. 42–48, 2015.

[14] L. He and D. K. Tafti, "Heat transfer in an assembly of ellipsoidal particles at low to moderate Reynolds numbers," *International Journal of Heat and Mass Transfer*, vol. 114, pp. 324–336, 2017.

[15] X. Li, M. Jiang, Z. Huang, and Q. Zhou, "Effect of particle orientation on the drag force in random arrays of prolate ellipsoids in low-Reynolds-number flows," *AIChE Journal*, vol. 65, no. 8, 2019.

[16] Q. Zhou and L.-S. Fan, "A second-order accurate immersed boundary-lattice Boltzmann method for particle-laden flows," *Journal of Computational Physics*, vol. 268, pp. 269–301, 2014.

[17] Z. Huang, C. Zhang, M. Jiang, H. Wang, and Q. Zhou, "Effects of particle velocity fluctuations on inter-phase heat transfer in gas-solid flows," *Chemical Engineering Science*, vol. 206, pp. 375–386, 2019.

[18] D. P. D. Frank and P. Incropera, *Fundamentals of Heat and Mass Transfer*, John Wiley & Sons, Hoboken, NJ, USA, 6th edition, 2007.

[19] Q. Zhou and L.-S. Fan, "Direct numerical simulation of moderate-Reynolds-number flow past arrays of rotating spheres," *Physics of Fluids*, vol. 27, no. 7, pp. 73306–73423, 2015.

[20] M. A. V. D. Hoef, R. Beetstra, and J. A. M. Kuipers, "Lattice-Boltzmann simulations of low-Reynolds-number flow past mono- and bidisperse arrays of spheres: results for the permeability and drag force," *Journal of Fluid Mechanics*, vol. 528, p. 233, 2005.

[21] W.-P. Breugem, "A second-order accurate immersed boundary method for fully resolved simulations of particle-laden flows," *Journal of Computational Physics*, vol. 231, no. 13, p. 4469, 2012.

[22] B. Sun, S. Tenneti, and S. Subramaniam, "Modeling average gas-solid heat transfer using particle-resolved direct numerical simulation," *International Journal of Heat and Mass Transfer*, vol. 86, pp. 898–913, 2015.

[23] E. M. Sparrow, J. P. Abraham, and J. C. K. Tong, "Archival correlations for average heat transfer coefficients for non-circular and circular cylinders and for spheres in cross-flow," *International Journal of Heat and Mass Transfer*, vol. 47, no. 24, pp. 5285–5296, 2004.

[24] Y. A. Cengel, *Heat Transfer: A Practical Approach with EES CD*, p. 896, McGraw-Hill Higher Education, New York, PA, USA, 2002.

[25] Z. Duan, B. He, and Y. Duan, "Sphere drag and heat transfer," *Scientific Reports*, vol. 5, no. 1, pp. 1–7, 2015.

Research Article

Novel Cubic Trigonometric B-Spline Approach Based on the Hermite Formula for Solving the Convection-Diffusion Equation

Aatika Yousaf,[1] **Thabet Abdeljawad** (ORCID),[2,3,4] **Muhammad Yaseen** (ORCID),[1] **and Muhammad Abbas** (ORCID)[1]

[1]*Department of Mathematics, University of Sargodha, Sargodha, Pakistan*
[2]*Department of Mathematics and General Sciences, Prince Sultan University, Riyadh, Saudi Arabia*
[3]*Department of Medical Research, China Medical University, Taichung, Taiwan*
[4]*Department of Computer Science and Information Engineering, Asia University, Taichung, Taiwan*

Correspondence should be addressed to Thabet Abdeljawad; tabdeljawad@psu.edu.sa and Muhammad Abbas; muhammad.abbas@uos.edu.pk

This paper introduces a cubic trigonometric B-spline method (CuTBM) based on the Hermite formula for numerically handling the convection-diffusion equation (CDE). The method utilizes a merger of the CuTBM and the Hermite formula for the approximation of a space derivative, while the time derivative is discretized using a finite difference scheme. This combination has greatly enhanced the accuracy of the scheme. A stability analysis of the scheme is also presented to confirm that the errors do not magnify. The main advantage of the scheme is that the approximate solution is obtained as a smooth piecewise continuous function empowering us to approximate a solution at any location in the domain of interest with high accuracy. Numerical tests are performed, and the outcomes are compared with the ones presented previously to show the superiority of the presented scheme.

1. Introduction

The CDE describes physical phenomena in which particles, energy, and other physical quantities are transferred within a physical system due to diffusion and convection. The CDE is given as

$$\frac{\partial v}{\partial t} + \alpha \frac{\partial v}{\partial \xi} = \beta \frac{\partial^2 v}{\partial \xi^2}, \quad a \le \xi \le b, t > 0, \qquad (1)$$

where α is the coefficient of viscosity and β is the phase velocity, respectively, and both are considered positive. Equation (1) is subject to the following initial condition:

$$v(\xi, 0) = \phi(\xi), \quad a \le \xi \le d, \qquad (2)$$

and the boundary conditions

$$\begin{cases} v(a, t) = g_0(t), \\ v(b, t) = g_1(t), \\ t > 0. \end{cases} \qquad (3)$$

Here, ϕ, g_0, and g_1 are known functions of sufficient smoothness.

In the literature, various numerical techniques have been developed for the one-dimensional CDE with specified initial and boundary conditions such as finite differences, finite elements, spectral methods, method of lines, and many more. Mohebbi and Dehghan [1] presented a high-order compact solution of the one-dimensional heat and advection-diffusion equation. Salkuyeh [2] used finite difference approximation to solve the CDE. Karahan [3, 4] worked on unconditional stable explicit and implicit finite difference techniques for the advection-diffusion equation using

spreadsheets. Restrictive Taylor approximation was used by Ismail et al. [5] to solve the CDE. Cao et al. [6] developed a fourth-order compact finite difference scheme for solving the CDE. The generalized trapezoidal formula was used by Chawla and Al-Zanaidi [7] to solve the CDE. Dehghan [8] used weighted finite difference techniques for the one-dimensional advection-diffusion equation. Furthermore, Dehghan [9] developed a technique for the numerical solution of the three-dimensional advection-diffusion equation. A second-order space and time nodal method for the CDE was conducted by Rizwan [10]. Kara and Zhang [11] introduced an ADI method for an unsteady CDE. Feng and Tian [12] presented an alternating group explicit method for the CDE. Mittal and Jain [13] redefined the cubic B-spline collocation method for solving the CDE. Kadalbajoo and Arora [14] presented the Taylor–Galerkin B-spline finite element method for the one-dimensional advection-diffusion equation. Sari et al. [15] used a high-order finite difference scheme for solving the advection-diffusion equation. Tsai et al. [16] used a characteristics method with cubic interpolation for the advection-diffusion equation. Daig et al. [17] presented a least-squares finite element method for the advection-diffusion equation. Chawla et al. [18] presented extended one-step time-integration schemes for the CDE. Ding and Zhang [19] presented a highly accurate difference scheme for CDE. Nazir et al. [20] obtained numerical solutions of the CDE CuTBS approach. Aminikhah and Alvi [21] solved the CDE using cubic B-spline quasi-interpolation. A new Rabotnov fractional-exponential function based fractional derivative for the diffusion equation under external force was presented by Kumar et al. [22]. A modified analytical approach with existence and uniqueness was presented by Kumar et al. [23] for fractional Cauchy reaction-diffusion equations. A numerical study of modeling and analysis of fractal and fractal-fractional differential equations was initiated in [24, 25].

Motivated by the boom of the spline approach in finding the numerical solutions of the partial differential equations, we have utilized a blend of the Hermite formula and the cubic B-spline for the discretization of the space derivative. This merger has significantly augmented the accuracy of the scheme. Another favorable advantage is that approximate solutions come up as a smooth piecewise continuous function permitting one to obtain approximation at any desired location in the domain. The approach used by von Neumann is utilized to confirm that the presented scheme is unconditionally stable. The scheme is applied to various test problems, and the outcomes are contrasted with those reported in [19–21].

The remaining portion of the paper is organized in the following sequence. Section 2 presents the proposed scheme that is derived out for the numerical treatment of the CDE. The stability analysis of the scheme is discussed in Section 3. The comparison of the numerical results is provided in Section 4. The outcomes of this study are presented in Section 5.

2. Derivation of the Scheme

For positive integers M and N, let $k = T/N$ and $h = b - a/M$ be the time and the space step sizes, respectively. The time domain is discretized as $t_n = $ nk, $n = 0, 1, 2, \ldots, N$. The spatial domain $[a, b]$ is partitioned as $\xi_j = $ jh, $j = 0, 1, 2, \ldots, M$, where $a = \xi_0 < \xi_1 < \cdots < \xi_{n-1} < \xi_M = b$. The procedure for finding the approximate solution of (1) involves determination of the approximate solution $V(\xi, t)$ to the exact solution $v(\xi, t)$ as follows [26]:

$$V(\xi, t) = \sum_{j=-3}^{M-1} \sigma_j(t) \mathrm{TB}_j^4(\xi), \tag{4}$$

where $\sigma_j(t)$ are time-dependent quantities to be determined and $\mathrm{TB}_j^4(\xi)$ are cubic trigonometric basis functions given in [26] as follows:

$$\mathrm{TB}_j^4(\xi) = \frac{1}{p} \begin{cases} y^3(\xi_j), & \xi \in [\xi_j, \xi_{j+1}], \\ y(\xi_j)(y(\xi_j)z(\xi_{j+2}) + z(\xi_{j+3})y(\xi_{j+1})) + z(\xi_{j+4})l^2(\xi_{j+1}), & \xi \in [\xi_{j+1}, \xi_{j+2}], \\ z(\xi_{j+4})(y(\xi_{j+1})z(\xi_{j+3}) + z(\xi_{j+4})y(\xi_{j+2})) + y(\xi_j)m^2(\xi_{j+3}), & \xi \in [\xi_{j+2}, \xi_{j+3}], \\ m^3(\xi_{j+4}), & \xi \in [\xi_{j+3}, \xi_{j+4}], \end{cases} \tag{5}$$

where

$$y(\xi_j) = \sin\left(\frac{\xi - \xi_j}{2}\right),$$

$$z(\xi_j) = \sin\left(\frac{\xi_j - \xi}{2}\right), \tag{6}$$

$$p = \sin\left(\frac{h}{2}\right)\sin(h)\sin\left(\frac{3h}{2}\right).$$

By applying the local support property of $TB_j^4(\xi)$, it is observed that only $TB_{j-3}^4(\xi), TB_{j-2}^4(\xi)$, and $TB_{j-1}^4(\xi)$ are survived. Consequently, the approximation v_j^n at (ξ_j, t_n) becomes

$$v(\xi_j, t^n) = v_j^n = \sum_{w=j-3}^{j-1} \sigma_j^n(t)TB_j^4(\xi). \tag{7}$$

Now, v_j^n and its necessary derivatives are approximated by applying the collocation conditions on $B_j^3(\xi)$. The obtained approximations are given by

$$\begin{cases} v_j^n = \vartheta_1 \sigma_{j-3}^n + \vartheta_2 \sigma_{j-2}^n + \vartheta_1 \sigma_{j-1}^n, \\ \left(v_\xi\right)_j^n = -\vartheta_3 \sigma_{j-3}^n + \vartheta_4 \sigma_{j-2}^n + \vartheta_3 \sigma_{j-1}^n, \\ \left(v_{\xi\xi}\right)_j^n = \vartheta_5 \sigma_{j-3}^n + \vartheta_6 \sigma_{j-2}^n + \vartheta_5 \sigma_{j-1}^n, \end{cases} \tag{8}$$

where

$$\vartheta_1 = \csc(h)\csc\left(\frac{3h}{2}\right)\sin^2\left(\frac{h}{2}\right),$$

$$\vartheta_2 = \frac{2}{1 + 2\cos(h)},$$

$$\vartheta_3 = \frac{3}{4}\csc\left(\frac{3h}{2}\right),$$

$$\vartheta_4 = 0, \tag{9}$$

$$\vartheta_5 = \frac{3 + 9\cos(h)}{4\cos(h/2) - 4\cos(5h/2)},$$

$$\vartheta_6 = -\frac{3\cot^2(h/2)}{2 + 4\cos(h)}.$$

Consider the Hermite formula at the knot (ξ_j, t_n) [27] given by

$$\left(v_{\xi\xi}\right)_{j-1}^n + 10\left(v_{\xi\xi}\right)_j^n + \left(v_{\xi\xi}\right)_{j+1}^n - \frac{12}{h^2}\left(v_{j-1}^n - 2v_j^n + v_{j+1}^n\right) = 0. \tag{10}$$

Substituting (8) in (10), we obtain

$$\left(v_{\xi\xi}\right)_j^n = \omega_1 \sigma_{j-4}^n + \omega_2 \sigma_{j-3}^n + \omega_3 \sigma_{j-2}^n + \omega_2 \sigma_{j-1}^n + \omega_1 \sigma_j^n, \tag{11}$$

where

$$\omega_1 = \frac{-\vartheta_5}{10} + \frac{6\vartheta_1}{5h^2},$$

$$\omega_2 = \frac{-\vartheta_6}{10} - \frac{12\vartheta_1}{5h^2} + \frac{6\vartheta_2}{5h^2}, \tag{12}$$

$$\omega_3 = \frac{-\vartheta_5}{5} + \frac{12\vartheta_1}{5h^2} - \frac{12\vartheta_2}{5h^2}.$$

Note that (11) provides new approximation of the second derivative. Now, applying the θ-weighted scheme to (1), we obtain

$$\left(v_t\right)_j^n = \theta h_j^{n+1} + (1 - \theta)h_j^n, \quad n = 0, 1, 2, \ldots, \tag{13}$$

where $h_j^n = \beta\left(v_{\xi\xi}\right)_j^n - \alpha\left(v_\xi\right)_j^n$. Using the difference scheme $(v_t)_j^n = (v_j^{n+1} - v_j^n)/k$ in (13), we obtain

$$v_j^{n+1} + k\alpha\theta\left(v_\xi\right)_j^{n+1} - k\beta\theta\left(v_{\xi\xi}\right)_j^{n+1} = v_j^n - k\alpha(1-\theta)\left(v_\xi\right)_j^n + k\beta(1-\theta)\left(v_{\xi\xi}\right)_j^n. \tag{14}$$

For the Crank–Nicolson approach, we choose $\theta = 0.5$ so that (14) reduces to

$$v_j^{n+1} + \frac{1}{2}k\alpha\left(v_\xi\right)_j^{n+1} - \frac{1}{2}k\beta\left(v_{\xi\xi}\right)_j^{n+1} = v_j^n - \frac{1}{2}k\alpha\left(v_\xi\right)_j^n + \frac{1}{2}k\beta\left(v_{\xi\xi}\right)_j^n. \tag{15}$$

Inserting (8) in (15) and replacing j with $j - 1$, we obtain

$$\left(\vartheta_1 - \frac{1}{2}k\alpha\vartheta_3 - \frac{1}{2}k\beta\vartheta_5\right)\sigma_{j-4}^{n+1} + \left(\vartheta_2 + \frac{1}{2}k\alpha\vartheta_4 - \frac{1}{2}k\beta\vartheta_6\right)\sigma_{j-3}^{n+1} + \left(\vartheta_1 + \frac{1}{2}k\alpha\vartheta_3 - \frac{1}{2}k\beta\vartheta_5\right)\sigma_{j-2}^{n+1} = \left(\vartheta_1 + \frac{1}{2}k\alpha\vartheta_3 + \frac{1}{2}k\beta\vartheta_5\right)\sigma_{j-4}^n$$

$$+ \left(\vartheta_2 - \frac{1}{2}k\alpha\vartheta_4 + \frac{1}{2}k\beta\vartheta_6\right)\sigma_{j-3}^n$$

$$+ \left(\vartheta_1 - \frac{1}{2}k\alpha\vartheta_3 + \frac{1}{2}k\beta\vartheta_5\right)\sigma_{j-2}^n, \quad j = 0, M. \tag{16}$$

Inserting (8) and (11) in (15), we obtain

$$-\left(\frac{1}{2}k\beta\omega_1\right)\sigma_{j-4}^{n+1}+\left(\vartheta_1-\frac{1}{2}k\alpha\vartheta_3-\frac{1}{2}k\beta\omega_2\right)\sigma_{j-3}^{n+1}$$

$$+\left(\vartheta_2+\frac{1}{2}k\alpha\vartheta_4-\frac{1}{2}k\beta\omega_3\right)\sigma_{j-2}^{n+1}$$

$$+\left(\vartheta_1+\frac{1}{2}k\alpha\vartheta_3-\frac{1}{2}k\beta\omega_2\right)\sigma_{j-1}^{n+1}-\left(\frac{1}{2}k\beta\omega_1\right)\sigma_j^{n+1}$$

$$=\left(\frac{1}{2}k\beta\omega_1\right)\sigma_{j-4}^{n}+\left(\vartheta_1+\frac{1}{2}k\alpha\vartheta_3+\frac{1}{2}k\beta\omega_2\right)\sigma_{j-3}^{n}$$

$$+\left(\vartheta_2-\frac{1}{2}k\alpha\vartheta_4+\frac{1}{2}k\beta\omega_3\right)\sigma_{j-2}^{n}+\left(\vartheta_1-\frac{1}{2}k\alpha\vartheta_3+\frac{1}{2}k\beta\omega_2\right)\sigma_{j-1}^{n}$$

$$+\left(\frac{1}{2}k\beta\omega_1\right)\sigma_j^{n},\quad j=1,2,3,\ldots,M-1.$$

$$(17)$$

Note that equations (16) and (17) together produce an inconsistent system of $(M+1)$ equations in $(M+3)$ unknowns. To obtain a consistent system, we need two additional equations which can be obtained using the given boundary conditions. Consequently, a consistent system of dimension $(M+3)\times(M+3)$ is obtained which can be solved using any Gaussian elimination-based numerical algorithm.

2.1. Initial State. The initial condition and the derivatives of initial condition are used to find initial vector σ^0 as follows:

$$\begin{cases}\left(v_\xi\right)_j^0=\phi'\left(\xi_j\right),&j=0,\\\left(v_j^0\right)=\phi\left(\xi_j\right),&j=0,1,\ldots,M,\\\left(v_\xi\right)_j^0=\phi'\left(\xi_j\right),&j=M.\end{cases}\quad(18)$$

System (18) produces an $(M+3)\times(M+3)$ matrix system of the following form:

$$H\sigma^0=b,\quad(19)$$

where

$$H=\begin{bmatrix}-\vartheta_3&\vartheta_4&\vartheta_3&0&\cdots&0&0\\\vartheta_1&\vartheta_2&\vartheta_1&0&\cdots&0&0\\0&\vartheta_1&\vartheta_2&\vartheta_1&0&\cdots&0\\\vdots&\vdots&\vdots&\vdots&\vdots&\vdots&\vdots\\\vdots&\vdots&\vdots&\vdots&\vdots&\vdots&\vdots\\\vdots&\vdots&\vdots&\vdots&\vdots&\vdots&\vdots\\0&0&\cdots&\cdots&\vartheta_1&\vartheta_2&\vartheta_1\\0&0&\cdots&\cdots&-\vartheta_3&\vartheta_4&\vartheta_3\end{bmatrix},$$

$$\sigma^0=\left[\sigma_{-4}^0,\sigma_{-2}^0,\sigma_{-1}^0,\ldots,\sigma_{M-2}^0\right]^T,$$

$$b=\left[\phi'\left(\xi_0\right),\phi\left(\xi_0\right),\ldots,\phi\left(\xi_M\right),\phi'\left(\xi_M\right)\right]^T.$$

$$(20)$$

3. Stability Analysis

The von Neumann stability technique is applied in this section to explore the stability of the given scheme. Consider the growth of error in a single Fourier mode, $\Omega_j^n=\delta^n e^{i\eta h j}$, where η is the mode number, h is the step size, and $i=\sqrt{-1}$. Inserting the Fourier mode into equation (15) yields

$$-\rho_1\delta^{n+1}e^{i\eta(j-4)h}+\rho_2\delta^{n+1}e^{i\eta(j-3)h}+\rho_3\delta^{n+1}e^{i\eta(j-2)h}$$

$$+\rho_4\delta^{n+1}e^{i\eta(j-1)h}-\rho_1\delta^{n+1}e^{i\eta(j)h}$$

$$=\rho_1\delta^n e^{i\eta(j-4)h}+\rho_5\delta^n e^{i\eta(j-3)h}+\rho_6\delta^n e^{i\eta(j-2)h}$$

$$+\rho_7\delta^n e^{i\eta(j-1)h}+\rho_1\delta^n e^{i\eta(j)h},$$

$$(21)$$

where

$$\rho_1=\frac{1}{2}k\beta\omega_1,$$

$$\rho_2=\vartheta_1-\frac{1}{2}k\alpha\vartheta_3-\frac{1}{2}k\beta\omega_2,$$

$$\rho_3=\vartheta_2+\frac{1}{2}k\alpha\vartheta_4-\frac{1}{2}k\beta\omega_3,$$

$$\rho_4=\vartheta_1+\frac{1}{2}k\alpha\vartheta_3-\frac{1}{2}k\beta\omega_2,\quad(22)$$

$$\rho_5=\vartheta_1+\frac{1}{2}k\alpha\vartheta_3+\frac{1}{2}k\beta\omega_2,$$

$$\rho_6=\vartheta_2-\frac{1}{2}k\alpha\vartheta_4+\frac{1}{2}k\beta\omega_3,$$

$$\rho_7=\vartheta_1-\frac{1}{2}k\alpha\vartheta_3+\frac{1}{2}k\beta\omega_2.$$

Dividing equation (21) by $\delta^n e^{i\eta(j-2)h}$ and rearranging the equation, we obtain

$$\delta=\frac{\rho_1 e^{-2i\eta h}+\rho_5 e^{-i\eta h}+\rho_6+\rho_7 e^{i\eta h}+\rho_1 e^{2i\eta h}}{-\rho_1 e^{-2i\eta h}+\rho_2 e^{-i\eta h}+\rho_3+\rho_4 e^{i\eta h}-\rho_1 e^{2i\eta h}}.\quad(23)$$

Using $\cos(\eta h)=(e^{i\eta h}+e^{-i\eta h})/2$ and $\sin(\eta h)=(e^{i\eta h}-e^{-i\eta h})/2i$ in equation (23) and simplifying, we obtain

$$\delta=\frac{2\rho_1\cos(2\eta h)+\rho_6+2A_1\cos(\eta h)-i2B_1\sin(\eta h)}{-2\rho_1\cos(2\eta h)+\rho_3+2A_2\cos(\eta h)+i2B_2\sin(\eta h)},$$

$$(24)$$

where

$$A_1=\vartheta_1+\frac{1}{2}k\beta\omega_2,$$

$$B_1=\frac{1}{2}k\alpha\vartheta_3,$$

$$(25)$$

$$A_2=\vartheta_1-\frac{1}{2}k\beta\omega_2,$$

$$B_2=\frac{1}{2}k\alpha\vartheta_3.$$

TABLE 1: Absolute errors when $k = 0.001$ at $h = 0.005$ for Example 1.

t	$\xi = 0.1$		$\xi = 0.3$		$\xi = 0.5$		$\xi = 0.7$		$\xi = 0.9$	
	Present	CNM [19]	Present	CNM [19]	Present	CNM [19]	Present	CNM [19]	Present	CNM [19]
0.2	9.19×10^{-7}	1.88×10^{-5}	7.52×10^{-8}	3.61×10^{-5}	6.83×10^{-6}	1.39×10^{-5}	3.06×10^{-5}	2.05×10^{-4}	8.13×10^{-5}	9.67×10^{-4}
0.4	1.52×10^{-6}	3.23×10^{-5}	1.39×10^{-7}	6.76×10^{-5}	1.27×10^{-5}	2.61×10^{-5}	5.71×10^{-5}	3.84×10^{-4}	1.41×10^{-4}	1.64×10^{-3}
0.6	1.88×10^{-6}	4.15×10^{-5}	1.86×10^{-7}	9.45×10^{-5}	1.78×10^{-5}	3.66×10^{-5}	7.97×10^{-5}	5.37×10^{-4}	1.84×10^{-4}	2.10×10^{-3}
0.8	2.10×10^{-6}	4.81×10^{-5}	1.99×10^{-7}	1.17×10^{-4}	2.22×10^{-5}	4.56×10^{-5}	9.89×10^{-5}	6.64×10^{-4}	2.16×10^{-4}	2.42×10^{-3}
1.0	2.22×10^{-6}	5.26×10^{-5}	1.68×10^{-7}	1.35×10^{-4}	2.58×10^{-5}	5.31×10^{-5}	1.15×10^{-4}	7.68×10^{-4}	2.39×10^{-4}	2.63×10^{-3}
10	6.19×10^{-8}	7.17×10^{-6}	1.90×10^{-6}	2.87×10^{-5}	1.12×10^{-5}	2.31×10^{-5}	3.52×10^{-5}	1.11×10^{-4}	4.78×10^{-5}	2.86×10^{-4}
20	1.57×10^{-8}	2.57×10^{-7}	1.58×10^{-7}	1.13×10^{-6}	6.85×10^{-7}	1.41×10^{-6}	1.85×10^{-6}	2.10×10^{-6}	2.27×10^{-6}	7.60×10^{-6}
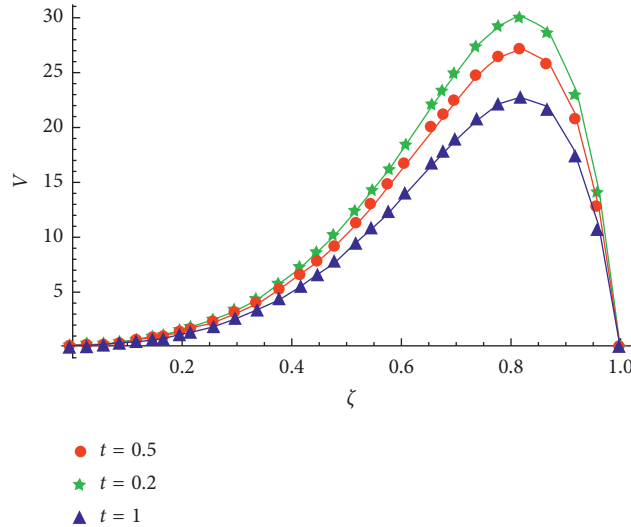
FIGURE 1: The approximate (stars, circles, and triangles) and exact (solid lines) solutions for various time stages when $h = 0.005, k = 0.001$ for Example 1.

Note that $\eta \in [-\pi, \pi]$. Without loss of generality, we can assume that $\eta = 0$ so that equation (24) takes the following form:

$$\delta = \frac{k\beta\omega_1 + \vartheta_2 - (1/2)k\alpha\vartheta_4 + (1/2)k\beta\omega_3 + 2\vartheta_1 + k\beta\omega_2}{-k\beta\omega_1 + \vartheta_2 + (1/2)k\alpha\vartheta_4 - (1/2)k\beta\omega_3 + 2\vartheta_1 - k\beta\omega_2},$$

$$= \frac{2\vartheta_1 + \vartheta_2 + k\beta(\omega_1 + \omega_2 + (1/2)\omega_3)}{2\vartheta_1 + \vartheta_2 - k\beta(\omega_1 + \omega_2 + (1/2)\omega_3)}$$

$$\leq 1,$$

(26)

which proves that the present computational scheme is unconditionally stable.

4. Numerical Experiments and Discussion

In this section, some numerical calculations are performed to test the accuracy of the offered scheme. In all examples, we use the following error norms:

$$L_\infty = \max_j \left| V_{\text{num}}(z_j, t) - v_{\text{exact}}(z_j, t) \right|,$$

$$L_2 = \sqrt{h \sum_{j=1}^{M+1} h \left| V_{\text{num}}(z_j, t) - v_{\text{exact}}(z_j, t) \right|}.$$

(27)

Example 1. Consider the CDE

$$\frac{\partial v}{\partial t} + 0.1\frac{\partial v}{\partial \xi} = 0.01\frac{\partial^2 v}{\partial \xi^2}, \quad 0 \leq \xi \leq 1, t > 0,$$

(28)

with the initial condition

$$v(\xi, 0) = \exp(5\xi)\sin(\pi\xi)$$

(29)

and the boundary conditions

$$v(0, t) = 0,$$
$$v(1, t) = 0.$$

(30)

The analytic solution of the given problem is $v(\xi, t) = \exp(5\xi - (0.25 + 0.01\pi^2)t)\sin(\pi\xi)$. The numerical results are obtained by utilizing the presented scheme. In Table 1, the absolute errors are compared with those obtained in [19] at various time stages. Figure 1 illustrates the comparison between the exact and numerical solutions at various time stages. Figure 2 shows the 2D and 3D error profiles at $T = 1$. A 3D comparison between the exact and numerical solutions is presented to exhibit the exactness of the scheme in Figure 3. The approximate solution when $t = 1, k = 0.01$, and $h = 0.05$ is given by

$$V(\xi, 1) = \begin{cases} 10.9843 \cos\left(\dfrac{\xi}{2}\right) - 10.9843\cos^3\left(\dfrac{\xi}{2}\right) + 54.9966\sin^3\left(\dfrac{\xi}{2}\right) - \\ \qquad\qquad\qquad\qquad\qquad\qquad\qquad\qquad\qquad\qquad\qquad \xi \in \left[0, \dfrac{1}{20}\right], \\ 41.2474 \csc\left(\dfrac{\xi}{2}\right)\sin^2(\xi) + \sin\left(\dfrac{\xi}{2}\right)(169.428 + 16.4765 \sin(\xi)), \\[2ex] 10.0258 \cos\left(\dfrac{\xi}{2}\right) - 10.0266\cos^3\left(\dfrac{\xi}{2}\right) + 67.7423\sin^3\left(\dfrac{\xi}{2}\right) - \\ \qquad\qquad\qquad\qquad\qquad\qquad\qquad\qquad\qquad\qquad\qquad \xi \in \left[\dfrac{1}{20}, \dfrac{1}{10}\right], \\ 50.8067 \csc\left(\dfrac{\xi}{2}\right)\sin^2(\xi) + \sin\left(\dfrac{\xi}{2}\right)(207.761 + 15.0399 \sin(\xi)), \\[2ex] 7.76173 \cos\left(\dfrac{\xi}{2}\right) - 7.77007\cos^3\left(\dfrac{\xi}{2}\right) + 82.6729\sin^3\left(\dfrac{\xi}{2}\right) - \\ \qquad\qquad\qquad\qquad\qquad\qquad\qquad\qquad\qquad\qquad\qquad \xi \in \left[\dfrac{1}{10}, \dfrac{3}{20}\right], \\ 62.0047 \csc\left(\dfrac{\xi}{2}\right)\sin^2(\xi) + \sin\left(\dfrac{\xi}{2}\right)((253.005 + 11.6551 \sin(\xi)), \\[2ex] \vdots \\ \vdots \\[2ex] 4135.9 \cos\left(\dfrac{\xi}{2}\right) - 3377.74\cos^3\left(\dfrac{\xi}{2}\right) - 1565.64 \sin\left(\dfrac{\xi}{2}\right)^3 + \\ \qquad\qquad\qquad\qquad\qquad\qquad\qquad\qquad\qquad\qquad\qquad \xi \in \left[\dfrac{17}{20}, \dfrac{9}{10}\right], \\ 1174.23 \csc\left(\dfrac{\xi}{2}\right)\sin^2(\xi) + \sin\left(\dfrac{\xi}{2}\right)(-10328.2 + 5066.61 \sin(\xi)), \\[2ex] 5855.3 \cos\left(\dfrac{\xi}{2}\right) - 4663.41\cos^3\left(\dfrac{\xi}{2}\right) - 1854.21\sin^3\left(\dfrac{\xi}{2}\right) + \\ \qquad\qquad\qquad\qquad\qquad\qquad\qquad\qquad\qquad\qquad\qquad \xi \in \left[\dfrac{9}{10}, \dfrac{19}{20}\right], \\ 1390.66 \csc\left(\dfrac{\xi}{2}\right)\sin^2(\xi) + \sin\left(\dfrac{\xi}{2}\right)(-13887.7 + 6995.11 \sin(\xi)), \\[2ex] 7812.87 \cos\left(\dfrac{\xi}{2}\right) - 6075.06\cos^3\left(\dfrac{\xi}{2}\right) - 2061.5\sin^3\left(\dfrac{\xi}{2}\right) + \\ \qquad\qquad\qquad\qquad\qquad\qquad\qquad\qquad\qquad\qquad\qquad \xi \in \left[\dfrac{19}{20}, 1\right]. \\ 1546.12 \csc\left(\dfrac{\xi}{2}\right)\sin^2(\xi) + \sin\left(\dfrac{\xi}{2}\right)(-17694.2 + 9112.59 \sin(\xi)), \end{cases} \tag{31}$$

Example 2. Consider the CDE

$$\frac{\partial v}{\partial t} + 0.22\frac{\partial v}{\partial \xi} = 0.5\frac{\partial^2 v}{\partial \xi^2}, \quad 0 \le \xi \le 1, t > 0, \tag{32}$$

(a)

(b)

FIGURE 2: 2D and 3D error profiles when $T = 1, h = k = 0.01$ for Example 1.

(a)

(b)

FIGURE 3: The exact and approximate solutions when $T = 1, h = k = 0.01$ for Example 1.

TABLE 2: Absolute errors when $k = 0.002$ and $h = 0.002$ for Example 2.

ξ	$t = 0.8$		$t = 1.0$	
	Present scheme	CNM [19]	Present scheme	CNM [19]
0.1	1.84×10^{-7}	2.12×10^{-7}	8.52×10^{-8}	1.79×10^{-7}
0.3	5.02×10^{-7}	5.85×10^{-7}	2.33×10^{-7}	4.92×10^{-7}
0.5	6.47×10^{-7}	7.62×10^{-7}	3.00×10^{-7}	6.40×10^{-7}
0.7	5.46×10^{-7}	6.49×10^{-7}	2.53×10^{-7}	5.45×10^{-7}
0.9	2.18×10^{-7}	2.61×10^{-7}	1.01×10^{-7}	2.19×10^{-7}

with the initial condition

$$v(\xi, 0) = \exp(0.22\xi)\sin(\pi\xi) \tag{33}$$

and the boundary conditions

$$\begin{aligned} v(0, t) &= 0, \\ v(1, t) &= 0. \end{aligned} \tag{34}$$

The analytic solution of the given problem is $v(\xi, t) = \exp(0.22\xi - (0.0242 + 0.5\pi^2)t)\sin(\pi\xi)$. By utilizing the proposed scheme, the numerical results are acquired. An excellent comparison between absolute errors computed by our scheme and the scheme in [19] is presented in Table 2. A close comparison between the exact and numerical solutions at different time stages is depicted in Figure 4. Figure 5 plots
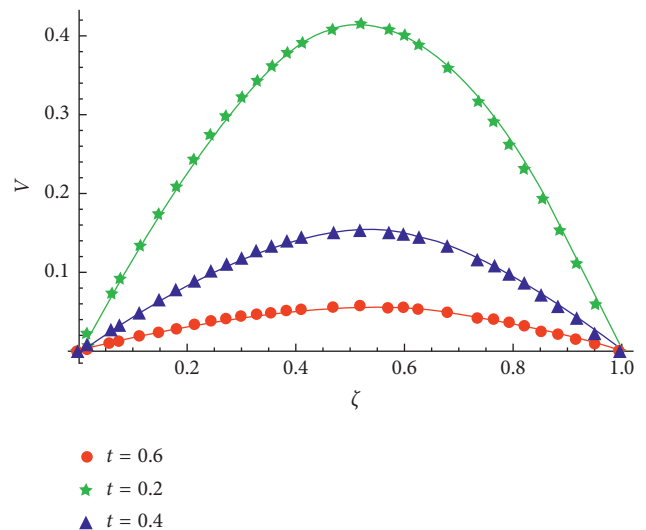
FIGURE 4: The approximate (stars, circles, and triangles) and exact (solid lines) solutions for various time stages when $h = k = 0.002$ for Example 2.

- $t = 0.6$
- $t = 0.2$
- $t = 0.4$

2D and 3D absolute errors at $T = 1$. Figure 6 deals with the 3D comparison that occurs between the exact and numerical solutions. The approximate solution when $t = 1, k = 0.01$, and $h = 0.05$ is given as

$$V(\xi, 1) = \begin{cases} 0.00705027 \cos\left(\dfrac{\xi}{2}\right) - 0.00705027\cos^3\left(\dfrac{\xi}{2}\right) - 0.107735\sin^3\left(\dfrac{\xi}{2}\right) + \\ \qquad\qquad\qquad\qquad\qquad\qquad\qquad\qquad\qquad\qquad \xi \in \left[0, \dfrac{1}{20}\right], \\ \sin\left(\dfrac{\xi}{2}\right)(-0.279207 + 0.0105754\sin(\xi)) + 0.0808013\csc\left(\dfrac{\xi}{2}\right)\sin^2(\xi), \\[2mm] 0.00365488 \cos\left(\dfrac{\xi}{2}\right) - 0.00365771\cos^3\left(\dfrac{\xi}{2}\right) - 0.0625858\sin^3\left(\dfrac{\xi}{2}\right) + \\ \qquad\qquad\qquad\qquad\qquad\qquad\qquad\qquad\qquad\qquad \xi \in \left[\dfrac{1}{20}, \dfrac{1}{10}\right], \\ \sin\left(\dfrac{\xi}{2}\right)(-0.143419 + 0.00548657\sin(\xi)) + 0.0469394\csc\left(\dfrac{\xi}{2}\right)\sin^2(\xi), \\[2mm] 0.00555436 \cos\left(\dfrac{\xi}{2}\right) - 0.00555086\cos^3\left(\dfrac{\xi}{2}\right) - 0.075112\sin^3\left(\dfrac{\xi}{2}\right) + \\ \qquad\qquad\qquad\qquad\qquad\qquad\qquad\qquad\qquad\qquad \xi \in \left[\dfrac{1}{10}, \dfrac{3}{20}\right], \\ \sin\left(\dfrac{\xi}{2}\right)(-0.181377 + 0.00832629\sin(\xi)) + 0.056334\csc\left(\dfrac{\xi}{2}\right)\sin^2(\xi), \\[2mm] \vdots \\[2mm] \vdots \\[2mm] -0.0808988 \cos\left(\dfrac{\xi}{2}\right) + 0.0700979\cos^3\left(\dfrac{\xi}{2}\right) - 0.00330615\sin^3\left(\dfrac{\xi}{2}\right) + \\ \qquad\qquad\qquad\qquad\qquad\qquad\qquad\qquad\qquad\qquad \xi \in \left[\dfrac{17}{20}, \dfrac{9}{10}\right], \\ \sin\left(\dfrac{\xi}{2}\right)(0.130845 - 0.105147\sin(\xi)) + 0.00247962\csc\left(\dfrac{\xi}{2}\right)\sin^2(\xi), \\[2mm] -0.114779 \cos\left(\dfrac{\xi}{2}\right) + 0.0954314\cos^3\left(\dfrac{\xi}{2}\right) + 0.00238008\sin^3\left(\dfrac{\xi}{2}\right) + \\ \qquad\qquad\qquad\qquad\qquad\qquad\qquad\qquad\qquad\qquad \xi \in \left[\dfrac{9}{10}, \dfrac{19}{20}\right], \\ \sin\left(\dfrac{\xi}{2}\right)(0.200982 - 0.143147\sin(\xi)) - 0.00178506\csc\left(\dfrac{\xi}{2}\right)\sin^2(\xi), \\[2mm] -0.0214135 \cos\left(\dfrac{\xi}{2}\right) + 0.0281036\cos^3\left(\dfrac{\xi}{2}\right) - 0.0075062\sin^3\left(\dfrac{\xi}{2}\right) + \\ \qquad\qquad\qquad\qquad\qquad\qquad\qquad\qquad\qquad\qquad \xi \in \left[\dfrac{19}{20}, 1\right]. \\ \sin\left(\dfrac{\xi}{2}\right)(0.0194332 - 0.0421554\sin(\xi)) + 0.00562965\csc\left(\dfrac{\xi}{2}\right)\sin^2(\xi), \end{cases} \tag{35}$$
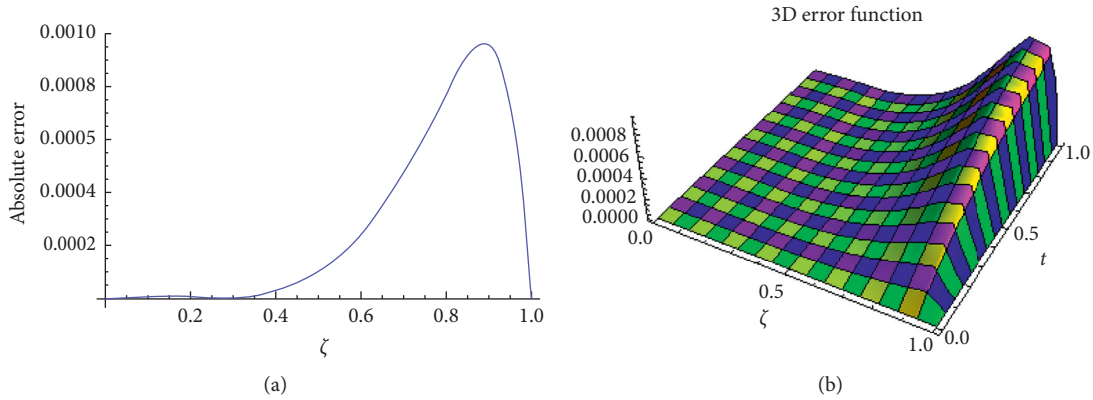
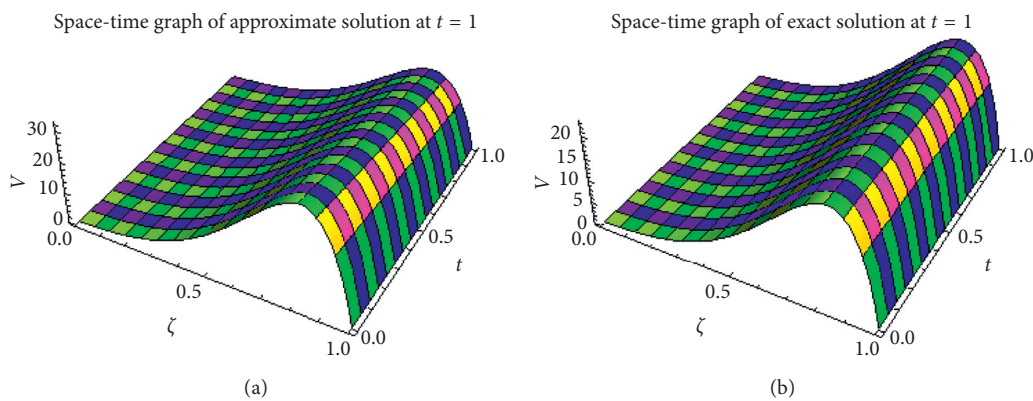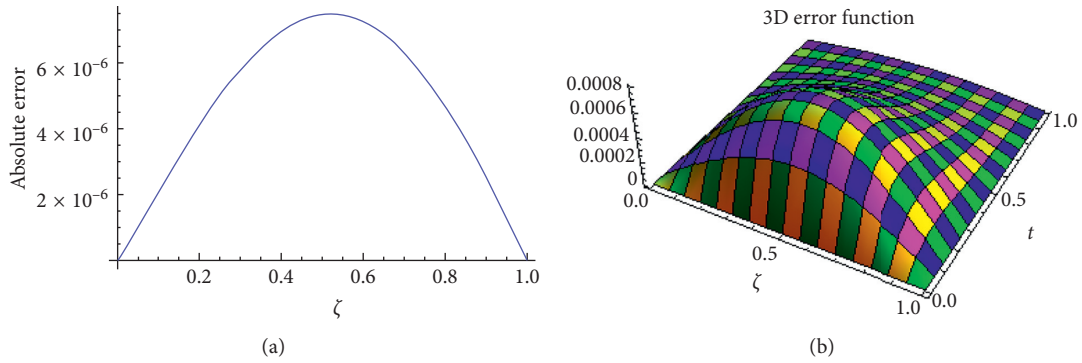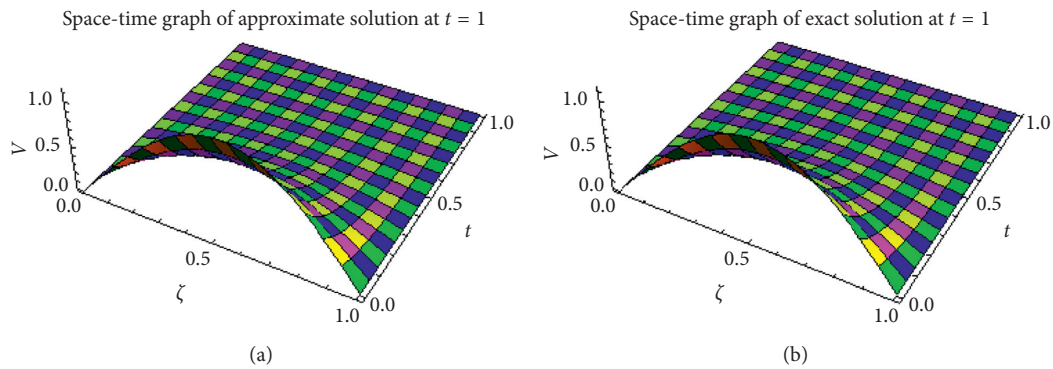FIGURE 5: 2D and 3D error profile when $T = 1, h = k = 0.01$ for Example 2.

FIGURE 6: The exact and approximate solutions with $T = 1, h = k = 0.01$ for Example 2.

TABLE 3: Absolute errors when $k = 0.005$ at $h = 0.01$ for Example 3.

t	$\xi = 0.1$		$\xi = 0.3$		$\xi = 0.5$		$\xi = 0.7$		$\xi = 0.9$	
	Present	CNM [19]	Present	CNM [19]	Present	CNM [19]	Present	CNM [19]	Present	CNM [19]
0.2	1.52×10^{-7}	3.72×10^{-6}	2.47×10^{-7}	1.02×10^{-5}	1.05×10^{-6}	1.32×10^{-5}	1.52×10^{-6}	1.12×10^{-5}	9.06×10^{-7}	4.48×10^{-6}
0.4	2.16×10^{-8}	2.80×10^{-6}	5.85×10^{-7}	7.68×10^{-6}	1.42×10^{-6}	9.93×10^{-6}	1.76×10^{-6}	8.41×10^{-6}	9.42×10^{-7}	3.36×10^{-6}
0.6	1.32×10^{-7}	1.57×10^{-6}	7.34×10^{-7}	4.29×10^{-6}	1.43×10^{-6}	5.55×10^{-6}	1.62×10^{-6}	4.69×10^{-6}	8.14×10^{-7}	1.88×10^{-6}
0.8	1.75×10^{-7}	7.77×10^{-7}	7.34×10^{-7}	2.13×10^{-6}	1.28×10^{-6}	2.75×10^{-6}	1.37×10^{-6}	2.33×10^{-6}	6.60×10^{-7}	9.29×10^{-7}
1.0	1.77×10^{-7}	3.61×10^{-7}	6.58×10^{-7}	9.88×10^{-7}	1.08×10^{-6}	1.28×10^{-6}	1.10×10^{-6}	1.08×10^{-6}	5.18×10^{-7}	4.31×10^{-7}

Example 3. Consider the CDE

$$\frac{\partial v}{\partial t} + 0.1 \frac{\partial v}{\partial \xi} = 0.2 \frac{\partial^2 v}{\partial \xi^2}, \quad 0 \leq \xi \leq 1, t > 0, \quad (36)$$

with the initial condition

$$v(\xi, 0) = \exp(0.25\xi)\sin(\pi\xi) \quad (37)$$

and the boundary conditions

$$v(0, t) = 0,$$
$$v(1, t) = 0. \quad (38)$$

The analytic solution of the given problem is $v(\xi, t) = \exp(0.25\xi - (0.012\xi + 0.2\pi^2)t)\sin(\pi\xi)$. The numerical outcomes are obtained utilizing the proposed scheme. An excellent comparison between absolute errors computed by our scheme and the scheme in [19] is discussed in Table 3. Figure 7 deals with the behavior of exact and approximate solutions at various time stages. Figure 8 plots 2D and 3D absolute errors at $T = 1$. In Figure 9, a tremendous 3D contrast between the exact and numerical solutions is shown. The approximate solution when $t = 1, k = 0.01$, and $h = 0.05$ is given as

$$V(\xi,1) = \begin{cases} \begin{aligned} &0.110325\cos\left(\frac{\xi}{2}\right) - 0.110325\cos^3\left(\frac{\xi}{2}\right) - 1.42017\sin^3\left(\frac{\xi}{2}\right) + \\ &\sin\left(\frac{\xi}{2}\right)(-3.3983 + 0.165487\sin(\xi)) + 1.06513\csc\left(\frac{\xi}{2}\right)\sin^2(\xi), \end{aligned} & \xi \in \left[0, \frac{1}{20}\right], \\[2em] \begin{aligned} &0.109556\cos\left(\frac{\xi}{2}\right) - 0.109557\cos^3\left(\frac{\xi}{2}\right) - 1.40995\sin^3\left(\frac{\xi}{2}\right) + \\ &\sin\left(\frac{\xi}{2}\right)(-3.36757 + 0.164336\sin(\xi)) + 1.05747\csc\left(\frac{\xi}{2}\right)\sin^2(\xi), \end{aligned} & \xi \in \left[\frac{1}{20}, \frac{1}{10}\right], \\[2em] \begin{aligned} &0.113008\cos\left(\frac{\xi}{2}\right) - 0.112997\cos\left(\frac{\xi}{2}\right)^3 - 1.43272\sin^3\left(\frac{\xi}{2}\right) + \\ &\sin\left(\frac{\xi}{2}\right)(-3.43655 + 0.169496\sin(\xi)) + 1.07454\csc\left(\frac{\xi}{2}\right)\sin^2(\xi), \end{aligned} & \xi \in \left[\frac{1}{10}, \frac{3}{20}\right], \\[1em] \vdots \\ \vdots \\[1em] \begin{aligned} &-1.70311\cos\left(\frac{\xi}{2}\right) + 1.4605\cos^3\left(\frac{\xi}{2}\right) - 0.0651712\sin^3\left(\frac{\xi}{2}\right) + \\ &\sin\left(\frac{\xi}{2}\right)(2.76626 - 2.19076\sin(\xi)) + 0.0488784\csc\left(\frac{\xi}{2}\right)\sin^2(\xi), \end{aligned} & \xi \in \left[\frac{17}{20}, \frac{9}{10}\right], \\[2em] \begin{aligned} &-1.90731\cos\left(\frac{\xi}{2}\right) + 1.6132\cos^3\left(\frac{\xi}{2}\right) - 0.0308979\sin^3\left(\frac{\xi}{2}\right) + \\ &\sin\left(\frac{\xi}{2}\right)(3.189 - 2.4198\sin(\xi)) + 0.0231734\csc\left(\frac{\xi}{2}\right)\sin^2(\xi), \end{aligned} & \xi \in \left[\frac{9}{10}, \frac{19}{20}\right], \\[2em] \begin{aligned} &-1.95402\cos\left(\frac{\xi}{2}\right) + 1.64688\cos^3\left(\frac{\xi}{2}\right) - 0.0259522\sin^3\left(\frac{\xi}{2}\right) + \\ &\sin\left(\frac{\xi}{2}\right)(3.27983 - 2.47032\sin(\xi)) + 0.0194642\csc\left(\frac{\xi}{2}\right)\sin^2(\xi), \end{aligned} & \xi \in \left[\frac{19}{20}, 1\right]. \end{cases} \tag{39}$$

Example 4. Consider the CDE

$$\frac{\partial v}{\partial t} + 0.8\frac{\partial v}{\partial \xi} = 0.1\frac{\partial^2 v}{\partial \xi^2}, \quad 0 \le \xi \le 1, t > 0, \tag{40}$$

with the initial condition

$$v(\xi, 0) = \exp\left(-\frac{(\xi - 2)^2}{80}\right) \tag{41}$$

and the boundary conditions

FIGURE 7: The approximate (stars, circles, and triangles) and exact (solid lines) solutions for various time stages when $h = 0.01, k = 0.005$ for Example 3.

(a)

(b)
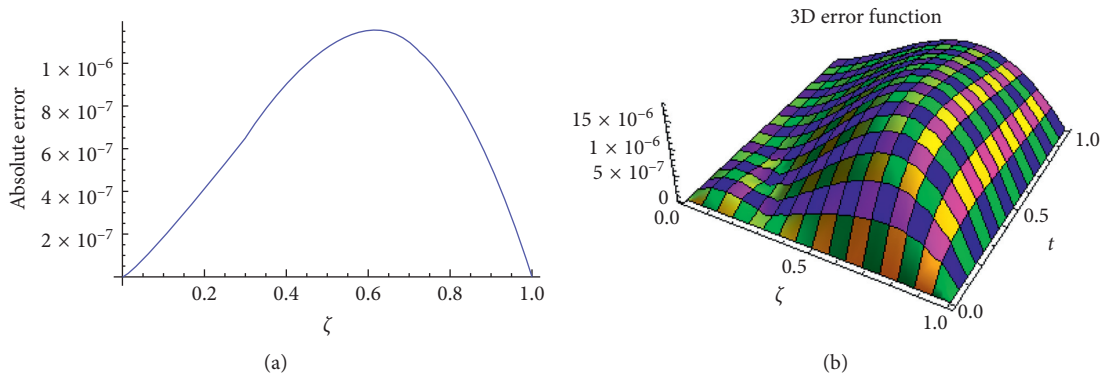
FIGURE 8: 2D and 3D error profiles when $T = 1, M = 100, k = 0.005$ for Example 3.

(a)

(b)
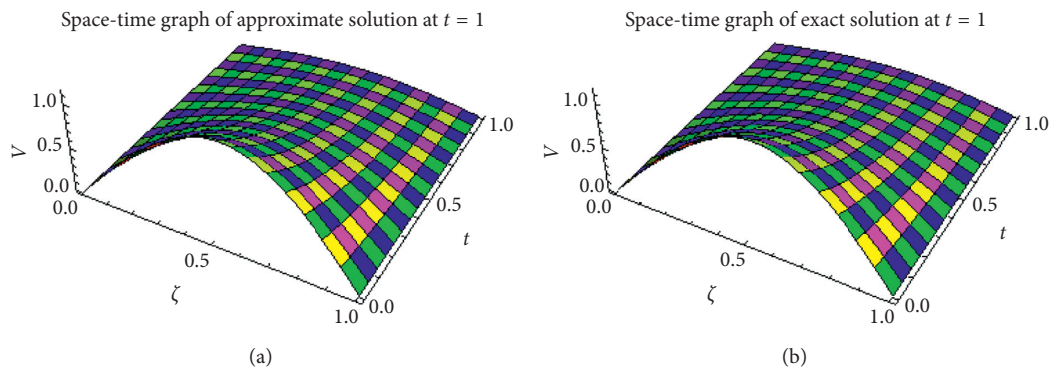
FIGURE 9: The exact and approximate solutions with $T = 1, h = 0.01, k = 0.005$ for Example 3.

TABLE 4: Error norms when $t = 1.0$ and $k = 0.001$ for Example 4.

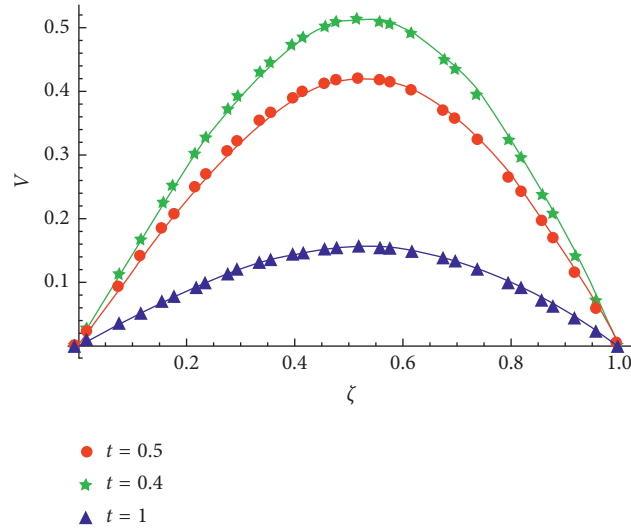| h	Present scheme		CuTBS [20]	
	L_2	L_∞	L_2	L_∞
1/4	8.17×10^{-6}	1.40×10^{-5}	1.20×10^{-4}	1.09×10^{-4}
1/8	2.87×10^{-6}	4.14×10^{-6}	2.98×10^{-5}	2.35×10^{-5}
1/16	7.95×10^{-7}	1.12×10^{-6}	7.56×10^{-6}	5.76×10^{-6}
1/32	2.05×10^{-7}	2.89×10^{-7}	1.91×10^{-6}	1.43×10^{-6}
1/64	5.32×10^{-8}	7.49×10^{-8}	4.77×10^{-7}	3.55×10^{-7}
1/128	1.49×10^{-8}	2.12×10^{-8}	1.17×10^{-7}	8.65×10^{-8}
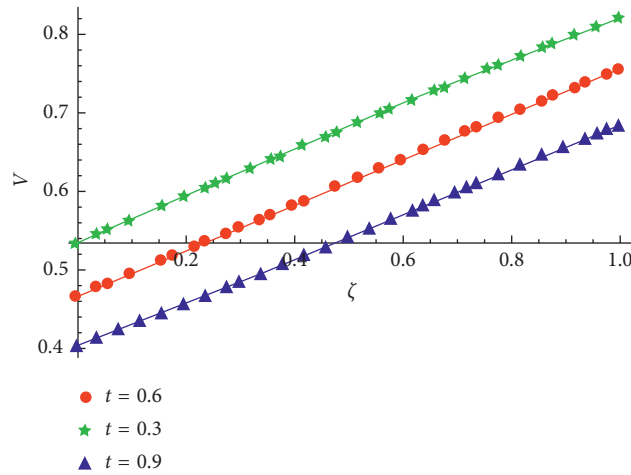
FIGURE 10: The approximate (stars, circles, and triangles) and exact (solid lines) solutions for various time stages when $h = 0.01, k = 0.001$ for Example 4.


(a)

(b)
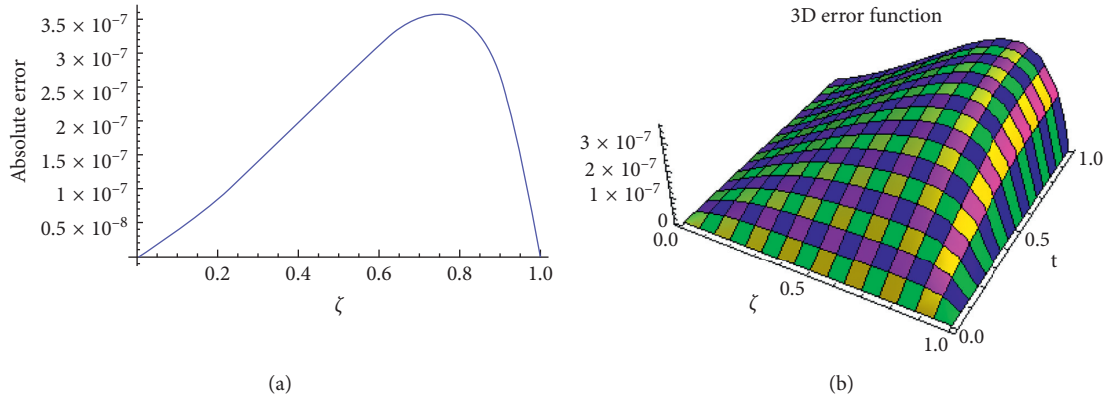
FIGURE 11: 2D and 3D error profile when $T = 1, h = k = 0.01$ for Example 4.

$$v(0,t) = \sqrt{\frac{20}{20+t}} \exp\left(-\frac{(-2-0.8t)^2}{0.4(20+t)}\right),$$

$$v(1,t) = \sqrt{\frac{20}{20+t}} \exp\left(-\frac{(-1-0.8t)^2}{0.4(20+t)}\right). \tag{42}$$

The analytic solution is $v(\xi, t) = \sqrt{20/20+t} \exp$ $(-(\xi - 2 - 0.8t)^2/0.4(20+t))$. In Table 4, the comparative analysis of absolute errors with those in [20] is provided. Figure 10 illustrates the behavior of numerical solutions at various stages of time. Figure 11 depicts the 2D and 3D graphs of absolute errors. Figure 12 shows the rattling accuracy that exists between the exact and numerical solutions.

The approximate solution when $t = 1, k = 0.01$, and $h = 0.05$ is given as

$$V(\xi, 1) = \begin{cases} 0.471308 \cos\left(\dfrac{\xi}{2}\right) - 0.0875439\cos^3\left(\dfrac{\xi}{2}\right) + 0.000784654\sin^3\left(\dfrac{\xi}{2}\right) + \\ \qquad \xi \in \left[0, \dfrac{1}{20}\right], \\ \sin\left(\dfrac{\xi}{2}\right)(0.514041 + 0.131316 \sin(\xi)) - 0.000588491 \csc\left(\dfrac{\xi}{2}\right)\sin^2(\xi), \\[4pt] 0.470916 \cos\left(\dfrac{\xi}{2}\right) - 0.0871524\cos^3\left(\dfrac{\xi}{2}\right) + 0.00599438\sin^3\left(\dfrac{\xi}{2}\right) + \\ \qquad \xi \in \left[\dfrac{1}{20}, \dfrac{1}{10}\right], \\ \sin\left(\dfrac{\xi}{2}\right)(0.529709 + 0.130729 \sin(\xi)) - 0.00449579 \csc\left(\dfrac{\xi}{2}\right)\sin^2(\xi), \\[4pt] 0.470136 \cos\left(\dfrac{\xi}{2}\right) - 0.0863755\cos^3\left(\dfrac{\xi}{2}\right) + 0.0111351\sin^3\left(\dfrac{\xi}{2}\right) + \\ \qquad \xi \in \left[\dfrac{1}{10}, \dfrac{3}{20}\right], \\ \sin\left(\dfrac{\xi}{2}\right)(0.545287 + 0.129563 \sin(\xi)) - 0.00835133 \csc\left(\dfrac{\xi}{2}\right)\sin^2(\xi), \\[4pt] \vdots \\ \vdots \\ 0.419092 \cos\left(\dfrac{\xi}{2}\right) - 0.0414767\cos^3\left(\dfrac{\xi}{2}\right) + 0.0611033\sin^3\left(\dfrac{\xi}{2}\right) + \\ \qquad \xi \in \left[\dfrac{17}{20}, \dfrac{9}{10}\right], \\ \sin\left(\dfrac{\xi}{2}\right)(0.750213 + 0.062215 \sin(\xi)) - 0.0458274 \csc\left(\dfrac{\xi}{2}\right)\sin^2(\xi), \\[4pt] 0.413674 \cos\left(\dfrac{\xi}{2}\right) - 0.0374249\cos^3\left(\dfrac{\xi}{2}\right) + 0.0620127\sin^3\left(\dfrac{\xi}{2}\right) + \\ \qquad \xi \in \left[\dfrac{9}{10}, \dfrac{19}{20}\right], \\ \sin\left(\dfrac{\xi}{2}\right)(0.761431 + 0.0561374 \sin(\xi)) - 0.0465095 \csc\left(\dfrac{\xi}{2}\right)\sin^2(\xi), \\[4pt] 0.407727 \cos\left(\dfrac{\xi}{2}\right) - 0.0331368\cos^3\left(\dfrac{\xi}{2}\right) + 0.0626424\sin^3\left(\dfrac{\xi}{2}\right) + \\ \qquad \xi \in \left[\dfrac{19}{20}, 1\right]. \\ \sin\left(\dfrac{\xi}{2}\right)(0.772993 + 0.0497052 \sin(\xi)) - 0.0469818 \csc\left(\dfrac{\xi}{2}\right)\sin^2(\xi), \end{cases}$$
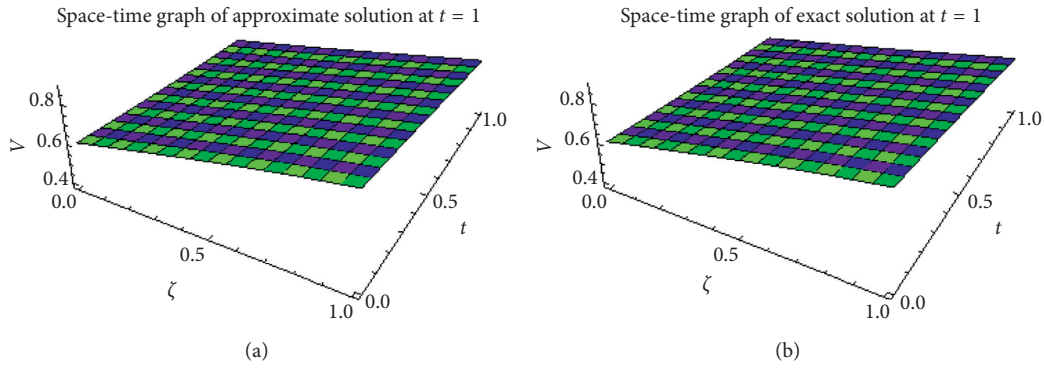
(43)

FIGURE 12: The exact and approximate solutions when $T = 1, h = k = 0.01$ for Example 4.

TABLE 5: Absolute errors when $h = 0.01$ and $k = 0.001$ for Example 5.

	$t = 1$		$t = 2$	
	CuBQI [21]	Present method	CuBQI [21]	Present method
$\xi = 0.1$	2.1506×10^{-6}	1.0675×10^{-7}	2.8217×10^{-6}	1.4143×10^{-7}
$\xi = 0.5$	7.0601×10^{-6}	3.2442×10^{-7}	1.2276×10^{-5}	5.6490×10^{-7}
$\xi = 0.9$	7.6594×10^{-6}	3.3157×10^{-7}	1.1643×10^{-5}	4.9986×10^{-7}

TABLE 6: Error norms when $h = 0.01$ and $k = 0.001$ for Example 5.

	$t = 1$		$t = 2$	
	CuBQI [21]	Present method	CuBQI [21]	Present method
L_2-norm	6.4790×10^{-7}	2.9393×10^{-7}	1.0719×10^{-6}	4.8607×10^{-7}
L_∞-norm	9.1107×10^{-6}	4.1329×10^{-7}	1.5204×10^{-5}	6.8951×10^{-7}

- $t = 0.5$
- $t = 0.1$
- $t = 0.9$
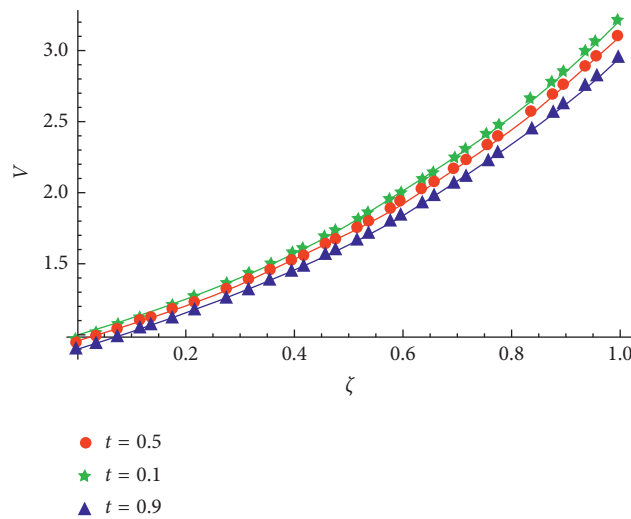
FIGURE 13: The approximate (stars, circles, and triangles) and exact (solid lines) solutions for various time stages when $h = 0.01, k = 0.001$ for Example 5.

Example 5. Consider the CDE

$$\frac{\partial v}{\partial t} + 0.1 \frac{\partial v}{\partial \xi} = 0.02 \frac{\partial^2 v}{\partial \xi^2}, \quad 0 \le \xi \le 1, t > 0, \quad (44)$$

with the initial condition

$$v(\xi, 0) = \exp(1.17712434446770\xi) \quad (45)$$

and the boundary conditions

$$v(0, t) = \exp(-0.09t),$$
$$v(1, t) = \exp(1.17712434446770 - 0.09t). \quad (46)$$

The analytic solution is $v(\xi, t) = \exp(1.17712434446770 \xi - 0.09t)$. The numerical outcomes are acquired by using

the introduced scheme. The error norms are computed and compared with those obtained in [21] in Tables 5 and 6. Figure 13 shows the behavior of exact and numerical solutions at various stages of time. Figure 14 depicts the 2D and 3D absolute error profiles at $T = 1$. In Figure 15, a 3D contrast between the exact and numerical solutions is presented and all the graphs are in good agreement. The approximate solution when $t = 1, k = 0.01$, and $h = 0.05$ is given as

$$
V(\xi, 1) = \begin{cases}
1.66078\cos\left(\dfrac{\xi}{2}\right) - 0.746853\cos^3\left(\dfrac{\xi}{2}\right) + 0.632987\sin^3\left(\dfrac{\xi}{2}\right) - \\
\qquad\qquad\qquad\qquad\qquad\qquad\qquad\qquad\qquad \xi \in \left[0, \dfrac{1}{20}\right], \\
0.47474\csc\left(\dfrac{\xi}{2}\right)\sin^2(\xi) + \sin\left(\dfrac{\xi}{2}\right)(4.05063 + 1.12028\sin(\xi)), \\[4pt]
1.65375\cos\left(\dfrac{\xi}{2}\right) - 0.739828\cos^3\left(\dfrac{\xi}{2}\right) + 0.726471\sin^3\left(\dfrac{\xi}{2}\right) - \\
\qquad\qquad\qquad\qquad\qquad\qquad\qquad\qquad\qquad \xi \in \left[\dfrac{1}{20}, \dfrac{1}{10}\right], \\
0.544853\csc\left(\dfrac{\xi}{2}\right)\sin^2(\xi) + \sin\left(\dfrac{\xi}{2}\right)(4.33178 + 1.10974\sin(\xi)), \\[4pt]
1.63814\cos\left(\dfrac{\xi}{2}\right) - 0.724265\cos^3\left(\dfrac{\xi}{2}\right) + 0.829444\sin^3\left(\dfrac{\xi}{2}\right) - \\
\qquad\qquad\qquad\qquad\qquad\qquad\qquad\qquad\qquad \xi \in \left[\dfrac{1}{10}, \dfrac{3}{20}\right], \\
0.622083\csc\left(\dfrac{\xi}{2}\right)\sin^2(\xi) + \sin\left(\dfrac{\xi}{2}\right)(4.64382 + 1.0864\sin(\xi)), \\[4pt]
\vdots \\
\vdots \\
-0.420769\cos\left(\dfrac{\xi}{2}\right) + 1.04963\cos^3\left(\dfrac{\xi}{2}\right) + 2.44322\sin^3\left(\dfrac{\xi}{2}\right) + \\
\qquad\qquad\qquad\qquad\qquad\qquad\qquad\qquad\qquad \xi \in \left[\dfrac{17}{20}, \dfrac{9}{10}\right], \\
\sin\left(\dfrac{\xi}{2}\right)(11.8844 - 1.57444\sin(\xi)) - 1.83242\csc\left(\dfrac{\xi}{2}\right)\sin^2(\xi), \\[4pt]
-0.768804\cos\left(\dfrac{\xi}{2}\right) + 1.30987\cos^3\left(\dfrac{\xi}{2}\right) + 2.50164\sin^3\left(\dfrac{\xi}{2}\right) + \\
\qquad\qquad\qquad\qquad\qquad\qquad\qquad\qquad\qquad \xi \in \left[\dfrac{9}{10}, \dfrac{19}{20}\right], \\
\sin\left(\dfrac{\xi}{2}\right)(12.6049 - 1.9648\sin(\xi)) - 1.87623\csc\left(\dfrac{\xi}{2}\right)\sin^2(\xi), \\[4pt]
-1.14283\cos\left(\dfrac{\xi}{2}\right) + 1.57959\cos^3\left(\dfrac{\xi}{2}\right) + 2.54124\sin^3\left(\dfrac{\xi}{2}\right) + \\
\qquad\qquad\qquad\qquad\qquad\qquad\qquad\qquad\qquad \xi \in \left[\dfrac{19}{20}, 1\right]. \\
\sin\left(\dfrac{\xi}{2}\right)(13.3322 - 2.36938\sin(\xi)) - 1.90593\csc\left(\dfrac{\xi}{2}\right)\sin^2(\xi),
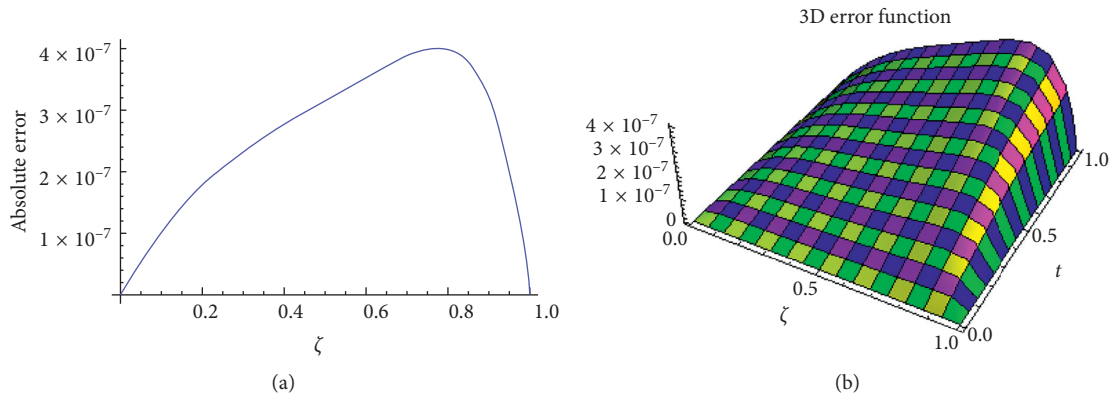\end{cases}
\tag{47}
$$

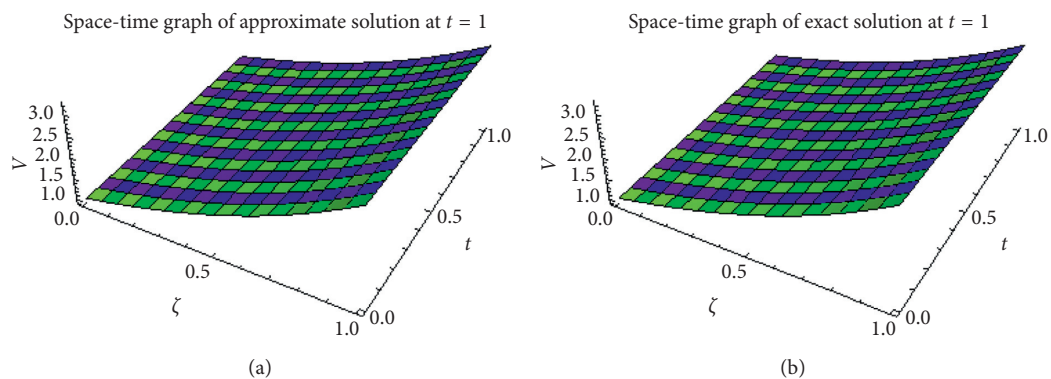FIGURE 14: 2D and 3D error profile when $T = 1, M = 100, k = 0.01$ for Example 5.

FIGURE 15: The exact and approximate solutions when $T = 1, h = k = 0.01$ for Example 5.

5. Concluding Remarks

In this study, a cubic trigonometric B-spline collocation method based on the Hermite formula is developed for the convection-diffusion equation. The smooth piecewise cubic B-spline has been used to approximate derivatives in space, whereas a standard finite difference has been used to discretize the time derivative. A combination of the Hermite formula and the cubic trigonometric B-splines for approximating the space derivative has considerably augmented the accuracy of the scheme. The solution comes up as a smooth piecewise continuous function so that one can find an approximate solution at any wanted location in the domain of interest. A special attention is devoted to the stability analysis of the scheme to confirm that the errors do not amplify. The numerical results are contrasted with some current numerical techniques. It is inferred that the presented scheme is more precise and provides better accuracy. It is also worthwhile to mention that the offered scheme is applicable to a variety of problems of applied nature in science and engineering.

Data Availability

The experimental data used to support the findings of this study are available within this paper.

Conflicts of Interest

The authors declare that they have no known conflicts of interest or personal relationships that could have appeared to influence the work reported in this paper.

Authors' Contributions

A. Y. and M. Y. wrote the original draft. M. A. and T. A. were involved in writing the review and editing. Visualization was performed by A. Y., M. Y., and M. A. T. A. was responsible for the resources. M. Y., M. A., and T. A. were involved in the conceptualization and methodology. All authors read and approved the final manuscript.

Acknowledgments

References

[1] A. Mohebbi and M. Dehghan, "High-order compact solution of the one-dimensional heat and advection-diffusion

equations," *Applied Mathematical Modelling*, vol. 34, no. 10, pp. 3071–3084, 2010.

[2] D. K. Salkuyeh, "On the finite difference approximation to the convection-diffusion equation," *Applied Mathematics and Computation*, vol. 179, no. 1, pp. 79–86, 2006.

[3] H. Karahan, "Unconditional stable explicit finite difference technique for the advection-diffusion equation using spreadsheets," *Advances in Engineering Software*, vol. 38, no. 2, pp. 80–86, 2007.

[4] H. Karahan, "Implicit finite difference techniques for the advection-diffusion equation using spreadsheets," *Advances in Engineering Software*, vol. 37, no. 9, pp. 601–608, 2006.

[5] H. Ismail, E. M. E. Elbarbary, and G. S. E. Salem, "Restrictive Taylor's approximation for solving convection-diffusion equation," *Applied Mathematics and Computation*, vol. 147, no. 2, pp. 355–363, 2004.

[6] H.-H. Cao, L.-B. Liu, Y. Zhang, and S.-m. Fu, "A fourth-order method of the convection-diffusion equations with Neumann boundary conditions," *Applied Mathematics and Computation*, vol. 217, no. 22, pp. 9133–9141, 2011.

[7] M. M. Chawla, M. A. Al-Zanaidi, and D. J. Evans, "Generalized trapezoidal formulas for convection-diffusion equations," *International Journal of Computer Mathematics*, vol. 72, no. 2, pp. 141–154, 1999.

[8] M. Dehghan, "Weighted finite difference techniques for the one-dimensional advection-diffusion equation," *Applied Mathematics and Computation*, vol. 147, no. 2, pp. 307–319, 2004.

[9] M. Dehghan, "Numerical solution of the three-dimensional advection-diffusion equation," *Applied Mathematics and Computation*, vol. 150, no. 1, pp. 5–19, 2004.

[10] U. Rizwan, "A second-order space and time nodal method for the one-dimensional convection-diffusion equation," *Computers & Fluids*, vol. 26, no. 3, pp. 233–247, 1997.

[11] S. Karaa and J. Zhang, "High order ADI method for solving unsteady convection-diffusion problems," *Journal of Computational Physics*, vol. 198, no. 1, pp. 1–9, 2004.

[12] X. F. Feng and Z. F. Tian, "Alternating group explicit method with exponential-type for the diffusion-convection equation," *International Journal of Computer Mathematics*, vol. 83, no. 10, pp. 765–775, 2006.

[13] R. C. Mittal and R. K. Jain, "Redefined cubic B-splines collocation method for solving convection-diffusion equations," *Applied Mathematical Modelling*, vol. 36, no. 11, pp. 5555–5573, 2012.

[14] M. K. Kadalbajoo and P. Arora, "Taylor-Galerkin B-spline finite element method for the one dimensional advection-diffusion equation," *Numerical Methods for Partial Differential Equations*, vol. 26, no. 5, pp. 2006–1223, 2009.

[15] M. Sari, G. Gürarslan, and A. Zeytinoğlu, "High-Order finite difference schemes for solving the advection-diffusion equation," *Mathematical and Computational Applications*, vol. 15, no. 3, pp. 449–460, 2010.

[16] T.-L. Tsai, S.-W. Chiang, and J.-C. Yang, "Examination of characteristics method with cubic interpolation for advection-diffusion equation," *Computers & Fluids*, vol. 35, no. 10, pp. 1217–1227, 2006.

[17] I. Daig, D. Irk, and M. Tombul, "Least-squares finite element method for the advection-diffusion equation," *Applied Mathematics and Computation*, vol. 173, pp. 554–565, 2006.

[18] M. M. Chawla, M. A. Al-Zanaidi, and M. G. Al-Aslab, "Extended one-step time-integration schemes for convection-diffusion equations," *Computers & Mathematics with Applications*, vol. 39, no. 3-4, pp. 71–84, 2000.

[19] H. Ding and Y. Zhang, "A new difference scheme with high accuracy and absolute stability for solving convection-diffusion equations," *Journal of Computational and Applied Mathematics*, vol. 230, no. 2, pp. 600–606, 2009.

[20] T. Nazir, M. Abbas, A. A. Majid, Ahmad, A. I. M. Ismail, and A. Rashid, "A numerical solution of advection-diffusion problem using new cubic trigonometric B-spline approach," *Applied Mathematical Modelling*, vol. 40, pp. 4586–4611, 2015.

[21] H. Aminikhah and J. Alavi, "Numerical solution of convection-diffusion equation using cubic B-spline quasi-interpolation," *Thai Journal of Mathematics*, vol. 14, no. 3, pp. 599–613, 2016.

[22] S. Kuamar, K. S. Nisar, R. Kumar, C. Cattani, and B. Samet, "A new Rabotnov fractional-exponential function-based fractional derivative for diffusion equation under external force," *Mathematical Methods in the Applied Sciences*, vol. 43, no. 7, pp. 4460–4471, 2020.

[23] S. Kuamar, A. Kumar, S. Abbas, M. A. Qureshi, and D. Baleanu, "A new Rabotnov fractional-exponential function-based fractional derivative for diffusion equation under external force," *Advances in Difference Equations*, vol. 28, p. 18, 2020.

[24] K. M. Owolabi, A. Atangana, and A. Akgul, "Modelling and analysis of fractal-fractional partial differential equations: application to reaction-diffusion model," *Alexandria Engineering Journal*, vol. 59, no. 4, pp. 2477–2490, 2020.

[25] A. Atangana, A. Akgül, and K. M. Owolabi, "Analysis of fractal fractional differential equations," *Alexandria Engineering Journal*, vol. 59, no. 3, pp. 1117–1134, 2020.

[26] M. Abbas, A. A. Majid, A. I. M. Ismail, and A. Rashid, "The Application of cubic Trigonometric B-Spline to the numerical solution of the hyperbolic problems," *Applied Mathematics and Computation*, vol. 239, pp. 74–88, 2014.

[27] M. H. Khader and M. H. Adel, "Numerical Solution of fractional wave equation using an efficient class of FDM based on the Hermite Formula," *Advances in Difference Equations*, vol. 34, p. 10, 2016.

[28] A. Yousaf, M. Yaseen, and M. Abbas, "A cubic trigonometric b-spline collocation method based on hermite formula for the numerical solution of the heat equation with classical and non-classical boundary conditions," (Submitted for publication).

Research Article

Hydrodynamic Analysis of the Flow inside the Submerged Entry Nozzle

Jesus Gonzalez-Trejo [iD],[1] **Cesar Augusto Real-Ramirez** [iD],[1] **Ignacio Carvajal-Mariscal** [iD],[2] **Florencio Sanchez-Silva** [iD],[2] **Francisco Cervantes-De-La-Torre** [iD],[1] **Raul Miranda-Tello** [iD],[1] **and Ruslan Gabbasov** [iD][1]

[1]*Universidad Autonoma Metropolitana, Mexico City, Mexico*
[2]*Instituto Politecnico Nacional, Mexico City, Mexico*

Correspondence should be addressed to Cesar Augusto Real-Ramirez; carr@correo.azc.uam.mx

The quality of steel produced by continuous casting depends mainly on the characteristics of the liquid steel flow pattern within the mold. This pattern depends on the flow dynamics of the nozzle that is immersed in liquid steel. This work characterizes the fluid dynamics within two separate submerged entry nozzle models with a square cross section bore. The Froude similarity criterion and water as working fluid have been used. The models consist of a square-shaped tube with one inlet and two lateral squared exits at the bottom. To enhance the flow visualization, the models do not have exit ports. Moreover, one of the models has a "pool," a volume at the bottom, and the other prescinds of it. The geometrical parameters and operational conditions of physical experiments were reproduced in the numerical simulations. The turbulence model used in this work is large eddy simulation (LES) with dynamic k-equation filtering. It was found that transient numerical simulations reproduce the dynamic nature of the internal flow pattern seen in physical experiments. The results show that the flow pattern within the pool nozzle is defined by only one large vortex; on the other hand, in the nozzle, without the pool, the flow pattern achieves a complex behavior characterized by two small vortexes. This study will allow to build nozzles that produce a symmetric, regular fluid flow pattern inside the mold, which leads to improvements on the process such as low energy consumption and finally in cost reductions.

1. Introduction

Molten steel continuous casting is an industrial process whose origins can be traced almost 200 years ago. Since the US Patent No. 1908 obtained by George Escol Sellers on December 17, 1840, titled "Machinery for making pipes continuously from lead," great experience has been gained in the operation of this process [1]. The continuous casting process can be seen in detail in the work [2]. Many theoretical and experimental investigations of the continuous casting process mainly aimed at obtaining high-quality homogeneous slabs were carried out. The aspect in which all research works have coincided is that the flow pattern of the jets of liquid steel emerging from the submerged entry nozzle (SEN) determines to a large extent the quality and

purity of the steel slabs. The SEN is designed to regulate the continuous flow of liquid steel that is supplied to the mold [3]. Several recent investigations have concurred with the fact that properties that characterize the internal and external geometry of the nozzle influence the flow pattern that the SEN produces inside the continuous casting mold. There are, however, differences in the influence that each of these geometric properties has on the flow pattern of liquid steel inside the nozzle and within the mold. For example, Calderon-Ramos et al. (2019) [4] studied the effect of both the transverse shape of the exit ports and the angle of inclination of the ports. They showed that the square-shaped ports produce symmetric and slow jets. Similarly, Zhang et al. (2019) [5] studied the influence of two fundamental aspects of the SEN exit ports on the liquid steel flow pattern within

the mold: the horizontal angle of inclination and the angle at which the ports' outlets diverge. The latter authors found an optimal combination of the port angle and immersion depth that reduces mold level fluctuations [6, 7]. Common to most of these works is the investigation at the same time of several factors that modify the flow pattern inside the mold [8, 9]. This approach, however, does not allow to separate the effects that each of them has on the flow inside the mold. On the other hand, previous works paid little attention to the exploration of the interior flow structure inside the SEN [10, 11].

The exit flow structure is developed in the bottom zone of the nozzle. However, factors such as the impurities dragged by liquid steel erode the internal walls which modify the internal volume of the SEN and thus the flow structure. The nozzles with a "pool," a volume at the bottom, suffer from a constant accumulation of the slag and impurities that fill the volume and change the fluid dynamics.

In order to numerically reproduce the flow pattern of the SEN, RANS and LES turbulence models were used previously to reproduce the internal flow pattern of the SEN [4, 12, 13]. In these works, it is possible to observe that RANS models could reproduce the average flow pattern; however, they do not obtain the transient dynamic flow behavior [2, 5–7, 9, 14–19]. On the other hand, the LES turbulence model reaches accurate results, and it is possible to compare their results with the physical experimental data [20–31].

Additionally, the flow behavior presented in this work has similarities to the fluid flow behavior in other science and engineering fields, for example, the problem of mixing and vortex formation in T-junctions found in pipes, arteries, venous systems, and microfluidic systems [31, 32].

The present work explores, using physical and numerical modeling, the effect of the well depth inside the SEN on the behavior of the jets that emerge from the nozzle ports. The box-type nozzle studied in this work has an inner bore with a square cross section that remains constant throughout all its length [16, 33]. In order to reproduce only the inner walls of the SEN, we model them as a thin shell that we termed nozzle internal prototype (NIP). The NIP employed in this work has two exit ports of square geometric shape. Since we analyze only the bifurcation of the flow of steel in nozzle interior, the effects of inert gas injection, port angle, and thickness of the port were not considered. We carry out both physical and numerical simulations of NIP that would correspond to a real 1 : 1/4 scaled bifurcated SEN, based on the Froude hydrodynamic similitude criterion.

2. Physical Simulations

2.1. Nozzle Internal Prototypes Geometry.
Figure 1 shows the NIP of two bifurcated SENs: one of them with a well (Figure 1(a)) and the other without a bottom well (Figure 1(b)), which will be named Case A and Case B, respectively. In addition, Figure 1(c) shows the photography of the experimental NIP corresponding to Case B. In this figure, there can be seen all the relevant geometrical aspects for this study: inner bore geometry, exit ports geometry, bore inner length, and depth of the bottom well. It is worth noting that both NIP studied have a flat bottom.

With regard to geometry, these prototypes have a square inner bore with 0.02 m per side and two square-shaped ports with a side length of 0.014 m. The areas of the two output ports sum roughly the transversal area of the bore nozzle. The depth of the nozzle bottom well for Case A is 0.007 m, which is half the height of the exit ports.

The volumetric flow used was 1.5 m^3/h. This flow is close enough to that occupied in previous works [3, 18]. Based on the Froude similitude criterion and considering that the working fluid is water, the NIPs used in the present study are 1 : 1/4 scaled models. The physical properties of the simulation fluid (water at 293.15 K) are listed in Table 1.

2.2. Physical Simulation Description.
Physical simulations were conducted under two distinct operating conditions. In all cases, the NIP discharged into a visualization cell, which is a rectangular prism with a square-shaped base of 0.015 m per side and a height of 0.5 m. The characteristics of the experimental setup are similar to those used in [26].

In the first operating condition, the NIP discharges both exit jets freely into the atmosphere, and following Gupta and Lahiri (1992) [11], this operating condition will be named as a "free-fall jet condition." This configuration allows better visualization of several significant phenomena, such as the shape, size, and direction of the outlet jets, as well as visualizes the behavior of the fluid flow inside the bifurcated nozzle between the exit ports [2, 12, 26].

In the free-fall jet condition, a high-speed camera was used to record the experiment at a rate of 1000 fps. The camera axis remains perpendicular to the axis formed by the centers of the exit ports. The camera was slightly tilted which permits better visualization of the NIP interior.

In the second operating condition, the NIP is submerged into the liquid. Following Gupta and Lahiri (1992) [11], this operating condition will be named as a submerged nozzle condition. The immersion depth measured between the free surface and the upper edge of the nozzle exit ports is 0.07 m. In this operating condition, a digital camera was used to take multiple pictures. The camera axis was aligned with the axis formed by the centers of the nozzle exit ports, such that the camera lens plane is parallel to the plane of the exit ports.

In the submerged nozzle condition, an approach called "light painting" was implemented to visualize the vortex structures generated inside the NIP. Light painting is a photography technique that records the movement of a light source by taking a long exposure photo. In our case, the light sources are hollow glass particles of the same type as those used in PIV studies, illuminated by a continuous wave 3 W power laser that generates a 0.001 m thick plane.

2.3. Physical Simulations: Case A

2.3.1. Free-Fall Jet Condition.
Figure 2 depicts a single vortex that forms on the bottom of the NIP captured at regular time intervals. The vortex rotation axis is almost parallel to the axis of the exit ports. This vortex emerges from the
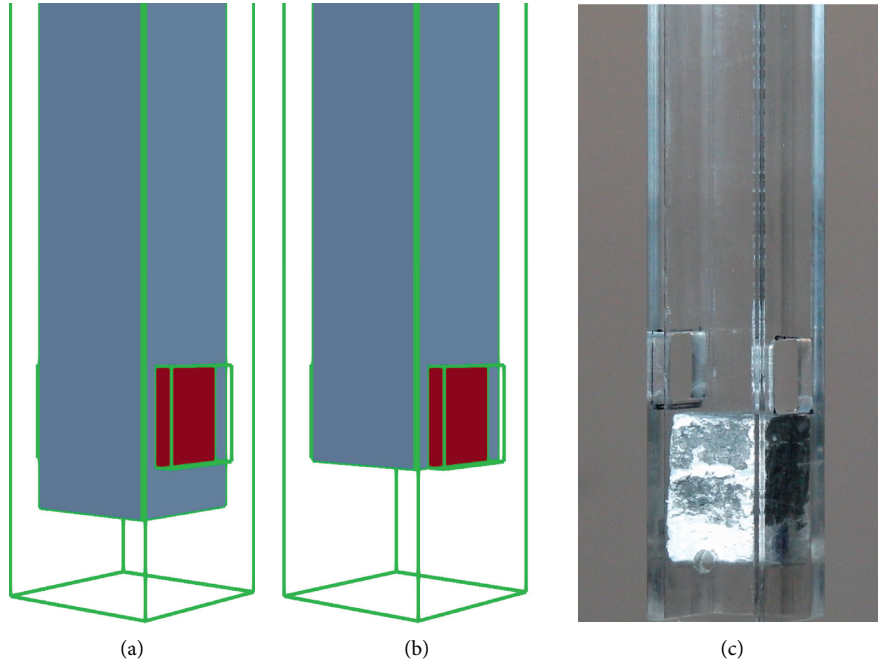
Figure 1: Representation of studied NIPs. (a) Numerical model of Case A. (b) Numerical model of Case B. (c) Photograph of Case B physical model.

Table 1: Physical properties of the simulation fluid.

Property	Value
Dynamic viscosity, μ (Kg/m · s)	$1 \cdot 10^{-3}$
Density, ρ (Kg/m^3)	$1 \cdot 10^3$
Kinematic viscosity, v (m^2/s)	$1 \cdot 10^{-6}$
Superficial tension, σ (N/m)	$7.5 \cdot 10^{-2}$

development of low-pressure zones and acts as a siphon, suctioning surrounding air through small regions at the exit ports. Therefore, the vortex at the bottom of the nozzle inner bore becomes visible and outlines some of the reverse flow zones developing inside of bifurcated SEN. Previously, several authors have discussed the influence that the reverse flow phenomenon has on the formation of an asymmetric flow pattern over the course of time, inside the mold of the slab continuous casting machine [14, 21].

Figure 2 illustrates the features and phenomena of the hydrodynamic evolution of the vortex inside the NIP throughout 0.05 s. Also, the hydrodynamic evolution of the heights of the upper and lower edges of the vortex inside the nozzle is plotted, which illustrates complex dynamic behavior with high-frequency components. The heights of the two edges were measured on the center plane of the nozzle. The plot includes the measurements for all frames in the 0.05 s time lapse.

Several six-second recordings were carried out; all of them had vortices with the same rotation direction. Nevertheless, high-speed videos have shown that at several times, the vortex breaks and loses continuity between the exit ports. The vortex rupture at that moment is caused by the increasing pressure values inside the reverse flow zone, as well as the ceasing of siphoning effect. In addition, these recordings register that the semicylindrical shape of the vortex frequently bends and sinks into the nozzle pool.

The images suggest that nozzle exit jets have not the same size. Indeed, the jet on the left side, most of the time, has a higher divergence angle than the jet on the right side. However, there are instants, where jet sizes become similar or the jet on the right side is broader than the jet on the left. These variations in the sizes and intensities of the jets will surely induce an asymmetrical behavior of the liquid steel flow pattern inside the continuous casting mold.

During the physical simulations, it was recorded a couple of air bubbles in the liquid stream which allowed a rough estimation of the flow velocity (Figure 3). Two bubbles traveled near the NIP central line, but their behavior near the vortex is distinct. When the vortex absorbs the right-hand side bubble (encircled in red), this one leaves the nozzle by the top of the exit port. Conversely, the left-hand side bubble (encircled in blue) surrounds the vortex and leaves the nozzle by the bottom of the exit port. If we assume that each bubble moves on a plane that is parallel to the observer, then the downstream velocity can be measured from the video
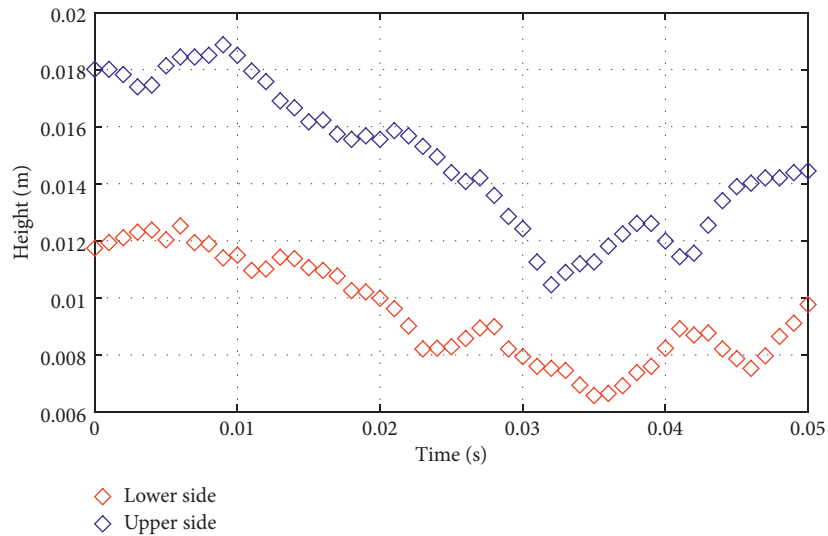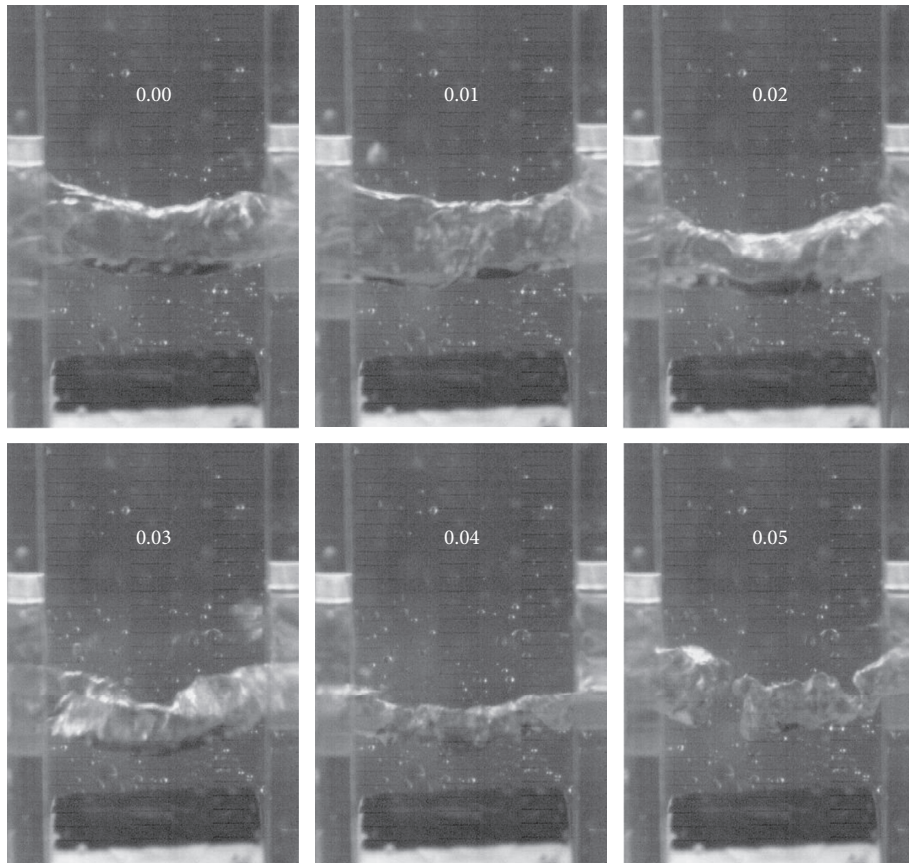
FIGURE 2: Dynamic evolution of the vortex inside the NIP, Case A, for a time interval of 0.05 s (upper panel). Also, in the bottom panel, the oscillation of the vortex position as its upper and lower side is shown.

recording as shown on the plot of the bottom of Figure 3. In both cases, the velocity grows as the bubbles approach the bottom of the NIP.

2.3.2. Submerged Nozzle Condition. In this operating condition, the NIP is submerged such that the jets are discharging into the liquid. In this case, also a single
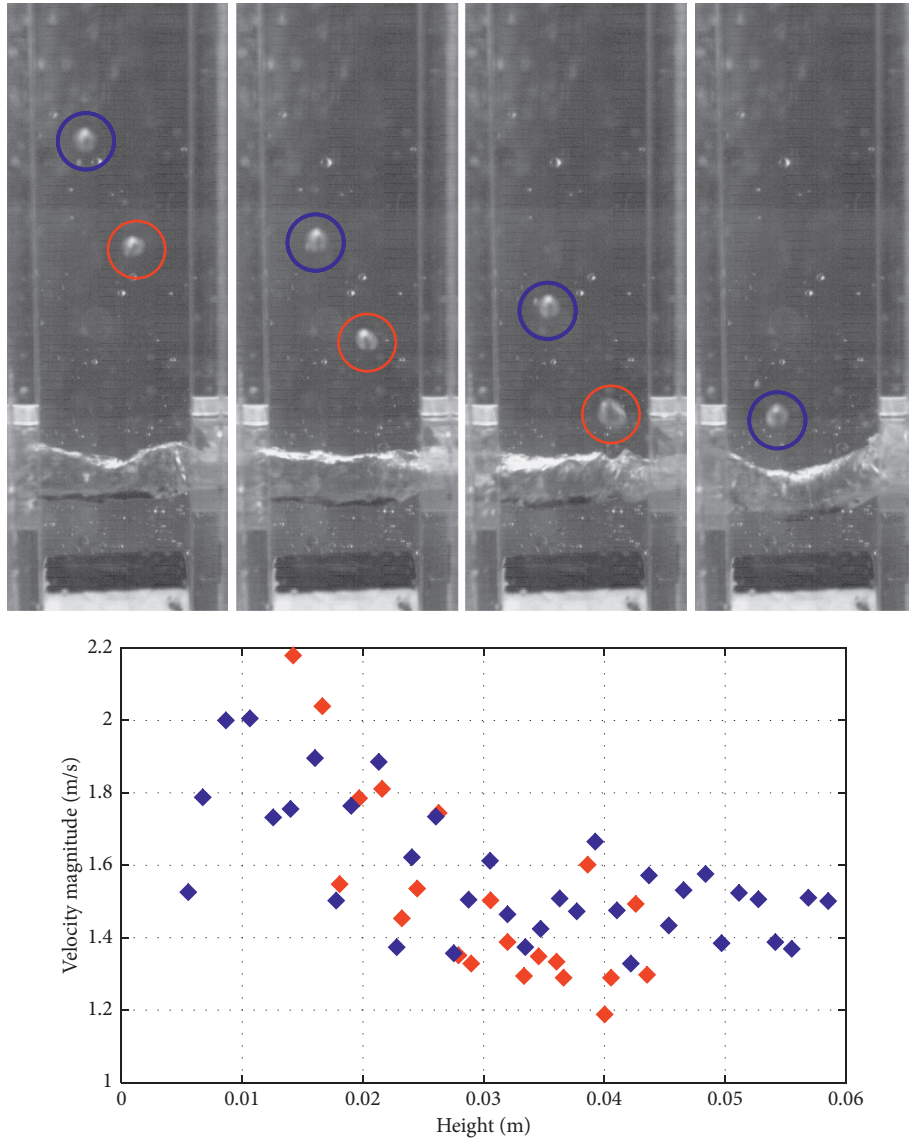
Figure 3: Dynamic evolution of two bubbles in Case A (top) and the velocities of the bubbles at different heights from the bottom of the nozzle (bottom).
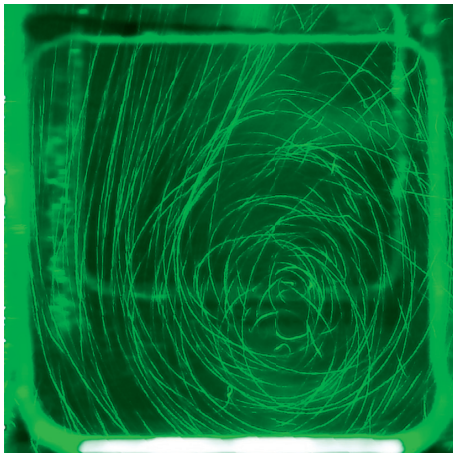
Figure 4: Vortical fluid flow pattern viewed from one of the exit ports for Case A submerged NIP.

pronounced vortex is formed. Figure 4 shows a close-up of the vortex with its rotation axis parallel to the exit ports' axis. The photograph confirms the fact that the vortex axis rotation does not remain static while the camera diaphragm is open. Notice also that the vortex occupies a considerable area of the exit ports.

2.4. Physical Simulations: Case B

2.4.1. Free-Fall Jet Condition. The flow behavior of the NIP without a bottom well is very different from the previous case. Two counterrotating vortices are now formed inside the prototype. The high-speed video recording shows that there are several significant differences between the vortices observed in the NIP with and without well. The first difference is that the two vortices of the NIP without bottom well rarely connect both exit ports entirely. Another
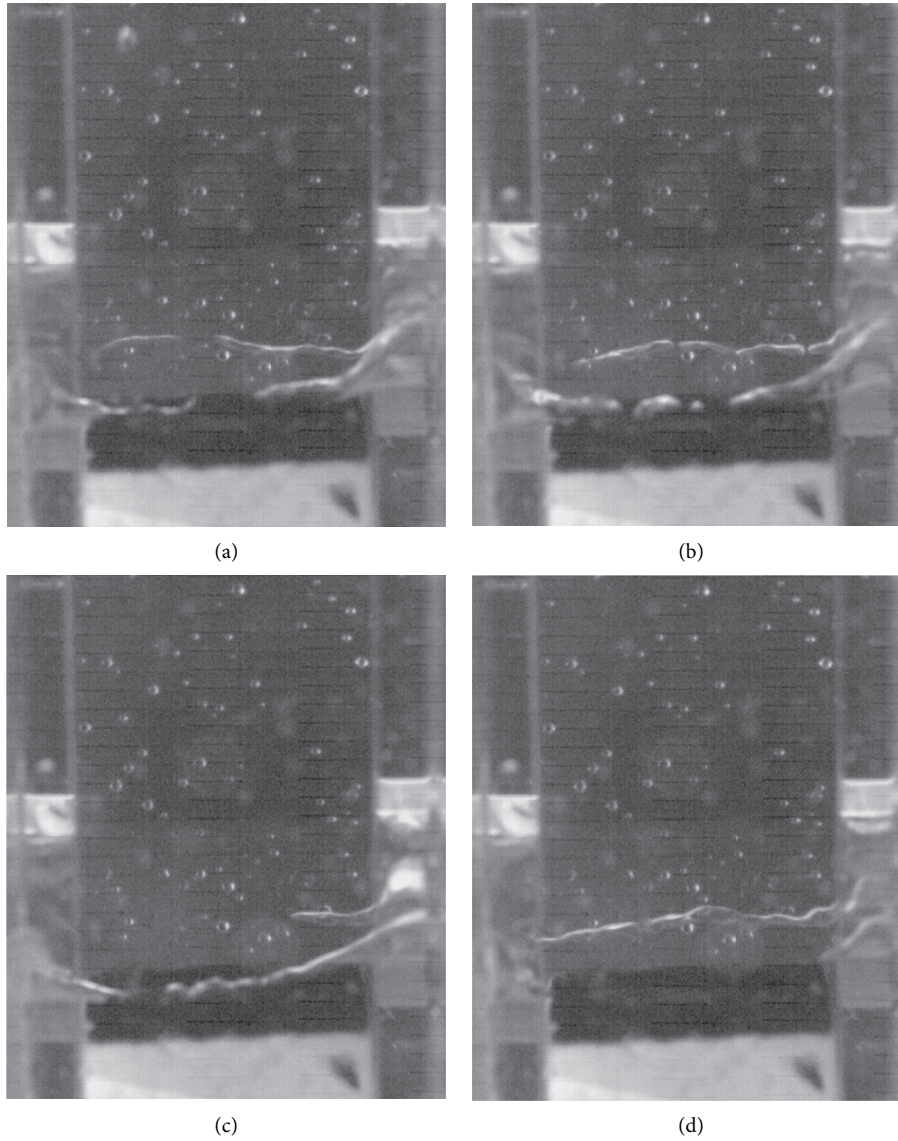
(a)

(b)

(c)

(d)

FIGURE 5: Dynamic evolution of the vortices inside the NIP, Case B, for a time interval of 0.036 s.

characteristic is that there are instants where only one vortex is visible. Although the axes of rotation of both vortices are not straight lines, they are moderately parallel to each other and parallel to the nozzle exit ports' axis. These vortices arise because the pressure inside these zones decreases and thus become reverse flow zones that suction air through the exit ports. Figure 5 shows some representative examples of the shapes acquired by the two vortexes generated inside the nozzle without well. A plausible explanation of the vortex continuity breaking and the temporary absence of one vortex is that the pressure is higher than required inside the low-pressure zones.

High-speed video recordings registered air bubbles in the flow stream, one of them remained visible for 0.052 s, and it was used as a tracer to estimate fluid velocity magnitude. Figure 6 depicts the trajectory of the bubble and the estimation of the fluid velocity as a function of the height relative to the bottom of the nozzle. The bubble travels near the NIP longitudinal axis with a constant velocity until it reaches the area near the exit ports. There, its speed decreases and the bubble moves away from the inner bore longitudinal axis. Later, the bubble accelerates when it passes in the middle of the two vortices and finally leaves the NIP at the bottom of the exit port.

The shapes, the sizes, and the dynamic behavior of the jets emerging from the nozzle without the pool are notably different in comparison with the nozzle with bottom well. Inspection of individual frames of video record suggests that despite the jets are not identical, the differences in sizes and shapes are quite small.

The jets emerging from the nozzle without a pool are compact in shape. Several authors [2, 21] named this
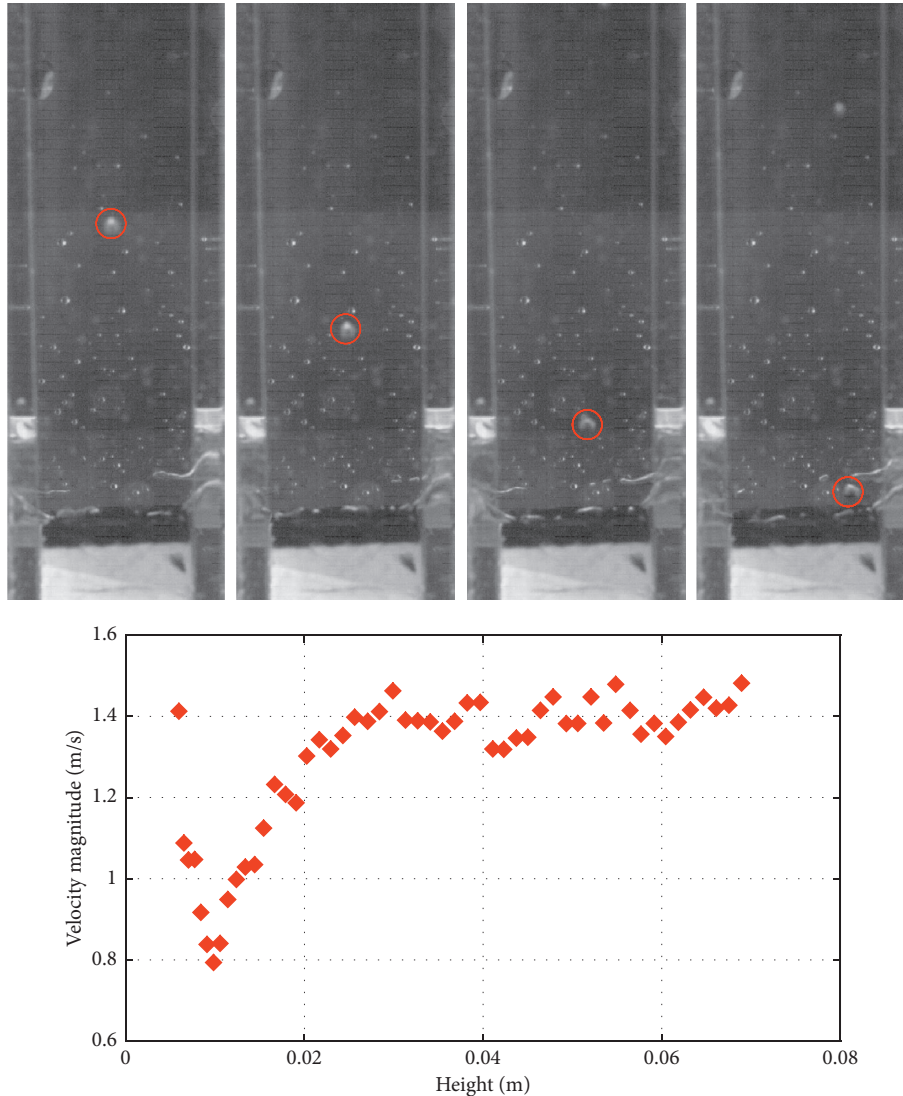
Figure 6: Bubble trajectory inside the NIP, Case B (top) and its measured velocity (bottom).

behavior as "smooth jets." The compact shape of the jets has two implications. The first one is related to the jet's impingement point. Due to their compact shape, the outlet jets do not collide directly with any of the mold walls and release much of their kinetic energy into the liquid steel within the mold. The second implication is that the compact shape of the outlet jets promotes uniform heat transfer between molten steel and mold walls. A practical implication of producing almost identical smooth outlet jets is a double-roll symmetric liquid steel flow pattern produced inside the mold. The distinctive characteristic of this flow pattern is the absence of extreme variations near the liquid steel-slag interface, which, in turn, decreases the undesirable slag trapping phenomenon.

2.4.2. Submerged Nozzle Condition. Figure 7 shows a visualization of the behavior of the fluid inside the NIP

without pool using the "light-painting" technique. Compared with the previous NIP, Case A, visualization of the vortex is much more complicated because of the vortex intensity. This picture shows a close-up of the region near the exit port; a filter was applied to enhance visualization of particle trajectories. Two vortexes rest in the lower half of the volume defined between the two exit ports.

3. Numerical Simulations

3.1. Governing Equations and Turbulence Model Considerations. For developing the mathematical model, the following system properties were considered. The working fluid is incompressible and has Newtonian behavior. The studied process is isothermal, and all temperature-dependent physical properties remain constant.
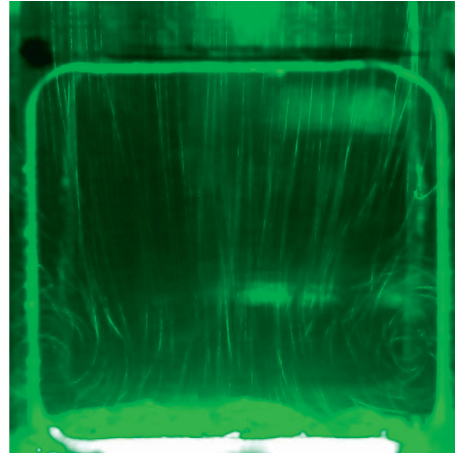
FIGURE 7: Two counterrotating vortexes located near the exit port of the NIP for the Case B.
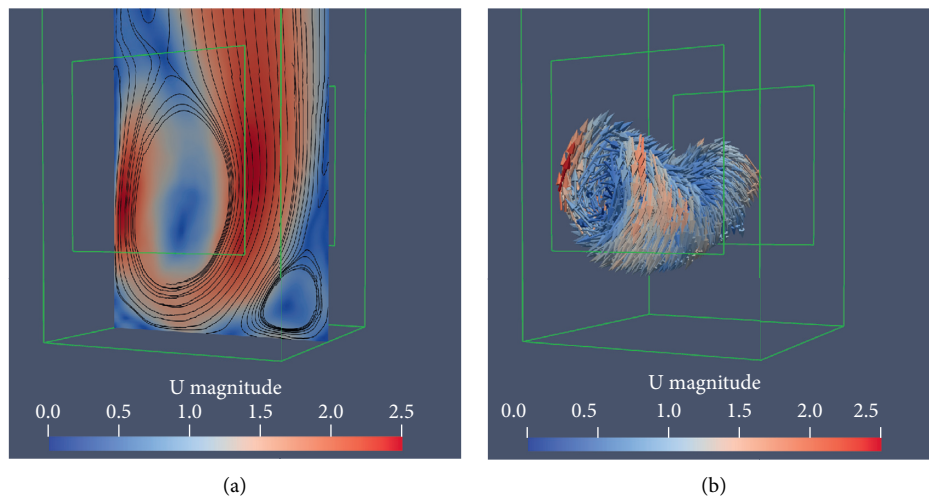

(a)	(b)

FIGURE 8: Turbulent fluid flow pattern inside the simulated NIP for Case A. (a) Plane parallel to nozzle exit ports colored by flow velocity magnitude and 2D streamlines and (b) vortex structure outlined by the fluid velocity vectors. The size of the vectors is the same, but they are colored according to their magnitude.

The governing equations of the fluid flow motion for incompressible fluid flow are the Navier–Stokes equations. However, for high Reynolds numbers, the adequate turbulence model is necessary to accurately reproduce the transient fluid flow behavior for a given system. Real et al. (2006) [12] compared the predictions of the fluid flow patterns inside a bifurcated SEN using two different turbulence models: the $(k - \varepsilon)$ and the large eddy simulation (LES) models. The authors found that the $(k - \varepsilon)$ model fails in recovering the transient behavior of the fluid flow inside the SEN observed experimentally.

Recently, Shukla and Dewan (2018) [13] presented a comparison of the prediction capabilities of four different subgrid stress (SGS) models for simulating the heat transfer in a slot jet impingement system with the Reynolds number of 20,000. The models analyzed in their work were Smagorinsky, WALE (wall-adapting local eddy-viscosity), k-equation, and dynamic k-equation. The authors of that work found that the velocity and turbulence profiles using the four LES models followed the trends of the experimental results. However, the authors also found that WALE and dynamic k-equation SGS models display superior performance in complex flow regions. Based on the preceding arguments, the transient numerical simulations presented in this work were done using an LES turbulence model with dynamic k-equation filtering.

The basic idea of LES is to directly resolve all turbulence scales larger than grid resolution in spatial and temporal while to model the effect of the turbulence scales smaller than that of the grid scale (GS) using the subgrid scale (SGS) model.

The LES turbulence model separates the fluid motion into small and large scales and directly resolves all turbulence scales larger than grid resolution while models the effect of the turbulence scales smaller than that of the grid scale using certain subgrid scale (SGS) model. The fluid
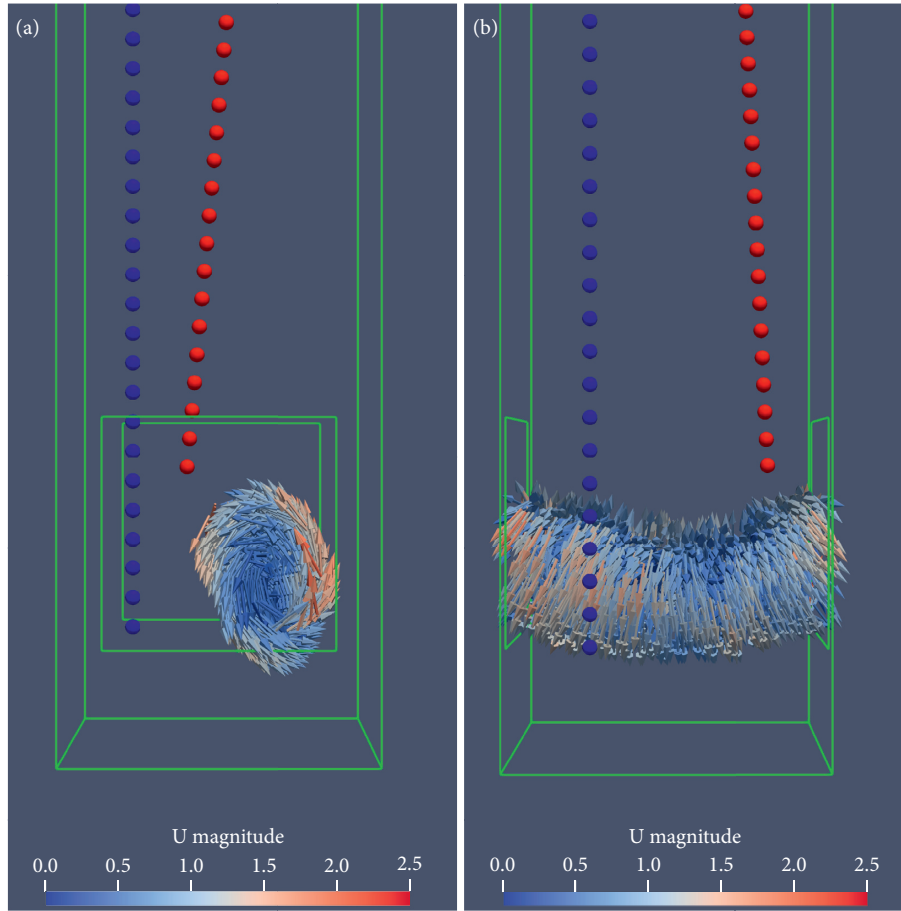
FIGURE 9: Vortex tube outlined by the velocity vectors shown in two projections (a) and (b) along with the paths used for velocity tracing. Bottom panel shows the comparison of experimental and numerical velocities.

motion separation is accomplished by means of a cutoff filter. The filtered governing equations are as follows:

$$\frac{\partial \overline{u}_i}{\partial x_i} = 0,$$

$$\frac{\partial \overline{u}_i}{\partial t} + \overline{u}_j \frac{\partial \overline{u}_i}{\partial x_j} = -\frac{\partial \overline{p}}{\partial x_i} - \frac{\partial T_{ij}}{\partial x_j} + \nu \frac{\partial^2 \overline{u}_i}{\partial x_j \partial x_j},$$

(1)

where $\overline{u}_i$ is the filtered fluid velocity vector i-component, $\overline{p}$ is the filtered density-normalized pressure, and ν is the kinematic viscosity of the fluid. Equation (3) also includes the components of a SGS stress tensor $\mathbf{T}$ defined as follows:

$$T_{ij} = \overline{u_i u_j} - \overline{u}_i \overline{u}_j.$$

(2)

In the dynamic k-equation SGS model, the SGS stress tensor is modeled using the velocity-strain tensor, $\overline{S}$, the
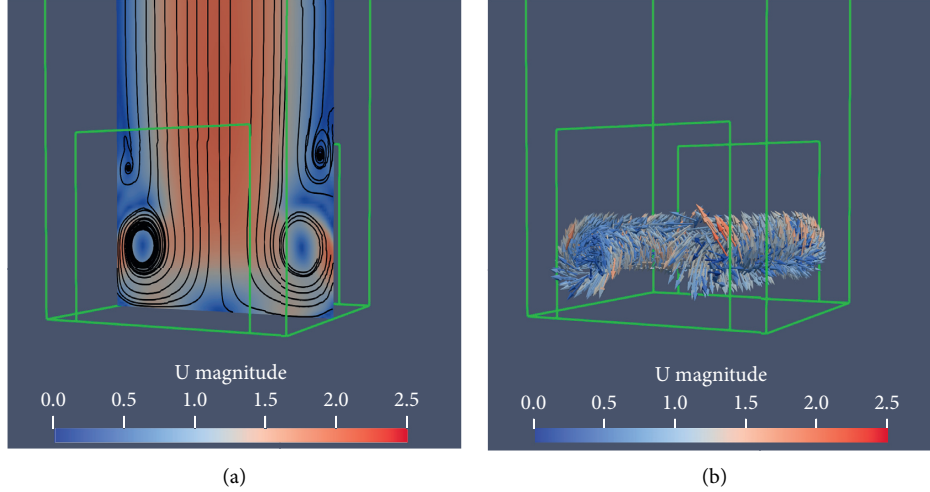
(a)

(b)

FIGURE 10: Turbulent fluid flow inside the simulated NIP for Case B. (a) Plane parallel to nozzle exit ports colored by flow velocity magnitude and 2D streamlines. (b) Two vortex structures outlined by the fluid velocity vectors. The size of the vectors is the same, but they are colored according to their magnitude.

subgrid scale kinematic eddy viscosity, ν_{SGS}, and the subgrid scale kinetic energy, k_{SGS}:

$$\overline{S} = \frac{1}{2}\left(\frac{\partial \overline{u}_i}{\partial x_j} + \frac{\partial \overline{u}_j}{\partial x_i}\right), \tag{3}$$

$$T_{\text{ij}} = -2\nu_{\text{SGS}}\overline{S}_{\text{ij}} + \frac{2}{3}k_{\text{SGS}}\delta_{\text{ij}}, \tag{4}$$

$$\nu_{\text{SGS}} = C_k\,\Delta\sqrt{k_{\text{SGS}}}. \tag{5}$$

In the previous equation, Δ is the subgrid characteristic length scale. In addition, k_{SGS} is obtained by solving the following transport equation:

$$\frac{\partial k_{\text{SGS}}}{\partial t} + \overline{u}_i\frac{\partial k_{\text{SGS}}}{\partial x_i} = -T_{\text{ij}}\frac{\partial \overline{u}_i}{\partial x_j} - C_e\frac{k_{\text{SGS}}^{(3/2)}}{\Delta} + \frac{\partial}{\partial x_i}\left(\nu_{\text{SGS}}\frac{\partial k_{\text{SGS}}}{\partial x_i}\right). \tag{6}$$

This additional transport equation overcomes some drawbacks of algebraic eddy-viscosity models, which may occur in high Reynolds number flows and/or in the cases of a coarse grid model resolution [28]. This SGS model has two coefficients, C_k and C_e, that must be calculated. Kim and Menon (1995) described in detail a localized dynamic formulation for obtaining these coefficients [29]. A remarkable feature of their formulation is its numerical consistency at high Reynolds numbers [30].

In this work, the OpenFOAM CFD toolbox was employed to accomplish numerical simulations. This computational program is an open-source software package and uses the finite volume method for numerical representation of the equations governing fluid motion. Several authors have recently shown that the program allows simulating a wide variety of complex fluid flow processes [20, 22–25, 27]. A detailed analysis of capabilities and validation study is presented in [17].

For solving the Navier–Stokes equations, OpenFOAM offers several methods to address the pressure-velocity coupling. This work used the PISO (pressure implicit with the split operator) method.

3.2. Numerical Simulation Setup. These are the boundary conditions for the mathematical model previously described:

(i) The inlet boundary condition was set as fully developed turbulent flow profile. The average inlet velocity is set to $\overline{u}_z = 1$ m/s.

(ii) The nonslip condition was considered for all the NIP solid walls ($u_i = 0$).

(iii) The inlet-outlet boundary condition was applied to both exit ports. Such condition switches to the inlet boundary if the local velocity vector next to the boundary is directed inside the domain (backward flow). This boundary condition allows to recover the reverse flow observed in physical experiments.

(iv) The nozzle discharges to the atmosphere.

In all the simulations, the convergence criterion is fulfilled when residuals for the modeled variables reached values of 1×10^{-5}. The convergence analysis was carried out using the results of the numerical simulations of the nozzle without the pool. The base for the convergence analysis was a model with a sufficiently large quantity of elements. Then, a second model was created by refining the mesh and increasing the amount of the elements. From the second model, a third model was built with four times the number of elements of the base model. We found that the hydrodynamic behavior obtained with the second numerical model entirely coincides with the results obtained in the physical simulations. The differences between the results of the numerical simulations with the second and the third model are negligible, so we take the mesh of the third model to carry out the numerical simulations. The third model also served as the base for creating the model for the nozzle with bottom
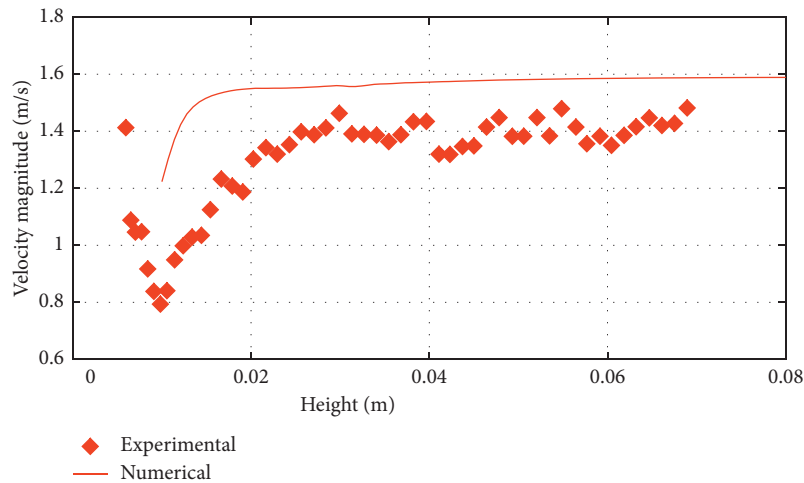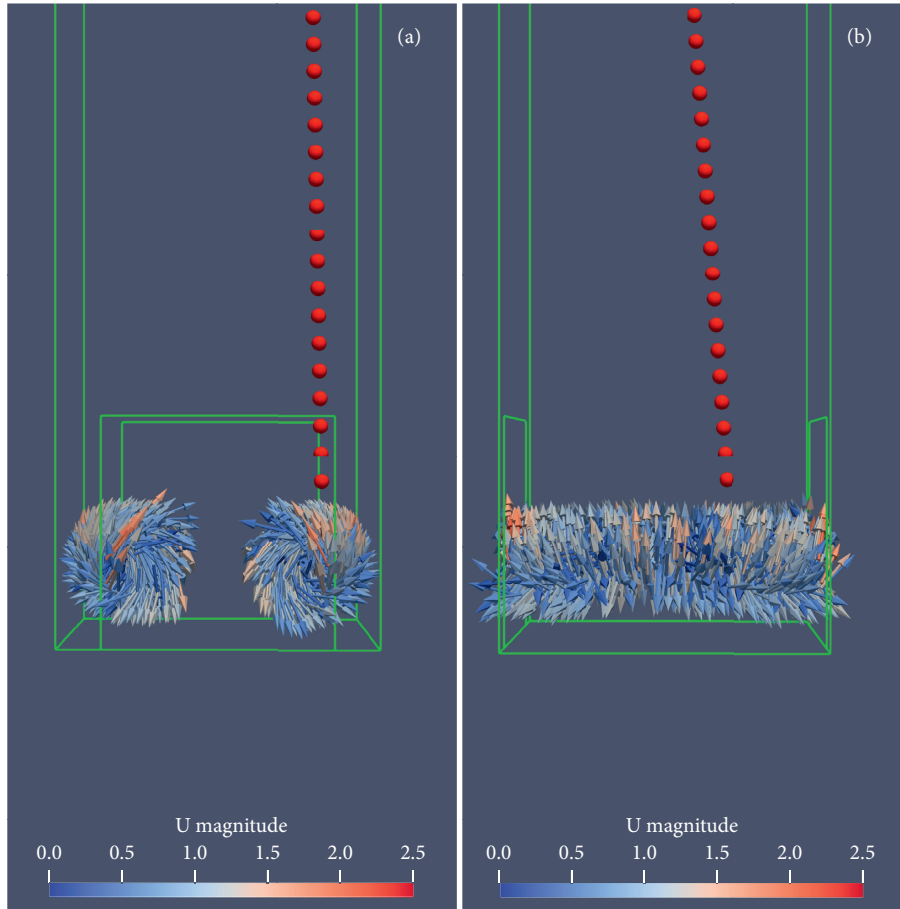
Figure 11: Vortex tubes outlined by the velocity vectors shown in two projections (a) and (b) along with the path used for velocity tracing. Bottom panel shows the comparison of experimental and numerical velocities.

well. In this case, the bottom well volume mesh has the elements of the same size as the elements in the central zone of the exit ports. The results of numerical simulations presented in this work are the average of 41 snapshots taken along an interval of two seconds.

3.3. Numerical Simulations: Case A. The results of numerical simulation of the NIP with the bottom well are shown in

Figure 8. The upper panel shows the velocity field and the streamlines along the plane perpendicular to the axis connecting exit ports, while the bottom panel shows the vortex surface where the fluid pressure is equal or lower than the atmospheric pressure along with the velocity vectors. This surface outlines the shape of the vortex produced inside the NIP. As can be noted from both panels, there is a dominant vortex that occupies a large fraction of the volume of the

nozzle bottom. There is also a small vortical structure on the bottom of the well. Its rotation direction is opposite to the big vortex rotation direction. The rotation axis of the small vortex is almost parallel to the exit ports' axis. Over time, major changes were observed in the shape and size of the large vortex, but it was found that the vortex was always present.

Although the axis of the vortex is nearly parallel to the axis of the output ports of the NIP, it is never located on the nozzle central zone. The analysis of the numerical simulations confirmed that there is always a bias of the vortex axis with respect to the central plane of the NIP. A close inspection of the low-velocity vectors directed towards the interior of the NIP shows the existence of reverse flow. Note that the area near the center of the port has a very low velocity and liquid emerges with high velocity mainly along the edges of the exit ports. The latter fluid flow pattern suggests that the liquid emerges through disperse, cone-shaped jets. This agrees with the findings obtained through physical simulations.

In order to investigate the velocity of the flow inside the NIP's bore, we extract the velocity magnitudes along two straight lines as depicted in the panels (a) and (b) of Figure 9. The bottom panel of Figure 9 shows the obtained velocities (blue and red lines) along with the measured velocities from the physical model (blue and red diamonds). It may be concluded that despite the different methods used for measuring velocities in both types of simulations, a qualitative agreement is obtained.

3.4. Numerical Simulations: Case B. Figure 10 shows an example of simulation where the two vortexes created inside the NIP without the pool. The analysis of the simulation led us to the following observations. The two vortexes located close to the bottom of the NIP are always present and preserve their cylindrical shape. Moreover, their axes remained roughly parallel to each other. The volumes of both vortexes oscillate continuously, tending, however, to preserve the similar size.

Figure 10 shows the magnitude of fluid velocity and the streamlines along the plane parallel to the exit ports (upper panel) and the zero-pressure surface of the vortexes together with the velocity vector magnitudes. The streamlines depict the presence of two dominant counterrotating vortexes located close to the bottom of the NIP and two smaller vortexes located just above the main ones. Overall, the velocity field is quite symmetric. As in the previous case, the low-velocity vectors indicate the presence of reverse flow inside the nozzle while high-velocity vectors are found close to the ports.

Notice that the velocity gradients are not as large as those observed in Case B. Furthermore, the largest velocity values are uniformly distributed at the bottom of the exit ports. This behavior agrees with smooth outlet jets found for the NIP without the pool.

Again, in order to compare the velocities inside the NIP obtained in the physical experiment with the numerical ones, we extract the velocity magnitude along a straight line as illustrated in Figure 11. As shown in the bottom panel, the agreement between both experiments is not as good as in the previous case. However, qualitatively, the velocity drop close to the bottom is reproduced, indicating the pattern of the smooth jets.

4. Conclusions

The nozzle internal prototype (NIP) studied in this work was constructed based on a box-type nozzle with an inner bore and a square cross section that remains constant throughout all its length. The NIP has two exit orifices of square geometric shape and satisfies the Froude similitude criterion.

In order to analyze hydrodynamics of the flow inside the nozzles, two different depths of pool inside the NIP were simulated using physical and numerical modeling. From the metallurgical industry perspective, Cases A and B reproduce two operational conditions. Case A shows the initial condition in the life cycle of the SEN, and Case B reproduces a condition when the liquid steel impurities were collected at the bottom zone of the nozzle.

The results show that the exit flow structure develops in the bottom zone of the nozzle; however, each case generates different turbulent flow conditions. Case A forms a single pronounced vortex that occupies a considerable area of the exit ports. Meanwhile, Case B develops dynamic flow behavior with two vortexes. The vortexes in both cases are located near the nozzle exit ports, and the reverse flow zones associated with them, emerge naturally, regardless of other factors.

The findings of this work are complementary to the information obtained using the circle cross section nozzle reported in 2006 [12] and are relevant for future works, especially for those regarding numerical simulations of inert gas injection in the stream flowing through the nozzle [10, 15, 19].

An accurate evaluation of the gas injection effect first requires a deep analysis of the process performance without gas injection and the influence of other process components such as the sliding gate, for example. Another factor is the inlet flow misalignment; the effect of this process characteristic will become significant when the nozzle length is too short.

This study will allow to build nozzles that produce a symmetric, regular fluid flow pattern inside the mold, which leads to improvements on the process such as low energy consumption and finally in cost reductions.

Data Availability

The data used to support the findings of this study are available from the corresponding author upon request.

Conflicts of Interest

The authors declare that they have no conflicts of interest.

Acknowledgments

References

[1] G. E. Sellers, "Machinery for making pipes continuously from lead, & C," US1908A, 1840.

[2] D. E. Hershey, B. G. Thomas, and F. M. Najjar, "Turbulent flow through bifurcated nozzles," *International Journal for Numerical Methods in Fluids*, vol. 17, no. 1, pp. 23–47, 1993.

[3] N. T. Mills and L. F. Barnhardt, "Development of submerged entry tundish nozzles," *JOM*, vol. 23, no. 11, pp. 37–43, 1971.

[4] I. Calderón-Ramos, R. D. Morales, R. Servín-Castañeda et al., "Modeling study of turbulent flow in a continuous casting slab mold comparing three ports SEN designs," *ISIJ International*, vol. 59, no. 1, pp. 76–85, 2019.

[5] H. Zhang, Q. Fang, T. Xiao, H. Ni, and C. Liu, "Optimization of the flow in a slab mold with argon blowing by divergent bifurcated SEN," *ISIJ International*, vol. 59, no. 1, pp. 86–92, 2019.

[6] D.-W. Li, Z.-J. Su, K. Marukawa, and J.-C. He, "Simulation on effect of divergent angle of submerged entry nozzle on flow and temperature fields in round billet mold in electromagnetic swirling continuous casting process," *Journal of Iron and Steel Research International*, vol. 21, no. 2, pp. 159–165, 2014.

[7] Z. Li, E. Wang, Y. Xu, and L. Xu, "Influence of SEN depth and port angle on vertical electromagnetic brake effects in continuous casting mould," *COMPEL-the International Journal for Computation and Mathematics in Electrical and Electronic Engineering*, vol. 36, no. 2, pp. 445–457, 2017.

[8] Z.-Q. Zhang, J.-B. Yu, Z.-M. Ren, and K. Deng, "Study on the liquid metal flow field in FC-mold of slab continuous casting," *Advances in Manufacturing*, vol. 3, no. 3, pp. 212–220, 2015.

[9] A. Asad, C. Kratzsch, and R. Schwarze, "Numerical investigation of the free surface in a model mold," *Steel Research International*, vol. 87, no. 2, pp. 181–190, 2015.

[10] Z. Wang, K. Mukai, and D. Izu, "Influence of wettability on the behavior of argon bubbles and fluid flow inside the nozzle and mold," *ISIJ International*, vol. 39, no. 2, pp. 154–163, 1999.

[11] D. Gupta and A. K. Lahiri, "Water modelling study of the jet characteristics in a continuous casting mould," *Steel Research*, vol. 63, no. 5, pp. 201–204, 1992.

[12] C. Real, R. Miranda, C. Vilchis, M. Barron, L. Hoyos, and J. Gonzalez, "Transient internal flow characterization of a bifurcated submerged entry nozzle," *ISIJ International*, vol. 46, no. 8, pp. 1183–1191, 2006.

[13] A. K. Shukla and A. Dewan, "OpenFOAM based LES of slot jet impingement heat transfer at low nozzle to plate spacing using four SGS models," *Heat and Mass Transfer*, vol. 55, no. 3, pp. 911–931, 2018.

[14] C. A. Real-Ramirez and J. I. Gonzalez-Trejo, "Analysis of three-dimensional vortexes below the free surface in a continuous casting mold," *International Journal of Minerals, Metallurgy, and Materials*, vol. 18, no. 4, pp. 397–407, 2011.

[15] Z.-Q. Liu, F.-S. Qi, B.-K. Li, and M.-F. Jiang, "Vortex flow pattern in a slab continuous casting mold with argon gas injection," *Journal of Iron and Steel Research International*, vol. 21, no. 12, pp. 1081–1089, 2014.

[16] K. K. Chen, C. W. Rowley, and H. A. Stone, "Vortex dynamics in a pipe *T*-junction: recirculation and sensitivity," *Physics of Fluids*, vol. 27, no. 3, 2015.

[17] E. Robertson, V. Choudhury, S. Bhushan, and D. K. Walters, "Validation of OpenFOAM numerical methods and turbulence models for incompressible bluff body flows," *Computers & Fluids*, vol. 123, pp. 122–145, 2015.

[18] J. Gonzalez-Trejo, C. A. Real-Ramirez, R. Miranda-Tello, F. Rivera-Perez, and F. Cervantes-De-La-Torre, "Numerical and physical parametric analysis of a SEN with flow conditioners in slab continuous casting mold," *Archives of Metallurgy and Materials*, vol. 62, no. 2, pp. 927–946, 2017.

[19] S. Sarkar, V. Singh, S. K. Ajmani, R. K. Singh, and E. Z. Chacko, "Effect of argon injection in meniscus flow and turbulence intensity distribution in continuous slab casting mold under the influence of double ruler magnetic field," *ISIJ International*, vol. 58, no. 1, pp. 68–77, 2018.

[20] G. R. Tabor and M. H. Baba-Ahmadi, "Inlet conditions for large eddy simulation: a review," *Computers & Fluids*, vol. 39, no. 4, pp. 553–567, 2010.

[21] S. Pirker, D. Kahrimanovic, and S. Schneiderbauer, "Secondary vortex formation in bifurcated submerged entry nozzles: numerical simulation of gas bubble entrapment," *Metallurgical and Materials Transactions B*, vol. 46, no. 2, pp. 953–960, 2015.

[22] Y. Cao and T. Tamura, "Large-eddy simulations of flow past a square cylinder using structured and unstructured grids," *Computers & Fluids*, vol. 137, pp. 36–54, 2016.

[23] E. Fooladgar, C. K. Chan, and K.-J. Nogenmyr, "An accelerated computation of combustion with finite-rate chemistry using LES and an open source library for in-situ-adaptive tabulation," *Computers & Fluids*, vol. 146, pp. 42–50, 2017.

[24] J. Mao, K. Zhang, and K. Liu, "Comparative study of different subgrid-scale models for large eddy simulations of magnetohydrodynamic turbulent duct flow in OpenFOAM," *Computers & Fluids*, vol. 152, pp. 195–203, 2017.

[25] J. Mao, Y. Yin, L. Yu, K. Xiang, and H. Wang, "Large eddy simulation of geometry sensitivity of magneotohydrodynamic turbulent flow in a rectangular duct," *Fusion Engineering and Design*, vol. 127, pp. 111–119, 2018.

[26] C. A. Real-Ramirez, I. Carvajal-Mariscal, F. Sanchez-Silva, F. Cervantes-De-La-Torre, J. Diaz-Montes, and J. Gonzalez-Trejo, "Three-dimensional flow behavior inside the submerged entry nozzle," *Metallurgical and Materials Transactions B*, vol. 49, no. 4, pp. 1644–1657, 2018.

[27] M. Kim, J. Lim, S. Kim, S. Jee, J. Park, and D. Park, "Large-eddy simulation with parabolized stability equations for turbulent transition using OpenFOAM," *Computers & Fluids*, vol. 189, pp. 108–117, 2019.

[28] S. Huang and Q. S. Li, "A new dynamic one-equation subgrid-scale model for large eddy simulations," *International Journal for Numerical Methods in Engineering*, vol. 81, no. 7, pp. 835–865, 2010.

[29] W.-W. Kim and S. Menon, "A new dynamic one-equation subgrid-scale model for large eddy simulations," in *Proceedings of the 33rd Aerospace Sciences Meeting and Exhibit*,

American Institute of Aeronautics and Astronautics, Reno, NV, USA, January 1995.

[30] S. Menon, P.-K. Yeung, and W.-W. Kim, "Effect of subgrid models on the computed interscale energy transfer in isotropic turbulence," *Computers & Fluids*, vol. 25, no. 2, pp. 165–180, 1996.

[31] K. K. Chen, C. W. Rowley, and H. A. Stone, "Vortex breakdown, linear global instability and sensitivity of pipe bifurcation flows," *Journal of Fluid Mechanics*, vol. 815, pp. 257–294, 2017.

[32] M. Kahshan, D. Lu, and M. Rahimi-Gorji, "Hydrodynamical study of flow in a permeable channel: application to flat plate dialyzer," *International Journal of Hydrogen Energy*, vol. 44, no. 31, pp. 17041–17047, 2019.

[33] D. Vigolo, S. Radl, and H. A. Stone, "Unexpected trapping of particles at a *T* junction," *Proceedings of the National Academy of Sciences*, vol. 111, no. 13, pp. 4770–4775, 2014.

Research Article

CFD-DEM Simulation of Reverse Circulation Pneumatic Cuttings Removal during Coal Seam Drilling

Xiaoming Han ⑩, Peibo Li, and Jialiang Li

School of Mechanical and Power Engineering, Henan Polytechnic University, Henan, Jiaozuo 454003, China

Correspondence should be addressed to Xiaoming Han; hanxmr@126.com

To solve the problems that the borehole depth is shallow and the borehole formation rate is low during the gas drainage drilling in soft coal seam with current cuttings removal method, a new technology of reverse circulation pneumatic cuttings removal is put forward. The CFD-DEM coupling method is used to establish the simulation model of cuttings-air two-phase flow in drill pipe. The effects of the air velocity for cuttings removal and the mass flow rate of cuttings on the flow characteristics, cuttings removal effect and pressure drop of cuttings-gas two-phase flow are analysed. The results show that the drag force of drilling cuttings becomes larger with the increase of air velocity and the stratified flow characteristic is obvious. The drill cuttings migration ratio is positively correlated with the air velocity for cuttings removal and negatively correlated with the mass flow rate of cuttings. When the mass flow rate of cuttings is constant, the increase of air velocity for cuttings removal leads to the increase of pressure drop in the inner hole of drill pipe. When the air velocity of cuttings removal is constant, the mass flow rate of cuttings and the pressure drop in the inner hole of drill pipe increases. Therefore, the appropriate air velocity should be selected considering the energy consumption during cuttings removal.

1. Introduction

Gas extraction is the main means to prevent and control gas outburst in coal seam. And, drill cuttings conveying during the borehole drilling in coal seam is the key to ensure the drilling depth and the drilling efficiency. The mechanical removal and the hydraulic removal of cuttings have a great impact on the stability of borehole wall, which is easy to cause the borehole collapse and blockage, sticking of the drill pipe, and other accidents [1]. The current cuttings removal method with pressure air removes the cuttings through the annular hole between drill pipe and borehole wall by the pressure air through the inner hole of drill pipe. It is difficult to collect the drill cuttings at the outlet of boreholes, which is easy to cause the dust pollution [2–4]. So, a new reverse circulation pneumatic cuttings removal technology is proposed that the annular hole between drill pipe and borehole wall is used as the air inlet and the inner hole of drill pipe is used as the cuttings removal channel [5, 6].

Numerical methods based on computational fluid dynamics (CFD) have mainly been used. Niu and Zhang [7] studied the critical wind speed under different cuttings removal rate and solid gas ratio as well as the pressure loss of air flow in drill pipe inner hole and annular hole. It is found that the critical wind speed and pressure loss are positively correlated with the solid gas ratio. Guo et al. [8] performed three dimensional and time-dependent calculations by using the finite volume CFD of sudden pipe expansion flows. Riaz and Sadiq [9] set up the governing equations with the help of similarity transformations and handled the solution of boundary value problems by perturbation procedure. So, the analytical solutions for fluid and particulate phase velocities, mean flow rates, and pressure gradient profile have been presented, while a numerical treatment has been carried out for pressure rise. And, the exact solutions of non-Newtonian multiphase fluid through peristaltic pumping characteristics in an annulus having complaint walls and applied magnetic field was studied [10]. Abdelsalam et al. [11] and Ijaz et al.

[12] studied the two-phase flows characteristics in the biologically inspired pumping systems.

The Computational Fluid Dynamics and Discrete Element Method Coupling Algorithm (CFD-DEM) is a well-developed method that has been proven effective in the study of liquid-solid and gas-solid two-phase flow system. The bilateral coupled CFD-DEM method was used to numerically simulate the coal particles flow pattern in the swirling pneumatic conveying process and the interaction between coal particles and pipe wall to reveal the mechanism of coal particle swirling pneumatic conveying [13, 14]. Based on the CFD-DEM coupling algorithm, the dust cyclone separator in negative pressure fixed-point sampling is simulated to study the effect of air velocity and coal mass flow rate on the coal-air two-phase separation process [15]. Akhshik et al. [16, 17] applied the CFD-DEM coupling method to study the effects of drill pipe rotation and drill cuttings shape on the cuttings flow characteristics in different inclined angle drilling holes. And, the numerical simulation is consistent with the experimental results. Based on the CFD-DEM coupling method, Shao et al. [18] simulated the migration of large-diameter unconventional drill cuttings particles to study the drill cuttings removal rule in borehole and reveal the influence of cuttings shape and content on the removal effect of cuttings. Sun et al. [19] used the CFD-DEM coupling method to simulate the trajectory of drill cuttings. The simulation results of the cuttings concentration coincided with the experimental data by Kim et al. [20], which proved the accuracy and feasibility of the CFD-DEM coupling method in the drill cuttings removal. Therefore, the CFD-DEM coupling method is also used to simulate the cuttings-gas two-phase flow in the inner hole of drill pipe during the horizontal drilling borehole in coal seam. The research can reveal the effects of the air velocity for cuttings removal and the mass flow rate of cuttings on the flow characteristics, cuttings removal effect, and pressure drop of cuttings-gas two-phase flow to improve the drilling efficiency in coal seam.

2. Materials and Methods

2.1. Introduction of the Reverse Circulation Pneumatic Cuttings Removal System.

As shown in Figure 1, the reverse circulation pneumatic cuttings removal system mainly includes drilling rig, drill pipe, drilling bit, cyclone separator, and Roots vacuum pump. The Roots vacuum pump provides the air force for the pneumatic conveying of drill cuttings. Under the suction effect of vacuum pump, air enters the bottom of the drill hole along the annular hole between drill pipe and borehole wall. The drill cuttings generated by the operating drilling bit are wrapped and carried into the inner hole of drill pipe through the discharge hole. And, the inner hole of drill pipe is used as the cuttings removal channel. The cyclone separator acts as the dust removal device to separate the drill cuttings from the cuttings-air two-phase flow. The drill cuttings are collected in the separator under the gravity while the filtered air is discharged through the Roots vacuum pump. The system has high removal efficiency of drill cuttings and plays a role of dust control and dust suppression by collecting the discharged cuttings.
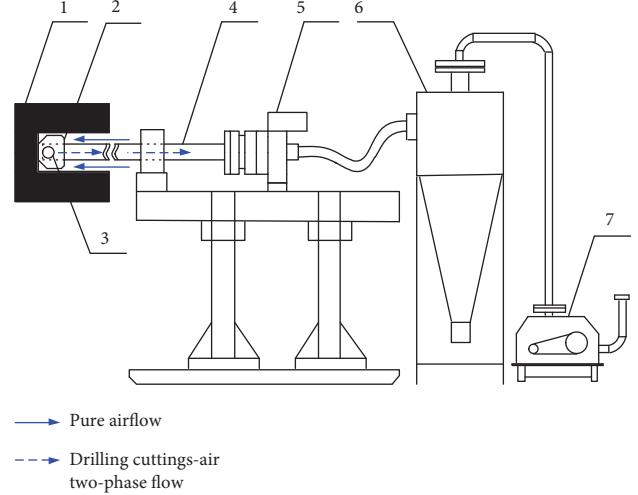

Figure 1: System composition of reverse circulation pneumatic cuttings removal. 1-Coal wall; 2-Drilling bit; 3-Discharge hole; 4-Drill pipe; 5-Drilling rig; 6-Cyclone separator; 7-Roots vacuum pump.

2.2. Drill Cuttings-Air Two-Phase Flow Control Equation.

The drill cuttings generated by the drilling bit breaking coal are smaller in size. Considering the continuity and fluidity of a large number of drill cuttings along the inner hole of drill pipe are similar to the movement of fluid, the dual-Eulerian model is used to describe the two-phase flow of drill cuttings and air. The air phase control equation includes the mass conservation and momentum conservation equations [16, 17, 21]:

$$\frac{\partial (\varepsilon_a \rho_a)}{\partial t} + \nabla \cdot (\varepsilon_a \rho_a \mathbf{v}_a) = 0,$$

$$\frac{\partial (\varepsilon_a \rho_a \mathbf{v}_a)}{\partial t} + \nabla \cdot (\varepsilon_a \rho_a \eta \mathbf{v}_a) = -\nabla p + \nabla \cdot (\varepsilon_a \eta \nabla \mathbf{v}_a) + \varepsilon_a \rho_a \mathbf{g} - \mathbf{S},$$

$$(1)$$

where, ε_a is the porosity, ρ_a is the air density, $\mathbf{v}_a$ is the air velocity, ∇ is the divergence operator, p is the pressure on a fluid mesh element, η is the aerodynamic viscosity, and $\mathbf{S}$ is the momentum sink which is the ratio of the sum of the forces between drill cuttings and air in the fluid mesh unit to the volume of the fluid mesh unit:

$$\mathbf{S} = \frac{\sum_{i=1}^{N} \mathbf{F}_{c-a,i}}{V_{\text{cell}}}, \qquad (2)$$

where N is the number of drill cuttings in the fluid mesh unit, $\mathbf{F}_{c-a,i}$ is the interaction force between drill cuttings and air, and V_{cell} is the fluid grid element volume.

$$\mathbf{F}_{c-a} = C_D \frac{\pi d_c^2}{8} (\mathbf{v}_a - \mathbf{v}_c)^2, \qquad (3)$$

where C_D is the resistance coefficient, d_c is the drill cuttings diameter, and $\mathbf{v}_c$ is the drilling speed.

The drill cuttings motion follows Newton's second law. So,

$$m_i \frac{d\mathbf{v}_i}{dt} = m_i\mathbf{g} + \mathbf{F}_{c-a,i} + \mathbf{F}_c, \tag{4}$$

$$\mathbf{I}_i \frac{d\boldsymbol{\omega}_i}{dt} = \sum_{j=1}^{k} \mathbf{T}_{ij} + \mathbf{T}_{DT,i}, \tag{4}$$

where m_i is the quality of drill cuttings, $\mathbf{v}_i$ is the drilling speed, $\mathbf{F}_c$ is the contact force of drill cuttings, $\mathbf{I}_i$ is the rotary inertia of drill cuttings, ω_i is the angular velocity of drill cuttings, and $\sum_{j=1}^{k} \mathbf{T}_{ij}$ is the resultant moment of drill cuttings:

$$\mathbf{T}_{ij} = \mathbf{F}_c \times r_\mathbf{i}, \tag{5}$$

where, $r_\mathbf{i}$ is the vector from the center of mass of cutting i to the contact point and $\mathbf{T}_{DT,i}$ is the moment produced by the slip-rotation:

$$\mathbf{T}_{DT,i} = \frac{\rho}{2}\left(\frac{d_i}{2}\right)^5 C_{DR}|\Omega|\Omega, \tag{6}$$

where ρ is the cutting density, d_i is the mean diameter of ith cutting, C_{DR} is the rotational drag coefficient, and Ω is the relative angular velocity of the cutting to the air.

2.3. Drill Cuttings Contact Model.

During the movement of drill cuttings along the inner hole of drill pipe, the Hertz–Mindilin contact model is used to describe the cuttings-cuttings contact and the contact between the cuttings and the inner wall of drill pipe. The contact forces of drill cuttings are shown in Figure 2. The contact forces between the cuttings or between the cuttings and the inner wall of drill pipe are divided into normal force $\mathbf{F}_n^c$, normal damping force $\mathbf{F}_n^d$, tangential force $\mathbf{F}_t^c$, and tangential damping force $\mathbf{F}_t^d$.

The normal force $\mathbf{F}_n^c$ is the function of normal overlap δ_n, equivalent Young's modulus Y^*, and equivalent radius R^* [13]:

$$\mathbf{F}_n^c = \frac{4}{3}Y^*\delta_n^{3/2}\sqrt{R^*}, \tag{7}$$

$$\frac{1}{Y^*} = \frac{\left(1 - v_i^2\right)}{Y_i} + \frac{\left(1 - v_j^2\right)}{Y_j}, \tag{8}$$

$$\frac{1}{R^*} = \frac{1}{R_i} + \frac{1}{R_j}, \tag{9}$$

where v_i, Y_i, and R_i and v_j, Y_j, and R_j are Poisson's ratio, Young's modulus, and radius of cuttings i and cuttings j, respectively.

The normal damping force $\mathbf{F}_n^d$ is

$$\mathbf{F}_n^d = -2\sqrt{5/6}\gamma\sqrt{S_n m^*}\mathbf{v}_n^{rel}, \tag{10}$$

$$S_n = 2Y^*\sqrt{R^*\delta_n}, \tag{11}$$

$$\gamma = \frac{\ln e}{\sqrt{\ln^2 e + \pi^2}}, \tag{12}$$

$$\frac{1}{m^*} = \frac{1}{m_i} + \frac{1}{m_j}, \tag{13}$$

where S_n is the normal stiffness, m^* is the equivalent mass, $\mathbf{v}_n^{rel}$ is the normal component of relative velocity between drill cuttings, e is the recovery coefficient, And m_i and m_j are the quality of drill cuttings i and drill cuttings j, respectively.

The tangential force $\mathbf{F}_t^c$ depends on the tangential overlap δ_t and the tangential stiffness S_t:

$$\mathbf{F}_t^c = -S_t\delta_t, \tag{14}$$

$$S_t = 8G^*\sqrt{R^*\delta_t}, \tag{15}$$

$$G^* = \frac{2 - v_i^2}{G_i} + \frac{2 - v_j^2}{G_j}, \tag{16}$$

where G^* is the equivalent shear modulus and G_i and G_j are the shear modulus of cuttings i and cuttings j, respectively.

The tangential damping force $\mathbf{F}_t^d$ is

$$\mathbf{F}_t^d = -2\sqrt{5/6}\gamma\sqrt{S_t m^*}\mathbf{v}_t^{rel}, \tag{17}$$

where $\mathbf{v}_t^{rel}$ is the normal component of relative velocity between drill cuttings.

When the tangential force between the drill cuttings is greater than the static friction force, the slip between the drill cuttings will occur. The tangential force is

$$\mathbf{F}_t^c = \varphi_s\mathbf{F}_n^c, \tag{18}$$

where φ_s is the sliding friction coefficient.

2.4. Simulation Model.

According to the working principle of the reverse circulation pneumatic cuttings removal system, the geometric model including borehole, drilling bit, and drill pipe is built, as shown in Figure 3.

According to the working principle of the reverse circulation pneumatic cuttings removal system, the diameter of drilling bit is 94 mm and the diameter of discharge hole in drilling bit is 40 mm. The outer diameter of drill pipe is 73 mm, and the inner hole diameter of drill pipe is 40 mm. The drilling bit is connected with the drill pipe. The diameter of the borehole in coal seam is about 100 mm. In order to analyze the flow characteristics of the drill cuttings along the inner hole of drill pipe, the length of drill pipe is set as 4.9 m and the drilling bit length is set as 0.1 m. So, the geometry model length of the drill pipe-bit reverse circulation pneumatic cuttings removal simulation is 5 m.

The hexahedral mesh is used to mesh the geometric model. A total of 53209 mesh elements and 47428 mesh nodes are generated. The mesh generation is shown in Figure 4. The annular hole between drill pipe and borehole wall is set as the inlet and the end of the inner hole of drill pipe is set as the outlet.
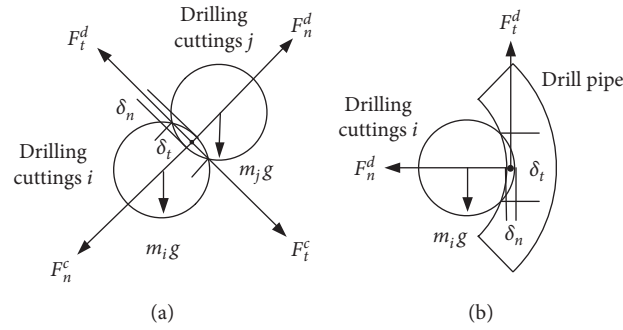
FIGURE 2: Scheme diagram of contact forces.
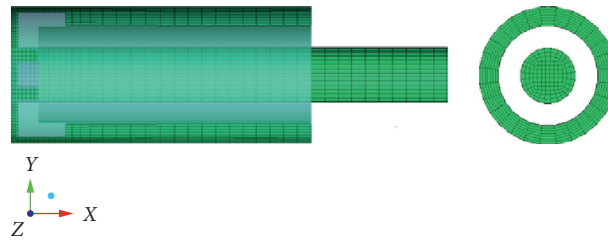

FIGURE 3: Geometric model.

FIGURE 4: Mesh generation.

To solve the air phase, the unsteady pressure solver with a gravitational acceleration of 9.81 m/s^2 along the negative Y direction is set. The turbulence model is the realizable k-ε turbulence model. The inlet is set as speed inlet with the air velocity of 5.13 m/s, 6.85 m/s、8.56 m/s、10.27 m/s, and 11.98 m/s, respectively. Correspondingly, the air velocity in the inner hole of drill pipe is 15 m/s, 20 m/s, 25 m/s, 30 m/s, and 35 m/s, respectively. The turbulence intensity is 5%, and the turbulent viscosity ratio is 0.5. The outlet is set as pressure outlet with the pressure of −3000 Pa. The finite volume method and the QUICK algorithm are used to discretize the air phase control equation and the momentum equation. The second-order upwind scheme is used to discretize the turbulent kinetic energy and the turbulent diffusion equation. The SIMPLE algorithm is used for the phase-to-phase coupling of pressure-velocity phase. The simulation parameters are set as Table 1.

The drill cuttings generated by the drilling bit in coal seam were collected, and the particle size analysis was carried out. It was found that the particle size of the cuttings was mainly less than 1 mm. Therefore, the spherical particles with the particle

diameter of 1 mm were used to simulate the drill cuttings. The drill cuttings are generated at the entrance of the discharge hole of drilling bit. And, the cuttings production is set as 0.06 kg/s, 0.08 kg/s, 0.10 kg/s, 0.12 kg/s, and 0.14 kg/s, respectively. In order to avoid the drill cuttings accumulating at the discharge hole when the cuttings are generated, the initial velocity of cuttings is set as 2 m/s in the X direction. The drill cuttings phase solution time step is set to be 2×10^{-6} s, and the air phase time step is set to be 1×10^{-4} s.

2.5. Model Verification.
To validate the simulation predictions, the reverse circulation pneumatic cuttings removal test device is built which is shown in Figure 5.

The Roots vacuum pump typed of QZSR125A is used as the power source of the experimental system. The boost range is −50~0 kPa, and the maximum flow is 6.38 m^3/min. During the test, the flow of Roots vacuum pump can be changed by adjusting the speed of variable frequency motor of Roots vacuum pump to adjust the air velocity. A feeding device is used to simulate the generation of drill

TABLE 1: Settings of simulation parameters.

Item	Parameter	Unit	Value
Drill cuttings	Poisson ratio	—	0.3
	Shear modulus	Pa	1×10^9
	Density	kg/m^3	1400
Drill pipe	Poisson ratio	—	0.29
	Shear modulus	Pa	7.9×10^{10}
	Density	kg/m^3	7800
Contact of cuttings and cuttings	Contact model	—	Hertz-mindlin
	Recovery coefficient	—	0.5
	Static friction coefficient	—	0.6
	Rolling friction coefficient	—	0.05
Contact of drill cuttings and drill pipe inner wall	Contact model	—	Hertz-mindlin
	Recovery coefficient	—	0.5
	Static friction coefficient	—	0.4
	Rolling friction coefficient	—	0.05
Atmosphere	Density	kg/m^3	1.225
	Dynamic viscosity	kg/(m·s)	1.7894×10^{-5}
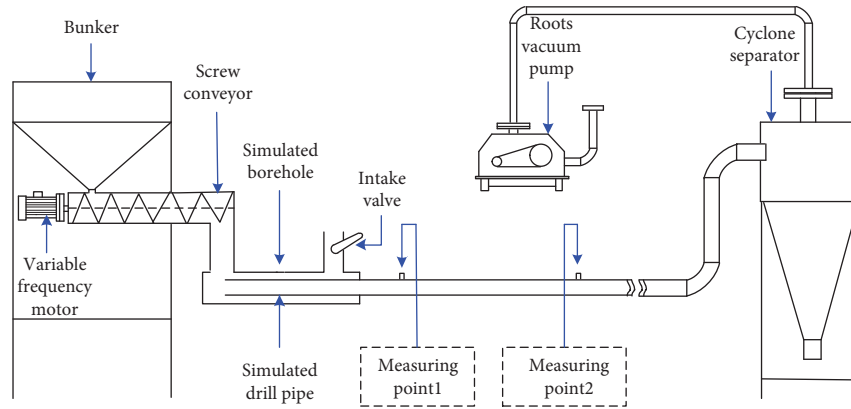
FIGURE 5: Experiment system of reverse circulation pneumatic cuttings removal.

cuttings. The feeding device is composed of bunker and screw conveyor. The mass flow rate of cuttings is controlled by adjusting the speed of screw conveyor. The transparent rigid plexiglass tube is used to simulate the drill pipe and borehole. The two-phase separation of drill cuttings and air is completed in the cyclone separator. In order to obtain the pressure drop of drill pipe under the steady flow of cuttings and air, the pressure measuring point 1 is set at the distance of 3 m from the drill pipe inlet, and the pressure measuring point 2 is set at the downstream 2 m from the pressure measuring point 1. Figure 6 is the actual experimental equipment.

In the experiment, the mass flow rate of cuttings was selected as 0.06 kg/s, 0.10 kg/s, and 0.14 kg/s, and the air velocity was selected as 15 m/s, 20 m/s, 25 m/s, 30 m/s, and 35 m/s. The pressure drop per unit length between measuring point 1 and measuring point 2 was tested and is shown in Figure 7. From the comparison of pressure drop per unit length, it shows that the results of CFD-DEM simulation reasonably agree with those of the experiment.

3. Results and Discussion

3.1. Flow Characteristics Analysis of Cuttings Phase

3.1.1. Drilling Cuttings Flow Pattern in Inner Hole of Drill Pipe. The cuttings flow patterns of 0~0.5 m and 4.5~5 m segments in the inner hole of drill pipe under different air velocities are shown in Figure 8 when the cuttings mass flow rate is 0.14 kg/s.

From Figure 8, it can be seen that the drilling cuttings are evenly generated at the entrance of the discharge hole of drilling bit. Then, the cuttings enter the inner hole of drill pipe at the initial speed of 2 m/s. Because the cuttings speed is less than the air velocity, the drilling cuttings accelerate and form obvious cuttings flow under the drag force of air flow, and then under the gravity action, the drilling cuttings flow gathers at the bottom of the inner hole of drill pipe and moves along the direction of the air flow until they are discharged from the inner hole of drill pipe.
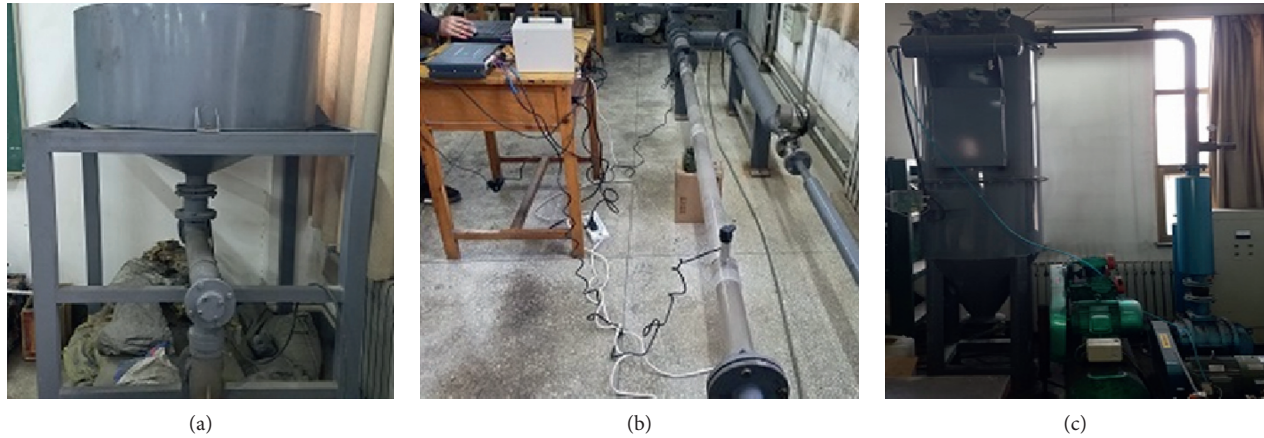
FIGURE 6: Experimental equipment: (a) feeding device, (b) cuttings removal channel, and (c) separator and vacuum pump.
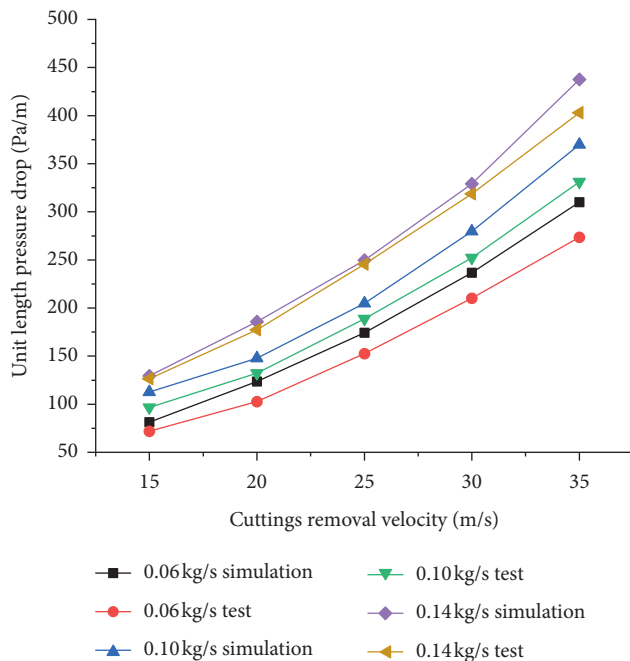

FIGURE 7: Comparison of pressure drop per unit length

When the air velocity is 15 m/s, the cuttings flow pattern is shown in Figure 8(a). Because of the low air velocity, the characteristic length of the cuttings flow is relatively short and deposits at the bottom of the inner hole of drill pipe. The typical characteristics of pipe bottom flow are presented along the flow direction and a thicker cuttings layer is formed. The moving speed of cuttings in the 4.5~5 m segment is obviously lower than that in the 0~0.5 m segment, which indicates that the cuttings have decelerated during the movement. When the air velocity is 20 m/s, the cuttings flow pattern is shown in Figure 8(b). With the increase of air velocity, the drag force of drilling cuttings becomes larger, and the characteristic length of drilling cuttings flow becomes longer. However, it still shows the characteristics of pipe bottom flow and the thickness of the drilling cuttings layer decreases. At this time, the moving speed of drilling

cuttings in the 4.5~5 m segment is higher than that in the 0~0.5 m segment. As shown in Figure 8(c), when the air velocity is 25 m/s, the characteristics of the cuttings flow are further lengthened, and the thickness of the cuttings layer decreases again along the flow direction. Individual drilling cuttings are distributed in the upper part of the inner hole of drill pipe. As shown in Figure 8(d), when the air velocity is 30 m/s, the characteristics length of the cuttings flow becomes longer. The characteristics of pipe bottom flow get weakened, and the thickness of the cuttings layer decreases further along the flow direction. A small amount of drilling cuttings distributes in the upper part of the inner hole of drill pipe, and the cuttings movement speed is higher than that of the bottom cuttings. The stratified flow characteristic is obvious. The stratified flow can be roughly divided into two layers: most of the cuttings move along the bottom of the inner hole to form the cuttings conveying layer, and some cuttings suspension movement forms the mixed conveying layer. Figure 8(e) shows that the amount of cuttings floating in the flow direction increases and the stratified flow characteristics is obvious when the air velocity is 35 m/s.

3.1.2. Cuttings Distribution along Flow Direction. The distribution of drill cuttings along the flow direction can reflect the accumulation of drill cuttings in the inner hole of drill pipe. The drill pipe-bit model is equally divided into 25 segments along the flow direction, and the amount of drill cuttings at different positions along the flow direction is counted at the time of 2 s, respectively. And, the ratio of the amount of cuttings in different positions to the total number of cuttings in the inner hole of drill pipe is defined as the amount proportion of cuttings along the flow direction which is used to characterize the distribution of cuttings along the flow direction, as shown in Figure 9.

Figure 9 shows that the amount proportion of cuttings along the flow direction increases gradually when the air velocity is 15 m/s. It reaches the maximum in the 3~5 m segment, and the maximum proportion increases with the increase of the mass flow rate of drill cuttings. When the air velocity is 20 m/s, 25 m/s, 30 m/s, and 35 m/s, respectively,
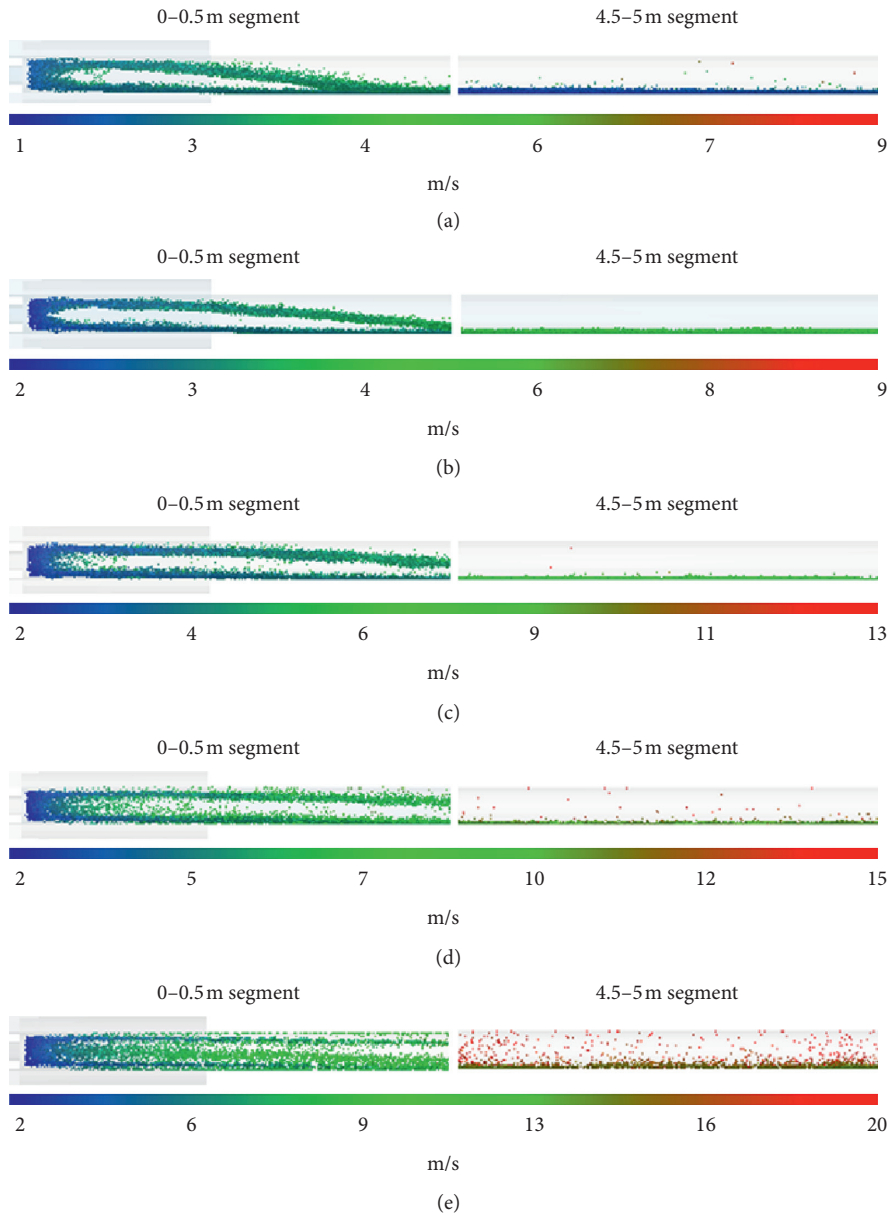
FIGURE 8: Cuttings flow pattern under different gas velocities: (a) $v_a = 15$ m/s, $M_c = 0.14$ kg/s, (b) $v_a = 20$ m/s, $M_c = 0.14$ kg/s, (c) $v_a = 25$ m/s, $M_c = 0.14$ kg/s, (d) $v_a = 30$ m/s, $M_c = 0.14$ kg/s, and (e) $v_a = 35$ m/s, $M_c = 0.14$ kg/s.

the amount proportion of cuttings along the flow direction shows the same trend of change, which gradually decreases along the flow direction and the maximum proportion occurs at the drill bit. The above phenomenon shows that when the air velocity is 15 m/s, the cuttings accumulate in the inner hole of drill pipe. The amount proportion of cuttings along the flow direction increases gradually. With the increase of the mass flow rate of cuttings, the accumulation of drill cuttings intensifies. When the air velocity is 20 m/s, 25 m/s, 30 m/s, and 35 m/s, the cuttings enter the drill bit at a lower initial speed and accelerate under the drag force of the air flow. The cuttings with higher speed are discharged from the inner hole of drill pipe in time, while the cuttings speed at the entrance of the discharge hole of drill bit is relatively low. The amount of cuttings at

the entrance of the discharge hole is higher than that at other positions. Therefore, the amount proportion of cuttings along the flow direction decreases gradually and the maximum proportion increases with the increase of the air velocity.

3.1.3. *Cuttings Velocity Variation along Flow Direction.* The variation of drill cuttings velocity along the flow direction can reflect the acceleration and motion characteristics of drill cuttings along the flow direction. The average velocity of drill cuttings at different positions along the flow direction is calculated at time of 2 s separately. The variation of drill cuttings velocity along the flow direction is shown in Figure 10.
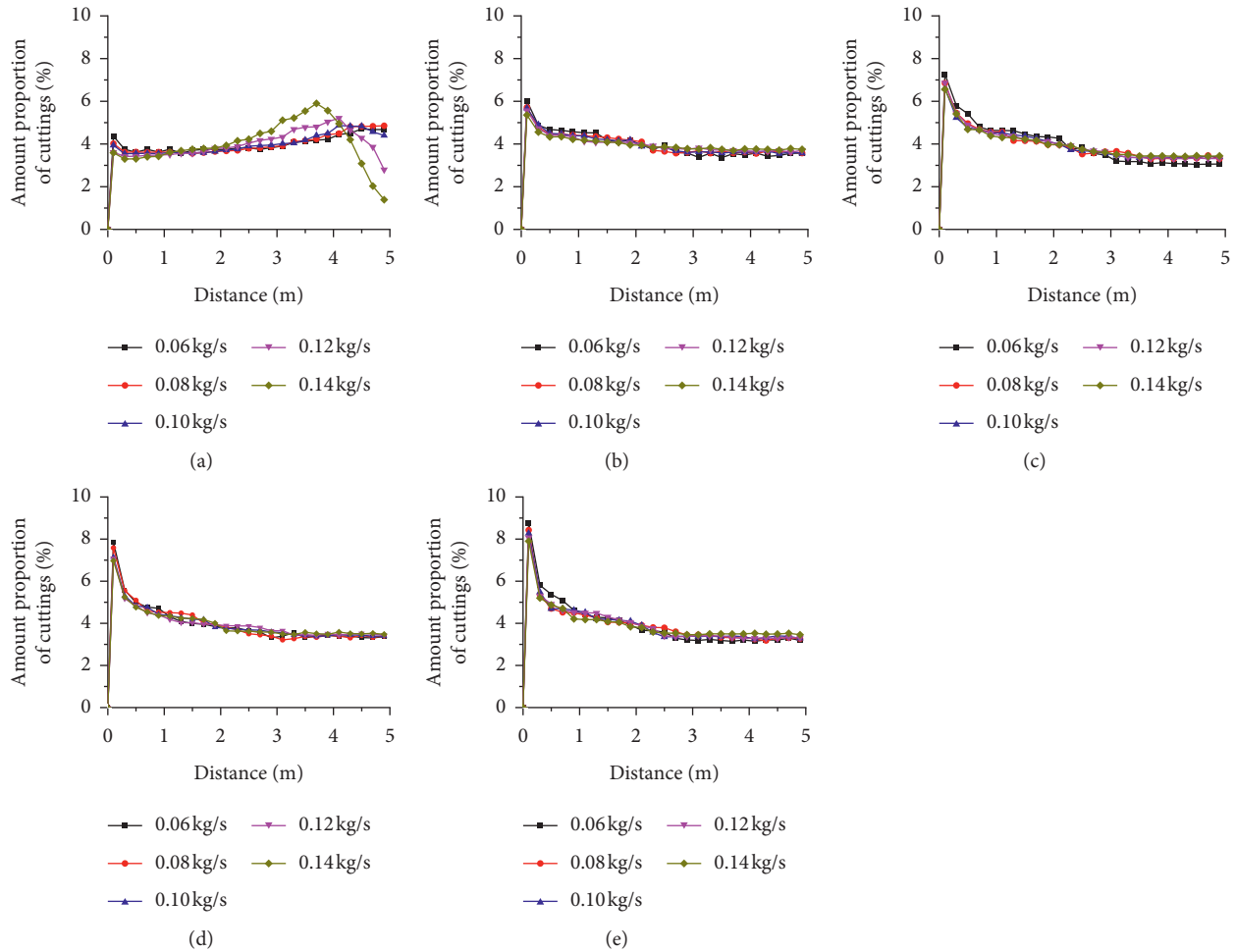
Figure 9: Amount distribution of cuttings along flow direction: (a) $v_a = 15$ m/s, (b) $v_a = 20$ m/s, (c) $v_a = 25$ m/s, (d) $v_a = 30$ m/s, and (e) $v_a = 35$ m/s.

As can be seen from Figure 10, when the air velocity is 15 m/s, the drill cuttings enter the inner hole of drill pipe at the initial speed of 2 m/s and accelerate under the drag force of air flow. Drill cuttings decelerate along the flow direction after short-distance acceleration movement. With the increase of the mass flow rate of drill cuttings, the acceleration distance of drill cuttings becomes shorter, the maximum velocity decreases, and the deceleration phenomenon is obvious. When the mass flow rate of cuttings is 0.12 kg/s and 0.14 kg/s, the cuttings decelerate along the flow direction first and accelerate at the end of the drill pipe. As the mass flow rate of drill cuttings increases, the accumulated cuttings increase, the cuttings layer becomes thicker, the area of air flow passage decreases and the air flow velocity increases at this position, which makes the cuttings located at the upper part of the cuttings layer accelerate again. When the air velocity are 20 m/s, 25 m/s, 30 m/s, and 35 m/s, respectively, the cuttings velocity increases along the flow direction. Under the same air velocity, the cuttings velocity at the same position decreases with the increase of the mass flow rate of cuttings. The drag force on the cuttings is proportional to the velocity difference between the cuttings and air flow. When

the cuttings enter the inner hole of drill pipe at a lower initial velocity, the drag force on the cuttings is larger because of the large velocity difference between the cuttings and the air flow. Therefore, the cuttings move in the inner hole of drill pipe with a higher acceleration. With the increase of cuttings velocity, the velocity difference between cuttings and air flow decreases, the drag force decreases, and the acceleration of the cuttings decreases. So, the velocity curve of drill cuttings in the 1~5 m segment is relatively flat compared with that in the 0~1 m segment.

Figures 9 and 10 show the distribution and velocity of the drill cuttings at different positions along the flow direction under different working conditions. In summary, when the air velocity is 15 m/s, the velocity of drill cuttings along the flow direction decreases and accumulates. The cuttings cannot effectively discharge from the inner hole of drill pipe in time and even block the inner hole of drill pipe, which makes the cuttings removal difficult and affects the drilling depth and drilling rate of borehole. When the air velocity is greater than 20 m/s, the velocity of drill cuttings increases along the flow direction, and no accumulation phenomenon occurs, so the cuttings removal can be achieved smoothly.
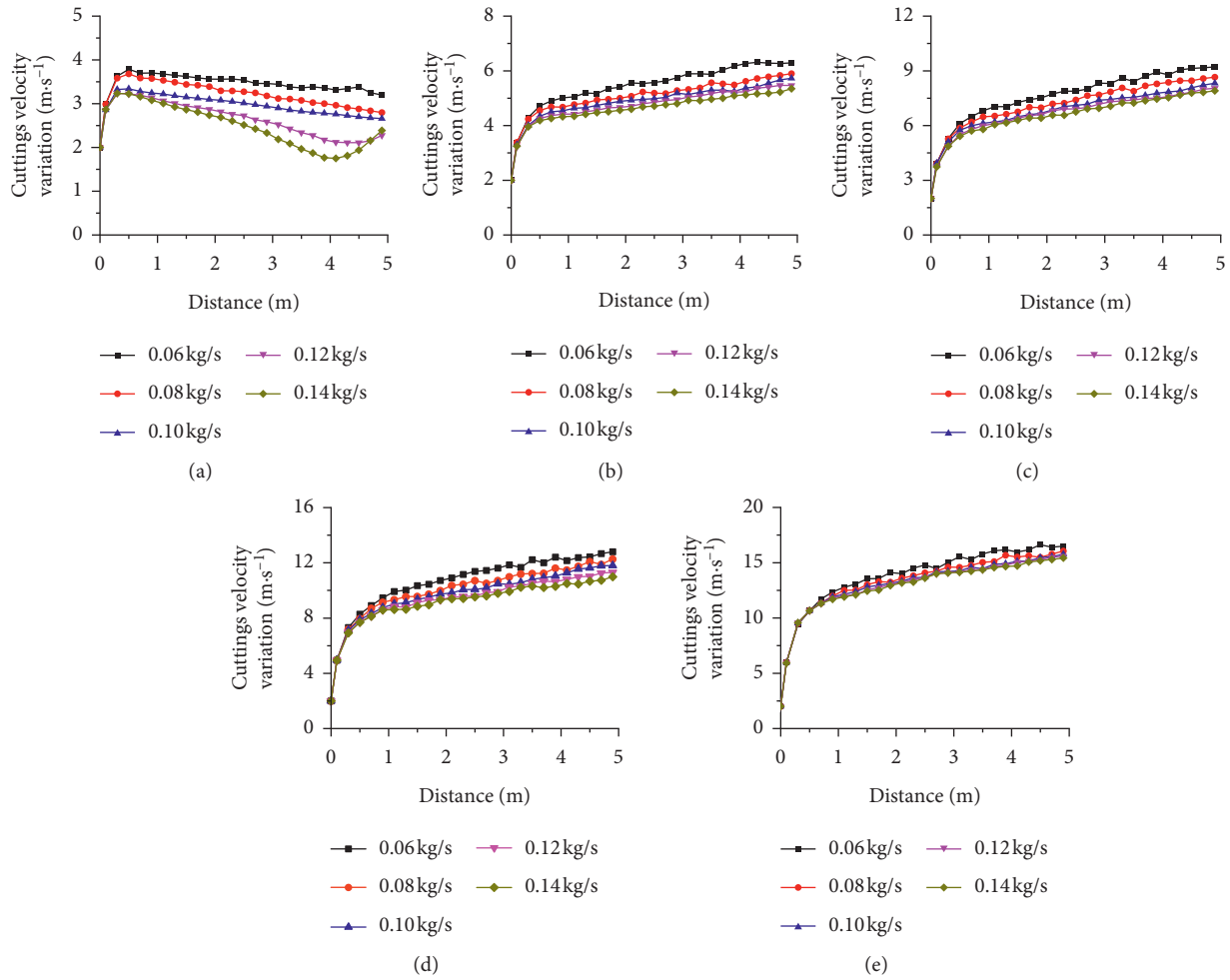
FIGURE 10: Cuttings velocity variation along flow direction: (a) $v_a = 15$ m/s, (b) $v_a = 20$ m/s, (c) $v_a = 25$ m/s, (d) $v_a = 30$ m/s, and (e) $v_a = 35$ m/s.

When the air velocity is constant, the cuttings mass flow rate increases from 0.06 kg/s to 0.14 kg/s, the amount of drill cuttings increases, and the individual cuttings energy obtained from the air flow decreases. Therefore, the cuttings velocity decreases along the flow direction with the increase of the mass flow rate of cuttings. Similarly, when the mass flow rate of drill cuttings is constant, the individual cuttings energy obtained from the air flow increases with the increase of air velocity. The drill cuttings accelerate faster and move in the inner hole of drill pipe at a higher speed. Therefore, in the application of the new technology of reverse circulation pneumatic cuttings removal, whether the drill cuttings can be discharged from the drilling hole directly depends on the air velocity and the mass flow rate of drill cuttings. In order to ensure that the cuttings are smoothly discharged from the drilling hole, the air velocity cannot be lower than 20 m/s.

3.2. Flow Characteristics Analysis of Air Phase. In order to analyze the influence of operating parameters on the air flow characteristics, the axial air flow velocity distribution at the position of 4.75 m under different cuttings mass flow rate and different air velocity is compared and analysed, as shown in Figure 11.

Figure 11(a) shows the axial airflow velocity distribution at the positon of 4.75 m under different mass flow rate of drill cuttings with the air velocity of 30 m/s. It can be seen from the figure that the maximum air flow velocity is distributed in the upper part of the inner hole of drill pipe due to the influence of drill cuttings. With the increase of the mass flow rate of cuttings, the air flow velocity in the lower part decreases while the air flow velocity in the upper part increases, and the position of the maximum air flow velocity moves upward. At the same air velocity, the increase of the mass flow rate of cuttings leads to the increase of the thickness of the bottom cuttings layer, which further reduces the area of air flow passage and aggravates the influence of drill cuttings on the air flow field. The air flow moves upward, and the position of the maximum air flow velocity moves upward.

Figure 11(b) shows the axial flow velocity distribution at the position of 4.75 m under different air velocities with the mass flow rate of 0.14 kg/s. It can be seen from the figure that the position with the maximum air velocity moves downward and gradually approaches the central axis with the increase of the air velocity. When
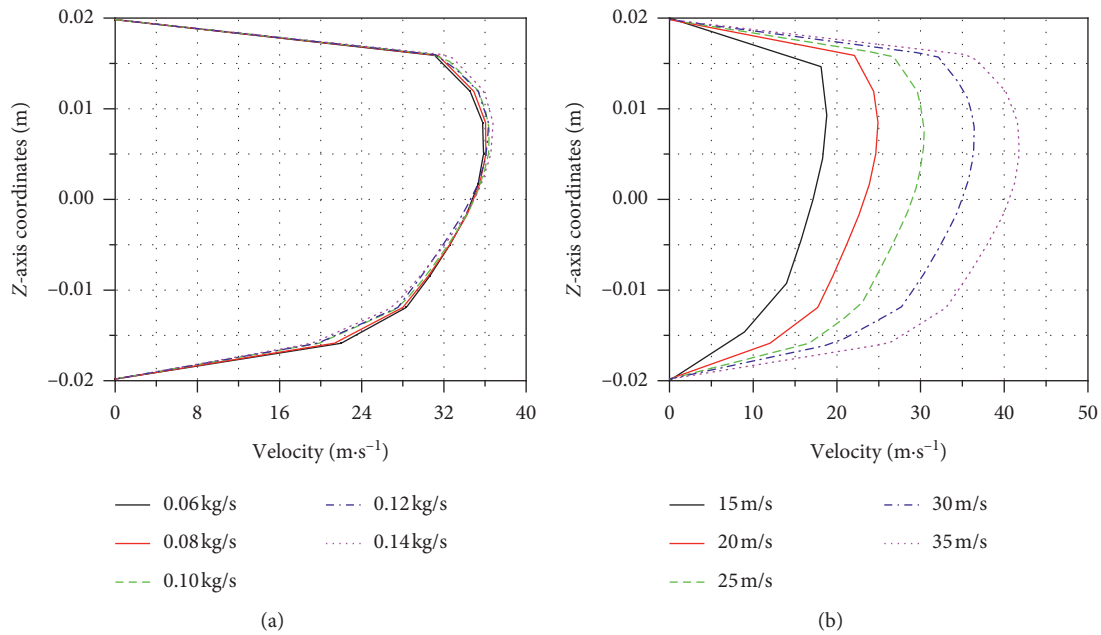
FIGURE 11: Air velocity distribution at position of 4.75 m.

the mass flow rate of cuttings is constant, the cuttings velocity becomes faster with the increase of the air velocity. The cuttings are timely and effectively discharged from the inner hole of drill pipe. So, the corresponding thickness of the bottom drill cuttings layer decreases. Under the higher air velocity, some cuttings move in suspension in the inner hole of drill pipe, which enlarges the air flow passage to weaken the influence of the drill cuttings layer at the bottom of pipe on the airflow. So, the position with the maximum air flow velocity moves downward.

3.3. Forces between Cuttings and Air under Different Working Conditions.
In the process of reverse circulation pneumatic cuttings removal, there is a relationship between the action force and the reaction force besides the momentum exchange between drill cuttings and air. The interaction forces between drill cuttings and air in 0~2 s under different working conditions are extracted. As shown in Figure 12, the variation of interaction forces between drill cuttings and air under different working conditions with time is analysed.

Figure 12(a) shows that the interaction forces between drill cuttings and air increase continuously with time when the air velocity is 15 m/s. When the mass flow rate of cuttings is 0.06 kg/s, the interaction forces between two phases increase slowly with time. With the increase of the mass flow rate of cuttings, the slope of the force curves between two phases increase and the forces between two phases increase. When the air velocity is 20 m/s, 25 m/s, 30 m/s, and 35 m/s, respectively, the interaction forces between the cuttings and air increase first. And then, the forces stabilize with time. The time-varying curves of the interaction forces between two phases are divided into the

"growth section" and the "stable section" for analysis. It can be seen that, under the same air velocity, with the increase of the mass flow rate of cuttings, the slope of the "growth section" increases, the corresponding time length increases, and the interaction forces between the two phases of the "stable section" increase. When the mass flow rate of cuttings is constant, the slope of the "growth section" curve increases with the increases of the air velocity, and the corresponding time length becomes shorter, while the interaction forces between the two phases in the "stable section" become larger. When the air velocity is greater than 20 m/s, there is no accumulation of drill cuttings in the inner hole of drill pipe. The amount of drill cuttings in the drill pipe reaches the dynamic balance state and the interaction forces between the two phases remain relatively stable. When the mass flow rate of cuttings keeps constant, with the increase of the air velocity, the movement speed of drill cuttings becomes faster, and the time of reaching the "stable section" of the interaction forces between two phases becomes shorter. Although the increase of air velocity decreases the number of cuttings in the drill pipe, the drag force of a single cuttings by the flow field increases significantly at this time. So, the interaction forces between the two phases tend to increase. At the same air velocity, with the increase of the mass flow rate of cuttings, the amount of cuttings in the drill pipe increases and the interaction forces between the two phases increase. At the same time, the increase of the number of drill cuttings slows down the cuttings velocity. So, the time when the interaction forces between two phases reach the "stable section" becomes longer. It can be seen that the variation of the interaction forces between drill cuttings and air with time can be used to judge whether the cuttings-air two-phase flow reaches a stable state in the simulation process.
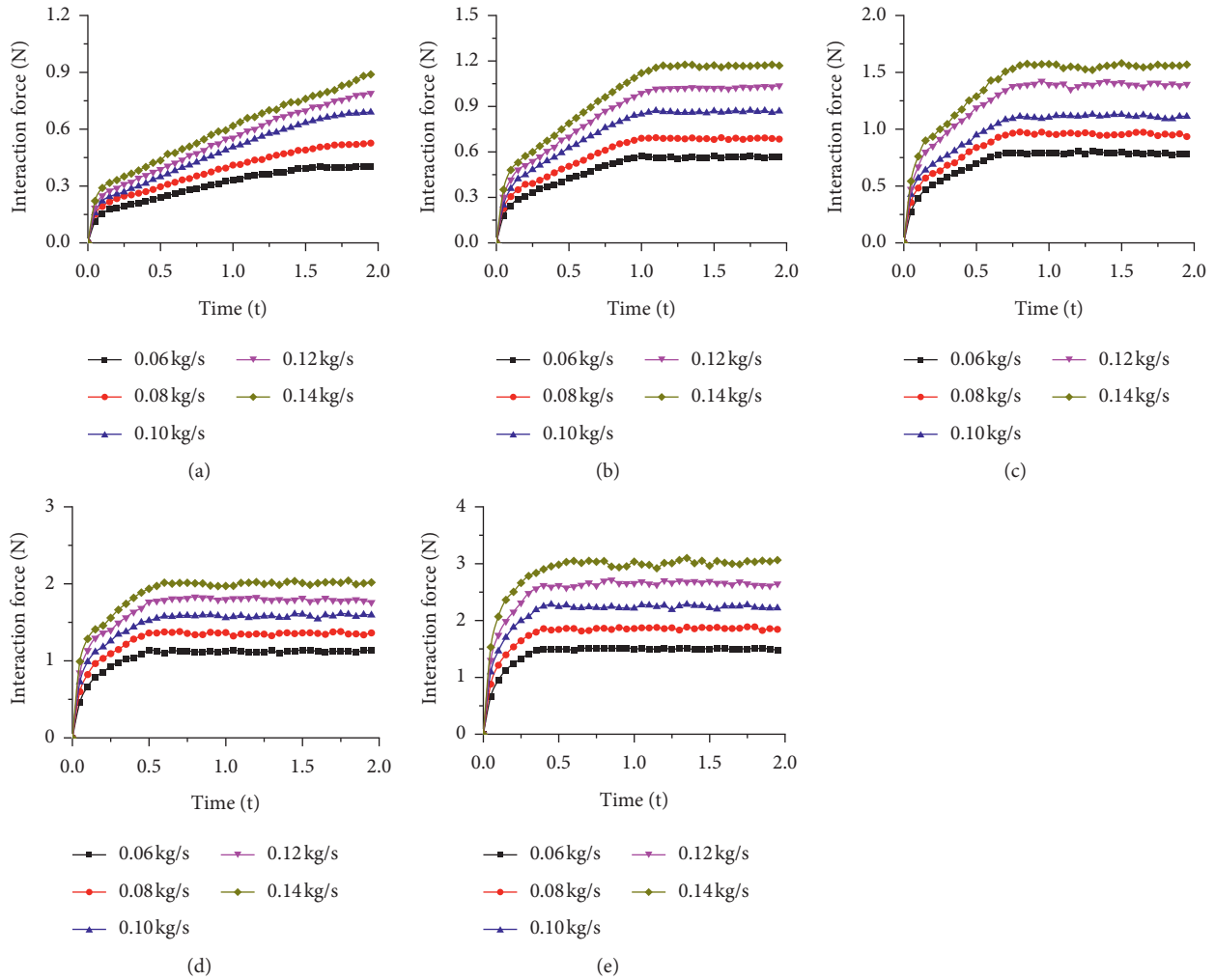
FIGURE 12: Interaction forces between cuttings and air: (a) $v_a = 15$ m/s, (b) $v_a = 20$ m/s, (c) $v_a = 25$ m/s, (d) $v_a = 30$ m/s, and (e) $v_a = 35$ m/s.

3.4. Cuttings Removal Effect under Different Working Conditions. In order to analyze the influence of different working conditions on the effect of reverse circulation pneumatic cuttings removal, the cuttings migration ratio is used to evaluate the cuttings removal effect [22]. The cuttings migration ratio is defined as the ratio of the average cuttings velocity in the drill pipe to the air velocity under the corresponding working conditions. Figure 13 shows the cuttings migration ratio under different working conditions.

Figure 13 shows that, when the mass flow rate of cuttings is constant, the cuttings migration ratio is positively correlated with the air velocity, while when the air velocity is constant, the cuttings migration ratio is negatively correlated with the mass flow rate of cuttings. In addition, when the air velocity is low, the difference between the cuttings migration ratios under different mass flow rate of cuttings is large. With the increase of the air velocity, the difference between the cuttings migration

ratios under different mass flow rate of cuttings decreases gradually. Drill cuttings move along the flow direction with the characteristics of pipe bottom flow under the action of airflow drag force and self-gravity after entering the inner hole of drill pipe. When the air velocity is low, the pipe bottom flow characteristics are significant. At this time, the collision and friction between cuttings-cuttings, drill pipe-cuttings have a greater influence on the cuttings movement, which result in the average velocity of drill cuttings far lower than the air velocity. The effect of cuttings removal is poor. With the increase of air velocity, the characteristics of pipe bottom flow weaken, and some drill cuttings move in suspension in the inner hole of drill pipe. The collision and friction between cuttings-cuttings, drill pipe-cuttings decrease. So, the cuttings migration ratio increases. When the air velocity is constant, the increase of the mass flow rate of cuttings increases the amount of cuttings in the drill pipe. The influence of collision and friction between cuttings-
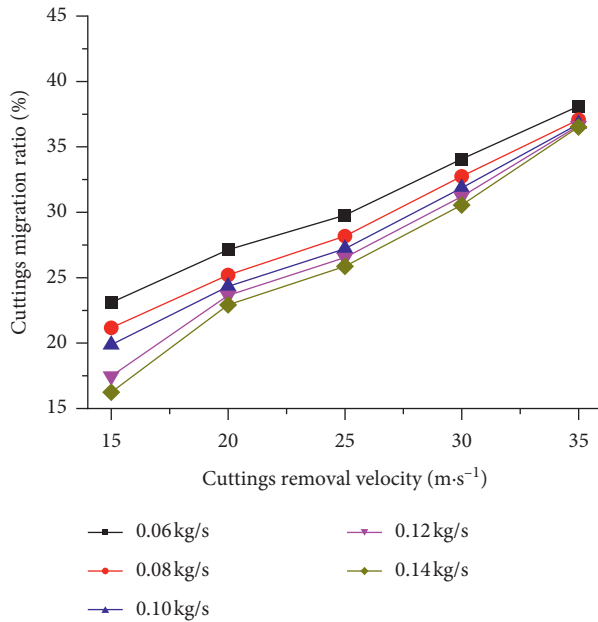
FIGURE 13: Cuttings migration ratio under different working conditions.

FIGURE 14: Air flow pressure drop under different working conditions.

cuttings, drill pipe-cuttings on the cuttings movement is intensified. So, the cuttings removal effect becomes worse. Compared with the low air velocity, the higher air velocity can make the drill cuttings be discharged from the drill pipe in time and effectively. The amount of drill cuttings in the drill pipe is relatively small. The increase of the mass flow rate of cuttings has little effect on the cuttings movement. Therefore, under the condition of low air velocity, the cuttings migration ratio varies greatly with different mass flow rate of cuttings. Under the condition of high air velocity, the increase of mass flow rate of cuttings has little effect on the cuttings migration ratio.

3.5. Pressure Drop of Cuttings-Air Two-Phase Flow.
The drill cuttings generated by the drilling bit breaking coal enter the inner hole of drill pipe under the action of air flow and discharge along the flow direction. In this process, all kinds of energy consumed by air flow and drill cuttings movement are compensated by the pressure energy of the air flow. So, the pressure drop of air flow can be used to characterize the energy consumption of cuttings-air two-phase flow [23]. The pressure drop of cuttings-air two-phase flow in the inner hole of drill pipe under different working conditions is shown in Figure 14.

As can be seen from Figure 14, the pressure drop of cuttings-air two-phase flow is significantly higher than that in the inner hole of drill pipe under the pure air flow, which indicates that the drill cuttings cause the greater energy consumption to the air flow. The pressure drop shows the same trend with the increase of air velocity under different mass flow rate of cuttings. At the same mass flow rate of cuttings, the pressure drop increases with the increase of air velocity. And, at the same air velocity, the pressure drop also increases with the increase of the mass flow rate of cuttings.
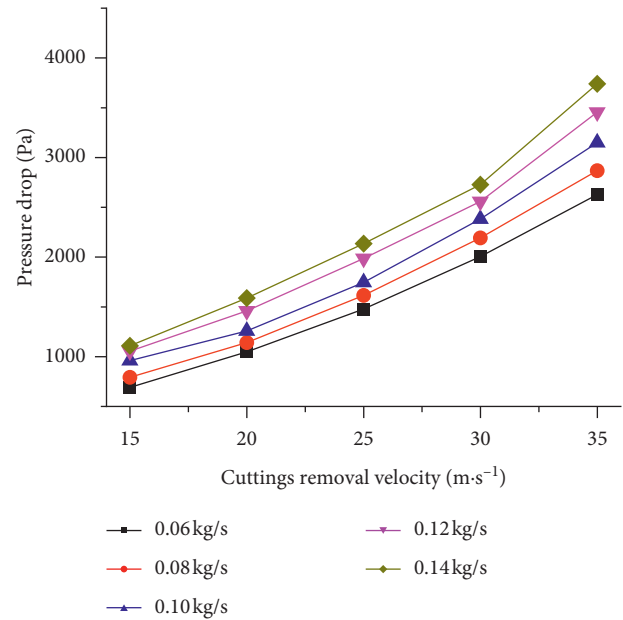
The pressure drop in the inner hole of drill pipe is mainly composed of two parts. One part is the friction pressure drop of air flow. The other part is the pressure drop caused by the drill cuttings which includes the energy consumption caused by the collision and friction among cuttings-cuttings and drill pipe-cuttings during the cuttings removal and the kinetic energy obtained by the drill cuttings. When the mass flow rate of cuttings is constant, the mixing ratio of drill cuttings to air decreases with the increase of the air velocity, but the friction pressure drop of air flow and the kinetic energy of drill cuttings increases. So, the pressure drop increases with the increase of the air velocity. At the same air velocity, with the increase of the mass flow rate of cuttings, the mixing ratio of cuttings and air increases and the porosity in the inner hole of drill pipe decreases. At this time, the energy consumption increases due to the collision and friction among cuttings-cuttings and cuttings-drill pipe, so the pressure drop also increases with the increase of the mass flow rate of cuttings.

In conclusion, the higher air velocity increases the pressure drop of air flow and the air consumption. Therefore, in order to avoid unnecessary energy consumption, on the premise of ensuring the smooth discharge of drill cuttings from the drill hole, the appropriate air velocity should be selected to determine the air volume of Roots vacuum pump. Taking the simulation model in this paper as an example, when the air velocity is 15 m/s, the amount of cuttings increases along the flow direction, and the velocity of cuttings decreases. So, the drill cuttings will accumulate in the inner hole of drill pipe. If the air velocity is greater than 20 m/s, the amount of cuttings will decrease along the flow direction. The speed and pressure drop of drill cuttings will increase. So, 20 m/s is selected as the appropriate air velocity of cuttings removal.

4. Conclusions

In this paper, the CFD-DEM coupling method is used to simulate the two-phase flow of drill cuttings and air in the inner hole of drill pipe with the reverse circulation pneumatic cuttings removal technology during the horizontal drilling in coal seam. The effects of the air velocity and the mass flow rate of cuttings on the two-phase flow characteristics, cuttings removal effect, and pressure drop of the flow field are analysed. The results show that the following:

(1) With the increase of air velocity, the drag force of drilling cuttings becomes larger. The characteristic length of drilling cuttings flow becomes longer. The thickness of the cuttings layer decreases further along the flow direction. A small amount of drilling cuttings distributes in the upper part of the inner hole of drill pipe and the cuttings movement speed is higher than that of the bottom cuttings. The stratified flow characteristic is obvious.

(2) When the air velocity of cuttings removal is 15 m/s, the proportion of drill cuttings along the flow direction increases, the forces between the cuttings and air increase continuously with time, and the cuttings velocity decreases. So, the drill cuttings are easy to accumulate in the inner hole of drill pipe. If the air velocity is greater than 20 m/s, the proportion of cuttings along the flow direction decreases and the cuttings velocity increases.

(3) When the mass flow rate of cuttings is constant, the cuttings migration ratio is positively correlated with the air velocity. When the air velocity is constant, the cuttings migration ratio is negatively correlated with the mass flow rate of cuttings. The interaction forces between drill cuttings and air increase first. And then, the forces stabilize with time.

(4) At the same mass flow rate of cuttings, the pressure drop of the cuttings-air two-phase flow increases with the increase of air velocity. At the same air velocity, the pressure drop of the cuttings-air two-phase flow increases with the increase of the mass flow rate of cuttings. So, 20 m/s is selected as the appropriate air velocity for cuttings removal considering the pressure drop of cuttings-air two-phase flow and the flow characteristics of drill cuttings.

Data Availability

The data used to support the findings of this study are available from the corresponding author upon request.

Conflicts of Interest

The authors declare that there are no conflicts of interest regarding the publication of this paper.

References

[1] C. Liu, *Study on mechanism and controlling of borehole collapse in soft coal seam*, Ph.D. thesis, China University of Mining and Technology, Xuzhou, China, 2014.

[2] N. Yao, X. Yin, Y. Wang, L. Wang, and Q. Ji, "Practice and drilling technology of gas extraction borehole in soft coal seam," *Procedia Earth and Planetary Science*, vol. 3, pp. 53–61, 2011.

[3] Y.-L. Wang, Y.-N. Sun, X.-X. Zhai, and Z.-F. Wang, "Study on new drilling technology in soft and outburst seam," *Journal of Mining and Safety Engineering*, vol. 29, no. 2, pp. 289–294, 2012.

[4] Y. L. Wang, Z. F. Wang, and W. Y. Lu, "Analysis on pressure loss of drill cuttings movement caused by gas-solid coupling in gas extraction borehole," *Science and Technology of Safety Production in China*, vol. 4, pp. 13–19, 2015.

[5] X.-M. Han, L.-L. Zhang, Y. Liu, and Z.-H. Tie, "Chip removal mechanism by air reverse circulation during horizontal drilling in soft outburst coal seam," *Science and Technology of Safety Production in China*, vol. 11, no. 5, pp. 26–31, 2015.

[6] X. M. Han, S. N. Song, and J. L. Li, "Pressure drop characteristics of reverse circulation pneumatic cuttings removal during coal seam drilling," *Science Progress*, vol. 103, no. 2, pp. 1–20, 2020.

[7] G. Niu and W. Zhang, "Study on critical air velocity and pressure loss of pneumatic coal dust removal for boreholes along coal seams," *China Safety Science Journal*, vol. 23, no. 11, pp. 60–65, 2013.

[8] B. Guo, T. A. G. Langrish, and D. F. Fletcher, "CFD simulation of precession in sudden pipe expansion flows with low inlet swirl," *Applied Mathematical Modelling*, vol. 26, no. 1, pp. 1–15, 2002.

[9] A. Riaz and M. A. Sadiq, "Particle-fluid suspension of a non-newtonian fluid through a curved passage: an application of urinary tract infections," *Frontiers in Physics*, vol. 8, p. 109, 2020.

[10] A. Riaz, A. Zeeshan, S. Ahmad, A. Razaq, and M. Zubair, "Effects of external magnetic field on non-Newtonian two phase fluid in an annulus with peristaltic pumping," *Journal of Magnetics*, vol. 24, no. 1, pp. 62–69, 2019.

[11] S. I. Abdelsalam, M. M. Bhatti, A. Zeeshan, A. Riaz, and O. A. Bég, "Metachronal propulsion of a magnetised particle-fluid suspension in a ciliated channel with heat and mass transfer," *Physica Scripta*, vol. 94, no. 11, Article ID 115301, 2019.

[12] N. Ijaz, A. Riaz, A. Zeeshan, R. Ellahi, and S. M. Sait, "Buoyancy driven flow with gas-liquid coatings of peristaltic bubbly flow in elastic walls," *Coatings*, vol. 10, no. 2, p. 115, 2020.

[13] J.-W. Zhou, C.-L. Du, S.-Y. Liu, and Y. Liu, "Comparison of three types of swirling generators in coarse particle pneumatic conveying using CFD-DEM simulation," *Powder Technology*, vol. 301, pp. 1309–1320, 2016.

[14] J.-W. Zhou, Y. Liu, S.-Y. Liu, C.-L. Du, and J.-P. Li, "Effects of particle shape and swirling intensity on elbow erosion in dilute-phase pneumatic conveying," *Wear*, vol. 380-381, pp. 66–77, 2017.

[15] P. W. Jian, H. T. Zhang, and Y. G. Wang, "The gas-solid flow characteristics of cyclones," *Powder Technology*, vol. 308, pp. 178–129, 2017.

[16] S. Akhshik, M. Behzad, and M. Rajabi, "CFD-DEM approach to investigate the effect of drill pipe rotation on cuttings transport behavior," *Journal of Petroleum Science and Engineering*, vol. 127, pp. 229–244, 2015.

[17] S. Akhshik, M. Behzad, and M. Rajabi, "CFD-DEM simulation of the hole cleaning process in a deviated well drilling: the effects of particle shape," *Particuology*, vol. 25, pp. 72–82, 2015.

[18] B. Shao, Y. F. Yan, and C. F. Bi, "Migration of irregular cuttings particles in big size by CFD-DEM coupled simulation model," *Science, Technology and Engineering*, vol. 17, no. 27, pp. 195–200, 2017.

[19] B. Sun, H. Xiang, H. Li, and X. Li, "Modeling of the critical deposition velocity of cuttings in an inclined-slimhole annulus," *SPE Journal*, vol. 22, no. 4, pp. 1213–1224, 2017.

[20] Y.-J. Kim, N.-S. Woo, Y.-K. Hwang, J.-H. Kim, and S.-M. Han, "Transport of small cuttings in solid-liquid flow with inclined slim hole annulus," *Journal of Mechanical Science and Technology*, vol. 28, no. 1, pp. 115–126, 2014.

[21] Z. L. Yuan, L. P. Zhu, and F. Geng, *Gas-Solid Two Phase Flow and Numerical Simulation*, Southeast University Press, Nanjing, China, 2013.

[22] M. Sorgun, "Simple correlations and analysis of cuttings transport with Newtonian and non-Newtonian fluids in horizontal and deviated wells," *Journal of Energy Resources Technology*, vol. 135, no. 3, Article ID 032903, 6 pages, 2013.

[23] C. Liang, L. Shen, P. Xu et al., "Comparison of pressure drops through different bends in dense-phase pneumatic conveying system at high pressure," *Experimental Thermal and Fluid Science*, vol. 57, pp. 11–19, 2014.

Research Article

Numerical and Computer Simulations of Cross-Flow in the Streamwise Direction through a Moving Surface Comprising the Significant Impacts of Viscous Dissipation and Magnetic Fields: Stability Analysis and Dual Solutions

Yu-Ming Chu [1,2] **Umair Khan,**[3] **A. Zaib** [4,5] **and S. H. A. M. Shah**[3]

[1]*Department of Mathematics, Huzhou University, Huzhou 313000, China*
[2]*Hunan Provincial Key Laboratory of Mathematical Modeling and Analysis in Engineering,*
 Changsha University of Science & Technology, Changsha 410114, China
[3]*Department of Mathematics and Social Sciences, Sukkur IBA University, Sukkur 65200, Sindh, Pakistan*
[4]*Department of Natural Sciences, The Begum Nusrat Bhutto Women University, Sukkur 65170, Pakistan*
[5]*Department of Mathematical Sciences, Federal Urdu University of Arts Science & Technology, Gulshan-e-Iqbal,*
 Karachi-75300, Pakistan

Correspondence should be addressed to A. Zaib; aurangzaib@fuuast.edu.pk

Received 18 July 2020; Revised 6 September 2020; Accepted 13 September 2020; Published 30 September 2020

Academic Editor: Marin Marin

The inspiration for this study is to explore the crucial impact of viscous dissipation (VISD) on magneto flow through a cross or secondary flow (CRF) in the way of streamwise. Utilizing the pertinent similarity method, the primary partial differential equations (PDEs) are changed into a highly nonlinear dimensional form of ordinary differential equations (ODEs). These dimensionless forms of ODEs are executed numerically by the aid of bvp4c solver. The impact of pertinent parameters such as the suction parameter, magnetic parameter, moving parameter, and viscous dissipation parameter is discussed with the help of plots. Dual solutions are obtained for certain values of a moving parameter. The velocities in the direction of streamwise, as well as cross-flow, decline in the upper branch solution, while the contrary impact is seen in the lower branch solution. However, the influence of suction on the velocities in both directions uplifts in the upper branch solution and shrinks in the lower branch solution. The analysis is also performed in terms of stability to inspect which solution is stable or unstable, and it is observed that the lower branch solution is unstable, whereas the upper branch one is stable.

1. Introduction

The investigations of CRFS started after the pioneering research by Blasius [1] and Prandtl [2] on the laminar flow from a flat surface through a miniature viscosity. Prandtl [3] seemed to be a primary researcher to give the result for the regular depress gradient flow through a yawed infinite cylinder. The study through cross-flow or secondary flow is significant in many engineering applications such as a flow of wind phenomena, mechanical, aerospace, and rotating disk. Jones [4] discussed the vital results involving the problem of CRF, where he scrutinized the influence of

sweepback on the boundary layer flow (BOUNLF). The three-dimensional flow past flat surface, as well as curved surfaces, was explored by Mager [5]. Bhattacharyya and Pop [6] examined the dissipation impact on forced convective flow in the way of CRF. Weidman [7] found the outcomes of the flow over an exponentially stretching surface involving the power law at which CRFS is shaped via the activity of the transverse wall shearing. Haq et al. [8] scrutinized the CRF in the direction of streamwise (STW) from a heated moving surface comprising the influence of viscous dissipation (VISD). Itu et al. [9] utilized the finite element technique to improve the rigidity of circular composite surfaces via radial

ribs. Khan et al. [10] considered the combined impacts of a chemical reaction (CHEMR) and activation energy (ACTIE) comprising nanoparticles through a CRF and STW direction with nonlinear radiation. They reported the dual nature of solutions. Recently, Nisar et al. [11] explored the nonlinear radiation impact on MHD flow of titanium and aluminum alloy particles in the CRF and STW flow direction.

The investigations of the properties of magnetic assets also named magnetohydrodynamics (MHD) flow on electrically conducting liquids conferred its importance in industrial and engineering fields such as heat insulation, geothermal systems, boilers, saltwater, nuclear process, energy storage, and biological transportation. Abbas [12] obtained the equation of frequency for radial vibrations through a poroelastic cylinder in a porous lid by utilizing Biot's theory for wave propagation. Groza and Pop [13] explored the fractional problems of linear multipoint as well as two-point boundary value and obtained the numerical solution by implementing the Haar wavelet technique. Niculita et al. [14] used the finite element technique by utilizing the skin panel for the adaptive wing. Ali [15] found the dual outcomes of magnetoviscous flow through a nonlinear permeable shrinking surface. Mabood et al. [16] analyzed the influence of CHEMR on magnetorotated liquid from a vertical surface entrenched in a permeable medium with a heat source. Kumar et al. [17] scrutinized the frictional heating impact on magneto flow (MAGF) comprising Ferro liquid in the existence of radiation. Bhatti and Rashidi [18] explored the entropy analysis on magnetonanoliquid through a stretching sheet. Abbas and Marin [19] established the generalized thermoelasticity through a pulsed laser and obtained the analytic solution. The stimulus of thermal and exponential space-dependent heat sources on MHD nanoliquid through a rotating disk was observed by Makinde et al. [20]. Riaz et al. [21] considered the impact of bioheat on the 3D flow of non-Newtonian fluid in a peristaltic motion through a rectangular cross-section. Mabood Shateyi [22] deliberated the time-dependent MAGF with heat and mass transport embedded in a porous stretching sheet with radiation. Recently, Ahmad et al. [23] investigated the magnetic field on time-dependent squeezing flow between two horizontal surfaces involving non-Newtonian liquid.

The fluctuating destruction of the velocity gradients through the viscous stresses is signified as viscous dissipation. This fractional irreversible process is frequently referred to as the conversion of kinetic energy into internal energy of the liquid (heating up the liquid owing to viscosity because dissipation is elevated in the regions through great gradients). The concept of VISD was first considered by Brinkman [24]. He utilized the viscous dissipation (VISD) concept in the capillary flows. Gebhart [25] scrutinized the impact of VISD in free convective liquid flows. The stimulus of VISD on free convective flow in the non-Darcy regime was explored by Murthy and Singh [26], and they explored the ten percent decrement in three split regions of fluids. Tunc and Bayazitoglu [27] utilized the technique of integral transform to solve the problem containing viscous dissipation along with the transfer of heat in microtubes. The influences of thermal radiation (THERMR) and VISD on

time-dependent magneto flow through a heated infinite vertical surface were inspected by Cookey et al. [28]. Partha et al. [29] discovered the VISD influence on mixed convective flow through an exponential stretched sheet. Ibrahim et al. [30] studied the combined effects of THERMR and VISD on time-dependent flow involving micropolar fluid. The BOUNLF and the transfer rate of heat involving Sisko liquid from an expanded or stretched cylinder through erratic thermal conductivity and VISD were inspected by Malik et al. [31]. Recently, Hussain et al. [32] discussed the impact of VISD on MAGF of a non-Newtonian liquid over a nonlinear heated stretched surface.

As discussed earlier, the problem containing combined effects of the magnetic field and viscous dissipation is not yet explored. Therefore, we are examining the viscous dissipation effect along with the magnetic field in the cross-flow and streamwise directions with the characteristic of heat transport. Another important contribution regarding the problem is the complex dual nature of solutions and the stability analysis which of most researchers missed out. This assessment added an innovative methodology for the researchers, engineers, and scientists to find out the key features of the transfer rate of heat in the STW direction of CRF. The subsequent model is numerically handled using bvp4c software. The effects of the important parameters are contested with the assistance of graphs. The problems involving cross-flow taken here are exceptional in that the transverse motion is believed to be fully developed. In several engineering conditions, the cross-flowing stream may be dependent strongly on the orientation and position of a second leading edge.

2. Problem Formulation

The current proposed model is measured using the approach of streamwise (STW) and cross-flow (CRF) directions within the boundary layer. The Cartesian coordinates and their corresponding velocities are symbolically denoted by (x, y, z) and (u, v, w), respectively. Based on the secondary flow phenomena, to deal with the three-dimensional (cross-flow and streamwise directions) flow over a heated surface under the variable applied magnetic field, $B(x) = B_0/\sqrt{2x}$. They accomplish a motion along with an unchanged velocity $-\lambda U_1$ into and out of the origin located at a position x equal zero, where the coordinate x is run in the path of a flat surface, while the dimensionless moving parameter and the unchanged velocity are denoted by λ and U_1, respectively. Also, T_w and T_∞ are the uniform wall and ambient temperature of the liquid, whereas the constant and ambient or free-stream concentration of the liquid are symbolically signified by C_w and C_∞, respectively. The problem is schematically captured in Figure 1. Also, it is presumed that the CRF has a range that is extended widely in the spanwise direction. So, the components of the momentum, energy, and concentration equation did not depend upon the z coordinate. The exercising of the aforementioned conventions along with the Boussinesq approximation and the BOUNDL scaling the leading PDEs is [6, 8, 11]
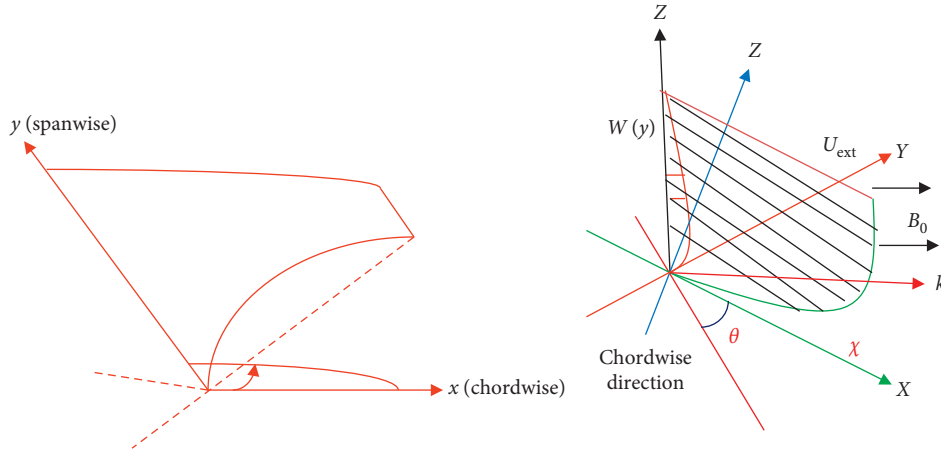
FIGURE 1: Diagram of the problem.

$$u_x + v_y = 0, \tag{1}$$

$$uu_x + vu_y - v_f u_{yy} = \frac{\sigma_f B^2}{\rho_f}(U_1 - u), \tag{2}$$

$$uw_x + vw_y - v_f w_{yy} = \frac{\sigma_f B^2}{\rho_f}(w_1 - w), \tag{3}$$

$$uT_x + vT_y - \alpha_f T_{yy} = \frac{\mu_f}{(\rho c_p)_f}\left(\left(u_y\right)^2 + \left(w_y\right)^2\right), \tag{4}$$

$$uC_x + vC_y = D_B C_{yy}, \tag{5}$$

with the corresponding boundary conditions

$$u(x, 0) = -\lambda U_1,$$
$$v(x, 0) = v_0,$$
$$w(x, 0) = 0,$$
$$T(x, 0) = T_w,$$
$$C(x, 0) = C_w, \tag{6}$$
$$u(x, y) \longrightarrow U_1,$$
$$w(x, y) \longrightarrow w_1,$$
$$T(x, y) \longrightarrow T_\infty,$$
$$C(x, y) \longrightarrow C_\infty \text{ as } y \longrightarrow \infty.$$

Here, the component velocities in the respective directions of $x-$, $y-$, and $z-$axes are signified by $u(x, y), v(x, y)$, and $w(x, y)$, respectively, while the subscript such as x and y of the velocity components is called the partial derivatives. The other symbols involved in equations (1)–(6) are abbreviated as the dynamic viscosity μ_f, density ρ_f, temperature of the liquid T, thermal diffusivity α_f, effective heat capacity $(\rho c_p)_f$, concentration C, Brownian diffusion coefficient D_B, and thermal conductivity k_f. For simplicity, the technique for solving the problem here by introducing the similarity transformations is as follows:

$$\eta = y\sqrt{\frac{U_1}{2xv_f}},$$

$$\psi = \sqrt{2xU_1 v_f}\,f(\eta),$$

$$w = w_1 g(\eta), \tag{7}$$

$$\phi(\eta) = \frac{C_\infty - C}{C_\infty - C_w},$$

$$\theta(\eta) = \frac{T_\infty - T}{T_\infty - T_w}.$$

Thus, equation (1) is true identically, while equations (2)–(5) are worked out by the similarity variables. The governing dimensional form of ordinary differential equations become as follows:

$$\frac{d^3 f}{d\eta^3} + f\frac{d^2 f}{d\eta^2} + M\left(1 - \frac{df}{d\eta}\right) = 0, \tag{8}$$

$$\frac{d^2 g}{d\eta^2} + f\frac{dg}{d\eta} + M(1 - g) = 0, \tag{9}$$

$$\frac{d^2\theta}{d\eta^2} + \Pr f\frac{d\theta}{d\eta} + \Pr\left[Ec_1\left(\frac{d^2 f}{d\eta^2}\right)^2 + Ec_2\left(\frac{dg}{d\eta}\right)^2\right] = 0, \tag{10}$$

$$\frac{d^2\phi}{d\eta^2} + Le f\frac{d\phi}{d\eta} = 0. \tag{11}$$

The converted boundary conditions are

$$f(\eta) = S,$$

$$\frac{df(\eta)}{d\eta} = -\lambda,$$

$$g(\eta) = 0,$$

$$\theta(\eta) = 1,$$

$$\phi(\eta) = 1, \text{ at } \eta = 0,$$

$$\frac{df(\eta)}{d\eta} \longrightarrow 1,$$

$$g(\eta) \longrightarrow 1,$$

$$\theta(\eta) \longrightarrow 0,$$

$$\phi(\eta) \longrightarrow 0 \text{ as } \eta \longrightarrow \infty. \tag{12}$$

In the aforementioned equations, the dimensionless sundry parameters are mathematically expressed as follows: $M = \sigma B_0^2 / \rho_f U_1$, $\Pr = \nu_f / \alpha_f$, $Le = \alpha_f / D_B$, $Ec_1 = U_1^2 / c_p$ $(T_w - T_\infty)$, and $Ec_2 = w_1^2 / c_p (T_w - T_\infty)$ are, respectively, called the magnetic parameter, Prandtl number, Lewis number, and Eckert numbers.

2.1. Skin Friction.
The coefficient of skin friction over the STW (C_{fx}) in the x-direction and CRF (C_{fz}) in the z-direction is written as

$$C_{fx} = \frac{\mu_f(u_y)_{y=0}}{\rho_f U_1} = \frac{f''(0)}{\sqrt{2Re_x}},$$

$$C_{fz} = \frac{\mu_f(w_y)_{y=0}}{\rho_f w_1^2} = \frac{g'(0)}{\sqrt{2Re_x}(w_1/U_1)}. \tag{13}$$

2.2. Nusselt Number.
The local rate of heat transfer in dimensionless form is written as

$$Nu_x = \frac{x(-k_f T_y)_{y=0}}{k_f(T_w - T_\infty)} = -\frac{\theta'(0)}{\sqrt{2Re_x}}. \tag{14}$$

2.3. Sherwood Number.
The local Sherwood number in dimensionless form is written as

$$Sh_x = \frac{x(-C_y)_{y=0}}{D_f(C_w - C_\infty)} = -\frac{\phi'(0)}{\sqrt{2Re_x}}, \tag{15}$$

where the correlation of the Reynolds number is $Re_x = xU_1/\nu_f$.

3. Stability Analysis

Within this section, the linear stability analysis of the solutions achieved is carried out to test their stability. Because of such purpose, we cited the work concluded through the study of Merkin [33]. Considering the time-dependent form of equations (2)–(5) along with BC (6), we may write

$$u_t + uu_x + vu_y - v_f u_{yy} = \frac{\sigma B^2}{\rho_f}(U_1 - u), \tag{16}$$

$$w_t + uw_x + vw_y - v_f w_{yy} = \frac{\sigma B^2}{\rho_f}(w_1 - w), \tag{17}$$

$$T_t + uT_x + vT_y - \alpha_f T_{yy} = \frac{\mu_f}{(\rho c_p)_f}\left((u_y)^2 + (w_y)^2\right), \tag{18}$$

$$C_t + uC_x + vC_y = D_B(C_{yy}), \tag{19}$$

subject to the boundary conditions

$$u(x, 0, t) = -\lambda U_1,$$
$$v(x, 0, t) = v_0,$$
$$w(x, 0, t) = 0,$$
$$T(x, 0, t) = T_w,$$
$$C(x, 0, t) = C_w, \tag{20}$$
$$u(x, y, t) \longrightarrow U_1,$$
$$w(x, y, t) \longrightarrow w_1,$$
$$T(x, y, t) \longrightarrow T_\infty,$$
$$C(x, y, t) \longrightarrow C_\infty \text{ as } y \longrightarrow \infty.$$

By letting the fresh time-dependent similarity variable τ, the old transformations (7) may be in mathematical form as follows:

$$\eta = y\sqrt{\frac{U_1}{2xv_f}},$$

$$\psi = \sqrt{2xU_1 v_f} f(\eta),$$

$$w = w_1 g(\eta), \tag{21}$$

$$\theta(\eta) = \frac{T - T_\infty}{T_w - T_\infty},$$

$$\phi(\eta) = \frac{C - C_\infty}{C_w - C_\infty},$$

where $\tau = U_1 t/2x$ and $\eta = y\sqrt{U_1/2xv_f}$.

Using (21), equations (16)–(19) along with the appropriate BC (20) reduce to the simplest form as follows:

$$\frac{\partial^3 f(\eta, \tau)}{\partial \eta^3} + \left(2\tau \frac{\partial f(\eta, \tau)}{\partial \eta} \frac{\partial^2 f(\eta, \tau)}{\partial \tau \partial \eta} - \frac{\partial^2 f(\eta, \tau)}{\partial \tau \partial \eta}\right)$$
$$+ f(\eta, \tau) \frac{\partial^2 f(\eta, \tau)}{\partial \eta^2} + \frac{\sigma_f B_0^2}{\rho_f U_1}\left(1 - \frac{\partial f(\eta, \tau)}{\partial \eta}\right) = 0, \tag{22}$$

$$\frac{\partial^2 g(\eta,\tau)}{\partial \eta^2} + \left(2\tau \frac{\partial f(\eta,\tau)}{\partial \eta} \frac{\partial g(\eta,\tau)}{\partial \tau} - \frac{\partial g(\eta,\tau)}{\partial \tau}\right)$$
$$+ f(\eta,\tau) \frac{\partial g(\eta,\tau)}{\partial \eta} + \frac{\sigma_f B_0^2}{\rho_f U_1}(1 - g(\eta,\tau)) = 0, \tag{23}$$

$$\frac{1}{\text{Pr}} \frac{\partial^2 \theta(\eta,\tau)}{\partial \eta^2} + Ec_1 \left(\frac{\partial^2 f(\eta,\tau)}{\partial \eta^2}\right)^2 + f(\eta,\tau) \frac{\partial \theta(\eta,\tau)}{\partial \eta}$$
$$+ Ec_2 \left(\frac{\partial g(\eta,\tau)}{\partial \eta}\right)^2 - \frac{\partial \theta(\eta,\tau)}{\partial \tau} = 0, \tag{24}$$

$$\frac{\partial^2 \phi(\eta,\tau)}{\partial \eta^2} + Le f(\eta,\tau) \frac{\partial \phi(\eta,\tau)}{\partial \eta} - \frac{\partial \phi(\eta,\tau)}{\partial \tau} = 0, \tag{25}$$

along with the corresponding BCs

$$f(\eta,\tau) = S,$$
$$\frac{\partial f(\eta,\tau)}{\partial \eta} = -\lambda,$$
$$g(\eta,\tau) = 0,$$
$$\theta(\eta,\tau) = 1,$$
$$\phi(\eta,\tau) = 1 \text{ at } \eta = 0, \tag{26}$$
$$\frac{\partial f(\eta,\tau)}{\partial \eta} \longrightarrow 1,$$
$$g(\eta,\tau) \longrightarrow 1,$$
$$\theta(\eta,\tau) \longrightarrow 0,$$
$$\phi(\eta,\tau) \longrightarrow 0 \text{ as } \eta \longrightarrow \infty.$$

The key physical dimensional constraints involved in the above equations are the same and are defined earlier. The stability analysis of the free time-dependent solution $f(\eta,0) = f_0(\eta)$ and $g(\eta,0) = g_0(\eta)$ for the momentum equation in both directions and further $\theta(\eta,0) = \theta_0(\eta)$ and $\phi(\eta,0) = \phi_0(\eta)$ signify the corresponding energy and concentration equations. Let

$$f(\eta,\tau) = f_0(\eta) + e^{-\beta t} F(\eta,\tau),$$
$$g(\eta,\tau) = g_0(\eta) + e^{-\beta t} G(\eta,\tau),$$
$$\theta(\eta,\tau) = \theta_0(\eta) + e^{-\beta t} \Theta(\eta,\tau), \tag{27}$$
$$\phi(\eta,\tau) = \phi_0(\eta) + e^{-\beta t} \Phi(\eta,\tau),$$

where β highlights the eigenvalues. Using (27) into (22)–(26), we may achieve the following linearized eigenvalue problem:

$$F''' + f_0 F'' + F f_0'' + \beta F' - MF' = 0, \tag{28}$$

$$G'' + f_0 G' + F g_0' + \beta G - MG = 0, \tag{29}$$

$$\Theta'' + \text{Pr}\left[f_0 \Theta' + F\theta_0' + Ec_1 (2f_0'F'')^2 + Ec_2 (2g_0'G')^2 + \beta\Theta\right] = 0, \tag{30}$$

$$\Phi'' + Le(f_0\Phi' + F\phi_0') + \beta\Phi = 0. \tag{31}$$

along with the appropriate BCs

$$F(\eta) = 0,$$
$$F'(\eta) = 0,$$
$$G(\eta) = 0,$$
$$\Theta(\eta) = 0,$$
$$\Phi(\eta) = 0 \text{ at } \eta = 0, \tag{32}$$
$$F'(\eta) \longrightarrow 0,$$
$$G(\eta) \longrightarrow 0,$$
$$\Theta(\eta) \longrightarrow 0,$$
$$\Phi(\eta) \longrightarrow 0 \text{ at } \eta = \infty.$$

The eigenvalue outcome of the linearized-type problem provides the class of eigenvalues. Because of the approach of linear stability analysis, the initial deceleration of disturbance, which is a physically reliable outcome (stable), is observed because of the positive coarse eigenvalue, while the initial development of disturbance is occurred owing to the negative coarse values which provide the unstable outcome. Furthermore, it is easy to note all of the positive smallest eigenvalues which indicates that the results achieved are stable and physically consistent. Therefore, in the current problem, equations (28)–(32) are solved for the eigenvalue β with the new BC $F'' = 1$ by relaxing the condition that $F' \longrightarrow 0$ as $\eta \longrightarrow \infty$.

4. Results and Discussion

In this current section, the numerical results of the streamwise and cross-flow problem governed by the set of nonlinear partial differential equations (PDEs) are presented. To solve the nonlinear PDEs (2)–(5), the similarity variables are first introduced to transform the problem into a system of highly nonlinear ODEs (8)–(11). These ODEs are very difficult to solve exactly; therefore, it can be tackled numerically by using the scheme of finite difference for boundary value problem based on the three-stage Lobatto IIIA. For the computations, the fixed values assigned to the parameters are $S = Le = 0.5, \lambda = -3.5$, $M = 0.1, Ec_1 = 0.1$, $Ec_2 = 0.2$, and $\text{Pr} = 6.2$. The dual or multiple solutions of the problem under consideration are obtained for the specific range of the stretching and shrinking constraints. In our results, the upper branch solution and the lower branch solution is depicted graphically with the solid and dotted lines, respectively.

4.1. Effects of Magnetic Parameter. The influence of the magnetic parameter M is captured in the STW and CRF directions in Figures 2(a) and 2(b), respectively. The
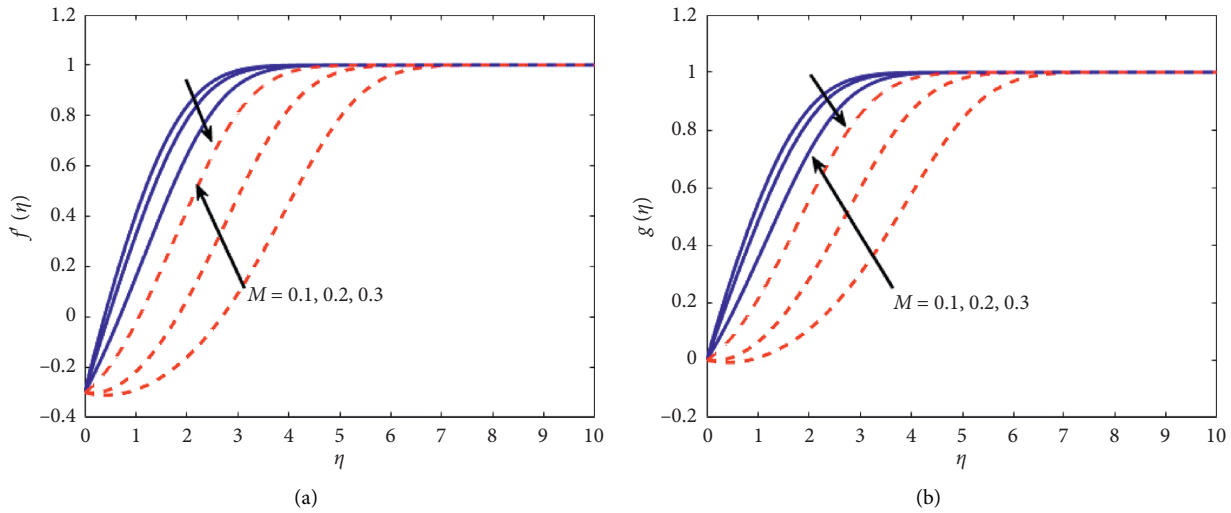
(a)

(b)

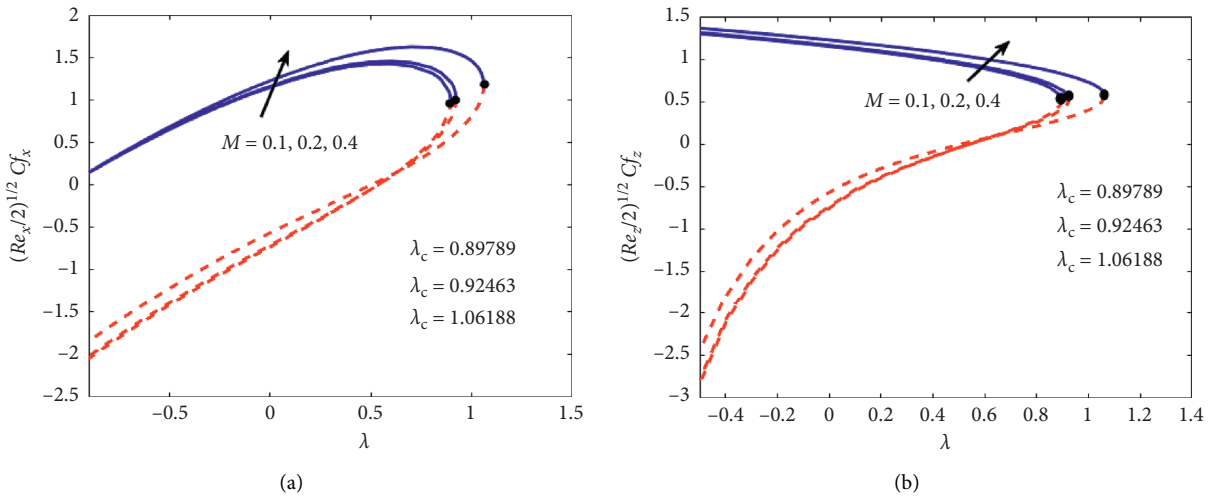Figure 2: (a, b) Impact of M on $f'(\eta)$ and $g(\eta)$.

(a)

(b)

Figure 3: (a, b) Impact of M versus λ on $(2\text{Re}_x)^{1/2}Cf_x$ and $(2\text{Re}_x)^{1/2}Cf_z$.

solutions obtained for $f'(\eta)$ and $g(\eta)$ satisfy the initial and boundary conditions. The velocity profiles in the STW and CRF directions decrease in the first branch solution and increase in the second branch solution. Physically, this is happening due to a larger amount of M which can slow down the liquid motion; this occurs due to retarding force known as Lorentz force. Figures 3(a) and 3(b) explain that the skin friction in both directions increases owing to the constraint M in the first branch solution, while the changed behavior is observed in the second branch solution. On the other hand, the rate of heat and mass transfer decreases in the first branch solution and enhances the second branch solution as portrayed in Figures 4(a) and 4(b), respectively. The huge magnetic limit develops the force called drag which is also entitled as Lorentz force. This force controls as mediators that resist the fluid flow and craft progress in the local transfer rate of heat and mass along with the local coefficient of skin coefficient.

4.2. Influence of Suction Parameter. In the porous medium, the mass suction/injection parameter is important and is defined with the expression $S = -v_0\sqrt{2x/v_fU_1}$. In case of suction, $(S > 0)$ and for injection, $(S < 0)$. If $(S < 0)$, the dual nature of solutions cannot be obtained. However, the dual solutions exist in the case of mass suction. In Figures 5(a) and 5(b), the variation of the suction parameter S on both the velocity profiles in the STW direction in terms of $f'(\eta)$ and the CRF in terms of $g(\eta)$ is displayed. These results suggest that the velocity of liquid augments due to increasing values of S in the upper branch solution which in turn reduces the velocity BOUNLF thickness, while there is a decline in the lower branch solution in the STW and CRF directions. Generally, because of S, the heated liquid is shoved toward a surface of the wall where the forces can retard the liquid owing to lofty control of the viscosity. The skin friction coefficients in both directions are displayed in Figures 6(a) and 6(b). These figures show that the
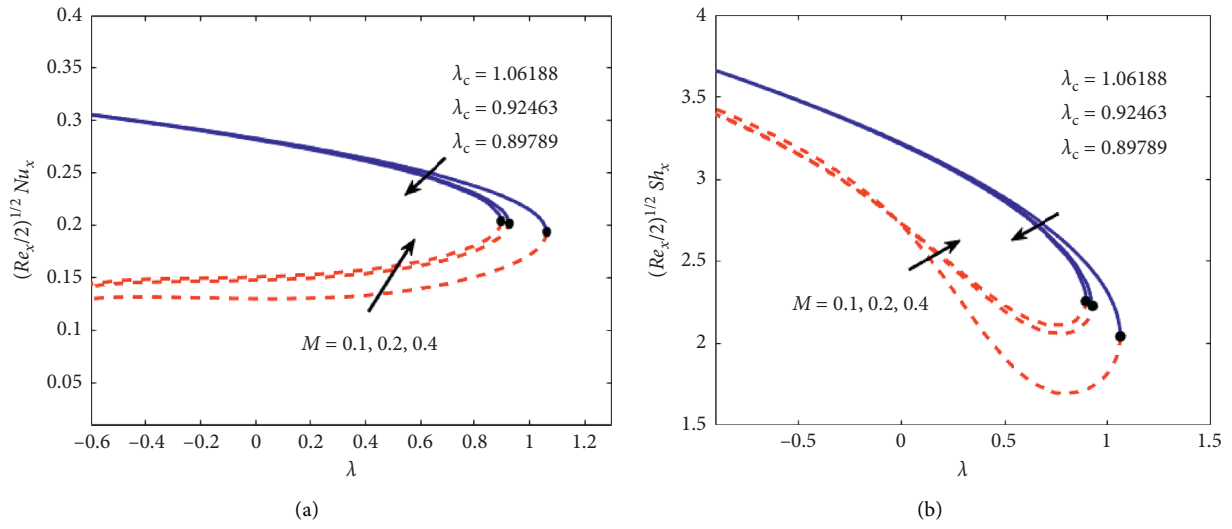
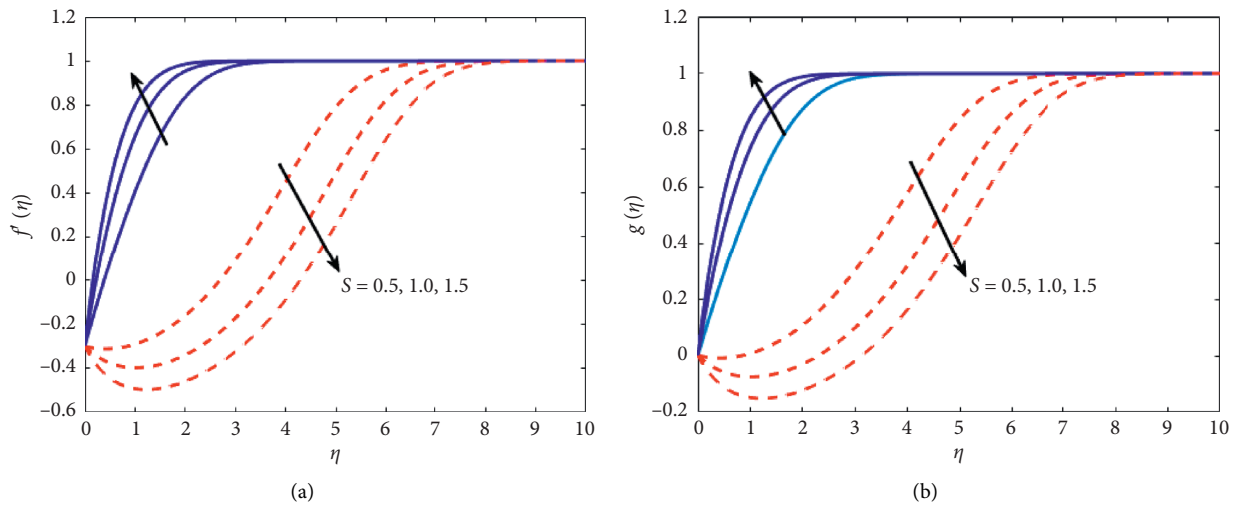Figure 4: (a, b) Impact of M versus λ on $(2\mathrm{Re}_x)^{1/2}Nu_x$ and $(2\mathrm{Re}_x)^{1/2}Sh_x$.

Figure 5: (a, b) Impact of S on $f'(\eta)$ and $g(\eta)$.
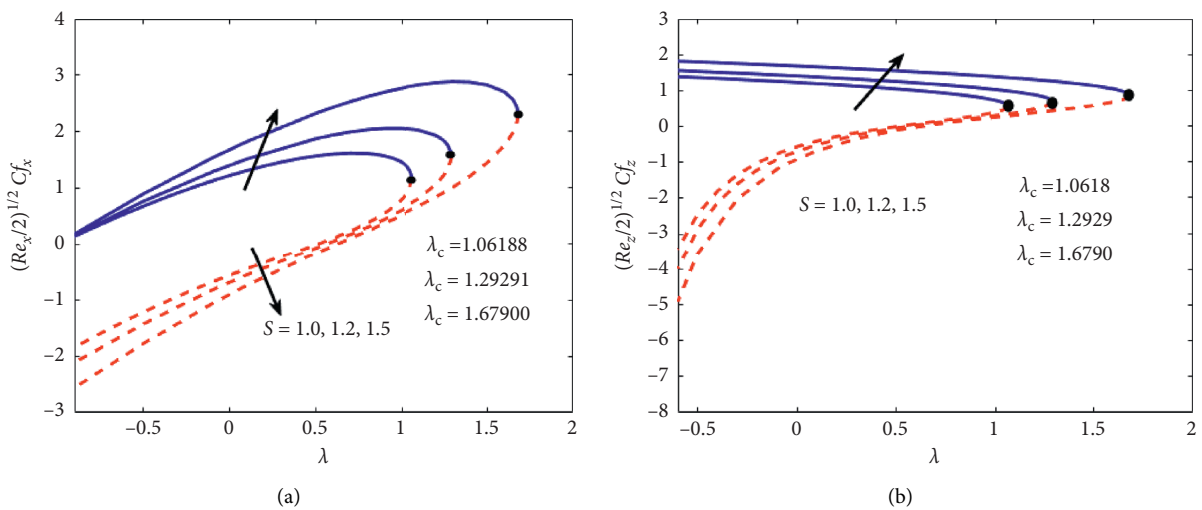
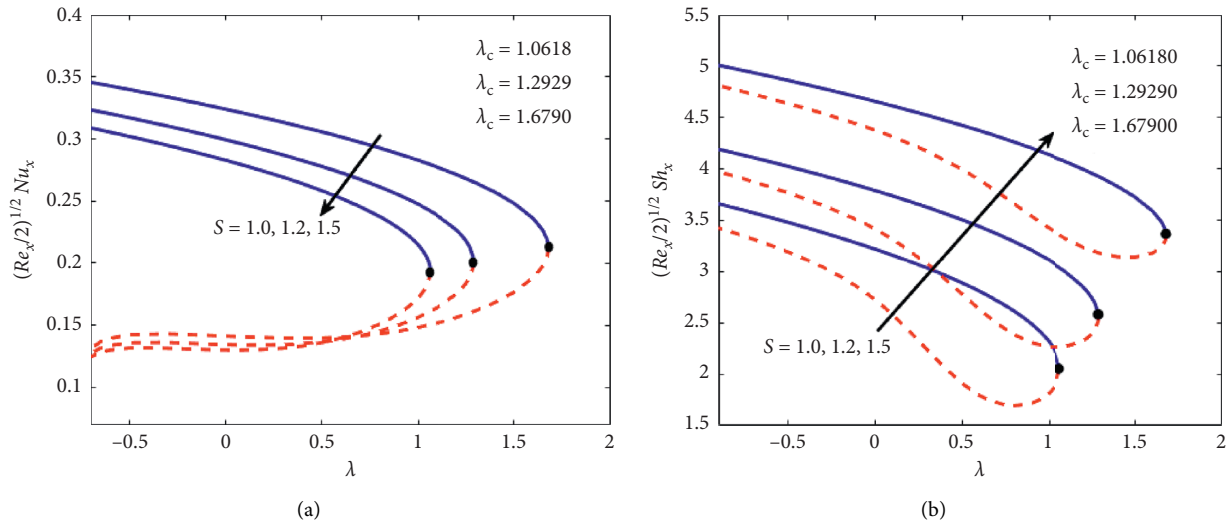Figure 6: (a, b) Impact of S versus λ on $(2\mathrm{Re}_x)^{1/2}Cf_x$ and $(2\mathrm{Re}_x)^{1/2}Cf_z$.

Figure 7: (a, b) Impact of S versus λ on $(2\mathrm{Re}_x)^{1/2} Nu_x$ and $(2\mathrm{Re}_x)^{1/2} Sh_x$.
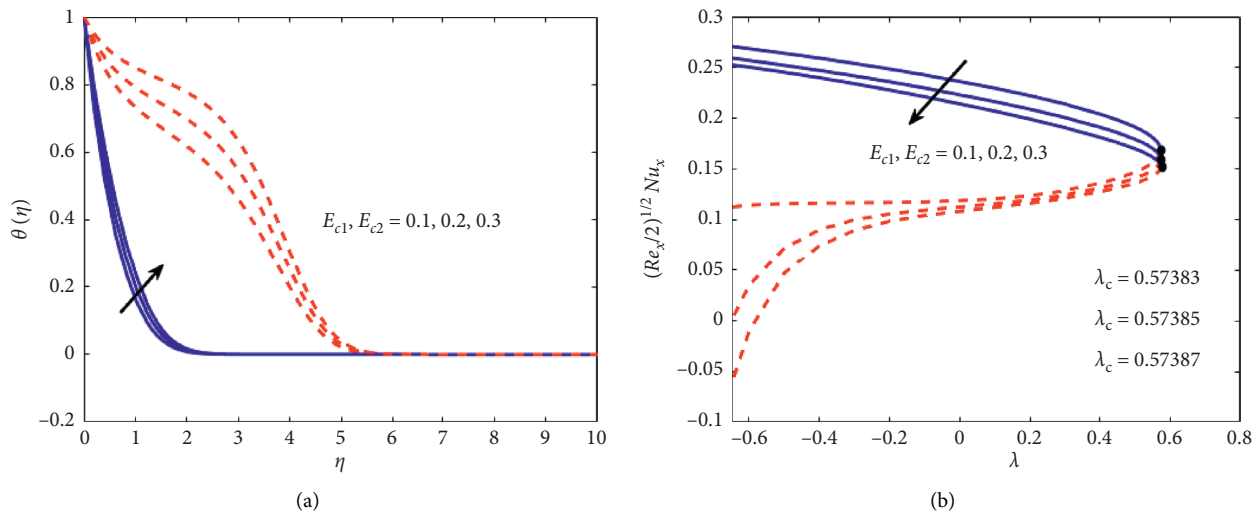

Figure 8: (a, b) Impact of E_{c1} and E_{c2} on $\theta(\eta)$ versus λ on $(2\mathrm{Re}_x)^{1/2} Nu_x$.

upper branch solution increases while the second branch result decreases as the mass suction parameter increases. The variation of S on the local transfer rate of heat and mass is presented in Figures 7(a) and 7(b), respectively. Figure 7(a) depicts the values of the local rate of heat transfer decline due to augmenting S in both branches of solutions, whereas the Sherwood number augments with S in the upper and lower branch solutions as revealed in Figure 7(b).

4.3. Effects of Eckert Numbers. The Eckert parameters appear in the energy equation due to the viscous dissipation term. The Eckert numbers have a direct impact on the rate of heat transfer. As the Eckert numbers upsurge, more heat is transferred from the surface due to which the thermal boundary layer increases. This impacts of E_{c1} and E_{c2} on temperature $\theta(\eta)$ is displayed in Figure 8(a). However, the increases in Eckert numbers show a decrease in Nusselt

number (Figure 8(b)). This is predictable since the implementation of the Eckert number proposes the ratio of kinetic energy and enthalpy. Thus, an augment in E_{c1} and E_{c2} suggests that the heat dissipated is stored in the liquid via fractional heating that enhances the liquid temperature and consequently declines the heat transfer rate.

4.4. Effects of Lewis Number. Lewis number L_e appears in the concentration equation and is a ratio of the kinematic viscosity and the Brownian diffusion coefficient. The influence of L_e on concentration $\phi(\eta)$ is demonstrated in Figure 9(a). The graphical result shows that the concentration profile decreases for both solutions. This implies that the heat will disperse more quickly than concentration. The concentration boundary layer becomes steeper as L_e enhances. Moreover, the increase in L_e shows an increase in the Sherwood number (Figure 9(b)).
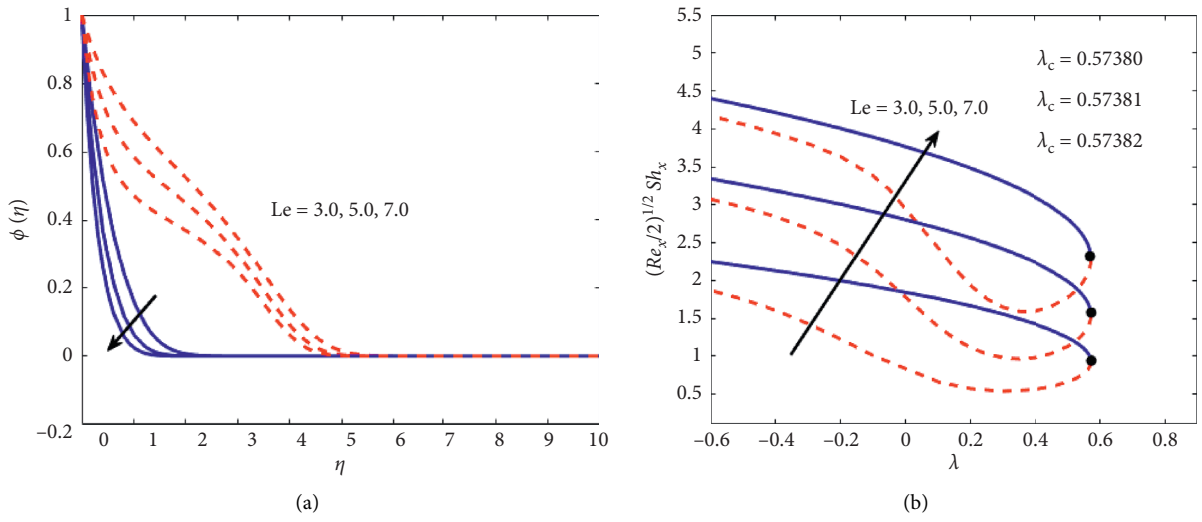
Figure 9: (a, b) Impact of L_e on $\phi(\eta)$ versus λ on $(2Re_x)^{1/2}Sh_x$.
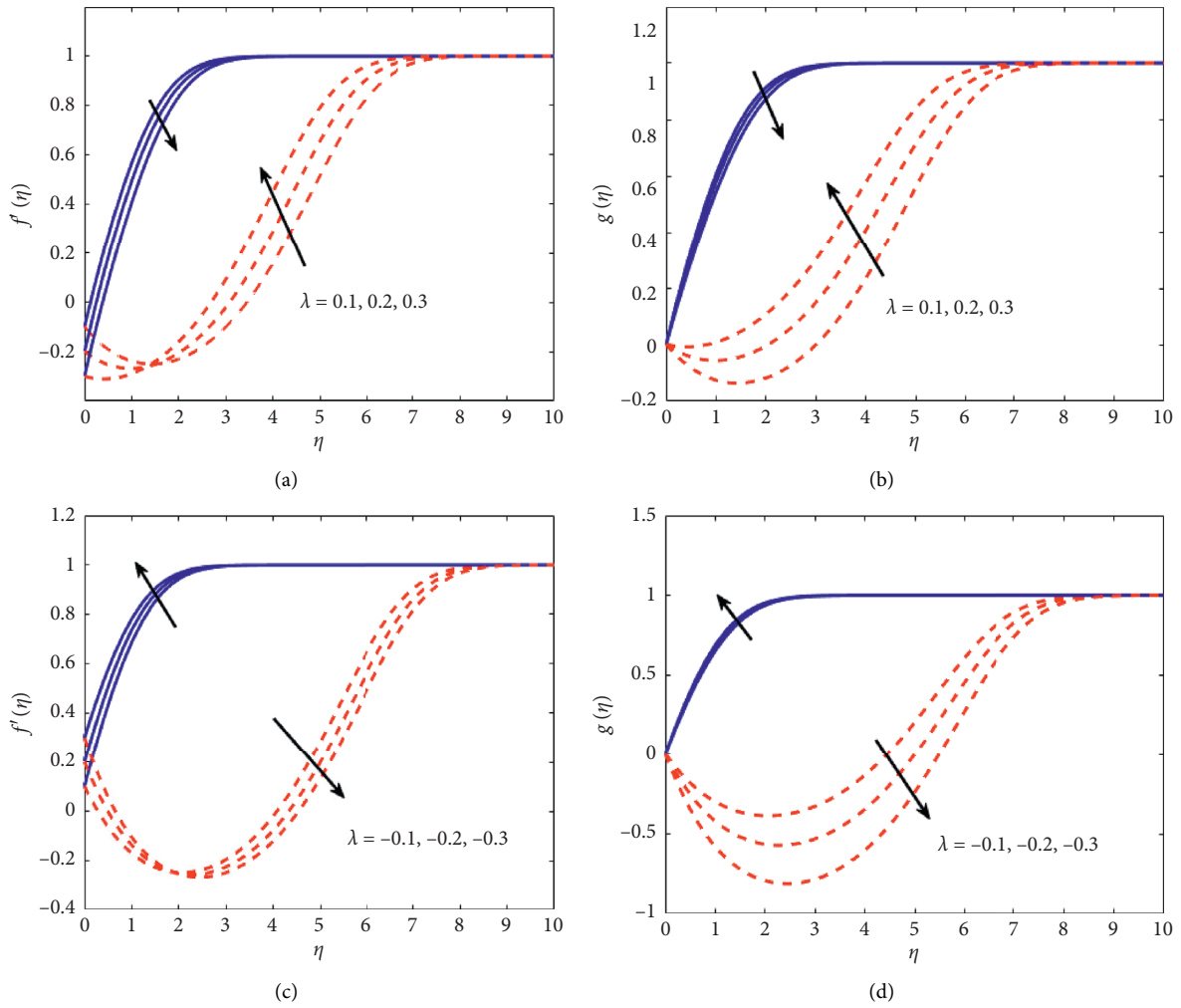

Figure 10: (a–d) Impact of λ on $f'(\eta)$ and $g(\eta)$.

4.5. Effects of Stretching and Shrinking Parameters. In Figures 10(a)–10(d), the variations of stretching/shrinking parameters on the velocities $f'(\eta)$ and $g(\eta)$ in both directions are displayed. The effect of the stretching parameter (Figures 10(a) and 10(b)) shows that the lower branch solution decreases while the upper branch solution increases. On the other hand, the altered behavior is noted for the shrinking parameter, as illustrated in Figures 10(c) and 10(d). It is also examined from these figures that, in the phenomenon of the lower branch solution, initially, the velocity profiles are negative, and then as the value of η progresses, it starts to augment and then becomes positive. Physically, this trend happens due to the contrary directions of shrinking and stretching velocities.

5. Conclusions

In the current investigation, the impact of VISD on MAGF near a stagnation point in the directions of STW and CRF through a moving surface is scrutinized. The leading PDEs are converted into nonlinear ODEs via suitable variables. These converted ODEs are worked out by utilizing bvp4c software based on 3-stage Lobatto IIIA. The influences of pertinent constraints on the flow fields such as concentration, velocity, and temperature are illustrated graphically and numerically scrutinized. The core finding of this exploration can be precised as follows:

(i) Because of some amount of moving parameter, multiple solutions are achieved

(ii) The velocity of liquid decays owing to M in the upper branch solution and upsurges in the lower branch solution in the STW and CRF directions

(iii) The friction factor in the STW and CRF directions augments because of the larger value of M in the upper branch solution, while the rate of mass and heat transfer decelerates in the upper branch solution and augments in the lower branch solution

(iv) The mass suction parameter enhances the velocity and friction factor in the upper branch solution and drops in the lower branch solution, whereas the rate of heat transfer declines and the Sherwood number upsurges in the first and second branch solutions

(v) The temperature distribution enhances due to the Eckert number, while the transfer rate of heat declines due to the Eckert number in the upper and lower branch solutions

(vi) The concentration profile decelerates with increasing values of L_e in the first branch (upper) solution and the second branch (lower) solutions

(vii) The values of the Sherwood number uplift in both branches of solutions due to L_e

Finally, this paper can be expanded by taking a time-dependent flow or mixed convective flow. Also, the non-Newtonian fluid or hybrid nanofluid may be added due to numerous applications.

Abbreviations

B_0:	Magnetic field intensity
C:	Concentration
C_∞:	Ambient fluid concentration
C_w:	Wall concentration
C_{fx} and C_{fz}:	Skin friction coefficients
D_B:	Brownian diffusion coefficient
Ec_1 and Ec_2:	Eckert numbers
f and g:	Dimensionless velocities
k_f:	Thermal conductivity
L_e:	Lewis number
M:	Magnetic parameter
Nu_x:	Nusselt number
Pr:	Prandtl number
R_d:	Radiation parameter
Re_x:	Local Reynolds number
S:	Suction
Sh_x:	Sherwood number
T:	Temperature
T_∞:	Free-stream temperature
T_w:	Temperature of wall
U_1:	Constant velocity
w_0:	Transverse velocity
(u, v, w):	Velocity components
(x, y, z):	Cartesian coordinates
α_f:	Thermal diffusivity
β:	Eigenvalues
λ:	Moving parameter
μ_f:	Dynamic viscosity
ρ_f:	Density
$(\rho c_p)_f$:	Effective heat capacity
θ:	Dimensionless temperature
v_f:	Kinematic viscosity
ψ:	Stream function
τ:	Time-dependent similarity variable
':	Derivative w. r. t. η.

Data Availability

No data were used to support this study.

Conflicts of Interest

The authors declare that they have no conflicts of interest.

Acknowledgments

References

[1] H. Blasius, "Grenzschichten in flüssigkeiten mit kleiner reibung," *Zeitschrift für angewandte Mathematik und Physik*, vol. 56, pp. 1–37, 1908.

[2] L. Prandtl, "Uber flussigkeitsbewegung bei sehr kleiner reibung," in *Interactive Mathematics.*Kongregate, San Francisco, CA, USA, 1904.

[3] L. Prandtl, "On boundary layers in three-dimensional flow," *Aeronautical Research Council*, vol. 9829, 1946.

[4] R. T. Jones, "Effects of sweepback on boundary-layer and separation,"*Technical report, National Advisory Committee 884 NTRS - NASA Technical Reports USA AmesAeronautical Laboratray*, Moffett Field, CA, USA, 1947.

[5] A. Mager, "Three-dimensional laminar boundary layer with small cross-flow," *Journal of the Aeronautical Sciences*, vol. 21, no. 12, pp. 835–845, 1954.

[6] K. Bhattacharyya and I. Pop, "Heat transfer for boundary layers with cross flow," *Chinese Physics B*, vol. 23, no. 2, Article ID 024701, 2014.

[7] P. Weidman, "Similarity solutions for power-law and exponentially stretching plate motion with cross flow," *International Journal of Non-Linear Mechanics*, vol. 89, pp. 127–131, 2017.

[8] R. U. Haq, F. A. Soomro, Z. H. Khan, and Q. M. Al-Mdallal, "Numerical study of streamwise and cross flow in the presence of heat and mass transfer," *European Physical Journal Plus*, vol. 132, no. 5, p. 214, 2017.

[9] C. Itu, A. Öchsner, S. Vlase, and M. I. Marin, "Improved rigidity of composite circular plates through radial ribs," *Proceedings of the Institution of Mechanical Engineers, Part L: Journal of Materials: Design and Applications*, vol. 233, no. 8, pp. 1585–1593, 2019.

[10] U. Khan, A. Zaib, I. Khan, and K. S. Nisar, "Activation energy on MHD flow of titanium alloy (Ti6Al4V) nanoparticle along with a cross flow and streamwise direction with binary chemical reaction and non-linear radiation: Dual Solutions," *Journal of Materials Research and Technology*, vol. 9, no. 1, pp. 188–199, 2019.

[11] K. S. Nisar, U. Khan, A. Zaib, I. Khan, and D. Baleanu, "Exploration of aluminum and titanium alloys in the streamwise and secondary flow directions comprising the significant impacts of magnetohydrodynamic and hybrid nanofluid," *Crystals*, vol. 10, no. 8, p. 679, 2020.

[12] I. A. Abbas, "Natural frequencies of a poroelastic hollow cylinder," *Acta Mechanica*, vol. 186, no. 1–4, pp. 229–237, 2006.

[13] G. Groza and N. Pop, "A numerical method for solving of the boundary value problems for ordinary differential equations," *Results in Mathematics*, vol. 53, no. 3-4, pp. 295–302, 2012.

[14] C. Niculita, S. Vlase, A. Bencze, M. Mihalcica, M. R. Calin, and L. Serbina, "Optimum stacking in a multi-ply laminate used for the skin of adaptive wings, Optoelect," *Advanced Material-Rapid Communications*, vol. 5, no. 11, pp. 1233–1236, 2011.

[15] F. M. Ali, R. Nazar, N. M. Arifin, and I. Pop, "Dual solutions in MHD flow on a nonlinear porous shrinking sheet in a viscous fluid," *Boundary Value Problems*, vol. 2013, no. 1, 2013.

[16] F. Mabood, S. M. Ibrahim, and G. Lorenzini, "Chemical reaction effects on MHD rotating fluid over a vertical plate embedded in porous medium with heat source," *Journal of Engineering Thermophysics*, vol. 26, no. 3, pp. 399–415, 2017.

[17] K. A. Kumar, V. Ramana Reddy Janke, S. Vangala, and S. Naramgari, "Impact of frictional heating on MHD radiative ferrofluid past a convective shrinking surface," *Defect Diffusion Forum*, vol. 378, pp. 157–174, 2017.

[18] M. M. Bhatti and M. M. Rashidi, "Numerical simulation of entropy generation on MHD nanofluid towards a stagnation point flow over a stretching surface," *International Journal of Applied and Computational Mathematics*, vol. 3, no. 3, pp. 2275–2289, 2017.

[19] I. A. Abbas and M. Marin, "Analytical solution of thermo-elastic interaction in a half-space by pulsed laser heating," *Physica E: Low-Dimensional Systems and Nanostructures*, vol. 87, pp. 254–260, 2017.

[20] O. D. Makinde, B. Mahanthesh, B. J. Gireesha, N. S. Shashikumar, R. L. Monaledi, and M. S. Tshehla, "MHD nanofluid flow past a rotating disk with thermal radiation in the presence of aluminum and titanium alloy nanoparticles," *Defect and Diffusion Forum*, vol. 384, pp. 69–79, 2018.

[21] A. Riaz, R. Ellahi, M. M. Bhatti, and M. Marin, "Study of heat and mass transfer in the eyring-powell model of fluid propagating peristaltically through a rectangular compliant channel," *Heat Transfer Research*, vol. 50, no. 16, pp. 1539–1560, 2019.

[22] F. Mabood and S. Shateyi, "Multiple slip effects on MHD unsteady flow heat and mass transfer impinging on permeable stretching sheet with radiation," *Modelling and Simulation in Engineering*, vol. 2019, pp. 1–11, 2019.

[23] S. Ahmad, M. Farooq, A. Anjum, and S. Sheriff, "Investigation of convective heat and mass conditions in squeeze flow of a hydro-magnetic sutterby fluid," *Journal of Magnetics*, vol. 24, no. 4, pp. 688–697, 2019.

[24] H. C. Brinkman, "Heat effects in capillary flow I," *Applied Scientific Research*, vol. 2, no. 1, pp. 120–124, 1951.

[25] B. Gebhart, "Effects of viscous dissipation in natural convection," *Journal of Fluid Mechanics*, vol. 14, no. 2, pp. 225–232, 1962.

[26] P. V. S. N. Murthy and P. Singh, "Effect of viscous dissipation on a non-Darcy natural convection regime," *International Journal of Heat and Mass Transfer*, vol. 40, pp. 1251–1260, 1977.

[27] G. Tunc and Y. Bayazitoglu, "Heat transfer in microtubes with viscous dissipation," *International Journal of Heat and Mass Transfer*, vol. 44, no. 13, pp. 2395–2403, 2001.

[28] C. I. Cookey, A. Ogulub, and V. B. Omubo-Peppleb, "Influence of viscous dissipation and radiation on unsteady MHD free-convection flow past an infinite heated vertical plate in a porous medium with time-dependent suction," *International Journal of Heat and Mass Transfer*, vol. 46, no. 13, pp. 2305–2311, 2003.

[29] M. K. Partha, P. V. S. N. Murthy, and G. P. Rajasekhar, "Effect of viscous dissipation on the mixed convection heat transfer from an exponentially stretching surface," *Heat and Mass Transfer*, vol. 41, no. 4, pp. 360–366, 2005.

[30] F. S. Ibrahim, A. M. Elaiw, and A. A. Bakr, "Influence of viscous dissipation and radiation on unsteady MHD mixed convection flow of micropolar fluids," *Applied Mathematics & Information Sciences*, vol. 2, pp. 143–162, 2008.

[31] M. Y. Malik, A. Hussain, T. Salahuddin, M. Awais, S. Bilal, and F. Khan, "Flow of sisko fluid over a stretching cylinder and heat transfer with viscous dissipation and variable thermal conductivity: A numerical study," *AIP Advances*, vol. 6, no. 4, Article ID 045118, 2016.

[32] A. Hussain, M. Y. Malik, T. Salahuddin, A. Rubab, and M. Khan, "Effects of viscous dissipation on MHD tangent hyperbolic fluid over a nonlinear stretching sheet with convective boundary conditions," *Results in Physics*, vol. 7, pp. 3502–3509, 2017.

[33] J. H. Merkin, "On dual solutions occurring in mixed convection in a porous medium," *Journal of Engineering Mathematics*, vol. 20, no. 2, pp. 171–179, 1986.

Research Article

The Shape Effect of Gold Nanoparticles on Squeezing Nanofluid Flow and Heat Transfer between Parallel Plates

Umair Rashid,[1] Thabet Abdeljawad [ID],[2,3,4] Haiyi Liang [ID],[1,5] Azhar Iqbal [ID],[6] Muhammad Abbas [ID],[7] and Mohd. Junaid Siddiqui[6]

[1]*CAS Key Laboratory of Mechanical Behavior and Design of Materials, Department of Modern Mechanics,*
 University of Science and Technology of China, Hefei, Anhui 230026, China
[2]*Department of Mathematics and General Sciences, Prince Sultan University, Riyadh 11586, Saudi Arabia*
[3]*Department of Medical Research, China Medical University, Taichung 40402, Taiwan*
[4]*Department of Computer Science and Information Engineering, Asia University, Taichung 40402, Taiwan*
[5]*IAT-Chungu Joint Laboratory for Additive Manufacturing,*
 Anhui Chungu 3D Printing Institute of Intelligent Equipment and Industrial Technology, Wuhu, Anhui 241200, China
[6]*Mathematics and Natural Sciences, Prince Mohammad Bin Fahd University, Al Khobar 31952, Saudi Arabia*
[7]*Department of Mathematics, University of Sargodha, Sargodha 40100, Pakistan*

Correspondence should be addressed to Thabet Abdeljawad; tabdeljawad@psu.edu.sa and Haiyi Liang; hyliang@ustc.edu.cn

The focus of the present paper is to analyze the shape effect of gold (Au) nanoparticles on squeezing nanofluid flow and heat transfer between parallel plates. The different shapes of nanoparticles, namely, column, sphere, hexahedron, tetrahedron, and lamina, have been examined using water as base fluid. The governing partial differential equations (PDEs) are transformed into ordinary differential equations (ODEs) by suitable transformations. As a result, nonlinear boundary value ordinary differential equations are tackled analytically using the homotopy analysis method (HAM) and convergence of the series solution is ensured. The effects of various parameters such as solid volume fraction, thermal radiation, Reynolds number, magnetic field, Eckert number, suction parameter, and shape factor on velocity and temperature profiles are plotted in graphical form. For various values of involved parameters, Nusselt number is analyzed in graphical form. The obtained results demonstrate that the rate of heat transfer is maximum for lamina shape nanoparticles and the sphere shape of nanoparticles has performed a considerable role in temperature distribution as compared to other shapes of nanoparticles.

1. Introduction

Nanotechnology has recently emerged and has become a worldwide revolution to obtain exceptional qualities and features over the last few decades. It developed at such a fast pace and is still going through a revolutionary phase. Nanotechnology is coming together to play a crucial and commercial role in our future world. Gold nanoparticles are one of the utmost stable metal nanoparticles and their current fascinating features include assembly of several types in material science, individual nanoparticles behaviors, magnetic, nanocytotoxic, optical properties, size-related electronic, significant catalysis, and

biological applications. Gold nanoparticles have attracted research attention due to their properties and various potential applications. This progression would go to the later generation of nanotechnology that requires products of gold nanoparticles with precise shape, controlled size, large production facilities, and pureness. Gold nanoparticles are widely used as preferred materials in numerous fields because of their unique optical and physical properties, that is, surface plasmon oscillation for labeling, sensing, and imaging. Recently, significant developments have been made in biomedical fields with superior biocompatibility in therapeutics and treatment of various diseases. Gold nanoparticles can be prepared and conjugate

with numerous functionalizing agents such as dendrimers, ligands, surfactants, RNA, DNA, peptides, polymers, oligonucleotides, drugs, and proteins [1].

Squeezing nanofluid flow with the effect of thermal radiation and magnetohydrodynamics (MHD) has important uses in the development of the real world. It has gained the consideration of researchers due to its extensive usages. Squeezing flow has increasing usages in several areas, particularly in the food industry and chemical engineering. The undertakings and properties of the squeezing flow of nanofluid for industrial usages such as electronic, transportation, biomechanics, foods, and nuclear reactor have been explained in many publications in the open literature. There are various examples concerning squeezing flow but the most significant ones are injection, compression, and polymer preparation.

The squeezing flow of nanofluid has gained significant consideration due to the valuable verities of applications in the physical and biophysical fields [2]. Hayat et al. [3] discussed the MHD in squeezing flow by using two disks. Dib et al. [4] examined the analytical solution of squeezing nanofluid flow. Duwairi et al. [5] addressed the heat transfer on the viscous squeezed flow between parallel plates. Domairry and Hatami [6] examined the time-dependent squeezing of nanofluid flow between two surfaces by applying differential transformation techniques. Sheikholeslami and Ganji [7] studied the heat transfer in squeezed nanofluid flow based on homotopy perturbation method. The thermal radiation effect in two-dimensional and time-dependent squeezing flow was investigated using homotopy analysis method by Khan et al. [8]. Sheikholeslami et al. [9] presented the effect of MHD on squeezing nanofluid flow in a rotating system. Gupta and Saha Ray [10] investigated the unsteady squeezing nanofluid flow between two parallel plates by using the Chebyshev wavelet expansion. The effects of MHD on alumina-kerosene nanofluid and heat transfer within two horizontal plates were examined by Mahmood and Kandelousi [11].

In the fields of engineering and science, there are various mathematical problems to find but the exact solution is almost complicated. Homotopy analysis method (HAM) is a well-known and critical method for solving mathematics-related problems. The main advantage of the homotopy analysis method is finding the approximate solution to the nonlinear differential equation without linearization and discretization. Earlier time in 1992, Liao [12–16] introduced this technique to find out the analytical results of nonlinear problems. The author concluded that homotopy analysis method (HAM) quickly converges to an approximate solution. The homotopy analysis method gives us a series of solutions. The approximate solution by homotopy analysis method is quite perfect since it contained all the physical parameters involved in a problem. Due to the effectiveness and quick convergence of the solution, various researchers, namely, Rashidi et al. [17, 18] and Abbasbandy and Shirzadi [19, 20], used homotopy analysis method (HAM) to find the solutions of highly nonlinear and coupled equations. Hussain et al. [21] presented the bioconvection model for squeezing flow using homotopy analysis method with the effect of thermal radiation heat generation/absorption.

Heat transfer can be increased by using several methodologies and techniques such as increasing the heat transfer coefficient or heat transfer surface which allows for a higher heat transfer rate in small volume fraction. Cooling is a major technical challenge faced by increasing numbers of industries involving microelectronics, transportation, manufacturing, and solid-state lighting. So, there is an essential requirement for innovative coolant with a better achievement that would be employed for enhanced properties [22]. Recently, nanotechnology has contributed to improving the new and innovative class of heat transfer nanofluid. Base fluids are embedded with nanosize materials to obtain nanofluids (nanofibers, nanoparticles, nanotubes, nanorods, nanowires, droplet, or nanosheet) [23]. Significantly, nanofluids have the ability to enhance heat transfer rate in several areas like nuclear reactors, solar power plants, transportation industry (trucks, automobiles, and airplanes), electronics and instrumentation, biomedical applications, microelectromechanical system, and industrial cooling usages (cancer therapeutics, cryopreservation, and nanodrug delivery) [24]. There are several studies to show the applications of nanofluid heat transfer. Kristiawan et al. [25] studied the convective heat transfer in a horizontal circular tube using TiO_2-water nanofluid. Turkyilmazoglue and Pop discussed the heat and mass transfer of convection flow of nanofluids containing nanoparticles of Ag, Cu, TiO_2, Al_2O_3, and CuO [26]. Sheikholeslami and Ganji [7] presented the analytical results of heat transfer in water-Cu nanofluid. Qiang and Yimin [27] investigated the experimental studies of convective heat transfer in water-Cu nanofluid. Elgazery [28] examined the studies of Ag-Cu-Al_2O_3-TiO_2-water nanofluid over a vertical permeable stretching surface with a nonuniform heat source/sink. Rea et al. [29] studied the viscous pressure and convective heat transfer in a vertical heated tube of Al_2O_3-ZrO_2-water nanofluids. Salman et al. [30] discussed by using a numerical technique the concept of affecting convective heat transfer of nanofluid in microtube using different categories of nanoparticles such as Al_2O_3, Cuo, SiO_2, and ZnO. Sheikholeslami et al. [31, 32] studied hybrid nanofluid for heat transfer expansion. Hassan et al. [33] discussed convective heat transfer in Ag-Cu hybrid nanofluid flow. Bhatti et al. [34] examined numerically hall current and heat transfer effects on the sinusoidal motion of solid particles. Furthermore, many researchers did work on heat transfer and thermal radiation; see [35–39].

In light of the above literature study, it has been observed that Cu, Ag, Al_2O_3, SiO_2, Cuo, and ZnO are mostly used to find the heat transfer. The gold (Au) was rarely used to find the heat transfer rate due to mixed convection [40]. The shape of nanoparticles is very significant in the enhancement of heat transfer. It is necessary to find the heat transfer rate in nanofluid under the exact shapes of nanoparticles [41]. From the literature survey, it is observed that no effort has been made on gold (Au) nanoparticles shape effect on squeezing flow. The basic purpose of the present study is to analyze the shape effect of gold (Au) nanoparticles on squeezing nanofluid flow and heat transfer. Various types of nanoparticles are under deliberation: column, sphere, hexahedron, tetrahedron, and lamina. The effects of various

physical parameters on velocity and temperature distributions are analyzed through plotted graphs.

2. Problem Description

Consider heat transfer in the incompressible, two-dimensional, laminar, and stable squeezing nanofluid between two horizontal plates at $y = 0$ and $y = h$. The lower plate is fixed by two forces which are equal and opposite. Both the plates are separated by distance h. A uniform B magnetic field is applied along y-axis. Moreover, the effect of nonlinear thermal radiation is also considered. The thermophysical properties of gold nanoparticles and water are presented in Table 1. The values of nanoparticles shapes-related parameters are presented in Table 2. The partial governing equations of the problem are modeled as [42]

$$\frac{\partial u}{\partial x} + \frac{\partial v}{\partial y} = 0, \tag{1}$$

$$u\frac{\partial u}{\partial x} + v\frac{\partial u}{\partial y} = -\frac{1}{\rho_{n_f}}\frac{\partial p}{\partial x} + \frac{\mu_{n_f}}{\rho_{n_f}}\left(\frac{\partial^2 u}{\partial x^2} + \frac{\partial^2 u}{\partial y^2}\right) - \frac{\sigma_{n_f}B^2 u}{\rho_{n_f}}, \tag{2}$$

$$u\frac{\partial v}{\partial y} = -\frac{1}{\rho_{n_f}}\frac{\partial p}{\partial y} + \frac{\mu_{n_f}}{\rho_{n_f}}\left(\frac{\partial^2 u}{\partial x^2} + \frac{\partial^2 u}{\partial y^2}\right), \tag{3}$$

$$u\frac{\partial T}{\partial x} + v\frac{\partial T}{\partial y} = \frac{k_{n_f}}{(\rho C p)_{nf}}\left(\frac{\partial^2 T}{\partial x^2} + \frac{\partial^2 T}{\partial y^2}\right) + \frac{\mu_{n_f}}{(\rho C p)_{nf}}$$
$$\cdot \left\{2\left[\left(\frac{\partial u}{\partial x}\right)^2 + \left(\frac{\partial v}{\partial y}\right)^2\right] + \left(\frac{\partial v}{\partial x}\right)^2\right\} \tag{4}$$
$$+ \frac{16\sigma^*}{3(\rho C p)_{nf}K^*}\frac{\partial^2 T}{\partial y^2}.$$

The reverent boundary value conditions are

$$f = 0, f' = 1, \theta = 1, \quad \text{at } \eta = 0,$$
$$f = \frac{v_0}{ah}, f' = 0, \theta = 0, \quad \text{at } \eta = 1. \tag{5}$$

The following similarity variables are induced to non-dimensionalize governing equations (1)–(4):

$$u = axf'(\eta),$$
$$v = -ahf(\eta),$$
$$\eta = \frac{y}{h}, \tag{6}$$
$$\theta(\eta) = \frac{T - T_1}{T_2 - T_1}.$$

Equation (1) is identically satisfied. Eliminating the pressure and by using equation (6) into equations (2), (3), and (4), one has the following nonlinear coupled boundary value problems:

Physical properties	Gold (Au)	Pure water
ρ (kg/m^3)	19300	998.3
Cp (J/kg·K)	129	4182
k (W/m·K)	318	0.60

Table 2: The values of nanoparticles shapes-related parameters as [44].

Shapes	Column	Sphere	Hexahedron	Tetrahedron	Lamina
ϕ	0.4710	1	0.8060	0.7387	0.1857
m	6.3698	3	3.7221	4.0613	16.1576

$$f'''' - R\frac{A_1}{A_2}\left(f'f'' - ff'''\right) - \frac{1}{A_2}Mf'' = 0, \tag{7}$$

$$(1 + \text{Rd})\theta'' + \text{Pr}\left(\frac{A_3}{A_4}Rf\theta' + 4\frac{A_2}{A_4}\text{Ec}f'^2\right) = 0, \tag{8}$$

$$f(0) = 0,$$
$$f'(0) = 1,$$
$$f(1) = A,$$
$$f'(1) = 0, \tag{9}$$
$$\theta(0) = 1,$$
$$\theta(\infty) = 0.$$

The dimensionless quantities are

$$A = \frac{v_0}{ah},$$

$$R = \frac{ah^2}{v_f},$$

$$\text{Pr} = \frac{\mu_f(\rho C p)_f}{\rho_f k_f},$$

$$\text{Ec} = \frac{\rho_f a^2 h^2}{(\rho C p)_f(T_w - T_\infty)}, \tag{10}$$

$$M = \frac{\sigma_{n_f}B^2 h^2}{v_f \rho_f},$$

$$\text{Rd} = \frac{16\sigma^* T_\infty^3}{3k_{n_f}k^*}.$$

Here, A, Pr, M, R, Ec, and Rd represent the suction parameter, Prandtl number, magnetic parameter, Reynolds number, Eckert number, and thermal radiation parameter, respectively. One has

$$A_1 = \frac{\rho_{n_f}}{\rho_f},$$

$$A_2 = \frac{\mu_{n_f}}{\mu_f},$$

$$A_3 = \frac{(\rho Cp)_{nf}}{(\rho Cp)_f}, \quad (11)$$

$$A_4 = \frac{k_{n_f}}{k_f}.$$

Here, A_1, A_2, A_3, and A_4 represent the ratio of density, viscosity, heat capacitances, and thermal conductivity, respectively.

In this study, we consider

$$\frac{\rho_{n_f}}{\rho_f} = (1 - \phi) + \frac{\rho_s}{\rho_f}\phi,$$

$$\frac{\mu_{n_f}}{\mu_f} = \frac{1}{(1 - \phi)^{2.5}},$$

$$\frac{(\rho Cp)_{nf}}{(\rho Cp)_f} = (1 - \phi) + \frac{(\rho Cp)_s}{(\rho Cp)_f}\phi, \quad (12)$$

$$\frac{k_{n_f}}{k_f} = \frac{\left[k_s + (m-1)k_f\right] - (m-1)\phi\left(k_f - k_s\right)}{\left[k_S + (m-1)k_f\right] + \phi\left(k_f - k_s\right)},$$

where k_f, μ_f, ρ_f, and $(\rho Cp)_f$ represent thermal conductivity, dynamic viscosity, density, and specific heat of the fluid, respectively, whereas k_s, μ_s, ρ_s, and $(\rho Cp)_s$ denote the thermal conductivity, dynamic viscosity, density, and specific heat of the solid, respectively. m and ϕ are the shape factor and volume fraction of nanoparticles, respectively.

The physical quantity of Nu (Nusselt number) is defined as

$$\text{Nu} = \left|A_4 \theta'(0)\right|. \quad (13)$$

3. Solution by HAM

The auxiliary linear operators are selected as follows:

$$\mathscr{L}_f(f) = \frac{d^4 f}{d\eta^4},$$

$$\mathscr{L}_\theta(\theta)\frac{d^2\theta}{d\eta^2}. \quad (14)$$

These auxiliary operators satisfy the following properties:

$$\mathscr{L}_f\left[C_1\frac{\eta^3}{6} + C_2\frac{\eta^2}{2} + C_3\eta + C_4\right] = 0,$$

$$\mathscr{L}_\theta\left[C_5 e^\eta + C_6 e^{-\eta}\right] = 0. \quad (15)$$

The initial guesses are chosen as

$$f_0(\eta) = (1 - 2A)\eta^3 + (3A - 2)\eta^2 + \eta,$$

$$\theta_0(\eta) = 1 - \eta. \quad (16)$$

3.1. Zeroth-Order Deformation.
The corresponding zeroth deformation problem is defined as follows:

$$(1 - q)\mathscr{L}_f\left[\widehat{f}(\eta, q) - f_0(\eta)\right] = q\hbar_f \mathscr{N}_f\left[\widehat{f}(\eta, q), \widehat{\theta}_0(\eta, q)\right],$$

$$\widehat{f}(0, q) = 0,$$

$$\widehat{f}'(0, q) = 1,$$

$$\widehat{f}(1, q) = A,$$

$$\widehat{f}'(1, q) = 0,$$

$$(1 - q)\mathscr{L}_\theta\left[\widehat{\theta}(\eta, q) - \theta_0(\eta)\right] = q\hbar_\theta \mathscr{N}_\theta\left[\widehat{\theta}_0(\eta, q), \widehat{f}(\eta, q)\right],$$

$$\widehat{\theta}(0, q) = 1,$$

$$\widehat{\theta}(1, q) = 0, \quad (17)$$

in which $q \epsilon [0, 1]$ is called an embedding parameter and $\hbar_f \neq 0$ and $\hbar_\theta \neq 0$ are the convergence control parameters such that $\widehat{f}(\eta, 0) = f_0(\eta), \widehat{\theta}(\eta, 0) = \theta_0(\eta)$ and $\widehat{f}(\eta, 1) = f(\eta), \widehat{\theta}(\eta, 1) = \theta(\eta)$; it means that when q varies from 0 to 1, $\widehat{f}(\eta, q)$ varies from initial guess $f_0(\eta)$ to the final solution $f(\eta)$ and $\widehat{\theta}(\eta, q)$ varies from initial guesses $\theta_0(\eta)$ to $\theta(\eta)$.

The nonlinear operators $\mathscr{N}_f$ and $\mathscr{N}_\theta$ are given by

$$N_f\left[\widehat{f}(\eta, q), \widehat{\theta}(\eta, q)\right] = \frac{\partial^4 \widehat{f}(\eta, q)}{\partial\eta^4} - \frac{A_1}{A_2}R\left(\frac{\partial\widehat{f}(\eta, q)}{\partial\eta}\frac{\partial^2\widehat{f}(\eta, q)}{\partial\eta^2} - \widehat{f}(\eta, q)\frac{\partial^3\widehat{f}(\eta, q)}{\partial\eta^3}\right) - \frac{1}{A_2}M\frac{\partial^2\widehat{f}(\eta, q)}{\partial\eta^2} = 0,$$

$$(18)$$

$$N_\theta\left[\widehat{\theta}(\eta, q), \widehat{f}(\eta, q)\right] = (1 + R_d)\frac{\partial^2\widehat{\theta}(\eta, q)}{\partial\eta^2} + \Pr\left(\frac{A_3}{A_4}R\widehat{f}(\eta, q)\frac{\partial\widehat{\theta}(\eta, q)}{\partial\eta} + 4\frac{A_2}{A_4}\text{Ec}\frac{\partial^2\widehat{f}(\eta, q)}{\partial\eta^2}\right) = 0.$$

Expanding $\hat{f}(\eta, q)$ and $\hat{\theta}(\eta, q)$ with respect to q Maclaurin's series and $q = 0$, we obtain

$$f(\eta, q) = f_0(\eta) + \sum_{m=1}^{\infty} f_m(\eta) q^m,$$

$$\theta(\eta, q) = \theta_0(\eta) + \sum_{m=1}^{\infty} \theta_m(\eta) q^m,$$

(19)

where $f_m(\eta) = (1/m!)((\partial^m f(\eta, q))/(\partial \eta^m))|_{q=0}$ and $\theta_m(\eta) = (1/m!)((\partial^m \theta(\eta, q))/(\partial \eta^m))|_{q=0}$.

3.2. Higher-Order Deformation Problem. The higher-order problems are as follows:

$$\mathscr{L}_f[f_m(\eta) - \chi_m f_{m-1}(\eta)] = \hbar_f \mathscr{R}_f^m(f_{m-1}(\eta), \theta_{m-1}(\eta)),$$

$$f_m(0) = 0,$$

$$f'_m(0) = 0,$$

$$f'_m(1) = 0,$$

$$f'_m(1) = 0,$$

$$\mathscr{L}L_f[\theta_m(\eta) - \chi_m \theta_{m-1}(\eta)] = \hbar_\theta \mathscr{R}_\theta^m(\theta_{m-1}(\eta), f_{m-1}(\eta)),$$

$$\theta_m(0) = 0,$$

$$\theta_m(1) = 0,$$

(20)

where

$$\chi_m = \begin{cases} 0, & \text{when } m \le 1, \\ 1, & m > 1, \end{cases}$$

$$\mathscr{R}_f^m f(\eta) = f''_{m-1}(\eta) - \frac{A_1}{A_2} R$$

$$\cdot \left(\sum_{z=0}^{m-1} f'_z f''_{m-1-z} - \sum_{z=0}^{m-1} f_z f''_{m-1-z} \right) - M f''_{m-1}(\eta),$$

$$\mathscr{R}_f^m \theta(\eta) = (1 + R_d) \theta''_{m-1} + \Pr \frac{A_3}{A_4} R$$

$$\cdot \left(\sum_{z=0}^{m-1} f_z \theta'_{m-1-z} + 4 \frac{A_2}{A_4} \text{Ec} \sum_{z=0}^{m-1} f''_z f''_{m-1-z} \right).$$

(21)

The mth-order solutions are

$$f_m(\eta) = f_m^* + C_1 \frac{\eta^3}{6} + C_2 \frac{\eta^2}{2} + C_3 \eta + C_4,$$

(22)

$$\theta_m(\eta) = \theta_m^* + C_5 e^\eta + C_6 e^{-\eta},$$

(23)

where $C_z^m (z = 1 - 6)$ are constants to be determined by using the boundary conditions.

3.3. Convergence of Series Solutions. Zeroth- and higher-order deformation problems are given in equations (7) and (8), which clearly show that the series solutions contain nonzero auxiliary parameters $\hbar_f$ and $\hbar_\theta$. The convergence of the solutions is checked through plotting $\hbar$-curves $\hbar_f$ and $\hbar_\theta$ as displayed in Figures 1 and 2. It is evident that the series solutions (22) and (23) converge when $-1.8 \ge \hbar_f \le -0.2$ and $-1.8 \ge \hbar_\theta \le -0.2$.

4. Results and Discussion

The physical insight of the problem is discussed in this present portion. The schematic model of squeezing nanofluid is shown in Figure 3. The dynamics of heat transfer in the squeezing nanofluid fluid flow are described under the variation of dimensionless solid volume fraction, thermal radiation, Reynolds number, magnetic field, Eckert number, suction parameter, and shape factor. The analysis is carried out using the following range of parameters $0.1 \ge \phi \le 0.2$, $0.5 \ge A \le 1.0, 0.5 \ge M \le 4.0, 0.5 \ge R \le 1.0, 0.01 \ge \text{Ec} \le 0.9$, and $0.5 \ge \text{Rd} \le 2.0$. It is evident from Figures 4–7 that nanoparticles which participate in heat transfer are lamina > column > tetrahedron > hexahedron > sphere.

ϕ is a very important parameter for squeeze flow of nanofluid. From Figure 8, it is noted that the impact of ϕ on primary velocity seemed ineffective. It is also observed that the primary velocity is increased with increase of R as displayed in Figure 9. It is because that the inertia with the viscous ratio is dominant. From Figure 10, it is observed that the effect of M on the primary velocity is decreased due to the Lorentz force produced by M. The Lorentz force acts against the motion of squeeze flow of nanofluid. The variation of A on the dimensionless primary velocity is shown in Figure 11. From Figure 11, it can be seen that the primary velocity is intensifying with the increase of A; physically, the wall shear stress increases with the increase of A.

The secondary velocity decreases in the half of the region as shown in Figure 12. In Figures 13 and 14, it is distinguished that secondary velocity changed in half of the region (the region above the central line between the plates). It happened due to the constraint of law of conservation of mass. The variation of A is plotted in Figure 15; secondary velocity is also increased with the increase of A.

The shape effects of nanoparticles on dimensionless temperatures profiles are shown in Figure 16. It is noted from Figure 16 that sphere > hexahedron > tetrahedron > column > lamina. It is also observed that lamina nanoparticles have minimum temperature because of maximum viscosity while sphere shape nanoparticles have maximum temperature because of minimum viscosity. From Figure 17, it is observed that the temperature profile has a direct relation with ϕ; the reason is that increasing the volume fraction causes enhanced thermal conductivity of the nanofluid which turns to increase the boundary layer thickness. From Figure 17, it is also observed that the sphere shape nanoparticles show a prominent role in temperature distribution. Figure 18 depicts the influence of R on the dimensionless temperature profile; with increasing R, the dimensionless temperature profile decreases because of decreasing the thermal layer thickness. Figure 18 showed
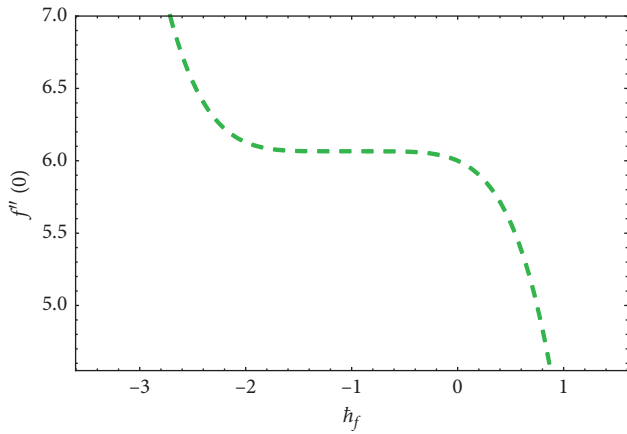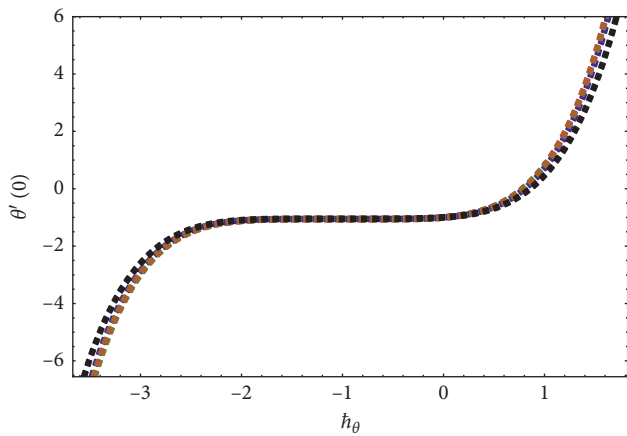
FIGURE 1: The $\hbar_f$–curve for $f''(0)$.

FIGURE 2: The $\hbar_\theta$–curve for $\theta'(0)$.

Column
Sphere
Hexahedron
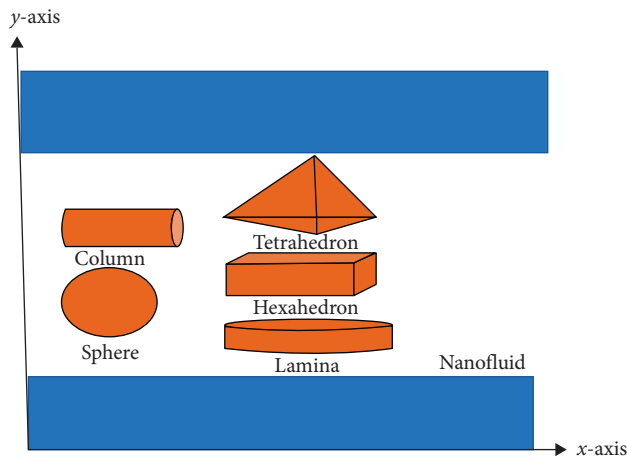Tetrahedron
Lamina

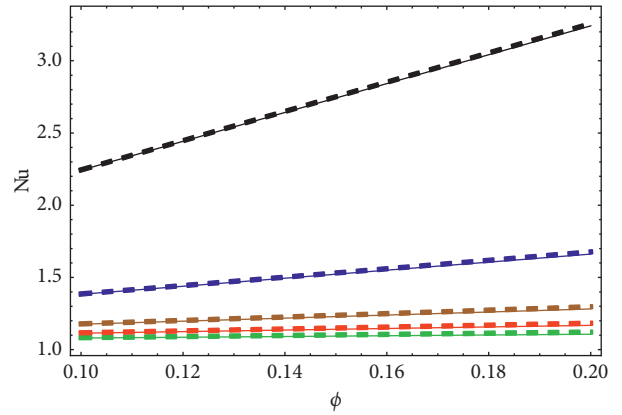FIGURE 3: Schematic model of squeezing nanofluid.

FIGURE 4: Nu for values of R and M, A, Rd = 0.5 and Ec = 0.3. Blue: column. Green: sphere. Red: hexahedron. Brown: tetrahedron. Black: lamina. $R = 0.5$ solid line; $R = 1.0$ dash line.
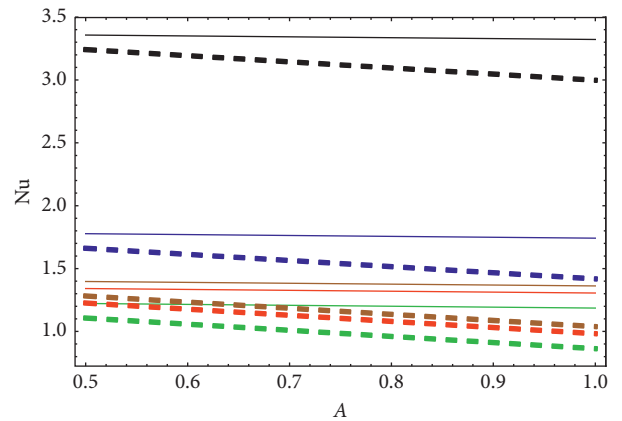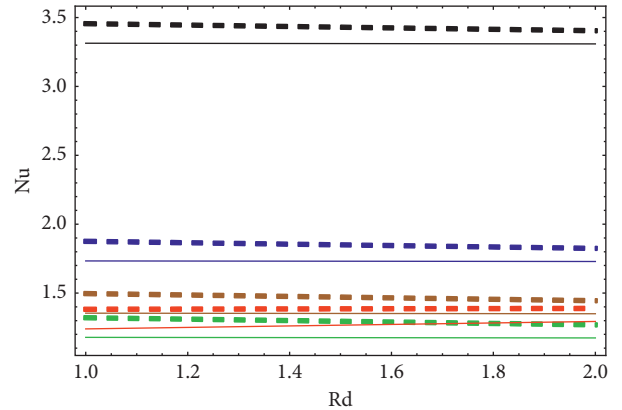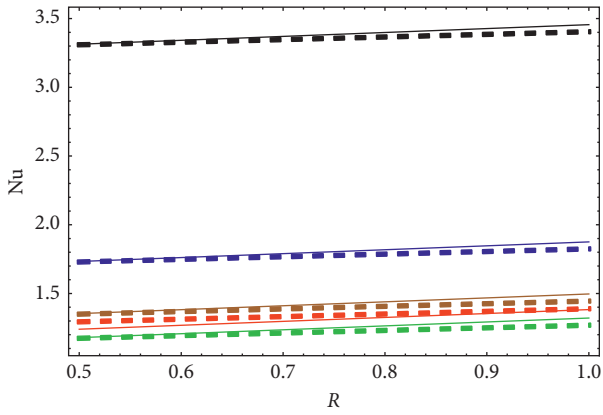

FIGURE 5: Nu for values of Ec and M, R, Rd = 0.5 and ϕ = 0.2. Blue: column. Green: sphere. Red: hexahedron. Brown: tetrahedron. Black: lamina. Ec = 0.01 solid line; Ec = 0.03 dash line.

FIGURE 6: Nu for values of R and M, A = 0.5, Ec = 0.3, and ϕ = 0.2. Blue: column. Green: sphere. Red: hexahedron. Brown: tetrahedron. Black: lamina. $R = 0.5$ solid line; $R = 1.0$ dash line.

Figure 7: Nu for values of Rd and M, $A = 0.5$, Ec $= 0.3$, and $\phi = 0.2$. Blue: column. Green: sphere. Red: hexahedron. Brown: tetrahedron. Black: lamina. Rd $= 1.0$ solid line; Rd $= 2.0$ dash line.
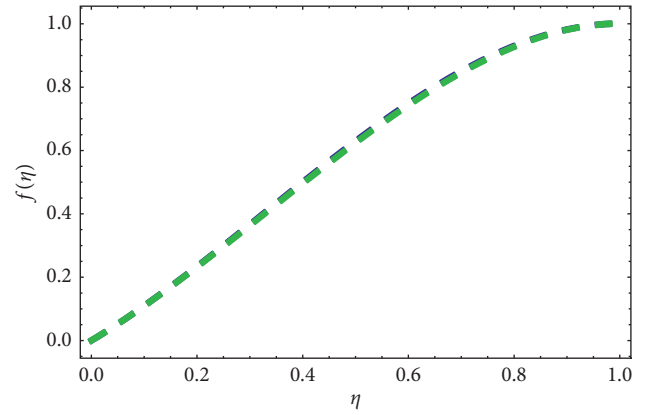

Figure 10: $f'(\eta)$ for values of M and $R = 0.3$, $A = 1.0$, and $\phi = 0.2$. Blue: $M = 0.5$. Green: $M = 4.0$.
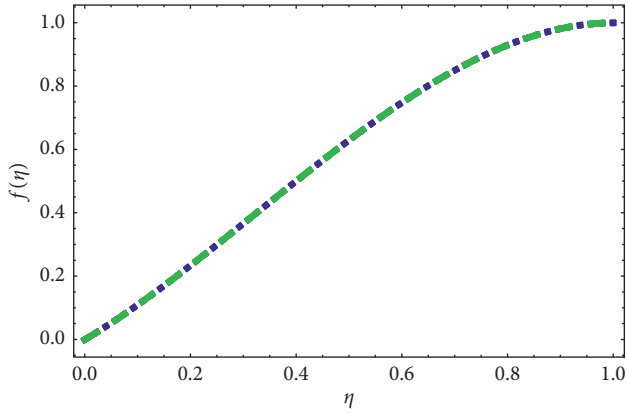

Figure 8: $f'(\eta)$ for values of ϕ and $R = 0.3$, $M = 0.5$, and $A = 1.0$. Blue: $\phi = 0.1$. Green: $\phi = 0.2$.
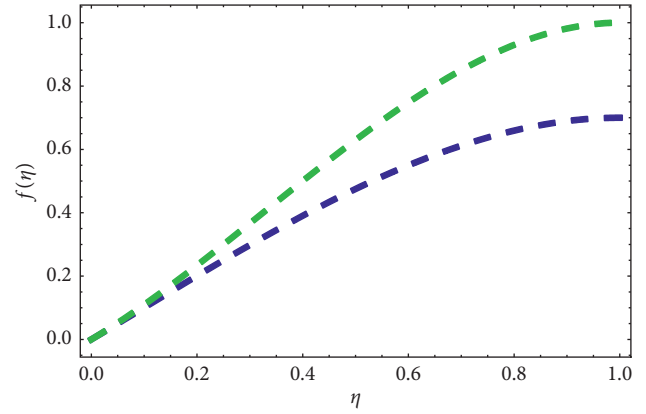

Figure 11: $f'(\eta)$ for values of A and $R = 0.3$, $M = 0.5$, and $\phi = 0.2$. Blue: $A = 0.5$. Green: $A = 1.0$.
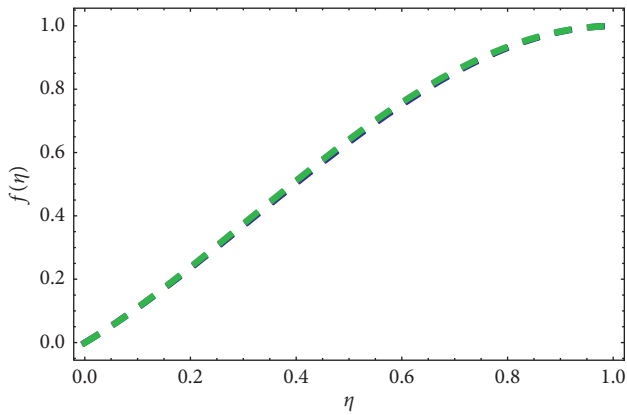

Figure 9: $f'(\eta)$ for values of R and $M = 0.5$, $A = 1.0$, and $\phi = 0.2$. Blue: $R = 0.5$. Green: $R = 1.0$.
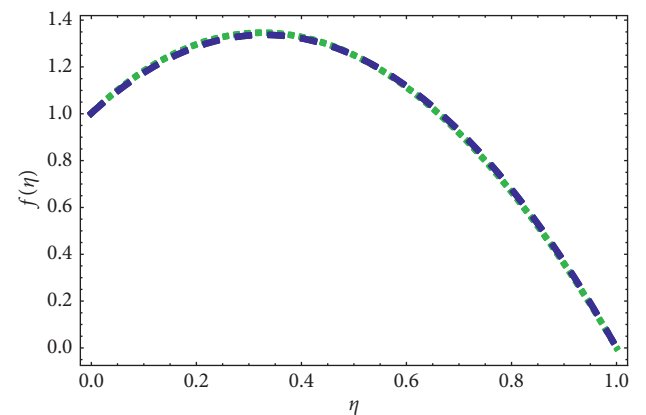

Figure 12: $f'(\eta)$ for values of M and $R = 0.3$, $A = 1.0$, and $\phi = 0.2$. Blue: $\phi = 0.1$. Green: $\phi = 0.2$.
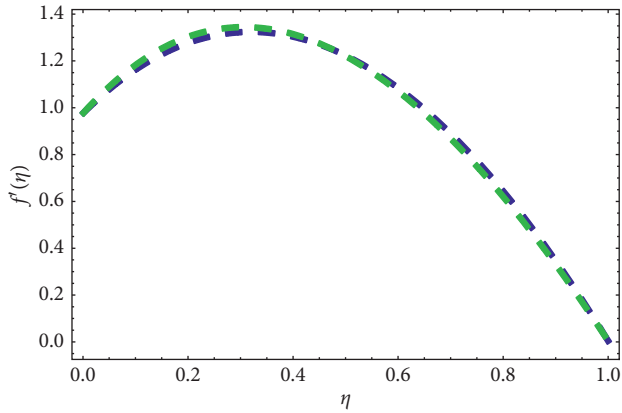
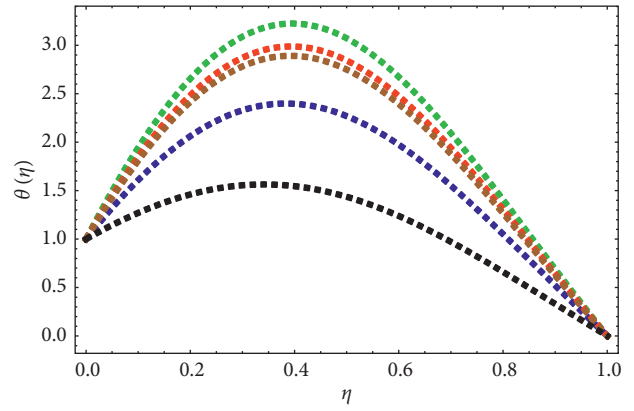Figure 13: $f'(\eta)$ for values of R and $M = 0.5$, $A = 1.0$, and $\phi = 0.2$. Blue: $R = 0.5$. Green: $R = 1.0$.

Figure 16: $\theta(\eta)$ for effect of the nanoparticles shapes and $R = 0.3$, Rd, $M = 0.5$, Ec $= 0.7$, $A = 1.0$, and $\phi = 0.2$. Blue: column. Green: sphere. Red: hexahedron. Brown: tetrahedron. Black: lamina.
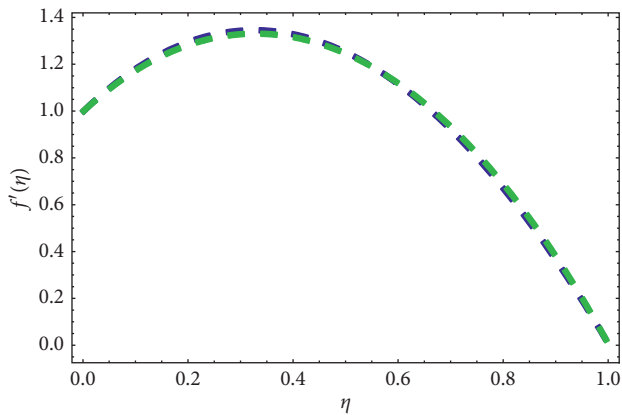

Figure 14: $f'(\eta)$ for values of M and $R = 0.3$, $A = 1.0$, and $\phi = 0.2$. Blue: $M = 0.5$. Green: $M = 4.0$.
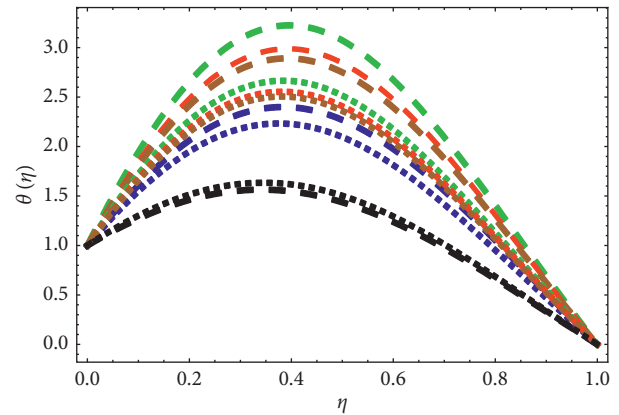

Figure 17: $\theta(\eta)$ for values of ϕ and Ec $= 0.7$, Rd, $M = 0.5$, $R = 0.3$, and $A = 1.0$. Blue: column. Green: sphere. Red: hexahedron. Brown: tetrahedron. Black: lamina. $\phi = 0.1$ dot line; $\phi = 0.2$ dash line.
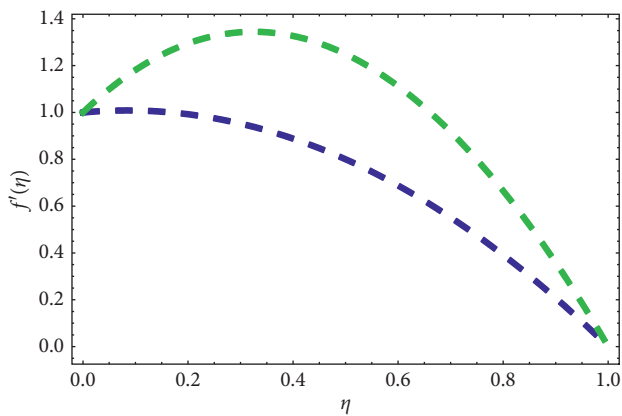

Figure 15: $f'(\eta)$ for values of A and $R = 0.3$, $M = 0.5$, and $\phi = 0.2$. Blue: $A = 0.5$. Green: $A = 1.0$.
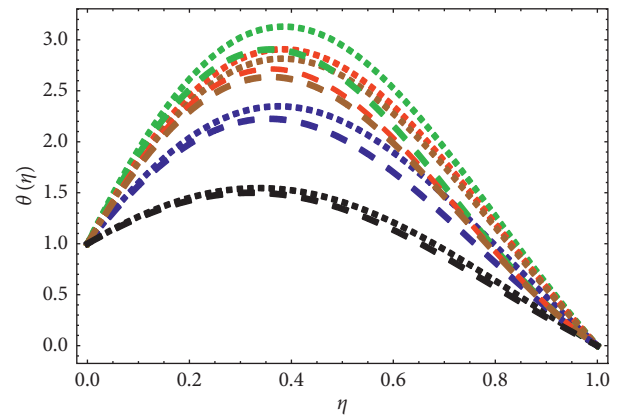

Figure 18: $\theta(\eta)$ for values of R and Ec $= 0.7$, Rd, $M = 0.5$, $A = 1.0$, and $\phi = 0.2$. Blue: column. Green: sphere. Red: hexahedron. Brown: tetrahedron. Black: lamina. $R = 0.5$ dot line; $R = 1.0$ dash line.

FIGURE 19: $\theta(\eta)$ for values of M and $R = 0.3$, Rd $= 0.5$, Ec $= 0.7$, $A = 1.0$, and $\phi = 0.2$. Blue: column. Green: sphere. Red: hexahedron. Brown: tetrahedron. Black: lamina. $M = 1.0$ dot line; $M = 3.0$ dash line.

FIGURE 21: $\theta(\eta)$ for values of Rd and Ec $= 0.7$, $R = 0.3$, $M = 0.5$, $A = 1.0$, and $\phi = 0.2$. Blue: column. Green: sphere. Red: hexahedron. Brown: tetrahedron. Black: lamina. Rd $= 0.5$ dot line; Rd $= 1.0$ dash line.

FIGURE 20: $\theta(\eta)$ for values of A and $R = 0.3$, Rd, $M = 0.5$, Ec $= 0.7$, and $\phi = 0.2$. Blue: column. Green: sphere. Red: hexahedron. Brown: tetrahedron. Black: lamina. $A = 0.7$ dot line; $A = 1.0$ dash line.
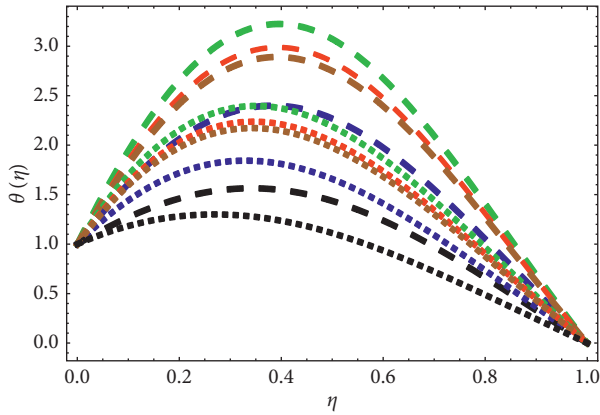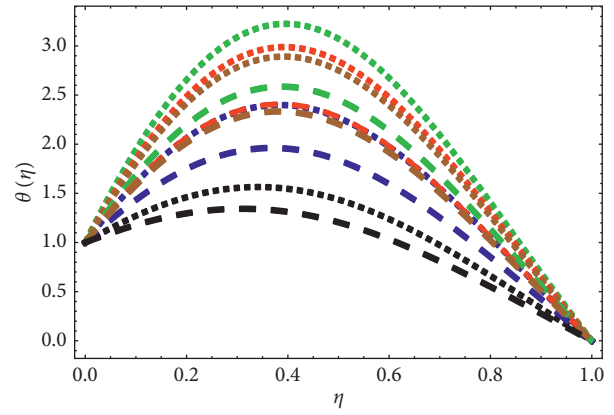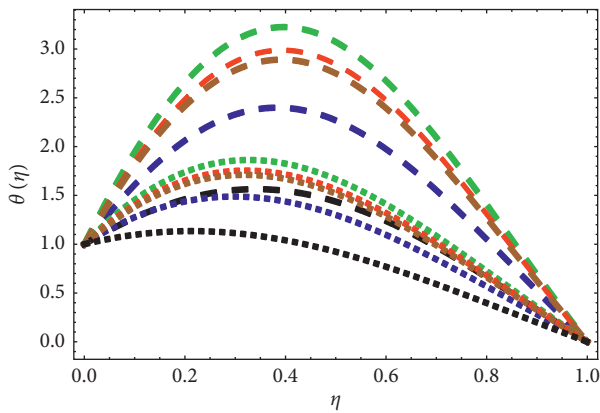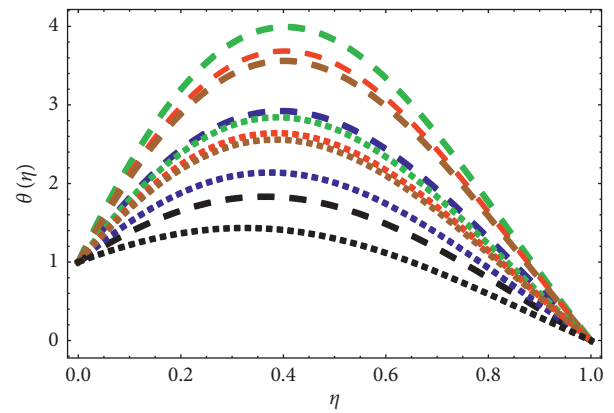

FIGURE 22: $\theta(\eta)$ for values of Ec and $R = 0.3$, Rd, $M = 0.5$, $A = 1.0$, and $\phi = 0.2$. Blue: column. Green: sphere. Red: hexahedron. Brown: tetrahedron. Black: lamina. Ec $= 0.6$ dot line; Ec $= 0.9$ dash line.

that the effect of sphere shape nanoparticles is more significant than other shapes of nanoparticles under the influence of R. Figure 19 describes the impact of M on thermal boundary layer thickness. From Figure 19, it is noted that the temperature increases with the increase of M. The reason is that M tends to increase a dragging force which produces heat in temperature profile. Figure 19 depicts that the sphere shape nanoparticles in Au-water play a leading role in the temperature profile. Figure 20 shows that the temperature profile increases with A; physically, the heated nanofluid is pushed towards the wall, where the buoyancy forces can intensify the viscosity. That is why it decreases the wall shear stress. Figure 21 shows the effect of Rd on temperature profile; from this figure, it is illustrated that the Rd has an inverse relation with temperature profile. Due to this, the greater value of Rd corresponds to an increase in the dominance of conduction over radiation and hence reduction in the buoyancy force and the thermal boundary layer thickness. Under the effect of Rd, sphere shape nanoparticles have an important role in temperature distribution. Figure 22 displays that the squeezed nanofluid flow

temperature increases with the increase of the Ec; the reason is that the frictional heat is deposited in squeezed nanofluid; however, thermal boundary layer thickness of sphere shape nanoparticles seems to be more animated in squeezed nanofluid by Ec effect.

5. Conclusion

In the present paper, the effect of gold (Au) nanoparticles on squeezing nanofluid flow has been thoroughly examined. The analytical solution was obtained by using homotopy analysis method (HAM) for a range of pertinent parameters such as shape factor, solid volume fraction, thermal radiation, Reynolds number, magnetic field, suction parameter, and Eckert number. The effects of various parameters have been illustrated through graphs. The Pr keeps fixed at 6.2. In the view of results and discussions, the following deductions have arrived:

(i) The nanoparticles of sphere shape show a remarkable role in the disturbance of temperature profiles

(ii) The nanoparticles of tetrahedron shape show a moderate role in the disturbance of temperature profiles

(iii) The nanoparticles of lamina shape play a lower role in the disturbance of temperature profiles

(iv) The nanoparticles of lamina shape play a principal role in the heat transfer rate

(v) The nanoparticles of tetrahedron shape show a moderate role in the heat transfer rate

(vi) The nanoparticles of tetrahedron shape show a lower role in the heat transfer rate

(vii) Performances of lamina and sphere shapes nanoparticles in the forms of disturbance on temperature profiles and the heat transfer are opposite to each other

(viii) Performances of hexahedron and tetrahedron shapes nanoparticles in forms of the disturbance temperature profiles and the heat transfer are opposite to each other

Abbreviations

PDEs: Partial differential equations
ODEs: Ordinary differential equations
RNA: Ribonucleic acid
DNA: Deoxyribonucleic acid
MHD: Magnetohydrodynamic
HPM: Homotopy perturbation method
HAM: Homotopy analysis method.

Data Availability

No data were used to support this study.

Conflicts of Interest

The authors declare no conflicts of interest.

Authors' Contributions

Umair Rashid, Azhar Iqbal, and Mohd. Junaid Siddiqui contributed to conceptualization; Umair Rashid, Thabet Abdeljawad, and Azhar Iqbal contributed to methodology; Umair Rashid, Haiyi Liang, Azhar Iqbal, and Muhammad Abbas contributed to software; Haiyi Liang, Umair Rashid, Thabet Abdeljawad, Azhar Iqbal, Mohd. Junaid Siddiqui, and Muhammad Abbas contributed to validation; Haiyi Liang, Umair Rashid, Thabet Abdeljawad, Azhar Iqbal, Mohd. Junaid Siddiqui, and Muhammad Abbas contributed to formal analysis; Haiyi Liang, Umair Rashid, Thabet Abdeljawad, Azhar Iqbal, Mohd. Junaid Siddiqui, and Muhammad Abbas contributed to investigation; Thabet Abdeljawad and Muhammad Abbas contributed to resources; Umair Rashid, Azhar Iqbal, and Muhammad Abbas are responsible for writing and original draft preparation; Haiyi Liang, Umair Rashid, Azhar Iqbal, and Muhammad Abbas are responsible for writing, review, and editing of the paper; Azhar Iqbal and Muhammad Abbas contributed to

visualization; Haiyi Liang, Thabet Abdeljawad, and Muhammad Abbas contributed to supervision; Thabet Abdeljawad and Muhammad Abbas contributed to funding acquisition. All authors have read and agreed to the published version of the manuscript.

Acknowledgments

References

[1] M. Das, K. H. Shim, S. S. A. An, and D. K. Yi, "Review on gold nanoparticles and their applications," *Toxicology and Environmental Health Sciences*, vol. 3, no. 4, pp. 193–205, 2011.

[2] S. Muhammad, S. Shah, G. Ali, M. Ishaq, S. Hussain, and H. Ullah, "Squeezing nanofluid flow between two parallel plates under the influence of MHD and thermal radiation," *Asian Research Journal of Mathematics*, vol. 10, no. 1, pp. 1–20, 2018.

[3] T. Hayat, T. Abbas, M. Ayub, T. Muhammad, and A. Alsaedi, "On squeezed flow of jeffrey nanofluid between two parallel disks," *Applied Sciences*, vol. 6, pp. 1–15, 2016.

[4] A. Dib, A. Haiahem, and B. Bou-said, "Approximate analytical solution of squeezing unsteady nanofluid flow," *Powder Technology*, vol. 269, pp. 193–199, 2015.

[5] H. M. Duwairi, B. Tashtoush, and R. A. Damseh, "On heat transfer effects of a viscous fluid squeezed and extruded between two parallel plates," *Heat and Mass Transfer*, vol. 41, pp. 112–117, 2004.

[6] G. Domairry and M. Hatami, "Squeezing Cu-water nanofluid flow analysis between parallel plates by DTM-Padé method," *Journal of Molecular Liquids*, vol. 193, pp. 37–44, 2014.

[7] M. Sheikholeslami and D. D. Ganji, "Heat transfer of Cu-water nanofluid flow between parallel plates," *Powder Technology*, vol. 235, pp. 873–879, 2013.

[8] S. I. Khan, U. Khan, N. Ahmed, and S. T. Mohyud-Din, "Thermal radiation effects on squeezing flow casson fluid between parallel disks," *Communications in Numerical Analysis*, vol. 2016, no. 2, pp. 92–107, 2016.

[9] M. Sheikholeslami, M. Hatami, and D. D. Ganji, "Nanofluid flow and heat transfer in a rotating system in the presence of a magnetic field," *Journal of Molecular Liquids*, vol. 190, pp. 112–120, 2014.

[10] A. K. Gupta and S. Saha Ray, "Numerical treatment for investigation of squeezing unsteady nanofluid flow between two parallel plates," *Powder Technology*, vol. 279, pp. 282–289, 2015.

[11] M. Mahmoodi and S. Kandelousi, "Kerosene–alumina nanofluid flow and heat transfer for cooling application," *Journal of Central South University*, vol. 23, no. 4, pp. 983–990, 2016.

[12] S. Liao, "An optimal homotopy-analysis approach for strongly nonlinear differential equations," *Communications in Nonlinear Science and Numerical Simulation*, vol. 15, no. 8, pp. 2003–2016, 2010.

[13] S. Liao, "An analytic solution of unsteady boundary-layer flows caused by an impulsively stretching plate," *Communications in Nonlinear Science and Numerical Simulation*, vol. 11, no. 3, pp. 326–339, 2006.

[14] S. Liao, "On the homotopy analysis method for nonlinear problems," *Applied Mathematics and Computation*, vol. 147, no. 2, pp. 499–513, 2004.

[15] S.-J. Liao, "On the analytic solution of magnetohydrodynamic flows of non-Newtonian fluids over a stretching sheet," *Journal of Fluid Mechanics*, vol. 488, pp. 189–212, 2003.

[16] S.-J. Liao, "An explicit, totally analytic approximate solution for Blasius' viscous flow problems," *International Journal of Non-linear Mechanics*, vol. 34, no. 4, pp. 759–778, 1999.

[17] M. M. Rashidi, A. M. Siddiqui, and M. Asadi, "Application of homotopy analysis method to the unsteady squeezing flow of a second-grade fluid between circular plates," *Mathematical Problems in Engineering*, vol. 2010, Article ID 706840, 18 pages, 2010.

[18] M. M. Rashidi and S. A. Mohimanian Pour, "Analytic approximate solutions for unsteady boundary-layer flow and heat transfer due to a stretching sheet by homotopy analysis method," *Nonlinear Analysis: Modelling and Control*, vol. 15, no. 1, pp. 83–95, 2010.

[19] S. Abbasbandy, "Homotopy analysis method for heat radiation equations," *International Communications in Heat and Mass Transfer*, vol. 34, no. 3, pp. 380–387, 2007.

[20] S. Abbasbandy and A. Shirzadi, "A new application of the homotopy analysis method: solving the Sturm-Liouville problems," *Communications in Nonlinear Science and Numerical Simulation*, vol. 16, no. 1, pp. 112–126, 2011.

[21] S. Hussain, S. Muhammad, G. Ali et al., "A bioconvection model for squeezing flow between parallel plates containing gyrotactic microorganisms with impact of thermal radiation and heat generation/absorption," *Journal of Advances in Mathematics and Computer Science*, vol. 27, no. 4, pp. 1–22, 2018.

[22] O. Manca, Y. Jaluria, G. Lauriat, K. Vafai, and L. Wang, "Heat transfer in nanofluids 2013," *Advances in Mechanical Engineering*, vol. 2014, Article ID 832415, 2 pages, 2014.

[23] W. Yu and H. Xie, "A review on nanofluids: preparation, stability mechanisms, and applications," *Journal of Nanomaterials*, vol. 2012, Article ID 435873, 17 pages, 2012.

[24] Y. Xuan and Q. Li, "Heat transfer enhancement of nanofluids," *International Journal of Heat and Fluid Flow*, vol. 21, no. 1, pp. 58–64, 2000.

[25] B. Kristiawan, B. Santoso, A. T. Wijayanta, M. Aziz, and T. Miyazaki, "Heat transfer enhancement of TiO_2/water nanofluid at laminar and turbulent flows: a numerical approach for evaluating the effect of nanoparticle loadings," *Energies*, vol. 11, no. 6, Article ID 1584, 2018.

[26] M. Turkyilmazoglu and I. Pop, "Heat and mass transfer of unsteady natural convection flow of some nanofluids past a vertical infinite flat plate with radiation effect," *International Journal of Heat and Mass Transfer*, vol. 59, pp. 167–171, 2013.

[27] L. Qiang and X. Yimin, "Convective heat transfer and flow characteristics of Cu-water nanofluid," *Science in China, Series E: Technological Sciences*, vol. 45, no. 4, pp. 408–416, 2002.

[28] N. S. Elgazery, "Nanofluids flow over a permeable unsteady stretching surface with non-uniform heat source/sink in the presence of inclined magnetic field," *Journal of the Egyptian Mathematical Society*, vol. 27, no. 1, pp. 1–26, 2019.

[29] U. Rea, T. McKrell, L.-w. Hu, J. Buongiorno, and J. Buongiorno, "Laminar convective heat transfer and viscous pressure loss of alumina-water and zirconia-water nanofluids," *International Journal of Heat and Mass Transfer*, vol. 52, no. 7-8, pp. 2042–2048, 2009.

[30] B. H. Salman, H. A. Mohammed, and A. S. Kherbeet, "Heat transfer enhancement of nanofluids flow in microtube with constant heat flux," *International Communications in Heat and Mass Transfer*, vol. 39, no. 8, pp. 1195–1204, 2012.

[31] M. Sheikholeslami, R. Ellahi, and C. Fetecau, "CuO–water nanofluid magnetohydrodynamic natural convection inside a sinusoidal annulus in presence of melting heat transfer," *Mathematical Problems in Engineering*, vol. 2017, Article ID 5830279, 9 pages, 2017.

[32] S. Manikandan and K. S. Rajan, "New hybrid nanofluid containing encapsulated paraffin wax and sand nanoparticles in propylene glycol-water mixture: potential heat transfer fluid for energy management," *Energy Conversion and Management*, vol. 137, pp. 74–85, 2017.

[33] M. Hassan, M. Marin, R. Ellahi, and S. Z. Alamri, "Exploration of convective heat transfer and flow characteristics synthesis by Cu-Ag/water hybrid-nanofluids," *Heat Transfer Research*, vol. 49, no. 18, pp. 1837–1848, 2018.

[34] M. M. Bhatti, R. Ellahi, A. Zeeshan, M. Marin, and N. Ijaz, "Numerical study of heat transfer and Hall current impact on peristaltic propulsion of particle-fluid suspension with compliant wall properties," *Modern Physics Letters B*, vol. 33, no. 35, Article ID 1950439, 2019.

[35] G. Palani and I. A. Abbas, "Free convection MHD flow with thermal radiation from an impulsively-started vertical plate," *Nonlinear Analysis: Modelling and Control*, vol. 14, no. 1, pp. 73–84, 2009.

[36] K. Sharma and M. Marin, "Reflection and transmission of waves from imperfect boundary between two heat conducting micropolar thermoelastic solids," *Analele Universitatii "Ovidius" Constanta—Seria Matematica*, vol. 22, no. 2, pp. 151–176, 2014.

[37] S. M. Atif, S. Hussain, and M. Sangheer, "Effect of viscous dissipation and Joule heating on MHD radiative tangent hyperbolic nanofluid with convective and slip conditions," *Journal of the Brazilian Society of Mechanical Sciences and Engineering*, vol. 41, no. 4, p. 189, 2019.

[38] S. M. Atif, S. Hussain, and M. Sagheer, "Heat and mass transfer analysis of time-dependent tangent hyperbolic nanofluid flow past a wedge," *Physics Letters A*, vol. 383, no. 11, pp. 1187–1198, 2019.

[39] U. Rashid and A. Ibrahim, "Impacts of nanoparticle shape on Al_2O_3-water nanofluid flow and heat transfer over a non-linear radically stretching sheet," *Advances in Nanoparticles*, vol. 9, no. 1, pp. 23–39, 2020.

[40] S. Aman, I. Khan, Z. Ismail, and M. Z. Salleh, "Impacts of gold nanoparticles on MHD mixed convection Poiseuille flow of nanofluid passing through a porous medium in the presence of thermal radiation, thermal diffusion and chemical reaction," *Neural Computing and Applications*, vol. 30, no. 3, pp. 789–797, 2018.

[41] R. Kandasamy, N. A. bt Adnan, and R. Mohammad, "Nanoparticle shape effects on squeezed MHD flow of water based Cu, Al_2O_3 and SWCNTs over a porous sensor surface," *Alexandria Engineering Journal*, vol. 57, no. 3, pp. 1433–1445, 2018.

[42] M. Mahmoodi and S. Kandelousi, "Semi-analytical investigation of kerosene-alumina nanofluid between two parallel plates," *Journal of Aerospace Engineering*, vol. 29, no. 4, Article ID 04016001, 2016.

[43] N. A. Adnan, R. Kandasamy, and R. Mohammad, "Nanoparticle shape and thermal radiation on marangoni water,

ethylene glycol and engine oil based Cu, Al_2O_3 and SWCNTs," *Journal of Material Sciences & Engineering*, vol. 6, no. 4, 2017.

[44] Y. Lin, B. Li, L. Zheng, and G. Chen, "Particle shape and radiation effects on Marangoni boundary layer flow and heat transfer of copper-water nanofluid driven by an exponential temperature," *Powder Technology*, vol. 301, pp. 379–386, 2016.

Research Article

Numerical Investigation of Heat and Mass Transport in the Flow over a Magnetized Wedge by Incorporating the Effects of Cross-Diffusion Gradients: Applications in Multiple Engineering Systems

Aisha M. Alqahtani,[1] **Adnan,**[2] **Umar Khan,**[3] **Naveed Ahmed,**[4] **Syed Tauseef Mohyud-Din,**[5] **and Ilyas Khan** (iD)[6]

[1]*Department of Mathematical Sciences, College of Science, Princess Nourah Bint Abdulrahman University, Riyadh, Saudi Arabia*
[2]*Department of Mathematics, Mohi-ud-Din Islamic University Nerian Sharif AJ&K, Trarkhel, Pakistan*
[3]*Department of Mathematics and Statistics, Hazara University, Mansehra, Pakistan*
[4]*Department of Mathematics, Faculty of Sciences, HITEC University Taxila Cantt, Taxila, Pakistan*
[5]*University of Multan, Multan, Pakistan*
[6]*Faculty of Mathematics and Statistics, Ton Duc Thang University, Ho Chi Minh City 72915, Vietnam*

Correspondence should be addressed to Ilyas Khan; ilyaskhan@tdtu.edu.vn

The flow over a wedge is significant and frequently occurs in civil engineering. It is significant to investigate the heat and mass transport characteristics in the wedge flow. Therefore, the analysis is presented to examine the effects of preeminent parameters by incorporating the cross-diffusion gradients in the energy and mass constitutive relations. From the analysis, it is perceived that the temperature drops against a higher Prandtl number. Due to concentration gradients in the energy equation, the temperature rises slowly. Moreover, it is examined that the mass transfer significantly reduces due to Schmidt effects and more mass transfer is pointed against the Soret number. The shear stresses increase due to stronger magnetic field effects. The local thermal performance of the fluid enhances against more dissipative fluid, and DuFour effects reduced it. Furthermore, the mass transport rate drops due to higher Soret effects and increases against multiple Schmidt number values.

1. Introduction

Importance of boundary layer flow cannot be ignored because of its diverse class of applications in daily life and industries as well. These comprised in civil engineering, aerodynamics, and many more.

The Newtonian flow over a stagnant wedge was firstly developed by Falkner and Skan [1]. They transformed a dimensional model to a third-order nonlinear self-similar differential equation by applying similarity variables. Afterwards, in 1937, Hartree [2] explored the boundary layer model approximately. Later, researchers turned toward the study of wedge flow under different flow conditions. In 1961, Koh et al. [3] explored the shear stresses and quantities of practical interest such as nusselt and Sherwood numbers over a wedge in the existence of a porosity parameter. They discussed the model by encountering the impacts of inconstant wall temperature and suction property. In 1987, Lin et al. [4] discussed the approximate solutions for wedge flow of any Prandtl number. They analyzed the temperature regimes in the existence of forced convection.

Lately, Hussanan et al. [5] examined the boundary layer model in the existence of porous media by considering constant concentration gradients and resistive heating.

Impacts of various physical quantities such as radiative heat flux and suction/injection on the chemically heating boundary layer model are reported in [6]. Chamber et al. [7] reported the boundary layer in the existence of a chemical reaction and diffusion gradients. The Falkner Skan flow model for a static or moving wedge saturated with nanofluid was discussed by Yacob et al. [8] in 2011. Flow in a wavering sheet was examined in [9]. They encountered the effects of natural convection and Ohmic heating. Su et al. [10] inspected the magnetohydrodynamic flow of Newtonian fluid composed by nanoparticles. Influences of applied Lorentz forces, slip flow condition, and ohmic heating were discussed in their study.

In 2016, Khan et al. [11] investigated the bioconvection model in the existence of a porosity parameter over a wedge. They explored the influence of viscous dissipation, resistive heating, and imposed Lorentz forces on the flow of a gyrotactic microorganism. They discussed the impacts of different self-similar physical parameter on the momentum, thermal, density motile, and concentration profiles of the microorganism. Graphical analysis for shear stresses, local mass, and heat transfer comprised in their study. They treated a particular model numerically and, for the accuracy of the results, made comparison with the prevailing literature. They investigated that velocity field increases for stronger magnetic field. Furthermore, significant analysis regarding to the characteristics of the flow behavior in various geometries under multiple flow conditions is perceived in [12–22].

In 2007, Ishak et al. [23] studied Falkner Skan flow through an accelerating wedge with the addition of suction/injection properties. Forced convection magnetohydrodynamic flow over a nonisothermal wedge by prevailing time-dependent viscosity was discussed by Pal et al. [24] in 2009. A magnetonanofluid model by considering the heat generation/absorption and the influence of a convective flow condition was inspected by Rahman et al. [25] in 2012.

Lately, Ullah et al. [26] investigated the non-Newtonian model past a wedge in the existence of imposed Lorentz forces. Ullah et al. [27] inspected the non-Newtonian model past a nonlinearly stretchable sheet by encountering the influences of various physical parameters. Aman et al. [28] studied a nanofluid model composed of gold nanoparticles. They also explored the influences of radiative heat flux and crisscross diffusion on the flow characteristics. Analysis of a ferrofluid composed of cylindrical-shaped nanoparticles was conducted in [29]. Various flow models under certain boundary flow conditions in different channels are investigated in [30–33]. Brinkman sort of a nanofluid model was examined in [34]. A natural convection flow model stretchable sheet was studied by Ullah et al. [35]. A nanofluid model bounded by Riga plates and a second-grade flow model between an oblique channel were studied in [36, 37], respectively. Impacts of the effective Prandtl model and thermal radiation on the Newtonian model between a converging/diverging channel were explored in [38, 39], respectively. For further study regarding nanofluids and regular fluid from different aspects, we can analyze [40–46].

From a careful science literature review, it is pointed that, to date, no one analyzed the energy and mass transportation in MHD wedge flow by prevailing crisscross diffusion gradients. Initially, formulation of the model is carried out, and then, mathematical analysis of the model is performed by means of the RK technique. Section 3 is dedicated to highlight the impacts of varying a nondimensional parameter in the flow characteristics. A fruitful comparison has been made for reliability of the study. In the end, major results of the work are highlighted in the last section.

2. Self-Similar Analysis

Consider the time-independent Newtonian flow past a wedge positioned in the main stream. The fluid is electrically conducting, and the effects of cross diffusion are also under consideration. The main stream velocity of the fluid is $U^*(x)$. The flow is considered in the Cartesian coordinate system, and x and y axis are chosen in such a way that the surface of the wedge is along the $x-$axis, and the $y-$axis makes a right angle with the $x-$axis and perpendicular to the wedge surface. Furthermore, the wedge surface is kept at variable temperature $T_w^*(x)$ and concentration $C_w^*(x)$. The ambient temperature and concentration of the fluid are denoted by T^* and C^*, respectively. Inconstant magnetic field $B^*(x)$ imposed perpendicularly to the wedge with the assumptions of a smaller magnetic Reynolds number and inconsequential induced magnetic field. The schematic theme of the MHD flow model is demonstrated in Figure 1:

In the light of the aforementioned restrictions, a particular flow model can be described in the existence of various physical quantities in the following manner [47]:

$$\frac{\partial u^*}{\partial x^*} + \frac{\partial v^*}{\partial y^*} = 0, \tag{1}$$

$$u^*\frac{\partial u^*}{\partial x^*} + v^*\frac{\partial u^*}{\partial y^*} = U^*(x)\frac{dU^*(x)}{dx^*} + \frac{\mu}{\rho}\left(\frac{\partial^2 u^*}{\partial y^{*2}}\right) + \frac{\sigma}{\rho}B^{*2}(U^*(x) - u^*), \tag{2}$$

$$u^*\frac{\partial T^*}{\partial x^*} + v^*\frac{\partial T^*}{\partial y^*} = \frac{k}{\rho c_p}\left(\frac{\partial^2 T^*}{\partial y^{*2}}\right) + \frac{DK_T}{\rho c_p C_s}\left(\frac{\partial^2 C^*}{\partial y^{*2}}\right), \tag{3}$$

$$u^*\frac{\partial C^*}{\partial x^*} + v^*\frac{\partial C^*}{\partial y^*} = D\left(\frac{\partial^2 C^*}{\partial y^{*2}}\right) + \frac{DK_T}{T_m}\left(\frac{\partial^2 T^*}{\partial y^{*2}}\right). \tag{4}$$

Equation (1) is the dimensional mass conservation law. Momentum, energy, and concentration equations by prevailing magnetic field and thermal and concentration gradients are embedded in equations (2)–(4), respectively. Furthermore, u^*, v^* represent the velocities along x and y coordinates. Moreover, $U^*(x)$ is the main stream velocity, dynamic μ, density ρ, imposed magnetic field B^*, temperature T^*, concentration C^*, heat capacity c_p, mass diffusivity D, mean temperature of the fluid T_m, thermal diffusion K_T, and concentration susceptibility C_s^*.
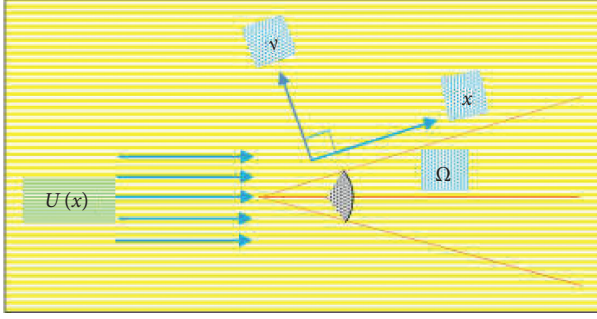
FIGURE 1: Physical configuration.

The feasible set of auxiliary conditions for the current wedge flow is as follows [47]:

$$u^* \uparrow^{y=0} = 0, \ v^* \uparrow^{y=0} = 0, \ T^* \uparrow^{y=0} = T_w^*(x), \ C^* \uparrow^{y=0} = C_w^*, \tag{5}$$

$$\left(u^* \uparrow^{y \to \infty}\right) \longrightarrow U^*(x) = u_0 x^m, \ \left(T^* \uparrow^{y \to \infty}\right) \\ \longrightarrow T_\infty^*, \ \left(C^* \uparrow^{y \to \infty}\right) \longrightarrow C_\infty^*. \tag{6}$$

The governing equations (1)–(4) can be reduced into the dimensionless form by utilizing the following defined nondimensional transformations and stream functions [47]:

$$u = \frac{\partial \psi}{\partial y},$$

$$v = -\frac{\partial \psi}{\partial x},$$

$$\psi = \sqrt{\nu u_0 x^{m+1}} \ F(\eta),$$

$$\eta = \sqrt{\frac{u_0 x^{m+1}}{\nu}} \ y x^{-1}, \tag{7}$$

$$\beta(\eta) = \frac{T^* - T_\infty^*}{T_w^* - T_\infty^*},$$

$$\phi(\eta) = \frac{C^* - C_\infty^*}{C_w^* - C_\infty^*}.$$

Here, B^* shows the applied magnetic field which is a function of x and is in the form $B = B_0 x^{(m-1/2)}$, where B_0 denotes the uniform magnetic field (for precedence, we can see [48, 49]), $U^*(x)$ denotes the free stream velocity and described in function of x, and is $U^*(x) = (u_0/x^{-m})$, in which u_0 is an invariable quantity and m ($0 \le m \le 1$) describes the Falkner Skan power law parameter. The expression $\beta = \beta(2 - \beta)^{-1}$, in which $\beta = (\Omega/\pi)$ describes the Hartree pressure gradient. Furthermore, $\beta = 0$ and $\beta = 1$ describe the cases along the x and y coordinates, respectively.

The following self-similar model is attained from the dimensional system after incorporating the feasible similarity variables which comprised the influences of cross diffusion and magnetic:

$$F''' - \left[mF'^2 - \left(\frac{m+1}{2}\right)FF' - m\right] + M^2(1 - F\prime) = 0, \tag{8}$$

$$\beta'' + \frac{\Pr(m+1)}{2} F\beta\prime + \Pr D_f \ \phi'' = 0, \tag{9}$$

$$\phi'' + \frac{Sc(m+1)}{2} F\phi\prime + SrSc\beta'' = 0. \tag{10}$$

The corresponding feasible boundary conditions are in the following manner:

$$\begin{aligned} F\left(\eta \uparrow^{\eta=0}\right) &= 0, \\ F'\left(\eta \uparrow^{\eta=0}\right) &= 0, \\ \beta\left(\eta \uparrow^{\eta=0}\right) &= 1, \\ \phi\left(\eta \uparrow^{\eta=0}\right) &= 1, \end{aligned} \tag{11}$$

$$\begin{aligned} F\prime\left(\eta \uparrow^{\eta \to \infty}\right) &\longrightarrow 1, \\ \beta\left(\eta \uparrow^{\eta \to \infty}\right) &\longrightarrow 0, \\ \phi\left(\eta \uparrow^{\eta \to \infty}\right) &\longrightarrow 0. \end{aligned} \tag{12}$$

In equations (8)–(10), with nonhomogeneous auxiliary conditions described in equations (11) and (12), self-similar quantities are the Hartmann number $(M = \sigma B_0^2/\rho u_0)$, Prandtl number $(\Pr = (\nu \rho C_p/k))$, Dufour number $(D_f = (Dk_T(C_w^* - C_\infty^*)/C_s C_p \nu(T_w^* - T_\infty^*)))$, Soret number $(Sr = (D_m k_T(T_w^* - T_\infty^*)/\nu T_m(C_w^* - C_\infty^*)))$, and Schmidt number $(Sc = (\nu/D))$.

The following are the formulas to estimate the shear stresses, local Nusselt (Nu_x), and Sherwood numbers Sh_x [47]:

$$C_F = \frac{\mu}{\rho U^2(x)} \left(\frac{\partial u^*}{\partial y^*}\right) \uparrow^{y=0}, \tag{13}$$

$$Nu_x = \left[\frac{kx}{k(T_w - T_\infty)}\right] \left(\frac{\partial T^*}{\partial y^*}\right) \uparrow^{y=0}, \tag{14}$$

$$Sh_x = \left[\frac{x}{C_w - C_\infty}\right] \left(\frac{\partial C^*}{\partial y^*}\right) \uparrow^{y=0}. \tag{15}$$

Hence, the nondimensional form for shear stress, local heat, and mass transfer is defined as follows:

$$\begin{aligned} C_F \sqrt{Re_x} &= F'(0), \\ Nu_x(Re_x)^{-(1/2)} &= -\beta\prime(0), \\ Sh(Re_x)^{-(1/2)} &= -\phi\prime(0), \end{aligned} \tag{16}$$

where $Re_x = (xU^*(x)/\nu)$ describes the local Reynolds number.

3. Mathematical Treatment

Usually, closed form solutions are very rare or not even exist for those models which are coupled and attain high non-linearity. It is better to tackle such sort of models either

numerically of asymptotically. A particular model is coupled and nonlinear in nature. Therefore, we adopted a numerical method called the Runge–Kutta method [50]. To initiate the technique, feasible substitutions are as follows:

$$
\begin{aligned}
y_1 &= F, \\
y_2 &= F\prime, \\
y_3 &= F\prime', \\
y_4 &= \beta, \\
y_5 &= \beta\prime, \\
y_6 &= \phi, \\
y_7 &= \phi\prime.
\end{aligned}
\tag{17}
$$

Then, the system of equations (8)–(10) is transformed into the following pattern:

$$
F''' = \left[mF'^2 - \frac{(m+1)}{2} FF'' - m \right] + M^2 (1 - F\prime), \tag{18}
$$

$$
\beta\prime' = -\frac{\Pr(m+1)}{2} F\beta\prime - \Pr D_f \, \phi\prime', \tag{19}
$$

$$
\phi\prime' = -\frac{Sc(m+1)}{2} F\phi\prime - SrSc\beta\prime'. \tag{20}
$$

By entreating the substitutions in equations (18)–(20), the following system is obtained:

$$
[y_1' \, y_2' \, y_3' \, y_4' \, y_5' \, y_6' \, y_7'] =
\begin{bmatrix}
y_2 \\[1mm]
y_3 \\[1mm]
\left[my_2^2 - \dfrac{m+1}{2} y_1 y_3 - m \right] + M^2 (1 - y_2) \\[1mm]
y_5 \\[1mm]
-\dfrac{\Pr(m+1)}{2} y_1 y_5 - \Pr D_f \, y_7' \\[1mm]
y_7 \\[1mm]
-\dfrac{Sc(m+1)}{2} y_1 y_7 - SrSc \, y_5'
\end{bmatrix}.
\tag{21}
$$

Consequently, supporting initial conditions are

$$
\begin{bmatrix}
y_1 \\
y_2 \\
y_3 \\
y_4 \\
y_5 \\
y_6 \\
y_7
\end{bmatrix}
=
\begin{bmatrix}
0 \\
0 \\
n_1 \\
1 \\
n_2 \\
1 \\
n_3
\end{bmatrix}.
\tag{22}
$$

After this, we performed the numerical calculation and obtained the tabulated results for the model. Table 1 presents the solutions for velocity, temperature, and concentration fields over the domain of interest.

4. Graphical Results and Discussion

The impacts of ingrained self-similar quantities on the momentum, temperature, and mass of the fluid are incorporated in this section. These physical quantities are M, $\Pr$,

D_f, Sr, and Sc. The impacts of the magnetic field and thermal and concentration gradients are also under consideration. It is very important to mention that, in the current nonlinear flow model, if $m = 1/2$, then it represents the wedge flow. If $m = 0$ and $m = 1$, it represents the flow of the horizontal plate and stagnation point flow, respectively. For an example, we can refer [47].

The flow behavior against an imposed magnetic field is given in Figure 2. It is explored that, against a stronger magnetic field, fluid motion increases. For horizontal plate flow, the velocity $F\prime(\eta)$ rises promptly comparative to the stagnation and wedge flow case. Physically, over a horizontal surface, the fluid particles move freely due to which the velocity upturns. Near the surface, these alterations are almost inconsequential. The physical reason behind this behavior is the force of friction between the surface and fluid layer adjacent to the surface. Due to the force of friction, the motion of fluid particles near the surface declines and rest of the fluid layer flow abruptly. Furthermore, for wedge and stagnation cases, increment in the velocity is observed quite slowly. Figure 2(b) presents a 3D image of the velocity against multiple values of M.

TABLE 1: Solutions for the velocity, temperature, and concentration.

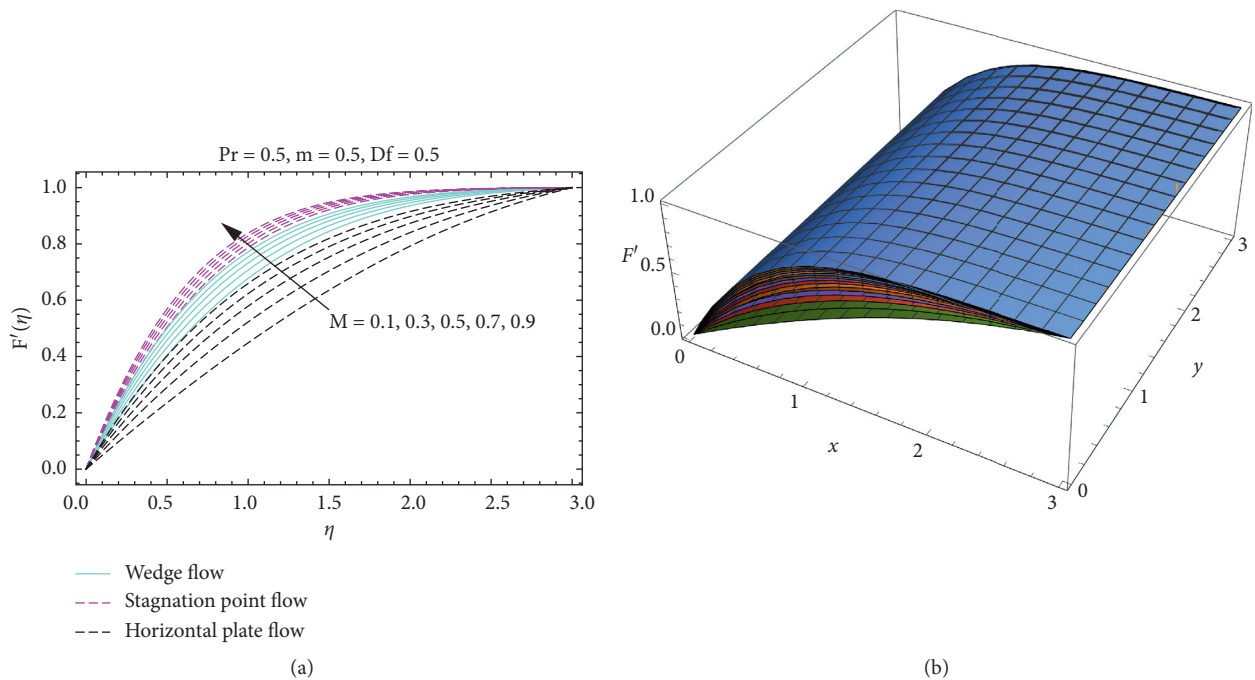| η	$F\prime(\eta)$	$\beta(\eta)$	$\phi(\eta)$
0.0	8.13152×10^{-20}	1.000000	1.000000
0.5	0.414545	0.855180	0.855180
1.0	0.680884	0.711965	0.711965
1.5	0.840408	0.573753	0.573753
2.0	0.927690	0.444814	0.444814
2.5	0.970631	0.329171	0.329171
3.0	0.989406	0.229747	0.229747
3.5	0.996641	0.147918	0.147918
4.0	0.999085	0.083486	0.083486
4.5	0.999809	0.034958	0.034958
5.0	1.000000	2.306680×10^{-9}	2.306680×10^{-9}

FIGURE 2: Influence of the magnetic number M on the velocity distribution $F'(\eta)$. (a) Two-dimensional; (b) 3D view.

The behavior of thermal performance $\beta(\eta)$ against Prandtl and Dufour parameters are given in Figures 3(a) and 3(b), respectively. The declines in $\beta(\eta)$ are noticed against stringer Prandtl values. For the stagnation point, these alterations are prompt, and maximum declines are perceived in the region $2 \le \eta \le 6$. The temperature $\beta(\eta)$ is against the horizontal plate flow case. Physically, the fluid flows abruptly over the horizontal surface due to which the collision between the particles increases; consequently, the temperature drops slowly. The significant increasing variations in $\beta(\eta)$ are pointed against Dufour effects. Due to the Dufour number, the temperature $\beta(\eta)$ upturns. However, maximum increment in the temperature is pointed against horizontal plate flow. Figures 4(a) and 4(b) show the 3D image of $\beta(\eta)$ against Prandtl and Dufour parameters, respectively.

The mass transfer for multiple values of Schmidt and Soret parameters is given in Figures 5(a) and 5(b), respectively. It is perceived that the mass transfer $\phi(\eta)$ is in inverse proportion to the Schmidt number. Due to higher Schmidt effects, less mass transfer at the surface is noted. However, maximum decrement is pointed against the stagnation point case. Near the surface, an almost inconsequential behavior of $\phi(\eta)$ is noted for wedge, stagnation, and horizontal flat plate cases. The Soret number which appears due to cross-diffusion gradients favor the mass transfer $\phi(\eta)$. The mass transfer profile rises against stronger Soret effects. For a horizontal plate, maximum alterations in the mass transfer trends are detected comparative to wedge and stagnation cases. The 3D behavior of the fluid concentration is shown against Sc and Sr in Figures 6(a) and 6(b), respectively.

The behavior of shear stress against the magnetic field and m is shown in Figures 7(a) and 7(b), respectively. It is pointed out that the shear stresses upturn against both the parameters. Due to stronger Hartmann effects, the fluid motion reduces; consequently, the shear stresses increase.

The local thermal performance and mass transfer rate against multiple parameters are shown in Figures 8 and 9, respectively. From inspection of the plotted results, it is
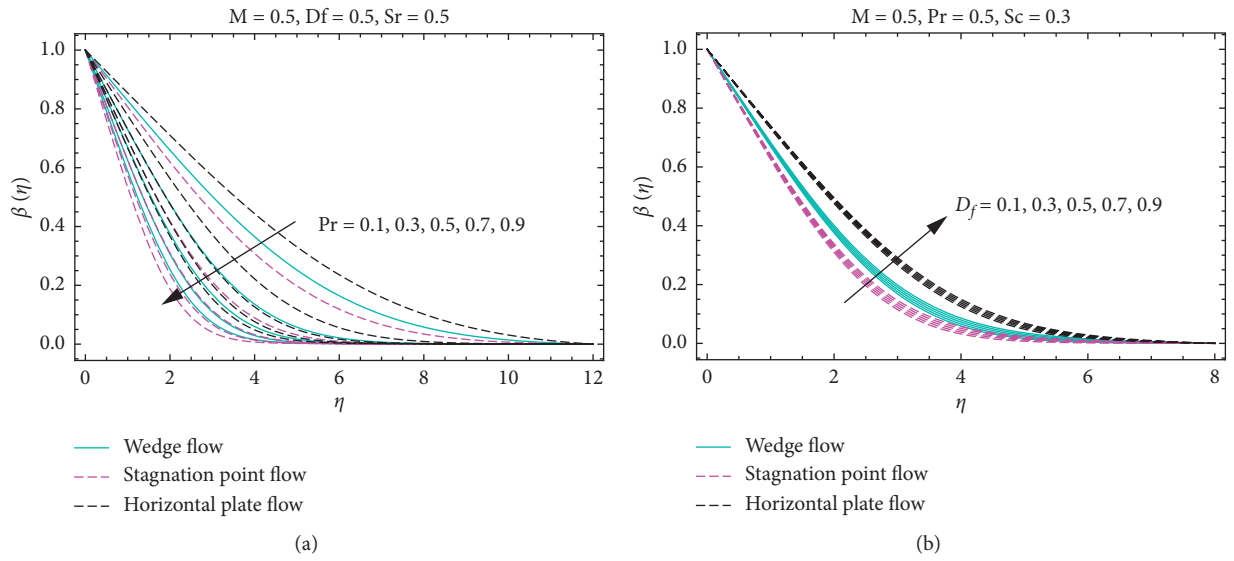
M = 0.5, Df = 0.5, Sr = 0.5

Pr = 0.1, 0.3, 0.5, 0.7, 0.9

Wedge flow
Stagnation point flow
Horizontal plate flow

(a)

M = 0.5, Pr = 0.5, Sc = 0.3

D_f = 0.1, 0.3, 0.5, 0.7, 0.9

Wedge flow
Stagnation point flow
Horizontal plate flow

(b)

FIGURE 3: Stimulus of the (a) Prandtl number Pr and (b) Dufour number D_f on $\beta(\eta)$.

(a)

(b)
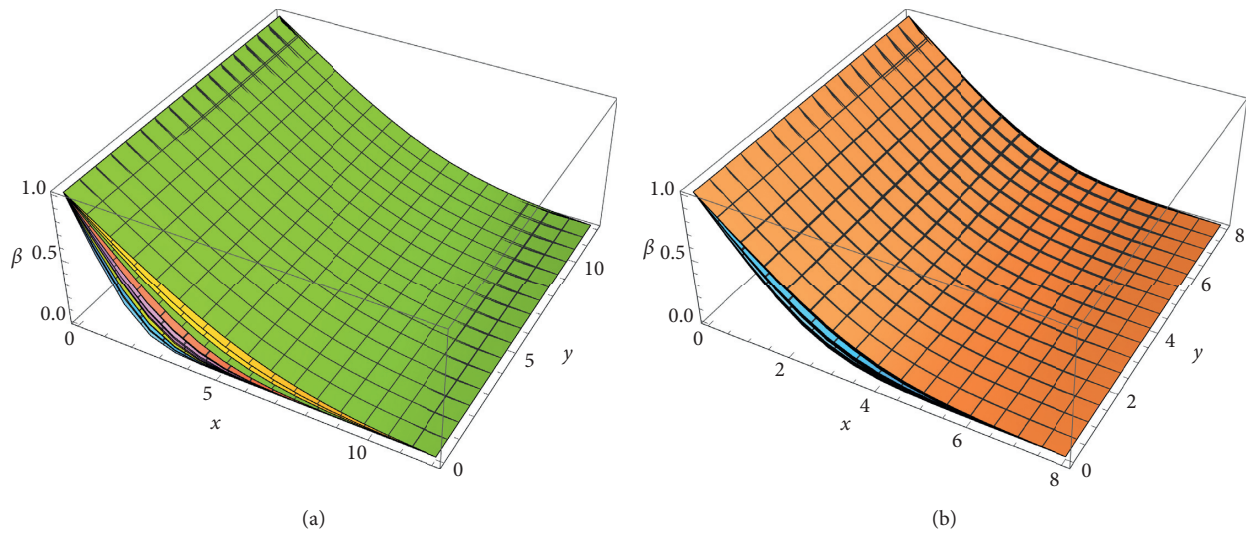
FIGURE 4: 3D Plot for temperature distribution $\beta(\eta)$ against the (a) Prandtl number Pr and (b) Dufour number D_f.

M = 0.5, Sr = 0.5, Pr = 0.5, D_f = 0.3

Sc = 0.1, 0.3, 0.5, 0.7, 0.9

Wedge flow
Stagnation point flow
Horizontal plate flow

(a)

M = 0.5, Sc = 0.5, Pr = 0.5, D_f = 0.5

Sr = 0.1, 0.3, 0.5, 0.7, 0.9

Wedge flow
Stagnation point flow
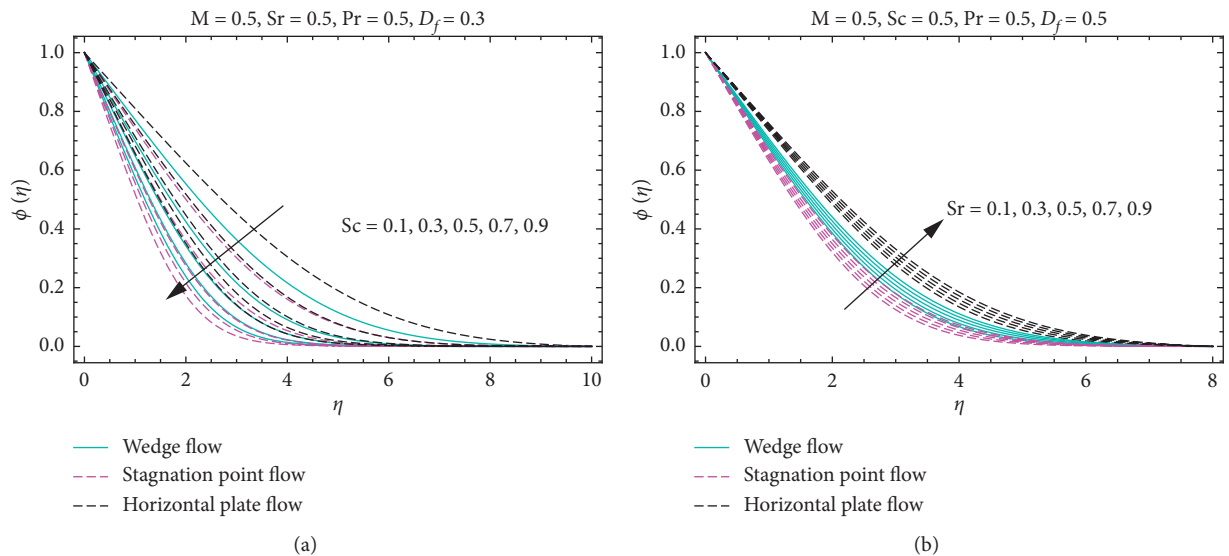Horizontal plate flow

(b)

FIGURE 5: Stimulus of the (a) Schmidt number Sc and (b) Soret number Sr on $\beta(\eta)$.
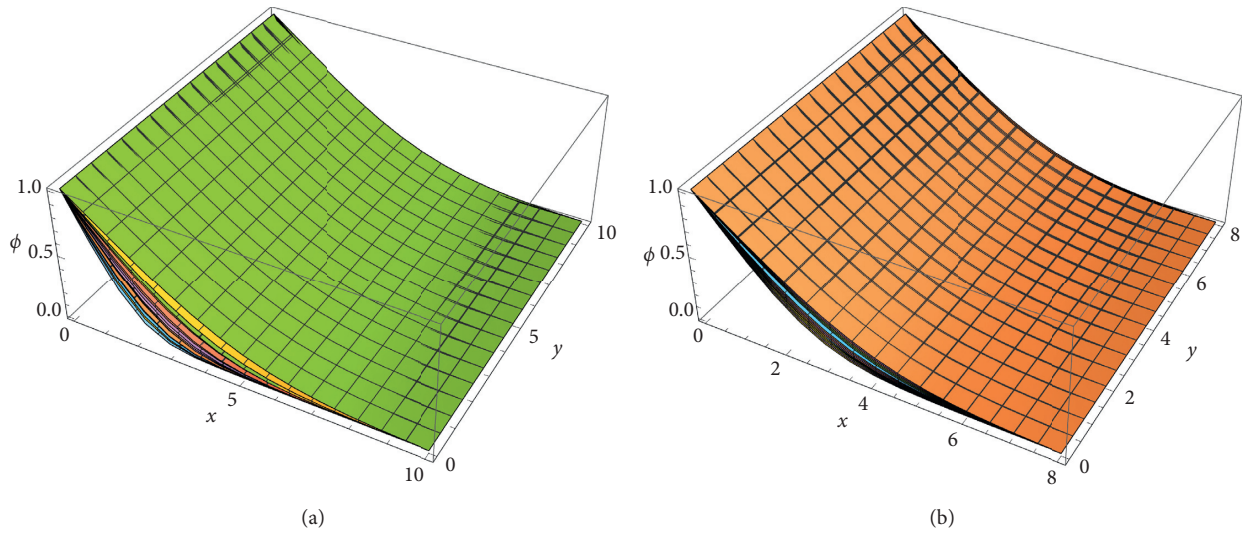
FIGURE 6: 3D Plot for mass distribution $\phi(\eta)$ against the (a) Schmidt number Sc and (b) Soret number Sr.
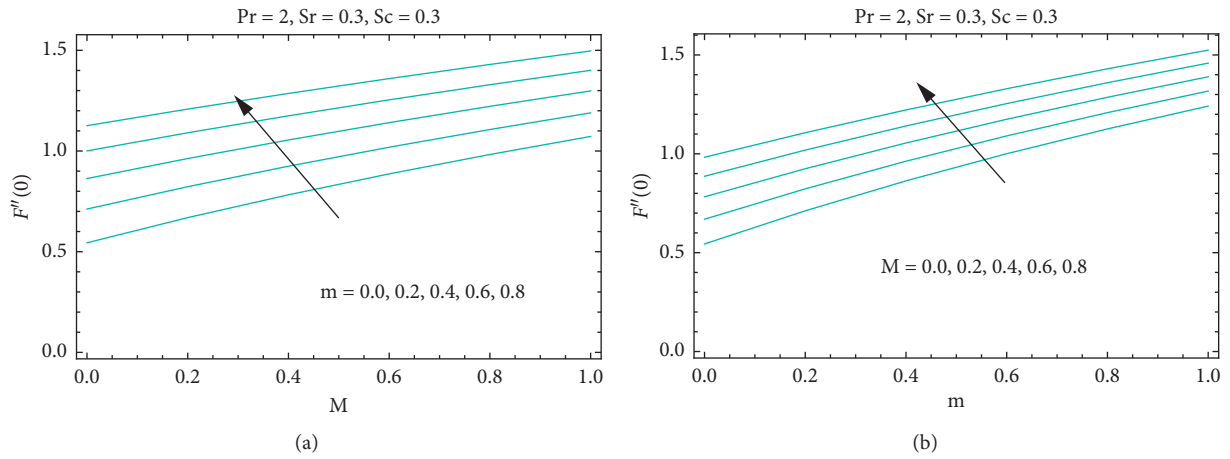

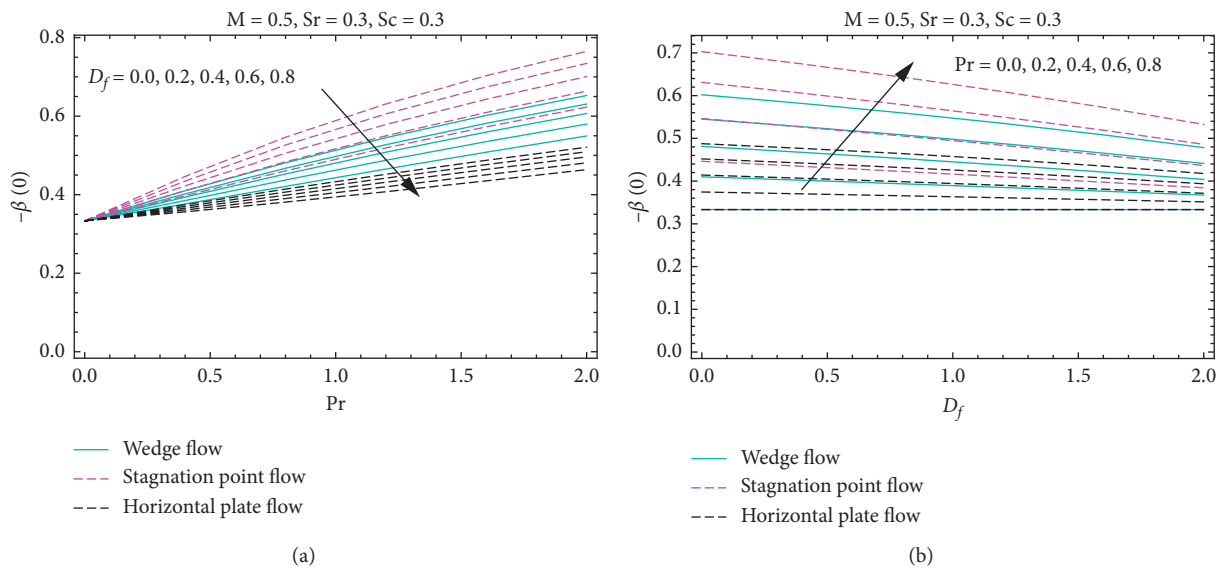FIGURE 7: Stimulus of (a) m and (b) the Hartmann number M on $F''(0)$.

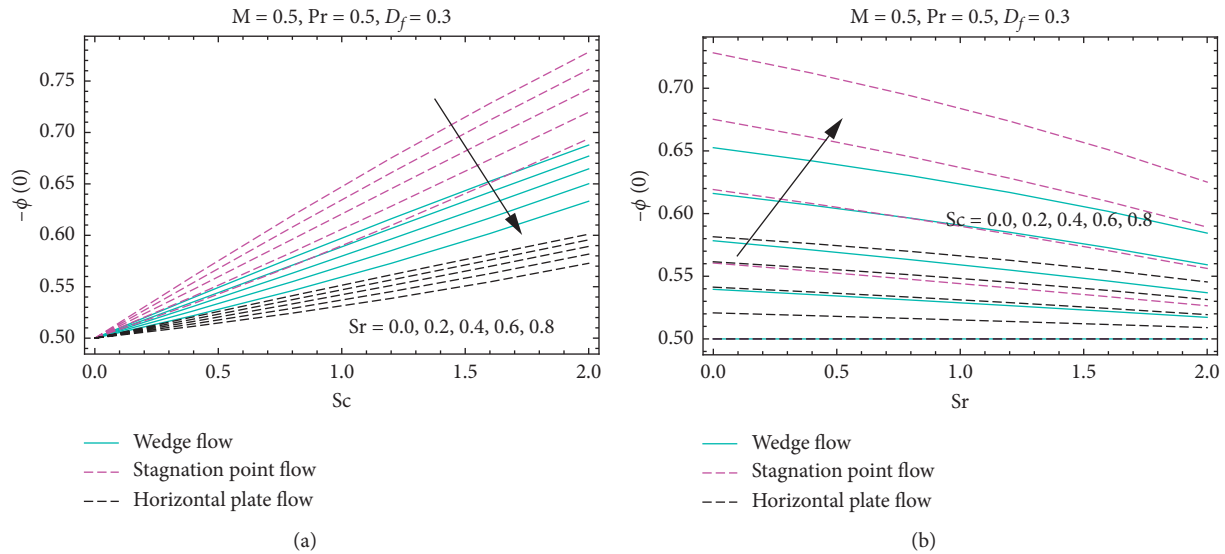FIGURE 8: Stimulus of the (a) Dufour number D_f and (b) Prandtl number Pr on $-\beta\prime(0)$.

FIGURE 9: Stimulus of the (a) Soret number Sr and (b) Schmidt number Sc on $\phi\prime(\eta)$.

TABLE 2: Comparison table for $F\prime(0)$.

M	Present	[51]	[47]
0	1.2328156765127756	1.232588	1.2325965196
0.2	1.248782822222880	1.248572	—
0.4	1.2955356976948873	1.295368	—
0.6	1.3700007639450016	1.369884	—
0.8	1.4680482127033443	1.467974	—
1.0	1.5853710319305012	1.585331	1.5852800424

noticed that the local thermal performance declines against the Dufour number. For the stagnation case, a drop in the local heat transfer rate is slow comparative to wedge and horizontal plate cases. On the other hand, viscous dissipative effects favor the local thermal performance rate. It is pointed out that, against more dissipative fluid, the local heat transfer rate increases. The mass transfer rate against Soret and Schmidt parameters is accessed in Figures 9(a) and 9(b), respectively. It is examined that the mass transfer rate enhances due to a stronger Schmidt number, and inverse variations are perceived against the Soret number.

Table 2 shows the comparative study against restricted flow parameters. The value of m is fixed at one and the computation is carried out. From the inspection of Table 2, it is perceived that the presented results and adopted technique are reliable and acceptable.

5. Conclusions

The presented work encountered MHD flow over a wedge. The stimuli of cross diffusion are taken under consideration. The model is effectively treated by using a numeric technique called the RK technique. The impacts of ingrained quantities on the flow behavior are presented, and lastly, the following key findings are noted:

(i) The fluid velocity $F\prime(\eta)$ is accelerating for increasing M, and in the case of stagnation point flow, these variations are rapid

(ii) The Dufour parameter favors the temperature $\beta(\eta)$, whereas the Prandtl number is against the fluid temperature

(iii) increasing Schmidt number leads to a decrease in the concentration of the fluid, and for a varying Soret number, these variations are reverse

(iv) Less heat and mass transfer are investigated for Dufour and Soret parameters

(v) More heat and mass transfer are noted for Prandtl and Schmidt parameters in the wedge, stagnation point, and horizontal plate flows

Data Availability

No data were used in the manuscript.

Conflicts of Interest

The authors declare that they have no conflicts of interest.

Acknowledgments

References

[1] V. M. Falkner and S. W. Skan, "Some approximate solutions of the boundary layer equations," *Philosophical Magazine*, vol. 12, pp. 865–896, 1931.

[2] D. R. Hartree, "On an equation occurring in Falkner and skan's approximate treatment of the equations of the

boundary layer," *Mathematical Proceedings of the Cambridge Philosophical Society*, vol. 33, no. 2, pp. 223–239, 1937.

[3] J. C. Y. Koh and J. P. Hartnett, "Skin friction and heat transfer for incompressible laminar flow over porous wedges with suction and variable wall temperature," *International Journal of Heat and Mass Transfer*, vol. 2, no. 3, pp. 185–198, 1961.

[4] H.-T. Lin and L.-K. Lin, "Similarity solutions for laminar forced convection heat transfer from wedges to fluids of any Prandtl number," *International Journal of Heat and Mass Transfer*, vol. 30, no. 6, pp. 1111–1118, 1987.

[5] A. Hussanan, Z. Ismail, I. Khan, A. G. Hussein, and S. Shafie, "Unsteady boundary layer MHD free convection flow in a porous medium with constant mass diffusion and newtonian heating," *European Physical Journal Plus*, vol. 129, no. 46, 2014.

[6] R. Kandasamy, W. Abd, and A. B. Khamis, "Effects of chemical reaction, heat and mass transfer on boundary layer flow over a porous wedge with heat radiation in the presence of suction or injection," *Theoretical and Applied Mechanics*, vol. 33, no. 2, pp. 123–148, 2006.

[7] P. L. Chambre and A. Acrivos, "Difiusion of a chemically reactive species in a laminar boundary layer flow," *Indian Engineering Chemical*, vol. 49, 1957.

[8] N. A. Yacob, A. Ishak, and I. Pop, "Falkner-Skan problem for a static or moving wedge in nanoluids," *International Journal of Thermal Sciences*, vol. 50, 2011.

[9] A. Hussanan, M. I. Anwar, F. Ali, I. Khan, and S. Shafie, "Natural convection flow past an oscillating plate with Newtonian heating," *Heat Transfer Research*, vol. 45, no. 2, pp. 119–135, 2014.

[10] X. Su and L. Xiaohong, "Hall effect on MHD flow and heat transfer of nanofluids over a stretching wedge in the presence of velocity slip and Joule heating," *Central European Journal of Physics*, vol. 11, no. 12, pp. 1694–1703, 2013.

[11] U. Khan, N. Ahmed, and S. T. Mohyud-Din, *Influence of Viscous Dissipation and Joule Heating on MHD Bio-Convection flow over a Porous Wedge in the Presence of Nanoparticles and Gyrotactic Microorganisms*, Springer, Berlin, Germany, 2016.

[12] M. K. Nayak, J. Prakash, D. Tripathi, V. S. Pandey, S. Shaw, and O. D. Makinde, "3D Bioconvective multiple slip flow of chemically reactive Casson nanofluid with gyrotactic microorganisms," *Heat Transfer*, vol. 49, no. 1, pp. 135–153, 2019.

[13] M. K. Nayak, J. Prakash, D. Tripathi, and V. S. Pandey, "3D radiative convective flow of ZnO-SAE50nano-lubricant in presence of varying magnetic field and heterogeneous reactions," *Propulsion and Power Research*, vol. 8, no. 4, pp. 339–350, 2019.

[14] M. K. Nayak, N. S. Akbar, D. Tripathi, and V. S. Pandey, "Three dimensional MHD flow of nanofluid over an exponential porous stretching sheet with convective boundary conditions," *Thermal Science and Engineering Progress*, vol. 3, pp. 133–140, 2017.

[15] M. K. Nayak, N. S. Akbar, D. Tripathi, Z. H. Khan, and V. S. Pandey, "MHD 3D free convective flow of nanofluid over an exponentially stretching sheet with chemical reaction," *Advanced Powder Technology*, vol. 28, no. 9, pp. 2159–2166, 2017.

[16] M. K. Nayak, N. S. Akbar, V. S. Pandey, Z. H. Khan, and D. Tripathi, "3d free convective mhd flow of nanofluid over permeable linear stretching sheet with thermal radiation," *Powder Technology*, vol. 315, pp. 205–215, 2017.

[17] A. Shahid, Z. Zhou, M. M. Bhatti, and D. Tripathi, "Magnetohydrodynamics nanofluid flow containing gyrotactic microorganisms propagating over a stretching surface by successive taylor series linearization method," *Microgravity-Science and Technology*, vol. 30, pp. 445–455, 2018.

[18] N. S. Akbar, D. Tripathi, and Z. H. Khan, "Numerical simulation of nanoparticles with variable viscosity over a stretching sheet," in *Numerical Simulations in Engineering and Science*, IntechOpen, London, UK, 2018.

[19] N. S. Akbar, D. Tripathi, and Z. H. Khan, "Numerical investigation of Cattanneo-Christov heat flux in CNT suspended nanofluid flow over a stretching porous surface with suction and injection," *Discrete & Continuous Dynamical Systems*, vol. 11, no. 4, pp. 583–594, 2018.

[20] N. S. Akbar, D. Tripathi, Z. H. Khan, and O. A. Bég, "A numerical study of magnetohydrodynamic transport of nanofluids over a vertical stretching sheet with exponential temperature-dependent viscosity and buoyancy effects," *Chemical Physics Letters*, vol. 661, pp. 20–30, 2016.

[21] M. Turkyilmazoglu, "Extending the traditional Jeffery-Hamel flow to stretchable convergent/divergent channels," *Computers & Fluids*, vol. 100, pp. 196–203, 2014.

[22] M. Turkyilmazoglu, "Slip flow and heat transfer over a specific wedge: an exactly solvable falkner-skan equation," *Journal of Engineering Mathematics*, vol. 92, no. 1, pp. 73–81, 2015.

[23] A. Ishak, R. Nazar, and I. Pop, "Falkner-Skan equation for flow past a moving wedge with suction or injection," *Journal of Applied Mathematics and Computing*, vol. 25, no. 1-2, pp. 67–83, 2007.

[24] D. Pal and H. Mondal, "Influence of temperature-dependent viscosity and thermal radiation on MHD forced convection over a non-isothermal wedge," *Applied Mathematics and Computation*, vol. 212, no. 1, pp. 194–208, 2009.

[25] M. M. Rahman, M. A. Al-Lawatia, I. A. Eltayeb, and N. Al-Salti, "Hydromagnetic slip flow of water based nanofluids past a wedge with convective surface in the presence of heat generation (or) absorption," *International Journal of Thermal Sciences*, vol. 57, pp. 172–182, 2012.

[26] I. Ullah, I. Khan, and S. Shafie, "Hydromagnetic Falkner-Skan flow of Casson fluid past a moving wedge with heat transfer," *Alexandria Engineering Journal*, vol. 55, no. 3, pp. 2139–2148, 2016.

[27] I. Ullah, K. Bhattacharyya, S. Shafie, and I. Khan, "Unsteady MHD mixed convection slip flow of casson fluid over nonlinearly stretching sheet embedded in a porous medium with chemical reaction, thermal radiation, heat generation/absorption and convective boundary conditions," *PLoS ONE*, vol. 10, no. 11, 2016.

[28] S. Aman, I. Khan, Z. Ismail, and M. Z. Salleh, "Impacts of gold nanoparticles on MHD mixed convection Poiseuille flow of nanofluid passing through a porous medium in the presence of thermal radiation, thermal diffusion and chemical reaction," *Neural Computing & Applications*, vol. 30, no. 3, pp. 789–797, 2016.

[29] A. Khalid, I. Khan, and S. Shafie, "Heat transfer in ferrofluid with cylindrical shape nanoparticles past a vertical plate with ramped wall temperature embedded in a porous medium," *Journal of Molecular Liquids*, vol. 221, pp. 1175–1183, 2016.

[30] A. Gul, I. Khan, and S. Shafie, "Energy transfer in mixed convection MHD flow of nanofluid containing different shapes of nanoparticles in a channel filled with saturated porous medium," *Nanoscale Research Letters*, vol. 10, 2015.

[31] I. Ullah, S. Shafie, and I. Khan, "Effects of slip condition and Newtonian heating on MHD flow of Casson fluid over a nonlinearly stretching sheet saturated in a porous medium,"

Journal of King Saud University, vol. 29, no. 2, pp. 250–259, 2016.

[32] A. Gul, I. Khan, S. Shafie, A. Khalid, and A. Khan, "Heat transfer in MHD mixed convection flow of a ferrofluid along a vertical channel," *PLOS One*, vol. 11, no. 10, pp. 1–14, 2015.

[33] M. Zin, N. Athirah, I. Khan, and S. Shafie, "The impact silver nanoparticles on MHD free convection flow of Jeffery fluid over an oscillating vertical plate embedded in a porous medium," *Journal of Molecular Liquids*, vol. 222, pp. 138–150, 2016.

[34] F. Ali, M. Gohar, and I. Khan, "MHD flow of water-based Brinkman type nanofluid over a vertical plate embedded in a porous medium with variable surface velocity, temperature and concentration," *Journal of Molecular Liquids*, vol. 223, pp. 412–419, 2016.

[35] I. Ullah, I. Khan, and S. Shafie, "MHD natural convection flow of casson nanofluid over nonlinearly stretching sheet through porous medium with chemical reaction and thermal radiation," *Nanoscale Research Letters*, vol. 11, p. 527, 2016.

[36] U. Khan, N. Ahmed, and S. T. Mohyud-Din, "Influence of thermal radiation and viscous dissipation on squeezed flow of water between Riga plates saturated with carbon nanotubes," *Colloids and Surfaces A: Physicochemical and Engineering Aspects*, vol. 522, pp. 389–398, 2017.

[37] U. Adnan, U. Khan, N. Ahmed, and S. T. Mohyud-Din, "Thermo-diffusion and diffusion-thermo effects on flow of second grade fluid between two inclined plane walls," *Journal of Molecular Liquids*, vol. 224, pp. 1074–1082, 2016.

[38] N. Ahmed, U. Khan, and S. T. Mohyud-Din, "Influence of an effective Prandtl number model on squeezed flow of γAl_2O_3-H_2O and γAl_2O_3-$C_2H_6O_2$ nanofluids," *Journal of Molecular Liquids*, vol. 238, pp. 447–454, 2017.

[39] M. Adnan, M. Asadullah, U. Khan, N. Ahmed, and S. T. Mohyud-Din, "Analytical and numerical investigation of thermal radiation effects on flow of viscous incompressible fluid with stretchable convergent/divergent channels," *Journal of Molecular Liquids*, vol. 224, pp. 768–775, 2016.

[40] M. Sheikholeslami and S. A. Shehzad, "Magnetohydrodynamic nanofluid convection in a porous enclosure considering heat flux boundary condition," *International Journal of Heat and Mass Transfer*, vol. 106, pp. 1261–1269, 2017.

[41] M. Sheikholeslami, T. Hayat, and A. Alsaedi, "Numerical study for external magnetic source influence on water based nanofluid convective heat transfer," *International Journal of Heat and Mass Transfer*, vol. 106, pp. 745–755, 2017.

[42] M. Sheikholeslami, "CuO-water nanofluid free convection in a porous cavity considering Darcy law," *The European Physical Journal Plus*, vol. 132, 2017.

[43] M. Sheikholeslami and K. Vajravelu, "Nanofluid flow and heat transfer in a cavity with variable magnetic field," *Applied Mathematics and Computation*, vol. 298, pp. 272–282, 2017.

[44] B. B. Mohsin, N. Ahmed, Adnan, U. Khan, and S. T. Mohyud-Din, "A Bioconvection model for squeezing flow of nanofluid between parallel plates in the presence gyrotactic microorganisms," *European Physical Journal Plus*, vol. 132, 2017.

[45] U. Khan, N. Ahmed, and S. T. Mohyud-Din, "Influence of viscous dissipation on copper oxide nanofluid in an oblique channel: implementation of KKL model," *The European Physical Journal Plus*, vol. 132, 2017.

[46] N. Ahmed, Adnan, U. Khan, S. T. Mohyud-Din, and A. Waheed, "Shape effects of nanoparticles on Squeezed flow between two Riga Plates in the presence of thermal radiation," *The European Physical Journal Plus*, 2017.

[47] D. Srinivasacharya, U. Mendu, and K. Venumadhav, "MHD boundary layer flow of a nanofluid past a wedge," *Procedia Engineering*, vol. 127, pp. 1064–1070, 2015.

[48] M. H. Cobble, "Magneto fluid dynamic flow with a pressure gradient and fluid injection," *Journal of Engineering*, vol. 11, no. 2, pp. 49–56, 1977.

[49] Z. Zhang and J. Wang, "Exact self-similar solutions of the magnetohydrodynamic boundary layer system for power-law fluids," *Zeitschrift für angewandte Mathematik und Physik*, vol. 58, no. 5, pp. 805–817, 2007.

[50] U. Khan, N. Ahmed, and S. T. Mohyud-Din, "Numerical investigation for three dimensional squeezing flow of nanofluid in a rotating channel with lower stretching wall suspended by carbon nanotubes," *Applied Thermal Engineering*, vol. 113, pp. 1107–1117, 2017.

[51] P. D. Ariel, "Hiemenz flow in hydromagnetics," *Acta Mechanica*, vol. 103, no. 1-4, pp. 31–43, 1994.